A study of alteration processes in bentonite

Macarena Leal Olloqui

A thesis submitted to the University of Bristol in accordance with the requirements for award of the degree of Doctor of Philosophy at the

Interface Analysis Centre, Faculty of Science

September 2019

72,808 words

Declaration of authorship

I declare that the work in this dissertation was carried out in accordance with the requirements of the University's Regulations and Code of Practice for Research Degree Programmes and that it has not been submitted for any other academic award. Except where indicated by specific reference in the text, the work is the candidate's own work. Work done in collaboration with, or with the assistance of, others, is indicated as such. Any views expressed in the dissertation are those of the author.

Signed: ……

Date: ……

“It is on a day like this one, a little later, a little earlier, that you discover, without surprise, that something is wrong, that, without mincing words, you don't know how to live, that you will never know”

Georges Perec, A man asleep

To my parents and siblings, who are my inspiration.

Abstract

At the present time, the solution considered as the most favourable and sustainable by the international community for the last stage of higher activity waste (HAW) management, whether consisting of irradiated fuel elements or vitrified radioactive waste, is storage at great depths, in underground facilities, within stable geological formations. This solution involves isolating the HAW from the biosphere by means of interposing a series of natural and engineered barriers, in the storage facilities at depths ranging between 200-1000m (UK). HAW is first embedded into extremely durable, corrosion-resistant containers. These are then arranged in galleries in stable geological formations surrounded by a buffer material, characterised by low permeability and high retention capacity. The isolation and confinement of HAW are therefore provided by the container, the buffer material and the natural barrier or host rock.

Bentonite is internationally considered as the most suitable buffer and backfill material. Nonetheless, for bentonite to accomplish the safety functions for which it has been selected, as a buffer and backfill material, it has to preserve its physicochemical characteristics over the expected timescales of a geological disposal facility. Under geological disposal conditions, the unpreventable corrosion of the containers, thermal gradients and mineral content of groundwaters will give rise to a highly-dynamic environment at the contact interface between the bentonite and containers. As a result, interactions between the clayey matrix and the released by-products of corrosion are expected to occur, inducing bentonite evolution via alteration and/or transformation into new mineral phases that may compromise the functionality of the buffer.

This research focuses on the physicochemical evaluation of different highly-compacted bentonite samples retrieved from the contact interface between bentonite and a simulated container. This research investigated the mineralogical evolution of the bentonite barrier to evaluate the presence of neoformed mineral phases, possibly arising from interactions between bentonite and corrosion by-products, and considering thermo-hydro-chemical-mechanical factors. A detailed characterisation of the samples was performed, and the results were used to assess the degree of alteration experienced by bentonite after 18 and 6.5 years, and 61, 122, 183 and 211 days of simulated experimental exposure respectively. This work has highlighted the key factors that could have altered the geotechnical barrier functionality after a relatively long-term exposure, as well as a short-term exposure to simulated geological conditions. This research has also highlighted the need to investigate the impact of a fully-reduced environment, as expected during mid-life of a repository, since a fully-reduced environment could accelerate clay alteration and/or transformation, potentially inducing the alteration of 2:1 phyllosilicates (smectite group) into 1:1 phyllosilicates (kaolinite-serpentine group) or Fe-rich smectites, which eventually will lead to a complete loss of the swelling capacity of bentonite and, therefore, its self-healing ability.

Acknowledgements

I would like to express my gratitude to many people that have helped my during this journey, without whom this thesis could not have been possible. First, I would like to thank **Professor Thomas Scott** for giving me the opportunity to do this Ph.D.

At the IAC, I would like to thank **Dr Keith Hallam** for his constant advice, his company at late hours in the tower and grammatical disagreements. To **John Nicholson** for his advices on any step in the experimental work presented in this thesis. I also very much appreciate the advice and constant help of **Dr Hugo Dominguez Andrade**.

I would also like to thank **Gareth Griffiths**, **Haris Paraskevoulakos**, **Jacek Wasik**, **Ian Ang**, **Chong Lui**, **Siqi He**, **Ilemona Okeme**, **Antonis Banos**, **Jolene Cook**, **Erin Holland** and **Dean Connor** for being such great colleagues in and out of the university, although I have never been officially invited to play badminton. Ah! Especially thanks to Gareth Griffiths for listening to my complaints.

Outside of University of Bristol, I would like to offer the greatest thanks to **Begoña de la Fuente Miranda**, **Anna López Mesa**, **Miriam Lisón Campos**, **Adriana Reixach García**, **María Mateu Reyes**, **María Eugenia López-Soriano** and **Ivan Granados Martínez** for their endless support, long conversations, drinks, live music and parties, in short, for being true friends; I never gave up because of you! Clearly, I could never have completed this journey without your support.

I would also like to thank **Sophie Davison**, **Ashley Lee**, **Emily Wride** and **James Bonney** for being the best flatmates I could have ever asked for. Sophie, thank you very much for your patience and for being such a wonderful flatmate and friend! Ashley, thank you very much for reading my 'boring uni stuff'.

Especially thanks to **Casey John Killin**, it would not be a 'mischi' without a 'vius'. You have been the pillar I have relied on during these years. Thank you so much for listening, for drawing me smiles, for dancing with me, for the trips, for the festivals, for your patience (even when I was determined to be grumpy), for the long night chats, for taking care of me, for *cabrearme* and for inspiring me every days. There are no words that can express my infinite gratitude to you. You are the real author of this thesis.

Finally, my heartfelt thanks goes to my family (and they are on top of everyone else in these acknowledgements) – **Armando Leal**, **Maria Dolores Olloqui**, **Mario Leal**, **Paula Leal** and **Nico Leal**. I would not have made it through this Ph.D. without you. Thank you for helping

me through the tough and stressful times, and for your limitless patience with my constant changing moods. I can clearly say without any doubt that I have the best family in the world. You always believe in me, even when I do not. I hope I have made you proud.

Publications

First author

'**A study of bentonite alteration at heated steel surfaces in a geological disposal facility setting**' M. Leal-Olloqui, C.P. Jones, K.R. Hallam, T.B. Scott, accepted by *Clay and Clay minerals*

M. Leal-Olloqui and T.B. Scott (2017). '**Study of the University of Bristol**'. Pp. 158–187 in: FEBEX-DP. Metal Corrosion and Iron-Bentonite Interaction Studies (P. Wersin and F. Kober, editors). NAB 16–016, Nagra, Wettingen, Switzerland

Second author

'**Monitoring the degradation of nuclear waste packages induced by interior metallic corrosion using synchrotron x-ray tomography**' H. Paraskevoulakos, A. Banos, C. Sttit, C.P. Jones, A.M. Adamska, J. Jowsey, M. Leal-Olloqui, G. Griffiths, K.R. Hallam, T.B. Scott. *Construction and Building Materials*. 2019 Aug 215:90-103

'**Development and validation of a high-resolution mapping platform to aid in the public awareness of radiological hazards**' P.G. Martin, D. Connor, O.D. Payton, M. Leal-Olloqui, A.C. Keatley, T.B. Scott. *Journal of Radiological Protection*. 2018 Mar 19;38(1):329-342

Conference paper

'**A study of geological disposal facility (GDF) ageing phenomena in bentonite**' M. Leal-Olloqui, F. Whitaker, T.B. Scott. WM Symposia, March 2017, Phoenix, Arizona, USA. *WMS Journal*, Volume 2, Issue 3

Contents

List of figures

List of tables

Abbreviations

ABM: **A**lternative **B**uffer **M**aterial

ATR: **A**ttenuated **T**otal **R**eflectance

Bq: **B**ec**q**uerel

CEC: **C**ation **E**xchange **C**apacity

CIEMAT: **C**entro de **I**nvestigaciones, **E**nergéticas **M**edio**a**mbientales y **T**ecnológicas

CoRWM: **C**ommittee on **R**adioactive **W**aste **M**anagement

CSIC: **C**onsejo **S**uperior de **I**nvestigaciones **C**ientíficas

cv: **c**is-**v**acant

DLS: **D**iamond **L**ight **S**ource

DSC: **D**ifferential **S**canning **C**alorimetry

DTA: **D**ifferential **T**hermal **A**nalysis

EBS: **E**ngineered **B**arrier **S**ystem

EBW: **E**lectron **B**eam **W**elding

EM: **E**lectro**m**agnetic radiation

Febex: **F**ull-Scale **E**ngineered **B**arriers **Ex**periment

FTIR: **F**ourier **T**ransform **I**nfra**r**ed Spectroscopy

GDF: **G**eological **D**isposal **F**acility

GTS: **G**rimsel **T**est **S**ite

HAW: **H**igher **A**ctivity **W**aste

HLW: **H**igh-**L**evel **W**aste

IC: **I**on **C**hromatography

ILW: **I**ntermediate **L**evel **W**aste

IR: **I**nfra**r**ed

LAW: **L**ower **A**ctivity **W**aste

LLW: **L**ow-**L**evel **W**aste

MAGW: **M**etal **A**ctive **G**as **W**elding

MPa: **M**ega **Pa**scal

NDA: **N**uclear **D**ecommissioning **A**uthority

OA: **O**riented **A**ggregates

OM: **O**riented **M**ounts

PAW: **P**lasma **A**rc **W**elding

P-EXAFS: **P**olarised **E**xtended **X**-ray **A**bsorption

PHA: **P**ulse **H**eight **A**nalyser

PWR: **P**ressurise **W**ater **R**eactor

PZC: **P**oint **Z**ero **C**harge

RWM: **R**adioactive **W**aste **M**anagement

SCA: **S**ingle **C**hannel **A**nalyser

SEM: **S**canning **E**lectron **M**icroscopy

SNF: **S**pent **N**uclear **F**uel

STT: **S**olid-**S**tate **T**ransformation

Sv: **S**ie**v**erts

TBT: **T**emperature **B**uffer **T**est

TGA: **T**hermo**g**ravimetric **A**nalysis

THC: **T**hermo-**H**ydro-**C**hemical

THCM: **T**hermo-**H**ydro-**C**hemical-**M**echanical

THM: **T**hermo-**H**ydro-**M**echanical

TMS: **T**ransmission **M**össbauer **S**pectrometer

tv: **t**rans-**v**acant

UPM: **U**niversitat **P**olitècnica de **C**atalunya

VLLW: **V**ery **L**ow-**L**e**v**el **W**aste

XRD: **X**-**r**ay **D**iffraction

XRT: **X**-**r**ay **T**omography

wt%: **W**eigh**t** percent

Chapter 1 Introduction

1.1 Introduction

In the United Kingdom (UK), the Clean Growth Strategy [1] delineates nuclear as a pillar of the national energy portfolio, with a 'sector deal' to ensure it reduces its costs to stay financially competitive.

With the building of the UK's first commercial nuclear reactor in 1956 [2], there is now a long-term commitment to nuclear energy. With anthropogenic climate change now being a widely-accepted phenomenon, there is a global drive to reduce carbon emissions by curbing fossil fuel burning. With numerous national and international accords in place [3], countries are quickly turning to low-carbon electricity generating sources - including nuclear power.

The UK's transition to a low-carbon future began with the adoption of the Climate Change Act in 2008, with the UK government legislating a target of an 80% reduction in greenhouse gas emissions by 2050 (from the 1990 baseline) [4]. In order to accomplish this, nuclear generation, along with renewable energies, is envisaged as a proven and efficient means of electrical energy production with reduced greenhouse gas emissions, especially in comparison to its homologous fossil fuels. Nevertheless, notwithstanding its numerous advantages, nuclear technology development has been significantly halted in the last decade, due to reignited debates related with health risk, nuclear security and, especially, the safe disposal of higher activity wastes (HAW) generated during power plant operations. These issues require continued attention to resolve the public uncertainties associated with its use [5]. Therefore, for nuclear energy to be considered a realistic option, one part of the solution is for an adequate waste management strategy to be developed for the UK. In this regard, the responsibility of developing a sustainable HAW management plan for the UK lies with Radioactive Waste Management (RWM), a UK public organisation belonging to the Nuclear Decommissioning Authority (NDA).

The HAW strategy in development must not only consider waste generated by the operation of the current nuclear power plants and decommissioning activities but also the legacy of existing

radioactive waste, and the radioactive waste yet to arise from new nuclear power plants. Additionally, there is significant HAW from reprocessing activities of nuclear fuel, the use of radioactive material in industry, medical research and defence-related nuclear programmes.

This chapter aims to give an overview of the current civil nuclear power situation in the UK and delineate the focus of the research presented herein.

1.2 Principles of nuclear energy

To achieve a good understanding of radioactive waste generation, it is crucial to understand the fission process and the operation of a nuclear power plant. A nuclear power plant is an industrial facility that utilises the heat produced by a 'controlled fission reaction' of a heavy atom or fissile material. In nature there are a variety of fissile materials such as: Uranium (^{233}U and ^{235}U); and Plutonium (^{239}Pu). However, the most utilised in nuclear reactors to generate heat and, thereby, electricity are ^{235}U and ^{239}Pu.

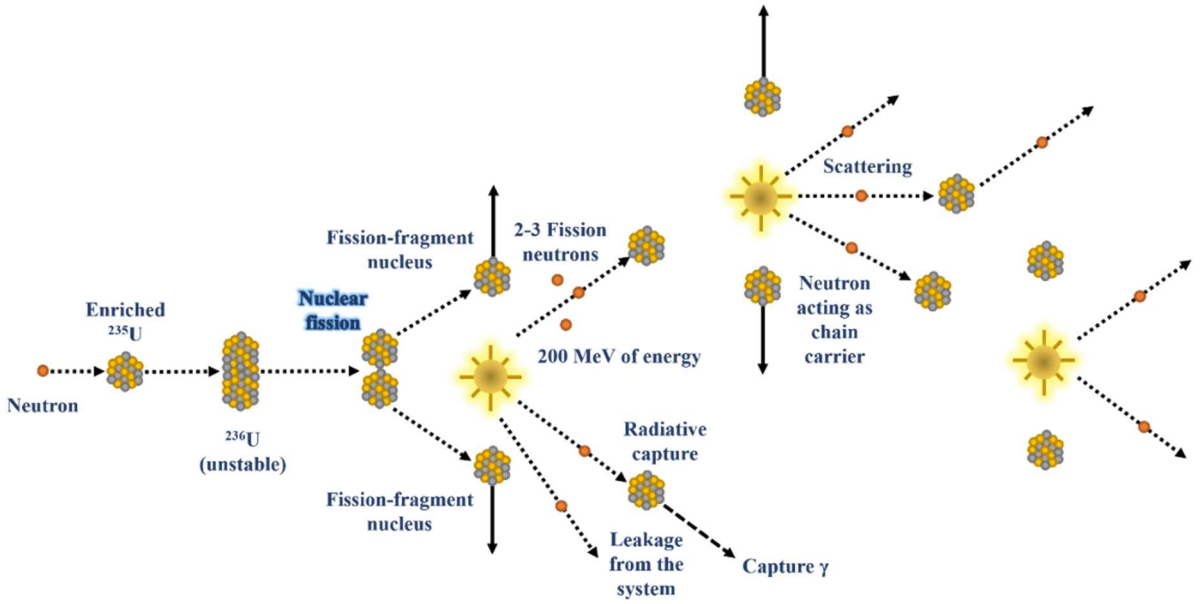

Figure 1.1: *Schematic of a fission chain reaction. Modified from* [6].

Nuclear fission requires the capture of a thermal neutron by a heavy nucleus or parent atom (^{235}U or ^{239}Pu), generating nuclear instability and causing its splitting into two fission nuclei, more neutrons and large amounts of energy [6]. The arising new neutrons will collide with other neighbouring atomic nuclei leading to propagate a chain reaction, as shown in Figure 1.1.

There are currently several different types of nuclear power plants and the differences between them are based on the type of fuel and moderator used to maintain the fission. Pressurised water reactors (PWR) constitute the large majority of the world's nuclear power plants. A conventional PWR consists of a reactor vessel accommodating between 150-200 fuel assemblies, each constituted of 200-300 zircaloy rods with enriched uranium dioxide pellets (UO_2) inside, which are stored within the reactor vessel and provide the fuel to sustain nuclear fission chain-reactions [7]. The thermal energy released by fission is transferred to the primary coolant (light water), which is pumped around the reactor vessel at high pressures. The primary coolant (heated light water) flows to a steam generator where it transfers its thermal energy to a secondary water loop system, generating steam [7]. The generated steam is used to drive turbines that, in turn, spin an electric generator producing electrical energy which, eventually, is added (once synchronised) to the electricity grid, Figure 1.2.

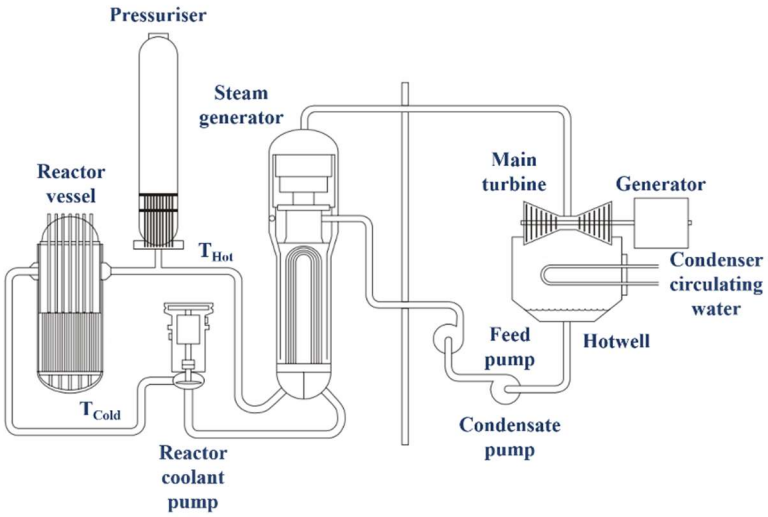

Figure 1.2: *Basic cycle of a PWR. Modified from* [8].

After irradiation of fuel in a reactor, the spent nuclear fuel (SNF) is one of the main contributors to radioactive waste. Figure 1.3 shows the composition of SNF of a standard PWR that has utilised 3.2% enriched uranium dioxide as fuel, irradiated to a burnup of 33GW per day and per tonne [9], with burnup defined as the loss of fissile material due to the fission of large amounts of ^{235}U during reactor operation [9]. The composition of the spent fuel varies with the degree of burnup and, thus, when the level of burnup increases, the number of trans-actinides increases, with a commensurate uplift in the level of radiotoxicity. From Figure 1.3 it follows that one tonne of SNF is approximately composed by: 95.5% uranium; and 4.5% stable fission products, plutonium, minor actinides, medium-lived and long-lived fission products.

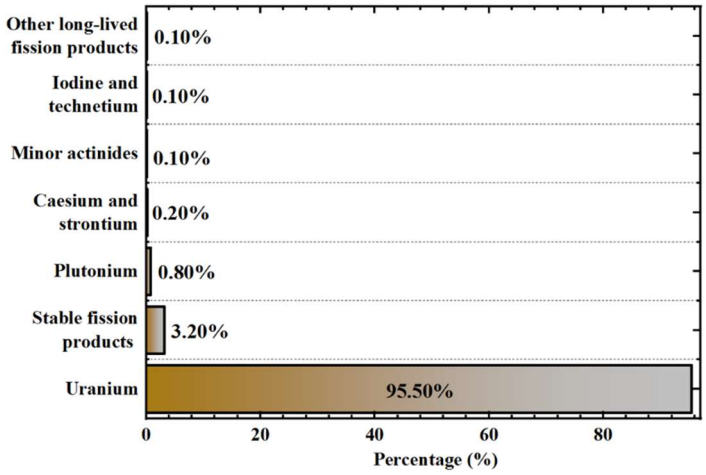

Figure 1.3: *Composition of one tonne of SNF (33GW/d/T) from a standard PWR after 10 years of cooling. Modified from* [9].

The risk level of these elements is measured by their radiotoxicity, using the uranium mineral radiotoxicity as a reference (Figure 1.4). The toxicity of a radionuclide (its radiotoxicity) is defined as 'its ability to produce injury by virtue of its emitted radiations when incorporated inside a body' [10], and is commonly expressed in Sieverts (Sv), or the dose ingested, inhaled or absorbed through the skin.

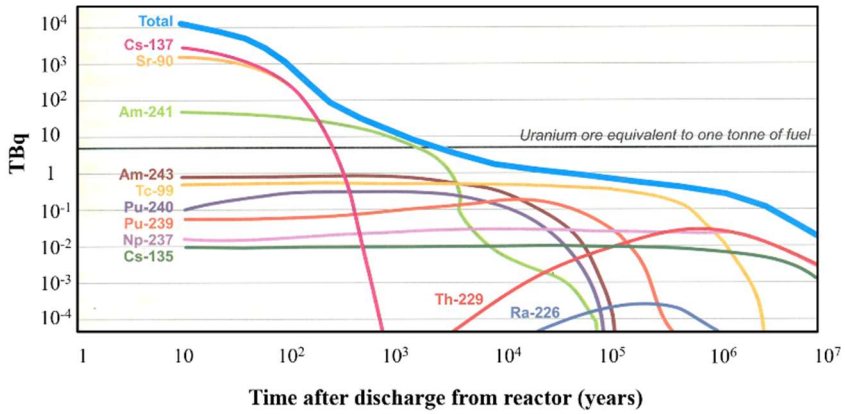

Figure 1.4: *Activity of HAW from one tonne of SNF. Adapted from* [9].

Figure 1.4 displays the hazard degree associated with some of HAW produced by one tonne of SNF. The changes in activity (TBq) are expressed as a function of time (years) after fuel discharge from reactor. From Figure 1.4, the following conclusions can be drawn: (*i*) firstly, the radiological risk declines by an approximate factor of 1,000 between 10 and 1,000 years due to the radioactive decay of medium half-life fission products which leave behind some minor actinides, such as americium and neptunium with longer half-lives [11]; and (*ii*) secondly, after 1,000 years, the radioactivity derived from the SNF is similar to the same corresponding amount of uranium ore, but still toxic if it is ingested [11].

The information relative to radioactive substances is usually given in terms of activity (Bq) and half-life. The activity of a radionuclide is 'the number of spontaneous nuclear transformations per second for a given quantity' [12]. If a nuclide shows high activity, it signifies that the nuclide decays rapidly to its decaying products, and therefore its half-life is short. Conversely, very long half-life radionuclides have a low activity. Tables 1.1 to 1.3 display some of the radioisotopes found in SNF, along with their half-lives and decay mode.

Table 1.1: *Some minor actinides fission products* [13].

Minor actinides	Isotope	Half-life (years)	Decay Mode
Neptunium	^{237}Np	$2.144 \cdot 10^{6}$	α
Americium	^{241}Am	432.2	α
Curium	Main curium isotopes; from ^{242}Cm to ^{250}Cm	Variety of half-lives. The longest are; ^{247}Cm: $1.56 \cdot 10^{7}$ ^{248}Cm: $3.40 \cdot 10^{5}$	Usually by α emission (but also by ε, spontaneous fission (SF) and β^-)

Table 1.2: *Medium-lived fission products* [13].

Medium-lived fission products	Isotope	Half-life (years)	Decay Mode
Caesium	^{137}Cs	30.17	β^- and γ
Strontium	^{90}Sr	28.90	β^-

Table 1.3: *Some long-lived fission products* [13], [14].

Long-lived fission products	Isotope	Half-life (years)	Decay Mode
Rubidium	^{87}Rb	$6.20 \cdot 10^{10}$	β^-
Zirconium	^{93}Zr	$1.53 \cdot 10^{6}$	β^-
Technetium	^{99}Tc	$2.13 \cdot 10^{5}$	β^-
Palladium	^{107}Pd	$5.00 \cdot 10^{6}$	β^-
Indium	^{115}In	$6.00 \cdot 10^{14}$	β^-
Iodine	^{129}I	$1.57 \cdot 10^{7}$	β^- and γ
Caesium	^{135}Cs	$3.00 \cdot 10^{6}$	β^-
Cerium	^{142}Ce	$5.10 \cdot 10^{15}$	α
Neodymium	^{144}Nd	$2.20 \cdot 10^{15}$	α
Samarium	^{147}Sm	$1.30 \cdot 10^{11}$	α

Besides the minor actinides, medium- and long-lived fission products (Tables 1.1 to 1.3), stable isotopes are also present in SNF.

Most of the longer-term radiological risk posed by SNF comes from a small collection of elements, such as plutonium, neptunium, americium, curium, and some long-lived fission products, such as iodine and technetium (Figure 1.4 and Table 1.3). In SNF, these elements are found in low concentrations (Figure 1.3) but, nevertheless, pose an unacceptable risk due to their high radiotoxicity and must be isolated from the biosphere and human environment (Figure 1.4). Therefore, the implementation of rigorous management proportional to the associated risk to the public and environment is of utmost importance, irrespective of future energy options, since worldwide there are already significant amounts of such radioactive waste and, therefore, a long-term solution is required.

1.3 Radioactive waste disposal

Radioactive waste is complex with regard to its varied chemical and physical forms, and some of the waste will remain radioactive over long periods of time. The main purpose of waste disposal is to isolate and confine radioactive waste from the biosphere, long enough to ensure that such waste has reached stable isotopic forms. Since some minor actinides and long-lived fission products have very long half-lives, these require isolation periods range between 100,000 to 1,000,000 years or beyond, as shown in Figure 1.4 and Tables 1.1 and 1.3.

The UK began research into geological disposal of radioactive waste after the publication of the Royal Commission on Environmental Pollution report on nuclear power in 1976 (the Flowers Report, 1976) [15]. Currently, the UK's existing intermediate and high-level radioactive wastes are in interim storage at Sellafield, Cumbria, or at one of 30 site locations distributed around the country [16]. Once, the interim storage period has expired, waste must be retrieved and finally disposed of. Due to the need for a rigorous plan for final radwaste disposal, in 2003 the UK government set up the Committee on Radioactive Waste Management (CoRWM), responsible for considering all possible options regarding radioactive waste management. Several long-term options have been considered and later discarded due to their complexity. These options included [17]: (*i*) interim or indefinite storage at or below surface level; (*ii*) direct rock injection into the rock strata; (*iii*) sea disposal; (i*v*) sub-seabed disposal;

(*v*) disposal in subduction zones; (*vi*) disposal in outer space; (*vii*) dilution and dispersal across large enough areas such that it does not pose a risk to the environment, (*viii*) transmutation; and (*ix*) volume reduction by incineration, burning or melting of wastes.

Few of these alternative options satisfied the necessary protection and security requirements sought, and also presented constraints regarding the viability of execution. In July 2006, CoRWM recommended geological disposal as the surest and most viable option for the management of the UK's radioactive waste legacy, after a preliminary period of interim storage which plays an important role due to the long timescales involved. That same year, the UK government accepted such a recommendation as the definitive option for final management of radioactive waste.

1.3.1 Radioactive waste categorisation

Radioactive waste has been defined as 'any material that has no further industrial use, and is contaminated by, or incorporates, radioactivity above certain levels' [18].

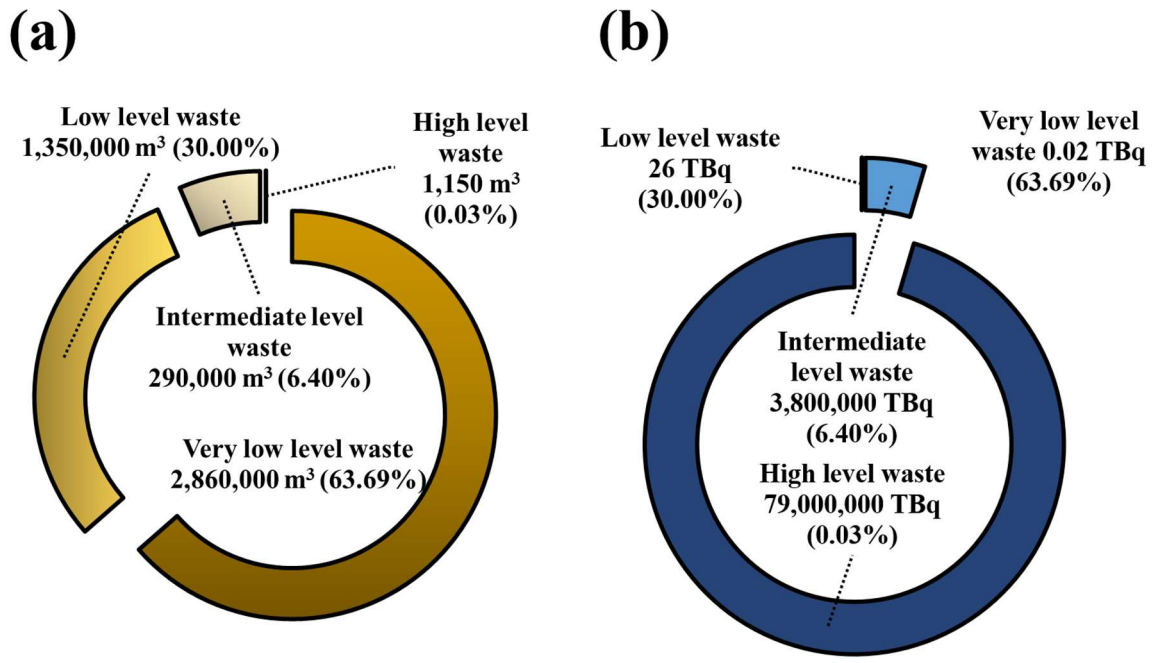

Figure 1.5: *Reported radioactive waste in the UK: (a) volumes (in m^3 and %), (b) radioactivity (in TBq). Modified from* [19].

Since, there is no international agreement for radioactive waste classification, the UK government has categorised radioactive waste, considering, its nature, activity and heat generated, into [18]: very low-level waste (VLLW), low-level waste (LLW), intermediate-level waste (ILW), and high-level waste (HLW).

Low-level waste: The majority of the waste comprising this category emanates from the operation and decommissioning activities of nuclear facilities. This category includes scrap metal, paper and plastics contaminated during these activities, and also incorporates some of the radioactive waste produced in hospitals and via research. These materials are characterised by relatively low levels of radioactivity which never exceeds 4-gigabecquerel (GBq) per tonne of alpha activity, or 12GBq per tonne gamma activity [18]. This category encompasses the sub-category of **very low-level waste,** which can be safely disposed of in conditioned landfill sites or with municipal, industrial or commercial waste. These wastes have a significantly lower activity of 400kBq of total activity per $1m^3$ of material, or single items containing less than 40kBq [18]. Around 94% of the reported volumes (LLW and VLLW) fall in this lower category and make up the majority of all UK nuclear waste by volume (Figure 1.5).

Intermediate-level waste: Most of the waste included in this category consists of nuclear reactor components, sludges from treatment of radioactive liquids and graphite from reactor cores and is characterised by a greater radioactive content than LLW. Therefore, its treatment and disposal are more complex. The waste in this category exceeds the upper boundaries of LLW but does not generate sufficient heat for this to have to be considered in the design of storage and disposal facilities. About 6% of the radioactive waste volumes reported pertain to this category, Figure 1.5 [19].

High-level waste: Waste within this category generates significant amounts of heat due to the high radioactive content and, therefore, heat management is an important factor to consider in the design of storage and disposal facilities. The reported volumes in this classification are less than 0.03% [19]. However, they contain the majority of the activity of the total UK radioactive inventory (Figure 1.5). This waste results primarily from the reprocessing activities of SNF and, typically, occurs in liquid form prior to its vitrification into a solid form for storage and final disposal. It is important to note that, SNF is not considered as a radioactive waste in the UK since it may have potential future use. But until then, it must be securely stored [18].

Radioactive wastes can also be categorised as: (*i*) **Higher activity waste** (HAW) - this category comprises HLW, ILW and LLW that is unsuitable for disposal in the existing UK low-level waste repositories (LLWR). HAW arises from activities such as reactor operation, SNF reprocessing and decommissioning [18], [20]; and (*ii*) **Lower activity waste** (LAW) comprises LLW and VLLW, and typically consists of plastic, paper, tissue, clothing, wood and metallic items, arising from routine monitoring and maintenance activities [21].

These categories and their reported volumes are regularly published by the NDA, aiming to foster a greater understanding of quantities, origin and properties of all radioactive waste generated in UK, including further arisings [18], [19]. From the most recent report published in March 2017 for stocks on 1st April 2016, it can be seen the UK has considerable reported volumes of radioactive waste that comprises a waste legacy of 4,490,000m^3 with a total reported activity of 83,000,000TBq, as shown in Figure 1.5 [19]. The majority of the radioactive waste constituting these reported volumes is due to the operation of the current nuclear facilities. The possibility of additional waste arising from future new facilities will increase the already existing national inventory.

1.4 Deep geological disposal

'Geological disposal' refers to the isolation of radioactive waste, at depth (~400-1000m), in a suitable host rock formation to ensure that no harmful quantities of radioactivity and non-radioactive contaminants ever reach the biosphere [22]. The complete isolation of radioactive waste will not only be achieved by placing it at great depth. Therefore, the installation will require the incorporation of multiple barriers (Figure 1.6). A multi-barrier system or engineered barrier system (EBS) is the means through which a geological disposal facility (GDF) is endowed with several failsafes by using the advantageous features of each material involved in the design [22], and comprises: (*i*) vitrified HLW waste in a borosilicate matrix ad HAW; (*ii*) waste container; (*iii*) geotechnical barrier or highly-compacted bentonite; (*iv*) engineering components that structurally support the installation; and (*v*) a stable rock formation in which the facility is sited.

The combination of these barriers must ensure that the radioactive waste is completely isolated, preventing unfavourable releases and radionuclide migration, until such waste has reached radioactivity values considered no longer harmful for humans and the environment. At the present time, the UK does not have a site for a GDF, since the design will depend to some extent on its final location and, by extension, the final design of the future UK geological disposal installation has not been decided yet.

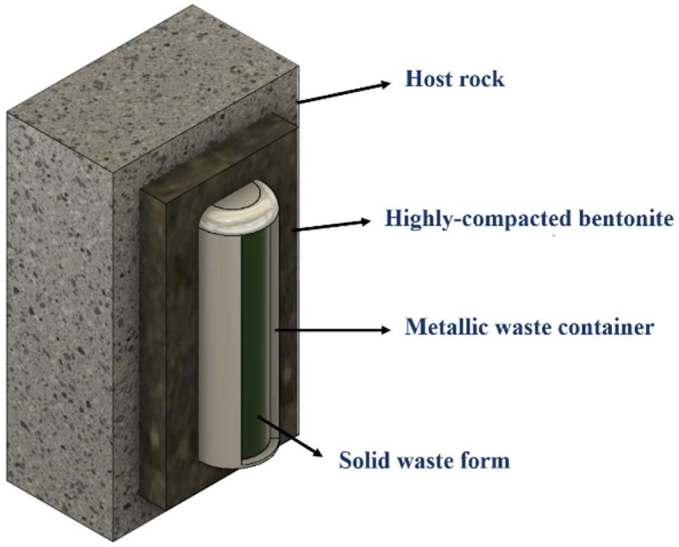

Figure 1.6: *Schematic of a multi-barrier system. Modified from* [22].

However, there are several model concepts that form the basis of the UK's current concept design and, each of them implements the multi-barrier concept. The following section presents a general description of the main concepts on which the UK design model is based. This review is not exhaustive and aims to provide an overall picture of the projects ongoing.

1.4.1 Deep geological disposal concepts

1.4.1.1 Scandinavian concept for deep geological disposal (SKB: KBS-3)

The Swedish nuclear fuel and waste management company (SKB) was established in the 1970s and is constituted by a consortium of several Swedish nuclear power companies. In 2009, the site was selected and, in 2011, plans were submitted to build a GDF at Forsmark (Sweden).

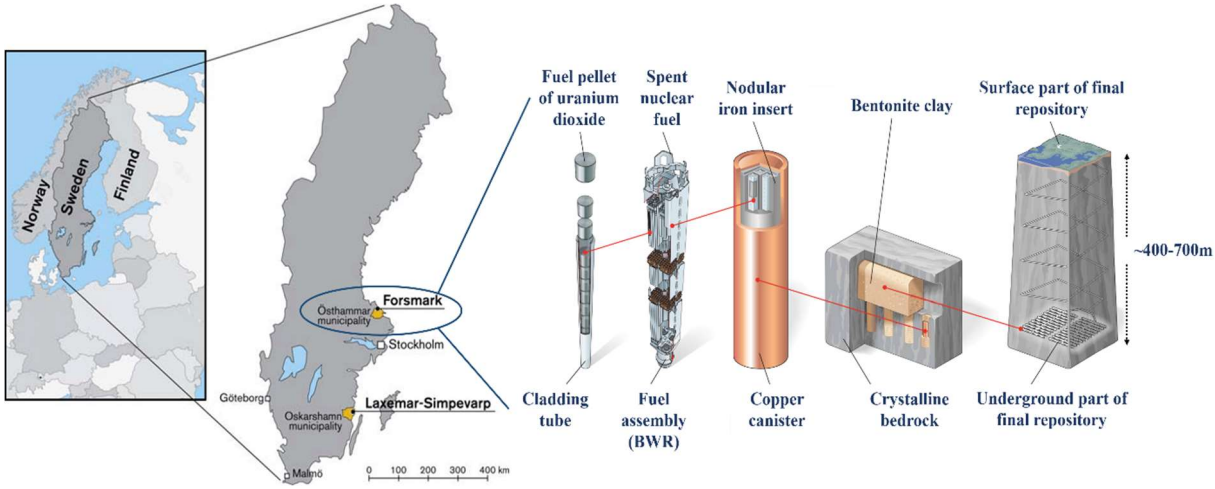

Figure 1.7: *Schematic of the KBS-3 concept and selected location. Modified from* [23], [24].

A schematic view of the KBS-3 concept, depicting the EBS concept, is shown in Figure 1.7. The KBS-3 repository is based on the multi-barrier concept. Spent fuel with no further use will be vitrified in cast iron and encapsulated within cylindrical canisters endowed with a copper shell. The canisters will be deposited deep underground, in granitic crystalline rock, at depths ranging between 400 and 700 metres in drilled boreholes surrounded by a buffer material. Finally, the facility's access tunnels will be backfilled with bentonite pellets, completely isolating the waste from the biosphere [25].

1.4.1.2 Swiss geological disposal concept (Nagra)

Nagra was established in 1972 by the Swiss nuclear power plant operators and the Federal Government to implement a safe disposal programme for radioactive wastes generated in Switzerland. The programme started with extensive research on available geological sites, followed by an investigation of container materials and multi-barrier configurations. The rock lithology selected for this concept is the argillaceous Opalinus clay deposit, recognised for its low permeability and groundwater flow. The extensive research performed by this country was supported by the Grimsel Test Site (GST) and the Mont Terri Project (rock laboratories), along with the collaboration of national and international partners, to accomplish a better understanding of chemical interactions, host rock properties and barrier components [26], [27], [28].

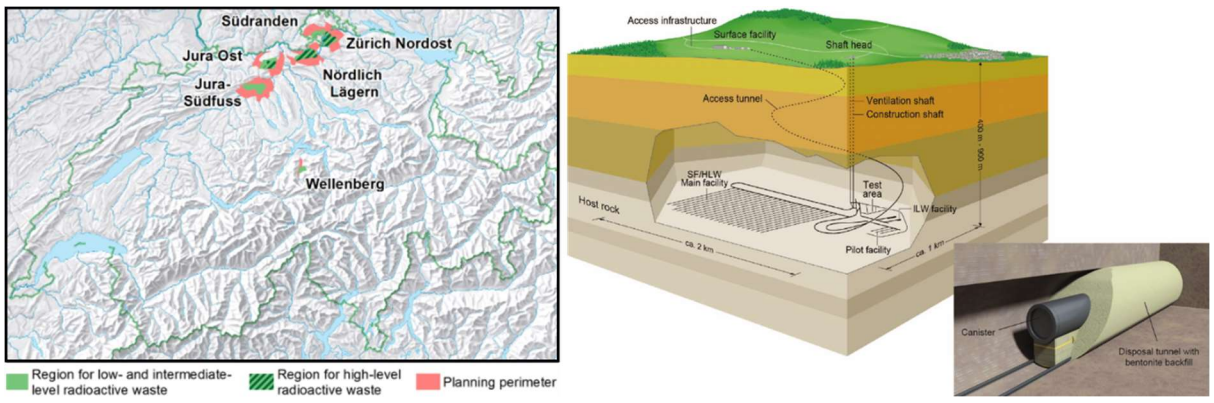

Figure 1.8: *Schematic of the Swiss concept for geological disposal of radioactive waste and locations under investigation. Modified from* [26], [29].

The design of this concept differs from that proposed by SKB in that the containers will be placed horizontally (rather than vertically), resting on compacted bentonite blocks and the space between the container and the argillaceous formation backfilled with bentonite pellets. The design also incorporates steel supporting arches that will eventually corrode, and the clay

host rock formation will provide an additional sealing environment. Accordingly, in this concept the need for a highly compacted barrier is not as imperative. Figure 1.8 shows a schematic view of the Swiss concept for geological disposal. Currently, Nagra is investigating six geological siting areas (Jura Ost, Jura Südfuss, Nördlich Lägern, Südranden, Wellenberg and Zürich Nordost) as shown in Figure 1.8.

1.4.1.3 Finnish geological disposal concept (POSIVA)

The Finnish geological disposal programme was initiated in the 1970s, with a concept very similar to the Scandinavian approach. The final GDF will be constructed at Olkiluoto. The considered bedrock is crystalline granitic in nature, and the radioactive waste containers will be placed vertically within boreholes drilled from the floor of the deposition tunnels. The radioactive waste containers will be designed with a copper-iron shell surrounding the solid waste form. Figure 1.9 displays a schematic view of the final Finnish GDF design [30].

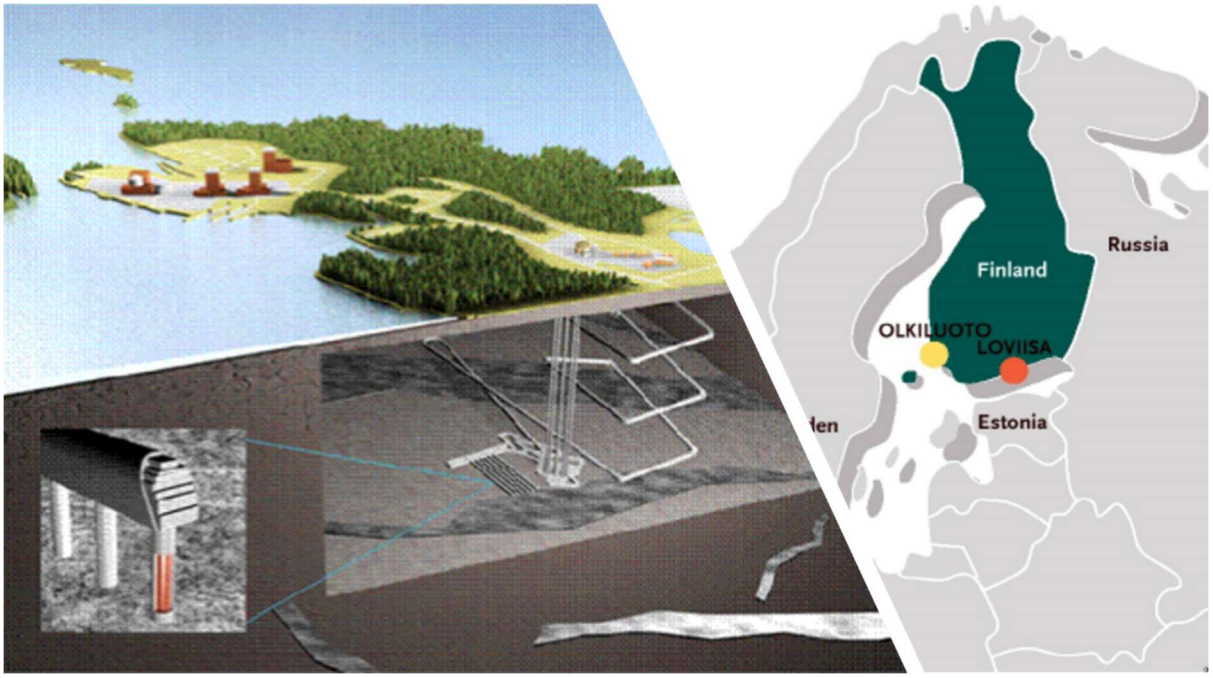

Figure 1.9: *Schematic of the KBS-3V design and location and selected location. Modified from* [30], [31].

1.4.1.4 French geological disposal concept (Andra)

The French National Radioactive Waste Management Agency (Andra) initiated a research programme, after approval of the French Waste Act on 30th December 1991, to define the best strategy for the long-term management of their radioactive waste. Andra's programme has

considered two main host media, argillaceous and crystalline formations. However, the argillaceous Callovo-Oxfordian formation seems to be the most probable candidate for a HAW repository and, therefore, is the likely location, since most of the research to date has been performed at the Meuse/Haute-Marne underground laboratory located in such a formation [32], [33]. Figure 1.10 depicts the geological features of the Callovo-Oxfordian formation.

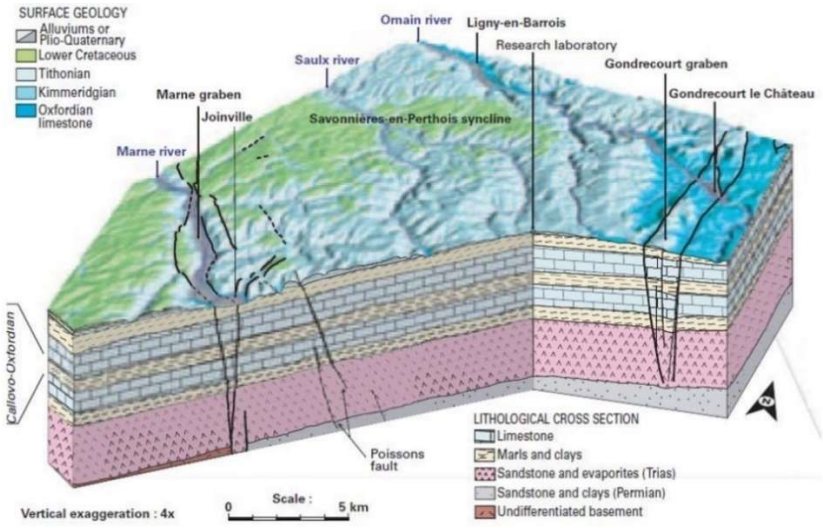

Figure 1.10: *Outline of the Callovo-Oxfordian formation. Adapted from* [32].

The French concept is somewhat similar to that developed by Nagra, and envisions radioactive waste encapsulation within steel containers which will be finally placed in horizontal deposition tunnels [34].

1.4.2 Bentonite as engineered barrier

Most of the geological disposal concepts for HAW include bentonite as a geotechnical barrier. However for bentonite to achieve the functions for which it has been selected as an isolating material, it must be technically engineered into highly compacted blocks [35]. Upon compaction, bentonite gains the desired properties which guarantee an adequate isolation of radioactive waste. These properties include an increase of its swelling capacity, and thermal and mechanical stability. The swelling capacity is its most conspicuous property since, in contact with water, bentonite exerts swelling pressure, leading to eventual sealing of the underground installation along with formed cracks and cavities.

Some of bentonite's required or desired properties will slightly vary, depending on the characteristics of the host rock selected and, therefore, of the selected concept. In crystalline

host rocks, such as granite, and due to groundwater flow through cracks, bentonite must keep water away from the canister surface and inhibit radionuclide release to the biosphere in the case of canister failure [35]. However, in argillaceous formations due to their low permeability and high plasticity, fractures are self-sealed. Consequently, the major concern is to favour flow of gases formed by the container corrosion and, simultaneously, keep the water away from the container [35]. Despite the host rock structural differences, the required or desired bentonite properties are similar between concepts. Table 1.4 presents a summary of the desired properties of bentonite in crystalline and argillaceous host rocks.

Table 1.4: *Desired and expected bentonite properties for HAW isolation in crystalline and argillaceous host rocks. Adapted from* [35].

Property	Bentonite function
Sealing capacity	Seal possible cavities, cracks and fractures formed
Radionuclide retention capacity	Radionuclide absorption in case of container failure
Thermal conductivity	Avoid heat accumulation in the vicinity of HAW containers
Mechanical stability	Maintain canister position
Gas permeability	Facilitate corrosion gas molecule diffusion
Erosion	Withstand erosion at the interface bentonite-canister
Nuclear radiation	Structurally withstand radiation
Drying	Uphold swelling capacity against extensive drying
Container corrosion	Structural and chemical stability against canister and metal components
Host rock water and cement pore water	Maintain its stability against porewater present in the host rock and cementitious materials

Research targeted at GDFs has been focused on underground rock laboratories to study bentonite behaviour under repository-like conditions, aiming to achieve a greater understanding of thermo-hydro-chemical (THC) and thermo-hydro-mechanical (THM) processes affecting bentonite under simulated repository conditions. On this basis, many field-based experiments have been performed. Tables 1.5 and 1.6 summarise the length-scale experiments conducted to date.

Table 1.5: Field-based EBS experiments [36].

Experiment name	Objective of study
Alternative Buffer Material (ABM)	Evaluate THC and THM processes on 11 different types of bentonite buffer
40% scale buffer test	Study early processes in bentonite buffer, including distribution of the heat, saturation rate from the gap to the middle of the buffer block, water effect, buffer erosion and swelling behaviour
BACkfilling Control Experiment for High level wastes in Underground Storage (BACCHUS 2)	Develop a process for backfilling tunnels with pellets and bentonite powders
Bentonite Rock Interaction Experiment (BRIE)	Study the interactions between rock and bentonite
Canister Retrieval Test (CRT)	Evaluate the effect of microbiological processes in the buffer performance
Demonstration Of Plugs And Seals. Experimental Pressure and Sealing Plug (DOPAS. EPSP)	Develop design and strategies for plugs and seals to be use in geological disposal facilities, using bentonite suspensions as a pressurisation media
Engineered Barrier Emplacement Experiment in Opalinus Clay (EB)	Demonstrate the feasibility of granular expansive barriers
Full-scale emplacement (FE)	Investigation of the repository induced THM coupled effects on the host rock
In situ Full-scale Engineered Barrier Experiment (Febex in-situ test)	Acquire a greater knowledge of the THM and THC processes affecting bentonite
Gas Permeable Seal Test (GAST)	Behaviour of a gas permeable seal under realistic boundary conditions

Table 1.6: Field-based EBS experiments [36].

Experiment name	Objective of study Objective of study
HE-B	Study the THM process in the buffer material
HE-E	Study the THM process in the clay formation
Isothermal test (ITT)	Examine the influence of heat on the performance of the buffer
Large Scale Gas Injection Test (LASGIT)	Examine the gas migration through the buffer
Long-term In-situ Test (LIT)	Investigate radionuclide migration in the presence of clay colloids under real conditions
Long-Term Test of Buffer Material (LOT)	Collect information concerning survival, activity and migration of bacteria in bentonite under repository-like conditions
Mock-up Josef	Mineralogical alterations on bentonite induced by heat emanating from the canister
Noyau de Scellement (NCS)	Analyse the permeability process of the seal (buffer)
PGZ2	Study the response of claystone caused by a repository
PRACLAY	Study the THM behaviour of the bentonite buffer
Prototype repository experiment	Study fundamental properties of bentonite pellets subjected to repository-like conditions
RESEAL	Increase knowledge of the basic parameters influencing the hydro-mechanical behaviour of the sealing material
SB-Experiment	Test and demonstrate maintenance of sand/bentonite admixtures under relevant conditions
SEALEX	Examine bentonite performance in the long-term
Temperature Buffer Test (TBT)	Improve understanding and basis for modelling of THM behaviour of the buffer

A geological disposal installation constructed deep (~200-1000m for the UK concept) within the terrestrial crust below ground level is widely acknowledged in both academic and industrial fields as a permanent solution for disposal of nuclear waste in many countries (Section 1.4.1). Currently, the waste management organisations mentioned in Section 1.4.1 are actively leading research and implementation of GDFs.

The primary purpose of a GDF is to isolate the radioactive waste and impede radionuclide transport to the biosphere. Therefore, it is crucial that all elements involved in the long-term operation and stability of a GDF are suitably investigated before carrying out its planning and final implementation. The design of a GDF incorporates a multi-barrier passive system for which the long-term durability depends on the features of each element involved in the design; included among the passive barriers is bentonite. The theory behind the utilisation of bentonite as a passive barrier resides in its low permeability and self-healing capacity, thus averting early radionuclide discharge to the biosphere as a consequence of rapid corrosion of the metal container.

Bentonite displays very high swelling properties which are primarily a function of its montmorillonite content (Chapter 2). The better the swelling capability, the more effective the barrier will be in delaying radionuclide transportation. Heat exuded by the decaying fission products is the main 'by-product' of expended reactor fuel. During HAW storage, the heat will easily reach the surface of the metallic container, driving off the water contained within the bentonite structure, and greatly facilitating oxygen migration inwards to the container's surface, which, in turn, will initiate a corrosion process in that region.

Thus far, research has been focussed on understanding the THC and THM processes affecting bentonite, interactions between bentonite and the host rock, gas and radionuclide migration through the buffer and bacteria interactions with bentonite (as listed in Tables 1.5 and 1.6). However, in spite of the numerous full-scale experiments performed to date, there is little or no information regarding interactions between the released corrosion by-products, as a result of container corrosion, and bentonite. From the length-scale experiments listed in Tables 1.5 and 1.6, only a few were focussed on the examination of the THCM processes and the influence of the corrosion processes expected on the surfaces of the metallic components. Therefore, only the most critical length-scale experiments are summarised below.

The 40% scale buffer test was conceived to simulate a GDF of HAW as per the reference design concept adopted by Finland (section 1.4.1.3) [37]. To that end, two experimental vertical holes, of 800mm diameter, were drilled into the testing tunnel TU1 located at 140m from the surface in Onkalo (Figure 1.11) [37]. Both experimental holes were of 3m depth, separated by 4m distance. In each hole, MX-80 bentonite buffer blocks, a heating container emulating HAW and monitoring equipment (thermocouples, relative humidity transducers, total and pore pressure sensors, displacement and force transducers) were installed [37]. The heating test started in November 2011 at a target temperature of 90°C. The duration of the 40% scale buffer test was planned to have a continuous monitoring for at least two years [37].

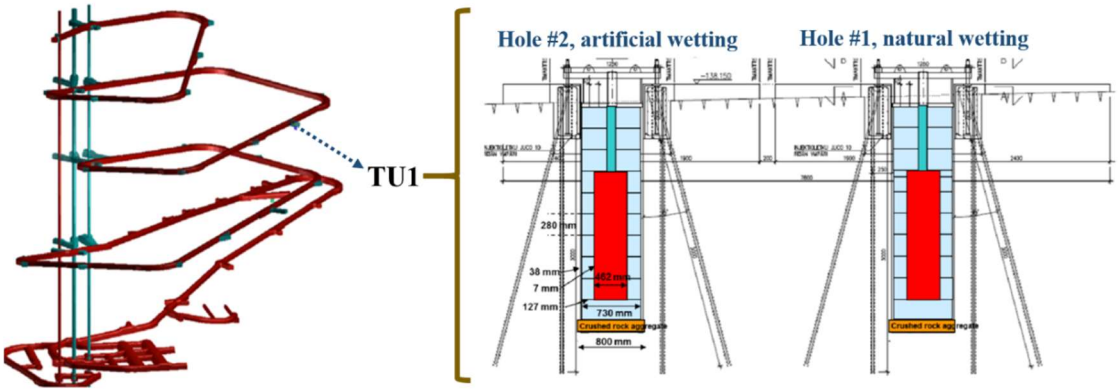

Figure 1.11: *Layout of the 40% scale buffer test. Adapted from* [37].

Despite the fact that the main aim of this medium-scale test was to obtain information regarding the early processes affecting bentonite such as distribution of the heat, the effect of saturation and the saturation rates of the buffer blocks, the swelling of buffer under repository-like conditions, as well as erosion processes [37]; relevant information with regard to the presence of traces of iron oxides and oxyhydroxides and traces of beidellite was also obtained during the characterisation of samples that were in direct contact with the simulated heater.

The full-Scale (FE) experiment was envisaged as a full-scale multiple heater test in the Opalinus Clay formation at the Mont Terri underground rock laboratory [38]. This length-scale in-situ test was designed according to the Swiss disposal concept (section 1.4.1.2) to simulate the construction, waste emplacement and the early post-closure stages of an underground repository [38]. The layout of this in-situ test consisted in three experimental heaters placed on top of compacted granulated bentonite mixture blocks (GBM) and the remaining space was backfilled with highly compacted pellets of GBM (Figure 1.12) [38]. The heating phase started in December 2014, with temperatures on the surfaces of the heaters ranging between 117 and 133°C [38]. The experiment was equipped with 238 sensors to investigate the induced THM

coupled effects within a HAW repository and validate the existing THM models [38]. The Full-Scale (FE) experiment was run for seven years [38].

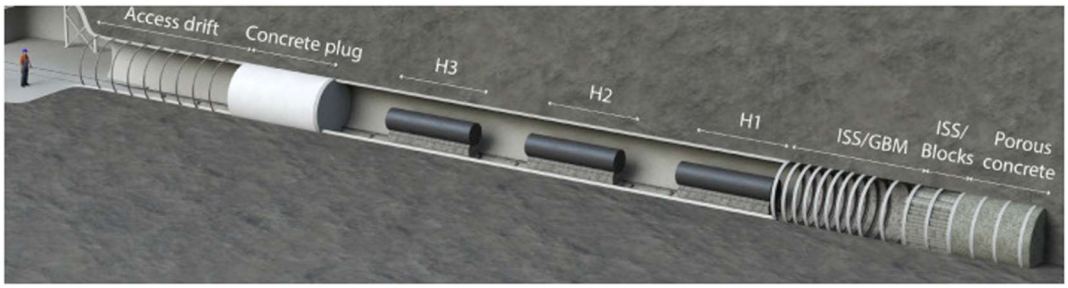

Figure 1.12: *Layout of the Full-Scale (FE) experiment. Adapted from* [39].

From this particular in-situ test, the following conclusions were drawn [39]: (*i*) the results from the in-situ monitoring FE experiment established that anoxic conditions may be reached within a few weeks to a maximum of a few months after closure; (*ii*) the oxygen concentration in the bentonite backfill decreases rapidly at the early post-closure stages; and (*iii*) mineral alterations and microbial respiration are expected to be irreversible at the boundary conditions of an underground repository.

The long-term test of buffer material (LOT) aimed to validate models and hypotheses concerning physical properties of MX-80 bentonite, regarding mineralogy, microbial effect, cation mobilisation through the buffer, copper corrosion and gas transport under conditions similar to those expected in the Swedish model (section 1.4.1.1) [40].

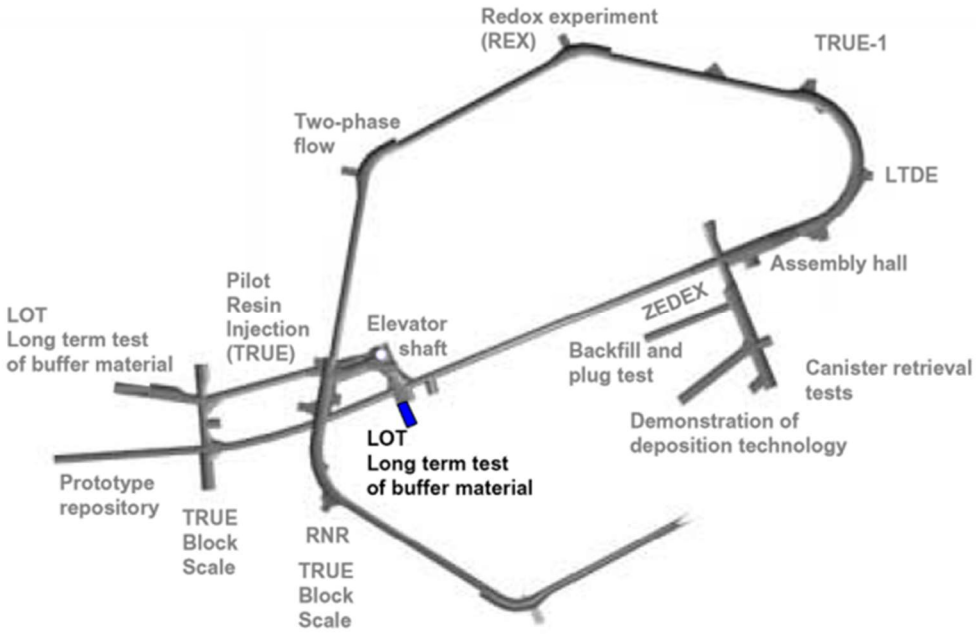

Figure 1.13: *Location of the long-term test of buffer material (LOT) at the Äspö Hard Rock laboratory. Adapted from* [40].

The test consisted of seven parcels run for one, five and 20 years. Each contained a heater, a central copper tube, pre-compacted clay buffer surrounding the copper tube and corresponding instrumentation to monitor the temperature among other parameters [40]. Each heater purported to emulate the radiated heat by the decaying HAW at standard KBS-3 conditions (90°C) and adverse condition (130°C) [40].

After the retrieval of several parcels the following findings were established [41]: (*i*) from the mineralogical point of view, no significant changes were found in the MX-80 bentonite compared to reference material; (*ii*) no changes in cation exchange capacity were observed; and (*iii*) the clay mineralogy and the proportion of accessory minerals within the clayey matrix remained close to those observed in the reference material. However, precipitation of gypsum was observed in the areas close to the copper tube, as well as an increase of calcium and sulphur.

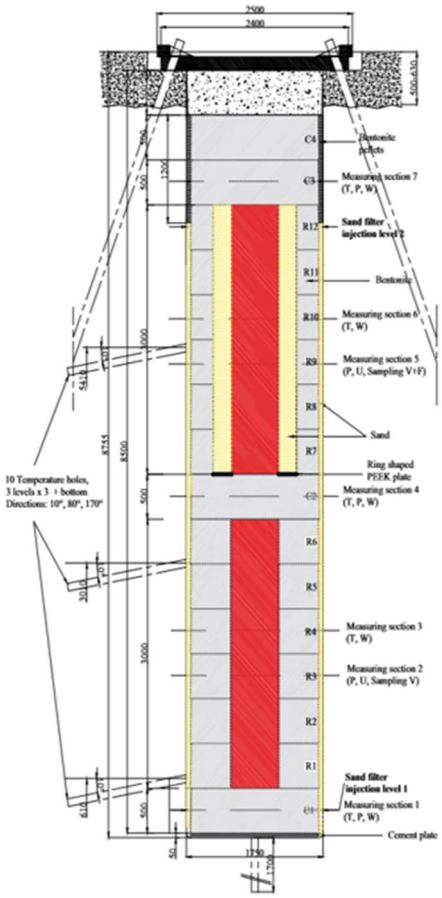

Figure 1.14: *Layout of the temperature buffer test (TBT). Adapted from* [42].

The temperature buffer test (TBT) aimed to provide better understanding of the THM behaviour of the bentonite buffer at 100°C during water saturation transient [42]. The experiment was installed in 2003 in a full-scale KBS-3 deposition hole at the Äspö Hard Rock

laboratory and dismantled in 2010, after seven years of artificial saturation [42]. The TBT consisted in two heaters made of carbon steel surrounded by MX-80 compacted bentonite blocks (Figure 1.14) [42].

With regard to chemical and mineralogical analyses, findings from this in-situ test were more conclusive than the previous experiments [42]: (*i*) analyses of aqueous leachates showed an irregular increase of chlorine within bentonite blocks, concluding that it was a consequence of the artificial saturation, besides an increase of sulphates in areas close to the heaters; (*ii*) an increase in the overall CEC was observed in the vicinity of the heaters; (*iii*) analysis of the exchangeable cations showed a partial replacement of Na^+ by Ca^{2+}; (*iv*) CP/AES+MS, EGA analyses confirmed the redistribution of the total sulphur, which increased towards the heater, as well as the presence of iron oxides and oxyhydroxides, such as hematite, magnetite and goethite in those bentonite samples retrieved from the contact with the C-steel heater; (*v*) x-ray diffraction (XRD) did not provided a clear evidence of any structural changes within the montmorillonite component of MX-80; (*vi*) Mössbauer analysis showed, in some of the samples, a larger isomeric shift, which is typical of divalent Fe, suggesting certain of structural Fe reduction; and finally (*vii*) Fourier transform infrared spectroscopy (FTIR) analysis showed a decrease in cristobalite towards the heater.

Despite the fact that numerous length scale experiments have been performed to date. The findings from these experiments are inconclusive, in particular concerning the interactions between released by-products and the buffer, as a result of container's corrosion. Therefore, those repositories that intend to use bentonite as a buffer must be suitably convinced that its performance over long periods (Section 1.4) can be maintained or at least predicted. Bentonite performance in a GDF over such timescales (Section 1.4) may be then affected by a locally-elevated temperature in combination with factors such as groundwater interactions and container corrosion. It still remains unclear if the montmorillonite component of bentonite will remain sufficiently stable, both chemically and structurally, to assure compliance with the desired safety functions for which bentonite has been selected. This potential deficiency must be investigated to underpin the integrity of any GDF relying on bentonite as a buffer. This PhD thesis attempts to address this knowledge gap. Hence, the present work is focussed on the study of bentonite stability against effects derived from canister corrosion by analysing several samples coming from the Febex in-situ test (Full-Scale Engineered Barriers Experiment) and ABM project (Alternative buffer material). Both in-situ full-scale tests were implemented with

heaters embedded within metallic containers to emulate the conditions that will possibly develop at the contact between the surfaces of the HAW containers and bentonite. Therefore, a brief description of these field-based experiments is given below.

1.4.2.1 Full-Scale Engineered Barriers Experiment in Crystalline Host Rock (Febex)

The Febex experiment at the GTS (Switzerland) consisted of an in-situ full-scale EBS test performed under natural conditions [43]. Febex was a pilot project designed for 'field-research' of a HAW repository hosted in a medium-crystalline rock, granodiorite [44], using two surrogate steel canisters with one inner heater each to emulate the heat released by the radioactive waste. Canisters were placed horizontally in drifts with a diameter of 2.28m, surrounded by compacted blocks of bentonite, and sealed by a concrete plug (Figure 1.15) [43]. The Febex experiment had two main objectives:

1. To provide evidence of the viability of assembling a deep geological storage facility for the disposal of HAW based on the Spanish concept of EBS for crystalline host rock [45].
2. To acquire a greater knowledge of the THM and THC processes affecting bentonite developing appropriate models and methodologies [45].

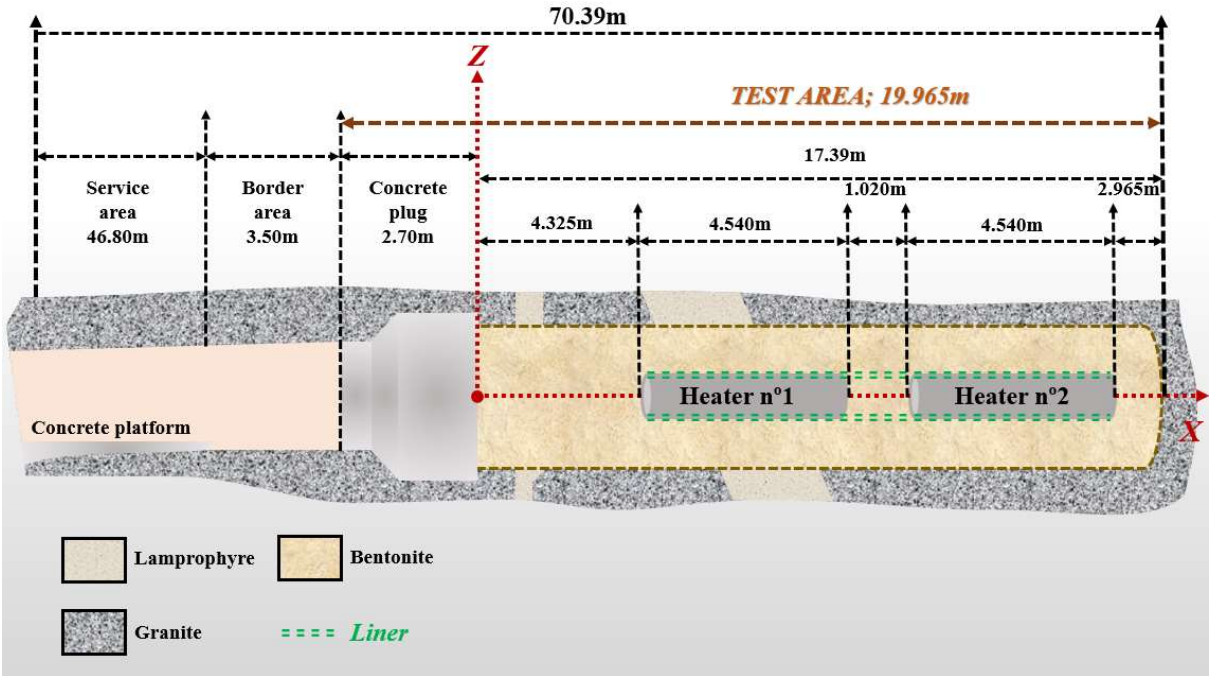

Figure 1.15: *Layout of the Febex in-situ test. Modified from* [43].

The Febex project was envisaged in three main parts: (*i*) an in-situ full-scale test under natural conditions; (*ii*) a mock-up test conducted at CIEMAT (Centro de Investigaciones, Energéticas, Medioambientales y Tecnológicas, Madrid, Spain); and (*iii*) a series of supporting laboratory tests [45]. The project was performed with Febex bentonite, selected by ENRESA S.A. (the Spanish Agency for Radioactive Waste Management) as a suitable buffer and backfill material and whose properties are mentioned in Chapter 3.

The in-situ heating test was initiated in February 1997, with the surface temperature of a surrogate HAW canister maintained at a constant 100°C and the bentonite buffer gradually hydrated by the inflow of groundwater from the surrounding rock. The ensemble was comprehensively monitored using 632 sensors to continuously chart the evolution of the major physical parameters such as temperature, humidity, total pressure, pore pressure and physical displacements, among others. Additionally, a data acquisition and control system was utilised to record, collect and store the data raised by the installed sensors, and control the power of the electrical heater inside the canister to ensure optimal temperature performance at all times [45].

After five years of operation a partial dismantling was conducted in 2002. The dismantling activities involved demolition of the concrete plug, retrieval of heater no.1 and, resealing operations with the intention of continuing the field-based test for several further years. During the dismantling process, several bentonite samples were taken to investigate the THM and THC processes under which bentonite was subjected [46].

The dismantling of heater no.2, after 18 years of operation, started in late 2015 and was scheduled to end in late 2016. The dismantling operations related to heater no.2 involved an entire sampling programme, including rock, buffer, sensors and, in general, all the metallic components used during the experiment, with the objective of analysing the bentonite barrier conditions following the experimental curating time. The dismantling operations were completed at the end of 2018 [45].

1.4.2.2 The Alternative Buffer Material in-situ test (ABM)

MX-80 bentonite has been the reference material for the Swedish KBS-3 GDF design. However, the alternative buffer material (ABM) project aimed to extend this knowledge to other expansible materials to optimise the safety functions, availability and costs of the future Swedish GDF [47] recognising that there was not an infinite availability of any one specific

bentonite material. Resources may become exhausted because bentonite is a physically mined commodity.

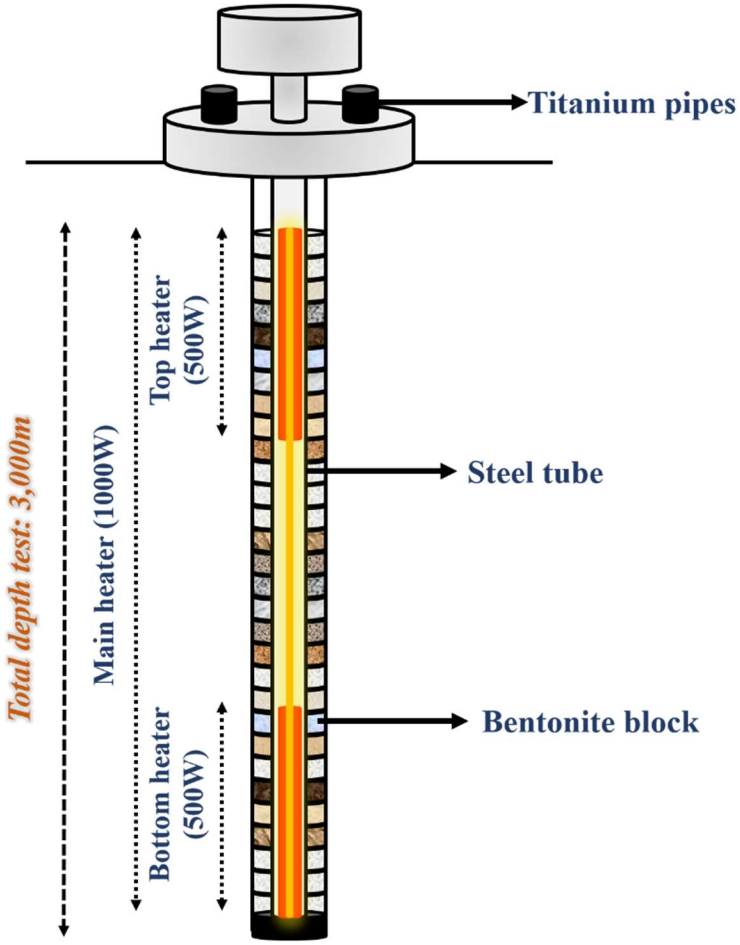

Figure 1.16: *Schematic of an ABM experimental package. Modified from* [47].

The ABM experiment was started at the Äspö Hard laboratory in 2006. The experiment layout consisted of three medium-scale test packages or parcels, consisting each of a central steel tube with a heater inside, surrounded by 11 different types of clay [47]:

- Ikosorb (Moroccan Ca, K, Na-bentonite, low Fe content)
- Deponit C-AN (Milos, natural Ca-bentonite)
- IbecoSeal (natural Georgian Na-bentonite)
- Friedland (low smectite content)
- Asha 505 (natural Na-bentonite, high Fe iron content)
- Calcigel (German Ca-bentonite)
- Febex bentonite (Spanish Ca-bentonite)
- Kunigel V1 (Japanese Na-bentonite)

- Callovo-Oxfordian (natural French claystone)
- Rokle (Czech Ca-bentonite, high Fe content)
- MX-80 (Wyoming bentonite)

The ABM project aimed to characterise the clays with respect to their THM and THC properties, mineralogy and chemical composition, and identify any differences in its behaviour or long-term stability under the simulated conditions. In addition to the use of diverse types of clay and simulated steel canisters, the performed experiment also focused on studies of iron-bentonite interactions.

A layout of an experimental parcel is shown in Figure 1.16 and its design was based on the KBS-3 concept, using steel canisters instead of copper and dimensionally smaller. The three packages were placed in separate excavated boreholes in granitic rock (diorite and greenstone). The boreholes had a diameter of 300mm and an estimated depth of 3,000m. Each package consisted of a central steel tube protecting three inner heaters, as shown in Figure 1.16. The steel tubes were surrounded by ring-shaped bentonite blocks and the corresponding monitoring instrumentation. The bentonite blocks were exposed to similar experimental conditions to those considered in KBS-3, but at higher temperatures (130°C) to accelerate any alteration process [47].

The three packages were designed with titanium pipes inserted in the upper outermost slot filled with sand. The pipes were equipped with drilled holes at different levels and connected to an artificial water saturation system. All three packages were naturally wetted from the existing host rock fractures (measured water inflow in the three packages was about 0.06l/min), although packages one and two were also artificially wetted. The dismantling operations were initially planned after one, three and five years of exposure to the targeted maximum temperature [47]. Each package was endowed with 20 thermocouples, two temperature indicators on the surface of each block and humidity sensors, and, after the installation, all instruments were connected to a data logger to register the humidity and temperature evolution.

The heating test of the three parcels started in December 2006. After 2.5 years of operation in May 2009, dismantling operations of the first parcel were initiated. The second parcel was dismantled in April 2013, after 6.5 years of experimental heating. Immediately after excavation at the Äspö Hard laboratory, bentonite samples were collected on site, and the samples were

transported to Clay Technology (Lund, Sweden) for more precise subsampling and preservation.

1.5 Concluding statement

Although the nuclear industry is a mature and well-established industry in the UK with 15 reactors in operation [48], there is still a great uncertainty associated with the management of the current radioactive waste legacy and future arisings. Such uncertainty has led to a change in the perception of the industry by the public, which has led to a restructuring of current operation strategies, further ensuring secure operation throughout the lifespan of a nuclear power plant, through its decommissioning and final disposal. Despite reported volumes of HLW are only 0.03% of the total radioactive waste generated by the UK (Figure 1.5). However, due to its extreme radiotoxicity and, the long timescales involved makes imperative a meticulous management plan. The UK has opted for a GDF as the most secure and viable option but, for this option to be realistic, bentonite must guarantee the preservation of its properties (Chapter 2) within the timescales considered for an underground repository. Over the course of this study, the implication of the released heat from the radioactive waste and corrosion processes of the canister surfaces containing such wastes upon bentonite were investigated, using a variety of laboratory techniques on bentonite samples from both the Febex in-situ test and the ABM project (Chapter 4 and 5). To complement this sample characterisation, and to achieve a greater understanding of bentonite properties evolution under expected repository conditions, a laboratory experiment over several days (61, 122, 183 and 211 days) has been performed and arising samples were analysed post-mortem by high-resolution diffraction at the Diamond Light Source (synchrotron facility). This post-mortem analysis was complemented by 3D imaging of the associated canister corrosion by using metallic body-wires embedded in the experiment utilising microcomputed tomography (Chapter 6). The design of the cells and devices used for the experiment are included in Appendix A (Plane A.1). Additionally, a full description of materials and analytical techniques used throughout this investigation are presented in Chapter 3.

Chapter 2 Principles for bentonite research

2.1 Introduction

As discussed in Chapter 1, a GDF is a multi-barrier system for disposing of radioactive waste involving both engineered and natural barriers. Overall, HAW is expected to be vitrified into a solid form and embedded within metal containers. The waste containers will be placed underground in tunnels or boreholes, and the remaining space between the host rock and the metal container will be infilled by a buffer material acting as a physical and chemical barrier to limit microbial and chemical attack. The long-term stability of wastes within a GDF will be determined by the design and construction of the engineered barriers, and the Thermo-Hydro-Chemical-Mechanical (THCM) interactions that may happen between the different engineered components as a result of coupled processes, such as the heat produced by radioactive decay and the ionic composition of the contacting ground water.

Internationally selected as one of the primary candidates to be used as a backfill and buffer for final disposal of HAW in a GDF is bentonite, a naturally occurring geomaterial, which is characterised by the following features: (*i*) high swelling capacity due to its montmorillonite content; (*ii*) low hydraulic and gas conductivity; (*iii*) high cation exchange capacity (CEC) owing to its ability to exchange cationic species; and (*iv*) high plasticity [49]. Due to these features, bentonite has been studied and used in many industrial engineering applications, such as landfill liners. The montmorillonite clay mineral component in bentonite provides the ability to absorb a large volume of water whilst keeping some shear resistance and ductile behaviour. As defined by Börjesson [50] the most prominent intrinsic properties of the buffer are its: (*i*) swelling pressure; (*ii*) hydraulic conductivity; (*iii*) strength; and (*iv*) stiffness, which are a function of montmorillonite content and dry density. Hence, bentonite is widely considered the most suitable backfill material to accomplish the safety functions desired in underground repositories.

2.2 Bentonite mineralogy: Structure and properties

Bentonite terminology was first suggested by Knight [51] when referring to a peculiar clay-like material with soapy properties from the cretaceous 'Bento Shale' (Wyoming, USA). Currently, the most widely-accepted definition is that established by Wright [52], who described bentonite as 'any clay which is composed dominantly of montmorillonite, a swelling clay mineral from the smectite group, and whose physical properties are dictated by this clay mineral'.

Many authors have listed the characteristic of the smectite group. However the best compilation is provided by Bergaya and Lagaly [53], who described the smectite group features as follows: (*i*) high degree of layer stacking; (*ii*) high specific surface area; (*iii*) variable layer charge; (*iv*) high CEC; (*v*) small anion exchange capacity; (*vi*) high interlayer absorption or interlayer ion exchange rate; and (*vii*) variable and extensive interlayer separation. This compilation provides an overview of why bentonite must be considered as the most appropriate geomaterial for long-term isolation of HAW waste packages.

Since bentonite is a natural geomaterial, it can be found in many deposits distributed across the globe. Bentonite deposits worldwide can be found in rocks of very different ages, being abundant in Cenozoic and Tertiary rocks, in the Cretaceous layers of the Mesozoic era, or the Jurassic era, while rarely found in Palaeozoic beds. It is generally assumed to have been formed through devitrification (weathering) of vitreous volcanic ash and tuff, frequently in the presence of water, followed by partial silica elimination, and final montmorillonite crystallisation. The chemical composition of the bentonite in a deposit depends on the temperature of the water in which the volcanic ash had formed [51].

2.1.1 Structure and properties of smectite-type clay minerals: Montmorillonite

For a better understanding of the properties of bentonite and its safety functions in a GDF, the present subsection provides a summary description of a typical structural configuration of smectite-type clay minerals, as well as a brief depiction of its fundamental properties.

Smectite clay minerals are the result of the association of tetrahedral and octahedral sheet-types. A tetrahedral sheet/entity is constituted by infinite tetrahedrons periodically repeated. A single tetrahedron consists of a central cation (T, commonly Si^{4+}, Al^{3+}, and Fe^{3+}),

coordinated with four oxygens. Of the four oxygen anions, three are basal oxygens (Ox_b) and one an apical oxygen (Ox_a), as shown in Figure 2.1 (a). Therefore, each tetrahedron unit is linked with other neighbouring tetrahedrons by sharing the three basal oxygens, forming a bidimensional hexagonal mesh pattern or tetrahedral sheet/entity along the crystallographic directions; a and b, as displayed in Figure 2.1 (b) [54]. An octahedral sheet/entity is composed of linked octahedrons, forming infinitely extending sheets lying on triangular faces, oblique to the tetrahedral sheets. Each octahedron is constituted by a central cation (O, usually Al^{3+}, Mg^{2+}, Fe^{3+} and Fe^{2+}) coordinated with six oxygens atoms which are linked to other octahedra by sharing edges (Figure 2.2 (a)).

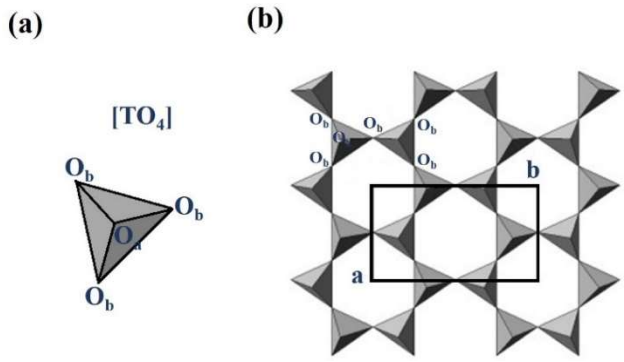

Figure 2.1: *(a) Tetrahedron unit, (b) tetrahedral sheet/entity where O_a refers to the apical oxygen, O_b refers to the three basal oxygens, a and b being the unit cell parameters. Adapted from* [54].

Linked octahedra tend to form different topologies relying upon the hydroxyls, OH, (Ox_o) positions, distinguishing: (*i*) cis-oriented octahedrons when positioning is along the edges (Figure 2.2 (a)); and (*ii*) trans-oriented octahedrons when positioning occurs along the diagonal (Figure 2.2 (b)) [54].

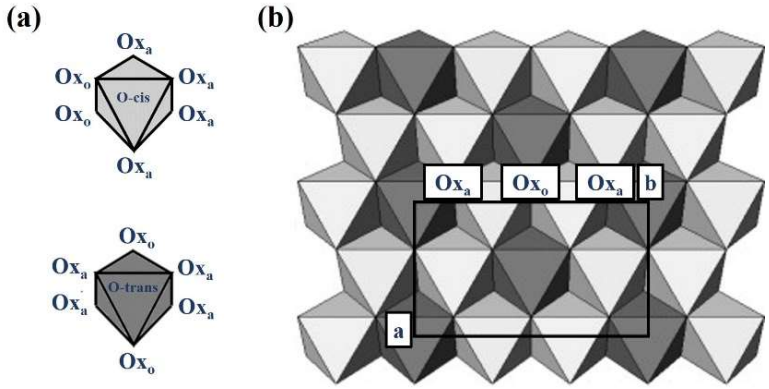

Figure 2.2: *(a) Ox_o (OH) topologies resulting in cis- and trans- octahedrons, (b) displays its respective location in the octahedral sheet or entity. Ox_a and Ox_o refers to the apical oxygens and anionic positions, a and b being the unit cell parameters. Adapted from* [54].

Tetrahedral and octahedral sheets are connected through the oxygen apical atoms of the tetrahedrally entities, forming a common plane with octahedral anionic positions Ox_o (OH^-, F^-, Cl^-, O^-), without being the latter's shared with the tetrahedra (Figure 2.3). A typical 2:1 smectite structure is formed by two tetrahedral sheets sandwiching a central octahedral entity, as depicted in Figure 2.3, where two tetrahedral entities pertaining to one layer each are oppositely oriented and facing the upper and lower surfaces of an octahedral sheet, with two-thirds of the OH groups replaced by tetrahedral apical oxygens atoms. The outer layer surface is comprised by the tetrahedral basal oxygen atoms [54].

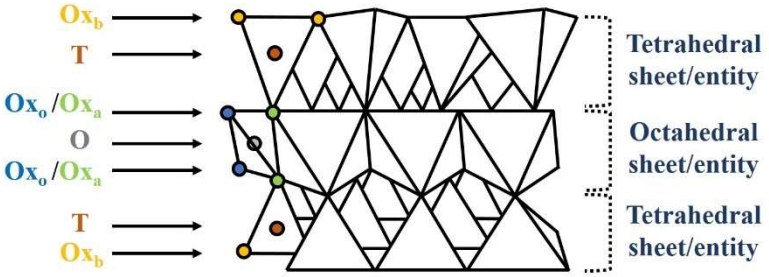

Figure 2.3: *Schematic of a typical 2:1 structure, showing the tetrahedral and octahedral sheet/entity configuration linked together. Modified from* [54].

In smectites, when tetrahedral and octahedral entities are joined together forming a layer, the final structure is usually negatively charged, with a total layer charge ranging between 0.2 to 0.6 per half unit cell [54]. Electrical neutrality is present when: (*i*) two central atoms of two octahedrons are occupied by trivalent cations (O^{3+}), while presenting a vacancy in a third octahedron; (*ii*) all the central atoms are occupied by divalent cations (O^{2+}) in the octahedral sheet; or (*iii*) all tetrahedrally central atoms (T) are occupied by Si^{4+} [54].

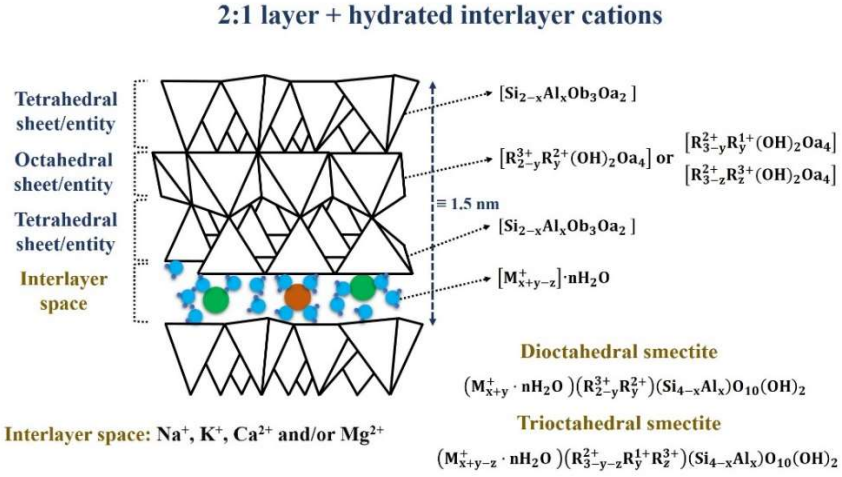

Figure 2.4: *Schematic of 2:1 layer structure with hydrated interlayered cations. Modified from* [54].

The characteristic negative charge of smectite-type clay minerals is balanced by inserting positively charged cations into the interlayer space located between two layers, with Na^{+}, K^{+}, Ca^{2+} and Mg^{2+} as the most common generic cations in the interlayer (Figure 2.4). A large range of different cations can occupy tetrahedral and octahedral positions, as well as the interlayer positions. Isomorphic substitutions along the tetrahedral and octahedral entities lead to different layer charge locations, affecting the hydration and cation speciation in the interlayer space. When substitution of Si^{4+} for trivalent cations (R^{3+}) occurs in tetrahedral positions, this creates an excess of negative charge on the three basal oxygens (Ox_b) and apical oxygen (Ox_a). Substitutions of trivalent cations (R^{3+}) for divalent cations (R^{2+}) in octahedral sites, and/or presence of vacancies in trioctahedral species, also induces an excess of negative charge. Therefore, isomorphic substitutions in tetrahedral and octahedral locations affect the local negative charge and the total layer charge of the 2:1 layer, and this is compensated by the speciation of the cations present in the interlayer spacing [54].

Furthermore, variable charging in smectite-type clay minerals can also arise by the presence of unsaturated bonds at edges and external surfaces, and dissociation of accessible hydroxyl groups. The latter variations in charge are strongly dependant on the pH of the aqueous environment and ionic activity in which the smectite clay minerals are residing, and its global contribution to the total layer charge varies between 10 and 20%, depending on particle morphology and the ratio of the edge surface [55], [56]. Negative charge emerging from isomorphic substitutions accounts for around 80% of the total layer charge and is independent of the pH and ionic activity of the medium, and it is designated as a permanent layer charge [55].

This particular structural arrangement has led to smectites being defined as 2:1 phyllosilicates, within which the following typologies can be established: (*i*) dioctahedral smectites; and/or (*ii*) trioctahedral smectites [54]. In dioctahedral smectites as montmorillonite, the octahedral sheet is mainly occupied by trivalent cations, whereas in trioctahedral smectites the octahedral sheet is mainly occupied by divalent cations. Therefore, the general formula for di- and tri-octahedral smectites can be expressed as in Equations 2.1 and 2.2:

$$\left(M^{+}_{x+y} \cdot nH_2O\right)\left(R^{2+}_{3-y}R^{2+}_{y}\right)(Si_{4-x}Al_x)O_{10}(OH)_2 \qquad \text{Equation 2.1 [54]}$$

$$\left(M^{+}_{x+y} \cdot nH_2O\right)\left(R^{2+}_{3-y}R^{+}_{y}\right)(Si_{4-x}Al_x)O_{10}(OH)_2 \qquad \text{Equation 2.2 [54]}$$

where x and y are the layer charges from tetrahedral and octahedral sites, R^{3+} and R^{2+} are the generic divalent and trivalent cations in octahedral positions, and M^{+} is the generic interlayer cation [54]. Figure 2.5 displays structural equations of the most common dioctahedral and trioctahedral smectites.

Dioctahedral smectite

Montmorillonite: $(M_y^+ \cdot nH_2O)(Al_{2-y}^{3+}Mg_y^{2+})Si_4^{4+}O_{10}(OH)_2$

Beidellite: $(M_x^+ \cdot nH_2O)Al_2^{3+}(Si_{4-x}^{4+}Al_x^{3+})O_{10}(OH)_2$

Nontronite: $(M_x^+ \cdot nH_2O)Fe^{3+}{}_2(Si_{4-x}^{4+}Al_x^{3+})O_{10}(OH)_2$

Volkonskoite: $(M_x^+ \cdot nH_2O)Cr_2^{3+}(Si_{4-x}^{4+}Al_x^{3+})O_{10}(OH)_2$

Trioctahedral smectite

Hectorite: $(M_y^+ \cdot nH_2O)(Mg_{3-y}^{2+}Li_y^+)Si_4^{4+}O_{10}(OH)_2$

Saponite: $(M_x^+ \cdot nH_2O)Mg_3^{2+}(Si_{4-x}^{4+}Al_x^{3+})Si_4^{4+}O_{10}(OH)_2$

Sauconite: $(M_x^+ \cdot nH_2O)Zn^{2+}{}_3(Si_{4-x}^{4+}Al_x^{3+})Si_4^{4+}O_{10}(OH)_2$

Figure 2.5: *Structural equations of di- and trio- octahedral smectites. Modified from* [54].

Hydration in smectite-type clay minerals occurs through different mechanisms and, therefore, water is present in different forms: (*i*) absorbed water in inner and outer surfaces; (*ii*) condensed water in structural micropores; and (*iii*) water in the interlayer space [54].

Smectite hydration by water uptake in the interlayer space defines its characteristic swelling capacity and, thus, its sealing capacity, guaranteeing its performance as an insulating barrier for HAW over long periods of time.

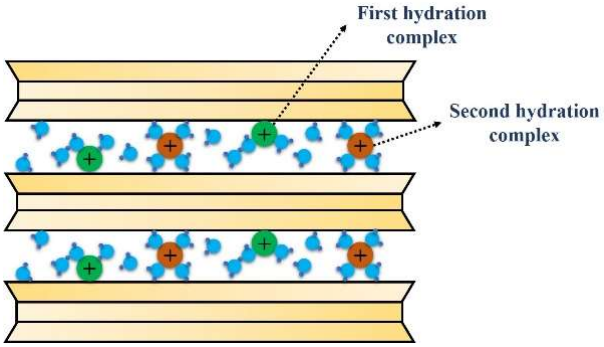

Figure 2.6: *Interlayer hydration complexes.*

The degree of interlayer hydration is associated with the nature of the interlayer cations present and the layer charge. Interlayer water uptake in smectites occurs in a staggered manner, progressively separating two adjacent layers, giving rise to the swelling phenomenon. This process mainly depends on: (*i*) the hydration energy of interlayer cations; (*ii*) polarisation

processes between interlayer cations and water molecules; (*iii*) cation-layer electrostatic attraction; and (*iv*) size and morphology of smectite particles [54]. Therefore, two different hydration complexes can be distinguished in the interlayer space (Figure 2.6). The first hydration complex is a direct consequence of the bonds formed between an interlayer cation and the clay mineral surface on one side, and with several water molecules on the other side [54]. The second hydration complex is formed when the surface of an interlayer cation is completely surrounded by water molecules, and it interacts with the upper and lower surfaces in the interlayer space though its water ligands [54].

Smectite-type clay minerals are also characterised by an ability to exchange cationic species, balancing the negative layer charge emerging from isomorphic substitutions. The CEC is, therefore, one of the fundamental properties of smectites, enabling exchange of ions fixed on the outer surface of smectite crystals, in the interlayer space, or in other interior spaces with a surrounding aqueous solution. The CEC is characterised by its reversible nature, controlled diffusion, stoichiometric features and the existing selectivity of one cation over another [54]. This ion-exchange capability strongly influences the smectite properties such as: (*i*) its cation retention; and (*ii*) diffusion processes of charged and uncharged molecules [57]. These processes will influence cation and molecule migration, which is an important consideration in the case of container failure within a GDF.

Since the Febex in-situ test was performed with Febex bentonite, which structurally is composed of the interstratified minerals illite and smectite, it is crucial to mention: (*i*) illite structural characteristics; (*ii*) transition mechanisms of illite-smectite mixed layers; and (*iii*) transformation mechanisms of smectite to illite, since the co-existence of expandable and non-expandable layers may be an important feature to consider when using this material as a buffer and backfill in future GDF.

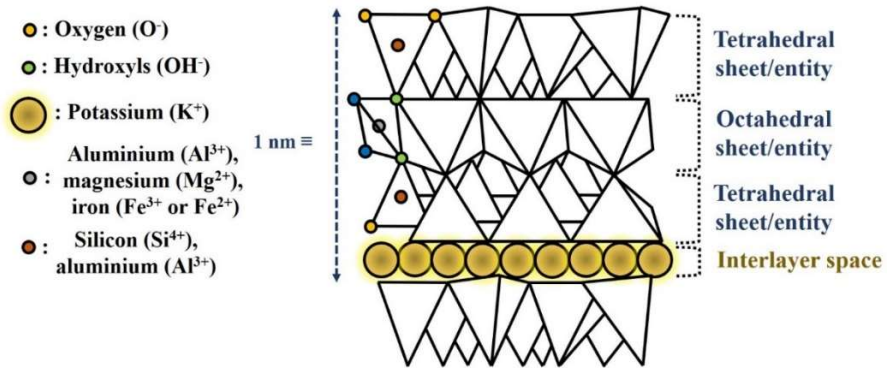

Figure 2.7: *Illite structure. Modified from* [54].

Illite is a dioctahedral 2:1 phyllosilicate characterised by a non-expansible interlayer due to its occupation by poorly hydrated potassium cations, hence it is not a swelling clay. Structurally, illite is similar to muscovite, but it differs from the latter in that on average it contains more silica, magnesium, iron and structural water, less aluminium in the tetrahedral layer and less potassium in the interlayer space. Its structure was Rietveld-refined by Gualtieri et al. [58]. This characterisation led to the following key conclusions: (*i*) the interlayer space is characterised by the presence of K^+ (~80%); (*ii*) the percentage of trans-vacant (tv) layers is higher than the cis-vacant (cv) layers; and (*iii*) the presence of 1M disordered domains or rotational disorder together with a 1M dominant polytype.

The existence of illite-smectite mixed layers in bentonite has attracted the attention of many researchers and such a stacked structure has been widely investigated using two proposed models: MacEwan [59] and Nadeau et al. [60]. The model developed by MacEwan [59] suggests that smectite-to-illite transition occurs through a solid-state transformation (SST) by remodelling the chemistry and structure of smectite without disrupting its layer stacking. Through transmission electron microscopy (TEM), Nadeau et al. [60] observed the existence of fundamental plate-like particles 1nm thick, able to absorb water and organic molecules. Thus, illite-smectite (I/S) particles, in this model, are composed of two units of said 1nm thick particles linked together by the interlayer K^+. Nadeau et al. [60] stated that this new particle is the precursor of mixed I/S layers.

The smectite-to-illite transformation is dominated by the following crystal-chemical parameters: (*i*) interlayer K^+ abundance; (*ii*) substitution of Al^{3+} by Si^{4+}; and (*iii*) interlayer hydration, in addition to time, temperature and pressure as physical parameters [54]. The dynamics of this process were modelled by Altaner and Ylagan [61], who proposed that the illite-smectite structure must be interpreted as: (*i*) chemically homogeneous non-polar 2:1 layers; and (*ii*) as polar 2:1 layers with charged smectite on one side and charged illite on the other. In the polar model, the subsequent reaction mechanisms are the precursors of smectite illitisation: (*i*) SST; (*ii*) dissolution and recrystallisation; and (*iii*) Ostwald ripening, providing that best approximates smectite illitisation in rock-dominated systems such as bentonite. Illite lacks water within its structure, enabling its layers to build up uniformly as illitisation of smectite progresses. As illite content increases, the thickness of the assembled layers increases as well, and in x-ray diffraction (XRD) this manifests itself as the 001 reflection becoming progressively sharper [54].

2.1.2 Importance of bentonite's rheological properties in HAW repositories

As bentonite, in many international repository programmes, is intended to be used as a buffer material, it will be a crucial component in a GDF design, and so will have a significant impact on the evolution and behaviour of the repository in the medium and long-term. Bentonite's main function is to provide a secure chemical and mechanical environment around the HAW storage container, limiting exposure of the container surface to aggressive chemical species and, in the long-term, inhibiting the transport of radioactive substances towards the geosphere. Therefore, this buffer material provides a major safety function during the installation, operation and subsequent closure of repositories.

Since one of the main objectives in a GDF is to provide mechanical protection, its rheological properties require consideration. Such properties have been researched over several decades. Some of the most important parameters to contemplate are its: (*i*) swelling pressure; (*ii*) hydraulic conductivity; (*iii*) suction or retention properties; and (*iv*) shear strength, along with (*v*) its thermal conductivity.

Bentonite swelling pressure has been rigorously studied, since it will determine the facility's sealing capability. As already indicated, when bentonite is in an aqueous medium it incorporates water into its structure and sequentially swells exerting pressure on boundary surfaces or materials. Swelling prevents a premature contact between the HAW container and groundwater in the surrounding host rock. This effect also enables the sealing of gaps already present in the installation, and those formed due to the existing erosion processes during repository evolution, besides maintaining the container in position despite any physical settlement. Research performed on bentonite swelling pressure concluded that this property is strongly dependant on parameters such as: (*i*) dry density; (*ii*) degree of saturation; (*iii*) temperature; and (*iv*) pore water chemistry (including pH), and its correlations have been widely predicted in the literature [62], [63], [64]. For bentonite to comply with its functions as an artificial barrier, it must initially be heavily compacted in block or pellet forms at its initial hygroscopic water content. During compaction, the dry density increases as pressure is applied, and the increase of dry density exponentially raises the bentonite's swelling pressure, since compaction reduces the number of air-filled pores, as displayed in Figure 2.8 (a). Hence, the

concept is that bentonite is emplaced heavily compacted at its hygroscopic water content before subsequently wetting and swelling in-situ to seal in the waste packages.

Controversial data have been published related with the water content or degree of saturation. Villar and LLoret [63] and Ye at al. [64] reported that the initial water content seems to have no influence on the swelling behaviour of bentonite upon compaction. Delage et al. [65], Romero et al. [66] and Tarantino and De Col [67] claimed that bentonite's degree of saturation increases when dry density increases due to a decrease in the void ratio associated with the presence of macropores. Conversely, Sudhakar and Ravi [68], observed at high dry densities, a decrease on swelling pressure while increasing the initial degree of saturation, as shown in Figure 2.8 (b).

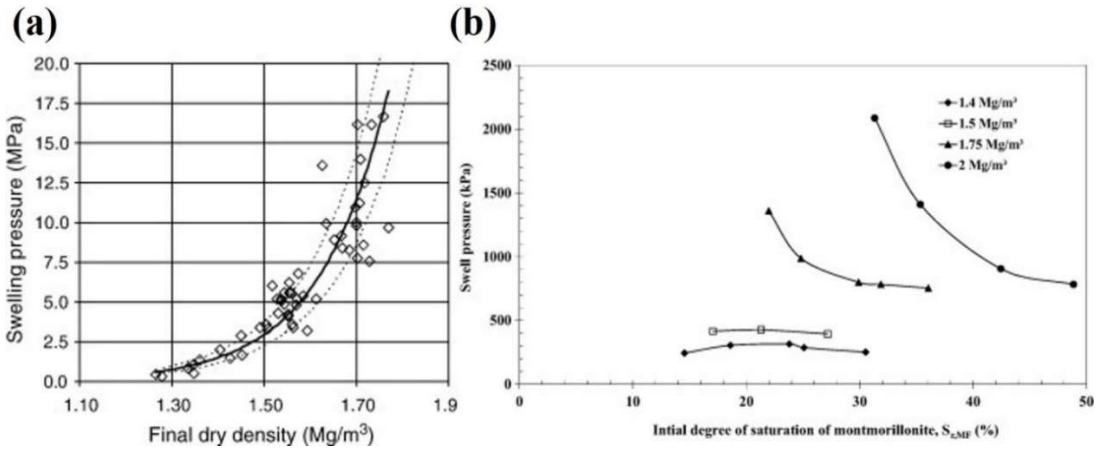

Figure 2.8: *(a) Bentonite swelling pressure vs degree of saturation. Adapted from* [63]*, (b) bentonite swelling pressure vs initial degree of saturation. Adapted from* [68].

With regard to the effect of temperature on bentonite swelling pressure, conflicting results are reported, since its determination depends on the experimental conditions, degree of compaction, water content and type of bentonite utilised. Both a decrease and increase of swelling pressure with temperature have been reported. The reduction of swelling pressure at increasing temperature has been attributed to the movement of water molecules from micro- to macro- pores [69], [70], loss of hydrating water [71] and cement formation [72], [73]. On the other hand, observed increases in swelling pressure have been ascribed to the influence of temperature on the pore pressure, hydration pressure and osmotic pressure [74], [75], as well as increase of ion diffusion and thermal energy [76]. The salt content in bentonite pores would seem to be another major factor that influences its swelling capability. Results derived from experiments at different solution concentrations led to the conclusion that the salinity of the pore water clearly decreases the swelling pressure [77], [78]. This observation may be

explained due to the influence exerted by the infiltrating solution which may trigger changes in the microstructure of bentonite and, therefore, over the swelling aggregates [78], [79], [80].

Bentonite, because of its fine particle size and consequent micropores and high surface charges, possesses low hydraulic conductivity, which is a desired feature for a GDF since impermeability will prevent fluxes of corroding agents reaching the waste container and delay the escape of radionuclides in the case of container failure. Bentonite's hydraulic conductivity after compaction is determined by the selected dry density, the degree of saturation, the chemistry of the pore water and the temperature, and it varies very much depending on whether it is determined in saturated or unsaturated conditions. Generally speaking, the hydraulic conductivity of bentonite decreases with an increase in dry density and resulting decrease in the degree of saturation due to the smaller pore space availability [69], [81], [82], as shown in Figure 2.10 (a). Furthermore, when compacted bentonite is exposed to temperatures in the range of 20-80°C, it shows an increase in its hydraulic conductivity. Cho et al. [83] explained this increase due to an increase in bentonite viscosity, while the effect of the temperature did not seems to have a great influence on bentonite hydraulic conductivity (Figure 2.10 (b)).

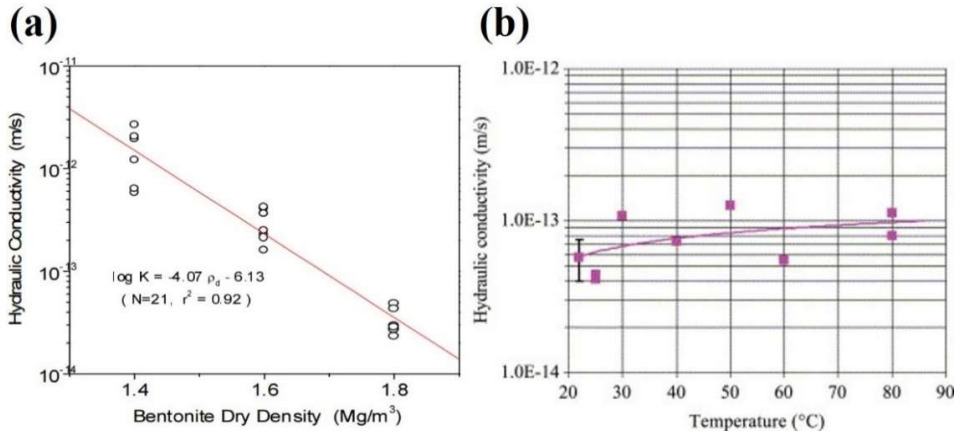

Figure 2.9: *(a) Bentonite hydraulic conductivity as a function of dry density variation. Adapted from* [84]*, (b) bentonite hydraulic conductivity as a function of temperature variation at an average dry density of 1.58g/cm³. Adapted from* [69].

Also, the presence of certain ionic species (Na^+ and Cl^-) in the pore fluid results in an increase of bentonite hydraulic conductivity [85], [86]. As interlayers are more charge satisfied by cations and, hence, water is not electrostatically hindered.

When bentonite is partially saturated, negative pressures can appear in pores, up to MPa in magnitude. The suction or retention properties of bentonite are defined by the accessibility of water at a boundary, and owing to the large gradients, flow occurs and increases the degree of

saturation until bentonite becomes completely saturated. As the degree of saturation increases, the hydraulic conductivity increases principally because of the availability of a bigger area for the flow to occur through. Two possible scenarios can be deduced from the suction or retention properties of bentonite: (*i*) if bentonite is constrained at its boundaries, swelling pressure increases as degree of saturation increases; and (*ii*) if on the contrary, bentonite is not constrained at its boundaries, it will absorb large amounts of water, and will freely expand as its degree of saturation gradually increases. This process may also be affected by the ionic species present in the absorbed water [78], [87], [88]. Basically, it will swell to fit the space available, ideally as a self-sealing backfill material.

In a GDF, the waste containers will be deposited in drilled boreholes within the host rock and surrounded by the bentonite buffer. As a consequence of the tectonic activity of the selected site, or stress alterations triggered by the excavation activities during repository construction, shear displacements in the rock may occur. Mechanically isolating the waste containers from externally displacements of the repository structure, Leupin et al. [89] provided a detailed description of buffer safety functions related with canister protection, and affirmed that the plasticity of bentonite will alleviate shear stress transfer into the canister in case of rock displacements. Nevertheless, the degree of bentonite compaction and, hence, its dry density must be limited for bentonite to exhibit a less ductile and more brittle behaviour. Conversely, in the event of a mass displacement in the host rock, bentonite must have a high dry density to prevent canister displacement and stress transfer. Consequently, the clay barrier must remain sufficiently ductile to absorb internal and external stresses and deform, but at the same time must maintain a high shear strength to prevent excessive canister displacement (Figure 2.10).

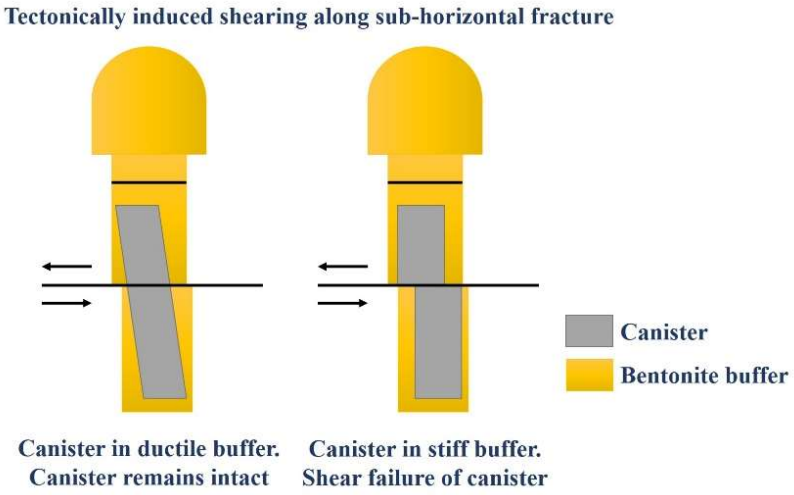

Figure 2.10: *Schematic view of barrier ductility importance. Modified from* [90].

Bentonite must also dissipate any emergent heat from the waste containers to avoid heat accumulation at the bentonite-container interface that might accelerate corrosion or cause local drying of the bentonite, recognising that its thermal conductivity is relatively poor versus crystalline rocks. Therefore, bentonite's thermal conductivity must be as large as possible. As with the swelling pressure, bentonite's thermal conductivity is determined by the compaction, since it is strongly correlated with the volume fraction of air present in pores. For a given dry density and after compaction, bentonite thermal conductivity becomes high due to the decline of air-filled pores. In response to water saturation, the same effect is observed owing to the larger conductivity of water compared to air [91], [92], [64]. Additionally, it has been seen that bentonite mineralogical composition also influences its thermal conductivity, since higher concentrations of certain accessory minerals, such as quartz, induces higher conductivities [92]. Despite the fact that higher dry density and water content lead to higher thermal conductivity, these are not alone expected to be sufficient for dissipating the heat generated by HAW. However, this will ultimately depend on the final thermal requirements of the disposal system [93]. Research on bentonite admixtures with graphite or quartz has shown a clear increase in thermal conductivity [64], [94], [95], [96], compared to unmodified bentonite.

2.3 Implications of bentonite alteration under expected repository conditions

Components manufactured from steel or other metals are present in most GDF designs and are not considered to be thermodynamically stable under geological disposal conditions. After repository closure, the geochemical environment at the interface between the enshrouding bentonite and the canister and, at the interface between bentonite and the host rock will evolve, conditioned by temperature and groundwater gradients. Landolt et al. [27] and Leupin et al. [89] reported a summary of the processes expected at the bentonite-container interface in the Opalinus clay formation, as depicted in Figure 2.11. Four main phases have been predicted after repository closure:

Phase 1 or aerobic dry: This phase begins after placing the containers in their respective boreholes drilled in the host rock. Approximately 5-10 years after container placement, the

interface-contact between the container and bentonite reaches 100-150°C. During this phase, there is a slow migration of groundwater away from the container surface, and the oxygen trapped at the interface is consumed as a result of container corrosion aided by the high temperatures. For the sake of simplicity, it is assumed that oxygen will reach the surface of the container uniformly, since oxygen diffuses rapidly through bentonite when it is partially saturated, although the bentonite blocks and pellets initially have a different dry density and water content. During this initial phase, the release of sulphates is expected due to the oxidation of sulphides present in the clay matrix, causing an acceleration of the oxidation process. In addition, there will be a redistribution of salts throughout the clay matrix, causing precipitation away from the container surface with commensurate bentonite desiccation.

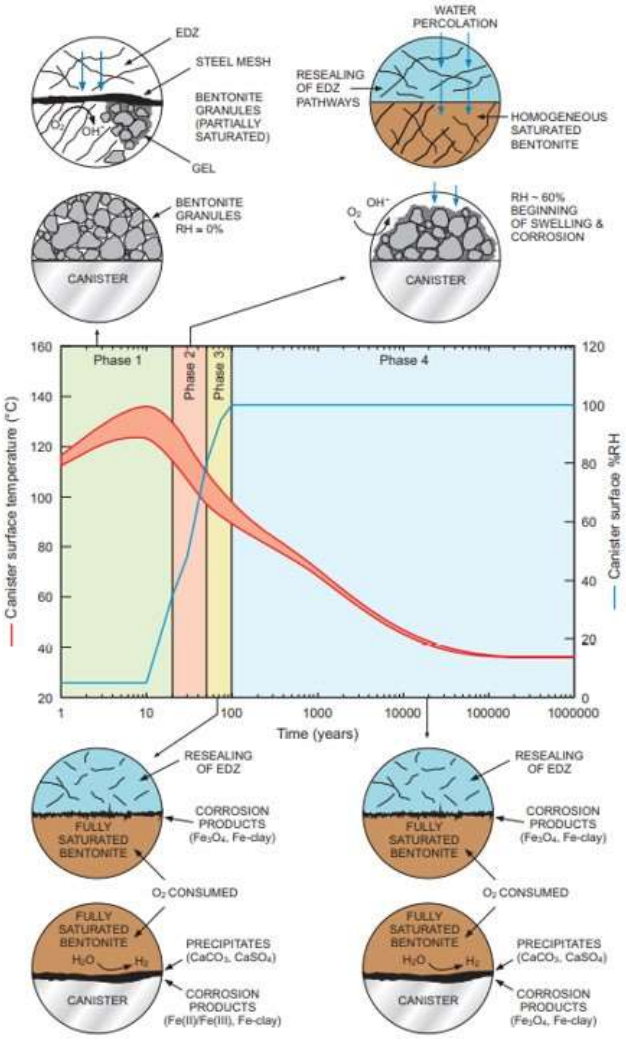

Figure 2.11: *Expected corrosion processes at the canister-bentonite interface and derived corrosion products. Adapted from* [27].

Phase 2 or aerobic unsaturated: This second phase is expected to last between 20 and 30 years. Once the maximum thermal peak of the HAW has been reached, as shown in the

Figure 2.11, a dry environment will have established itself around the container. As a result, there will have been a loss of bentonite volume owing to the water egress from the bentonite's voids. However, due to the migration of groundwater inwards from the clay barrier towards the container, the bentonite will slowly re-saturate. Under these conditions, and assuming that no significant mineralogical alterations have occurred in this time, the bentonite surrounding the container should recover its initial volume providing once again a completely sealed environment. Salts that may have precipitated during Phase 1 will re-dissolve and the bentonite's water content will progressively increase due to the gradual migration of water inwards into the repository from the bounding host rock. The saline content of the incoming water will result in changes in osmotic gradients and cation exchange. Due to the relatively high residual HAW temperatures, high pressures will develop inside the bentonite pores.

Phase 3 or anaerobic unsaturated: This phase corresponds to the transition period between aerobic and anaerobic conditions and is expected to last 50 years or beyond. The temperature at the HAW container surfaces will fall to values between 90-60°C, as shown in Figure 2.11. All the corrosion products formed in the aerobic phases will now to start to undergo chemical reduction. Therefore, further container corrosion will go anaerobic and hence rates will slow. In addition, the progressive saturation of the bentonite continues and, therefore, its swelling. At the end of phase 3, the bentonite should have reached full saturation and, thus, its swelling will have plateaued.

Phase 4 or anoxic: At the onset of this phase, bentonite is fully saturated, and all the corrosion products have been chemically reduced. Therefore, the only oxidant agent now available in the EBS is water. Under these circumstances, corrosion processes lead to hydrogen gas formation due to the reduction of protons and water. In addition, those initially dissolved secondary minerals can re-precipitate in carbonates or other phases and react with bentonite. After approximately 1,000 years, the pore water pressure decreases, resulting in bentonite consolidation. Furthermore, the mobile Fe cations may migrate through the clay matrix, possibly leading to the formation of Fe-rich minerals. The temperature at the canister surface will continuously decrease until eventually reaching values below 40°C after 10,000 years. This would mark the cessation of hydrothermal reactions.

The lifetime phases of a GDF described above are those expected in argillaceous host rock. However, Leupin et al. [89] also provides details of the expected evolution and boundary conditions for a concept set in crystalline host rocks. Leupin et al. [89] stated that the expected

phases in crystalline host rocks will be similar to those described for the Opalinus clay formation, only differentiated by the thermal limits and the hydraulic dynamics of the host rock. The potential iron corrosion processes on steel surfaces were described by Madsen [97]. As re-saturation occurs, the water absorbed by the clay barrier will access the contact interface, giving rise to a wet corrosion process that will result in magnetite and hydrogen formation. Once oxygen has been consumed at the interface, hydrogen and iron hydroxides are produced as a result of deprotonation of water molecules (Equation 2.3).

$$Fe_{(s)} + H_2O \rightarrow Fe(OH)_2 + H_2 \qquad \text{Equation 2.3 [97]}$$

The expected alkaline and anoxic environment at the contact interface at phase 4 will favour the formation of ferrous hydroxide which, in turn, will evolve readily to form magnetite and additional hydrogen (Equation 2.4):

$$3Fe(OH)_2 \rightarrow Fe_3O_4 + H_2 + 2H_2O \qquad \text{Equation 2.4 [98]}$$

Reduced iron species released during phase 3 and 4 might diffuse and interact with the buffer material, impairing its main chemical and mineralogical properties and, thus, its rheological properties, jeopardising its engineering barrier performance within a GDF. Therefore, induced corrosion under repository conditions may have two possible interaction paths through or with the buffer: (*i*) iron ion sorption processes via cation exchange or iron ion complexation at the edge sites; and (*ii*) chemical reduction of structural iron in the clayey matrix.

2.3.1 Sorption processes

Under reducing HAW repository conditions, released Fe^{2+} may be incorporated into the smectite structure by cation exchange in the interlayer space or by its complexation to edge sites. Sorption data reported in the literature posit that Fe^{2+} sorption by montmorillonite is strongly dependent on the pH conditions of the enveloping media [99], concluding:

(i) at acidic pH (~3.5-4), Fe^{2+} sorption is extremely strong,

(ii) at intermediate pH values (~3.5-4 to 7), the dominant Fe^{2+} sorption process is due to complexation into the edge sites and,

(iii) at basic pH media (>7), Fe^{2+} sorption shows a selectivity coefficient very similar to that of Ca^{2+}.

2.3.2 Reduction of smectite structural iron

In smectite-type minerals, iron seems to be the principle element in its structure that may potentially coexist in two relatively stable, but different, oxidation states; Fe(II) and Fe(III). The reduction of structural iron in smectite has been the subject of numerous scientific studies over the last few decades. Results indicate that the oxidation state of iron may profoundly alter the physicochemical properties of bentonite, and these changes may have important effects on its fundamental mineralogical, chemical and rheological properties.

Reduction of structural iron may lead to: (*i*) transformation of the smectite component to non-swelling minerals (1:1 or 2:1 phyllosilicates); and/or (*ii*) alter the smectite constituent to an iron-rich smectite. These two scenarios may lead to loss of the advantageous swelling capacity and, thus, its capability as a buffer. Smectite alteration into new neoformed minerals entails an increase in its crystallinity. As the degree of smectite crystallinity increases, its CEC, sorption properties and radionuclide retention capability would be progressively degraded due to the loss of interlayer sites, and OH edge-site accessibility, compromising the overall performance of the bentonite as a geotechnical barrier [100], [101], [102], [103].

Due to the instability of Fe(II)-rich trioctahedral smectites under atmospheric conditions, only a few experimental studies have been reported in the literature regarding their properties and the kinetics of the alteration process. Kohyama, Shimoda and Sudo [104] reported a rapid oxidation in less than an hour under atmospheric conditions of several trioctahedral Fe(II)-rich saponite samples. Collected from the glassy rhyolitic tuffs at Oya, Tochigi Prefecture (Japan), these samples provided crystallographic data which suggested that the oxidation process implied the consumption of structural hydroxyls. The resulting oxidation showed an increase of Fe^{3+} content, without loss of the smectite 2:1 structure. Badaut et al. [105] also reported the instability of a trioctahedral Fe(II) smectite retrieved from its natural environment of formation (Atlantis II Deep, SW basin (Red Sea)), observing a rapid oxidation of samples during desiccation under laboratory conditions.

Many studies have been performed on air-stable Fe(III)-rich smectites, such as nontronite. Stucki and Roth [106], Stucki, Golden and Roth [107], Stucki and Tessier [108], and Stucki, Bailey and Gan [109] performed experiments for reduction of structural iron on different ferruginous smectites and montmorillonites, using Na-dithionite ($Na_2S_2O_4$) as a strong reducing agent. Results revealed that the chemical reduction of Fe^{3+} in smectite leads to

an increase of the layer charge, causing layers to collapse and stack, showing a greater order in the *a-b* dimension. Other reversible changes in mineralogical structure and smectite composition were also observed during Fe^{3+} reduction that affected, among other properties, its effective surface. During smectite structural iron reduction experiments, small amounts of silica and iron were dissolved, but it was concluded that this effect was independent of smectite oxidation state.

Other mechanisms for accommodating the reduction of Fe^{3+} to Fe^{2+} have been suggested; Manceau et al. [110] used several analytical techniques to investigate the coordination number and crystallographic occupation of Fe^{2+}, changes in-plane and out-of-plane in layer structure, and monitor possible changes in OH and H_2O structural groups in highly-reduced Garfield nontronite samples. Conclusions were: (*i*) after a complete reduction, Fe^{2+} remains six-fold coordinated; (*ii*) polarised extended x-ray absorption (P-EXAFS) revealed some of the reduced iron atoms occupy trans-vacant (tv) positions, and out-of-plane P-EXAFS data relative to the layer structure showed that the structural iron reduction revoked the corrugation of basal oxygens of dioctahedral smectites, leading to the formation of a flat basal surface typical of trioctahedral layers; (*iii*) x-ray diffraction data revealed iron migration from cis- to trans-vacant positions (around 28% of the reduced iron); and (*iv*) infrared analyses unveiled the loss of nontronite's dioctahedral nature and the formation of a new vibrational band close to that assigned to OH of structural hydroxyl groups associated with trioctahedral $[Fe^{2+}]_3OH$ stretching vibrations. The gathering of these results allowed the development of a model to explain the reduction mechanism of Garfield nontronite.

Subsequently, Drits and Manceau [111] proposed a model to reassess the experimental data published on chemical reduction of structural iron in smectites. The proposed model aimed to predict the chemical composition of smectite, considering the modification of its properties as a function of the degree of reduction. In the reduced state, structural Fe^{2+} cations are six-fold coordinated (as previously stated by Manceau et al. [110]), which induces an increase in the negative layer charge usually compensated by Na^+ and H^+ uptake. These incorporated cations can react with structural hydroxyl groups, causing dehydroxylation and/or link up with unsaturated octahedral oxygens atoms. On this basis, Drits and Manceau [111], proposed two equations to explain the amount of Na^+ and H^+ incorporated into the smectite structure as a function of the amount of iron reduction. Results based on this model showed that the structural mechanism of Fe^{3+} reduction in montmorillonite differs from that determined in nontronite and

beidellite. Montmorillonite possess cis-vacant (cv) 2:1 layers, whereas nontronite and beidellite possess trans-vacant (tv) 2:1 layers, thus explaining the deviations between models. In cv octahedral sheets, hydroxyl pairs are bonded to three octahedral cations, while in tv sheets, OH pairs are bridged to two octahedral cations. In the montmorillonite framework, dehydroxylation requires the simultaneous migration of three neighbouring Fe^{2+} cations, so the required energy for this process to occur would be excessively high. Drits and Manceau [111] were able to conclude, therefore, that dehydroxylation in montmorillonite is very unlikely to occur, and the deficit in charge created by Fe^{3+} reduction is compensated for by increased Na^{+} sorption.

Iron reduction in smectite has been reported in tests performed with iron-reducing bacteria. Bio-reduction of structural Fe^{3+} in smectites is an area of research that has evolved rapidly since its discovery in 1987. Recent publications have shown that the reduction of Fe^{3+} in the octahedral sheet of smectites by bacteria results in a decrease of its specific surface area and ability to swell, and to an increase in its CEC [112], [113], [114]. This correlates with the work of Drits and Manceau [111], suggesting that Fe^{3+} reduction is compensated for by a more general increased cation sorption and an increased CEC.

2.3.2.1 Low temperature experiments within the framework of geological disposition of higher activity waste

In the scope of geological disposition of HAW, the majority of research has focussed on the study of metallic package corrosion in contact with bentonite. This has included examinations of the destabilising effects iron corrosion might have on montmorillonite, including conversion into new minerals. Many studies have centred on bentonite-iron admixtures and their behaviour when exposed to a range of temperatures. After interim storage, the heat emitted by the radioactive waste is expected to be around 100-125ºC [26], [115], [116], [117]. Thus, many countries have delimited a maximum acceptable surface container temperature of that value, which, moreover will prevent excessive damage to the geotechnical barrier material that envelops the waste containers [118], [119].

At temperatures below and in the range of 80-100ºC, Mueller-Vonmoos et al. [120] evaluated the effect of magnetite and iron powders in sodium and calcium bentonites (MX-80 and Montigel, respectively) under hydrogen-saturated steam conditions to evaluate swelling behaviour, variations in CEC and exchangeable cation population. They also investigated the behaviour of trivalent iron in the interlayer space. The experiments simulated the conditions

expected in a repository, assuming a surface HAW canister temperature of 80ºC under anoxic conditions for 100 days. Under these experimental conditions, formation of magnetite and hydrogen were noticeable, but no significant changes were observed on swelling pressures, CEC, exchangeable cation population and layer charge in both bentonites, and no evidence of iron uptake by the clay and/or transformation were detected. Later experiments conducted by Madsen [97], which consisted of MX-80 bentonite admixtures with zero-valent iron, resulted in similar conclusions.

Experimental work carried out by Lantenois et al. [101], Perronnet et al. [121], Osacký et al. [122], De Combarieu et al. [123], and Lanson et al. [124] showed bentonite destabilisation at experimental temperatures similar to those utilised by Mueller-Vonmoos et al. [120] and Madsen [97]. Lantenois et al. [101] conducted an experiment to investigate the interactions between iron powders and a variety of natural and synthetic smectite samples (dioctahedral and trioctahedral smectites) at 80ºC for 45 days. At basic pH, systematic destabilisation of smectite and metal iron was apparent, leading to the formation of magnetite and 1:1 phyllosilicate phases, odinite and cronstedtite. From these results, Lantenois et al. [101] proposed a model which involved the deprotonation of $Fe^{3+}OH$ released from the smectite structure, while the metal Fe acted as a proton acceptor, giving rise to metal corrosion. The resulting Fe^{2+} was absorbed at the edges of the smectite particles, inducing the reduction of structural Fe^{3+} and favouring its migration into the smectite interlayer to compensate for the layer-charge deficit. Hereafter, the interlayered Fe^{2+} migrated to octahedral locations to compensate for the extremely large deficit formed in the interlayer. As a consequence, newly formed trioctahedral domains emerged due to the migration of Fe^{2+} cations.

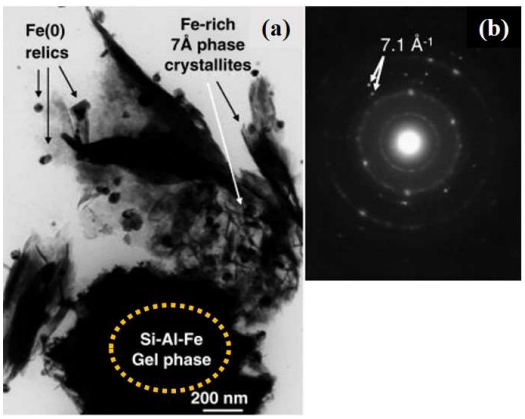

Figure 2.12: *(a) Fe-rich 7Å clay minerals associated with high density of Si-Al-Fe gels, (b) diffuse SAED pattern of transformed material. Adapted from* [121].

Using the same temperatures as Mueller-Vonmoos et al. [120] and Lantenois et al. [101], Perronnet et al. [121], carried out an experiment, consisting of admixtures of bentonite and metallic iron at different ratios exposed at 80ºC for 45 days. This study showed that kaolinite and smectite from different bentonite samples were altered into Si-Al-Fe gels (Figure 2.12) when in contact with metallic iron, evolving into iron-rich di- and tri-octahedral phyllosilicates (odinite and greenalite), in addition to the presence of magnetite as the main iron corrosion product. Different considered ratios underlined that bentonite-iron interaction is strongly dependant on the metallic iron availability. Osacký et al. [122] investigated the stability of seven different dioctahedral smectites, montmorillonite, beidellite and a ferruginous smectite, all representing bentonites from different formations. This work consisted of bentonite admixtures with pure iron powder subjected to 75ºC temperatures for 35 days in a nitrogen atmosphere. Analytical data from the samples showed that magnetite was the main arising corrosion product and the bentonites reacted differently with iron, the Fe-rich smectite being highly affected by the interaction (nascent forms of berthierine-like minerals). Results suggested that the octahedral iron cations may be responsible for smectite decomposition, causing partial dehydroxylation and altering the octahedral and tetrahedral sheets, leading to a decrease of thickness and layer charge.

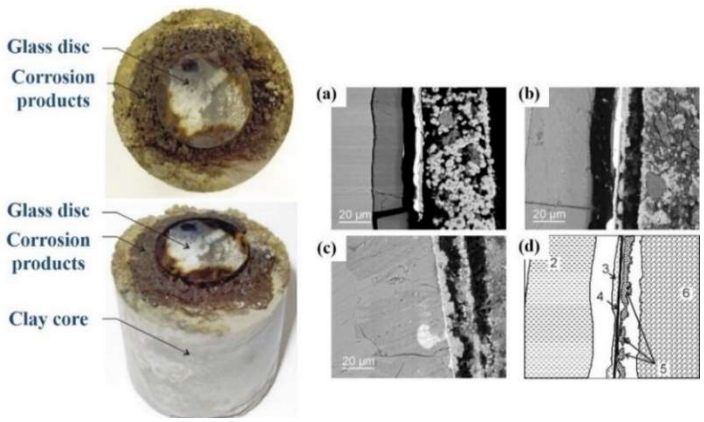

Figure 2.13: *(a-c) Scanning electron microscopy (SEM) images in backscattered electron (BSE) mode showing the glass-iron-clay interface after (a) six months, (b) ten months, (c) 16 months of reaction, (d) structural interpretation where (4) shows the thin layer belonging to Fe-rich silicates. Adapted from* [123].

In the same temperature range (90ºC), De Combarieu et al. [123] experimented with glass-iron-clay set ups (Figure 2.13) to investigate the coupled interactions between the glass, the corroded iron, and clay alteration for 6-18 months, characterising the developing interface regions. Iron corrosion led to magnetite and siderite formation as principal corrosion products; the presence of iron-rich phyllosilicates in the interface were also observed. These Fe-rich

phyllosilicates mainly consisted of 1:1 and 2:1 phyllosilicates (Figure 2.13), suggesting the presence of berthierine, nontronite and/or minnesotaite.

Lanson et al. [124] also contacted iron with bentonite heated to 80ºC to characterise the crystal-chemistry of the newly formed phyllosilicates. In accordance with results obtained by Lantenois et al. [101] and Perronnet et al. [121], the neoformed minerals originated from Si-Al-Fe gel maturation, resulting in smectite destabilisation in which iron predominates over magnesium. In iron-admixtures with beidellite and montmorillonite, Lanson et al. [124] identified two different particle populations (Type I; thicker particles and type II; thinner particles). In octahedral allocations, the presence of Type I was higher than the Type II the oxidation state of Type I lower that of type II. In the reacted nontronite, the particles found were an intermediate particle between Types I and II. These results refuted the already-mentioned formation by other authors of 1:1 phyllosilicate as berthierine, odinite and cronstedtite-like. More recently, Rivard et al. [125] conducted a series of experiments, using callovo-oxfordian clay mixed with iron powders, quartz, calcite and pyrite, subjected to temperatures of 90ºC for 1, 3 and 9 months. Experiments were also carried out in the presence of NaCl and $CaCl_2$ solutions. Formation of serpentine-like minerals were the predominant arising products, along with magnetite.

Experimental work at lower temperatures, 30ºC and 50ºC [126], has been also implemented to investigate the iron uptake by bentonite and the extent of changes induced in montmorillonite structure. The results did not show any evidence of montmorillonite alteration, although iron diffusion through the expansible material was apparent. However, Bildstein et al. [127] modelled clay-iron interactions, considering a canister temperature of 50ºC over 10,000 years to predict mineralogical transformation of the bentonite buffer. Calculations made through this model showed that the main arising corrosion products are magnetite and siderite at the bentonite-container interface. In immediate contact with the canister, the primary clay minerals were destabilised into iron-rich smectite-like minerals (cronstedtite and berthierine), with lower CEC, swelling capability and porosity. Modelling work performed by Savage et al. [128] contemplated the Ostwald step sequence to address the slow growth of bentonite alteration products. Simulations showed the following sequence of alteration products: magnetite→cronstedtite→berthierine→chlorite. It was concluded that chlorite formation/growth is not achieved until after 5,000 years of simulation time. Table 2.1 collects the main results from experimental work performed in the scope of low temperatures.

Table 2.1: *Experimental data on smectite transformation at low temperatures.*

Reference	Bentonite	Time	T (°C)	Reactants	Corrosion products	Neo-formed iron phases
Mueller-Vonmoos et al.	MX-80 and Montigel	100 days	80	Metallic iron in the form of iron powder	Magnetite	None
Madsen	MX-90	180 day	80	Metallic iron	Magnetite	None
Lantenois et al.	Natural and synthetic smectite samples (di-and tri- octahedral)	45 days	80	Metallic iron	Magnetite	Odinite and cronstedtite
Carlson et al.	MX-80	900 days	30-50	Coupons and wires	Magnetite, goethite, hematite	No iron silicates detected
Perronnet et al.	FoCa7 bentonite	45 days	80	Metallic iron	Magnetite	Odinite and greenalite
Osacký et al.	Montmorillonite, beidellite and ferruginous smectite	35 days	75	Pure iron powder (nitrogen atmosphere)	Magnetite	Berthierine
De Combarieu et al.	Callovo-Oxfordian clay	6-18 months	90	Pure iron foil	Magnetite and siderite	Berthierine, nontronite and/or minnesotaite
Lanson et al.	Montmorillonite and beidellite	45 days	80	Metallic iron	Magnetite	Berthierine, odinite and cronstedtite
Rivard et al.	Callovo-Oxfordian clay	1, 3, 9 months	90	Metallic iron	Magnetite	Serpentine particles

2.3.2.2 High temperature experiments within the framework of geological disposition of higher activity waste

Thus far, a compilation of the most critical experimental and modelled data within the scope of 'low temperatures' completed to date has been provided. Simultaneously, research considering high temperatures along with low temperatures has been also performed, and a summary of the results achieved are given below.

Wilson et al. [102] investigated montmorillonite stability at the buffer-container interface using thermodynamic modelling to estimate the thermodynamic properties of Fe-rich clay minerals. Modelled results suggested that if pore water is oversaturated with respect to magnetite from the encasement, the most probable alteration product is the formation of Fe(II)-rich saponite, concluding that the alteration of montmorillonite under repository conditions will not be so harmful as long as the swelling capacity is maintained. To corroborate the modelled results Wilson et al. [103] performed two series of experiments. The first consisted of Na-montmorillonite admixtures with native Fe, calcite and NaCl solutions which were exposed to 250ºC for 93 and 114 days. In the second series, admixtures including Na-montmorillonite, magnetite, native Fe and solutions of $FeCl_2$ were exposed to temperatures of 80ºC, 150ºC and 250ºC for 90 and 92 days. From the first series, Wilson et al. [103] observed that the montmorillonite alteration to Fe-rich smectite (saponite-like) occurred when native iron was predominantly added to magnetite. The Fe-rich smectite was initially formed as an Fe^{2+}-rich smectite which when exposed to air, was oxidised to Fe(III)-rich smectite. In the second series, significant alteration was only observed at 250ºC, resulting in the presence of berthierine. Post-mortem analysis showed less expansion capability of the new neoformed mineral and partial dissolution of the tetrahedral sheet (Figure 2.14).

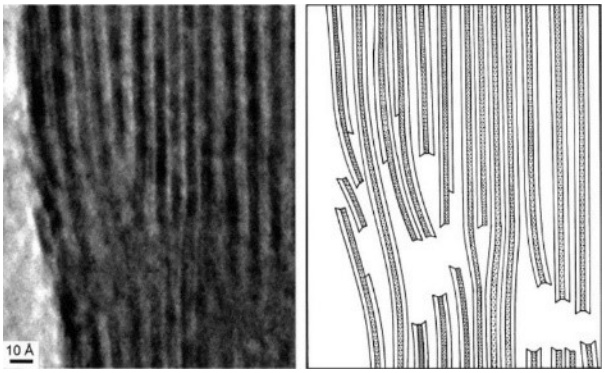

Figure 2.14: *TEM image and schematic interpretation of altered Fe-rich smectite Adapted from* [103].

Other experiments at high temperatures were conducted by Guillaume et al. [129] consisting of several batches of admixtures of MX-80 bentonite and metallic Fe and magnetite powders in low-salinity solutions at 300ºC to simulate the conditions expected in a GDF. Guillaume et al. [129] claimed the formation of new minerals (chlorite and saponite) due to montmorillonite alteration, while simulating the expected hydrothermal repository conditions over a period of nine months (Figure 2.15). Guillaume et al. [130] performed similar experiments on MX-80 bentonite at 80 ºC and 300ºC, using hematite and magnetite as an iron reactants in the presence of low-salinity solutions. At 80ºC non-significant changes were apparent, confirming the observations by Muller-Vonmoos et al. [120], while at 300ºC the presence of Fe oxides led to the formation of Fe(II)-rich smectite (saponite-like), thus supporting the results previously obtained by Wilson et al. [103].

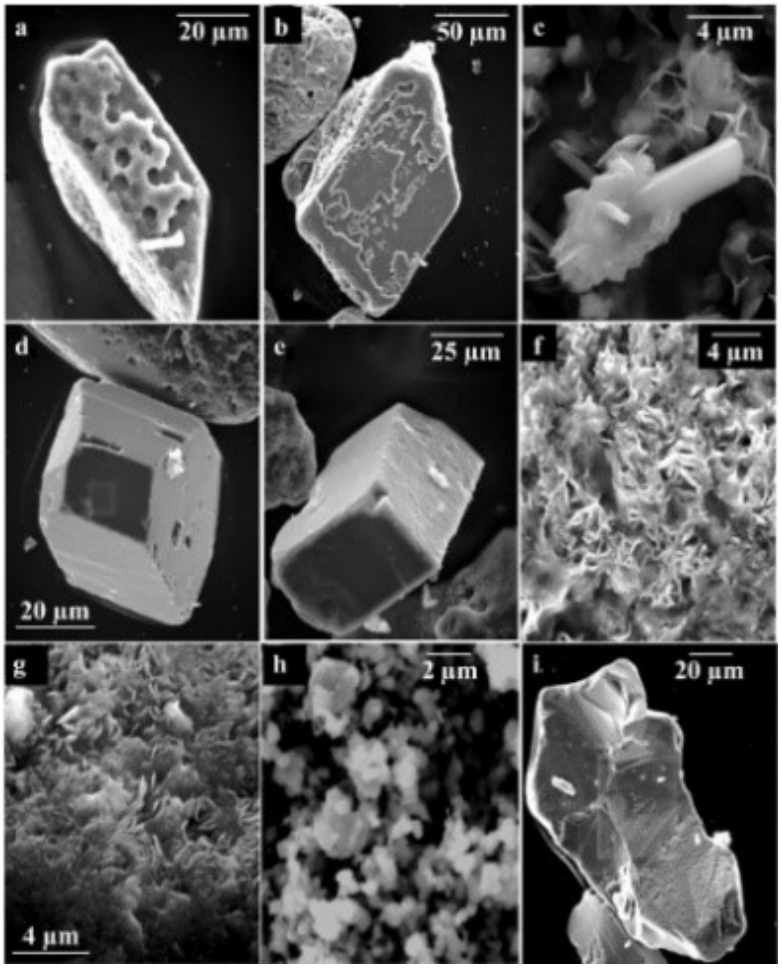

Figure 2.15: *Morphology of primary minerals and newly formed minerals as seen by SEM: (a) growth of quartz on a quartz particle, (b) growth of K-feldspar on a plagioclase, (c) zeolite crystal associated with the clay, (d) newly formed plagioclase, (e) newly formed K-feldspar (f) clay in the starting bentonite, (g) clay in the 3 month run, (h) magnetite powder added to the starting bentonite, (i) large euhedral crystal with magnetite composition. Adapted from* [129].

Cathelineau et al. [131] undertook similar experiments to those already mentioned, studying the alteration of MX-80 montmorillonite at temperatures of 80ºC, 150ºC and 300ºC over a one year period, in low-salinity solutions in the presence of magnetite, hematite and iron metal, considering different liquid/metal mass ratios. Results obtained were a close match to those observed in prior studies at low temperatures. However, at 300ºC the presence of iron oxides led to a partial replacement of montmorillonite, giving rise to trioctahedral domains (saponite).

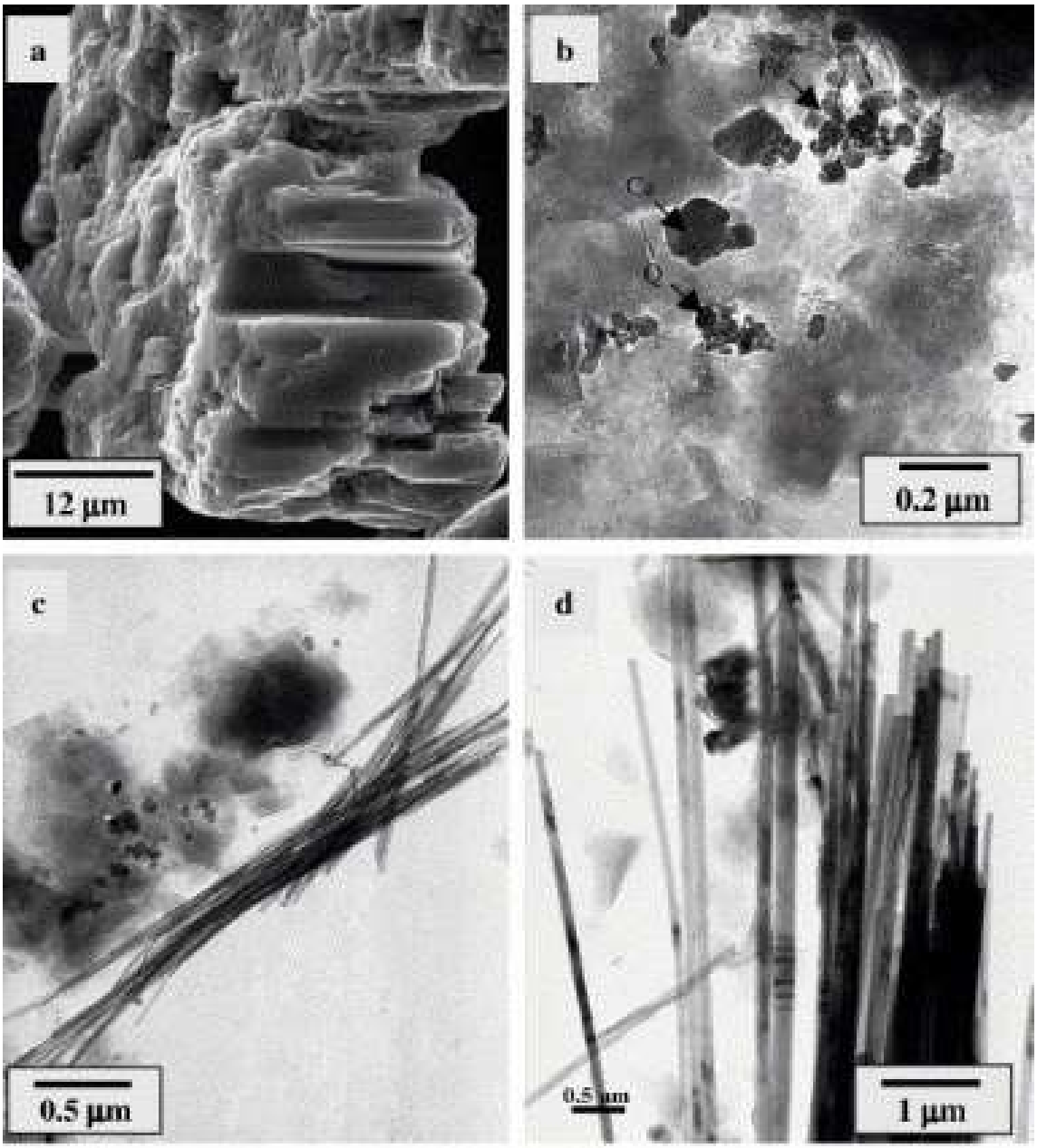

Figure 2.16: *Results obtained by Charpenteira et al.* [132] *where (b) clearly shows the zeolite-type mineral. Adapted from* [132].

Charpenteira et al. [132] also studied clay-iron interactions in alkaline solutions considering three different temperatures (80ºC, 150ºC and 300ºC), by mixing MX-80 bentonite with

powdered magnetite and metallic iron. The admixtures were also placed in contact with a metallic iron plate for three, six and nine months respectively. Charpenteira et al. [132] determined that temperature and distance to the iron plate are two fundamental parameters that govern the nature and rate of clay alteration.

The obtained results enabled them to conclude that at high temperature (300ºC) saponite and mordenite (zeolite-type mineral) were the main arising products (Figure 2.16) while at lower temperatures (80ºC and 150ºC) dioctahedral smectite remained as the predominant clay, observing Fe enrichment in the vicinity of the iron plate. In addition to the clay alterations seen, Charpenteira et al. [132] also reported a progressive dissolution of feldspars.

Since HAW containers will emanate heat originating from the waste contained therein, Jodin-Caumon et al. [133] evaluated the effect of a thermal gradient in clay-iron admixtures, developing an experimental device for this purpose. MX-80 bentonite mixed with iron metallic powder and magnetite was subjected to a thermal gradient from 80ºC to 300ºC over a period of 10 months. The main mineralogical alterations involved the smectite destabilisation into a Fe-enriched trioctahedral smectite, and chlorite. These neoformed minerals were found in the vicinity of the device walls or hottest areas, and their chemistry was undoubtedly different. As a consequence of the created thermal gradient, diffusion principally of Mg^{2+} towards the hottest areas was also observed. Jodin-Caumon et al. [134] performed another similar experiment to re-evaluate the thermal gradient effect in an Fe-claystone at 150ºC and 300ºC mixed with zero-valent iron in chloride aqueous solution as an enveloping media. Once the experimental time elapsed, the presence of neoformed minerals was conspicuous. Iron corrosion caused the surrounding medium to turn very basic and reductive and the temperatures applied resulted in the presence of Fe-serpentine, Fe-saponite, mixed-layer chlorite-smectite and mixed-layer serpentine-smectite. Migration of Mg^{2+} towards the hottest areas was confirmed.

Table 2.2 compiles the main results derived from the experimental work performed in the scope of high temperatures.

Table 2.2: *Experimental data on smectite transformation at high temperatures.*

Reference	Bentonite	Time	T (°C)	Reactants	Neo-formed iron phases
Guillaume et al.	MX-80	9 months	300	Metallic iron and magnetite powders. Low-salinity solution	Chlorite and saponite
Guillaume et al.	MX-80	9 months	300	Hematite and magnetite. Low-salinity solution	Saponite
Cathelineau et al	MX-80	1 year	300	Hematite, magnetite and iron metal. Low-salinity solution	Berthierine
Wilson et al.	Kunipa	180 days	250	Native iron and magnetite in $FeCl_2$	Saponite (first experiment) and berthierine (second experiment)
Charpenteira et al.	MX-80	9 months	300	Mix of metallic iron and magnetite	Zeolite and saponite
Jodin-Caumon et al.	MX-80	10 months	80 to 300	Metallic iron powders and magnetite	Fe-enriched trioctahedral smectite and chlorite
Jodin-Caumon et al.	Fe-claystone	3 to 6 months	150 and 300	Metallic iron and chloride solution	Fe-serpentine, Fe-saponite, mixed-layer chlorite-smectite and mixed-layer serpentine-smectite

2.3.2.3 Length-scale EBS experiments and natural analogues

The effect of corrosion products upon bentonite and, thence, iron-bentonite interactions in future GDFs were first identified by Nagra in mid-1980. Since then, length-scale EBS and mock-up experiments have been performed aiming to provide a better understanding of bentonite-related THCM processes, under repository-like conditions, since the preservation of its properties in the long-term is of paramount importance.

Post-mortem analyses from these experiments have been partly aimed at analysing the kinetics of iron-enrichment processes affecting bentonite, considering coupled reactions resulting from certain expected processes in a GDF. These processes relate to the canister temperature and ionic character of the surrounding medium as the precursors of a concatenation of initial reactions leading to bentonite alteration and/or transformation. These relatively 'long-term' experiments have given inconclusive results regarding kinetics of the processes that govern bentonite alteration and/or transformation, and some of the results are commented below.

Preliminary assessments of Fe impact on the buffer were performed by Wersin et al. [135] for the KBS-3H concept, evaluating the iron-bentonite interactions considering: (*i*) a mass balance estimation; and (*ii*) reactive transport modelling. Results from the mass balance estimations denoted that under the most severe scenario in which the entire container has been corrosion-consumed, only 10-30% of the smectite component of bentonite could be evolved or converted to an Fe(II)-rich clay. From the modelled data, it was concluded that, despite the fact that bentonite transformation to a non-expandable material is evident, the extent of this transformation will be spatially limited (a few centimetres), over long periods, to the vicinity of the container. By analysing several MX-80 bentonite samples from the ABM 1 experiment, Wersin et al. [136] observed the formation of a 10mm-thick area of different bentonite colouration in direct contact with the simulated canister, confirming, on a 'small scale', the results obtained in previous simulations. This layer was formed contiguous to a primary corrosion-container layer composed of siderite, magnetite, goethite and lepidocrocite, suggesting iron diffusion and possible iron-bentonite interactions. Later analyses did not evidence the presence of neoformed minerals or any clay transformation. However, signs of Mg^{2+} enrichment in the contact interface between the simulated canister and bentonite were observed, together with the dissolution of SiO_2.

Using multiple analytical techniques, Svensson and Hansen [137] characterised diverse samples form ABM 1 and TBT experiments to study mineralogy and redox conditions. Bentonite-ABM 1 samples were exposed to 130°C for 2.5 years. Samples in contact with the simulated container showed a higher proportion of Fe^{2+}/Fe^{3+} than those analysed from slight to major distances from the container. In addition, kinetic data showed a rapid oxidation in those samples enriched with Fe^{2+} when they were oxygen exposed. Therefore, reducing conditions were achieved during the performance of the ABM experiment. Conversely, TBT samples (130°C for 7 years) displayed less alteration than the ABM samples, though the samples were also collected from the bentonite contact interface with the simulated container, concluding that due to the larger dimensions of the TBT experiment large quantities of oxygen remained trapped in the clay matrix, and this, combined with a longer period taken to achieve saturation, provided more oxygen for corrosion after installation.

Recently, Torres et al. [138] studied the exchangeable cations, CEC, adsorbed iron and mineralogy of three Febex bentonite samples retrieved in the vicinity of heater nº2 of the Febex in-situ test. Soluble ions showed that Ca^{2+} and Mg^{2+} tended to migrate towards the heater, as previously observed by Wilson et al. [136], whereas Fe cations measured in exchange complex showed negligible values (0.002cmol(+)/kg)). Results from Fourier transform infrared spectroscopy (FTIR) of octahedral cations distribution were in accordance with those obtained from soluble ions analyses, concluding that bentonite did not undergo a significant iron enrichment.

As stated earlier, most of the performed research has been undertaken in laboratory or field-based experiments. The studies discussed above have provided crucial information about THCM processes that could affect bentonite in the long-term. Nonetheless, the experimental data from these studies is clearly limited by the relatively short-time observation (from several months to several years), since bentonite must preserve its fundamental properties over long timescales. Beyond the time-scale limitation, the laboratory and length-scale experiments are also restricted by the spatial-scale due to limitations encountered with reproducing a repository system within the host rock. The combination of these constraints makes it difficult to replicate the complexity of a 'real' repository system. To provide information that will represent the complexity of a GDF system under relevant time periods, considering the half-lives of the contained HAW, it has been proposed and suggested that the stability of bentonite in an underground repository must be investigated by considering natural analogues [139].

The use of natural analogues to study the long-term stability of a repository could provide consistency between short-term experiments, field-based experiments and expected geological evolution once a repository was closed. Since the relative effects of pressure, temperature, permeability or flow rate, and fluid composition under repository conditions can be predicted from data reported in natural analogues [139].

The main process driving loss of bentonite performance in a GDF is its mineralogy alteration. Most attention has been paid to illitisation of the smectite component, which requires K^+ addition, and to a lesser extent Al^{3+}. Interlayered water is egressed during the alteration and, thus, the phase becomes less ordered and less dense [139]. Smectite-to-illite alteration is purported to take place at specific temperature and pressure conditions, accompanied by changes in density, permeability and chemistry [140].

Geological surveys relating to the illitisation process are a starting-point for understanding the progression of such a process in future GDFs: (*i*) in sedimentary formations, it has been reported that the transition from smectite to illite is a slow process occurring at temperatures between 55°C and 120°C and depths of about 2000m to 4000m, with an alteration rate of 0.3% per million years [139]; while (*ii*) in metamorphic contact formations, the illitisation rate is of 40% at temperatures between 240°C and 105°C in an estimated period time of 3.4 million years [139]. The cited natural analogues indicate that the illitisation process is conditioned by the temperature, precursor material, water presence and time-scale [139]. Therefore, under repository conditions, where the temperatures are limited to 100°C, the smectite component of bentonite is expected to remain unaltered for more than 10^6 years. In this regard, the most studied case is the Kinnekulle natural analogue. Wilson et al. [90] affirm that the Ordovician Kinnekulle bentonite, after magmatic intrusion, was formed at a temperature of 120°C and, after 1,000 years the temperature decreased to 90°C. Therefore, the examination of these bentonites is vital to understand the evolution of a repository.

Nevertheless, there is not much information available in the literature about natural analogues related to iron-rich interactions. Consequently, some insights can be obtained from natural analogues on other Fe-bearing clays formations as given in Table 2.3. However, these comparisons should be treated with a suitable degree of scepticism because they cannot closely reproduce the ‘material conditions’ a GDF would present.

Table 2.3: *Occurrence of natural analogues of Fe-bearing clays* [98].

Fe-bearing clays	Occurrence
Fe-rich smectites such as: nontronite; and Fe-rich saponite	May occur in a wide variety of geological settings. Nontronite and Fe-saponite tend to form in hydrothermal systems. Nontronite formation is associated with intermediate redox conditions and low temperatures, while Fe-saponite formation is related with high temperatures
1:1 Fe-rich phyllosilicates such as: berthierine; and cronstedtite	Present in a variety of environments and associated with ironstones. Berthierine tends to form mixed layers with chlorite, acting as a precursor of chlorite at temperatures of 70-130°C in diagenetic sediments

The chloritisation process of smectites has been observed in variety of geological settings, occurring via: hydrothermal alteration of volcanoclastic rocks [141]; metamorphism of pelitic rocks [142]; hydrothermal and regional metamorphism of Mg-silicates and glass in basic igneous rocks [143], [144]; and the hydrothermal alteration of mafic minerals in amphibolites and gneisses [145]. Merriman and Peacor [146] suggested that the chloritisation of smectites in late-stage diagenetic to early-stage metamorphic systems may implicate the gradual conversion of trioctahedral smectite to chlorite via corrensite.

From these analogue studies, it can be concluded that the alteration of smectite via application of: (*i*) temperature; (*ii*) fluid composition (pH); and (*iii*) time occurs under conditions that may be comparable to those expected in the evolution of the repository over the long-term.

2.4 Concluding statement

This chapter has given an overview of the structural, physical and chemical features of bentonite and associated implications for those repositories that intend to use it as a buffer and

backfill material, due to its transformation and/or alteration that might slowly alter it over time. Nevertheless, there are large discrepancies within the literature regarding the alteration and transformation processes affecting bentonite. These discrepancies are fundamentally derived from the geological and hydrogeological nature of the selected site and geological disposal system considered by each country. In addition, many countries have delimited a target maximum temperature of 100ºC. Therefore, research focussed on the THCM implications at temperatures above 100ºC may not be necessarily representative of the long-term expected conditions within a repository, since the alteration products and/or transformation processes affecting bentonite might be exacerbated by high temperatures and result in mineral phases that probably would not occur at low temperatures. Consequently, considering unrealistic temperatures as compared to those expected in an underground repository, may lead to underestimating or overestimating the processes that govern such alterations and/or transformations. Thus, experimental work is key to achieving a better understanding of the coupled processes between bentonite and corrosion products. Given the complexity of the involved parameters and timescales considered, laboratory replication of such processes is clearly impossible. Therefore, experimental studies must be accompanied by modelling work and study of relevant natural analogues to achieve an approximate knowledge.

There is clear evidence that the hydrogeological evolution of the site, in combination with temperature, may have a strong impact on the performance of the smectite component, triggering permanent reduction in the physicochemical parameters conditioning the long-term evolution of a GDF. The precipitation, and later cementation in inter-aggregate spaces, of some natural components of bentonite, such as silicate and calcium hydrates, gypsum, cristobalite and silica seems to initiate such a permanent reduction. The cementation process will be favoured by the release of silica, magnesium, aluminium and iron in the aqueous enveloping solution which, in turn, will also facilitate iron migration and its incorporation in octahedral sites. In addition, progressive concentration of sulphates and carbonates at the bentonite-container interface could be assigned to initial high temperatures that leads to the drying of bentonite in the interface environment. As bentonite re-saturation progresses favoured by groundwater movement, re-dissolution of precipitated salts will also occur, increasing the salinity of the groundwater, which will act as an aggressive corrosive agent. The emanating heat from the waste container continues to fall and, hence, the silica in solution will re-crystallise forming a mass of silica cementitious. If these processes develop throughout the repository lifespan, it is believed that certain bentonite properties, such as its plasticity,

swelling capacity and shear strength, could be adversely affected, along with detrimental implications upon its thermal and hydraulic conductivity.

From the previously reviewed studies, it can be clearly stated that magnetite is the most likely corrosion product of steel HAW container corrosion. It is thought to form a stable layer on the container surface, limiting further corrosion. However, previous studies also lead to speculation that, due to the direct contact of bentonite with the container surface, the formation of said stable layer may be inhibited or heterogeneous, allowing iron ion release until through its thickness complete corrosion of the container occurs. In this case, the corrosion layer would be composed of an outer layer mainly consisting of goethite, hematite, maghemite, lepidocrocite and other corrosion products, and a second inner ferrous layer. These conditions could favour the incorporation of Fe into bentonite octahedral sites, partitioning into complexing at edges sites and/or interlayer via exchange, which would sequentially drive bentonite alteration and/or transformation. Likely transformation by-products are the kaolinite-serpentine group (1:1 phyllosilicates), while alteration by-products would be dominated by Fe-rich smectites, trioctahedral smectites and possibly chamosite, a Fe-rich phyllosilicate from the chlorite group. It is believed that the kinetics of such reactions will be controlled by the nature of the site groundwater, the thermal gradients created by the heat emanating from the waste containers and the type of buffer material utilised. Therefore, the combination of these factors in a confined environment could ultimately lead to permanent bentonite destabilisation, however the exact timescales for such alterations are unclear.

Overall, due to the dynamism and complexity of the factors possibly involved in bentonite alteration and/or transformation, it is necessary to combine laboratory tests, along with field-based analysis, to seek the conditions that define the kinetics of such reactions and achieve better understanding of the physicochemical processes affecting the bentonite-container interface and, better define the timescales over which transformations and/or alterations manifest.

2.5 Aims and objectives

It has been demonstrated in the previous sections that the stability of bentonite under repository conditions is an important challenge that needs to be addressed. This study is primarily focussed on characterising physicochemical changes at the clay/metal-interface within a GDF to gain enhanced understanding of the THCM effects on bentonite evolution under repository conditions in crystalline bedrock. This will be approached by studying the following aspects of bentonite research:

- Perform advanced characterisation of Febex and ABM bentonite samples by implementing a suitable laboratory methodology for THCM investigations at heated clay/metal interfaces by:
  - Examination of cation exchange capacity to determine changes in bentonite ability to exchange cations after several years of experimental exposure to simulated repository conditions.
  - Examination of exchangeable cations in the exchange complex.
  - Examination of any mineralogical changes and the presence of new neoformed minerals.
  - Determination of chemical bonding behaviour and identification of chemical changes on bentonite samples.
  - Provide specific information of magnetic and structural changes occurring within bentonite samples.
  - Identification of evolving corrosion layer thickness, composition and corrosion products present on metallic coupon samples.
- Develop an experimental cell design to replicate the expected conditions within an EBS:
  - To evaluate the significant mineralogical changes in the bentonite buffer after seven months of THCM exposure and combine the results to determine the extent of initial bentonite transformation and/or alteration under repository-like conditions.
  - Define how the results relate advance understanding of predicted bentonite-waste package evolution in a geological disposal environment.

Chapter 3 Materials and analytical techniques

3.1 Chapter overview

In general, two main types of bentonite have been deemed suitable for engineering barriers, sodium (Na^{+}) and calcium (Ca^{2+}) bentonites, both considered of homoionic nature. Research has been carried out into the performance of both bentonites, with Na-bentonites showing greater swelling capacity than Ca-bentonites. In the research described henceforth different bentonite samples are examined: (*i*) Febex bentonite from the Febex in-situ test; (*ii*) four different bentonites from the ABM in-situ test; and (*iii*) 24 Febex bentonite samples arising from a batch test performed at the University of Bristol. This chapter aims to provide general information of the bentonite samples further analysed, including provenance, on-site retrieval and a description of the analytical techniques utilised to evaluate the state of the samples.

3.2 Samples for characterisation

3.2.1 Full-scale Engineered Barrier Experiment in Crystalline Host Rock (Febex) experimental samples

3.2.1.1 Febex bentonite

The Febex in-situ test was performed with Febex bentonite from the Cortijo de Archidona deposit belonging to the volcanic region of Cabo de Gata, Almería, Spain (Figure 3.1). Febex bentonite was selected by the Spanish radioactive waste management agency (ENRESA S.A.) as a suitable backfill and buffer material for higher activity waste repositories based on the Spanish concept for a geological disposal facility (GDF) [147].

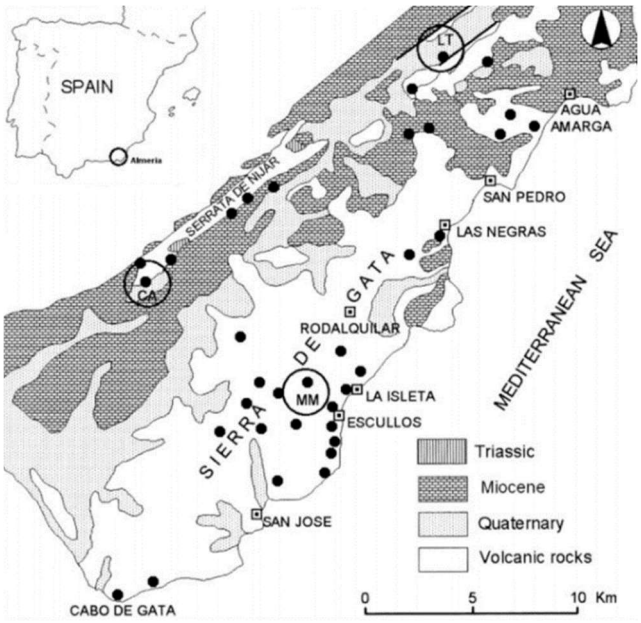

Figure 3.1: *Map of principal quarries in Cabo de Gata. CA: Cortijo de Archidona deposit. Adapted from* [148].

The Febex bentonite is predominantly composed of Ca-Mg montmorillonite, with excellent swelling capacity, permeability, adsorption capacity and thermal conductivity properties. In addition to the aforementioned properties, the Febex bentonite was also selected as an optimal buffer and backfill material because of: (*i*) its purity in terms of mineralogical composition; (*ii*) its specific surface area; (*iii*) its plasticity; (*iv*) its high proportion of fraction less than 2μm; and (*v*) its behaviour when pressure is applied (during compaction) [149]. The properties of Febex bentonite have been widely investigated over the past 20 years. Several publications exhaustively describe the properties of the Spanish clay material [43], [149], [150], [151], [152], [153], [154], [155], [156], [157], [158]. A brief summary of the relevant properties of Febex bentonite, obtained from some of the cited references, are given in Tables 3.1 to 3.3.

Table 3.1: *Mineralogical composition of Febex bentonite measured by x-ray diffraction. Adapted from* [81].

Mineralogical phases present	**wt%**
Montmorillonite content	92 ± 3
Smectitic phases; smectite-illite mixed layer	10-15
Quartz	2 ± 1
Plagioclase	2 ± 1
K-feldspar	2 ± 1
Calcite	2 ± 1
Opal-CT (cristobalite-trydimite)	2 ± 1

Table 3.2: *Febex bentonite properties determined by CIEMAT (Centro de Investigaciones Energéticas, Medioambientales y Tecnológicas) and UPC (Universitat Politècnica de Catalunya). Adapted from* [81].

Property	CIEMAT	UPC
Water content in equilibrium with the air in the laboratory (%)	13.7 ± 1.3	13.3 ± 1.3
Liquid limit (%)	102 ± 4	93 ± 1
Plastic limit (%)	53 ± 3	47 ± 2
Plasticity index (%)	49 ± 4	46 ± 2
Specific weight or particle density (g/m^3)	2.70 ± 0.04	-
Grain size distribution		
Fraction less than 74 μm (%)	92 ± 1	87
Fraction less than 2 μm (%)	68 ± 2	45
Specific surface area (m^2/g)		
Total	725 ± 47	-
External, BET	32 ± 3	-

Table 3.3: *Major exchangeable cations and cation exchange capacity of Febex bentonite. Adapted from* [81].

Exchangeable cations	wt%
Ca^{2+}	38
Mg^{2+}	28
Na^{+}	23
K^{+}	2
Cation exchange capacity (CEC)	111±9meq/100g

In addition, the Febex bentonite rheological properties have been widely investigated and information can be found in the literature [151], [152], [159].

3.2.1.2 Febex samples for characterisation

The main focus of the Febex in-situ test was to evaluate the performance of near-field repository components for HAW disposal in a granite formation [160].

The final sealing with concrete was completed in October 1996, and the gradual heating operation was initiated during February 1997. The temperature at the interface between the simulated heater and the bentonite barrier was maintained at 100°C. Simultaneously, the bentonite buffer was slowly hydrated by groundwater from the surrounding granite host rock [160]. Five years from initial commissioning, the first heater was dismantled (Figure 1.15). Once the dismantling operations were completed, sealing of the remaining part of the installation was carried out, which remained uninterrupted until 2015. In 2015 the final dismantling of the Febex in-situ test was conducted, following 18 years of continuous heating (Figure 3.2). The final dismantling operation consisted of the complete sampling of the geotechnical barrier, relevant interfaces, metal components and the embedded sensors to perform a complete analysis of the condition of the barriers after experiencing the simulated conditions of a radioactive waste underground repository.

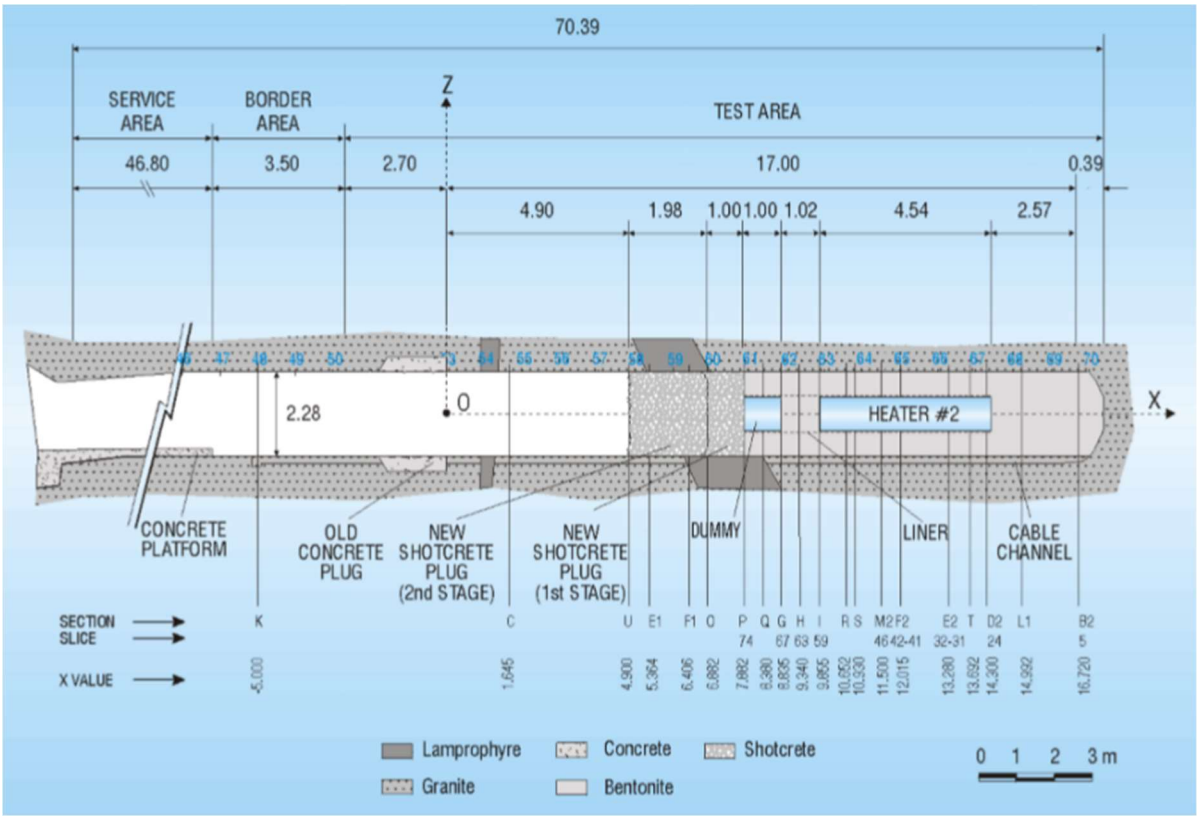

Figure 3.2: *In-situ test configuration after the initiation of the second phase in 2015. After* [160].

During the dismantling of heater no.2, most of the sensors remained operational to monitor the thermodynamic evolution of the in-situ experiment. Data of temperature evolution of each section was provided by Bárcena et al. [161] and Martínez et al. [162] and is presented in Table 3.4. The Febex in-situ test was designed with highly compacted bentonite blocks

arranged in the shape of a circular-crown around both heaters. The block geometries and their arrangements around each heater are presented in Figure 3.3. From Figure 3.3, it can be stated that the bentonite and coupon samples belonged to block-types BB-G-01 (S-S-54-15-A, B, C, D and E) and BB-G-03 (BM-B-41-1 and M-S-48-1) respectively. Considering the block-type (Figure 3.3), location (Figures 3.8, 3.10 and 3.14) and instrumentation section (Table 3.4), the temperature at which each sample was exposed can be approximately deducted (Table 3.5).

Table 3.4: *Temperatures (°C) measured in the bentonite barrier before dismantling. Adapted from* [161], [162].

	Reference	Section G	Section I	Section S	Section F2	Section D2	Section B2
Outer ring (BB-G-01)	Bárcena et al.	44-46	44-45			36-38	21-23
	Martínez et al.	30-34	37-39			37-38	22
Intermediate ring (BB-G-02)	Bárcena et al.	58-60	58-61			51-53	
	Martínez et al.	34-39	54-63	72	71-73	54-56	
Inner ring 1 (BB-G-03)	Bárcena et al	80-84	84-88		95-100	82-90	
	Martínez et al.	36-34	84-87	93	94-99	83-88	
Inner ring 2 (BB-G-04)	Bárcena et al.						21-23
	Martínez et al.						20-22
Core (BB-G-05)	Bárcena et al.	100-104					21-23
	Martínez et al.						22

In addition to temperature, other important information on the preliminary state of the samples was: (*i*) the water distribution; (*ii*) the dry densities; and (*iii*) the degree of saturation. Villar et al. [160] carried out an exhaustive analysis of several samples belonging to different sectors, determining the degree of saturation, the dry densities and the water content of each sector to which the samples belonged. In the absence of specific information on the sections to

which the samples evaluated in this chapter pertained, the computed results of Villar et al. [160] have been used to inform the expected 'local' conditions of the samples at the point before their retrieval in 2015.

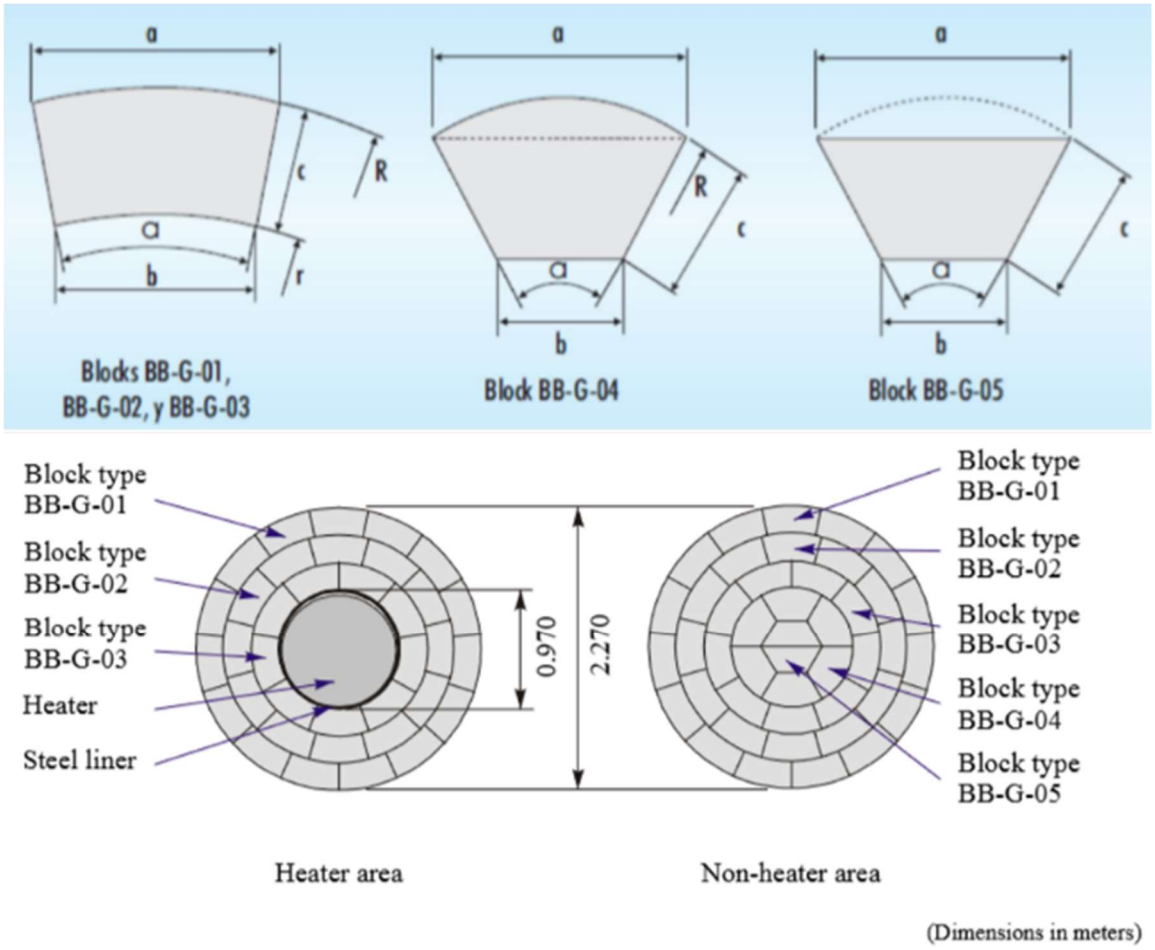

Figure 3.3: *Block-types and configuration of bentonite slices at Febex in-situ test. Adapted from* [43].

Table 3.5: *Approximate temperature at which each sample was exposed during the experiment operation.*

ID sample	Section	Slice	Block type	Instrumentation section	Temperature (°C)
BM-B-41-1	41	63	BB-G-03	H	-
M-S-48-1	48	42	BB-G-03	F2	~94-100
S-S-54-15-A	54	24	BB-G-01	D2	~36-38
S-S-54-15-B	54	24	BB-G-01	D2	~36-38
S-S-54-15-C	54	24	BB-G-01	D2	~36-38
S-S-54-15-D	54	24	BB-G-01	D2	~36-38
S-S-54-15-E	54	24	BB-G-01	D2	~36-38

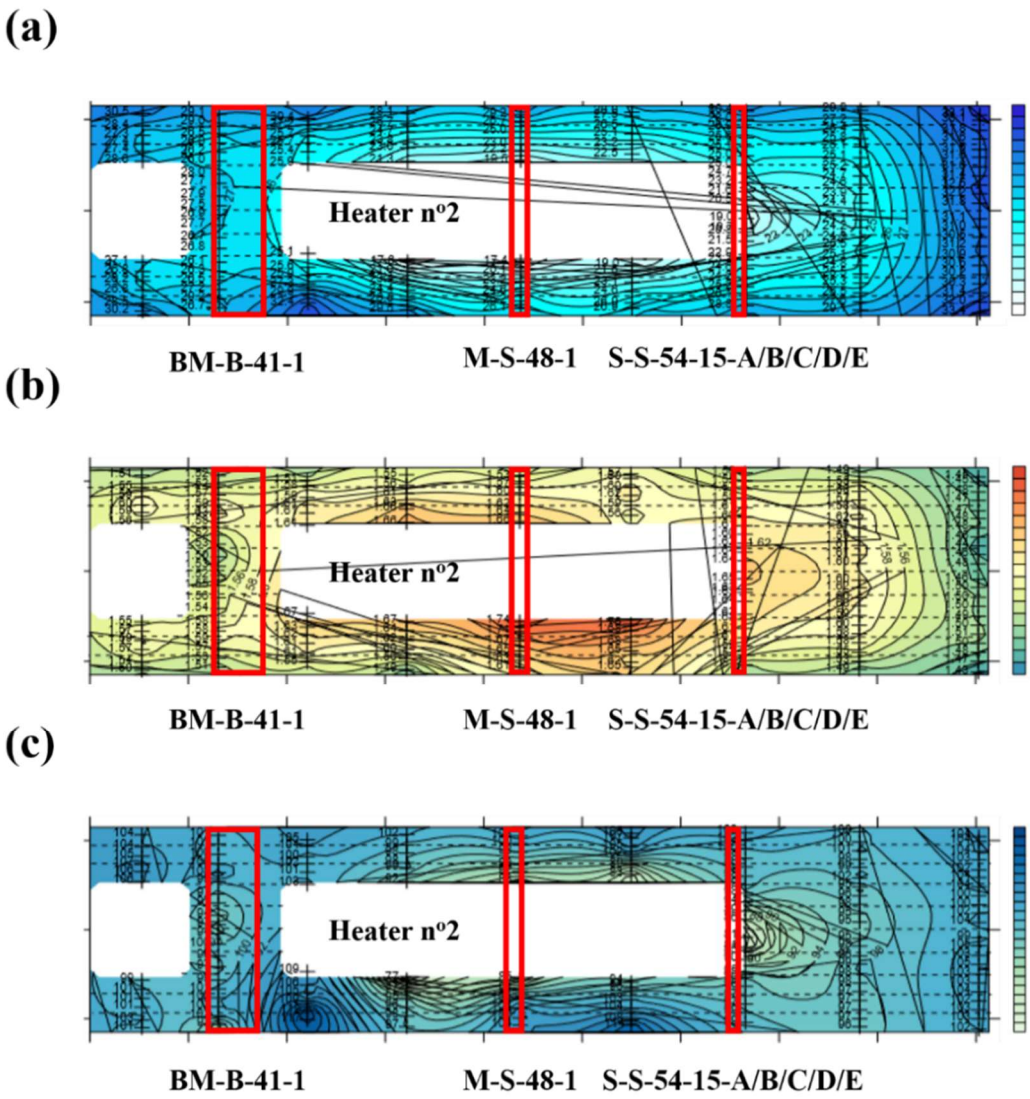

Figure 3.4: *(a) Water distribution in vertical longitudinal section. (b) Dry density distribution in vertical longitudinal section. (c) Degree of saturation distribution in vertical longitudinal section. Red squares indicate approximate locations of the samples. Modified from* [160].

Figure 3.4 shows the results obtained by Villar et al. [160] along with the approximate location of the samples examined in this chapter. Since the samples were retrieved from Section 41 (BM-B-41-1, Slice 63), Section 48 (M-S-48-1, Slice 42) and Section 54 (S-S-54-15-A/B/C/D/E, Slice 24), the information provided in Figures 3.5 and 3.6 is assumed to give an accurate approximation of the values of water content, dry density and degree of saturation. The information provided actually belongs to Section 39 (Slice 64), Section 49 (Slice 40) and Section 56 (Slice 22), which are section/ slices adjacent or nearly adjacent to the location of the bentonite samples evaluated in the Chapter 4. We assumed that these values can be applicable to our samples in view of the lack of other sources for this information. We also believe that the error induced by this assumption does not invalidate the conclusions of the

work presented in Chapter 4. Table 3.6 displays the approximate values of water content, dry density and degree of saturation of the Febex samples evaluated.

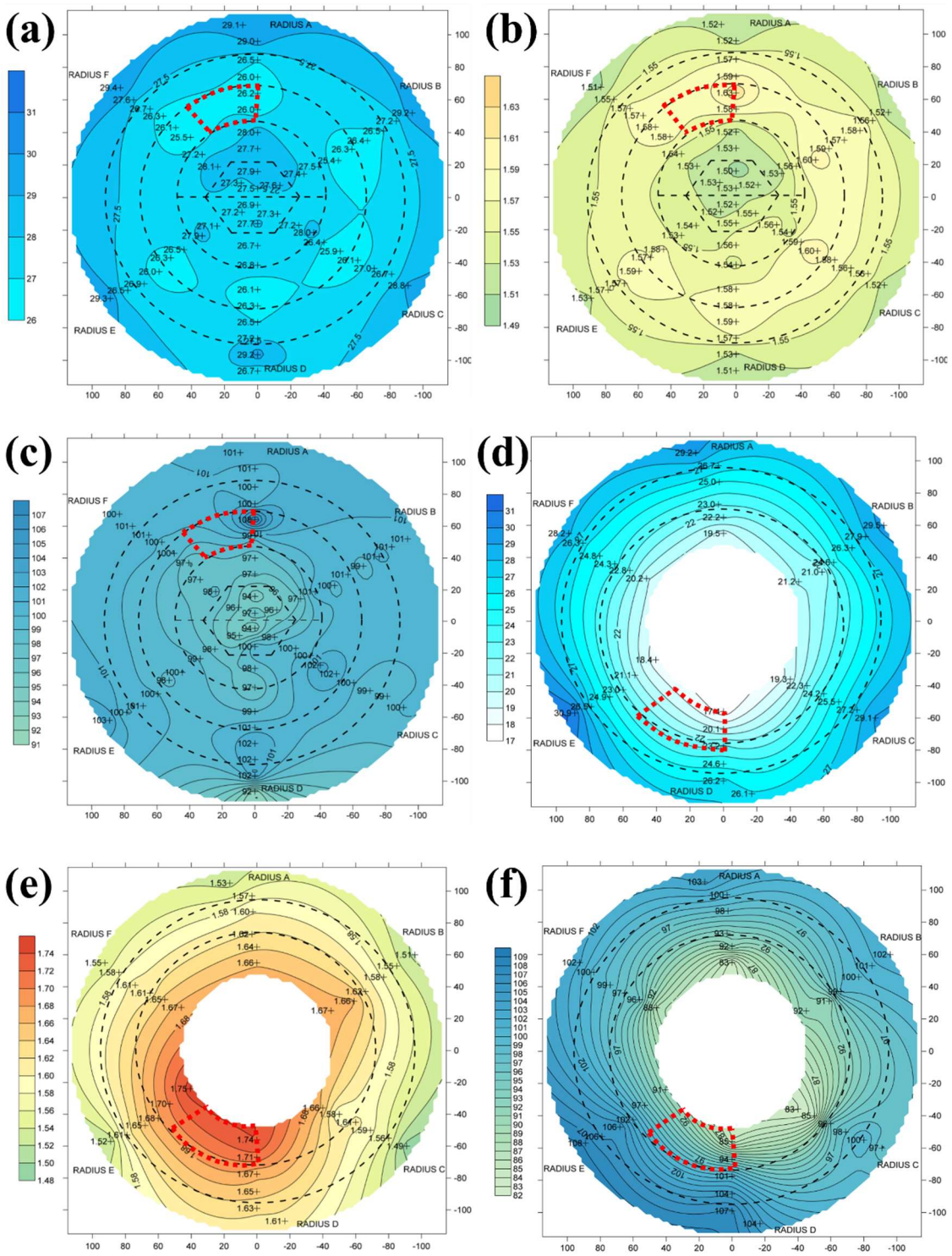

Figure 3.5: *(a) and (d) Water distribution and approximate location of sample BM-B-41-1 and M-S-48-1 at Section 39 and 49, respectively. (b) and (e) Dry density and approximate location of samples BM-B-41-1 and M-S-48-1 at Section 39 and 49, respectively. (c) and (f) Degree of saturation and approximate locations of sample BM-B-41-1 and M-S-48-1 at Sections 39 and 49, respectively. Modified from* [160].

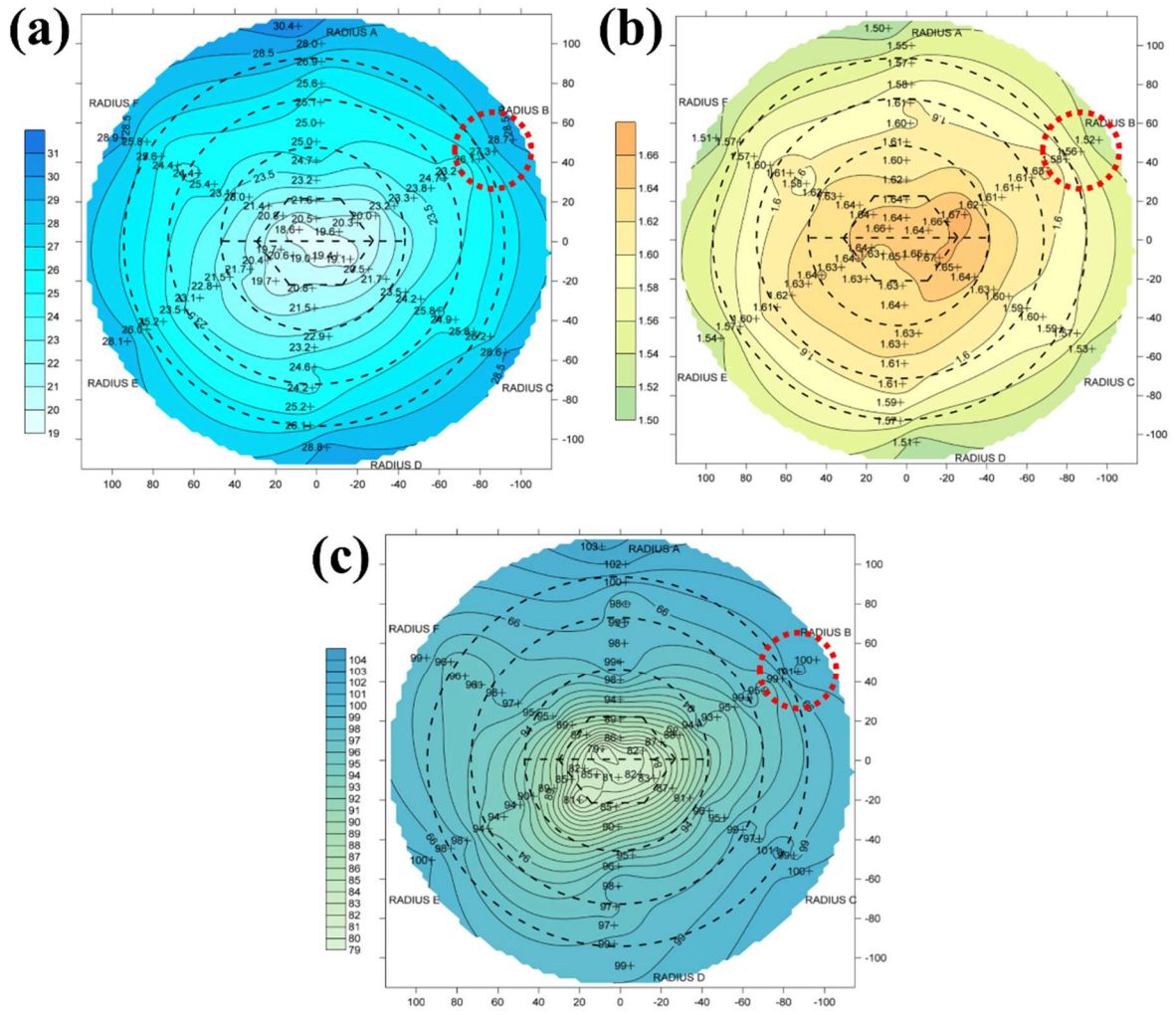

Figure 3.6: *(a) Water distribution at Section 56 and the approximate location of samples S-S-54-15-A/B/C/D/E. (b) Dry density at Section 56 and the approximate location of sample S-S-54-15-A/B/C/D/E. (c) Degree of saturation at Section 56 and the approximate location of sample S-S-54-15-A/B/C/D/E. Modified from* [160].

Table 3.6: *Approximate water distribution, dry density and degree of saturation of Febex samples. Values in parenthesis corresponds to the actual section and slices of the assessed samples in this work.*

ID sample	Section	Slice	Water distribution (%)	Dry densities (g/cm^3)	Degree of saturation (%)
BM-B-41-1	39 (41)	64 (63)	~25.5-26.2	~1.58-1.63	~97-108
M-S-48-1	49 (48)	40 (42)	~17.4-21.1	~1.70-174	~85-97
S-S-54-15-A	56 (54)	22 (24)	~27.3-28.5	~1.52-1.58	~99-101
S-S-54-15-B	56 (54)	22 (24)	~27.3-28.5	~1.52-1.58	~99-101
S-S-54-15-C	56 (54)	22 (24)	~27.3-28.5	~1.52-1.58	~99-101
S-S-54-15-D	56 (54)	22 (24)	~27.3-28.5	~1.52-1.58	~99-101
S-S-54-15-E	56 (54)	22 (24)	~27.3-28.5	~1.52-1.58	~99-101

All seven Febex in-situ test samples under study in the present work arose from the dismantling of heater no.2. This specific field test was conceived and performed within a horizontal shaft, 70.93m long, driven into the granite host rock, with a total bentonite backfilled test length of 17.00m. Heater no.2 was located approximately 14.00m into the backfilled volume (Figure 1.11). Samples from the bentonite barrier were retrieved from different slices or layers, with each slice or layer corresponded to a different sampling section. All Febex samples were received in aluminium packages, freshly vacuum-sealed on-site to maintain the experimental conditions. The Febex samples characterised in Chapter 4 were specifically selected by RWM.

3.2.1.2.1 Extensometer samples: S-S-54-15-A/B/C/D/E

Samples S-S-54-15-A/B/C/D, core samples of similar provenance regarding the area of retrieval, were extracted by hammering steel Shelby tubes into the sampling face of the bentonite edifice. Each steel Shelby tube had an approximate diameter of 35mm. Sample S-S-54-15-E was in direct contact with the extensometer and was received as loose bentonite pieces (Figure 3.7).

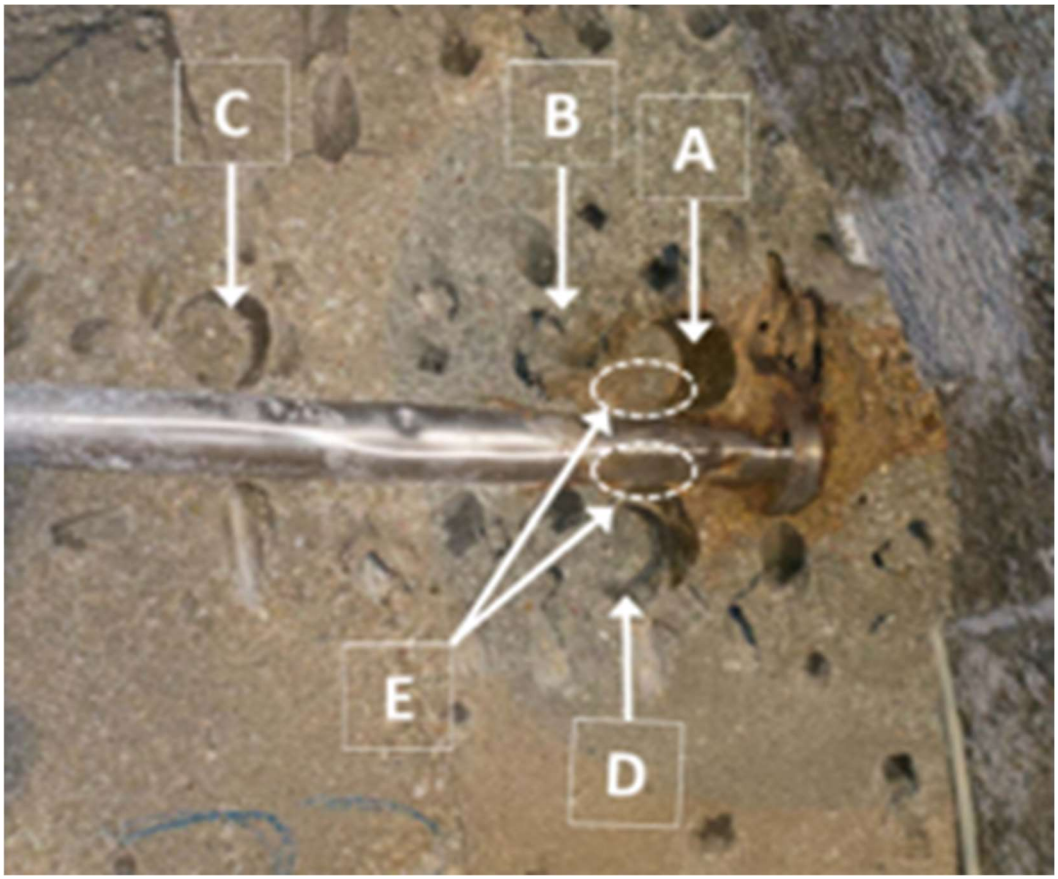

Figure 3.7: *Former position of samples S-S-54-15-A/B/C/D/E around the extensometer (SH-SD2-03). Adapted from* [163].

The five samples were extracted from the region immediately adjacent to extensometer SH-SD2-03, in what was known as the 'halo' zone, characterised by a visibly distinguishable discolouration assumed to result from corrosion suffered by the extensometer (Figure 3.7). Each core sample and sample S-S-54-15-E was collected from bentonite slice (or layer) 24, corresponding to the sampling section 54 at a horizontal distance of 14.30m into the backfilled test volume (Figure 3.8). The sensor, or extensometer, was a part of the instrumentation used to continuously read and measure possible displacements of heater no.2 and was protected by an external tube manufactured from AISI 316L stainless steel (Figure 3.7). Information concerning the colouration, bulk density, thickness, volume and weight of each core sample is given in Tables 3.7 and 3.8.

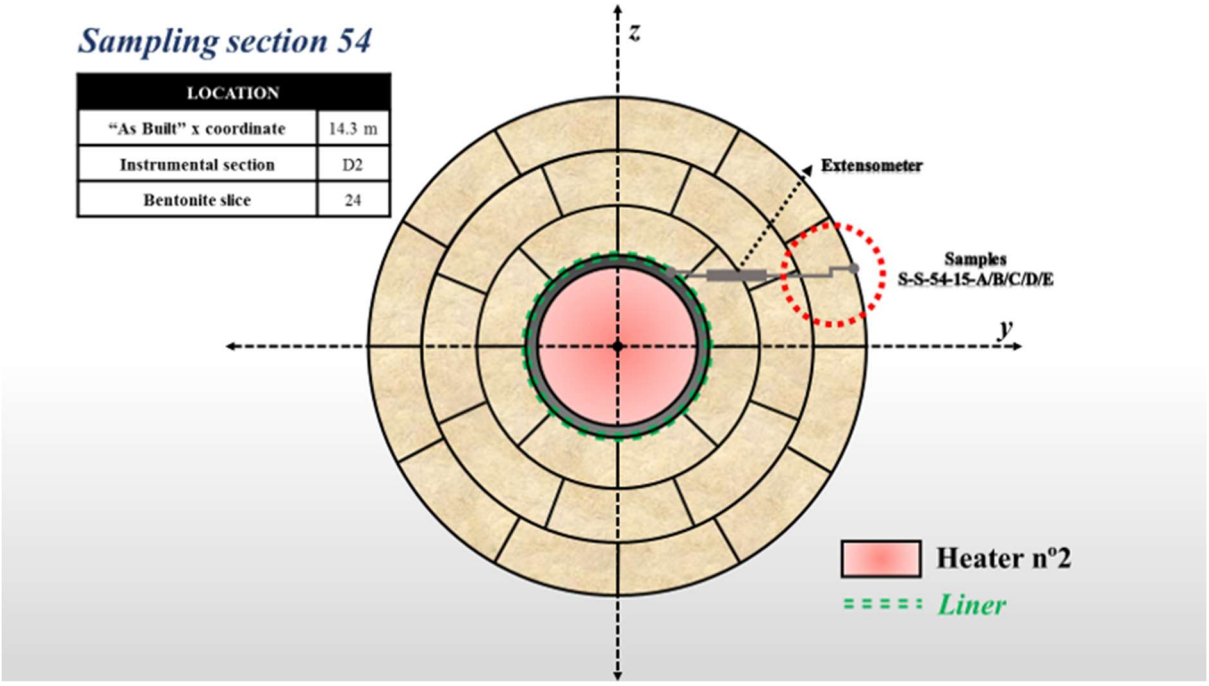

Figure 3.8: *Schematic view of extensometer samples slice/layer retrieval.*

Table 3.7: *Physical characteristics of Febex samples S-S-54-15-A/B/C/D. Adapted from* [163].

Bulk density	1950kg/m^3
Thickness (L)	0.20m
Radius (r)	0.017m
Volume (V)	2 10^{-5}m^3
Weight (w)	35.4±0.50g

Table 3.8: *Physical characteristics of Febex samples S-S-54-15-A/B/C/D.*

Sample	Colouration description
S-S-54-15-A	Collected from the 'red' corroded area
S-S-54-15-B	Collected at the interface of 'blue' and "red" corroded areas
S-S-54-15-C	Collected next to the corroded 'blue' area but with normal grey bentonite colouration characteristic of the Febex bentonite
S-S-54-15-D	Collected at the interface of 'blue' and 'red' corroded areas (similar to S-S-54-15-A and S-S-54-15-B)
S-S-54-15-E	In direct contact with the extensometer, it presented a red-dark colouration

3.2.1.2.2 Corrosion coupon samples: Sample M-S-48-1

Sample M-S-48-1 consisted of a series of rectangular coupons manufactured from TStE355 carbon steel. The coupons were different candidate wall metals for manufacturing the high activity waste containers and were included in the experiment to evaluate bentonite behaviour when gradual corrosion of metal occurs. During the experiment, four racks with metallic coupons were installed into rectangular cavities around the liner margins and backfilled with powdered bentonite to seal them in place.

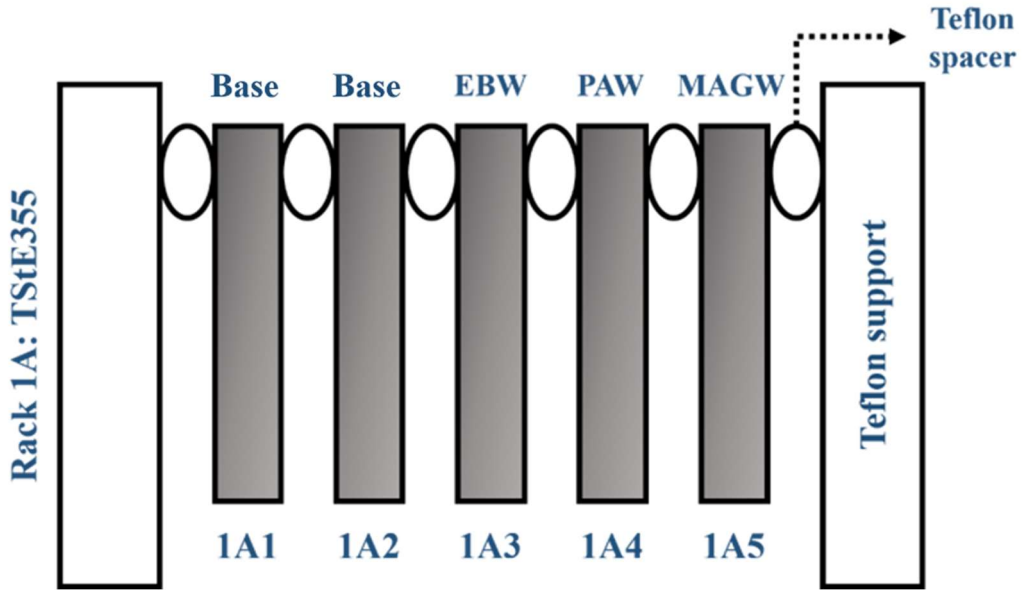

Figure 3.9: *Outline appearance of rack 1A (TStE355 carbon steel).*

The corrosion coupons (M-S-48-1 sample) were designed with a hole in the upper part allowing them to be mounted together. Each coupon was placed on Teflon supports at both ends and separated by Teflon spacers which held each carbon steel 'piece' or coupon (Figure 3.9).

Rack 1A contained (Table 3.9): (*i*) two base coupons; (*ii*) one coupon welded by electron-beam welding (EBW); (*iii*) one coupon welded by plasma arc welding (PAW); and (*iv*) one coupon welded by metal active gas welding (MAGW). Each coupon was classified upon reception as follows: Two base material coupons identified as 1A1 and 1A2, and three test coupons with welded joints were identified as: 1A3; 1A4; and 1A5 (Figure 3.9).

Table 3.9: *Rack 1A, material and type of coupons.*

Rack	Material	Type of coupons (and quantity)				Total
1A	Carbon steel TStE355	Base x2	EBW	PAW	MAGW	5

Sample M-S-48-1 was taken from rack 1A, located in bentonite slice/layer 42, sampling section 48, at a horizontal distance of 12.015m into the backfill volume (Figure 3.10). It is noteworthy that a period of one month separated the excavation process and physical sample retrieval. Over this period, the inner liner and surrounding excavated face of bentonite were exposed to air, possibly resulting in chemical alteration of the outermost material, through drying and/or corrosion.

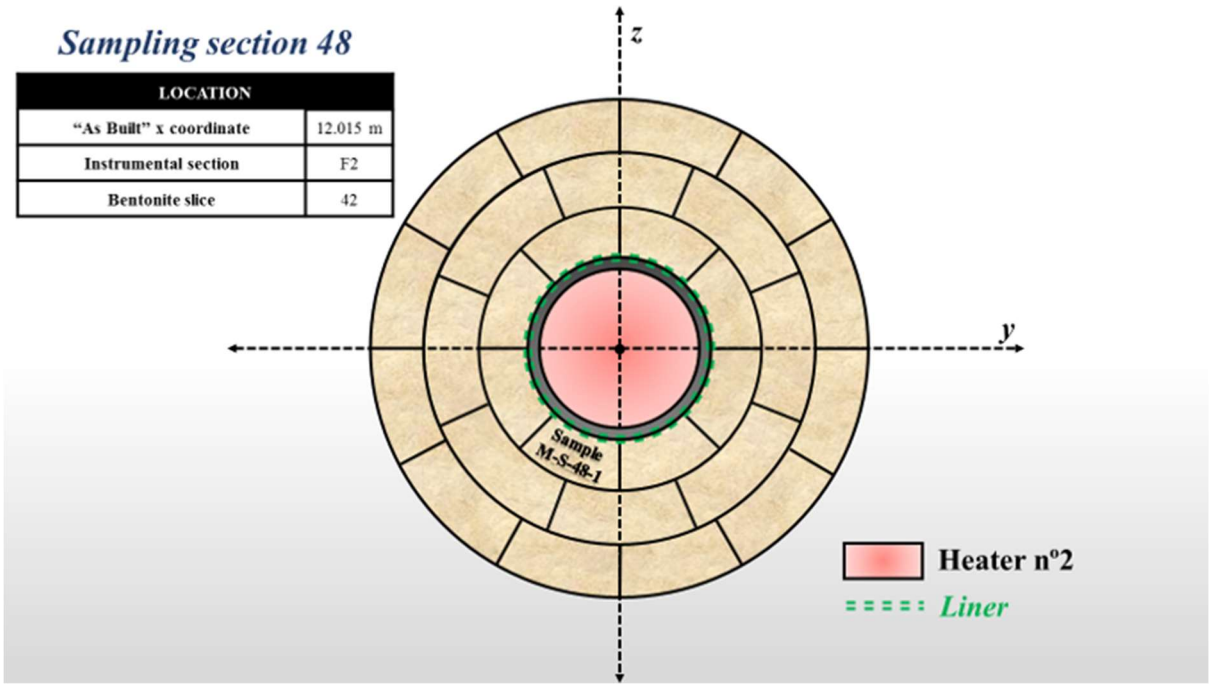

Figure 3.10: *Rack 1A location. Slice/layer 42, section 48.*

In addition to the carbon steel coupon samples described above, other metallic coupon samples were also included in the Febex in-situ test to evaluate not only the behaviour of carbon steel but also the performance of other metals considered suitable for HAW containers. Table 3.10

lists the metal corrosion probes or coupons emplaced at different sections within the compacted clay body that surrounded heater no.2.

Table 3.10: *Rack 2A, 3A and 4A, material and type of coupons.*

Rack	Material	Type of coupons (and quantity)						Total
2A	Stainless steel 316L	Base x2	EBW	GTAW	-	-	-	4
3A	Titanium	TiGr2	TiGr7 x2	TiGr12 x2	Ti2EBW	Ti7EBW	Ti7PAW	8
4A	Copper	Cu 99% x2	Cu10Ni x2	Cu30Ni	-	-	-	5

Results from characterisation of the different corrosion coupons were published in the Nagra report NAB 16-16 [164]. A brief summary of the results is presented hereinafter. Generally speaking, all coupons were exposed to low-humidity conditions due to their emplacement close to the heater. The two base materials were labelled as 2A1 and 2A2, and the two welded coupons were identified as: 2A3 and 2A4 [164].

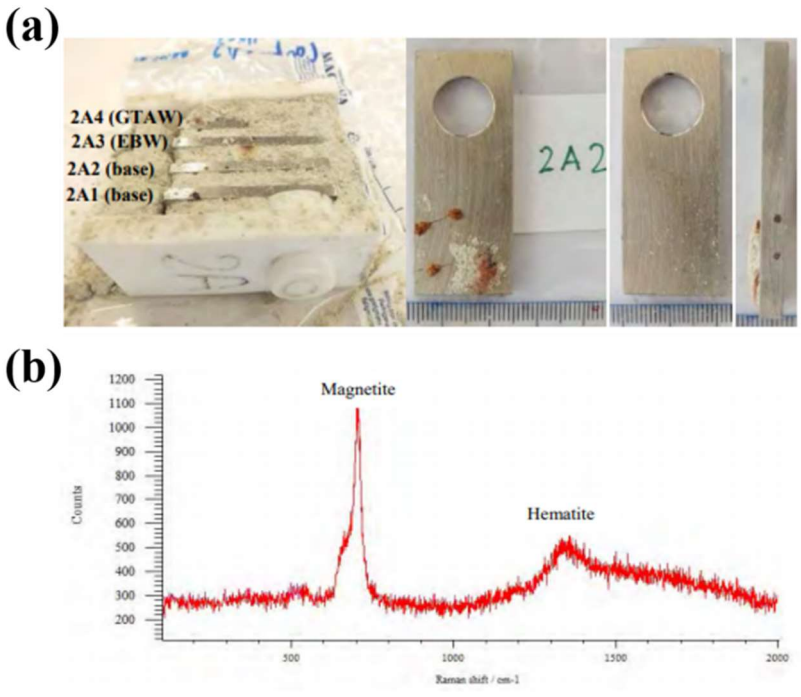

Figure 3.11: *(a) Visual appearance of Rack A2 and three faces of coupon 2A2. (b) Raman spectrum of the corrosion by-products located at one of the pits of sample 2A2. Modified from* [164].

The four coupons comprising Rack 2A (stainless steel) did not exhibit any visual sign of general corrosion. Figure 3.11 (a) shows the physical state of 2A2 probe. The corrosion of the

stainless steel coupons was manifested as pitting. Different laboratory techniques such as, SEM/EDX, XRD and μ-Raman spectroscopy were utilised to analyse the nature of the corrosion by-products filling the pits. EDX analysis revealed that the compounds filling the pits were composed of Fe and O, while also containing Cr and Cl [164]. However, due to the poorly-crystalline nature of the corrosion products present in the pits, their phases could not be identified by XRD. However, μ-Raman spectroscopy showed the presence of hematite and magnetite in one pit area of sample 2A2 (Figure 3.11 (b)) [164].

The five coupons from Rack 4A (copper) consisted of different copper alloys. The Cu-ETP coupons (Cu 99%) were identified as 4A1 and 4A2, the two Cu10Ni probes were labelled as; 4A3 and 4A4 and the Cu30Ni was identified as 4A5 [164]. Signs of corrosion were specially apparent on the surfaces of Cu-ETP coupons (Cu 99%). Corrosion appeared to be generally uniform with small localised corrosion areas at the edges of the Cu-ETP coupons [164]. Figure 3.12 (a) shows the physical state of 4A2 probe.

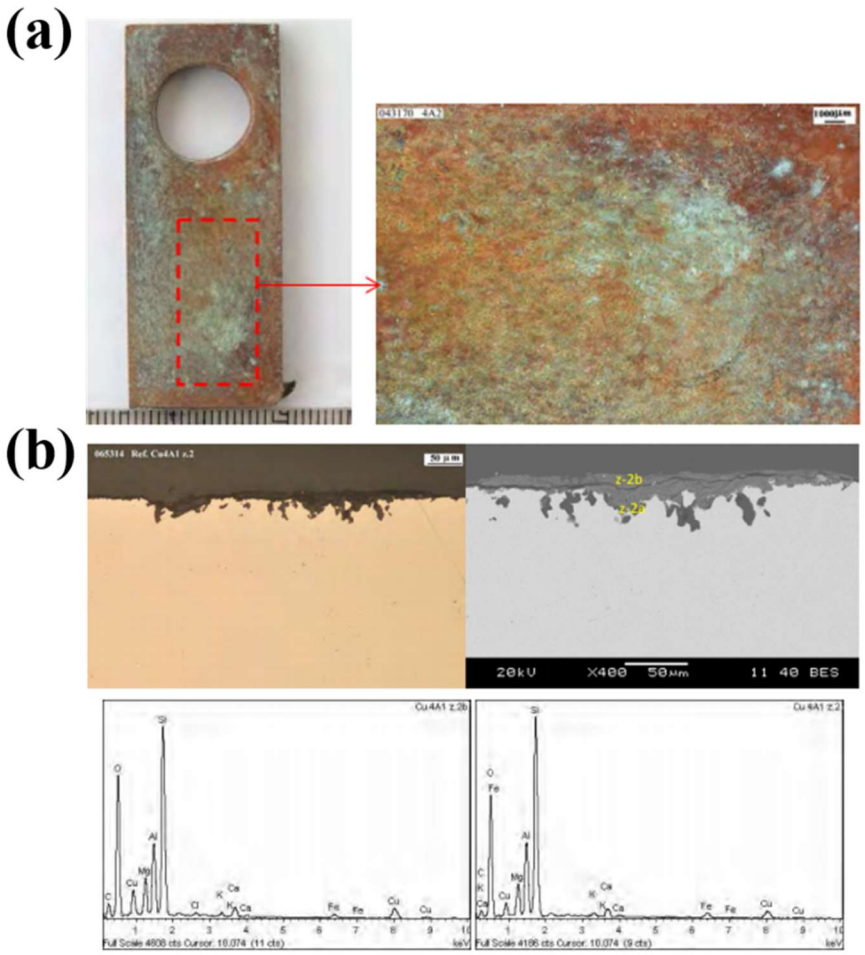

Figure 3.12: *(a) Photographs showing the Cu alloy coupon (4A2) and details of the corroded area. (b) Uniform corrosion layer present at the surface of 4A1. Modified from* [164].

SEM/EDX analysis revealed that the surfaces were composed of Cu and O. SEM/EDX analysis also unveiled the presence of chlorine in the two Cu-ETP corrosion coupon surfaces, whose enrichment increased in the greenish areas [164]. Metallographic analysis confirmed the generation of a relative uniform corrosion layer on the surface of 4A2 probe, as shown in Figure 3.13 (b).

Finally, from the titanium coupons, no surface corrosion was observed and no difference between the welded and unwelded samples was noted [164].

3.2.1.2.3 Liner bentonite sample: BM-B-41-1

BM-B-41-1 was extracted from bentonite slice/layer 63, sampling section 41, at a horizontal distance of 9.340m (Figure 3.13). The sample was extracted close to the liner and belonged to a 20kg block. Sample BM-B-41-1 was vacuum-package at site, after 20 minutes from its extraction. Table 3.11 shows data of the retrieval operation.

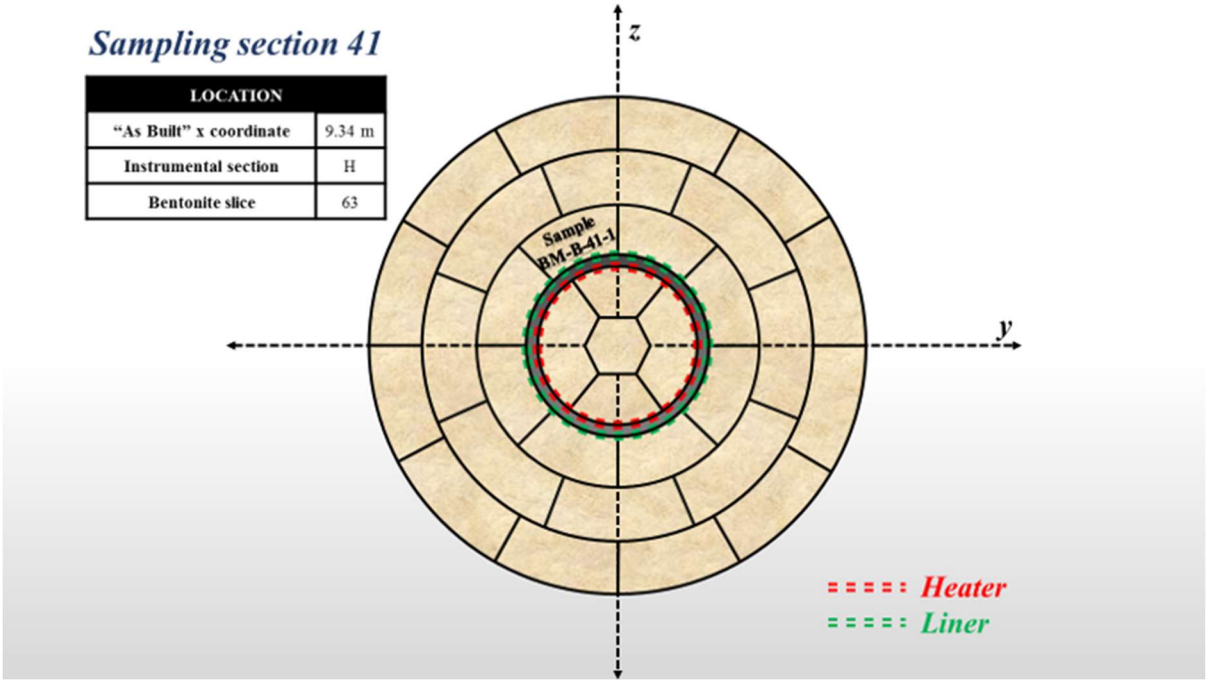

Figure 3.13: *BM-B-41-1 sample location. Slice/layer 63, section 41.*

The 20kg block was sent to the University of Bern and cut into five slabs, which involved 30 minutes of atmospheric exposure, and vacuum-sealed again.

The liner guide tube used in the experiment was a perforated steel tube, 970mm in diameter and 15mm thick. The liner was used to construct the storage receptacle and facilitate insertion

of the heater in its experimental storage position. The liner was designed and constructed with 11 segments. Each segment was made of conventional alloyed steel plate more typically used for boilers and pressure vessels (15 Mo 3 after DIN 17155).

Table 3.11: *Collection data at retrieval time. Adapted from* [165].

Date	29/05/2015	
Time	14:05	
Approximate air exposure time	10 min	
Temperature	13.5ºC	
Humidity	55%	
Dimensions (cm)	Δx	13.50
	Δy	54.00
	Δz	22.00

3.2.2 Alternative buffer material bentonite samples

The ABM in-situ test was originally envisaged and designed to investigate the chemical and mineralogical stability of different bentonite clay materials in the long-term [47]. The in-situ test was initially conceived to replicate the thermal, mechanical and geochemical conditions expected in an underground repository, utilising three steel tubes, each equipped with inner heaters. Each parcel was surrounded by cylindrical bentonite blocks of 11 different types of bentonite. Samples were compacted on-site, at the underground Äspö Hard Rock Laboratory, using a conical shape mould with chamfered edges, specifically designed to acquire the circular shape sought. Bentonite blocks of each parcel were compacted at their initial water content and grain size by applying 100MPa of pressure [47].

The first ABM parcel was dismantled in May 2009 after 2.5 years, and the second in April 2013 after 6.5 years of field test. The different buffer materials from both parcels were naturally wetted. The second parcel was also equipped with an artificial wetting system to guarantee complete material saturation. Both parcels were exposed to the maximum targeted temperature of 130°C from the early stages of the experiment [47]. Figure 3.14 and Table 3.12 collect information regarding the bentonite type, parcel and block. The ABM samples analysed in the present work were selected by Radioactive Waste Management (RWM) in preparation for this PhD project. The differences between the selected samples within the ABM experiment are their calcic or sodium nature (Table 3.12), as well as the thermal loading, while the sample

Kunigel V1 ABM 1 was exposed to the maximum thermal loading (130°C) over 2.5 years, the samples from the package 2 were exposed to temperatures on the range between 120-130°C over a period of 6.5 years.

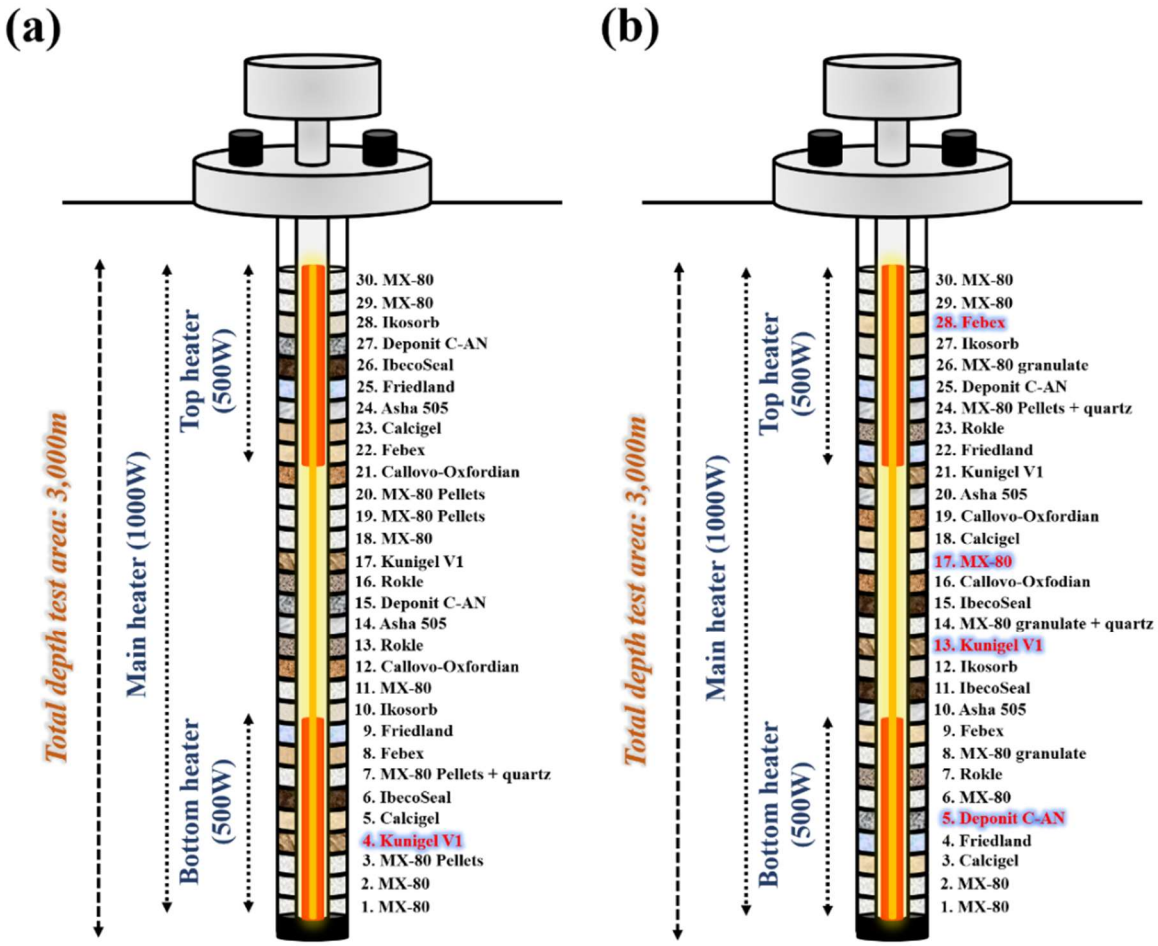

Figure 3.14: *(a) Schematic view of package 1. (b) Schematic view of package 2. The blocks highlighted belong to the position of samples under study. Modified from* [166].

Table 3.12: *ABM samples under study.*

Sample	Bentonite type	Parcel or package	Block
Kunigel V1	Na-bentonite	1	4
Kunigel V1	Na-bentonite	2	13
Deponit C-AN	Ca-bentonite	2	5
Febex	Ca-bentonite	2	28
MX-80	Na-bentonite	2	17

The scope of the present section is to provide information about the provenance and main features of the different materials under characterisation. Therefore, a summary description is provided herein.

3.2.2.1 Kunigel V1 bentonite

Kunigel V1 bentonite is originally from underground mines located in the Tsukinuno district, northern Japan (Figure 3.15). The bentonite used in the ABM in-situ test was mined and provided by Kunimine Industries Ltd., (Japan).

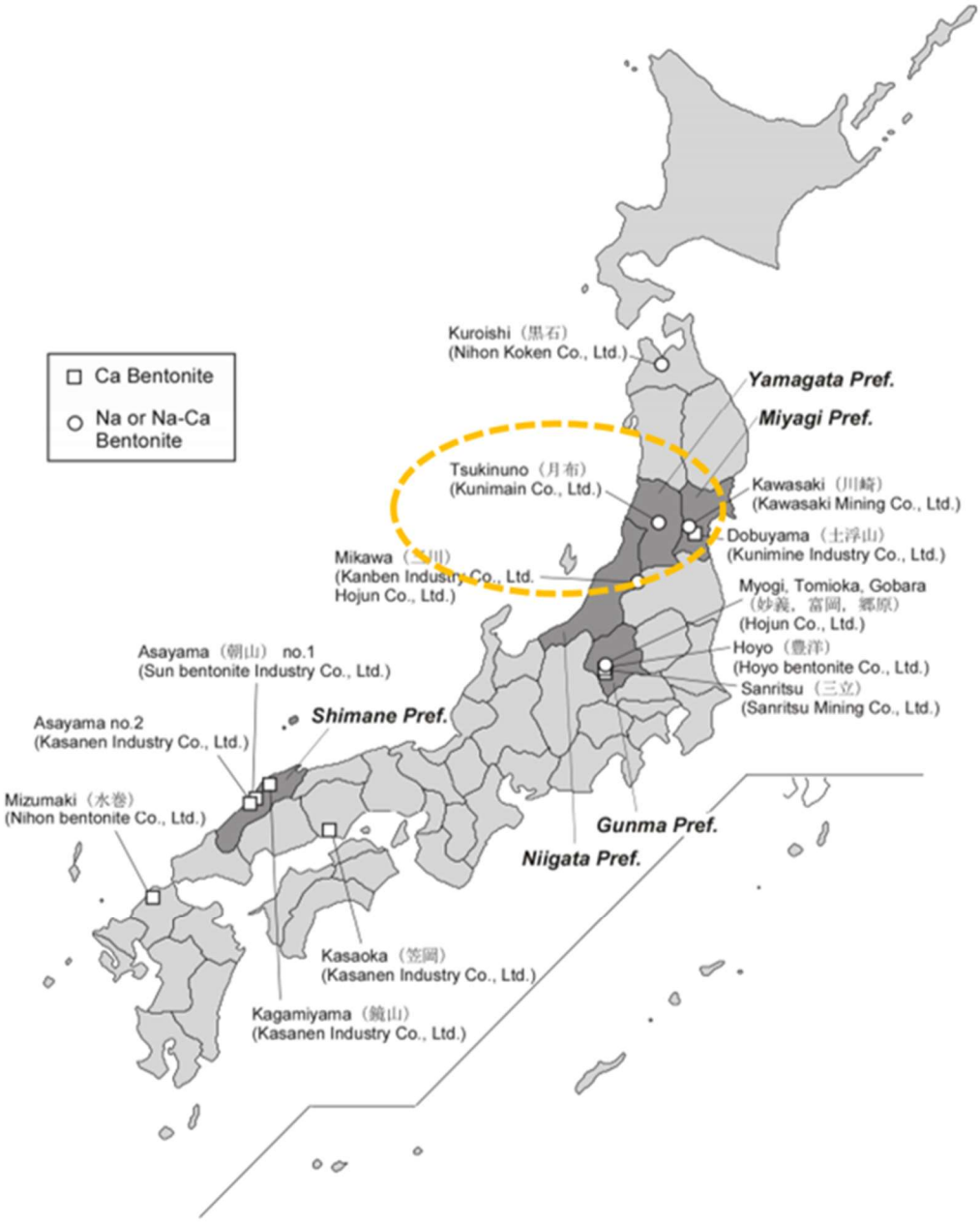

Figure 3.15: *Location of Kunigel V1 bentonite deposit. Adapted from* [167].

Kunigel V1 is a sodium bentonite whose characteristics has been examined and studied for possible use as buffer material and engineering barrier for HAW repositories in Japan. Tables 3.13 and 3.14 present summaries of the main mineralogical characteristics and other fundamental properties of Kunigel V1 bentonite.

Table 3.13: *Main physical properties of Kunigel V1 bentonite. Adapted from* [64], [168].

Parameters	***Kunigel V1 bentonite***
Specific gravity (G_S)	2.70
Liquid limit (W_L)	416%
Plastic limit (W_P)	21%
Plasticity index (L_P)	383
Specific density	2700kg/cm^3
Specific surface area	525m^2/g
Grain-size distribution	
Fraction less than 74μm	>90%
Fraction less than 2μm	58%

Table 3.14: *Mineralogical composition, cation exchange capacity and exchangeable cation information of Kunigel V1 bentonite. Adapted from* [169].

Parameters	**Kunigel V1 bentonite**
Phase mineral present	**wt%**
Montmorillonite	46-49
Quartz (chalcedony)	29-38
Feldspar	2.7-5.5
Calcite	2.1-2.6
Dolomite	2.0-3.8
Zeolite	3.0-3.5
Pyrite	0.5-0.7
Soluble impurities	**molg^{-1}**
Calcium sulphate ($CaSO_4$)	1.79×10^{-5}
Calcium chloride ($CaCl_2$)	6.14×10^{-7}
Surface sites and exchangeable cations	
SOH sites (edges sites)	2.07×10^{-5}molg^{-1}
Cation exchange capacity, CEC	60.1meq(100g)$^{-1}$
Na^+	51.4meq(100g)$^{-1}$
K^+	0.57meq(100g)$^{-1}$
Ca^{2+}	0.66meq(100g)$^{-1}$
Mg^{2+}	7.41meq(100g)$^{-1}$

In addition, extensive research related with its rheological properties has been performed; and information can be found in elsewhere [170], [171], [172], [173].

3.2.2.2 Febex bentonite

The Febex bentonite utilised in this particular field test was provided by CIEMAT. Information related to its provenance and properties can be found in section 3.2.1.1.

3.2.2.3 MX-80 bentonite

MX-80 or Wyoming bentonite is one of many bentonites selected as an optimal engineered clay barrier for underground HAW repositories. MX-80 bentonite is a worldwide-known commercial material, which was supplied by American Colloid Co. MX-80 bentonite is quarried in Wyoming and other American states, such Montana and South Dakota (Figure 3.16).

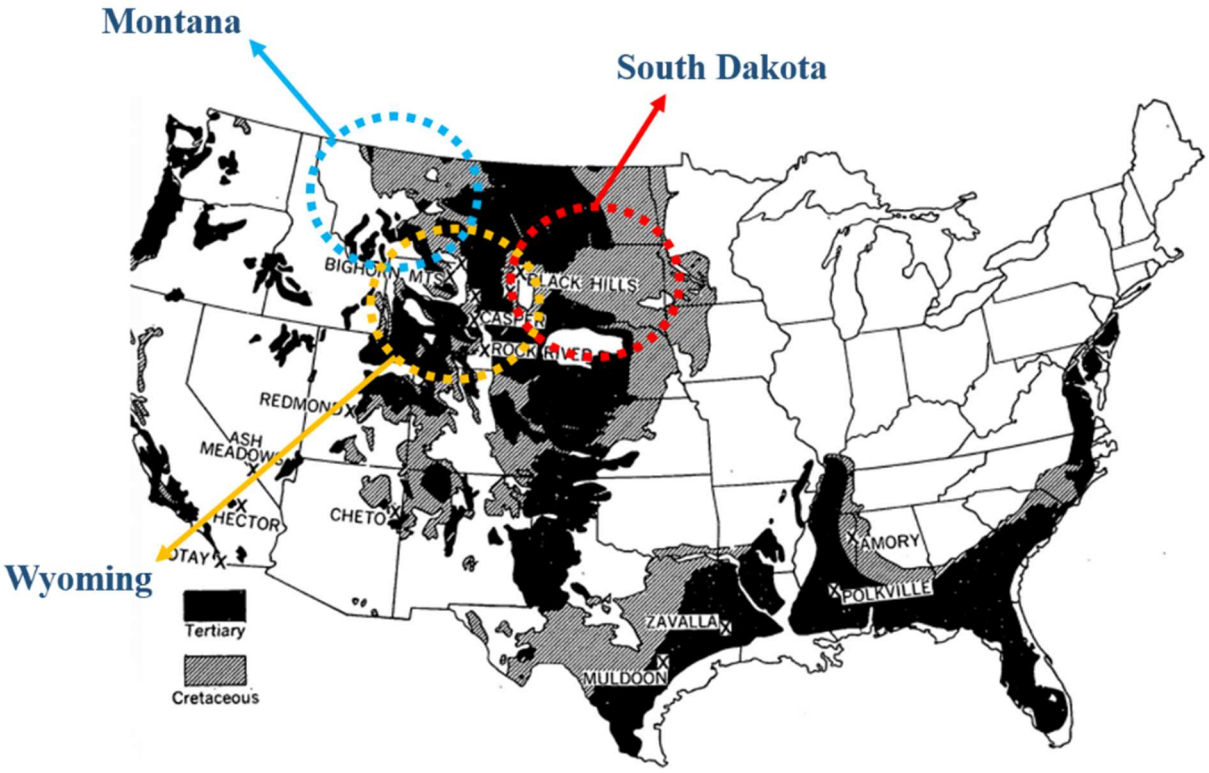

Figure 3.16: *Map showing the mining districts of Wyoming or MX-80 bentonite of Cretaceous and Tertiary ages. Adapted from* [174].

MX-80 bentonite is a sodium-montmorillonite, with outstanding swelling properties, permeability, absorption capacity and thermal conductivity. Many of its characteristics have

been comprehensively studied since this bentonite is endowed with the sought properties as a sealing and insulating material for HAW repositories.

The main properties of MX-80 bentonite have been well characterised from mineralogical, chemical and mechanical points of view. A brief summary of its relevant features are given in Tables 3.15 to 3.17.

Table 3.15: *Mineralogical composition of MX-80 bentonite. Adapted from* [175].

Mineralogical phases present	**wt%**
Montmorillonite content	62-82
Quartz	4-12
K-feldspars	5-8
Traces of cristobalite, calcite and pyrite	-

Table 3.16: *MX-80 bentonite properties. Adapted from* [87], [175], [176]. *[1]The fraction less than 2 μm of this bentonite is 80-90% of the total.*

Property	**MX-80 bentonite**
Water content in equilibrium with the air in the laboratory (%)	8-11
Liquid limit, w_l (%)	519
Plastic limit, w_p (%)	35
Plasticity index (%)	484
Specific weight or particle density, (Mg/m^3)	2.76
Grain size distribution (%)	
Fraction less than 2 μm (%)[1]	60
Specific surface (m^2/g)	
Total	562

Table 3.17: *Major exchangeable cations and cation exchange capacity of MX-80 bentonite. Adapted from* [175].

Exchangeable cations	**MX-80**
Ca^{2+}	10meq/100g
Mg^{2+}	3meq/100g
Na^{+}	61meq/100g
Cation exchange capacity (CEC)	74meq/100g

Since MX-80 bentonite is one of the most promising candidates, its rheological properties have been deeply investigated and results can be found elsewhere [92], [175].

3.2.2.4 Deponit C-AN bentonite

Deponit C-AN is a Greek bentonite whose mine is located in the north-east of Milos Island, Greece (Figure 3.17). Deponit C-AN is a calcium-dominated bentonite supplied to the ABM in-situ test by Silver and Baryte mining company.

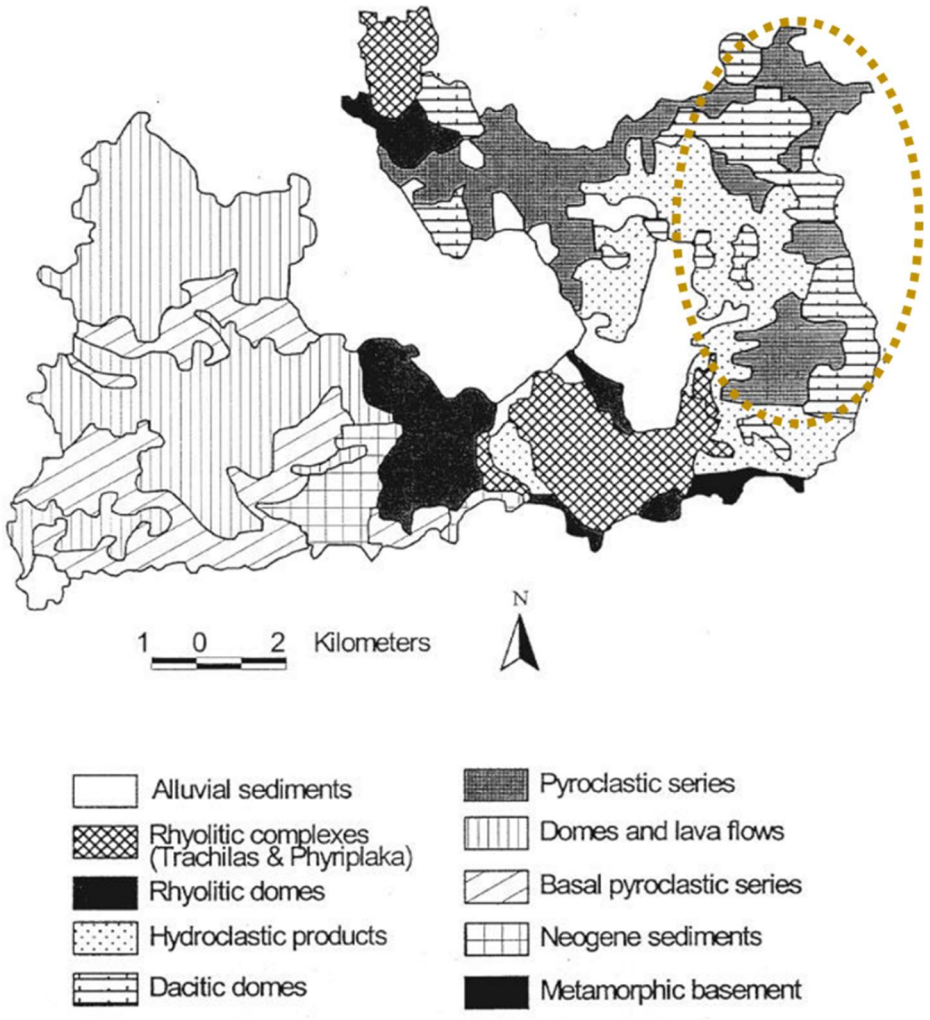

Figure 3.17: *Location of Deponit C-AN bentonite deposit (yellow). Adapted from* [177].

Deponit C-AN was originated via volcanic activity on Milos. The bentonite was formed due to hydrothermal reactions between permeable volcanic rocks and groundwaters heated at 90°C during the volcanism period [178]. The formation temperatures of Deponit C-AN were under the established limit for a buffer material (100ºC). This characteristic regarding its formation indicates its potential stability under repository-like conditions.

Table 3.18 to 3.20 collect information related to Deponit C-AN and its mineralogical composition and physical properties.

Table 3.18: *Mineralogical composition of Deponit C-AN bentonite. Adapted from* [178].

Mineralogical phases present	**wt%**
Montmorillonite content	79.5-82.5
Illite	4.5-5.1
Calcite	3.6-6.2
Gypsum	0.2-0.6
Pyrite	1.0-1.2
Quartz	0.1-0.5

Table 3.19: *Deponit C-AN bentonite physical properties. Adapted from* [178], [179].

Property	**Deponit Ca-N**
Liquid limit, w_l (%)	115
Plastic limit, w_p (%)	33
Plasticity index (%)	82
Specific weight or particle density, (Mg/m^3)	2.72
Grain size distribution (%)	
Fraction less than 2 μm (%)[1]	65
Specific surface (m^2/g)	
Total	797

Table 3.20: *Major exchangeable cations and cation exchange capacity of Deponit C-AN bentonite. Adapted from* [178].

Exchangeable cations	**Deponit Ca-N**
Ca^{2+}	45%
Mg^{2+}	29%
Na^{+}	24%
K^{+}	2%
Cation exchange capacity (CEC)	81meq/100g

Although there is little information with regards to the characterisation of Deponit C-AN bentonite, information of its rheological properties can be found elsewhere [77].

3.2.3 Bentonite synchrotron study: Cell design and manufacture of bentonite samples

Due to uncertainties regarding the likelihood of bentonite alteration and/or transformation, an experimental programme was conceived and designed to provide insights of the kinetics governing the alteration and/or transformation of bentonite.

3.2.3.1 Experimental cells design

A series of batch tests in small-scale cells (24 in total), of internal diameter 20.30mm and inner length 49.50mm, was designed, considering different periods of time (61, 122, 183 and 211 days) and thermal loadings (55°C, 65°C, 75°C; 85°C, 95°C, and 100°C). The experimental cells were designed with an inner Teflon liner of 1.35mm thickness due to its proved stability against the thermal loadings considered and to prevent possible interactions between the bentonite and the cell wall.

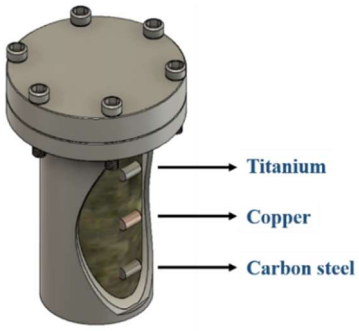

Figure 3.18: *Experimental cell* .

Externally, the cell bodies were made of aluminium 6082 to avoid possible deformations as a consequence of bentonite swelling over the heating period (Figure 3.18). A total of 24 pellets of Febex bentonite saturated clay were compacted at initial dry density of 1.65g/cm^3 to simulate the expected conditions in an underground repository, in accordance with the Spanish concept for final disposal of HAW [150]. Within each bentonite pellet, three metallic wires were inserted with an approximate positioning as represented in Figure 3.19. The body of the test cells (62.00mm total length) consisted of: (*i*) a cylindrical main aluminium body with a length of 57.00mm; and (*ii*) an aluminium upper lid with a total thickness of 7.00mm. The thickness of the aluminium cell wall was 1.08mm. The upper closing consisted of a cylindrical aluminium 6082 disc of 40mm diameter and 7.00mm thickness provided with six threaded holes around the perimeter of the disc. The lid of the cell was attached using six bolts, 20mm

long, and held in place with double locking nuts. The upper lid was provided with a Teflon disc to avoid any possible aluminium contact. The water-tightness of the contact between the lid and the body cell was assured using Viton O-rings capable of withstanding temperatures up to 200°C [180]. A schematic of the cell design can be found in Appendix A (Plane A.1).

3.2.3.2 Sample preparation technique for the embedded wires

In deep geological repositories, several materials, such as titanium, copper and carbon steel have been considered as potentials for HAW containers [181], [182]. Therefore, for the batch test carbon steel, titanium and copper specimens were considered. Originally, the metallic specimens were received in the shape of 1m wire lengths. These were precisely cut into 24 pieces of 2mm length. However, to guarantee a smooth finish on both ends, each piece was inserted into a grid plate endowed with multiple holes of 2mm length and 1.60mm diameter, and specimens were polished until reaching a final length of 2mm, assuring the same length for each specimen.

In the long-term or mid-life of a repository, the predominant mechanism will be anaerobic corrosion. To minimise the oxide on specimen surfaces at the commencement of the experiment, the specimens were chemically pickled. Specimen pickling was carried out using different acid solutions depending on the nature and chemical composition of the metallic samples. Tables 3.21 and 3.22 summarise the chemical pickling methodologies.

Table 3.21: *Pickling conditions for copper-base materials and carbon steel specimens. Adapted from* [183].

Sulfuric acid solution	
Sulfuric acid (H_2SO_4)	15-20vol%
35% hydrogen peroxide (H_2O_2)	3-5vol%
Water	Rinse with deionised water
Temperature of solution	Room temperature to 60°C
Immersion time	15 seconds to 5 minutes
Hydrochloric acid bath	
Hydrochloric acid (HCl)	40-90vol%
Water	Rinse with deionised water
Temperature of solution	Room temperature
Immersion time	1 to 3 minutes

The proportions of each acid were adapted to the dimensions and number of samples to be pickled. Despite the elevated number of samples, 24 in total of each material (titanium, copper and carbon steel), the dimensions of the samples were small. Therefore, just a few millimetres of each solution were needed.

Copper specimens were firstly subjected to a sulphuric acid 'bath' (Table 3.21). Subsequently, 25ml of sulphuric acid (H_2SO_4) and hydrogen peroxide (H_2O_2) solution were prepared. 15.5ml of distilled water were poured in a 50ml glass beaker and 5ml of H_2SO_4 (98%) and 4.5ml of H_2O_2 (28%) were slowly added. The solution was swirled for 5 min to ensure complete dissolution of the H_2SO_4 and H_2O_2. Copper-based specimens were placed inside the beaker containing the sulphuric acid solution for 5 min. After the sulphuric acid bath, the solution was decanted and specimens were rinsed with deionised water until the acid was washed out.

Following the sulphuric acid 'bath', copper samples were subjected to a hydrochloric acid 'bath'. For this, 25ml of HCl (35 %) were poured in a glass beaker and left settle for 3 min. Once the acid was settled, copper specimens were added and left to react for 3 min. Subsequently, specimens were rinsed with deionised water until the hydrochloric acid was completely removed. Carbon steel specimens were hydrochloric acid pickled following the procedure previously described for copper-based samples (Table 3.21).

Table 3.22 summarises the methodology utilised for titanium samples pickling.

Table 3.22: *Pickling conditions for titanium materials. Adapted from* [184].

Nitric acid and hydrofluoric acid solution	
Nitric acid (HNO_3)	15-40wt%
Hydrofluoric acid (HF)	1.0-2.0wt%
Water	Rinse with deionised water
Temperature of solution	Room temperature
Immersion time	5 min

14ml of HNO_3 (70%) and 1ml of HF (50%) were dissolved in 10 ml of distilled water in a plastic beaker and swirled for 5 min to ensure complete solution mixing. Titanium specimens were pickled for 5 min. After the pickling, the remaining solution was decanted into 500ml plastic beaker containing 10g of $CaCO_3$ in 100ml of distilled water. Titanium specimens were rinsed with deionised water until the acid was washed out. Once specimen pickling was

completed samples were stored in a nitrogen-purged glove-box (Saffron Scientific Equipment Ltd).

3.2.3.3 Bentonite sample manufacture

3.2.3.3.1 Material

The batch tests were conducted with Febex bentonite provided by CIEMAT. A summary of its physical and chemical properties can be found in section 3.2.1.1.

3.2.3.3.2 Bentonite sample preparation

3.2.3.3.2.1 Bentonite sample crushing

Initially, the Febex bentonite was a poorly-sorted mixture of various grain sizes ranging from micrometres to a few millimetres.

The Febex bentonite has a high cohesive nature when a significant amount of force is applied. Therefore, to attain a more equigranular matrix, the bentonites were placed in a sealed plastic bag and set on a large metallic slab. The bentonite was then crushed with a hammer to reduce the maximum grain size to approximately 2mm. This method was chosen as it provided the cleanest way of crushing the bentonite with the least possibility of contamination. After the bentonite had been crushed, it was removed from the plastic bag and sieved in a shaker for five min. A 2mm mesh sieve was used to allow all grains smaller than 2mm to pass through and be collected. The resulting bentonite particulate that was too large to pass through the sieve was recollected and placed back in the sealed plastic bag for further crushing. This process was repeated until the desired amount of granulate bentonite had been crushed.

3.2.3.3.2.2 Bentonite sample saturation

In a GDF, groundwater will percolate through the host rock into the buffer material, and thus slowly hydrate the bentonite. The main purpose of the bentonite saturation in the laboratory was to replicate repository-like conditions. Consequently, two different natural granitic water compositions were considered to simulate the water geochemistry that might be reasonably expected in a granite hosted GDF. A total of 22 bentonite samples were saturated with granitic water supplied by Pure Dartmoor Water Ltd. Table 3.23 shows the chemical composition of the water provided.

To provide a set of samples for comparison, two experimental cells were saturated with granitic water sampled from the Grimsel Test Site (GTS). The water was extracted from the BOUS 85.003 borehole (approximate total length of 150m). Figure 3.19 and Table 3.24 show the location and chemical composition of BOUS 85.003 borehole (GTS).

Table 3.23: *Chemical analysis of water composition provided by Pure Dartmoor Water ltd.*

Chemical species	Concentration (mg/l)
Cl^-	11.1
F^-	0.36
NO_2^-	Less than 0.003
NO_3^-	5.6
SO_4^{2-}	9.0
Ca^{2+}	8.0
Mg^{2+}	7.2
Na^+	5.9
K^+	1.3
pH	6.45

Table 3.24: *ADUS 96.001 borehole chemical composition. Adapted from* [185].

Chemical species	Concentration (ppm)
Na^+	8.60±0.06
Ca^{2+}	7.35±0.24
Mg^{2+}	0.40±0.01
K^+	0.88±0.10
SO_4^{2-}	5.90±0.22
Cl^-	0.82±0.04
F^-	4.13±0.10
Alk (HCO_3^-)	24.25±0.37
SiO_2	11.40±0.08
pH	9.70±0.13
Eh	-153mV

The hygroscopic water content of any soil is the ratio between the weight of water and the weight of dry solid expressed as a percentage, at room temperature and atmospheric pressure [186]. Bentonite saturation was carried out with a calculated volume of water solution to simulate the conditions expected in a HAW repository buffer barrier.

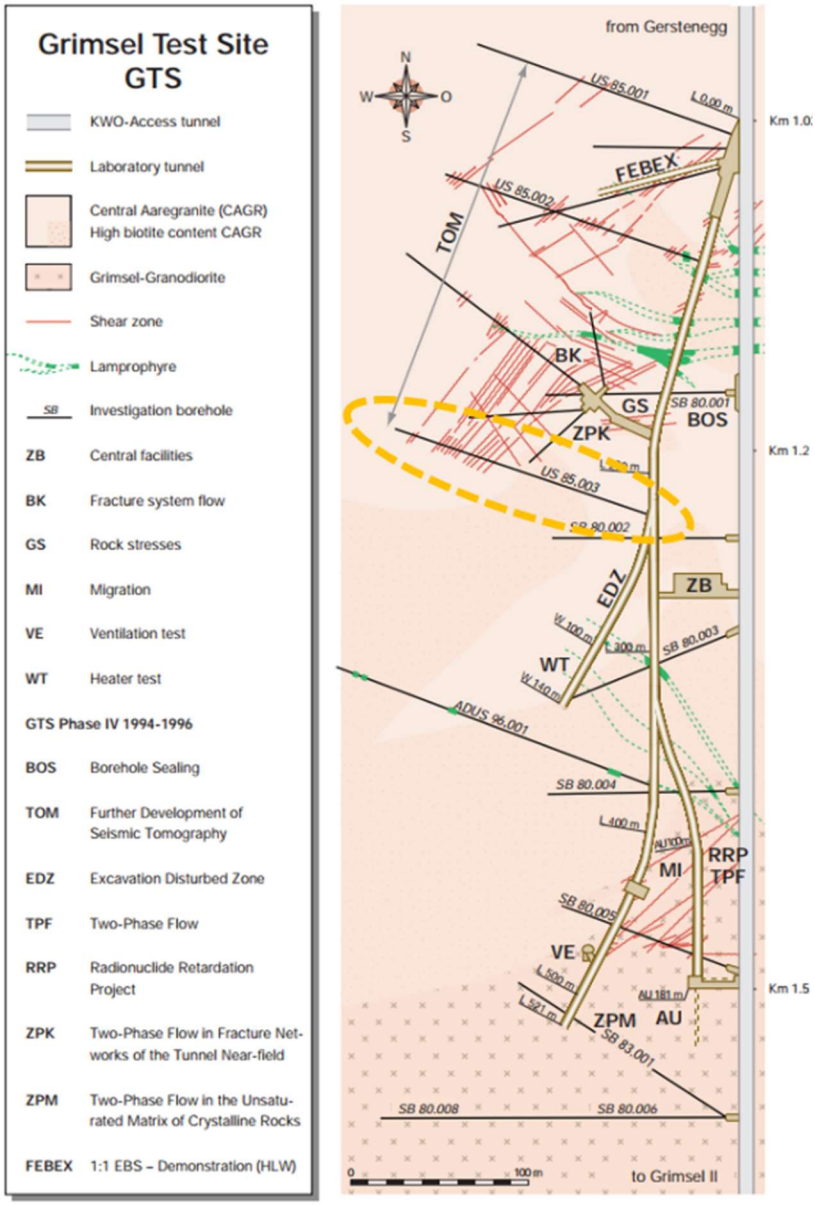

Figure 3.19: *Location of BOUS 85.003 borehole at the Grimsel Test Site. Adapted from* [185].

To calculate the volume of the water required to saturate the bentonite sufficiently, a succession of calculations was performed considering the inner dimensions of the compaction mould that was used for the pellet manufacture (49.50mm inner length and 20.25mm inner diameter). The inner mould compaction volume was calculated using the Equation (3.1). The arising volume is reported in Table 3.25.

$$V = \pi r^2 L$$ Equation (3.1)

Table 3.25: *Calculated inner volume of compaction mould.*

Inner compaction mould volume	15.90±0.30cm^3

Once the inner volume of the compaction mould was known, the mass of Febex bentonite for compaction into pellets was determined using Equation (3.2). A nominal density of 1.65g/cm^3 was chosen for the dry density of the bentonite as representative of repository-like conditions and in accordance the Spanish concept [150]. The mass for each loaded experimental pellet is reported in Table 3.26.

$$Total\ mass = Density \cdot Volume$$ Equation (3.2)

Table 3.26: *Calculated bentonite mass considering a dry density of 1.65g/cm^3.*

Total bentonite mass	26.30±0.03g

The hygroscopic water content of Febex bentonite under laboratory conditions is 13.70% [150]. Knowing the amount of bentonite to be used was calculated using the assumption that the Febex bentonite, when weighed, was at its hygroscopic content using Equation (3.3). Table 3.27 shows the calculated amount of bentonite at its hygroscopic water content.

$$M_{dry\ density} = Mass \cdot \left(1 + \frac{Water\ content}{100}\right)$$ Equation (3.3)

Table 3.27: *Calculated bentonite mass considering its hygroscopic water content.*

Bentonite mass considering its hygroscopic water content	29.90±0.03g

The experiment was designed to be isothermal. In view of the difficulties associated with the installation of a constant water supply, it was necessary to calculate the mass the bentonite would be, if it was saturated, using Equation (3.4). Consequently, bentonite samples were saturated assuming a hygroscopic water content of 13.70%, with the aim to reach a hygroscopic water content of 29% or a degree of saturation of 100% [150]. Table 3.28 reports the calculated bentonite mass, assuming water saturation.

$$M_{saturated\ bentonite} = Mass_{bentonite} \cdot \left(1 + \frac{Desired\ water\ content}{100}\right)$$ Equation (3.4)

Table 3.28: *Calculated bentonite mass considering water saturation.*

Bentonite mass considering water saturation	33.90±0.03g

Finally, to calculate the mass of granitic water needed to achieve sample saturation, the measured saturated mass was subtracted from the calculated mass of bentonite at 29% water content (Equation (3.5)). The amount of water to add to attain saturation is given in Table 3.29.

$$M_{water} = M_{saturated\ bentonite} - M_{dry\ bentonite} \quad \text{Equation (3.5)}$$

Table 3.29: *Calculated bentonite mass considering water saturation.*

Amount of water to achieve saturation	4.025±0.010g

Once the mass of water was calculated, it could be converted into a volume since 1g equals 1ml. Bentonite is characterised by its cohesive nature, so that, when adding water, it tends to form small saturated granules, and water distribution seems to be non-homogeneous. Given the difficulties to perform the experiment with an uninterrupted water supply, the most feasible solution was to achieve the saturation considering a 1:1 ratio. E.g. 29.90g of Febex bentonite must be mixed with 4.025ml of water to achieve saturation and reach a total of 33.90g. To the same amount of bentonite, 29.90g, must be added the same amount of water, 29.90ml. The mixture then oven-heated until a weight of approximately 33.90±0.10g is reached. To ensure water in the samples was homogeneously distributed, four initial samples were prepared and oven-heated at an initial temperature of 80°C. A heating period of 23 hours was required for samples to reach the theoretical weight calculated. Once heated, samples were left to stabilise for three days and weighed again. Sample weights before and after compaction are shown in Table 3.30. Table 3.31 displays pressure applied during compaction. After compaction, sample weights were slightly lower than before compaction, this may be due to the egression of air or water retained in pores.

Table 3.30: *Weight of bentonite samples before and after compaction.*

Sample ID	***Mass before compaction(g)***	***Sample ID***	***Mass after compaction (g)***
Sample 1	33.6444	A	32.0030
Sample 2	33.7112	B	32.5360
Sample 3	33.7779	C	32.1530
Sample 4	33.7623	D	30.8228

Table 3.31: *Pressures applied during compaction.*

Sample ID	*Applied pressures (MPa)*
A	11.768
B	13.729
C	14.710
D	14.416

To guarantee a homogeneous water distribution, samples were cut into three 'proportional' pieces using a diamond wire saw (model STX-2024) and weighed. Subsequently, samples were heated at 100°C for 8 hours to measure if the water distribution was similar across the samples. After heating, samples were weighed again and water content was calculated (Equation 3.6). Table 3.32 shows the water loss for each test sample.

$$Water\ content = \left(\frac{Mass_{saturated\ sample} - Mass_{dry\ sample}}{Mass_{dry\ sample}}\right) \cdot 100 \qquad \text{Equation (3.6)}$$

Table 3.32: *Water lost after heating in sample A and B.[1]Standard deviation water content sample A = 0.048%, [2]Standard deviation water content B = 0.034%,[3]Standard deviation water content sample A = 0.077%, [4]Standard deviation water content B = 0.374%*

Sample ID	*Mass before heating (g)*	*Mass after heating (g)*	*Water content[1, 2, 3, 4](%)*
A1	10.251	7.941	29.088
A2	10.079	7.811	29.038
A3	10.966	8.494	29.099
B1	11.217	8.761	28.088
B2	10.935	8.542	28.012
B3	10.304	8.049	28.009
C1	11.131	8.711	27.782
C2	11.269	8.816	27.822
C3	9.585	7.517	27.539
D1	9.310	7.361	26.488
D2	11.783	9.539	23.529
D3	9.307	7.468	24.623

Figure 3.20 shows the water distribution for test samples A, B, C and D. Test samples A, B and C showed a homogeneous water distribution, while the water distribution in sample D seemed

to be less homogeneous. Despite this, water content in sample D did not deviate from the average water content across the same sample in comparison with the other samples.

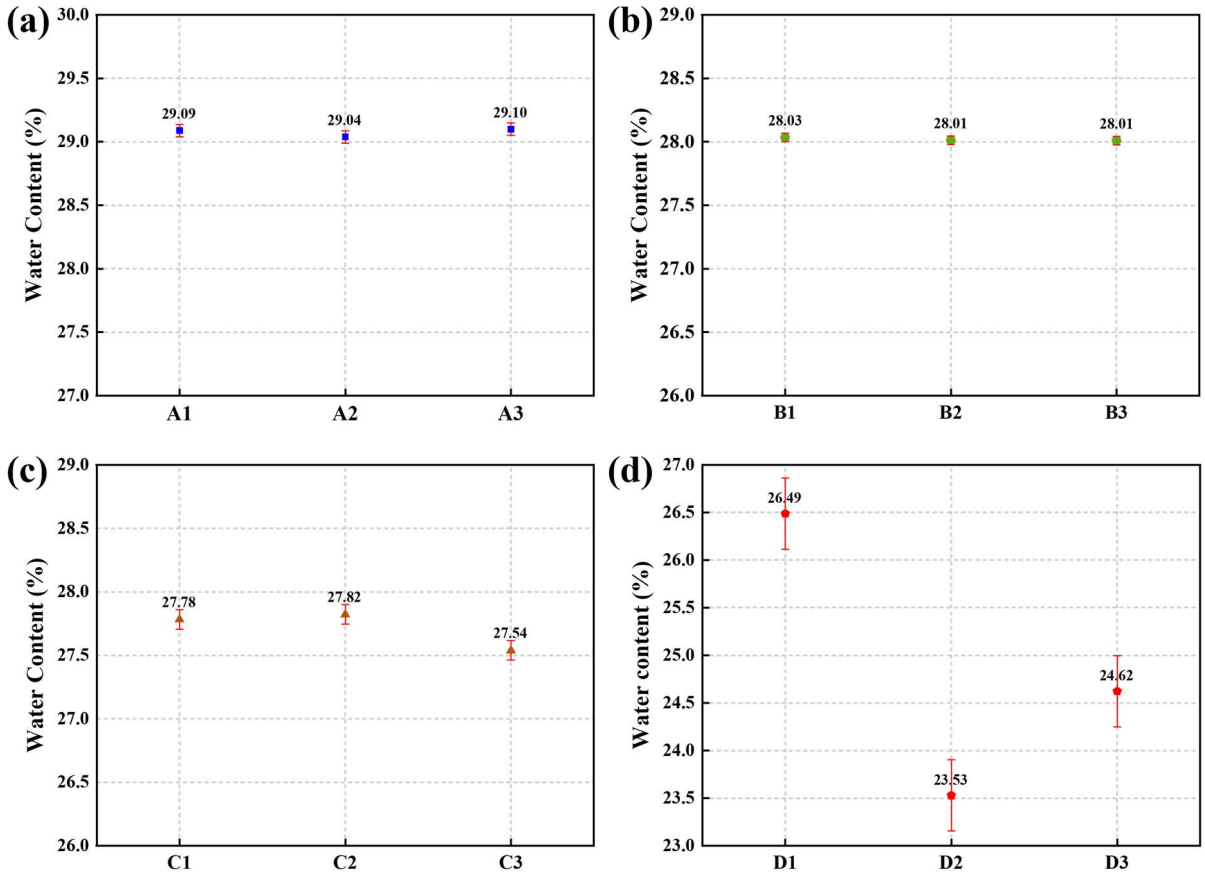

Figure 3.20: *(a) Water content distribution in test sample A. (b) Water content distribution in test sample B. (c) Water content distribution in test sample C. (d) Water content distribution in test sample D.*

3.2.3.3.2.3 Bentonite sample compaction

Following stabilisation of the samples, they were compacted into pellet form to fit inside the cells. This required the stabilised bentonite to be subjected to high pressures to form a cylindrical pellet with similar dimensions to those of the inner volume of the compaction mould, thus assuring that pellets fitted within the experimental cells. Accordingly, a specific mould was manufactured to perform the compaction (Figure 3.21).

The compaction mould consisted of a cylindrical AISI 316L stainless steel base, with an inner bore of 20.25mm diameter and an inner length of 49.50mm, to perform the compaction of bentonite into usable pellets. Externally, the cylindrical base had an outer 75.00mm diameter and 64.50mm length. An auxiliary element was necessary since the volume of the

uncompressed and saturated bentonite would be greater than the inner bore mould. A schematic of the compaction mould can be found in Appendix A (Plane A.1).

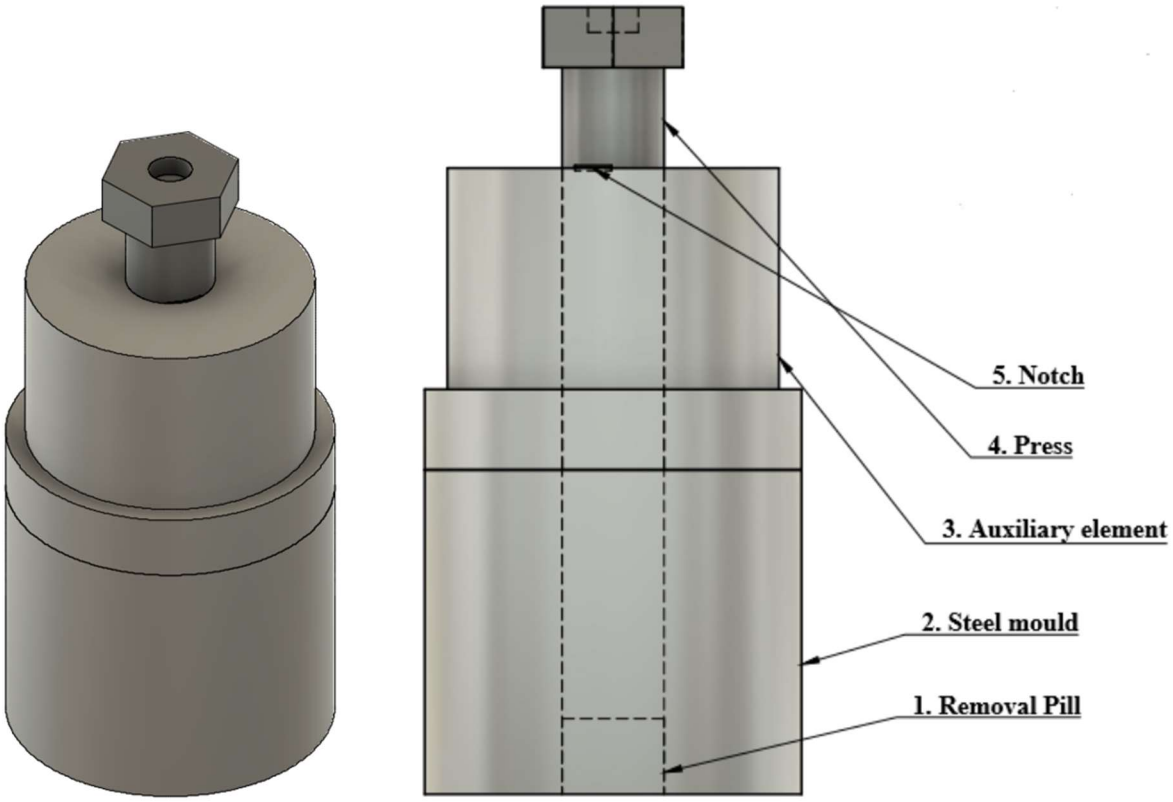

Figure 3.21: *Compaction mould.*

The mould was composed of a large cylindrical AISI 316L stainless steel press-rod measuring 80.00mm long and 20.25mm in diameter. Located in the centre of the mould, a bore, measuring 64.50mm across, pierced through the whole length. A removable pill of diameter 20.25mm and length of 15.00mm, was inserted into the bore, resulting in a bore height of 49.50mm. In order to increase the volume of the bore so that the saturated bentonite could be added, the auxiliary element was tailored on top of the mould, thus resulting in a new bore length of 124.50mm. A steel locating device was designed to guarantee that the bores of the mould and auxiliary element were perfectly aligned. This is then screwed into a base plate to avoid any movement during the compaction process. Finally, when the press-rod was inserted into the assembly, the resulting bore length would be 49.50mm, i.e. the desired length. The bentonite samples were compressed to densities in the region of 1.65g/cm^3 by applying pressures in the range of 20-15MPa, as representative of repository-like conditions as per the Spanish Reference concept [150]. Tables 3.33 and 3.34 present data relating to sample preparation.

Table 3.33: *Data sample preparation for bentonite synchrotron study. [1]Standard error = 0.0345g. [2]Standard error = 0.2199g.*

Sample ID	T (°C)	Time (days)	Mass of bentonite (g)	Volume of water (ml)	Final amount of bentonite in granular form[1] (g)	Sample mass after pelletisation[2] (g)	Pellet final dimension	
							Diameter (mm)	Length (mm)
1	55	61	33.90	33.90	33.0594	30.0824	20.25	49.50
2	65	61	33.90	33.90	33.2344	31.0234	20.25	49.50
3	75	61	33.90	33.90	33.7748	33.6093	20.25	49.50
4	85	61	33.90	33.90	33.0546	30.0299	20.25	49.50
5	95	61	33.90	33.90	33.0564	31.8165	20.25	49.50
6	100	61	33.90	33.90	33.0770	31.4665	20.25	49.50
7	55	122	33.90	33.90	33.9513	30.9015	20.25	49.50
8	65	122	33.90	33.90	33.0185	32.6927	20.25	49.50
9	75	122	33.90	33.90	33.0057	31.5334	20.25	49.50
10	85	122	33.90	33.90	33.9968	33.1182	20.25	49.50
11	95	122	33.90	33.90	33.9632	32.5208	20.25	49.50
12	100	122	33.90	33.90	33.8866	31.8705	20.25	49.50

Table 3.34: *Data sample preparation for bentonite synchrotron study. [1]Standard error = 0.0345g. [2]Standard error = 0.2199g.*

Sample ID	T (°C)	Time (days)	Mass of bentonite (g)	Volume of water (ml)	Final amount of bentonite in granular form[1] (g)	Sample mass after pelletisation[2] (g)	Pellet final dimensions	
							Diameter (mm)	Length (mm)
13	55	183	33.90	33.90	34.9425	32.6913	20.25	49.50
14	65	183	33.90	33.90	33.9603	32.2860	20.25	49.50
15	75	183	33.90	33.90	33.9892	33.7227	20.25	49.50
16	85	183	33.90	33.90	34.9102	32.0994	20.25	49.50
17	95	183	33.90	33.90	34.8846	32.0904	20.25	49.50
18	100	183	33.90	33.90	34.0070	32.7728	20.25	49.50
19	55	211	33.90	33.90	33.8596	32.3432	20.25	49.50
20	65	211	33.90	33.90	34.8528	29.0785	20.25	49.50
21	75	211	33.90	33.90	34.9655	31.5075	20.25	49.50
22	85	211	33.90	33.90	33.9181	31.0634	20.25	49.50
23	95	211	33.90	33.90	33.7421	33.1302	20.25	49.50
24	100	211	33.90	33.90	33.9161	31.4241	20.25	49.50

3.2.3.3.2.4 Sample preparation for synchrotron analysis

Following completion of the experiment, samples were sequentially drawn from the ovens and subjected to x-ray tomography to visually analyse any physical change. Once micro-CT was completed, samples were opened in a nitrogen-purged glovebox (Saffron Scientific Equipment Ltd), and carefully cut with a ceramic knife. For each wire-bentonite interface, powdered samples were prepared. Powders were obtained by grinding each sample in an agate mortar until reaching a grain size of <53µm. Given the difficulties encountered to embed the samples in microcapillaries inside the glovebox, samples were sequentially removed from the glovebox and embedded in borosilicate microcapillaries of 0.5mm inner diameter and 0.01mm wall thickness in normal atmosphere. Finally, each microcapillary was cut into a length between 40-50mm and rapidly sealed using 61 Norland optical adhesive by applying 385nm UV light ensuring the sealing of the microcapillary tops in minutes.

3.2.4 Summary of samples for characterisation

Tables 3.35 to 3.36 collect a summary of bentonite samples under study in the present work.

Table 3.35: *Summary list of bentonite and metal samples from Febex in-situ test.*

Sample ID	**Sampling section**	**Bentonite type**
S-S-54-15-A	54	Ca-bentonite
S-S-54-15-B	54	
S-S-54-15-C	54	
S-S-54-15-D	54	
S-S-54-15-E	54	
M-S-48-1	48	Carbon steel samples
BM-B-41-1	41	Ca-bentonite
Kunigel V1 ABM 1	Parcel 1, block 4	Na-bentonite
Kunigel V1 ABM 2	Parcel 2, block 13	Na-bentonite
Deponit C-AN ABM 2	Parcel 2, block 5	Ca-bentonite
MX-80 ABM 2	Parcel 2, block 17	Na-bentonite
Febex ABM 2	Parcel 2, block 28	Ca-bentonite

Table 3.36: *Summary list of experimental bentonite samples.*

Bentonite type	Sample ID	Temperature (°C)	Exposure time (days)
Febex bentonite	**1**	55	61
Febex bentonite	**2**	65	
Febex bentonite	**3**	75	
Febex bentonite	**4**	85	
Febex bentonite	**5**	95	
Febex bentonite	**6**	100	
Febex bentonite	**7**	55	122
Febex bentonite	**8**	65	
Febex bentonite	**9**	75	
Febex bentonite	**10**	85	
Febex bentonite	**11**	95	
Febex bentonite	**12**	100	
Febex bentonite	**13**	55	183
Febex bentonite	**14**	65	
Febex bentonite	**15**	75	
Febex bentonite	**16**	85	
Febex bentonite	**17**	95	
Febex bentonite	**18**	100	
Febex bentonite	**19**	55	211
Febex bentonite	**20**	65	
Febex bentonite	**21**	75	
Febex bentonite	**22**	85	
Febex bentonite	**23. Grimsel**	95	
Febex bentonite.	**24. Grimsel**	100	

3.3 Material characterisation techniques

To evaluate the state of the samples, a wide variety of laboratory techniques were used throughout this work and are detailed in this section. Most of the techniques used aimed to identify any bentonite chemical and structural changes.

3.3.1 Ion chromatography

3.3.1.1 Overview

Ion-exchange chromatography (IC) relies upon the affinity between ions and polar molecules in solution with an ion exchange material enabling their segregation [187].

3.3.1.2 The IC instrument and operation

IC measures the concentration of certain mixtures of ionic species by segregating them based on their electrostatic affinity with an ion exchanger contained within a column (Figure 3.22). Therefore, IC is a physical separation process based on coulomb interactions, in which the components to be separated are distributed between two phases, one that is stationary (the ion exchange bed) and the other moving in a certain direction (the liquid phase). The immobile ion exchange material in the bed has terminating ionic functional groups at its surface which interact with ions of opposite charge in the analyte. This type of chromatography is subdivided into two different techniques. The present analyses are focussed on cation-exchange chromatography which strips the positively charged cations from solution.

An IC system operates via several stages (Figure 3.22). A liquid sample is initially injected by means of an automated sampler which passes a controlled flow of the sample analyte into the IC system. Concurrently, the sample is mixed with an eluent and, inside the IC system, this mixed solution is pumped through a separator column, a chemically-inert tube packed with a polymeric resin (stationary phase), where the ion separation (ion exchange) takes place. The separation is based on the premise that different sample ions migrate through the IC column at different rates, depending upon interactions with the ion exchange sites available. After the eluent and sample leave the column, they flow through the suppressor, whose selectivity enhances detection of the sample ions while suppressing the conductivity of the eluent.

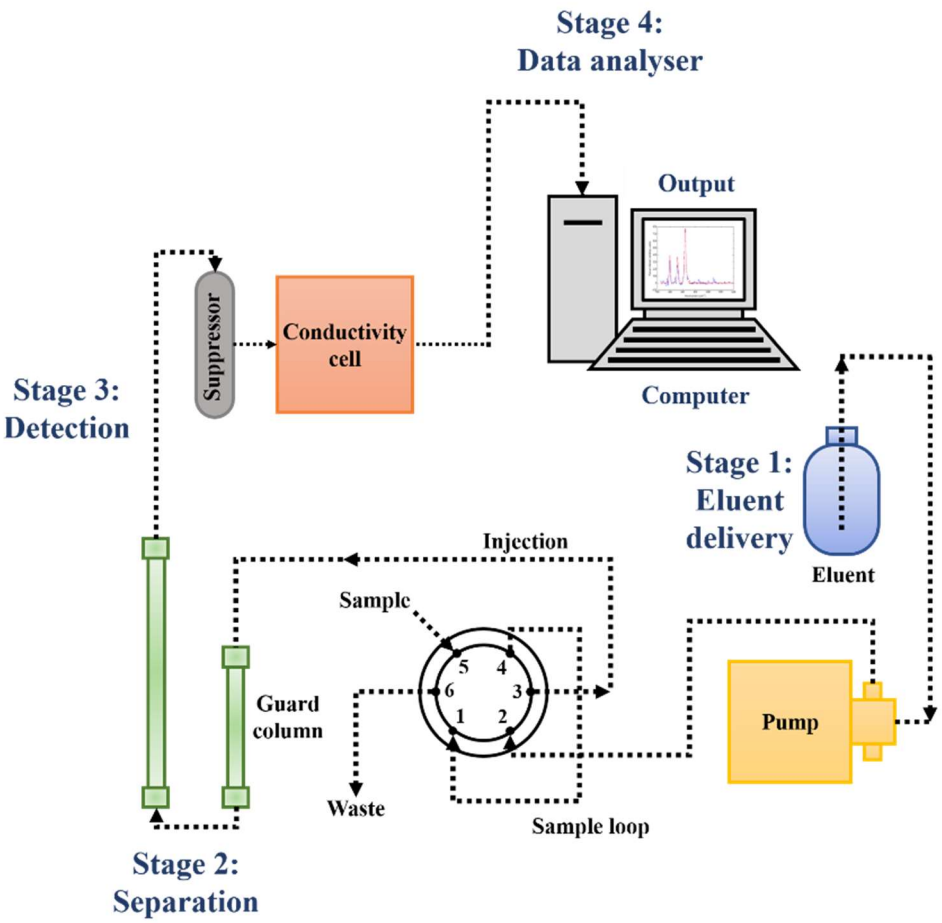

Figure 3.22: *Schematic of typical components of an ion exchange chromatograph, as used in the present work. Modified from* [188].

The electrical conductance of the solution is measured and registered by a conductivity cell, as sample ions emerge from the suppressor and produce an electrical signal based on the chemical and physical properties of the analyte [188]. The instrument used in this work was a Dionex ICS-90 ion chromatography system, fitted with an IonPac CS12A-8µm column (provided with styrene/divinylbenzene surface functionalised with carboxylic acid and phosphonic acid), a CSRS 300 4mm suppressor and a conductivity cell. The instrument was also fitted with a Dionex AS40 sampler to automatically upload the samples. The system uses methanesulphonic acid as an eluent (20mM) at a flow rate of 1ml/min.

3.3.1.3 Sample preparation

Ion chromatography was utilised to analyse the major exchangeable cations (Na^+, K^+, Mg^{2+} and Ca^{2+}) present in the exchangeable complex of each sample from Febex and ABM in-situ experiments. Exchangeable cation analyses were performed following the method developed by Sawhney [189].

A 0.5N caesium nitrate ($CsNO_3$) solution was prepare by diluting 94.455g of $CsNO_3$ in a litre of Milli-Q water. The solution was left to stabilise for 24 hours to permit ionic equilibration of the solution. Once the solution was stabilised, 40ml was added into each powdered sample (<53μm). Samples were dispersed by ultrasonic treatment (20kHz, 400W) for 5min, and magnetically stirred using several multiple-position magnetic stirrers (IKA Werke RO 15 power) for 24 hours of reaction time. Subsequently, the suspensions were transferred into 50ml capacity nalgene centrifuge tubes and centrifuged at 15,000rpm using a Beckman Coulter Avanti J-20 XPI refrigerated centrifuge for 22min. The upper 3ml of the supernatant was carefully removed using disposable pipettes, filtered using 0.45μm syringe filters and finally transferred into glass vials. Before carrying out any IC analysis, samples were diluted using ultrapure water type 1 as a solvent (Milli-Q).

3.3.1.4 Data processing

The ionic concentration measurements are based on the existence of a proportional relation between aqueous concentration of the ion of interest and the analytical/electrical signal or response generated by the instrument. Generally, this relation is linear. Therefore it can be expressed as:

$$y = a + b \cdot C_A \qquad \text{Equation (3.7)}$$

where y is the analytical signal, a is the intercept with ordinate axis, b is the slope of the regression curve and C_A is the analyte concentration.

Table 3.37: *Molecular weight (g), equivalent weight (g) and valence of cations of interest.*

Cation	Molecular weight (g)	Equivalent weight (g)	Valence
Ca^{2+}	40.078	20.039	2
Na^{+}	22.989	22.989	1
K^{+}	39.098	39.098	1
Mg^{2+}	24.305	12.152	2

Calibration standards with varied concentrations (1.25ppm, 2.50ppm, 5.00ppm, 10.00ppm, 25.00ppm and 50.00ppm), of the cations of interest, were prepared and run to obtain the linear equation from the measurement of the analytical signal (peak area) generated by the calibration standards, assuring good quality data. The pairs of concentration-analytical signal values were

fitted by the least-square method to acquire the explicit linear equation from which were obtained the analyte concentrations in the experimental Febex and ABM bentonite samples. Since the samples were diluted, a correction factor was applied to establish the true concentrations. Finally, to express the concentration in cmol(+)/kg the equivalent weight of each cation was considered (Table 3.37).

3.3.2 Thermal analysis techniques

3.3.2.1 Overview

Thermal analysis techniques encompass all those characterisation techniques which measure possible physical and chemical changes in a sample or in its reaction products as a function of temperature variation [190]. Several methods can be subsumed under this denomination, including: (*i*) differential thermal analysis (DTA); (*ii*) differential scanning calorimetry (DSC); and (*iii*) thermogravimetric analysis (TGA). For the present thesis, only the latter was used and, therefore, only this will be further discussed.

In TGA, mass of a sample is monitored versus time or temperature, while linearly increasing its temperature under a controlled atmosphere. Through this technique is observed the evolution of the mass of a sample, allowing the evaluation of possible gains or losses of weight suffered by the sample, caused by dehydration, absorption, desorption, vaporisation or sublimation. The analysis output is known as a thermogram, where mass or mass percentage is plotted as a function of time or temperature.

3.3.2.2 TGA instrument

A standard TGA instrument consists of several components, as presented in Figure 3.23. Any TGA instrument is equipped with a thermobalance, which allows the detection of small changes in sample mass. The thermobalance consists of a sample holder designed to tolerate high temperatures. The sample holder houses a thermocouple to provide control of the sample temperature. Nonetheless, achieving the exact sample temperature is not possible, since direct contact of the thermocouple with the sample may alter the measurement. Samples are accommodated in a crucibles made of various materials and ranging in volume. Samples are loaded into the furnace and deposited onto the thermobalance (located inside the furnace) by

means of an automatic sampler or arm to automate the whole process from sample weighing and loading, through heating and final sample removal after furnace cooling.

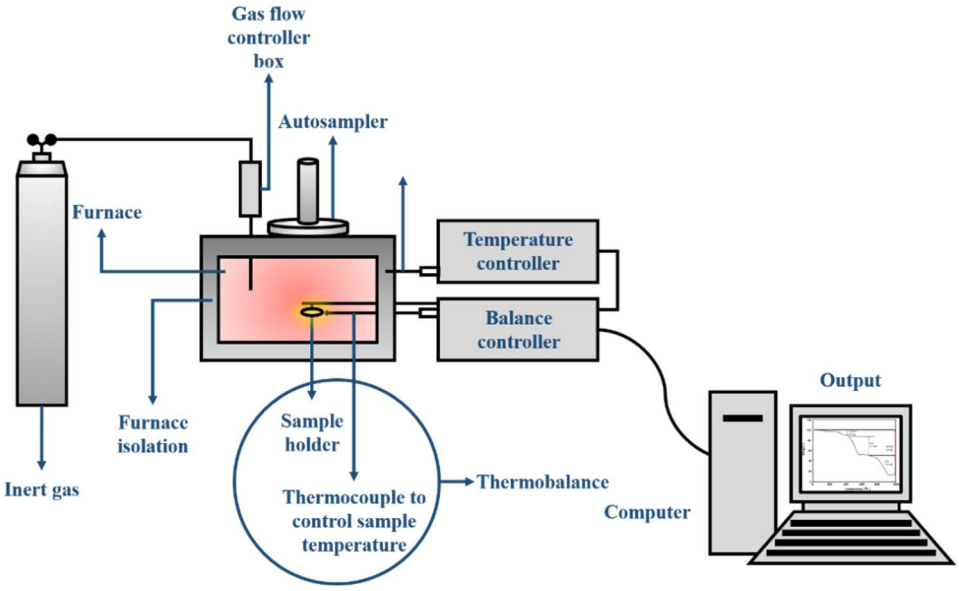

Figure 3.23: *Schematic of a TGA system, as used in the present work.*

To alter sample temperatures, TGA instruments are equipped with a relatively small furnace which covers a wide range of temperatures from ambient to for example 900ºC or 1200ºC. TGA instruments are also endowed with automatic systems to pump an inert gas into the chamber (nitrogen or argon) to inhibit undesirable reactions, and which also allow the control of flow rate into the chamber. The flow rate is specific for each sample under analysis since a low gas flow could lead to the inhibition of some intermediate products involved in elementary stages of a chemical reaction, whereas a high gas flow could affect the precision of the equilibrium through turbulence that will appear in the thermogram. Finally, TGA instruments are provided with computer software for instrument control data collection band processing.

3.3.2.3 Sample preparation, instrument operation and data processing

For TGA analysis, samples were prepared in a nitrogen-purged glovebox (Saffron Scientific Equipment Ltd) to preserve their redox conditions. 0.5g of each sample, plus a reference sample, were ground in an agate mortar until reaching a micrometric grain size (>53µm). A few milligrams of each sample (between 15-30mg) were sequentially removed from the glovebox and TGA analysed.

The instrument used in this work was a Mettler Toledo TGA/DSC with associated STARe software for instrument control and data collection. Samples were measured in 70µl alumina

crucibles using a dry nitrogen purge gas rate of 50ml/min and a heating rate of 10ºC/min in the temperature range from ambient to 1000°C. Data were analysed by comparison with literature sources.

3.3.3 Scanning electron microscopy

In scanning electron microscopy (SEM), a high energy electron beam is rastered across a sample surface. The resulting interactions between the sample and the beam are utilised for chemical analysis and image generation. A typical SEM is composed of: (*i*) an electron source; (*ii*) a column which allows adjustment of the beam through a set of electromagnetic lenses; (*iii*) detectors; and (*iv*) a display system.

3.3.3.1 Overview

The electron beam in a SEM can be generated in three different ways. However, the device utilised in the present work generates the electron beam by field emission. Therefore, this will be further described.

In field emission or cold field electron emission, the emission of electrons is induced by producing an electrostatic field on the 'head' of a tungsten filament of less than 50nm size, when applying a negative potential with regards to the anode. This causes the potential barrier to narrow, and the released primary electrons can tunnel though the potential barrier and abandon the cathode. The primary electrons will collide with sample electrons, giving rise to elastic or inelastic scattering. Figures 3.24 and 3.25 illustrate the derived phenomena from the interactions of primary electrons with the sample surface, which include: (*i*) secondary electrons (SE) due to the ionisation of atoms present in an specimen; (*ii*) backscattered electrons (BSE) arising as a result of Coulomb repulsions between the primary electrons and the nucleus of the sample atoms, resulting in the scattering back of primary electrons (the emission intensity of BSE is directly related with the atomic number (Z) of the atoms in the sample. Therefore, the higher the Z, the greater the number of emitted electrons.); (*iii*) x-rays during SE production, electrons from internal levels can be expelled, leaving behind a vacancy that can be occupied by an electron from high energy levels, causing the x-ray emission (x-ray emission is related to the every level configuration, and this is utilised to acquire information of the elemental composition of a sample); and (*iv*) Auger electrons emitted following interactions of x-rays with neighbouring electrons and the transfer of energy.

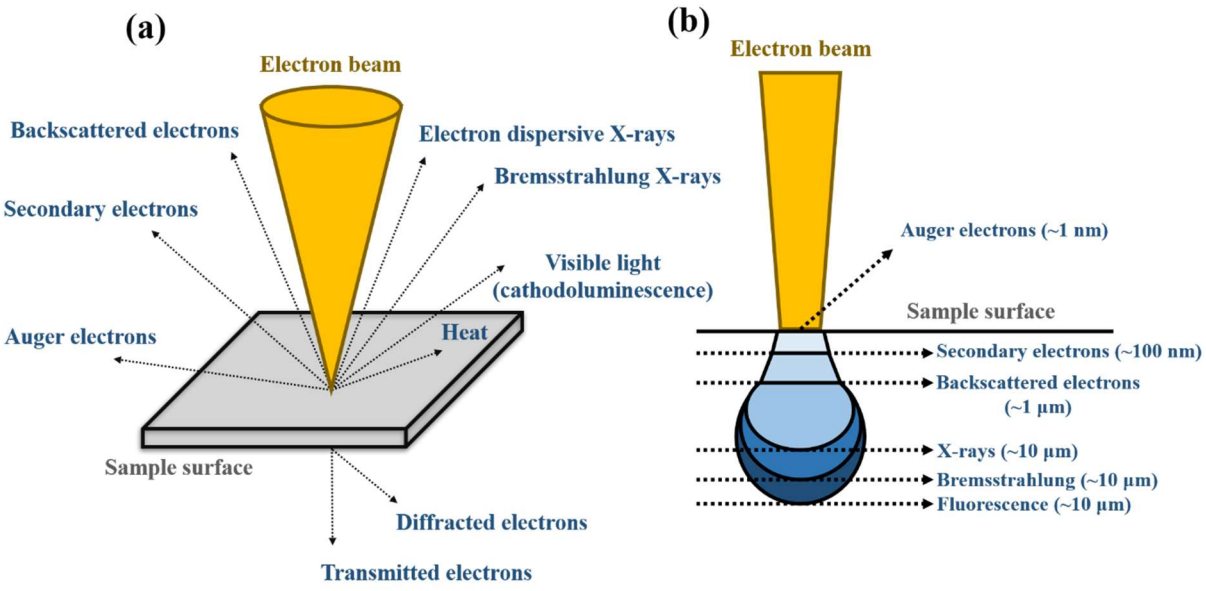

Figure 3.24: *(a) Different electron-sample interactions. (b) Origin of the different signals detectable by SEM. Modified from* [191].

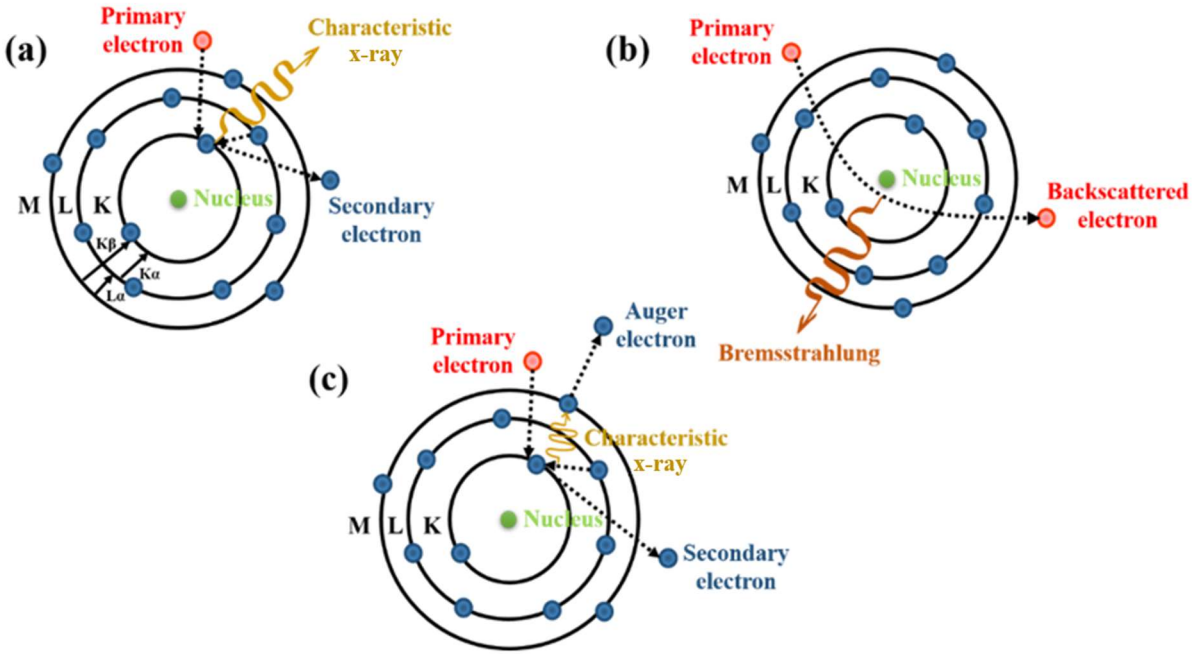

Figure 3.25: *Modes of electron emission owing to the incidence of an electron beam. Modified from* [191].

The described emissions are utilised to acquire images and perform analyses at the points of interest of a sample by means of the use of different detectors placed in the SEM chamber.

The combination of atomic weight of the atoms comprising a sample, and the energy of the incident beam determine the volume of interactions, as shown in Figures 3.24 and 3.25. The

volume of interactions proportionally increases with the energy of the incident beam, and decreases with the atomic weight of the atoms in a sample.

3.3.3.2 The SEM instrument

Figure 3.26 shows a schematic configuration of a SEM, as utilised in the present work. In a SEM instrument, the electron gun releases the primary electrons which are accelerated up to dozens of keV. The accelerated primary electrons are focussed through electromagnetic lenses and objective lenses to finally be driven onto the specimen surface, and give rise the emissions described in section 3.3.3.1. Depending on results desired, several analyses can be carried out and the signal is registered by the SE, BSE and x-ray detectors. Finally, images are obtained by synchronising the amplified current signal and the monitor.

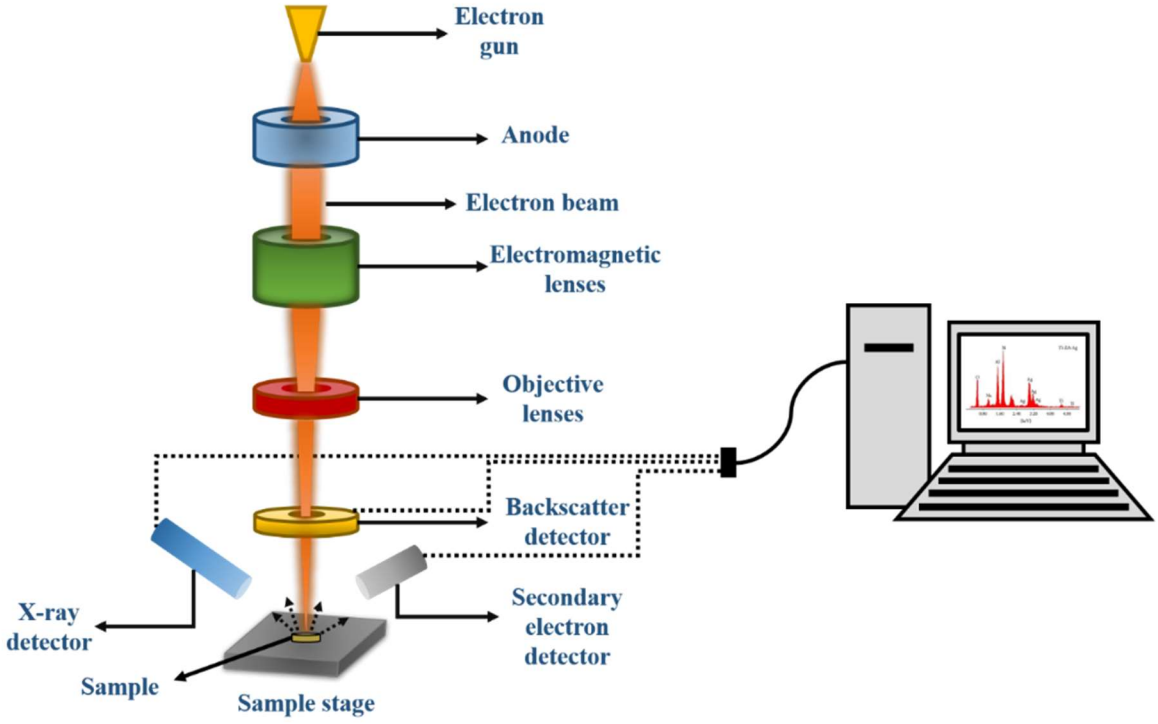

Figure 3.26: *Outline of an SEM instrument, as used in the present work.*

3.3.3.3 Sample preparation, instrument operation and data processing

SEM was utilised for morphological analysis on corrosion coupon sample, and to identify the nature of the corrosion layer. The encapsulated specimens in resin were observed and analysed under SEM (Zeiss Sigma HD VP Field Emission SEM with EDAX EBSD and Octane Plus EDX with tungsten filament). Elemental surface analyses were accomplished by energy dispersive x-ray (EDX) analysis.

3.3.4 X-ray characterisation techniques

3.3.4.1 X-ray production

X-rays are electromagnetic radiation (EM or EMR) of the same nature as radio waves, microwaves, infrared, visible light, ultraviolet and gamma rays, with a wavelength ranging from 0.01 to 10nm. X-rays differ from gamma rays in their origin. Gamma rays are produced by de-energisation of a nucleon from an excited level to a lower energy level, and during the radioactive decay of radioactive isotopes. X-rays arise from an 'extra-nuclear' phenomenon at electron orbit level, fundamentally produced by deceleration of electrons. X-ray energies lie between ultraviolet radiation and naturally-occurring gamma rays, and is classified as ionising radiation due to the ionisation of atoms when interaction with matter takes place, that is, it originates 'charged particles' or ions [192].

The fundamental principle of x-ray production for surface analysis techniques is based on the conversion of the kinetic energy of an electron into electromagnetic radiation. In x-ray diffraction and x-ray tomography, x-rays are generated within an x-ray tube (Figure 3.27) by applying a large voltage between a cathode and an anode, enclosed inside a high vacuum encasement. When the filament (cathode) is heated, an emission of electrons is produced via the thermionic effect creating an electron cloud. Due to the difference of electric potential between the electrodes, the electrons are attracted towards the anode [192].

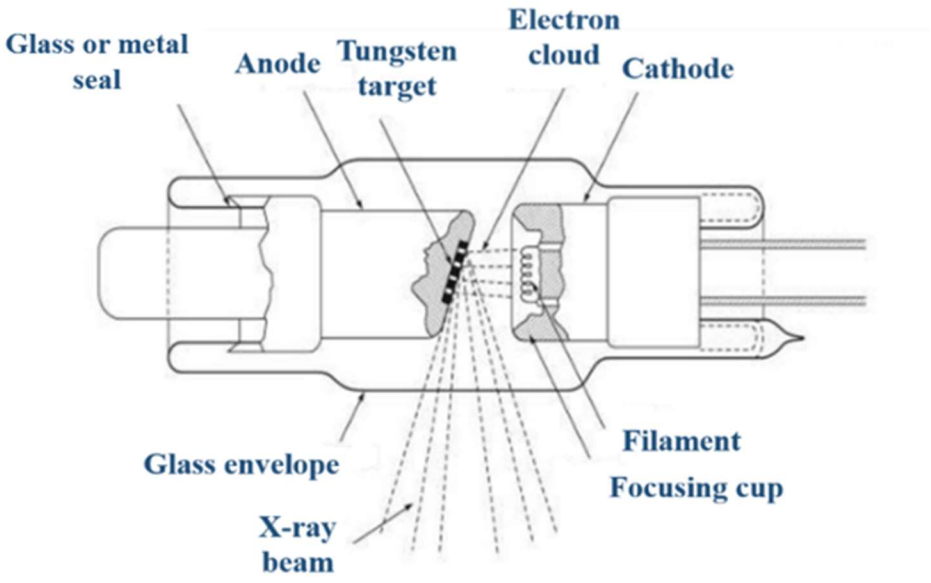

Figure 3.27: *Schematic of the major components of an x-ray tube, as used in XRD and XRT instruments. Modified from* [193].

Once electrons impact with the anode or target, they cede their kinetic energy by its conversion into other forms (mostly heat) due to interactions with nuclei and cortical electrons. Some electrons are rapidly decelerated when encountering with a positively-charged nucleus in the target, losing its kinetic energy by discharging an x-ray photon. This type of electromagnetic radiation is known as bremsstrahlung, or 'braking radiation'. Furthermore, if the kinetic energy of an electron exceeds the binding energy of an electron in the target, then ionisation of an atom occurs through ejection of an electron. If the ejected electron pertains to a very deep orbital layer (typically K or L) then the return to ground state is via emission of a very energetic photon, called an x-ray [192].

3.3.4.2 X-ray diffraction

3.3.4.2.1 Overview

X-ray diffraction discloses information relating to the crystallographic structure, chemical composition and physical properties of a sample. The basis of this technique lies in the phenomenon known as 'scattering', which consists of the deviation of an incident photon from its original direction of propagation with equal (elastic scattering) or lesser (inelastic scattering) energy owing to its collision with an electron. Thereby, when an x-ray beam collides with the electron cloud of the atoms of a sample part of the x-ray energy is transmitted into the electrons, causing them to oscillate at the same frequency, reaching an excited state. To return to the ground state, the electrons radiate their excess energy.

In a crystalline solid, atoms are ordered in space, and form a three-dimensional crystallographic network; thus crystals are periodic stacks. The x-radiation has an undulatory nature with wavelengths (λ) comparable to the distances between atoms. Consequently, x-rays, when entering into a sample, are diffracted at angle θ, that is to say in a certain direction from a d_{hkl} distance, interfering constructively when the phase difference between the emitted radiation by different atoms is proportional to 2π. This condition is illustrated by Bragg's law in Equation 3.6 and Figure 3.28.

$$n\lambda = 2d_{hkl} \cdot sin\,(\theta) \qquad \text{Equation (3.6)}$$

where n is a positive integer, λ is the wavelength of x-ray incident, d_{hkl} is the spacing between successive planes and θ is the incident angle.

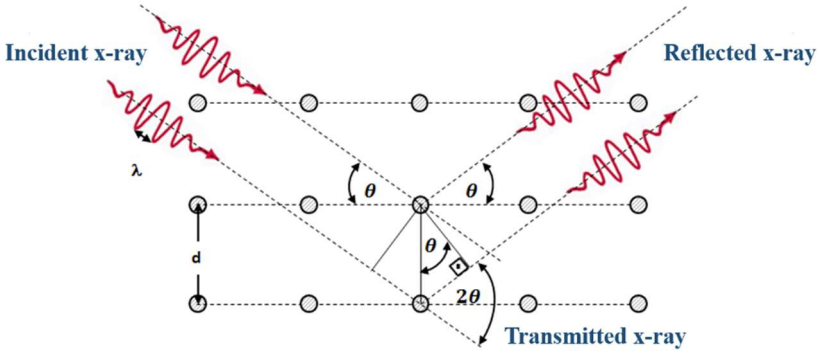

Figure 3.28: *Schematic of Bragg's law condition* [194].

3.3.4.2.2 The XRD instrument

The main components of an XRD instrument are shown in Figure 3.29. In x-ray diffraction, the x-rays are monochromated, since it is desirable to restrict their wavelength range. The monochromator consists of a pair of collimators (divergent and soller slits) composed of a series of closely-spaced metal 'plates' that absorb all radiation beams except parallel ones.

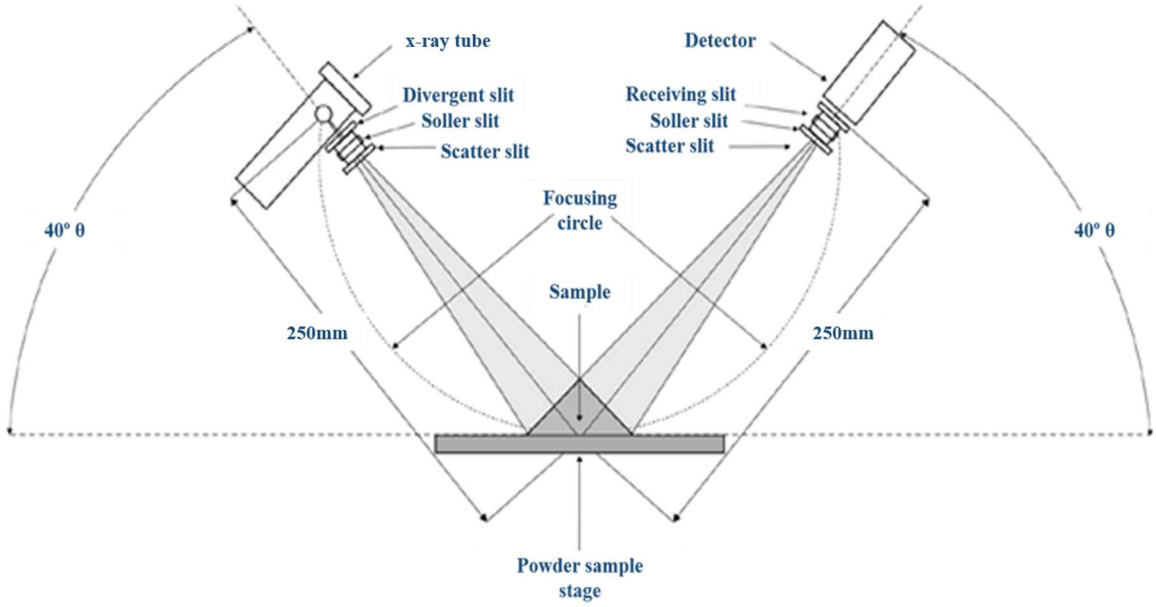

Figure 3.29: *Schematic of the main components of an x-ray diffractometer. Adapted from* [195].

The collimated beam is focussed onto the sample mounted on a goniometer (first plate), allowing determination of the angle θ. From Equation 3.6 it is evident that at any angle chosen with the goniometer, only a few wavelengths are diffracted to contribute towards a spectrum, it is necessary that when the sample rotates to an angle θ, the detector simultaneously moves to angle 2θ. Therefore, the collimated output beam and the detector are mounted on a second plate which rotates at twice the speed of the first.

For the present work, two different instruments were used: (*i*) a Bruker D8 Advance diffractometer equipped with a CuKα 1.54056Å x-ray source and energy dispersive Sol-X detector, for bentonite analysis; and (*ii*) a Phillips X'pert Pro Diffractometer equipped with a CuKα 1.54056Å x-ray source, for corrosion coupon analysis.

3.3.4.2.3 Sample preparation

The bulk mineralogy of bentonite samples were determined by random powder analysis. To minimise air exposure and, thereby, limit oxidative alteration of materials, sample preparation was undertaken in a nitrogen-purged glove-box (Saffron Scientific Equipment Ltd). Each sample was analysed as rapidly as possible. Powders were obtained by grinding 1g of each sample in an agate mortar to a particle size less than 53µm; each sample was sieved using a 53µm nylon mesh. Through this sample preparation, the samples have their crystals arranged in every possible crystallographic direction, so that there will always be a larger number of crystals non-oriented, and it is possible to identify maximum diffractions for a given group.

Randomly-oriented samples were measured using a Bruker D8 Advance diffractometer equipped with a CuKα X-ray source and energy dispersive Sol-X detector (operating at 40kV and 40mA). Scans were carried out from 2 to 65° in 2θ, with a dwell time of 1s and a step size of 0.02°.

The morphology of clay minerals is mainly phyllosilicates with 00l orientation. Random powder XRD for this group of minerals is not as conclusive and unequivocal as in many other groups, which do not present the preferred orientation evident in clay minerals. Therefore, it is essential to arrange a spatial mineral order. This additional arrangement for clay minerals is achieved by taking advantage of the fact that these minerals, due to their laminar structure, develop two-dimensional shapes which, by suitable preparation, can be arranged in parallel layers 'like the leaves of a book'.

The oriented mounts aim to intensify the basal reflections of clay minerals present in bentonite. To accomplish a semi-quantitative analysis of bentonite samples, it is all-important to separate the clay fraction (<2µm) from the bulk sample. Overall, the decantation technique is used to 'force' the clay bentonite mineral particles to lie flat based on 'Stokes' law to achieve a separation of the fraction less than 2µm. To analyse the clay mineralogy in the oriented mounts, the following treatments were performed: (*i*) air drying; (*ii*) solvation with ethylene glycol; and (*iii*) thermal treatment to 550ºC [196].

For each sample three oriented aggregates (OA) were prepared, which were allowed to air dry. The first OA was analysed directly, the second OA was analysed once subjected to an ethylene glycol (EG) atmosphere at 60ºC for at least 24 hours. The third OA was analysed once heated at 550ºC for at least two hours.

Oriented mount (OM) samples were measured using a Bruker D8 Advance diffractometer equipped with a CuKα X-ray source, operating at 40kV and 40mA and energy dispersive Sol-X detector. Scans were carried out over 2 to 35° in 2θ with a dwell time of 1s and a step size of 0.02°.

XRD analysis was also performed on the surface of the metallic coupon samples for which no sample preparation was required. Surface metallic coupons were measured using a Phillips X'pert Pro Diffractometer with a CuKα x-ray source and point Xe proportional detector, operating at 40kV and 40mA. Scans were carried out over 15 to 100° in 2θ with a dwell time of 4s and a step size of 0.05°.

3.3.4.2.4 Data processing

Phase identification of random powder and clay mineralogy on OA for each bentonite sample were performed by using DIFFRAC.EVA software. Phase identification on metallic coupons samples were carried out using MATCH! Phase identification programme.

3.3.4.3 X-ray tomography

3.3.4.3.1 Overview

X-ray tomography (XRT), x-ray micro-tomography (μXRT) or micro-computed tomography (μCT) is a non-destructive technique which provides high-resolution three-dimensional images, allowing study of the inner structure of materials. Micro-computed tomography is based on the attenuation of x-rays passing through a sample which is being imaged. Starting from the premise that an axial section of a sample can be considered as an area composed of voxels or discretised regions of an object, with a spatial resolution of Δx, Δy, Δx, each voxel having an effective attenuation, μ (ability to absorb photons) [197]. When an incident beam with I_0 intensity penetrates a sample, throughout an L trajectory, passing through each sample voxel with an inhomogeneous distribution of attenuations $\mu(x)$. The beam intensity $I(x)$ that

reaches the detector depends on: (*i*) the distance, *x*, traversed; and (*ii*) the attenuation at each point on its trajectory, obeying Beer-Lambert's law:

$$I(x) = I_0 \cdot e^{-\int_L^0 \mu(x)dx} \qquad \text{Equation (3.7)}$$

Since it is possible to know the initial beam intensity I_0 and the intensity of the beam that reaches the detector $I(x)$, Equation (3.7) can be re-written as:

$$P(x) = -ln\left(\frac{I(x)}{I_0}\right) = \int_L^0 \mu(x)dx \qquad \text{Equation (3.8)}$$

The resolution of Equation (3.8) provides the projections $P(x)$ and has two important implications: (*i*) the detector registers the integral lines which depend on the attenuation of each voxel; and (*ii*) although volumetric information as each area is composed of voxels, the detector is registering projections $p(x)$ which are no more than a unidimensional signal of θ angle, with such projections being stored in a matrix, $p(x,\theta)$, known as a sinogram. After the reconstruction, a two-dimensional image is obtained where each pixel has an intensity proportional to the estimated value of its attenuation μ (Figure 3.30).

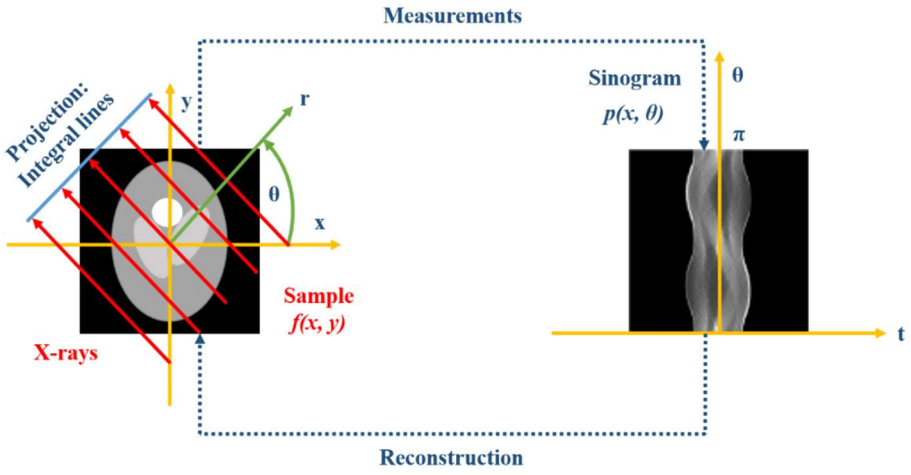

Figure 3.30: *Schematic of reconstruction process. Modified from* [197].

The major problem during the image reconstruction is the assignment of an appropriate attenuation, μ, to each voxel used to discretise the sample. This assignment is done by using analytical or iterative methods. The analytical method involves the direct solution of a linear equation system, the retro-projection and filtered back projection (FBP). The iterative method is referred to as the algebraic reconstruction technique (ART), and involves the use of iterative

statistical methods [197]. For the purpose of this section, the focus here is on the iterative method, since it is the one used by the instrument utilised in the present work. The iterative method is based on a comparison between the projections (p^i) of a proposed object (f^i) and the original projections measured by the detector (p^0). The proposed object (f^{i+1}) is upgraded considering the difference between the projections. Mathematically, this process can be expressed as:

$$p^i = A \cdot f^i + e \qquad \text{Equation (3.9)}$$

where A corresponds to a matrix that depends on such parameters as: (*i*) system geometry; (*ii*) detector response; and (*iii*) other physical parameters of the utilised device, and e is the noise induced error (i.e. by the detector) [197].

3.3.4.3.2 The XRT instrument

Figure 3.31 illustrates the main components of a transmission μXRT instrument. The x-ray tube releases the x-rays by the same principle described in section 3.3.4.1. The x-ray beam is collimated using filters that focus the beam geometry in a cone-beam projection, removing the low-energy x-rays.

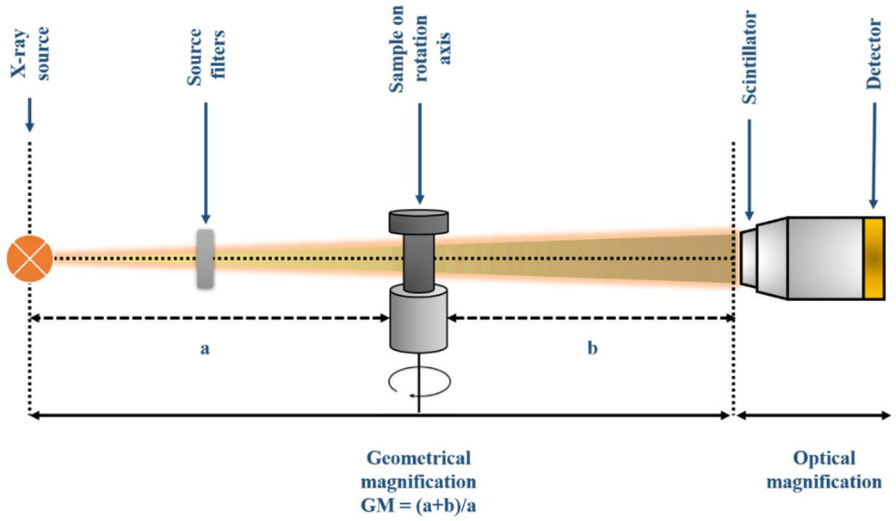

Figure 3.31: *Schematic of the principal components of a microcomputed tomography scanner.*

The sample is positioned between the x-ray source and the x-ray detector. For μCT to be possible, a rotational motion of the sample with regards to the detector is needed, so that 2D image projections are acquired as the x-ray beam passes through the sample, while the sample

is rotating. The attenuated and transmitted x-ray beam from high energy photons is captured by a detection system, which converts them to visible light by means of a scintillator. The visible light is magnified by an optical objective before it reaches a charge-coupled device camera (CCD). The CCD counts with a sensor that converts the images into digital signals which are sent out to a computer for further processing. 3D images of a sample are created by mathematically-reconstructing the 2D image projections, and each voxel represents the x-ray absorption at that point.

3.3.4.3.3 Sample preparation and instrument operation

µCT was utilised on bentonite samples intended for synchrotron study. Samples were scanned before and after thermal loading to visualise any changes at the boundary of the embedded metal bodies. µCT was also utilised on the BM-B-41-1 sample. Tomography reconstructions of samples were produced using a lab-based x-ray µCT (Zeiss Xradia 520 Versa). The µCT system has the characteristic spectrum from a tungsten target. The setting of the accelerating voltage and tube current was based on the x-ray absorption coefficients of the samples. The parameters of the µCT scans are listed in Table 3.38. Resolution of 2D images was of 2,048x2,048 (corresponding with binning 2). The transmission images form all the scans were automatically reconstructed by the scout-and-scan control system associated with the equipment.

Table 3.38: *µCT scanning parameters.*

CT Scan	High magnification synchrotron samples	BM-B-41-1 Febex sample
CT instrument	Zeiss Xradia 520 Versa	Zeiss Xradia 520 Versa
Accelerating voltage (kV)	140	160
Source power (W)	10	10
Optical magnification	4x	0.4x
Source to sample distance (mm)	Depending wires position	29
Sample to detector distance (mm)	35	150
Exposure time (s)	1	5
Number of Projections	2001	2001
Binning	2	2

3.3.4.3.4 Data processing

Reconstructed volumes were imported to XM3D Viewer (commercial software) to produce representative digital volumes of the BM-B-41-1 sample. Avizo was utilised to produce 3D volumes of metal bodies.

3.3.4.4 Synchrotron

3.3.4.4.1 Overview

The synchrotron source utilised for this thesis work was Diamond Light Source (DLS), located at Harwell, Oxfordshire (UK). DLS is a third-generation synchrotron because it combines the use of insertion devices with traditional bending magnets to produce synchrotron light. The 3GeV storage ring became operational in 2007, and it produces a wide range of wavelengths from x-rays to infrared. In synchrotrons, the EM is emitted by particles travelling close to the speed of light, and this is known as synchrotron light or synchrotron radiation.

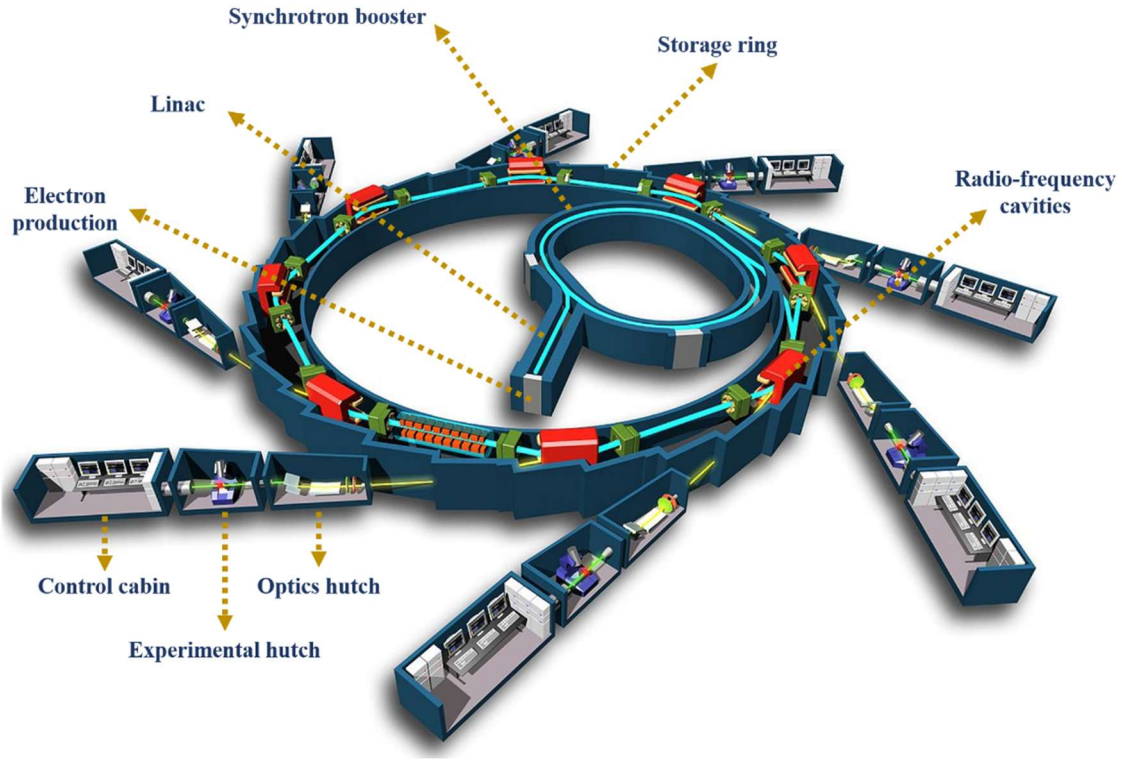

Figure 3.32: *Main components of a third-generation synchrotron. Modified from* [198].

Figure 3.32 shows the main components of a third-generation synchrotron facility [199]. DLS is accommodated in a toroidal building, containing: (*i*) a linear accelerator, or linac; (*ii*) a synchrotron booster; (*iii*) storage ring; and (*iv*) the associated beamlines. In a third-generation

synchrotron, the synchrotron light is produced by heating a cathode subjected to high voltage, all within high vacuum to produce electrons. The electrons pass to a linear accelerator, or linac, which imparts to them an energy of 1GeV using radio-frequency cavities. Subsequently, the electrons are injected into a synchrotron booster which imparts them the final energy (3GeV) through additional radio-frequency cavities, before their injection into the storage ring. In DLS, the storage ring is not completely circular, and is composed of 48 sections with 48 dipolar or bending magnets (one per section). This configuration gives rise to changes in the direction of electrons when passing by the vicinity of the magnets, curving the electron beam while circulating through the storage ring, which produces the synchrotron light. In addition, DLS is also equipped with insertion devices in the straight sections of the storage ring, increasing the beam intensity. As electrons circulate through the ring, they lose energy in the form of light. This light is channelled into the experimental beamline, composed of: (*i*) an optics hutch, where the light is filtered and focussed; (*ii*) an experimental hutch, where the experiments are performed; and (*iii*) a cabin, where the experiments are controlled. DLS has several beamlines but only I11 was utilised in this work.

3.3.4.4.2 The I11 instrument

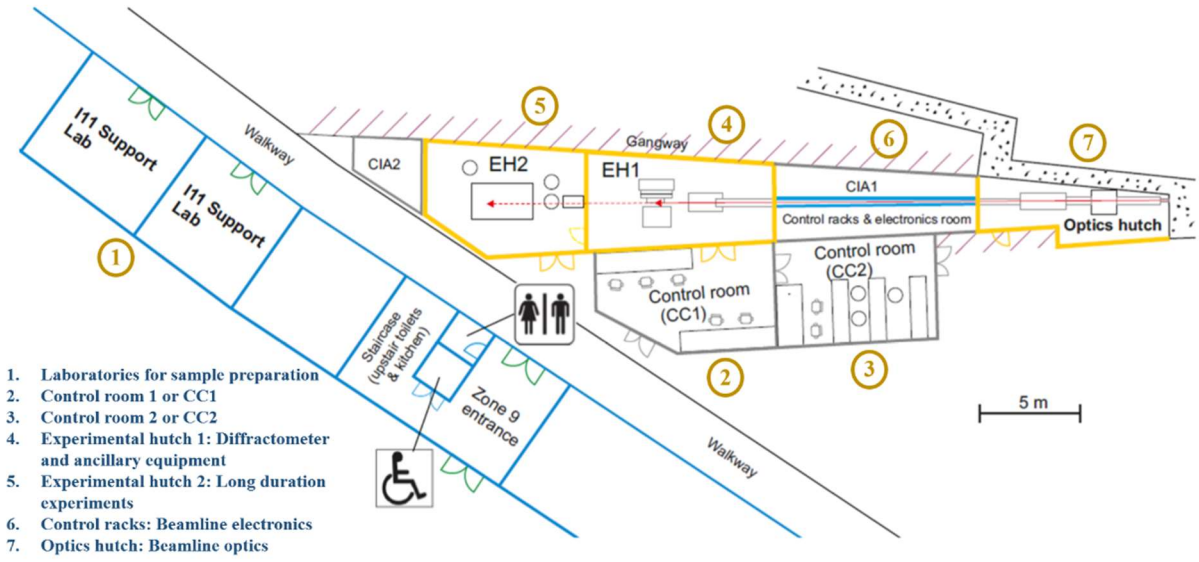

Figure 3.33: *Schematic of I11. Modified from* [200].

Figure 3.33 displays a schematic of the I11 beamline facility. The beamline is equipped with two experimental hutches: EH1; and EH2 [200]. However, only the first was utilised in the present work. Therefore, a description of the diffraction instrument and associated ancillary elements present in EH1 is given below.

Figure 3.34 presents a representation of EH1 and its ancillary elements [201], [202]. The optics hutch houses: (*i*) slit systems: (*ii*) beam diagnosis; (*iii*) monochromators; and (*iv*) harmonic rejection mirrors.

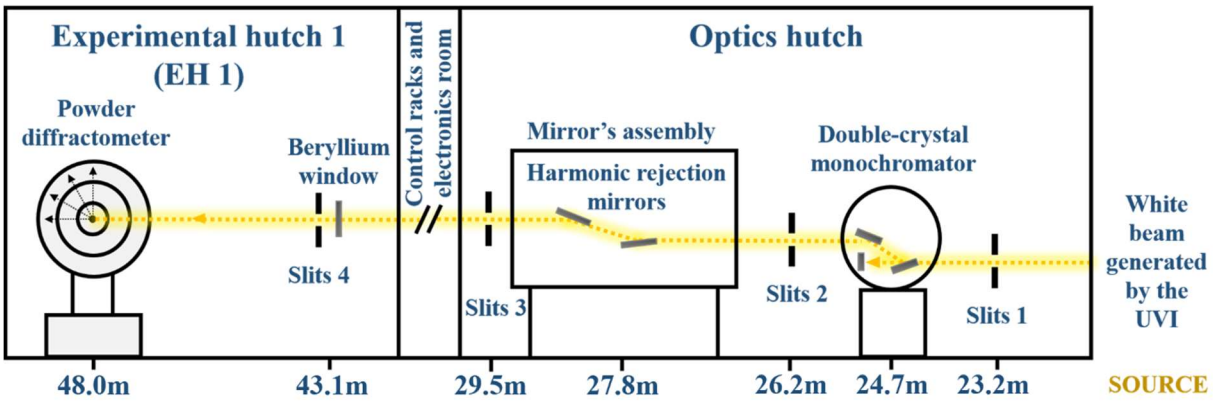

Figure 3.34: *Schematic of EH1 and associated ancillary elements. Modified from* [201].

The white beam is generated by the in-vacuum hybrid undulator, and is trimmed and defined by slits 1 (23.2m from the source). At 27.4m from the source there is a double-crystal monochromator that stabilises and provides a fixed exit of the beam geometry. The output beam passes though slits 2 (26.2m from the source), and impinges onto a sequence of harmonic rejection mirrors (27.8m from the source) that clean the beam, rejecting high energy photons and preventing 'contamination' of measurements, while working at low energies. The 'clean' beam passes through slits 3, and is directed into EH1, where it passes through a beryllium window and slits 4 (43.10m from the source) to be finally focussed onto the sample.

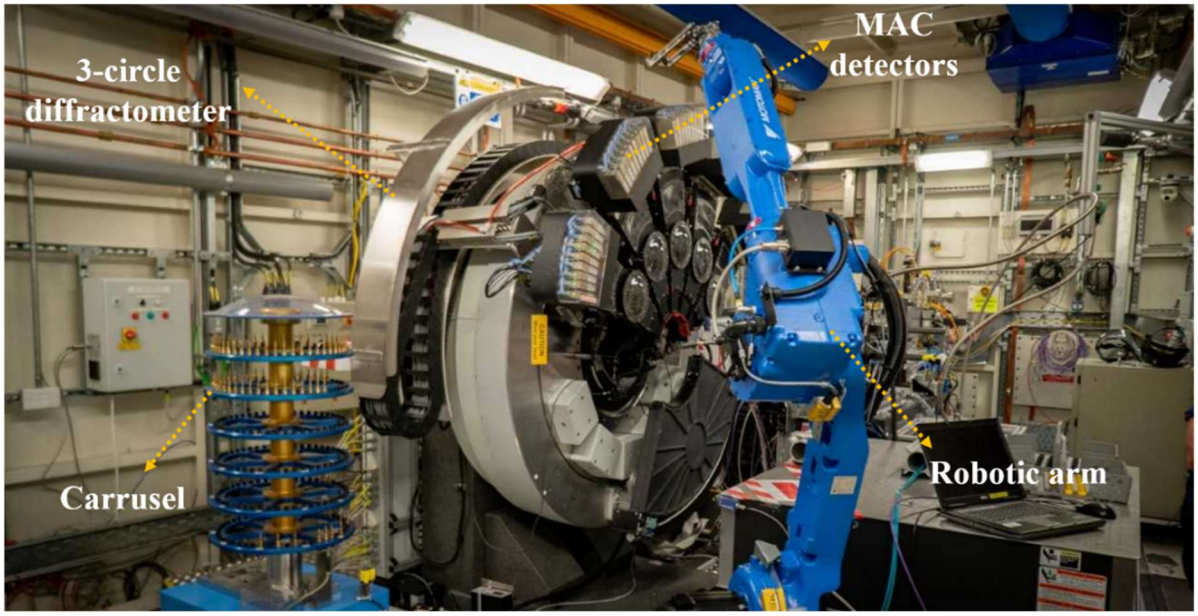

Figure 3.35: *Photo of I11 diffractometer.*

EH1 is located just after the control racks and electronics room, and holds all the instrumentation related to the diffractometer. The experimental hutch is endowed with a three-circle diffractometer (Figure 3.35 and Table 3.39) with three co-axial high precision rotary stages (θ-, 2θ-, δ-circle), 48.0m from the source. The 45 individual silicon crystals speed up the collection of data. Bentonite powder specimens embedded in microcapillaries and mounted onto a brass holder were positioned on the inner θ-circle. Specimens were loaded in the instrument by means of a robotic arm and aligned at the diffractometer centre of rotation, which itself is aligned with the x-ray beam.

Table 3.39: *Three-circle diffractometer components.*

High resolution diffraction: Multi-analysing crystal (MAC): X5 MAC-arms with 45 MAC channels.	MAC1	2θ coverage: 0-30°
	MAC2	2θ coverage: 30-60°
	MAC3	2θ coverage: 60-90°
	MAC4	2θ coverage: 90-120°
	MAC5	2θ coverage: 120-150°

3.3.4.4.3 Instrument operation and data processing

Table 3.40 collects the specifications of EH1 set up for high-resolution diffraction on bentonite samples at I11. A total of 88 samples were measured.

Table 3.40: *Specifications of EH1 set-up for high resolution diffraction.*

Source	90 pole in-vacuum undulator (U22)
Energy range (keV)	15
Wavelength (Å)	0.824523
Beamsize at sample (FHMW) (mm)	-0.8(v) x 2.5(h)
Photon flux at sample at 300 mA	1.70 x1013 ph/s/0.1%bw at 15keV
Resolution (Δ2θ, analysing crystal)	0.006405°
Temporal resolution (PSD)	30-60 mins per pattern

Peak identification was performed using MATCH! Phase identification programme.

3.3.5 Optical spectroscopy techniques

The geometry of a polyatomic system is determined by its lengths and bonding angles. As a matter of principle, these lengths and bonding angles can be obtained from spectroscopy data.

Spectroscopy refers to any experimental technique that is based on the interaction of EM with matter, resulting in emission, absorption and scatter phenomena.

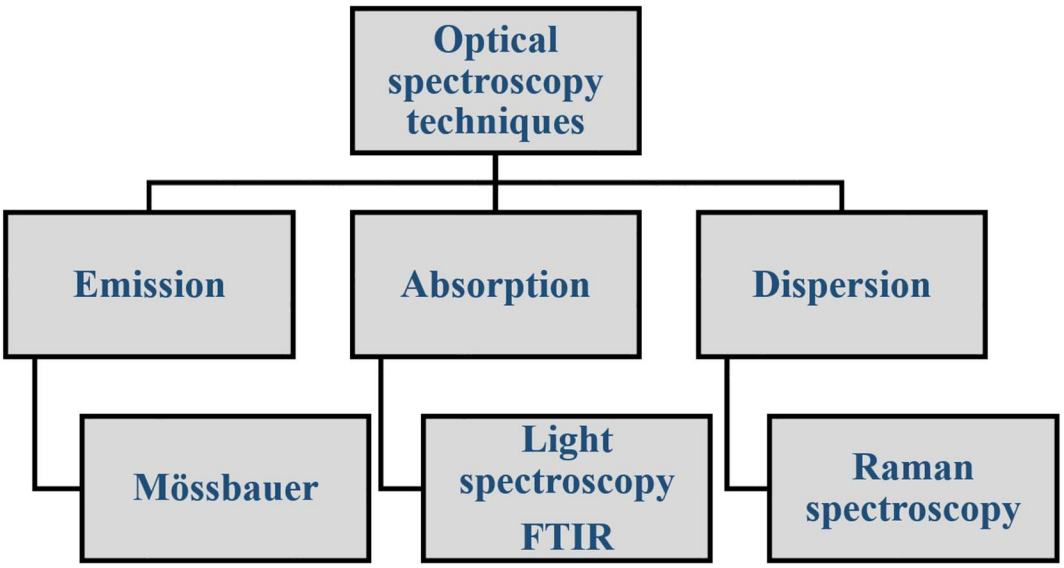

Figure 3.36: *Optical spectroscopy techniques.*

EM is characterised by a certain intensity (I_0) and frequency (v_0), and its interaction with matter can induce changes in both parameters. These interactions lead to one of the three general types of spectroscopies noted above (Figure 3.36). Therefore, the same physical phenomenon can be studied from different point of views: (*i*) absorption (when using infrared radiation); and (*ii*) scattering (when using Raman spectroscopy). This section explains succinctly the fundamentals of the optical spectroscopy techniques used in the present thesis.

3.3.5.1 Light spectroscopy

3.3.5.1.1 Ultraviolet-visible spectrometry

3.3.5.1.1.1 Overview

The underlying physical principles of light spectroscopy techniques are based on photon interactions with one or more substances present in a sample.

Light spectroscopy involves the absorption of an ultraviolet-visible photon by an atom, causing the transition of an electron from a basal state up to an excited state or higher energy level, attaining an unstable position. The electron then quickly falls back to the ground state and, in so doing, emits a photon with the same energy as the difference between the energy levels, as shown in Figure 3.37.

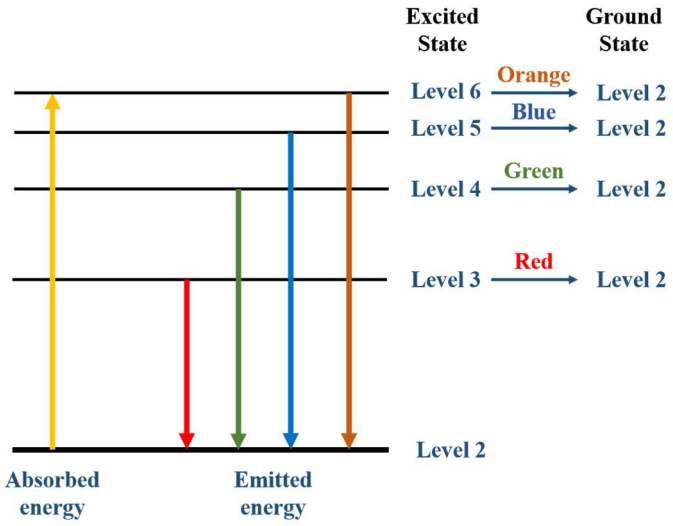

Figure 3.37: *Absorbed and emitted energy by an electron. Modified from* [203].

When light photons are focused on a solution containing an absorbent analyte, they can either pass through unaffected or be absorbed by valence electrons, and thus be promoted to excited states of higher energy. This absorption phenomenon can be expressed by the Beer-Lambert law, which states that absorption by a solution is linearly related to the concentration of the absorbing species and the path length of the radiation in the absorbing medium [203].

$$A = \varepsilon \cdot l \cdot c \qquad \text{Equation (3.10)}$$

where A is the measured absorbance, ε is the wavelength-dependent molar absorptivity coefficient or molar absorption coefficient ($M^{-1}cm^{-1}$), l is the path length and c is the analyte concentration.

3.3.5.1.1.2 The UV-Vis instrument

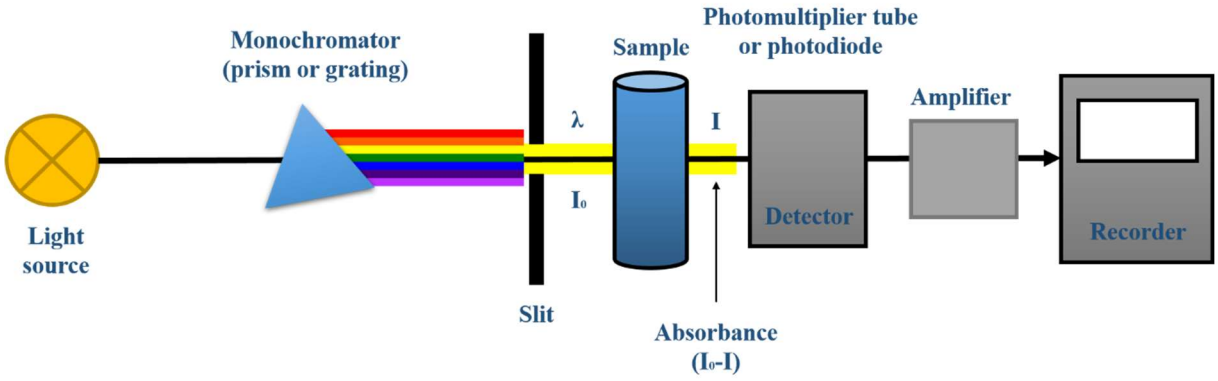

Figure 3.38: *Layout of the main components of a typical single beam UV-Vis spectrometer, as used in the present work.*

Figure 3.38 shows the main components of a UV/Vis spectrometer. A visible or UV light beam (with wavelengths between 400-800nm and 200-400nm respectively) is focussed onto a prism or diffraction grating (monochromator), which separates the light into its discrete wavelengths. The diffracted spectrum of light passes through a further slit before transiting the sample, contained within a 4mm cuvette in the sample chamber. The intensity emitted by the photons is collected by the detector (photomultiplier tube or photodiode) and the signal is processed and recorded. The spectrometer automatically scans all the component wavelengths in the manner described.

3.3.5.1.1.3 Sample preparation and instrument operation

UV-Vis spectroscopy was utilised for analysis of the cation exchange capacity (CEC) on samples from the Febex and ABM in-situ tests. The ion-exchange capability of smectites greatly influence their cation retention properties and diffusion processes of charged and uncharged molecules, having, therefore an important role in cation and molecule migration through the clay barrier in a GDF. Sample preparation was performed following the method described by Meier and Kahr [57]. A total of 18 samples were analysed. This method was selected to determine the CEC of the bentonite samples due to the high affinity of the Cu in the blue Cu(II) ethylenediamine complex for clay minerals [57]. Therefore, Cu(II) complexes with triethylenetetramine allow a rapid and easy determination of the CEC of clay minerals by photometrical determination [57].

To achieve the preparation of Cu(II)-trien, two solutions were prepared. The first solution was prepared by dissolving 1.4632g of triethylenetetramine in 100ml of Milli-Q water. The second solution should have contained 1.596 of $CuSO_4$ in a litre of distilled water. However, for availability reasons, copper(II) sulphate pentahydrate ($CuSO_4 \cdot 5H_2O$) was used. Consequently, some calculations were needed to estimate the right amount of $CuSO_4 \cdot 5H_2O$ to be use. The amount of copper(II) sulphate pentahydrate was obtained considering the molecular weight and the amount of copper sulphate described in the selected method.

$$n = \frac{mass\ of\ CuSO_4 in\ grams}{molar\ mass\ of\ CuSO_4} \qquad \text{Equation (3.11)}$$

Table 3.41: *Moles of CuSO4 to be use proposed in Meier and Kahr method.*

Moles of CuSO4	0.009996 ± 0.004g

Having estimated the number of moles (Table 3.41), and knowing the molarity of the solution intended to prepare (0.01M). The next step was to estimate the amount (g) of $CuSO_4 \cdot 5H_2O$ to use, considering the molecular weight of $CuSO_4 \cdot 5H_2O$ (249.593g/mol).

$$0.01\ moles\ of\ CuSO_4 \cdot \frac{1\ mol\ of\ CuSO_4 \cdot 5H_2O}{1\ mol\ of\ CuSO_4} \cdot \frac{249.593\ g\ of CuSO_4 \cdot 5H_2O}{1\ mol\ of\ CuSO_4 \cdot 5H_2O} = \mathbf{2.49593\ grams\ of\ CuSO_4 \cdot 5H_2O}$$

2.4960g of $CuSO_4 \cdot 5H_2O$ were weighed using digital scales and mixed with Milli-Q water to obtain 0.900ml of solution. Finally, both solutions were mixed together to obtain a litre of 0.01M Cu(II)-trien sulphate solution.

Two batches of samples were prepared. For that purpose, 200mg of ground air-dried samples were weighed using digital scales. Subsequently, 40ml of Milli-Q water was added, and samples were dispersed by ultrasonic treatment (20kHz, 400W) for five mins, and magnetically stirred using a multiple position magnetic stirrer (IKA Werke RO 15 power). While stirring, 10ml of the Cu-trien solution were added and left to stir for 1 hour reaction time. Subsequently, the 50ml suspension was transferred into 50ml nalgene centrifuge tubes, and the suspension was centrifuged at 15,000rpm using a Beckman Coulter Avanti J-20 XPI refrigerated centrifuge for 22 mins. The upper 3ml of the supernatant was carefully removed using disposable pipettes and transferred into spectrophotometer cuvettes (4ml) and the extinction was measured at 620nm against a blank prepared without sample.

3.3.5.1.1.4 Data processing

Finally, the cation exchange capacity (CEC) was determined on the basis of uptake of Cu-complex by bentonite samples. All CEC determinations were done in duplicate to assure the analysis repeatability, and the CEC estimation was performed using Equation 3.12 [57].

$$CEC\ (mmol/100g) = \frac{(E_b - E_m)}{E_b} \cdot 100 \qquad \text{Equation (3.12)}$$

3.3.5.2 Fourier transform infrared spectroscopy

3.3.5.2.1 Overview

Infrared spectroscopy techniques are based upon the absorption of infrared radiation by molecules in vibration, which leads to changes in the vibrational state of molecules, since molecules can rotate and vibrate at different frequencies.

Essentially, radiation energy located in the infrared wavelength range (Table 3.42) can be absorbed by a molecule (or part of it), which is vibrating in its basal state at the same wavelength as the incident infrared radiation, causing a change in the intensity of its vibration.

Table 3.42: *Wavelength (λ), wavenumber ($\bar{\upsilon}$) and frequency (υ) of the ultraviolet, visible and microwave regions of the electromagnetic radiation. Adapted from* [204].

Region	λ (cm)	$\bar{\upsilon}$ (cm^{-1})	υ (Hz)
Ultraviolet			
Far	$1 \cdot 10^{-6}$ to $2 \cdot 10^{-5}$	$1 \cdot 10^{6}$ to $5 \cdot 10^{4}$	$3 \cdot 10^{16}$ to $1.5 \cdot 10^{15}$
Near	$2 \cdot 10^{-5}$ to $3.8 \cdot 10^{-5}$	$5 \cdot 10^{4}$ to $2{,}63 \cdot 10^{4}$	$1.5 \cdot 10^{15}$ to $7.9 \cdot 10^{14}$
Visible	$3.8 \cdot 10^{-5}$ to $7.8 \cdot 10^{-5}$	$2{,}63 \cdot 10^{4}$ to $1{,}28 \cdot 10^{4}$	$7.9 \cdot 10^{14}$ to $3.8 \cdot 10^{14}$
Infrared			
Near	$7.8 \cdot 10^{-5}$ to $2.5 \cdot 10^{-4}$	$1{,}28 \cdot 10^{4}$ to $4 \cdot 10^{3}$	$3.8 \cdot 10^{14}$ to $1.2 \cdot 10^{14}$
Middle	$2.5 \cdot 10^{-4}$ to $5 \cdot 10^{-3}$	4,000 to 200	$1.2 \cdot 10^{14}$ to $6 \cdot 10^{12}$
Far	$5 \cdot 10^{-3}$ to $1 \cdot 10^{-1}$	200 to 10	$6 \cdot 10^{12}$ to $3 \cdot 10^{11}$
Microwave	$1 \cdot 10^{-1}$ to $1 \cdot 10^{2}$	10 to 0.1	$1 \cdot 10^{12}$ to $3 \cdot 10^{8}$

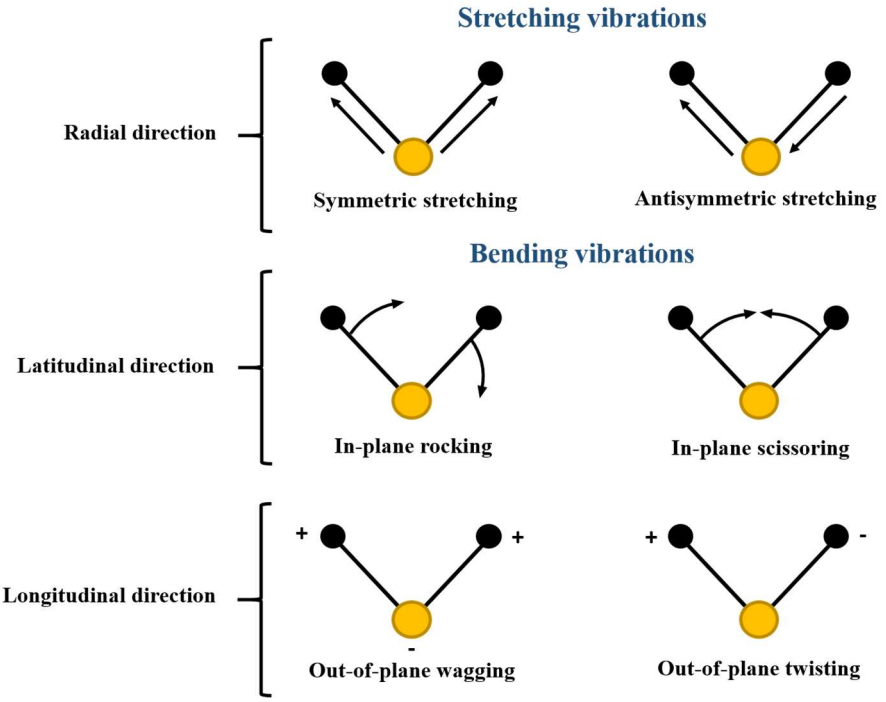

Figure 3.39: *Vibrational molecule modes. Modified from* [205].

The vibrational movements of a molecule can be broken down into oscillations in which atoms move in phase, giving rise to normal vibrational modes with characteristic frequencies. Two basic categories of vibrational modes can be distinguished: (*i*) stretching; and (*ii*) bending. Figure 3.39 shows the different vibrational modes of a molecule [204]. The stretching

vibrations are changes in the interatomic distances along the axis of the bond between two atoms, while bending vibrations are caused by changes in the angle formed by atomic bonds.

As displayed in Figure 3.39, the atoms of a molecule are not fixed with respect to each other but instead vibrate around their equilibrium positions. The energy needed to generate a vibration depends on the binding energy and the mass of the atoms involved, so that molecules vibrate with a certain energy value. The existence of these values to produce a vibration implies that only photons with sufficient energy in the infrared will be absorbed by those atomic bands with a dipole moment [206]. Therefore, a necessary condition for a vibration to occur in a molecule is the presence of a dipole moment. Consequently, if the dipole moment is zero there is no absorption of infrared radiation.

Any non-centrosymmetric molecule with regards to its electric charge, has a permanent dipole moment, which is a function of its geometrical characteristics. Due to internal vibrations (Figure 3.39), changes can occur in its geometrical characteristics leading to changes in dipole moment. Thus, when the frequency of these changes and the frequency of the incident infrared radiation is the same, there will be a reinforcement 'in-phase' of the interaction, and the dipole will absorb the energy. Therefore, the ultimate mechanism of interaction is the electrostatic coupling between the periodically-changing dipolar molecule and the electric field electromagnetic radiation. In addition, non-polar molecules can create an instantaneous dipole moment driven by the asymmetry produced by an inner vibration. This enables molecules to interact with infrared frequencies, giving rise to vibrational transitions [206].

These vibrational transitions can induce oscillations that come into resonances with the infrared beam, producing an energy exchange between the infrared beam and molecules or energy absorption by resonance. Therefore, there is a characteristic behaviour for a molecule with an atomic type, chemical environment and concentration of certain bonds. It can be said that the infrared spectrum bands associated with virtually all molecular compounds can be observed with each of these bands corresponding to a vibrational movement of one of the bonds within the molecule, creating a fingerprint for the compound.

Infrared analyses are based on the measurement of beam intensity before (I_0) and after (I) interaction with the sample, since molecules can absorb infrared radiation without later reemission by exciting certain vibrational frequencies. Results are expressed as a function of the frequency of the incident beam. To understand the behaviour of diatomic molecules in

vibration and study their vibrational frequencies, the harmonic oscillator model based on Hooke's law is used as the simplest vibrating system [207]. The harmonic oscillator model considers a molecule as two masses 'joined' by a spring with a constant given force (k), leading to changes in internuclear distances. Consequently, the force can be expressed as:

$$F(x) = -k \cdot x \qquad \text{Equation (3.13)}$$

where x is the displacement from equilibrium. Combining Hooke's law with Newton's force law, the vibrational frequency corresponds to:

$$\bar{\upsilon} = \frac{1}{2\pi}\sqrt{\frac{k}{\mu}} \qquad \text{Equation (3.14)}$$

where μ is the reduced mass of two bonded atoms, k is the force of constant the bond and $\bar{\upsilon}$ is the frequency of the absorbed band. From this equation, it can be seen that the frequency of a vibration and its energy are a function of the bond strength. However, vibrational energy is quantised, so that a harmonic oscillator has no continuum for vibrational energy level, but only certain discrete energy levels:

$$E_v = h\bar{\upsilon}\,(v + \tfrac{1}{2}) \qquad \text{Equation (3.15)}$$

In reality, a chemical bond is not truly a harmonic oscillator, which implies that energy levels are not equally spaced. Although, the vibrational energy of a system is quantised, the absorption takes place if, and only if, the frequency of the incident beam coincides with the vibrational frequency of the molecule ($\bar{\upsilon}$).

3.3.5.2.2 The FTIR instrument

FTIR instruments are based on the Michelson interferometer, but also include other components such as: (*i*) the infrared source (IR); (*ii*) the detector; and (*iii*) a data recording system. Figure 3.40 displays a schematic of an FTIR instrument of the type used in the present work. The polychromatic infrared beam emerging from the source enters into the optical interferometer and passes through a beam splitter, which directs half of the radiation towards a fixed mirror and the other half to a moveable mirror. The two rays recombine in the beam splitter in a constructive or destructive manner depending on the position of the mirrors,

resulting in an interferogram. The output beam from the interferometer passes through the sample cubicle, where it is transmitted or reflected by the sample depending on the results intended to achieve.

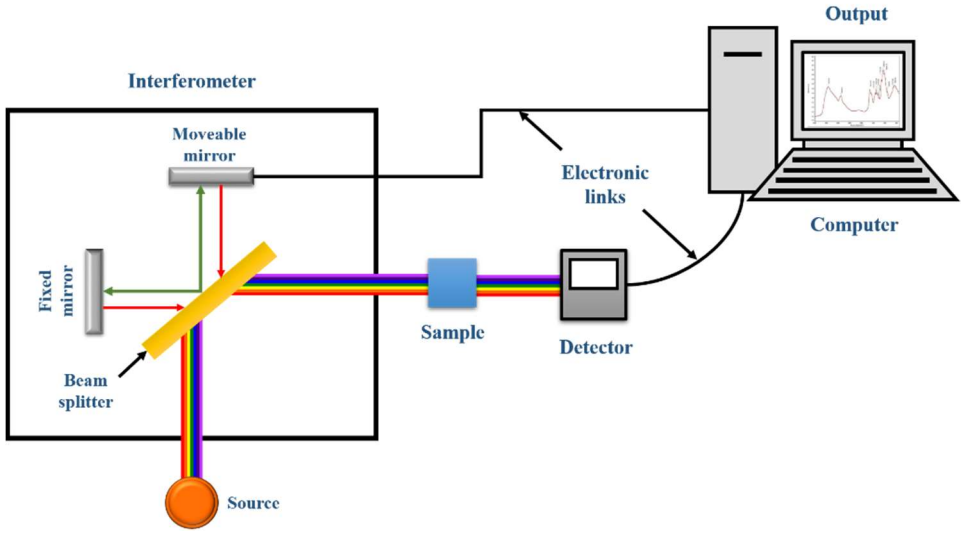

Figure 3.40: *Schematic of an FTIR instrument, as used in the present work.*

The detector monitors the full wavenumber range of infrared radiation to collect data for the Fourier transformation. The Fourier transformation is a tedious mathematical method which converts the interferogram into an absorption spectrum.

3.3.5.2.3 Sample preparation and instrument operation

FTIR spectroscopy was performed in the mid-infrared spectra region (MIR). Two sampling techniques were considered [208]: (*i*) attenuated total reflectance (ATR); and (*ii*) the potassium bromide (KBr) pressed disc technique.

Attenuated total reflectance was used for bentonite powdered samples. Samples were ground to a fine powder (<53µm), and no further preparation was needed. The ATR spectra in the MIR region were collected using a Perkin Elmer Spectrum Two FTIR spectrometer provided with a single reflection diamond ATR accessory. The sampling plate device was equipped with a diamond crystal, which allowed analysis of the powdered samples in the range of 4000-400cm^{-1}. The powdered samples (~0.50g of each sample approximately) were placed on the diamond crystal, and pressure was applied using the movable pressure arm which enabled good contact between the sample and the crystal to obtain high-quality spectra. For each powdered sample, 128 scans in the 4000-400cm^{-1} spectral range were recorded with a resolution of 4cm^{-1} at room temperature.

The potassium bromide (KBr) pressed disc technique is the most widespread method used to prepare a solid sample for routine scanning in the MIR region, due to the transparency of potassium bromide throughout the spectral region. Sample preparation was implemented within an argon-purged glovebox (MBRAUN unilab pro sp) owing to the hygroscopic features of the KBr. Therefore, KBr must be preserved as dry as possible, since water absorbs intensely in the infrared, and water traces can spoil the spectrum. The purpose of utilising the KBr technique was to better visualise the Si-O stretching modes (550-450cm^{-1}) from the tetrahedral entities, which cannot clearly be identified with the ATR technique.

Bentonite samples from both experiments were ground to fine powder (<53µm). 2mg of each sample were weighed using digital scales. Sequentially, 200mg of KBr were also weighed for each sample. Powdered bentonite samples were mixed with the KBr and transferred into an agate mortar, and the mixture was ground until the samples were well dispersed and reached the consistency of 'fine flour'. Finally, to produce and obtain usable pellets, a manual hydraulic press pellet (Specac) provided with a pressure gauge, was used. The admixtures of bentonite and KBr were compacted into fine discs of 13mm diameter by applying pressure in the range of 6-10t. This sample preparation was intended to allow recording of a good spectrum in the region of 4000-400cm^{-1}, with special attention being paid to the infrared region between 950-750cm^{-1}, corresponding to the octahedral cation-OH deformation bands. The FTIR spectra were recorded using a Perkin Elmer Spectrum Two FTIR spectrometer, equipped with an IR source, and a standard room temperature $LiTaO_3$ MIR detector. Additionally, the spectrometer was provided with a standard base plate which allowed us to fit and hold horizontally in place the sample holder to perform the measurements in the MIR. For each pellet sample, 128 scans in the 4000-400cm^{-1} spectral range were recorded with a resolution of 4cm^{-1} at room temperature.

3.3.5.2.4 Data processing

Data obtained were processed by manual comparison with published reference data.

3.3.5.3 Raman spectroscopy

3.3.5.3.1 Overview

The Raman effect was predicted by Smekal (1923) and Kramers-Heisenberg (1925), and shown to the world by C.V. Raman in 1928 [209]. Since then, the technique has been commonly used

to obtain chemical and structural information from organic and inorganic compounds, and many advances in the technique have led to its continued used today.

The Raman Effect is defined as an inelastic scattering phenomenon of light with matter. Analysis through Raman spectroscopy is based on impinging a monochromatic light beam of frequency v_0 upon a sample, and examine the light scattered by said sample. Most of the scattered light has the same frequency as the incident light, but a small fraction presents a frequency change as a result of the interaction of light with matter [209]. The frequency variations observed in Raman scattering are equivalent to energy variations. Ions and atoms are chemically-bound to form molecules and crystalline lattices, and are subject to constant vibrational and rotational movements. These oscillations are carried out at well-determined frequencies depending on the mass of the particles involved and the dynamic behaviour of the existing bonds. Each of the vibrational and rotational movements of molecules correspond to a determined value of molecular energy [209].

When photons of an incident light beam, with energy $h \cdot v_0$ (where h is the Plank constant) much greater than the energy difference between two vibrational (or rotational) levels of the molecule, collide with it, the majority of photons pass through, but a small fraction is scattered. The incident photon brings the molecule transiently to a disallowed level of vibrational (or rotational) energy, which is quickly lost leading to an allowed energy level by release of a photon. The frequency at which this photon is released depends on the energetic 'jump' made by the molecule (Figure 3.41).

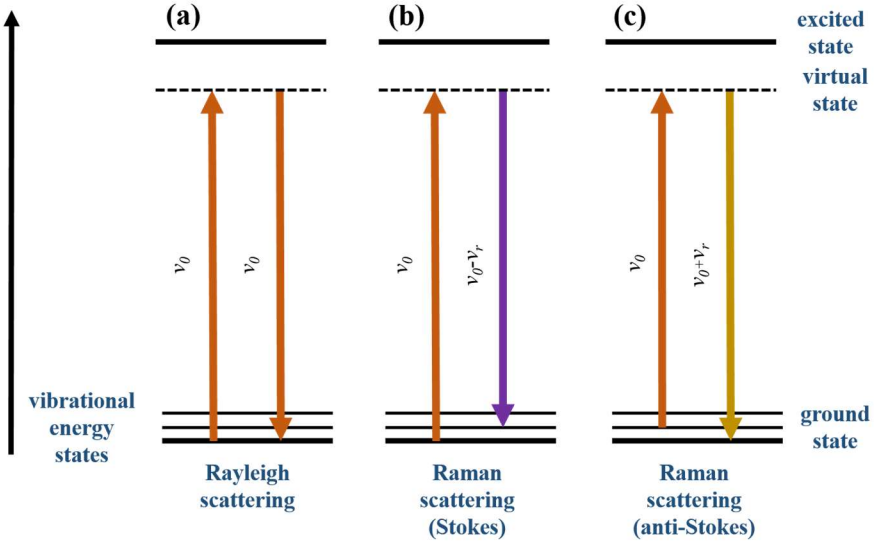

Figure 3.41: *Schematic view of energy transitions involved in: (a) Rayleigh scattering; (b) Raman scattering Stokes; and (c) Raman scattering (anti-Stokes). Adapted from* [210].

Figure 3.41 presents the different vibrational states in which the transitions between energy states for different light-matter interactions are shown [206]. When the result of photon-molecule interaction is a scattered photon at the same frequency of the incident photon, then the impact is said to be elastic, since neither the photon or molecule suffer any variation in their energetic state. The molecule returns to the same energy level that it had before; the scattered photon has the same v_0 frequency as the incident photon, giving rise Rayleigh scattering (Figure 3.41 (a)). If the result of the photon-molecule interaction is a scattered photon at a different frequency compared to, then the incident photon the impact is said to be inelastic. Some energy is transferred between the photon and the molecule. In this case two phenomena can occur: (*i*) if the scattered photon has lower frequency than the incident photon, some of energy from the incident photon has been transferred to the molecule. Thereupon, the molecule returns to an energetic state greater than the initial, and the emergent photon is scattered with v_0-v_r frequency, i.e. Raman Stokes scattering (Figure 3.41 (b)); and (*ii*) if the scattered photon has higher energy than the incident photon, some of the molecule energy has been transferred to the incident photon, meaning that the molecule is no longer at its fundamental vibrational state, but instead at higher energy level. Therefore, the released photon is scattered with v_0+v_r frequency and Raman anti-Stokes scattering takes place (Figure 3.41 (c)). Raman spectra collect the aforementioned phenomena by representing the scattered optical intensity as a function of the normalized wavenumber, υ, to which it is produced. The normalised wavenumber is a magnitude proportional to the frequency, ν, and inversely proportional to the wavelength λ, and is expressed in cm^{-1} (Equation (3.16)) [206]:

$$\upsilon = \nu/c = 1/\lambda \qquad \text{Equation (3.16)}$$

where υ is the normalized wavenumber, ν is the frequency and λ is the wavelength.

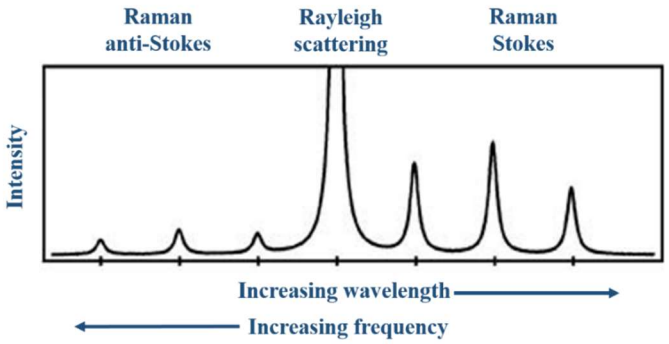

Figure 3.42: *Schematic of Rayleigh, Raman Stokes and Raman anti-Stokes bands. Adapted from* [211].

Raman spectra are composed of a primary Rayleigh band and two series of secondary bands corresponding to the Stokes and anti-Stokes bands, symmetrically-located on either side of the Rayleigh band (Figure 3.42) [209]. At room temperature, according to the Maxwell-Boltzmann's law of energy distribution, 99% of molecules are in the lower energy vibrational state and, therefore, the probability of energy transfers that give rise to Stokes scattering is much larger than for anti-Stokes scattering. This means that the intensity of Stokes scattering is 100 times greater than the intensity of anti-Stokes scattering [211]. Considering the difference in intensity between Stokes and anti-Stokes, the present work has been performed measuring only the Stokes effect.

3.3.5.3.2 The Raman instrument

Figure 3.43 shows a schematic of the Raman instrument used in the present work. A typical Raman system utilises a laser excitation source (ultraviolet (UV), visible or near infrared (IR)). The monochromatic light is guided and focused onto the sample through an optical head. The light scattered by the sample is collected by the same optical head and guided through a notch filter, which spectrally separates the Rayleigh scattered light to obliterate its optical effect on the spectrum. Subsequently, the scattered light is directed to the diffraction grating to be separated into its constituent wavelengths. The CCD detector converts the photons of scattered light into digital-electrical signals and the spectrum is sent to the computer.

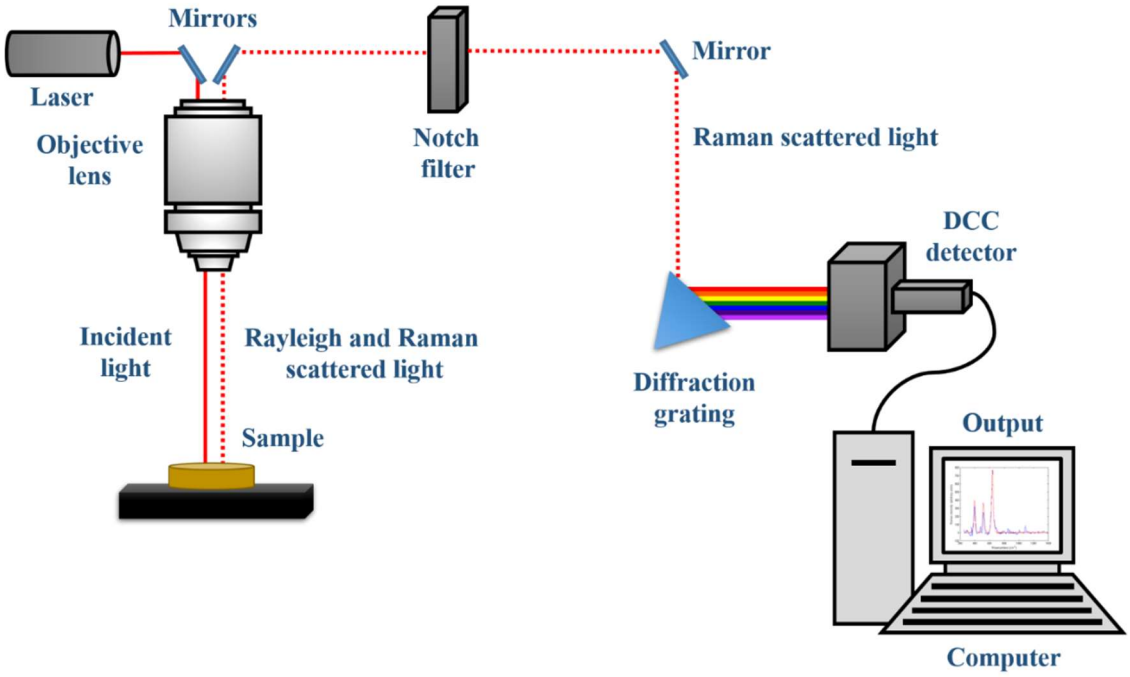

Figure 3.43: *Schematic view of Raman spectrometer, as used in the present work.*

3.3.5.3.3 Sample preparation and instrument operation

Raman spectroscopy was undertaken on the surface of metallic corrosion coupons (M-S-48-1). Therefore, no sample preparation was needed. Raman spectra were obtained using a Renishaw Ramanscope model 2000. The system was equipped with a HeNe laser (excitation wavelength of 632.8nm). Analyses were performed focusing the laser with a 50x objective lens onto the sample surface through a Leica optical microscope, corresponding to a laser spot diameter of 4μm. The Raman signal was collected in reflection mode, and spectra were measured over the Raman shift range of 100-1700cm^{-1} at a dwell time for each step of 10 sec and laser power of 4mV.

3.3.5.3.4 Data processing

Data obtained were processed by manual comparison with published reference data.

3.3.5.4 Mössbauer spectroscopy

Mössbauer spectroscopy is a well-known characterisation technique to conduct hyperfine interaction studies, providing specific information on magnetic, structural and chemical features of materials, depending on the emitted photon energy from the radioactive source.

3.3.5.4.1 The Mössbauer effect

The Mössbauer effect, or nuclear resonance fluorescence, was discovered by the German physicist Rudolf Ludwig Mössbauer, while experimenting with iridium-191 in 1958, which led to him being awarded the Nobel Prize in 1961 [212].

The Mössbauer effect is the phenomenon of emission and absorption of gamma rays without recoil energy loss by the involved nucleus [213]. When a nucleus in an excited state emits a gamma photon, the gamma photon imparts a recoil to the nucleus. Therefore the photon emerges with lower energy [213]. Likewise, if the same emitted photon were to impinge upon another nucleus, its energy must be higher to promote absorption and to provide the recoil energy. An increase in temperature of the gamma ray source causes an increase in the photon energy due to an increase in the atom velocity, broadening the gamma ray line shape via the doppler effect [213]. The energy lost by recoil is compensated by raising the temperature.

Nuclei, just like atoms, are characterised by the existence of energy levels that undergo a variety of transitions normally associated with emission or absorption of gamma rays. These energy levels are influenced by the electrical and magnetic environment that may induce changes or separate such energy levels, allowing one to obtain information concerning the chemical environment of atoms within a system [214], [215]. Transitions between nuclear energy levels occur by radiation processes that involve recoil. In recoil emission, for momentum conservation to occur, the nucleus must carry away a momentum equal and opposite to the gamma ray emitted. For this to occur, the kinetic energy of the nucleus must absorb part of the available energy during the transition [214], [215].

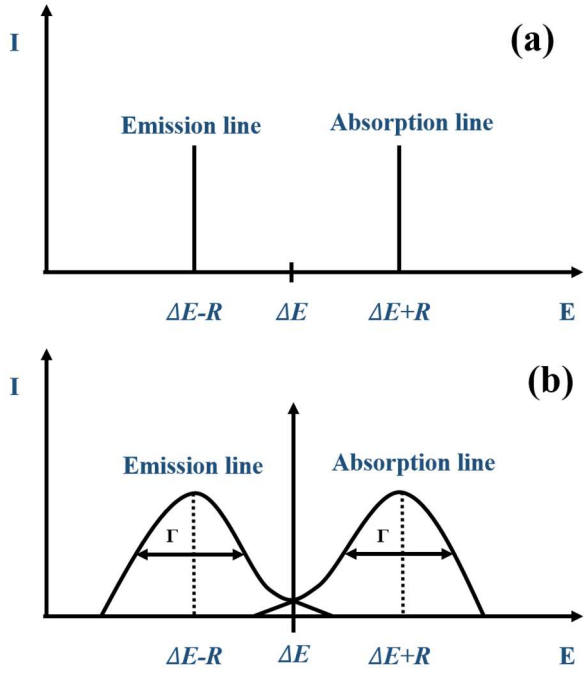

Figure 3.44: *(a) Emission and absorption line shifts. (b) Overlap between emission and absorption lines favouring the Mössbauer effect. Modified from* [216].

While absorption by recoil requires a gamma ray with energy greater that the transition energy, since as it occurs during recoil emission, part of the energy is absorbed as kinetic energy of the nucleus [214], [215]. Since, the energy shifts of the gamma-ray during emission and absorption are large in comparison to the width of the transition line (determined by the half-life of the exited state, and in accordance with the Heisenberg relation, $\Delta E' \cdot \Delta t' \geq h$), the overlap is non-existent. Thus, a gamma ray emitted by a nucleus in transition from state 2 to state 1 never excites the transition from state 1 to state 2 in another neighbouring nucleus (Figure 3.44 (a)) [214], [215]. Hitherto, the Mössbauer effect has been considered in relation to the mass of a nucleus. However, nuclei pertain to crystalline lattices, so the mass of the crystal to which the

nuclei is bound plays an important role in the Mössbauer effect, since recoil energy becomes vanishingly small when transferred to the crystal [214], [215]. Thus, if a nucleus emits a free-recoil gamma ray, favouring the transition from state 2 to state 1, overlap occurs between emission and absorption lines (Figure 3.44 (b)), allowing the absorption of this gamma ray by another nucleus, which then promotes the transition from state 1 to state 2, and this resonant absorption is key to the Mössbauer effect. Isotopes that can show free-recoil processes are limited to those whose first excited state is of very low energy, since free-recoil resonance, or the Mössbauer effect takes place when gamma rays are of very low energy. The source used for Fe^{57} Mössbauer spectroscopy is Co^{57} [217].

Energy changes caused by interactions at the nuclear level are very small. Therefore, to detect these changes, it is necessary to vary the gamma energy effect. This is achieved by the movement of the gamma ray source, that promoting small energy changes, with a velocity of mm/s, and recording the spectrum in discrete steps. The energy scale of Mössbauer is registered in terms of relative velocity within the source and absorber (Figure 3.45) [217].

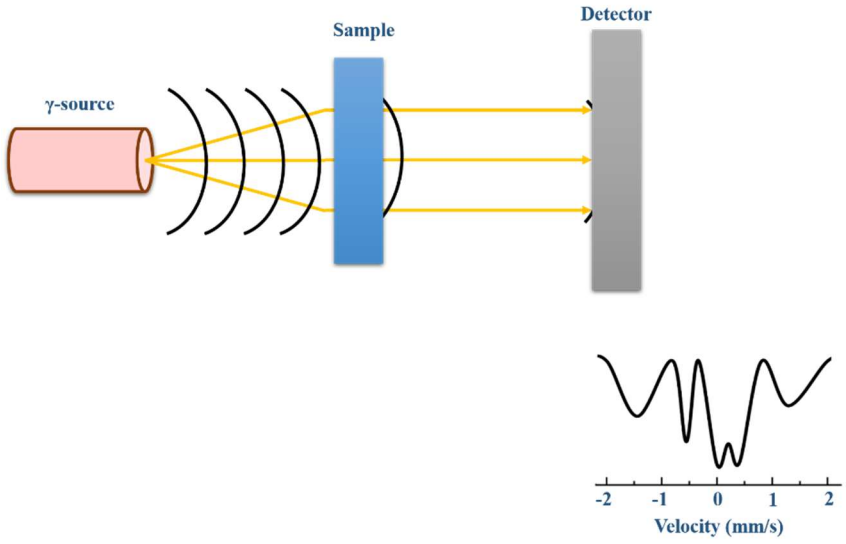

Figure 3.45: *Schematic view of source oscillation and spectrum obtainment.*

Nuclei involved in Mössbauer are surrounded by a charge distribution belonging to their own electrons and neighbouring ions. Interactions between this charge distribution and nuclear charge could cause alterations in the energetic levels of nuclei, providing information about the chemical environment of Mössbauer nuclei, facilitating Mössbauer spectroscopy on the samples under study that contain nuclei susceptible to this effect. Interactions are manifested as isomeric shifts, quadrupole splitting and magnetic or Zeeman splitting. These interactions are also known as hyperfine interactions.

3.3.5.4.2 The Mössbauer instrument

Figure 3.46 shows the basic configuration of a Mössbauer spectrometer [218]. A typical Mössbauer instrument consist of: (*i*) a radioactive source of Co^{57} encapsulated in a matrix to avoid the shifting of emitted frequencies; (*ii*) an electromechanical speed transducer to modulate the Doppler effect; and (*iii*) a radiation detector normally equipped with a series of complementary systems to allow analysis of the detected signal and, subsequently, synchronise the signal with the different velocities to which the speed transducer is moving the radioactive source.

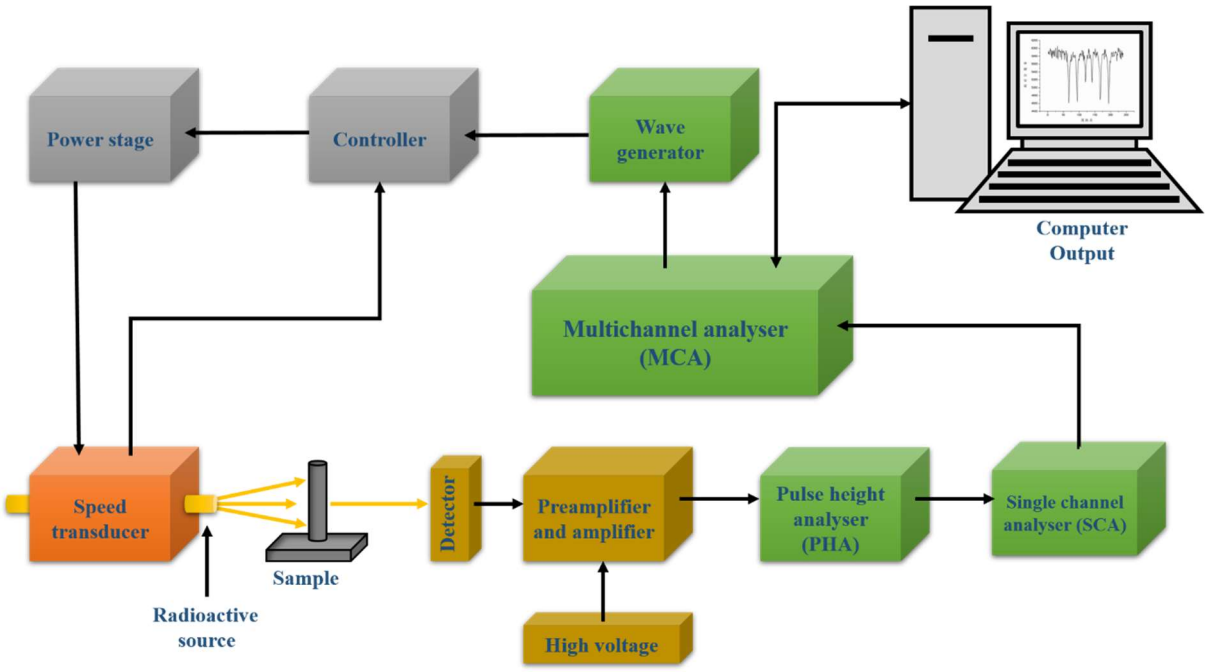

Figure 3.46: *Schematic of a Mössbauer spectrometer, as used in the present work.*

The work presented in this thesis has been performed utilising a Transmission Mössbauer Spectrometer (TMS) equipped with a gaseous ionisation detector. Therefore, a TMS will be further discussed. The instrument belongs to the Consejo Superior de Investigaciones Cientificas (CSIC), Madrid (Spain).

In a TSM, when gamma rays are focused into a sample some of them are absorbed by the sample, while the remaining radiation reaches the detector, so that the inverse of the absorption is known, as shown in Figure 3.47 (a) [218]. The gaseous ionisation detector consists of a cylindrical shell or cathode surrounding a thin filament or anode, and, in that cavity, there are a mixture of inert gases, such as Ar/He or Ar/CH_4 (Figure 3.48 (b)). Gamma radiation produced by the source excites the iron nuclei contained in the samples, and their return to the ground

state is carried out by the emission of x-rays, gamma rays and electrons. When gamma radiation from the sample (Figure 3.47 (a)) reaches the detector (Figure 3.47 (b)) and excites the gas, electrons and argon ions are released. These ions remain free in the high electrical field, initialising the displacement of electrons towards the filament or anode, and the displacement of ions towards the cathode. Due to the electrical field present between the electrodes, the electrons gain speed and collide with other atoms, causing the emission of more electrons, thus causing an avalanche of electrons towards the filament. Once the electron avalanche reaches the anode, a current pulse or signal in the measurement circuit is generated.

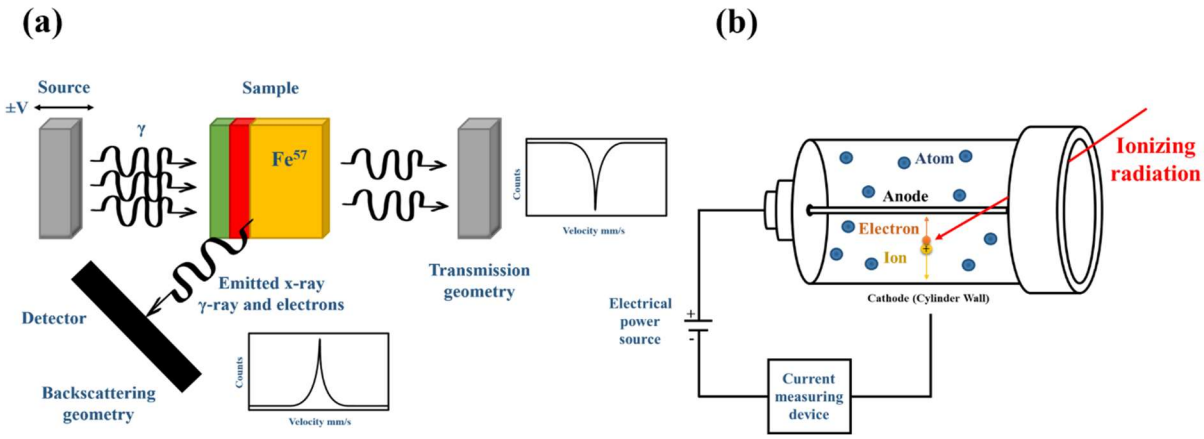

Figure 3.47: *(a) Schematic of signal production and detection. (b) Schematic of a gaseous ionisation detector. Modified from* [218].

Despite the high voltage generated in the detector, the voltage of the signal is of small magnitude. Therefore, the coupled preamplifier and amplifier assign a greater and proportional value to the signal (Figure 3.46). Subsequently, a pulse height analyser (PHA) classifies each signal as a function of its amplitude, enabling us to know whether the registered signal corresponds to the radiation of interest. Finally, a single channel analyser (SCA) coverts the signals that correspond with the energy of interest into a logic pulse or count, which are stored in the multichannel analyser memory (MCA). The systematic counts accumulation for each radioactive source velocity results in a Mössbauer spectrum, which is finally visualised in the computer.

3.3.5.4.3 Sample preparation and instrument operation

Samples were obtained by grinding and sieving 1g of each bentonite sample until reaching a grain size of <53µm. Sample preparation was performed within an argon-purged glovebox (MBRAUN unilab pro sp). Samples were vacuum-sealed and sent to CSIC for further analysis.

Spectra were recorded using ^{57}Fe Mössbauer spectroscopy in transmission mode. A conventional constant acceleration spectrometer with a $^{57}Co(Rh)$ source was used. The transmission experiments were carried out at room temperature. The velocity scale was calibrated using a 6μm thick iron foil and the isomer shifts were referred to the centroid of the alfa-Fe spectrum at room temperature.

3.3.5.4.4 Data processing

Mössbauer spectra for each sample were analysed using the RECOIL program by Dr. María Sánchez Arenillas and Dr. Juan de la Figuera Bayón from Consejo Superior de Investigaciones Científicas (CSIC, Spanish National Research Council).

3.4 Concluding statement

The work presented in the following chapters (Chapter 4, 5 and 6) is a multidisciplinary study, and therefore many solid and liquid techniques were used to tackle the unique challenge of studying the possible interactions between bentonite and the released corrosion by-products. Due to the considerable number of analytical techniques utilised through the present work, the description of each technique provided in the present chapter is intended to aid the understanding of the results discussed in the following chapters.

Thus, this chapter has discussed the analytical techniques and testing methodologies employed to meet the research objectives (Chapter 2, section 2.5). The suite of analytical techniques selected allows bentonite observation from the chemical and structural perspective; considering that bentonite, as a clay, is featured by its heterogeneous nature and its characteristics are strongly correlated with its bulk mineralogy. Thus, macro-scale alterations may be the result of mineralogical transformation and/or alteration. The batch test aimed to gain a parallel and complementary vision of the results obtained from the analysis of bentonite samples from the Febex and ABM in-situ tests, and so, improve the understanding of the symbiosis of the processes that may induce the transformation and/or alteration of bentonite within the engineering barrier system. The results of the analyses outlined within this chapter are presented in the following chapters.

Chapter 4 Effect of iron corrosion on bentonite from Febex in-situ test

4.1 Chapter overview

The present chapter focusses specifically on the physicochemical evolution of several highly-compacted bentonite samples and corrosion coupon samples from the dismantling of heater no.2 at the Febex in-situ test (Figure 3.2). The information provided hereinafter, enables us to have an initial derivation of the local conditions to which the bentonite samples evaluated in this chapter were exposed. The provenance, the sample conditions and the sampling protocol of each sample has been described in Chapter 3.

The majority of the geological disposal concepts developed internationally all envisage the encapsulation of the irradiated fuel and/or vitrified higher activity waste within iron or copper canisters which, in turn, will be surrounded by highly-compacted blocks of bentonite within a stable host rock at great depths. Since the metallic components and the clay barrier are important parts of an EBS, their deterioration could compromise the performance of the system in the long-term. Therefore, its integrity will be conditioned by: (*i*) corrosion of the containers that encapsulate the radioactive waste; (*ii*) degradation of the bentonite barrier due to the heat emitted by the decaying radioactive waste; and (*iii*) bentonite interactions with other metallic structures that provide support to the installation. For these reasons, the Febex in-situ test was conceived with a great variety of different metal components, integrated in the bentonite compacted body, which included the heaters, the perforated liner, small metallic coupons and several metal sensors.

Most of the metallic components utilised in the in-situ test were carbon-based steel materials. Under the simulated disposal conditions, the unpreventable corrosion of metallic components initiated by the consumption of oxygen trapped in the bentonite matrix led to the appearance of Fe^{3+} oxide corrosion products, such as lepidocrocite, goethite and hematite [164]. This process could be also promoted by the heat emanating from the radioactive waste, the local

relative humidity and the concentration of dissolved salts in the percolating groundwater. Once the total consumption of free oxygen (dissolved and gaseous) had occurred, iron corrosion is expected to be governed by the anaerobic environment created around the metal components, which involve the reduction of Fe^{3+} oxides to Fe^{2+} oxides, giving rise to the formation of magnetite and green oxides [164], in addition to siderite and iron sulphides. As predicted in the literature [164], these reactions would have been profoundly influenced by the initial oxygen concentration trapped in the clayey matrix, post-closure expected temperatures, gas composition, and nature of the groundwater. The combination of all these factors would have determined the evolution of the local environment at the interface contact between the metallic canister and the clay barrier. Anaerobic corrosion would also have continued, thereby additional 'reduced' iron corrosion products would have formed, just as much slower rates.

Characterisation of the Febex in-situ test samples aims to explore any physicochemical alteration and/or transformation experienced by the bentonite fraction over the 18 years duration of the experiment, which may provide some insight of potential adverse alterations that may affect the Febex bentonite under disposal conditions. Comprehensive results from physicochemical analysis on Febex bentonite samples and corrosion coupons are provided herein.

4.2 Characterisation of anaerobically-corroded metallic components and their influence on the surrounding Febex bentonite

4.2.1 Corrosion evolution on metallic sample: M-S-48-1

In a conventional EBS, metallic components and the clay barrier might be susceptible to deterioration processes. The expected corrosion of the container and structural metallic components, along with the thermal gradients and hydraulic dynamics of the bedrock, seem to lead to degradation of the clayey matrix. To understand the dynamics of such degradation, the Febex in-situ test was designed with numerous subsumed metal components within the compacted bentonite body, such as multiple metallic coupons.

This present chapter aims to examine the physicochemical state of bentonite and metallic coupons after 18 years in-situ test. The results presented hereinafter intend to provide information regarding the corrosion experienced by the metallic coupon surfaces (M-S-48-1) and, thus, establish a correlation between the by-products released during the metal corrosion process and their effects on bentonite.

The coupons were received as described in Chapter 3. Figure 4.1 shows the physical conditions of the recovered corrosion coupon sample at reception. The loose pieces of bentonite that remained in the plastic pouch, as well as those intercalated bentonite pieces that came off during coupon disassembly, were collected and further analysed.

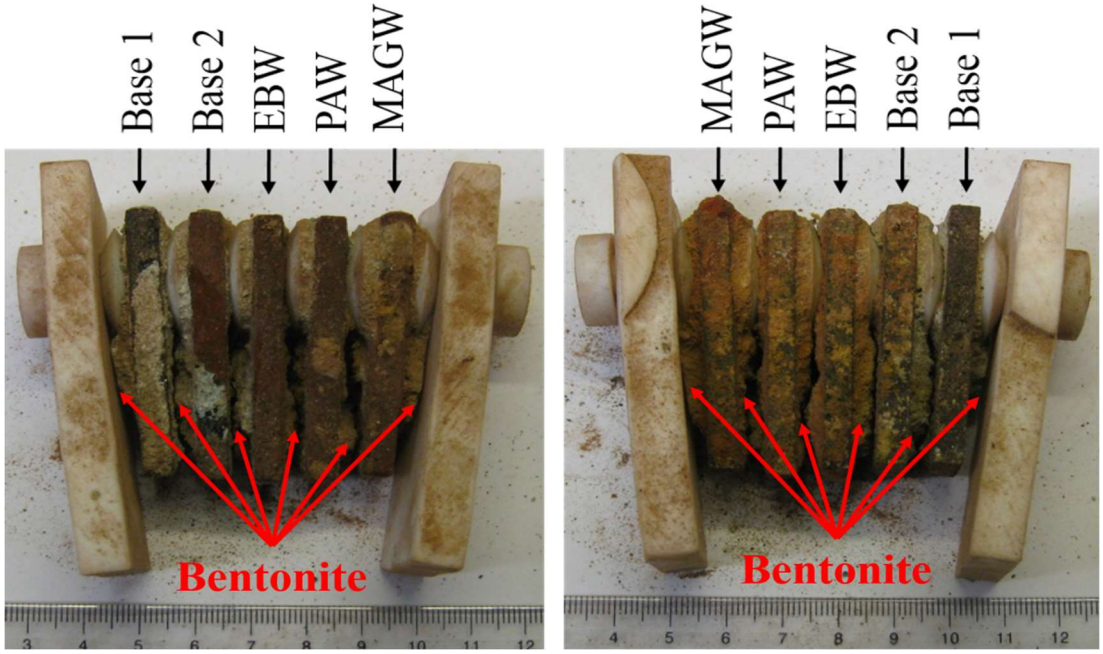

Figure 4.1: *Physical appearance of M-S-48-1 test sample at reception.*

At the University of Bristol, the samples were initially opened in a nitrogen-purged glovebox (Saffron Scientific Equipment Ltd). The metallic rack was disassembled into its metallic coupons, for visually inspection and photography (Figure 4.2).

From Figures 4.1 and 4.2, it can be observed that all coupons were covered in corrosion compounds, and it was possible to distinguish different colouration types unevenly distributed over the coupon surfaces. The different coloured areas suggested different degrees of degradation which may involve different corrosion products.

Overall, the surface of each coupon showed black-reddish colouration, and greenish areas blended with bentonite adhered to the surface (Figure 4.2).

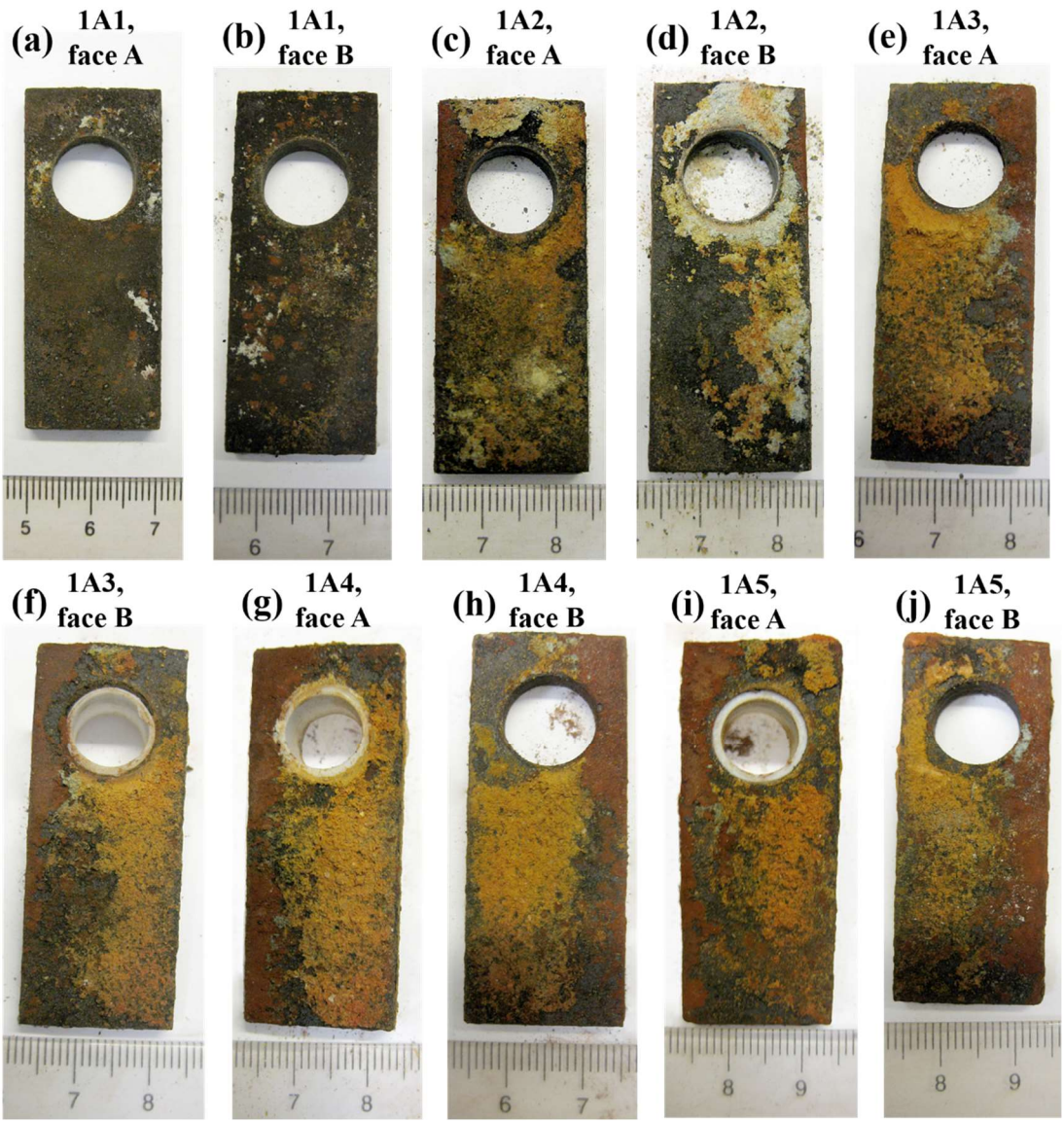

Figure 4.2: *(a) Visual appearance of 1A1, face A. (b) Visual appearance of 1A1, face B. (c) Visual appearance of 1A2, face A. (d) Visual appearance of 1A2, face B. (e) Visual appearance of 1A3, face A. (f) Visual appearance of 1A3, face B. (g) Visual appearance of 1A4, face A. (h) Visual appearance of 1A4, face B. (i) Visual appearance of 1A5, face A. (j) Visual appearance of 1A1, face B.*

The adhered bentonite showed an intense reddish colouration and seemed to have a lower water content in comparison with the bentonite samples later analysed. From visual inspection, it can be affirmed that corrosion damage in all carbon steel coupons was present as general corrosion, as shown in Figure 4.2.

4.2.1.1 Analysis of the surfaces of the corrosion coupons

The observed general corrosion over the surface of each coupon explained the need to accomplish an initial surface analysis to identify specific corrosion products. Therefore, SEM

was used for morphological analysis. Overall, no significant differences between samples were observed, with regards to surface analyses. This comprised both base material (1A1 and 1A2) and welded samples (1A3, 1A4 and 1A5). Thus, the data presented in Figure 4.3 is typically representative of all samples but belongs to the surfaces or faces of 1A1 and show the spectra and EDS micrographs collected. From Figure 4.3 and Table 4.1, it can be affirmed that the formed corrosion products were comprised mostly of iron and oxygen, together with structural bentonite elements, such as silicon, calcium and aluminium. The presence of chlorine was also observed on almost all surfaces of the coupons.

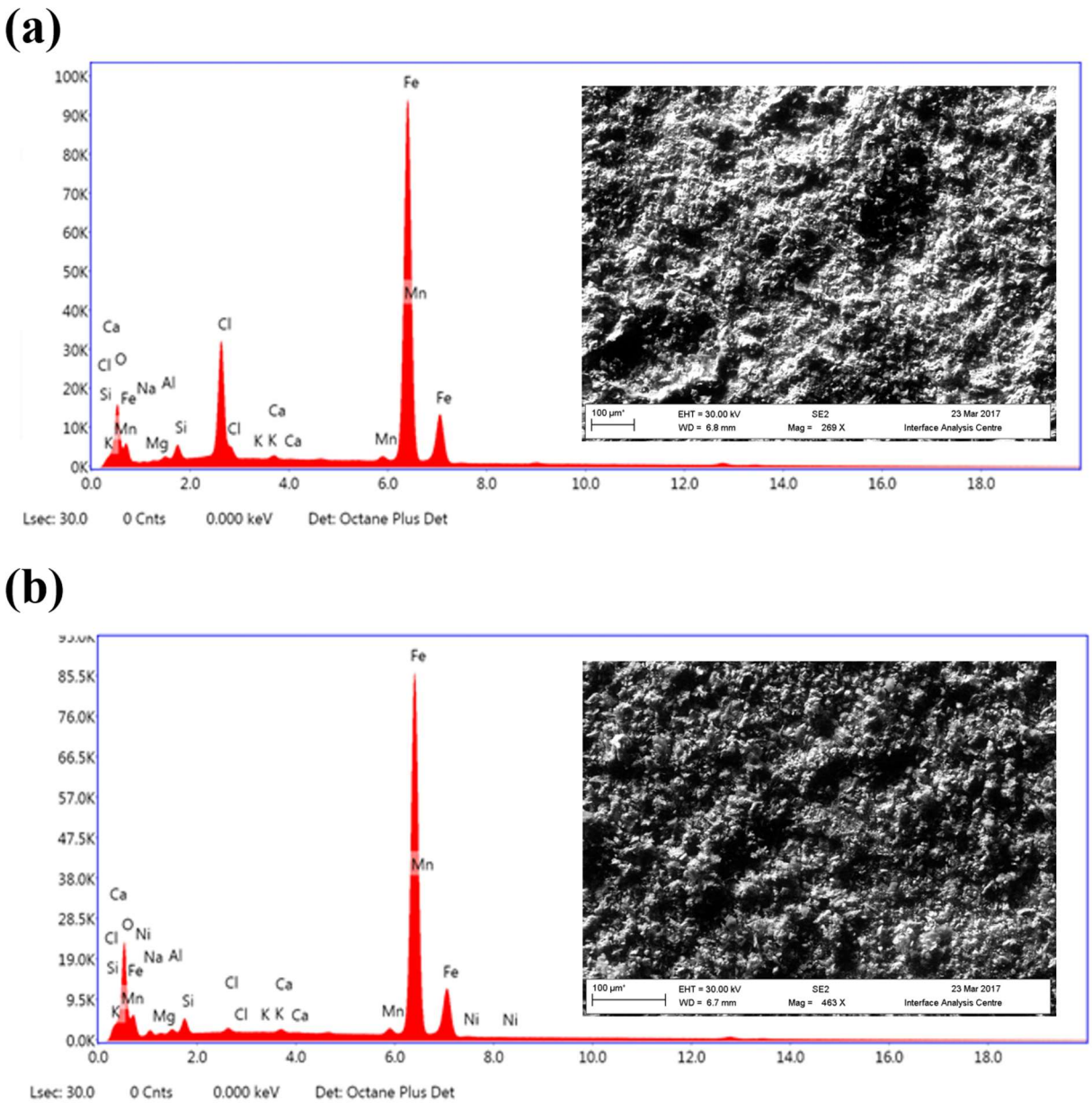

Figure 4.3: *(a) EDS spectra and micrographs of 1A1, face A. (b) EDS spectra and micrographs of 1A1, face B.*

Table 4.1: *Semi-quantitative results obtained in the EDS analysis performed on the coupons samples.*

EDS analyses	Element (wt%)										Total
	O	Na	Mg	Al	Si	Cl	K	Ca	Mn	Fe	
1A1. Face A	24.73	3.79	1.00	0.85	1.78	9.86	-	0.29	0.79	56.91	100
1A1. Face B	28.63	7.76	1.98	1.56	2.22	0.30	0.03	0.28	0.94	56.30	100
1A2. Face A	36.98	-	3.82	7.44	17.80	3.16	-	-	-	30.80	100
1A2. Face B	23.92	8.14	-	-	1.68	4.76	-	-	-	61.50	100
1A3. Face A	36.53	2.49	2.57	6.34	19.55	2.72	1.44	0.43	0.97	26.87	100
1A3. Face B	28.65	-	4.47	3.02	6.39	1.65	-	-	-	55.82	100
1A4. Face A	29.98	7.64	2.42	1.06	1.26	0.60	0.09	0.29	0.63	56.03	100
1A4. Face B	38.36	3.60	4.29	7.58	16.46	1.74	0.69	1.95	0.51	24.82	100
1A5. Face A	25.23	-	-	7.25	2.87	-	-	-	1.18	63.48	100
1A5. Face B	17.17	4.87	-	-	1.10	0.86	-	-	1.08	74.93	100

4.2.1.2 Identification of the by-products released by x-ray diffraction

The iron and chlorine identified by SEM/EDS dominated the subsequent surface analyses. Therefore, XRD was performed on sample surfaces to pinpoint the nature of the corrosion by-products released during the in-situ test. Although XRD analysis was carried out on each surface or sample face, the results presented in Figure 4.4 pertain to the face A of 1A1, since no differences were found between samples.

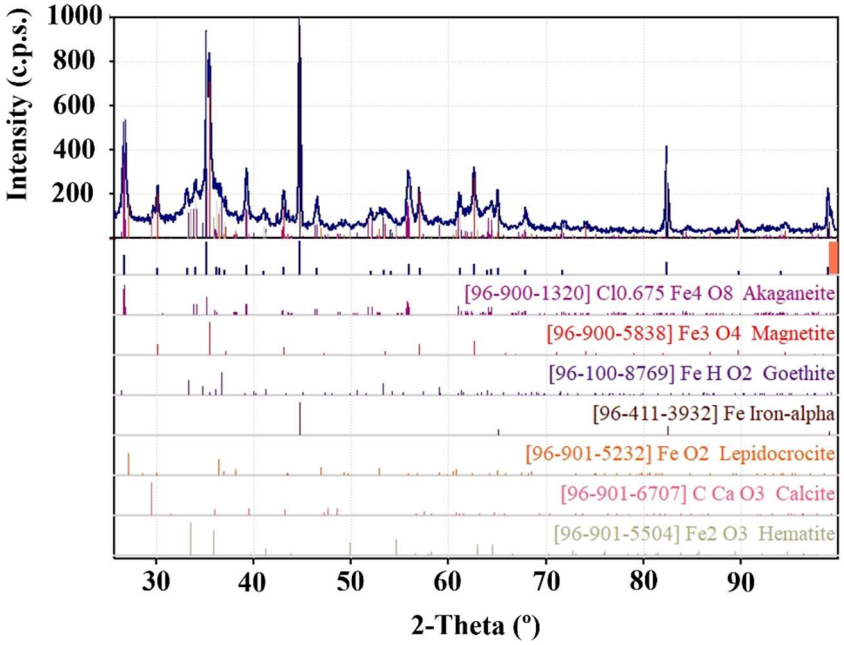

Figure 4.4: *XRD results of 1A3 (face A).*

XRD analysis revealed the presence of iron oxides, such as magnetite (Fe_3O_4) and hematite (Fe_2O_3), and oxyhydroxides, such as goethite (FeO(OH)), lepidocrocite (γ-FeO(OH)) and akaganeite (β-FeO(OH,Cl)), together with traces of calcite.

4.2.1.3 Identification of the by-products released by Raman spectroscopy

In combination with XRD, Raman spectroscopy was utilised to confirm the nature of the corrosion by-products observed. Due to the generalised corrosion, Raman spectroscopy was carried out at 18 points on the surfaces of each coupon. The results presented in Figures 4.5 and 4.6 pertain to the most relevant spectra together with their micrographs. Table 4.2 shows the Raman bands identified in Figures 4.5 and 4.6.

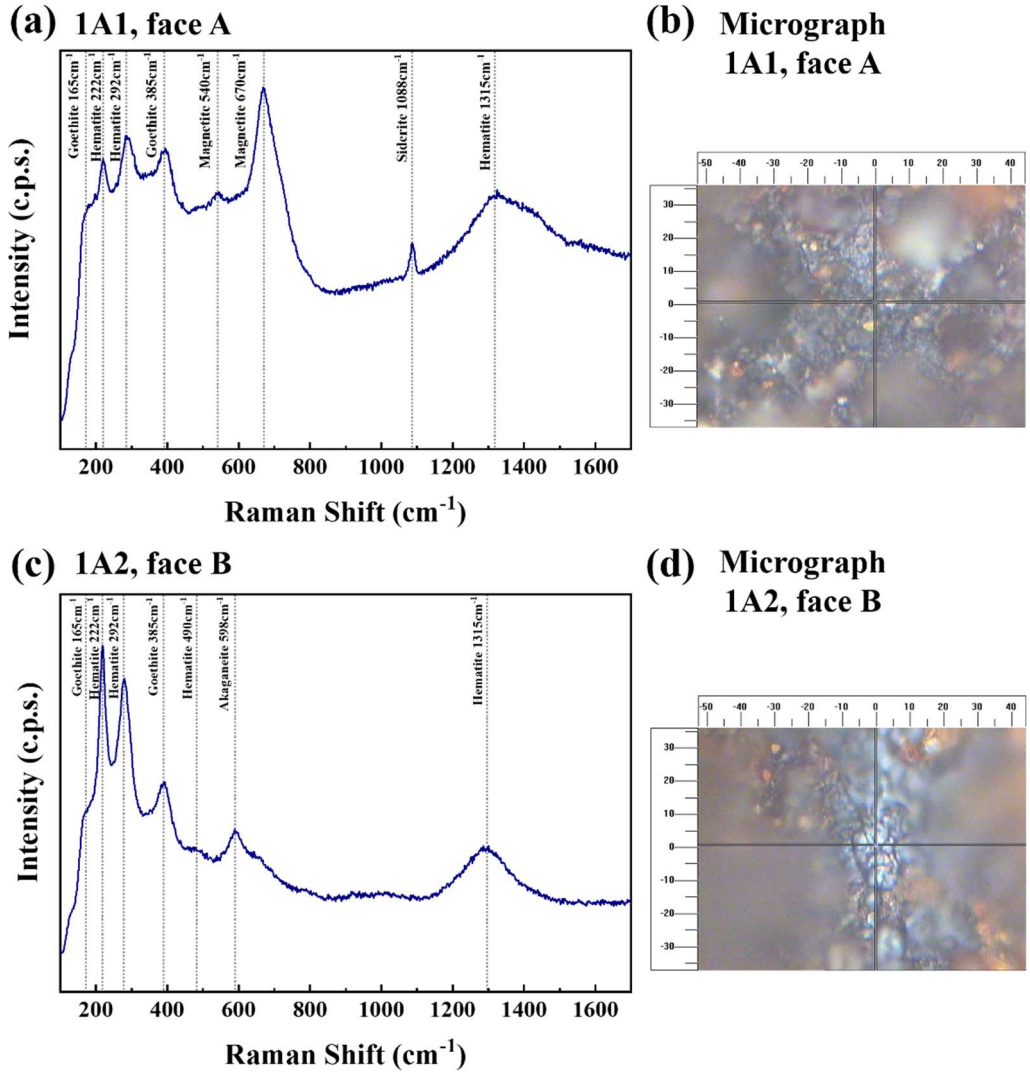

Figure 4.5: *(a) Raman surface spectra of 1A1 (face A). (b) Optical micrograph showing the location from where the Raman spectra was collected. (c) Raman surface spectra of 1A2 (face B). (d) Optical micrograph showing the location from where the Raman spectra was collected.*

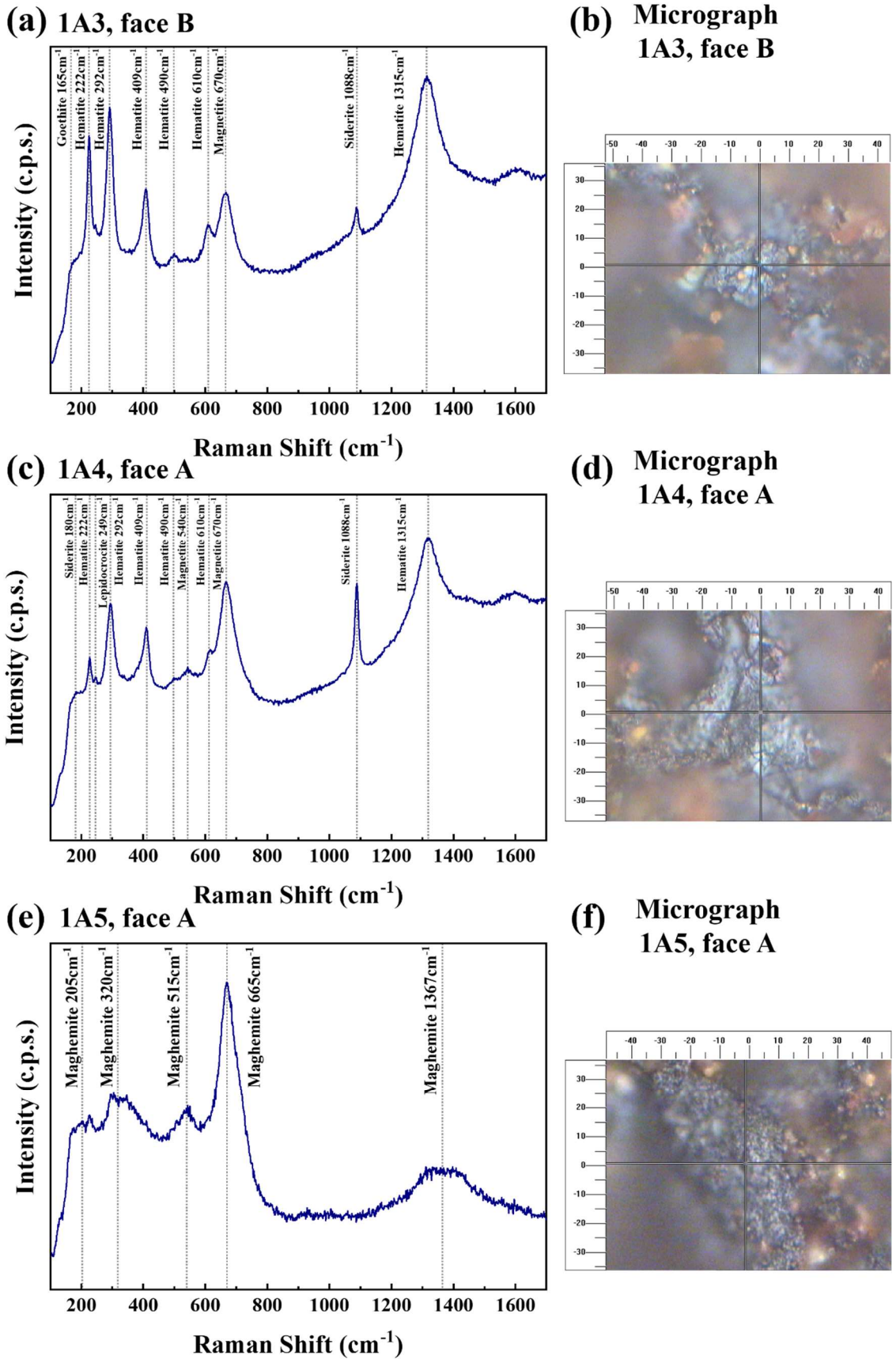

Figure 4.6: *(a), (c) and (e) Raman surface spectra of 1A3 (face B), 1A4 (face A) and 1A5 (face A). (b) (d) and (f) Optical micrograph showing the location from where the Raman spectra was collected on 1A3 (face B), 1A4 (face A) and 1A5 (face A).*

Table 4.2: *Raman bands of corrosion products detected on corrosion coupon surfaces.*

Mineral coupon sample	Chemical formula	Raman shift (cm^{-1})	Published Raman shift (cm^{-1})	References
Siderite	$FeCO_3$	180, 286, 1088	180, 282, 1087	[219], [220]
Hematite	α-Fe_2O_3	222, 292, 409, 490, 610, 1315	227, 293, 414,497,612,1320	[220], [221], [222]
Magnetite	Fe_3O_4	540, 670	532, 670	[222]
Goethite	α-FeO(OH)	165, 385	162, 384	[220], [221], [222],
Maghemite	γ-Fe_2O_3	205, 320, 515, 665, 1367	200, 300, 350, 515, 660, 1425	[220], [221], [222]
Akaganeite	β-FeO(OH,Cl)	598	597	[220]

Overall, the raman spectra confirmed the presence of the by-products identified using XRD. It is important to highlight the presence of akaganeite in XRD and Raman spectroscopy analyses. The presence of akaganeite has been previously addressed in the literature [164], in liner samples that belonged to sections 45 and 52 respectively. Chlorine accumulation at the heater surfaces due to the experimental temperatures and Cl^- concentration in the groundwaters (Table 3.24) at the GTS could have led to the formation of Cl-bearing Fe(III) oxyhydroxide, such as akageneite [164].

Since, the corrosion coupon samples pertained to Rack 1A, which in turn was retrieved from the contact with the liner (section 3.2.1.2.1). The presence of akaganeite at the surfaces of the coupon samples could be explained due to the combined effect of the thermal loading and the Cl^- concentration in the groundwaters. Besides, the presence of magnetite and hematite together with identified oxyhydroxides suggest that the conditions at the vicinity of the liner were anaerobic.

4.2.1.4 Study of the nature of the corrosion layer by scanning electron microscopy

To further evaluate the extent of corrosion of each coupon; coupons were cut lengthwise, and micrographs were taken at five points of each sample. Figure 4.7 shows the corrosion layer on face A of 1A2 sample.

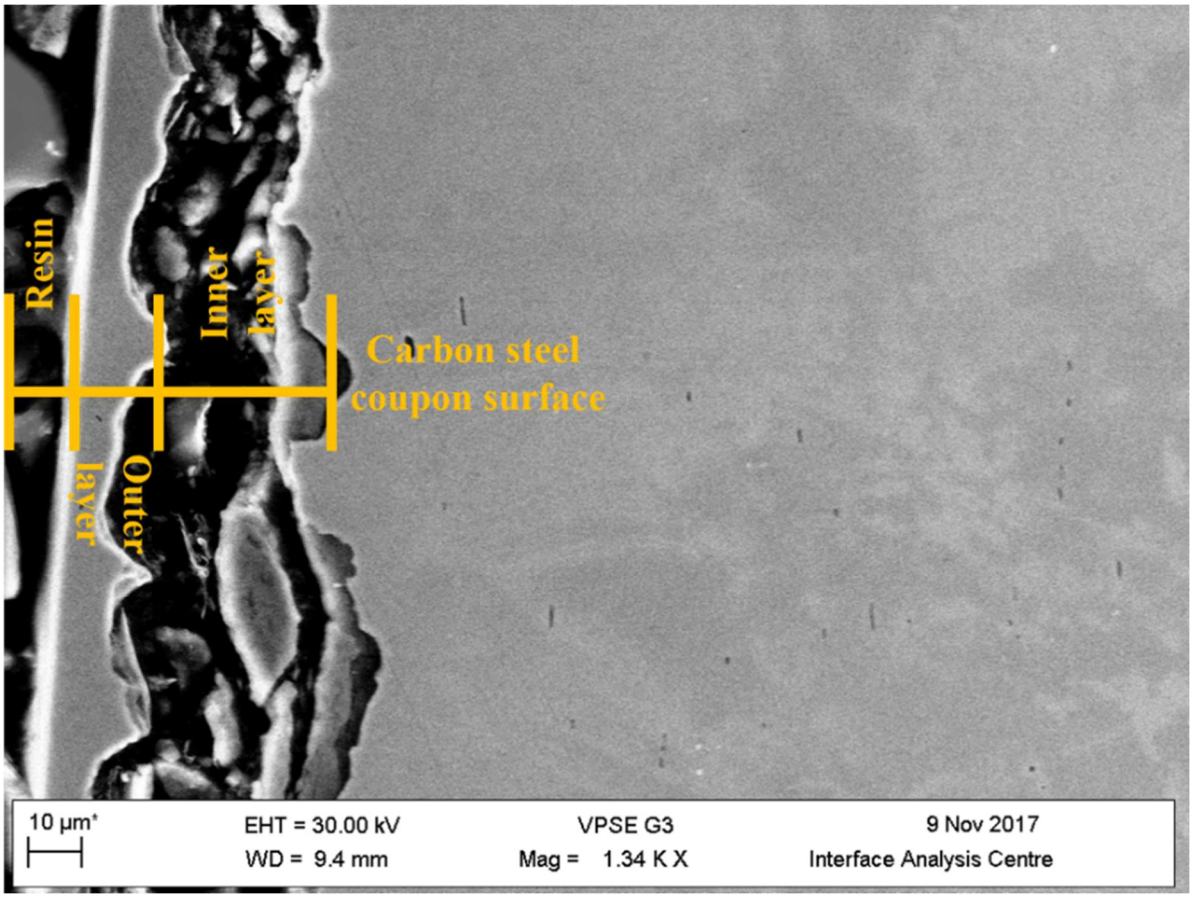

Figure 4.7: *SEM micrographs of 1A2 (face A).*

From SEM micrographs it was observed that the corrosion layer consists of: (*i*) a heterogeneous layer formed by mixed iron oxides and oxyhydroxides; and (*ii*) an inner layer of more coherent iron oxide ascribed to magnetite. This composition was determined by XRD and Raman spectroscopy. Additionally, the thickness of the corrosion layer was estimated from the micrographs and determinations are presented in Table 4.3.

Table 4.3: *Thickness of corrosion layer on corrosion coupons sample.*
[1]σ: Standard deviation. [2]SE: Standard error.

	Point 1 (µm)	Point 2 (µm)	Point 3 (µm)	Point 4 (µm)	Point 5 (µm)	σ[1] (µm)	SE[2] (µm)	Average corrosion (µm)	Average corrosion rate (µm/a)
1A1	13.29	48.22	52.93	18.05	22.78	18.21	8.14	31.05	1.73
1A2	41.74	72.67	58.07	103.47	63.94	22.83	10.21	67.98	3.78
1A3	26.86	29.29	51.68	29.98	24.76	10.91	4.88	32.51	1.81
1A4	11.48	19.66	17.13	33.24	28.06	8.70	3.89	21.91	1.22
1A5	46.99	31.17	42.37	54.05	38.22	8.66	3.87	42.56	2.36

Table 4.6 shows the estimation of the thickness of the corrosion layer at five different points along each coupon sample. From Table 4.6, it can be concluded that corrosion does not seems to be uniform along the surface of the carbon steel coupons. The average corrosion rate, assuming 18 years of corrosion time, is presented in Table 4.3.

This finding led to conclude that the C-steel components under simulated geological conditions are thermodynamically unstable, leading to the formation of a double corrosion layer that will facilitate the continuous release of corrosion by-products, that in turn could diffuse and interact with the bentonite buffer. The following sections shows the evaluation of the state of the bentonite samples in contact with metallic components.

4.2.2 Visual documentation of the Febex in-situ samples after 18 years of experiment

The Febex bentonite test samples were received as described in Chapter 3. At the University of Bristol, the samples were initially opened in a nitrogen-purged glovebox (Saffron Scientific Equipment Ltd), and visually inspected and photographed as a first pass analysis method.

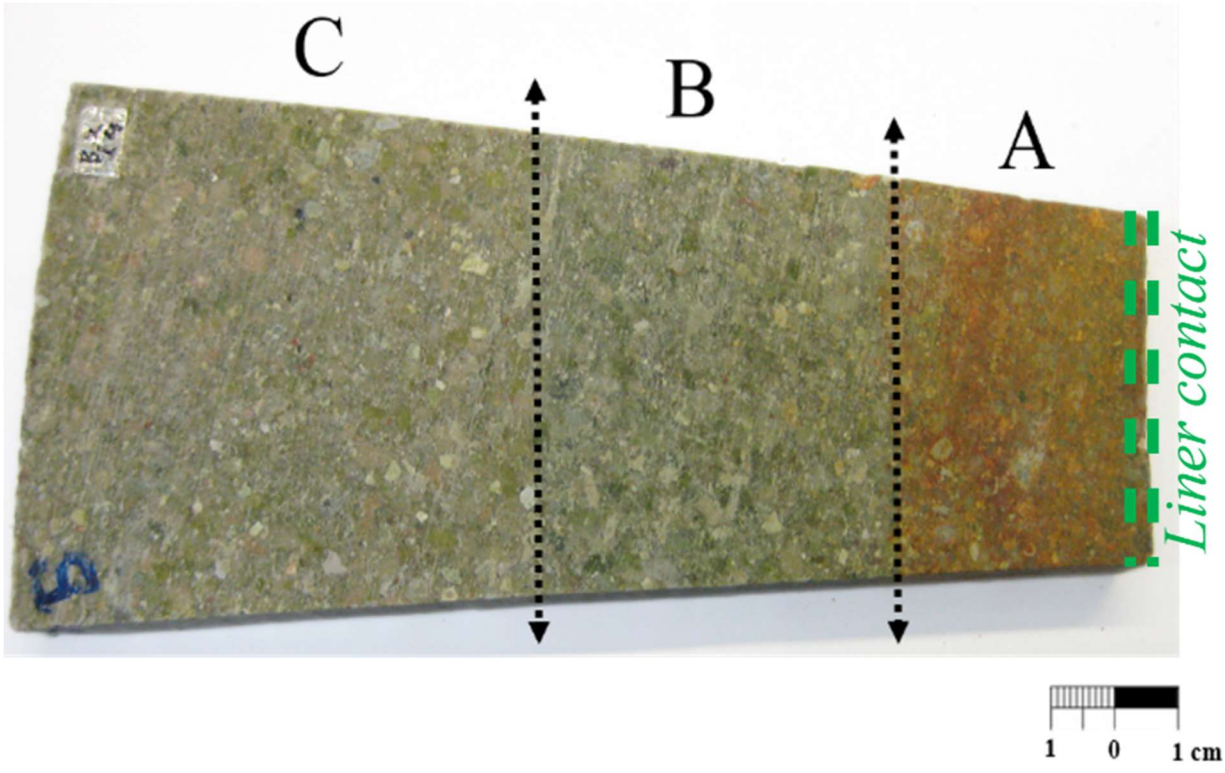

Figure 4.8: *Physical appearance of BM-B-41-1 test sample at reception.]*

Figures 4.8 and 4.9 depict the physical appearance of the samples upon inspection. Visually, the Febex bentonite typically exhibits a light grey colouration. However, the sample extracted in the vicinity of the liner of BM-B-14-1 sample (Figure 4.8) showed a gradational colour change from orange-brown in the immediate zone of contact with the liner, to a greenish-blue and then the normal colour of Febex bentonite. Therefore, to facilitate later analyses the sample was subdivided using a cutting wire into three different sections, or parts A, B and C.

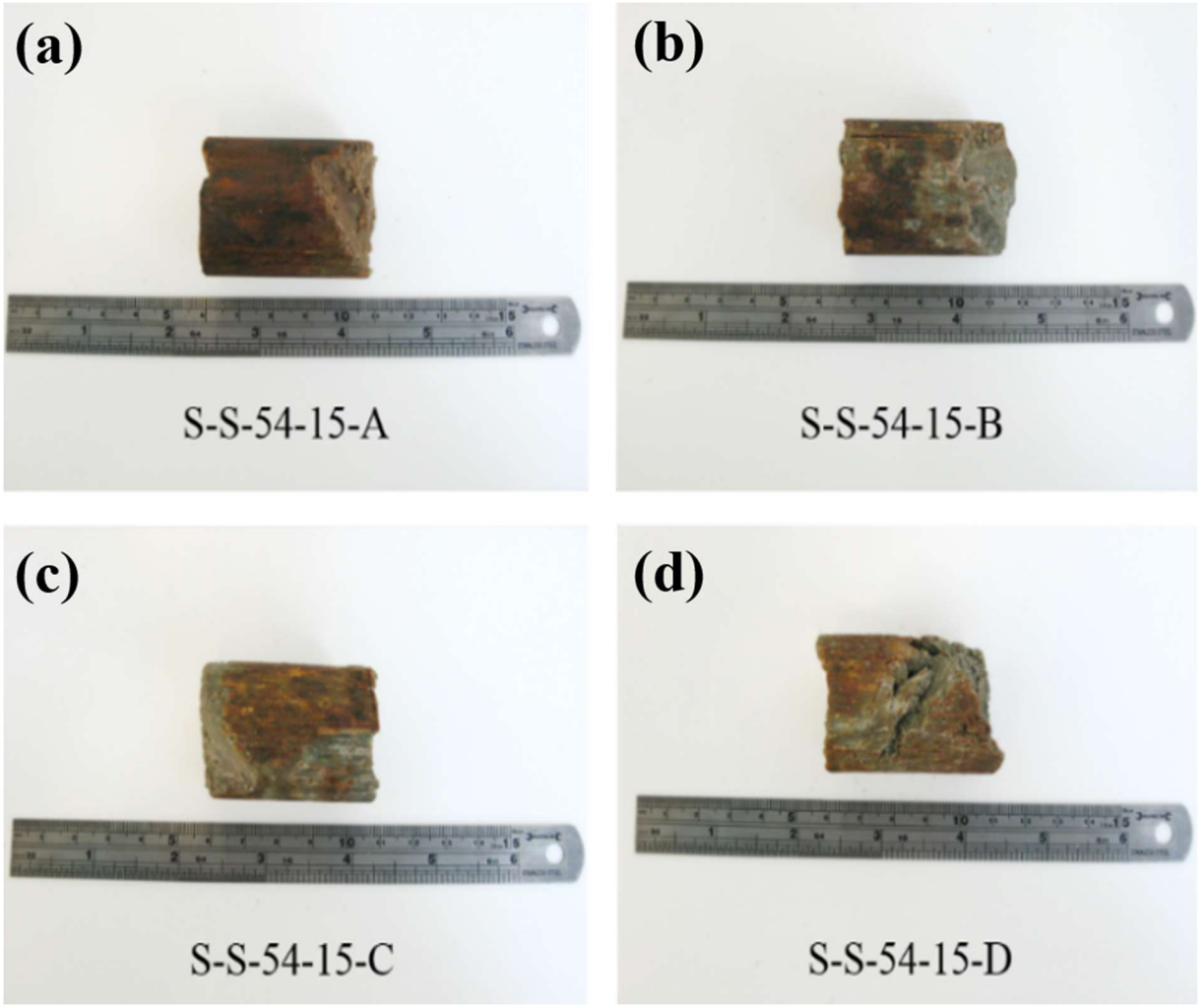

Figure 4.9: *Physical appearance of S-S-54-15-A/B/C/D test samples at reception.*

Figure 4.9 displays the physical state of the extensometer samples (S-S-54-15-15-A/B/C/D). For this samples, the reddish colouration was found only on external surfaces but not internally, when split/cut open. This evidence of oxidation is suggestive that it occurred during post-handling processing of the samples.

4.2.2.1 X-ray tomography: Sample BM-B-41-1. Transition between section A and B

Due to the different colouration present in part A of BM-B-41-1, x-ray tomography was performed as a second screen analysis of possible alteration and/or transformation.

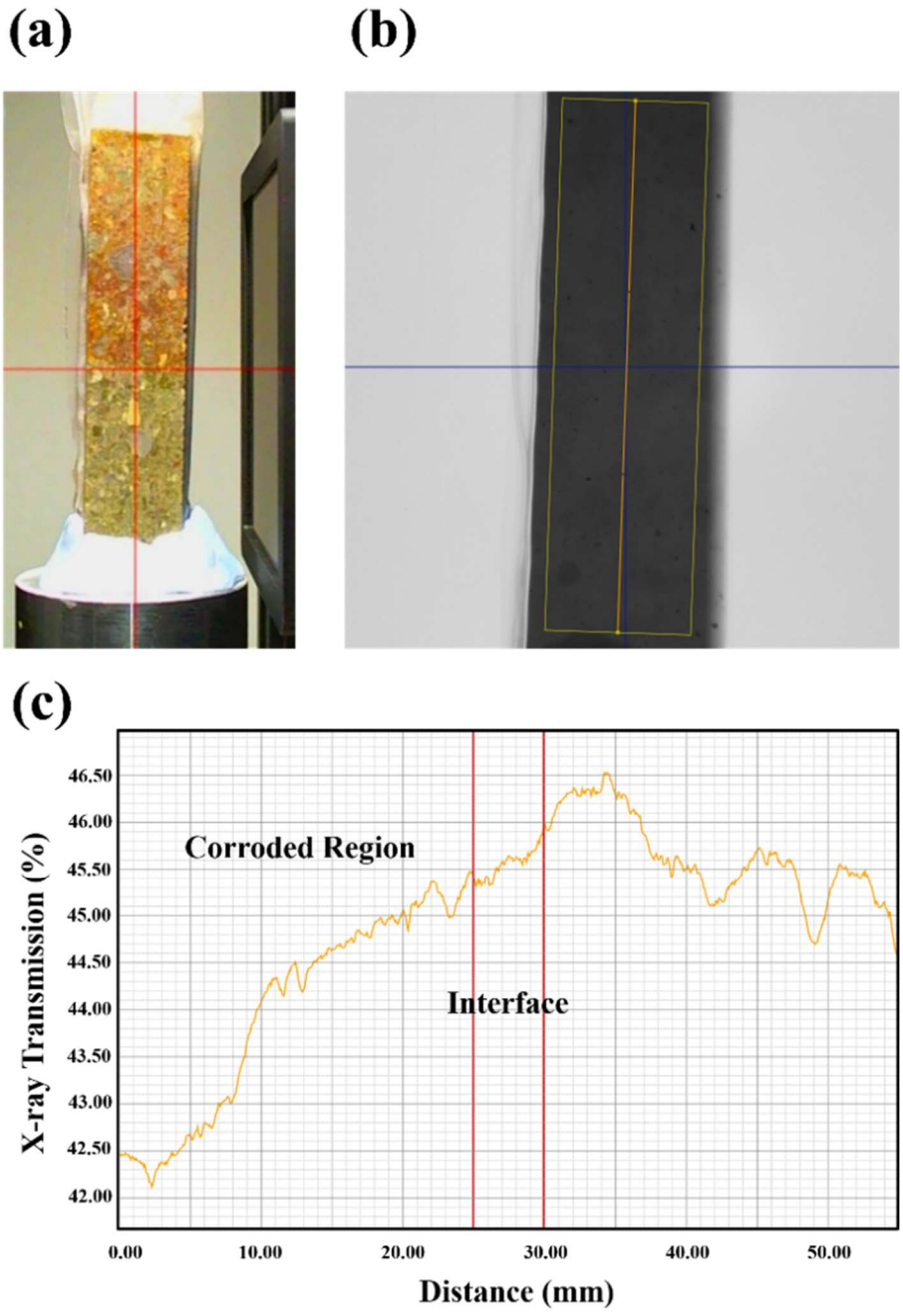

Figure 4.10: *(a) Photograph showing positioning of the sample with the interface positioned at the centre of the image. (b) X-ray radiograph showing the region from which the line-scan was extracted. The transmission percentage was averaged across the width of the sample. (c) Line-scan showing a marked increase in sample attenuation between 25-30mm (from the top to the bottom of the sample) into the corroded region.*

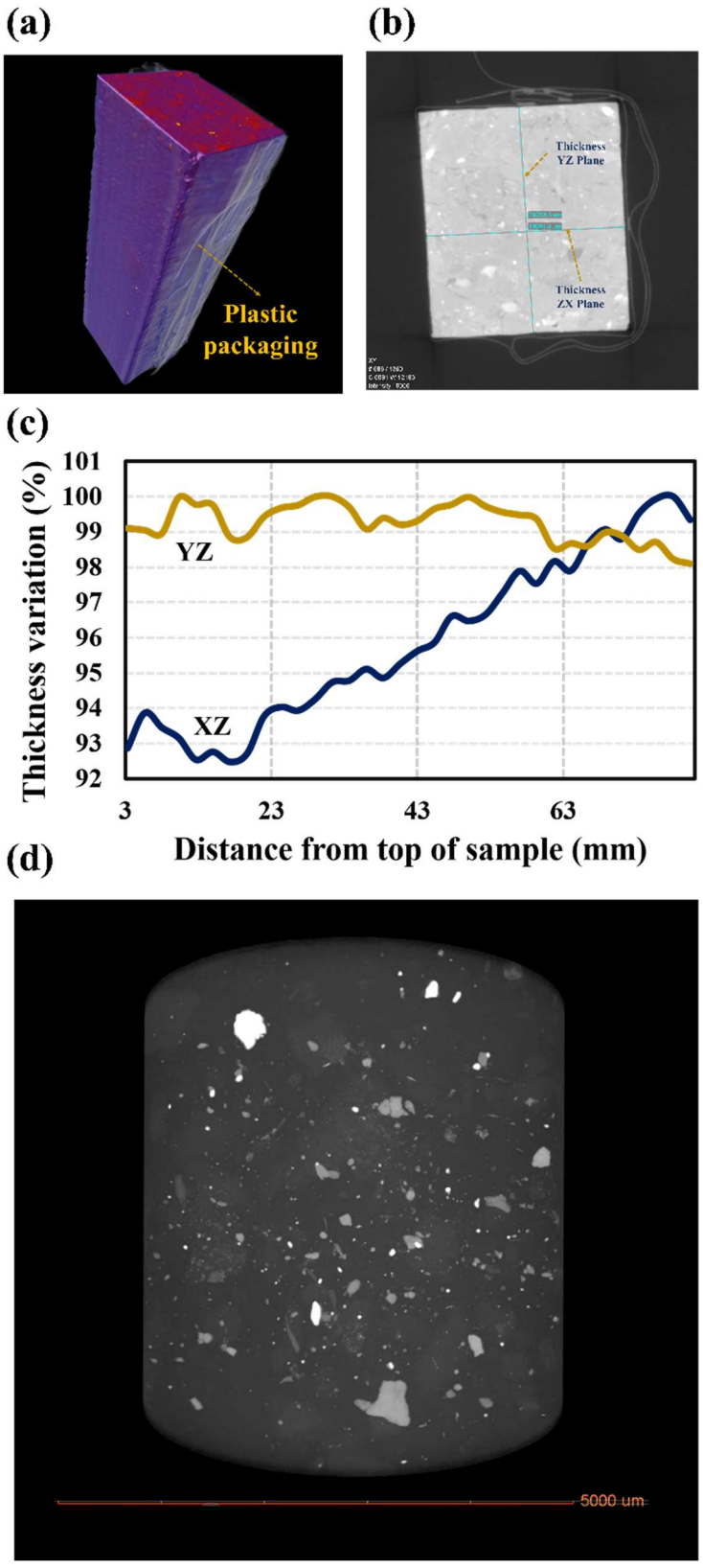

Figure 4.11: *(a) 3D render volume of BM-B-41-1, part/section A. (b) Cross-section reconstruction of BM-B-41-1, part/section A. (c) Thickness variation across the sample length. (d) Density-thresholded 3D render of a 5mm diameter volume of BM-B-41-1, part/section A. The plastic packaging prevented oxidation of the bentonite whilst inside the XRT instrument.*

X-ray attenuation is primarily controlled by the density and thickness of material it impinges; with Z-number also important for photon energies under 1MeV. A sample exhibiting uniform thickness but a variation in x-ray absorption will, therefore, be non-uniform in either density, quantity of high Z-number material or both. 2D x-ray projection images (Figure 4.10 (b)) were acquired from the sample to investigate attenuation variation in the visibly-corroded region. The recorded x-ray attenuation was determined to vary by up to 4.4% (a relative change of 9.46%) across the region analysed, grading from the assumed unaltered bentonite into the visually orange-brown material. The interface defined by the visible colour change was positioned at the centre of the scan (between 25-30mm from the edge of the extracted line-scan).

To confirm the uniformity of the sample, the 3D data were examined and a line profile showing the variation in transmission length through the sample as a function of distance from the edge was plotted (Figure 4.11). Figure 4.11 (a) shows the 3D volume render, while Figure 4.11 (b) shows a tomographic reconstructed cross-section through the 3D render and highlights the measurements taken in XZ and YZ, where YZ is the direction of the x-ray transmission. Figure 4.11 (c) shows the variation in thickness along the length of the sample, which (for the absorption orientation) are minimal.

The observed gradational change in x-ray attenuation could be positively ascribed to a density increase occurring within the sample towards the heater interface. This indicates a measurable physicochemical difference between the orange-brown bentonite and the bentonite further away from the liner interface. High magnification x-ray tomography analysis of a section of bentonite immediately proximal to the liner interface (Figure 4.11 (d)) indicated the presence of many micro-particles of denser material within the bentonite, typically forming plate-like structures up to 50μm in maximum dimension. These particles were easily resolved by density thresholding of the data, which indicated that these particles had a substantially greater attenuation coefficient than the surrounding bentonite.

This would be consistent with the presence of iron oxide phases which have approximately twice the density of bentonite (magnetite: 5.18g/cm^3 [223]; goethite: 4.26g/cm^3 [224]; hematite: 5.26g/cm^3 [225] and Febex bentonite 1.65g/cm^3 [81]). Consequently, the observation of possible iron oxide phases within the clayey matrix requires an exhaustive evaluation of potential interactions between the montmorillonite component of bentonite and the released corrosion by-products that might lead to bentonite alteration and/or transformation.

4.2.3 Cation exchange capacity determinations in the contact area between the bentonite and structural metallic components of the Febex in-situ test samples

CEC analysis was carried out to evaluate if: (*i*) corrosion products released by either the container and/or metallic structural components; or (*ii*) changes in the saline content of the surrounding aqueous medium, had affected the bentonite's capability to exchange cations. The higher the CEC value, the greater the capacity to retain, sorb or retard the transport of radionuclides. CEC is frequently used in soil analysis since it determines the ability of a material to retain cations. CEC values are usually presented in meq/100g, meq/100ml or mmol(+)/100g, that is to say concentration per unit mass or volume of the material. High CEC is one of the fundamental properties of the smectites [226]. The CEC of clay minerals is related to the layer charge and, consequently, is strongly linked with the layer isomorphic substitutions and the coordination of edge cations. When there is an excess of charge generated by isomorphic substitutions in octahedral and tetrahedral entities, this event is charge compensated by the cations present in the interlayer space. The interlayer cations are not usually fixed in the clay minerals and, so, are easily exchangeable. The coordination of edge cations is pH dependant and varies with the nature of the surrounding solution (strength and pH).

In an EBS, CEC will determine the geotechnical barrier's ability to absorb or retain certain radionuclides in case of canister failure. The analytical evaluation of this property of bentonite is of utmost importance as it allows cationic radionuclide retention or transport retardation towards the biosphere. One of the main characteristics of smectites is therefore their high cation exchange capacity in comparison with other clay minerals groups, such as kaolinite. This high capacity is determined by the large surface area exhibited by montmorillonite, which theoretically is about 750 $m^2 \cdot g^{-1}$ [227].

Table 4.4: *Specific surface area of some clay minerals. Modified from* [228].

Mineral	Source	S (m^2/g)
Na-montmorillonite	Upton, Wyoming	800
Ca-montmorillonite	Upton, Wyoming	800
Kaolinite	Georgia Kaolin Company	35

Smectites are considered to have the greatest surface area since, due to their layered structure, they present both internal and external surfaces available for cation sorption, as indicated by

Carroll & Starkey [229], who studied the CEC of several phyllosilicate minerals, concluding that bentonite shows a notably higher exchange capacity. Mulla et al. [228] also analysed the specific surface area of some montmorillonite and kaolinite samples showing that smectites have much greater sorption area than other clay minerals (Table 4.4).

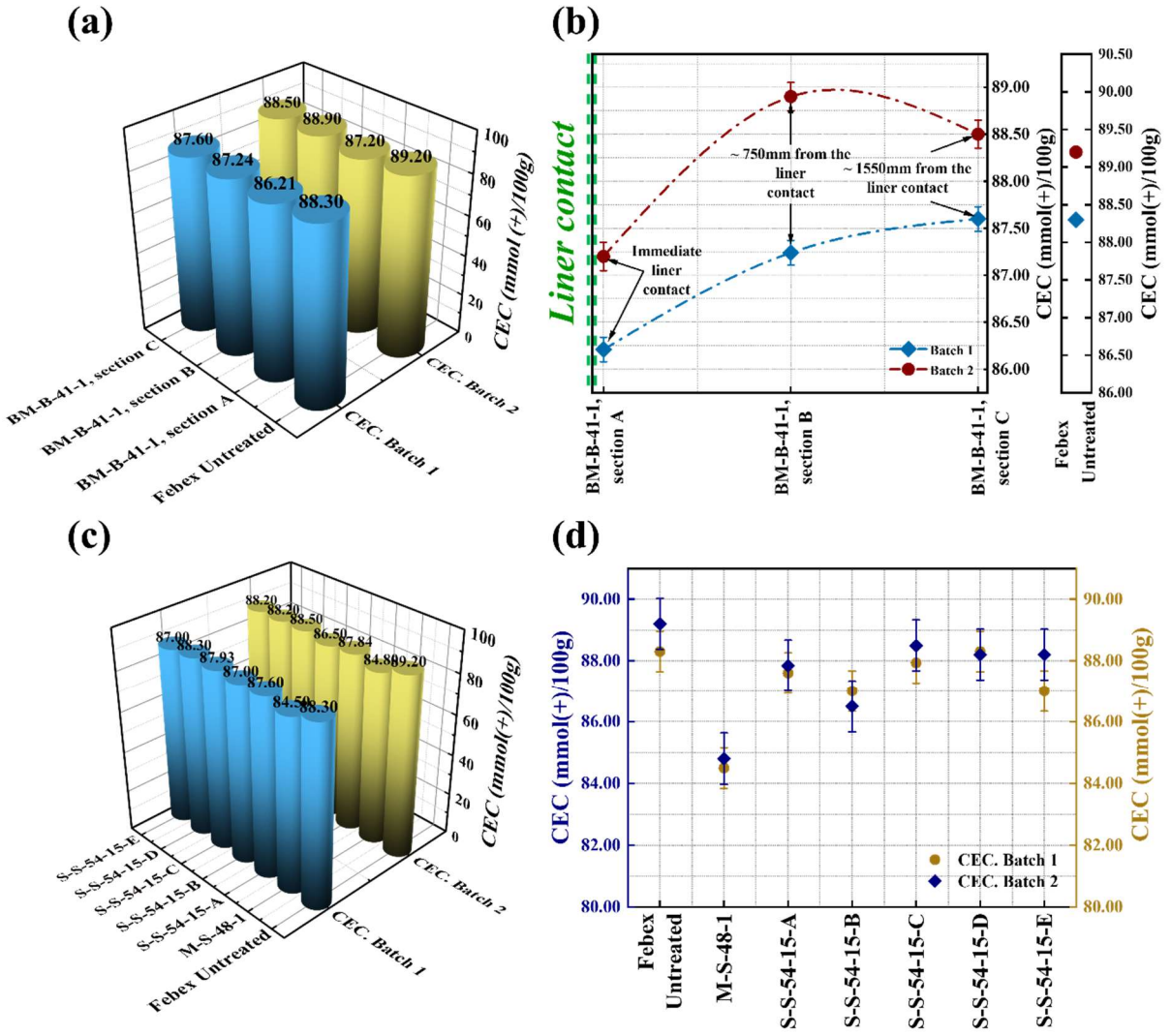

Figure 4.12: *(a)-(c) Cation exchange capacity (CEC, mmol(+)/100g) measured in all Febex bentonite samples. (b) Cation exchange capacity (CEC, mmol(+)/100g) values as a function of distance from the liner in sample BM-B-41-1. (d) Variability of CEC in samples retrieved close to the extensometer.*

However, deviations away from the normal CEC values for the smectite component of bentonite may be an indicator of mineralogical alteration. The degradation of bentonite CEC could occur as a consequence of the alteration of the permanent layer charge due to: (*i*) isomorphic substitutions driven by the replacement of Al^{3+} by Fe^{2+} in octahedral allocations; and (*ii*) the reduction of the Fe^{3+} in octahedral positions to Fe^{2+} due to redox perturbations caused by local corrosion processes. CEC alteration can also emerge as a result of variations

in pH-dependant charge. The pH value at which the net surface charge of a clay is neutral is denominated as the point of zero charge (PZC). Neumann [230] reported a PZC for smectite at pH 7.2. Neumann [230] concluded that changes in the saline content of the surrounding medium can lead to alterations in the net surface charge as a result of the absorption of H^+ or OH^-. Therefore, at high pH values, the edge sites tend to show a high CEC, whereas at low pH the anion exchange capacity is predominant [230]. Consequently, the higher the pH, the greater the CEC due to less availability of H^+. Accordingly, variation in CEC values for bentonite might be indicative of its alteration and/or transformation, driven by the described processes. Due to the relevance of CEC in the overall performance of bentonite as an EBS material. CEC analysis was run on each Febex sample, along with a reference/untreated sample supplied courtesy of CIEMAT to provide baseline data. CEC analysis was run following the method of Meier and Kahr [57], using Cu^{2+} as the index cation. The CEC calculated parameter is expressed as millimoles per 100grams (mmol(+)/100g).

Table 4.5: *CEC measured for each Febex sample.* $^{1}SE_{(standard\ error\ first\ batch)} = 1.36 mmol(+)/100g$, $^{2}SE_{(standard\ error\ second\ batch)} = 1.42 mmol(+)/100g$.

ID sample	CEC (mmol(+)/100g) First batch[1]	CEC (mmol(+)/100g) Second batch[2]
Febex reference	88.30	89.20
BM-B-41-1, section A	86.21	87.20
BM-B-41-1, section B	87.24	88.90
BM-B-41-1, section C	87.60	88.50
M-S-48-1	84.50	84.80
S-S-54-15-A	87.60	87.84
S-S-54-15-B	87.00	86.50
S-S-54-15-C	87.93	88.50
S-S-54-15-D	88.30	88.20
S-S-54-15-E	87.00	88.20

CEC results using the Cu-trien method are presented in Figure 4.12 (a)-(b) and tabulated in Table 4.5. Overall, CEC values from each sample were similar to those obtained in the reference sample and, correspond well with other literature sources that analysed the same bentonite [138], [231], [232]. However, as shown in Figure 4.12 (d) and Table 4.5, CEC values from sample M-S-48-1 are significantly lower than those obtained from the reference sample. CEC values for sample BM-B-41-1 (Table 4.5) were calculated in the different sections of the

sample. CEC values plotted as a function of the increasing distance from the liner are provided in Figure 4.12 (b). CEC values in both determinations record a CEC decrease in the immediate vicinity of the metallic liner, increasing again as the distance from the liner increases. CEC values between ~750-1500mm away from the liner were close matches to those observed in the reference sample, suggesting this was unaltered material. Despite the absolute differences between duplicates, especially in the different sections of sample BM-B-41-1 (retrieved from contact with the liner, section 3.2.1.2.3), there is an internal consistency of trends in each duplicate set (Figure 4.12 (b)). Besides, the presented uncertainties cannot be considered as an overestimation, if only because of all uncertainties on manipulated volumes (for example, the precision on the volume of a micropipette is usually about 1%). Overall difference between values is only 1-2 % of the value, clearly within the precision of the measurements.

There are a small differences between the CEC values obtained from the reference sample and the in-situ test samples. The observed deviations, particularly in section A of sample BM-B-41-1 and sample M-S-48-1, might be attributable to possible isomorphic substitutions in combination with chemical reduction of structural iron favoured by the Fe^{2+} migration through the clayey matrix. In addition, salinity changes in the enveloping aqueous medium favoured by the precipitation and re-dissolution of natural components, such as silicate and calcium hydrates, cristobalite and silica, could have slightly altered the overall CEC values observed.

4.2.4 Study of the evolution of exchangeable cations after 18 year of in-situ test

Although only subtle differences have been found in CEC between the Febex in-situ test samples and Febex reference material, they were deemed to be sufficiently significant to warrant determination of the exchangeable cations present in different samples. This could provide valuable information on any alteration and/or transformation induced in the bentonite samples over the course of the in-situ test and, therefore, the presence of newly formed minerals.

Variations in chemical composition found in most clay minerals are due to isomorphic substitutions in both tetrahedral and octahedral positions, those containing the exchangeable cations responsible for balancing the charge excess or deficit caused by such substitutions. For instance, the kaolinite-serpentine group exhibit little or no swelling capability. It follows that

the nature of cation concentration in the interlayer space, and on outer surfaces and edges, has an important effect on the bentonite's properties, especially its swelling capability. Hence, the dominant exchangeable cations (usually sodium or calcium in bentonite) dictate the swelling capability. Sodium bentonites are characterised by a greater swelling capability than calcium bentonites. The high water up-take capacity of sodium bentonites might be explained by the larger hydration force of Na^+ with respect to Ca^{2+}. In other words, since the charge/size ratio of Na^+ is greater than Ca^{2+}, the effective ion-dipole interaction would be larger and, thus, a greater number of water molecules would be attracted by a single Na^+ ion [233].

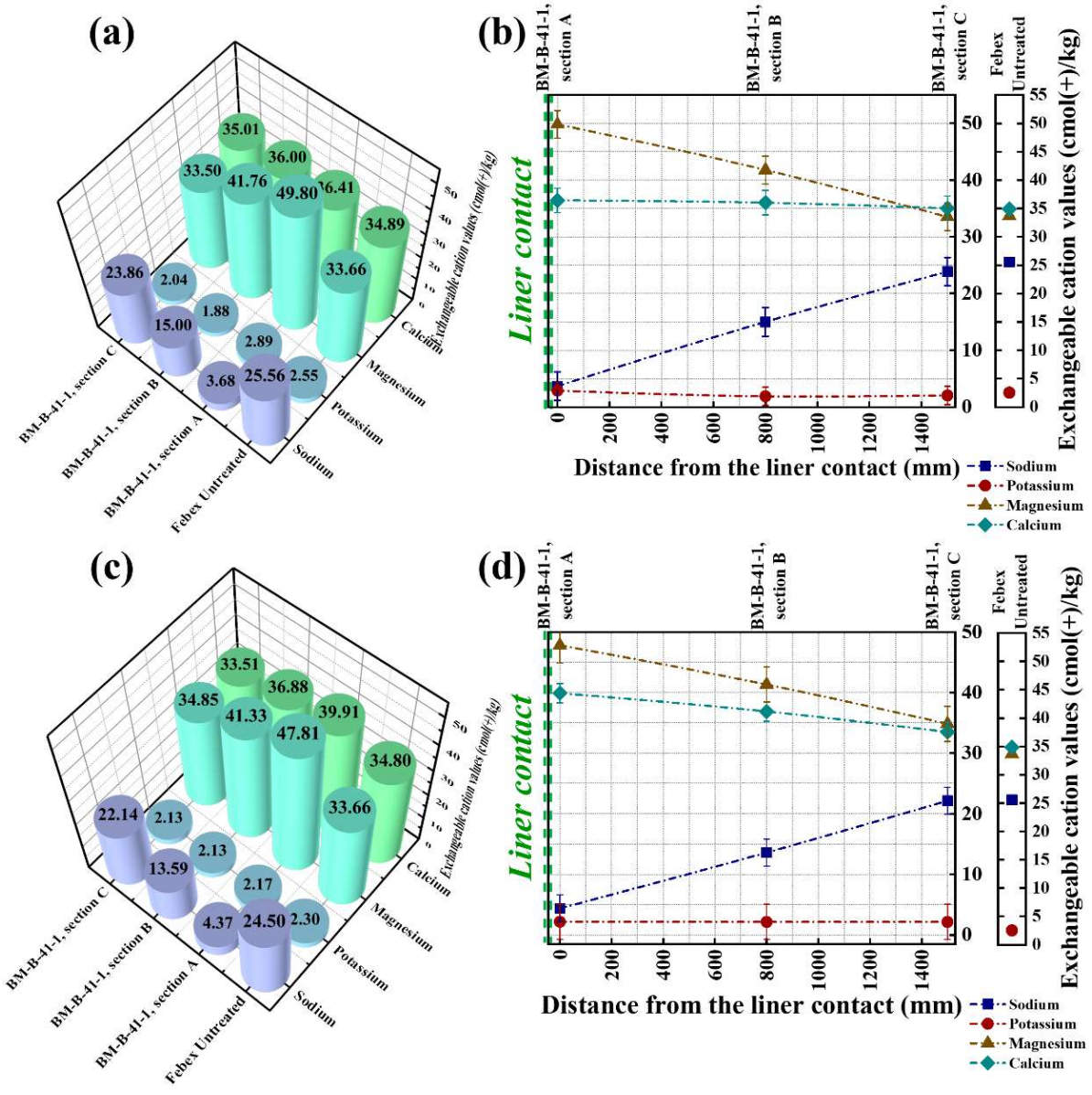

Figure 4.13: *(a)-(c) Results of exchangeable cation analysis (cmol(+)/kg), in two determinations of the different sections of sample BM-B-41-1. (b)-(d) Variation of exchangeable cations as function of distance from the liner contact, obtained in two determinations of the different sections (A/B/C) of sample BM-B-41-1.*

Table 4.6: *Results of exchangeable cation values variation (measured in cmol(+)/kg) estimated in parts A, B and C of sample BM-B-41-1expressed as a function of the distance from the liner.*

Determination 1						
Distance from the liner	Total CEC	**Na^+**	**K^+**	**Mg^{2+}**	**Ca^{2+}**	**Sample**
Immediate liner contact	92.78	3.68	2.89	49.80	36.41	**BM-B-41-1, section A**
~800mm from the liner	94.64	15.00	1.88	41.76	36.00	**BM-B-41-1, section B**
~1500mm from the liner	94.41	23.86	2.04	33.50	35.01	**BM-B-41-1, section C**
-	96.66	*25.56*	*2.55*	*33.66*	*34.89*	***Febex Untreated***
Determination 2						
Distance from the liner	Total CEC	**Na^+**	**K^+**	**Mg^{2+}**	**Ca^{2+}**	**Sample**
Immediate liner contact	94.26	4.37	2.17	47.81	39.91	**BM-B-41-1, section A**
~800mm from the liner	93.93	13.59	2.13	41.33	36.88	**BM-B-41-1, section B**
~1500mm from the liner	92.63	22.14	2.13	34.85	33.51	**BM-B-41-1, section C**
-	96.66	*24.50*	*2.30*	*33.66*	*34.80*	***Febex Untreated***

As reported by Pusch [234], cation replaceability is determined by factors such as: (*i*) experimental conditions; (*ii*) nature of the cations involved; (*iii*) cation concentration; (*iv*) cation valence; and (*v*) smectite type. Although the replacement of interlayer cations is dominated by a wide variety of factors, the most significant is the cationic valence. Thus, the greater the valence of the cation, the higher its replacement potential. Nevertheless, for ions of the same valence, the replacement of one for another is dictated by their ionic diameter, i.e. by the size of the cation. In this case, the replacement potential increases as the size of the cation decreases. Albeit, it is usually the size of the hydrated cation that controls the replacement ability. Therefore, for ions of equal valence but different hydration state, those less hydrated will have higher replacement energy, and will be, therefore, more difficult to replace. Besides the described factors, the cation replaceability is also ruled by their concentration in the surrounding solution. As stated by Pusch [234], the probability of exchange of Ca^{2+} by Na^+, in a Ca-montmorillonite, is ascertained via the Na^+ concentration in the solution. Therefore, the higher the concentration is, the greater the replaceability. It is usually accepted that the

amount of water sorbed by smectites increases as the ionic potential of the exchangeable cations increases. This is because it is strongly correlated to hydration energy of the actions. Thus, we see an ordering from Na<Ca<Mg. On this basis, the GTS water composition (Table 3.24) should be an initial parameter to consider due to its salinity, dominated by the presence of Na^+ which might have favoured cation exchange towards the Na^+-dominant composition.

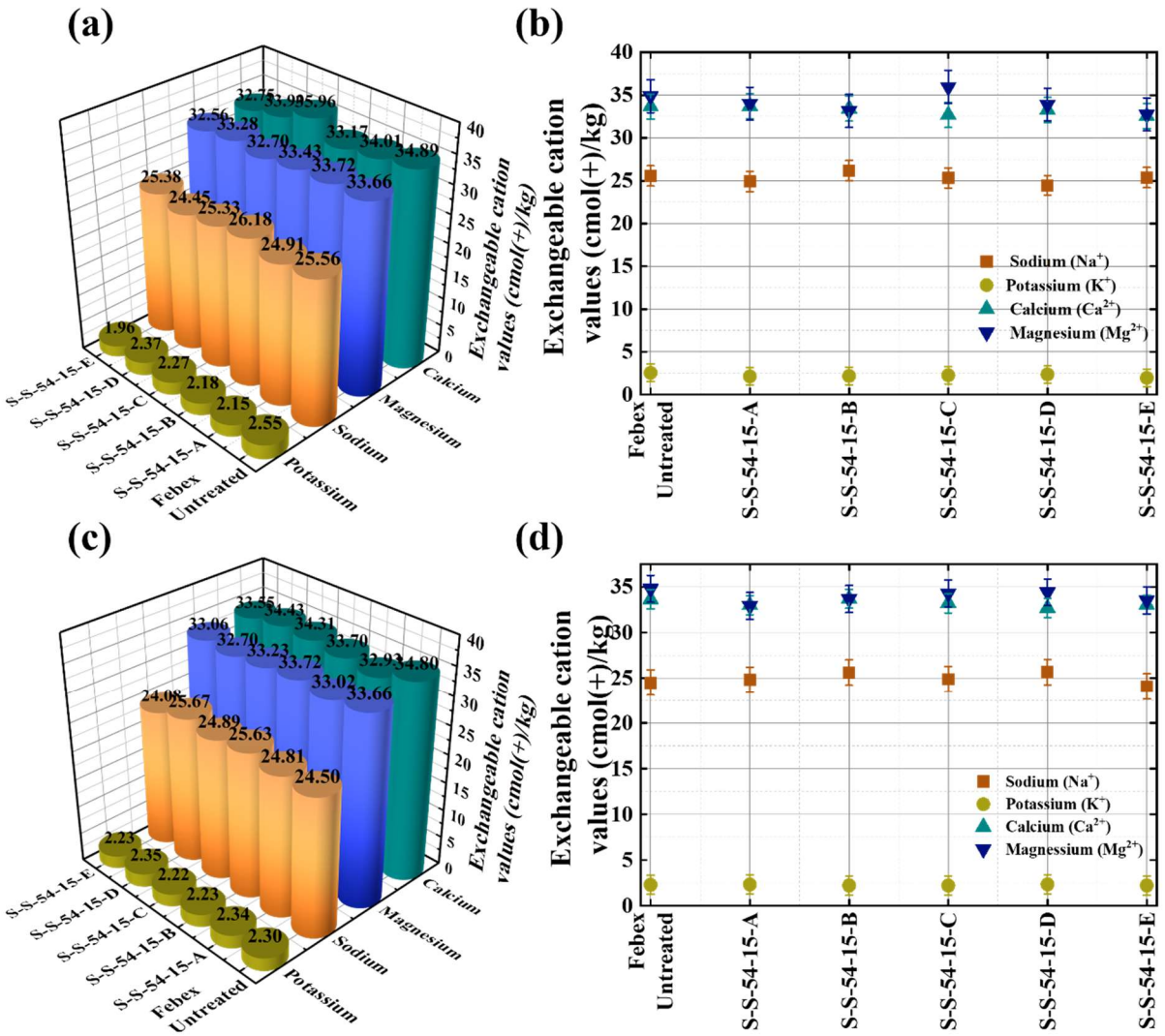

Figure 4.14: *(a)-(c) Exchangeable cation analysis (cmol(+)/kg), form two determinations of the extensometer bentonite samples. (b)-(d) Variation of exchangeable cations form two determinations of the extensometer bentonite samples.*

Evolution of the exchangeable cations replaceability was firstly determined in the reference sample and in the three different sections of the BM-B-41-1 sample. Exchangeable cation analyses were duplicated to ensure consistency, and a $CsNO_3$ solution was used for cation displacement and results are presented as centimoles per kilogram (cmol(+)/kg). The derived

results are shown in Figure 4.13 and tabulated in Table 4.6. Figure 4.13 (a) and (c), and Table 4.6 show the soluble ion values obtained from the pristine material and BM-B-41-1 sample.

Since the test sample was sliced into three sections or parts, measurements were performed at different distances from the liner interface, as presented in Figure 4.13 (b) and (d), and Table 4.6. Results showed a distinct ionic grading. Ca^{2+} and Mg^{2+} were the major cations in bentonite in immediate contact with the liner (section A). However, when distance from the liner increased (at ~800mm and ~1500mm), the concentrations of those cations decreased, with a commensurate increase in Na^{+} concentration, reaching values close to those determined in the reference sample.

Table 4.7: *Results of exchangeable cation values variation (measured in cmol(+)/kg) estimated in samples S-S-54-15-A/B/C/D/E.*

Determination 1					
Sum exchangeable cations	**Na^{+}**	**K^{+}**	**Mg^{2+}**	**Ca^{2+}**	**Sample**
94.78	24.91	2.15	33.72	34.00	**S-S-54-15-A**
94.96	26.18	2.18	33.43	33.17	**S-S-54-15-B**
96.26	25.33	2.27	32.70	35.96	**S-S-54-15-C**
93.99	24.45	2.37	33.28	33.90	**S-S-54-15-D**
92.64	25.37	1.96	32.56	32.75	**S-S-54-15-E**
96.66	*25.56*	*2.55*	*33.66*	*34.89*	***Febex Untreated***
Determination 2					
Sum exchangeable cations	**Na^{+}**	**K^{+}**	**Mg^{2+}**	**Ca^{2+}**	**Sample**
93.10	24.81	2.34	33.02	32.93	**S-S-54-15-A**
95.27	25.63	2.23	33.72	33.70	**S-S-54-15-B**
94.65	24.89	2.22	33.23	34.31	**S-S-54-15-C**
95.16	25.67	2.35	32.70	34.43	**S-S-54-15-D**
92.92	24.08	2.23	33.06	33.55	**S-S-54-15-E**
95.26	*24.50*	*2.30*	*33.66*	*34.80*	***Febex Untreated***

Exchangeable cation determinations were also carried out on the extensometer samples and the obtained results are presented in Figure 4.14 and Table 4.7. These specific samples were retrieved in the periphery of the bentonite-host rock contact, where water saturation was higher than in the areas close to the liner.

From Figure 4.14 and Table 4.7 it can be observed that there was no variability in the exchangeable cation determinations from the experimental samples and the unaltered sample. From exchangeable cation analysis, it was observed that samples retrieved close to the liner, specifically section A of the sample, showed a proportionally higher concentration of Mg^{2+}, relative to Ca^{2+}, Na^{+} and K^{+}, compared to the unaltered samples. Conversely, the observed exchangeable cation values in the extensometer samples were close matches to those observed in the reference sample. This was not unexpected as the extensometer was not heated and, hence, the variations observed in sections of BM-B-41-1 sample might be thermally induced.

Overall, from exchangeable cation determinations on section A (BM-B-41-1), it can be concluded that there was a cation migration (Mg^{2+}) towards the areas close to the liner or hottest areas as previously reported by Torres et al [138], where the saturation degree and water content were lower than the estimated values in areas close to the host rock. Despite this, the sum of the total exchangeable cations seems to vary in the immediate areas close to the heater, increasing again with increasing distance from the liner. In addition, the sum of exchangeable cations of the extensometer samples showed values close to those obtained from the pristine material. However, sample S-S-54-15-E showed a general value deviations with regard to the reference sample.

4.2.5 Mössbauer spectroscopy analysis of iron valence states

Determination of the iron oxidation state on clays can be relatively straightforward through Mössbauer spectroscopy, thus, this technique was utilised to establish the coordination state and deduce the magnetic properties induced by the presence of iron in the Febex bentonite matrix. To achieve a good understanding of the coordination state and magnetic properties of the Febex bentonite sample, the spectral analysis requires the identification of several parameters: *(i)* isomeric shifting; *(ii)* quadrupole splitting and; *(iii)* magnetic hyperfine parameters to locate the presence of iron.

As stated by Murad [235], the presence of iron oxides and hydroxides is likely in clays and can be detected by Mössbauer spectroscopy. Ideally, the magnetic ordering temperatures of iron oxyhydroxides are characterised by being relatively high, ranging from 300-900K in the case of hematite [236], around 400K in the case of goethite [237], and lower, 77K, in the case of lepidocrocite [238]. Nonetheless, due to clays presenting a mixed structure as a result of the association of numerous embedded accessory minerals, the behaviour of iron oxides and

oxyhydroxides against the Mössbauer effect deviates from the ideal. This deviation may be explained by several reasons [235], [239]. One of the major reasons is due to the replacement of iron by aluminium in iron oxyhydroxides. Since aluminium is of diamagnetic character, this substitution decreases the magnetic ordering temperatures, which results in a reduction of the magnetic hyperfine fields for all temperatures [235], [239].

Another important reason that must be outlined is the spontaneous change in the direction of magnetisation due to the presence of small particles of iron oxides and hydroxides in the clay matrix. This phenomenon is known as superparamagnetic relaxation and produces a reduction of the hyperfine field owing to line broadening. Mössbauer analyses aimed to determine the presence of iron within the different Febex in-situ test samples.

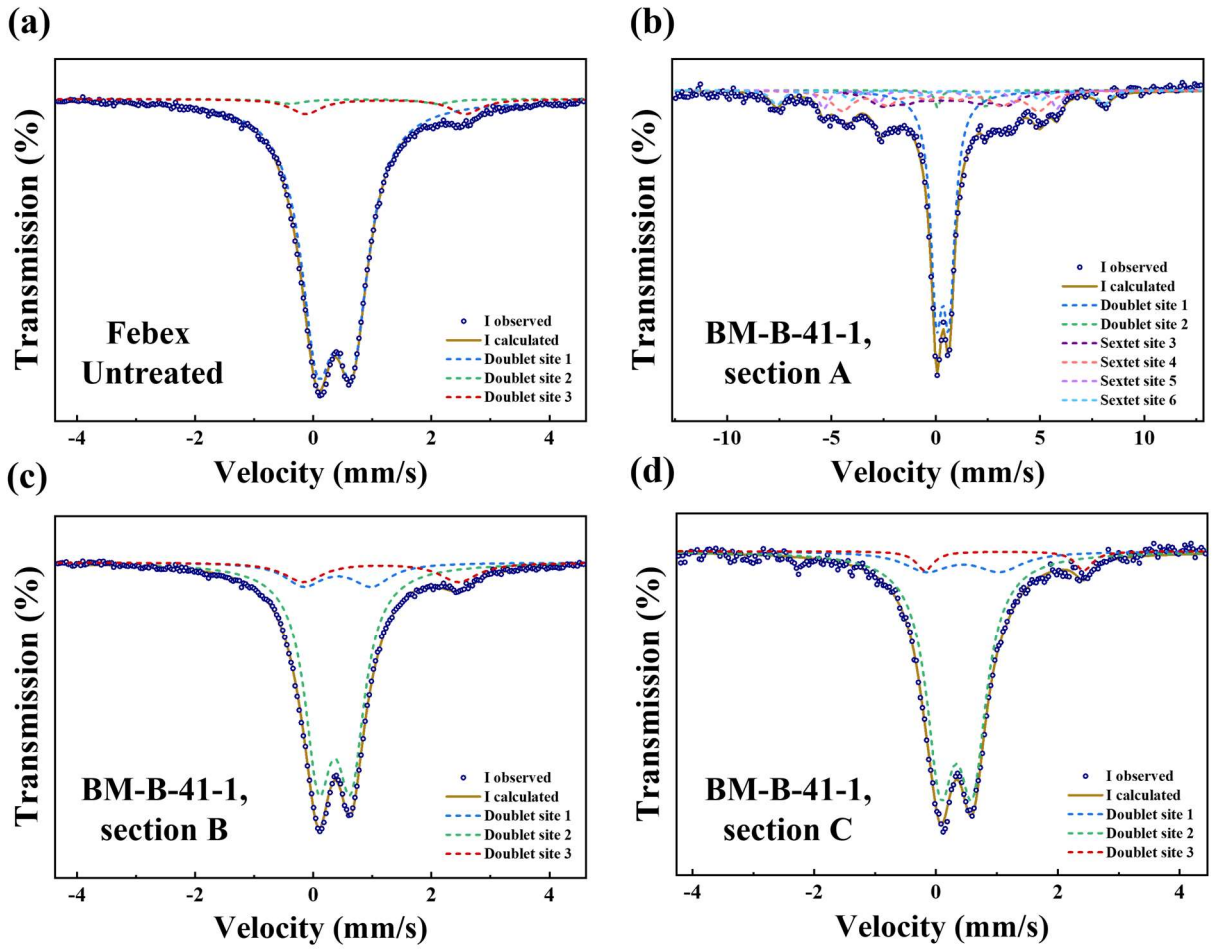

Figure 4.15: *(a), (b), (c) and (d) fitted Mössbauer spectra corresponding with Febex Untreated and sample BM-B-41-1, sections A, B and C (data acquired by Dr. María Sánchez Arenillas and Dr. Juan de la Figuera Bayón from Consejo Superior de Investigaciones Científicas (CSIC, Spanish National Research Council)).*

Analyses were carried out firstly on a reference or unaltered sample to provide baseline data, and subsequently on the experimental samples. Mössbauer analyses were performed under

contract by Dr. María Sánchez Arenillas and Dr. Juan de la Figuera Bayón from Consejo Superior de Investigaciones Científicas (CSIC, Spanish National Research Council).

Table 4.8: *Mössbauer data of reference sample and sections A, B, and C of sample BM-B-41-1. Sections A, B, and C. Measurement performed at room temperature (298K). B_{hf}: hyperfine magnetic field, δ: Isomer shift relative to ^{57}Fe, Δ: Quadrupole splitting, and RA: Relative spectral area (data acquired by Dr. María Sánchez Arenillas and Dr. Juan de la Figuera Bayón from Consejo Superior de Investigaciones Científicas (CSIC, Spanish National Research Council)). $^{1}SE_{(standard\ error\ RA)}$ =6%.*

Sample	Assignment	B_{hf} (T)	δ (mmS^{-1})	Δ (mmS^{-1})	RA (%)[1]
Febex Untreated	Fe^{3+} OH	-	0.36	0.59	92
	Fe^{2+} Td	-	0.85	2.50	2
	Fe^{2+} OH	-	1.22	2.70	6
BM-B-41-1, section A	Fe^{3+} OH	-	0.34	0.60	46
	Fe^{2+} OH	-	1.24	2.32	2
	Superparamagnetic Contribution Fe^{3+} oxides and/or Oxyhydroxides	19.63	0.36	0.10	15
	Goethite	29.28	0.30	-0.16	18
	Goethite	34.69	0.37	-0.14	8
	Hematite	49.68	0.35	-0.12	8
BM-B-41-1, section B	Fe^{3+} OH very distorted (because Δ is big)	-	0.41	1.15	12
	Fe^{3+} OH	-	0.36	0.55	77
	Fe^{2+} OH	-	1.15	2.6	11
BM-B-41-1, section C	Fe^{3+} OH very distorted (because Δ is big)	-	0.44	1.21	12
	Fe^{3+} OH	-	0.34	0.53	83
	Fe^{2+} OH	-	1.12	2.61	5

The comparison of the hyperfine parameters between the unaltered sample and the samples from the Febex in-situ test enabled some quantification of Fe^{2+} and Fe^{3+} in the unaltered material and experimental samples. The Mössbauer determinations of Fe^{2+} versus Fe^{3+}content for sections A, B and C of sample BM-B-41-1 and reference sample are shown in Figure 4.15 and Table 4.8. The Mössbauer spectra at room temperature (298K) of the unaltered sample (Figure 4.15 (a) and Table 4.8), and sections A, B and C (Figures 4.15 (b), (c) and (d), and Table 4.8), consist of three spectral components. It can be, therefore, stated that the iron cations

in octahedral positions are mostly trivalent. However, section A of sample BM-B-41-1 consist of two doublets, a superparamagnetic component and three discrete sextets. Fitted parameters (Figure 4.15 (b) and Table 4.8) showed the presence of goethite and hematite.

Table 4.9: *Mössbauer data of samples S-S-54-15-A/B/C/D/E and M-S-48-1. Measurement performed at room temperature. B_{hf}: hyperfine magnetic field, δ: Isomer shift relative to ^{57}Fe, Δ: Quadrupole splitting, and RA: Relative spectral area (data acquired by Dr. María Sánchez Arenillas and Dr. Juan de la Figuera Bayón from Consejo Superior de Investigaciones Científicas (CSIC, Spanish National Research Council)). $^{1}SE_{(standard\ error\ RA)}$ =6%.*

Sample	Assignment	B_{hf} (T)	δ (mmS^{-1})	Δ (mmS^{-1})	RA (%)[1]
S-S-54-15-A	Fe^{3+} OH	-	0.34	1.10	21
	Fe^{3+} OH	-	0.34	0.49	79
S-S-54-15-B	Fe^{3+} OH	-	0.37	0.60	91
	Fe^{2+} OH	-	1.12	2.64	9
S-S-54-15-C	Fe^{3+} OH	-	0.48	1.18	11
	Fe^{3+} OH	-	0.36	0.55	80
	Fe^{2+} OH	-	1.10	2.70	9
S-S-54-15-D	Fe^{3+} OH	-	0.34	0.54	87
	Fe^{3+} OH	-	0.43	1.15	5
	Fe^{2+} Td	-	0.80	2.60	8
S-S-54-15-E	Fe^{3+} OH	-	0.37	0.57	83
	Fe^{3+} OH	-	0.48	1.18	8
	Fe^{2+} OH	-	1.06	2.60	9
M-S-48-1	Fe^{3+} OH	-	0.34	0.59	36
	Hematite	49.3	0.36	-0.21	28
	Goethite	0.17	0.36	0.10	36

Section A of sample BM-B-41-1 showed Fe^{3+} and Fe^{2+} coexisting in octahedral positions. Also, the spectra of the sample displayed a superparamagnetic contribution that could be assigned to the presence of small microparticles of Fe^{3+} containing oxides and/or oxyhydroxides. The assignment of this component from a room temperature spectrum to specific Fe^{3+} compounds is not possible, since at room temperature, superparamagnetism causes magnetic order to disappear in goethite particles smaller that 15nm and hematite particles smaller than 8nm [235]. Therefore, and in order to distinguish between iron oxyhydroxides and phyllosilicates, the Mössbauer spectrum, in this specific case, should have been recorded at lower temperatures to minimise substitutional and particle-size affects in iron oxyhydroxides, and re-establish its

magnetic order but, at the same time, the temperature must be high enough to avoid magnetic order phyllosilicates [235]. Thus, the two goethite sextets might be associated with two fractions of this compound having different particles sizes, which would correlate with microXRT observations that showed different particle sizes.

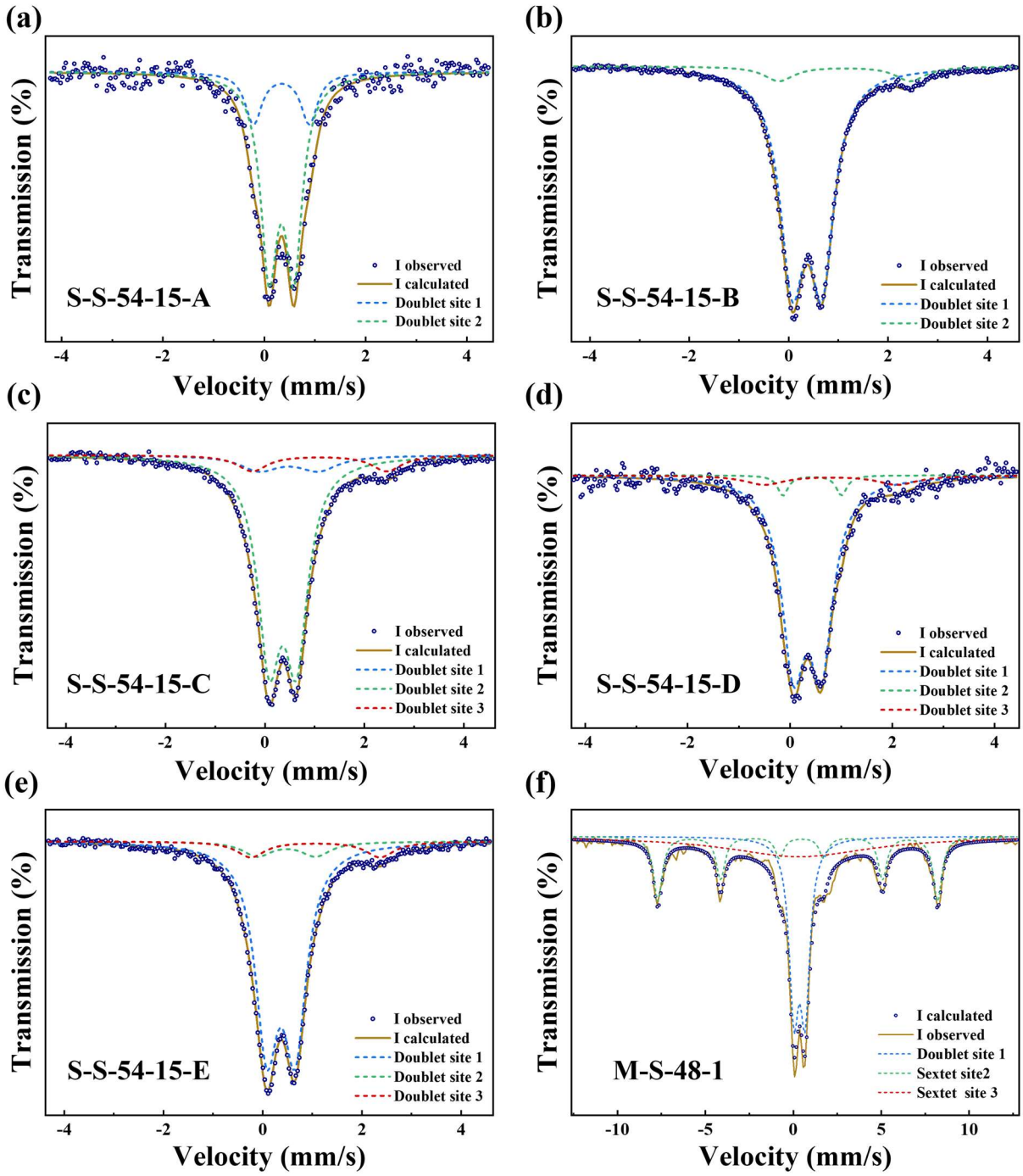

Figure 4.16: *(a), (b), (c), (d) and (e) fitted Mössbauer spectra corresponding with sample S-S-54-15-A/B/C/D/E. (f) Displays the fitted Mössbauer spectra corresponding with sample M-S-48-1 (data acquired by Dr. María Sánchez Arenillas and Dr. Juan de la Figuera Bayón from Consejo Superior de Investigaciones Científicas (CSIC, Spanish National Research Council)).*

Mössbauer spectra were also recorded from the extensometer samples (S-S-54-15-A/B/C/D/E), and the obtained results are presented in Table 4.9 and Figures 4.16 (a), (b), (c), (d) and (e). From comparison with the unaltered sample results, it can be concluded that the Mössbauer spectra of these samples mostly consists of three spectral components, concluding that iron cations in octahedral positions are also mostly trivalent. Finally, Mössbauer analysis was also carried out in the bentonite collected between the corrosion coupons sample and the results obtained are presented in Figure 4.16 (f) and Table 4.9. The M-S-48-1 Mössbauer spectrum consists of one doublet and two discreet sextets. The Mössbauer fitted parameters for this sample show the presence of goethite and hematite and are also characterised by the presence of Fe^{3+} in octahedral positions.

Examination of the Mössbauer profiles and hyperfine parameters obtained at room temperature (Figures 4.15 and 4.16, Tables 4.8 and 4.9) indicate that both Fe^{2+} and Fe^{3+} are present. The central doublets present in the spectrums and close to 0mm/s are indicative of the presence of iron within the silicate structure. Notable important is the presence of goethite and hematite in section A of BM-B-41-1, but more so is the coexistence of Fe^{2+} and Fe^{3+} within the clay crystallographic. This might suggest the migration of iron released from the corroded liner and, its incorporation on octahedral sites in the smectite, or due to structural iron reduction again in the smectite component. Both scenarios might lead to the formation of new minerals and, therefore, the alteration and/or transformation of the montmorillonite component.

4.2.6 X-ray diffraction studies of Febex bentonite samples in contact with metallic structural components

X-ray diffraction (XRD) analysis is one of the most common practices in analysis of crystallographic soil structures and post determination of mineralogical species. Therefore, XRD was utilised as a part of the physicochemical analyses performed to determine the presence of iron phases, as well as possible mineralogical alteration and/or crystallographic transformation of bentonite over the course of the Febex in-situ test.

Carlson [240] utilised a variety of laboratory techniques, among them XRD, to evaluate the iron content in bentonite samples from different worldwide deposits. Carlson [240] concluded that the examined bentonite samples were structurally composed of variable amounts of Fe^{3+}, in concentrations ranging between 5-10%. From this study, it was also clear that the most common iron oxide species were goethite and hematite.

To evaluate the iron content and determine any alteration and/or transformation of the smectite component, preliminary random powder diffraction analysis was run on the unaltered/untreated Febex bentonite. This initial analysis provided a baseline composition of Febex bentonite, which was subsequently used for comparative analyses with the Febex experimental samples. XRD analysis were also performed on random powders prepared from subsamples of each Febex in-situ test sample to identify the mineral phases and provide a semi-quantitative determination of their bulk mineralogy in comparison with the reference sample as shown in Figure 4.17 and Table 4.10.

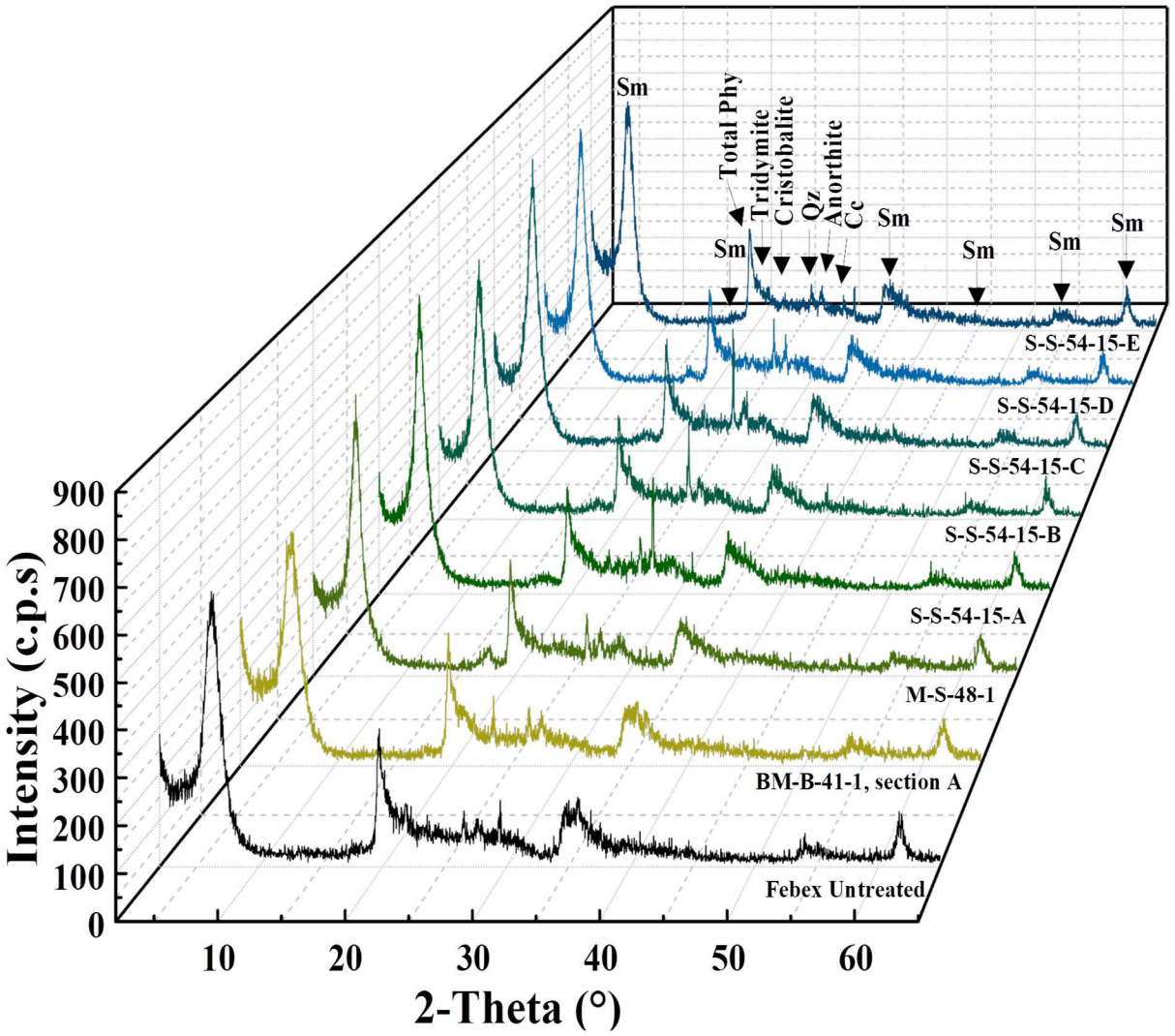

Figure 4.17: *XRD patterns of Febex bentonite samples. Sm: Smectite, Total Phy: Total phyllosilicates, Qz: Quartz, Cc: Calcite.*

No appreciable differences in mineralogy between the virgin material and the Febex bentonite samples analysed were found (Table 4.10). The mineral phases observed were a close match. Thus, it can be inferred, that from a compositional point of view, the Febex in-situ test samples

and the reference sample were similar. No iron phases were detected, and no evidence of alteration or mineralogical transformation was apparent.

Table 4.10: *Mineralogical composition of Febex bentonite samples compared with the Febex reference sample. [1]Standard error quartz (SE_{quartz}) = 0.26%, [2]Standard error ($SE_{tridymite}$) = 0.60%, [3]Standard error ($SE_{phyllosilicates}$) = 0.45%, [4]Standard error ($SE_{calcite}$) = 0.19%, [5]Standard error ($SE_{plagioclase}$) = 0.63%, [6]Standard error ($SE_{cristobalite}$) = 0.16%.*

Sample	Mineral (%)					
	Quartz[1]	Tridymite[2]	Phyllosilicates[3]	Calcite[4]	Plagioclase (albite/ anorthite)[5]	Cristobalite[6]
Febex Untreated	2	4	88	1	4	1
BM-B-41-1, section A	2	Traces	86	1	5	1
M-S-48-1	2	3	87	1	7	Traces
S-S-54-15-A	3	4	87	Traces	6	Traces
S-S-54-15-B	4	6	85	Traces	5	Traces
S-S-54-15-C	2	3	87	Traces	8	Traces
S-S-54-15-D	3	4	84	Traces	9	Traces
S-S-54-15-E	3	4	86	1	8	Traces

To determine any possible montmorillonite alteration and/or transformation, we can examine the characteristic (001) reflection. The 001 spacing of smectites varies between 12Å and 15Å, depending on the ambient relative humidity and other factors [241]. Therefore, the 001 spacings of Febex bentonite samples and untreated sample were determined (Table 4.11 and Figure 4.18). The majority of the samples exhibit a basal spacing similar to that measured in the raw material, confirming the Ca-Mg character. Overall, there are no clear differences in basal spacings between samples. However, the sample extracted from the vicinity of the liner (BM-B-41-1, section or part A) showed a lower value than the reference sample, but still close to the original value. This finding suggests that there may have been a slight increase of the basal spacing of bentonite in the immediate vicinity of the liner. This could be explained by a possible exchange of Na^+ for Ca^{2+} or Mg^{2+} already observed in the estimation of the exchangeable cations, and supported by previous assumptions by Villar et al. [242].

Table 4.11: *001 spacings values of Febex samples and unaltered samples. Standard error d-spacing ($SE_{d\text{-}spacing}$) = 0.41%.*

Sample	d-spacing (Å)
Febex Untreated	14.02
BM-B-41-1, section A	13.83
M-S-48-1	14.97
S-S-54-15-A	14.67
S-S-54-15-B	14.58
S-S-54-15-C	14.86
S-S-54-15-D	14.84
S-S-54-15-E	14.43

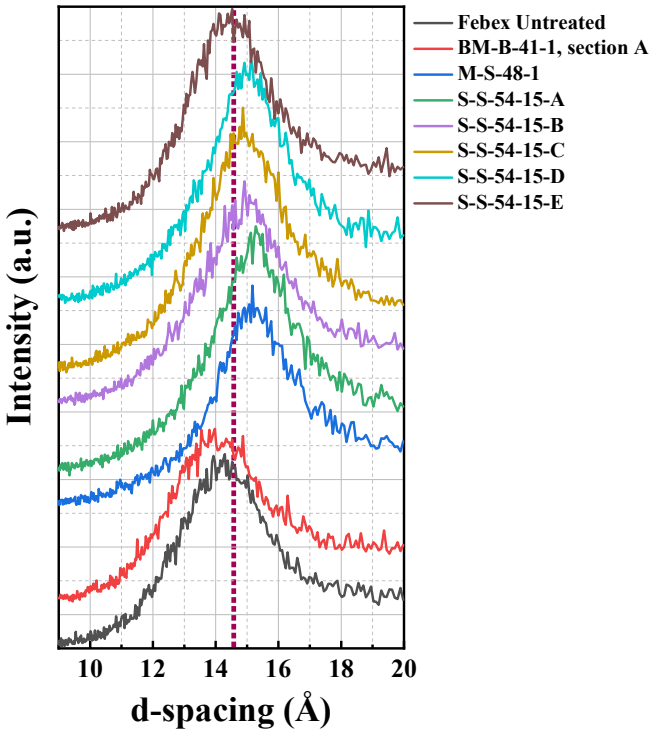

Figure 4.18: *XRD peak positions of 001 spacings of Febex bentonite samples and unaltered sample.*

Nonetheless, to perform a better identification of clay minerals, and visualise any alteration and/or transformation of the montmorillonite component as well as the presence of other aggregates, oriented mounts (OM) were created. Ethylene glycol sample saturation shifts the smectite 001 spacing from 12-15Å to 16-17Å. The shifting of the smectite 001 spacing depends on the layer charge density, type of interlayer cation, hydration state and the presence of other interstratified clay minerals [241]. Furthermore, smectite hydration state varies as a function of the degree of saturation, vapour pressure, ion size and concentration within the interlayer spacing. Bergaya and Lagaly [243] defined the hydration state of 2:1 phyllosilicate minerals as 'pseudo-layers', quantifying said states as tabulated in Table 4.12. Figures 4.19 and 4.20, and Tables 4.13, 4.14 and 4.15 display the results obtained after sample treatment.

Table 4.12: *2:1 phyllosilicate mineral hydration state. Adapted from* [243].

Hydration state	d-spacing (Å)
0	~10
1 (pseudo-monolayer)	~11.80-12.50
2 (pseudo-bilayer)	~14.50-15.50
3 (three water pseudo-layers)	~18.50
4 (four water pseudo-layers)	~19.00-20.00

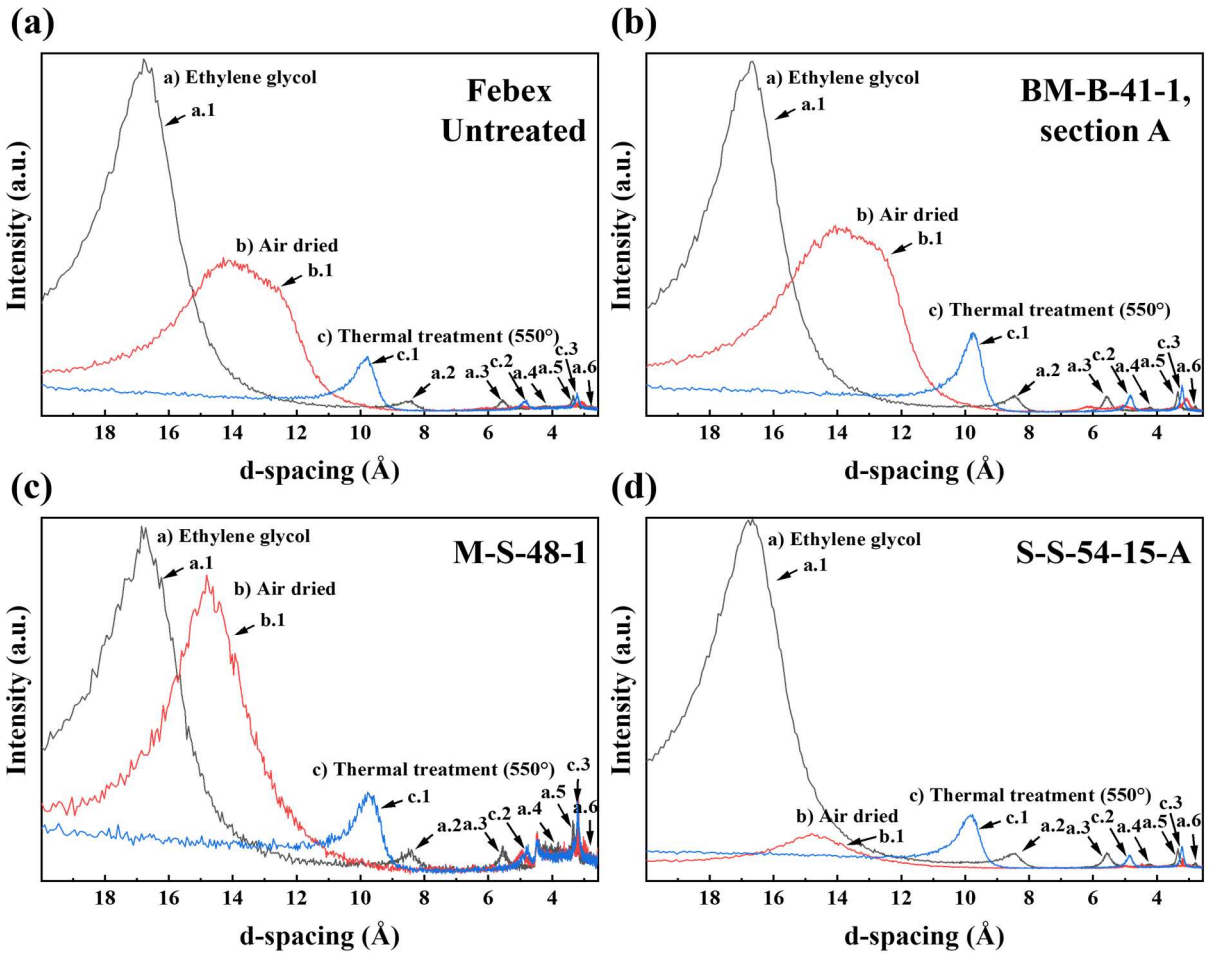

Figure 4.19: *(a) OM patterns of Febex Untreated. (b) OM patterns of sample BM-B-41-1, section A. (c) OM patterns of sample M-S-48-1. (d) OM patterns of sample S-S-54-15-A.*

In air-dried patterns, we observe a predominant peak around ~12-13Å (b.1) (Table 4.13), that after glycolation is displaced to values around ~16Å (a.1) (Table 4.14).

Table 4.13: *d-spacing values of air-dried patterns.*

Positions in Figures 4.19 and 4.20	Febex untreated	BM-B-41-1, section A	M-S-48-1	S-S-54-15-A	S-S-54-15-B	S-S-54-15-C	S-S-54-15-D	S-S-54-15-E
	d-spacing (Å)							
b.1 d(001)	12.63	12.69	12.84	12.84	12.80	12.70	12.70	13.63

From Figures 4.19 and 4.20 (air-dried patterns, b.1) and Table 4.13, it can be stated that the Febex experimental samples were in a 1-2 hydration state, confirming the presence of smectite minerals.

Table 4.14: *d-spacing values of glycolated patterns.*

Positions in Figures 4.19 and 4.20	Febex untreated	BM-B-41-1, section A	M-S-48-1	S-S-54-15-A	S-S-54-15-B	S-S-54-15-C	S-S-54-15-D	S-S-54-15-E
	d-spacing (Å)							
a.1 d(001)	16.74	16.65	16.80	16.71	16.73	16.73	16.72	16.77
a.2 d(002)	8.53	8.53	8.52	8.54	8.53	8.54	8.54	8.54
a.3 d(003)	5.55	5.56	5.55	5.55	5.55	5.55	5.55	5.55
a.4 d(004)	4.23	4.22	4.48	4.20	4.21	4.20	4.20	4.21
a.5 d(005)	3.34	3.35	3.33	3.35	3.34	3.34	3.34	3.34
a.6 d(006)	2.80	2.80	2.94	2.80	2.80	2.80	2.80	2.80

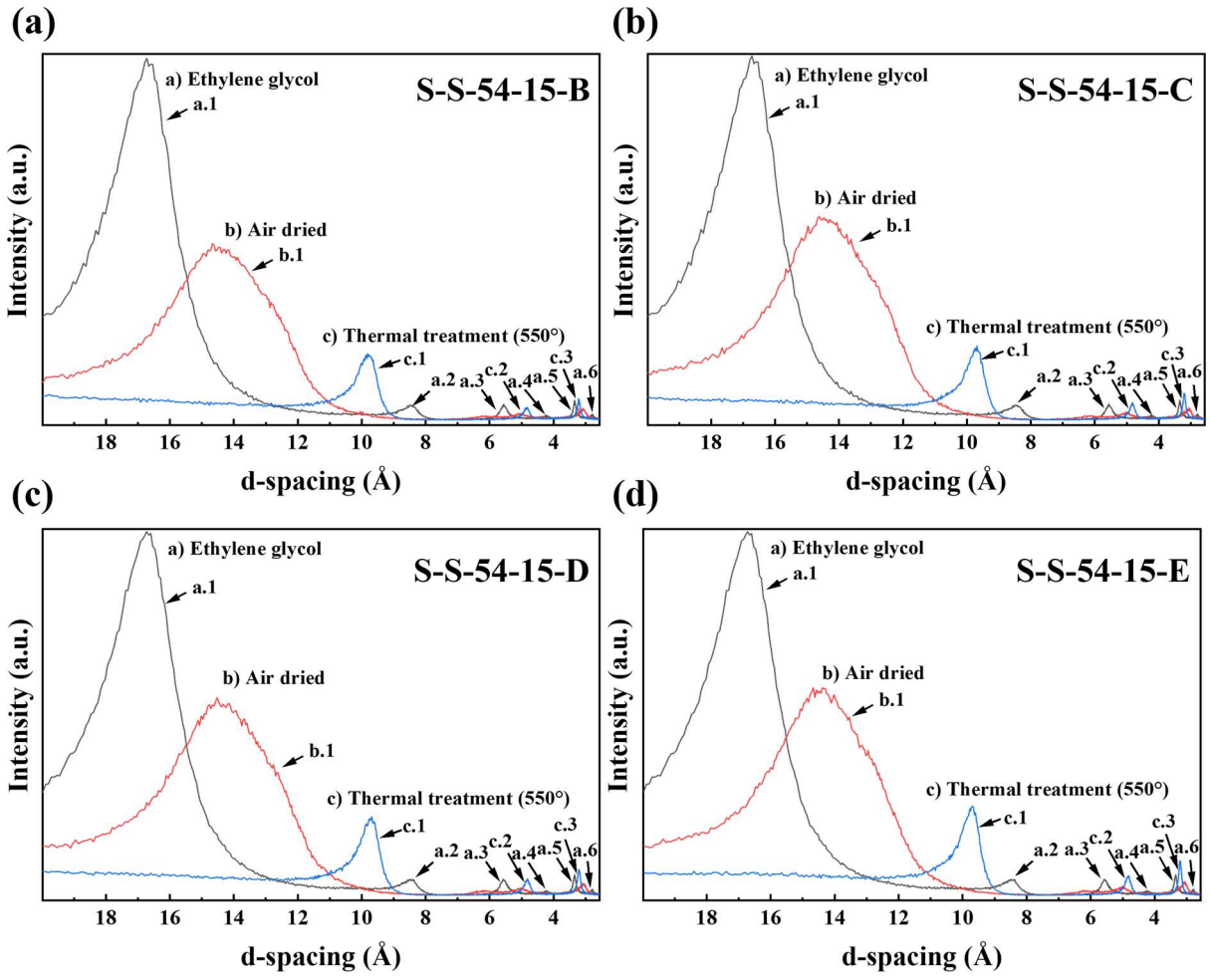

Figure 4.20: *(a) OM patterns of sample S-S-54-15-B. (b) OM patterns of sample S-S-54-15-C. (c) OM pattern of sample S-S-54-15-D. (d) OM patterns of sample S-S-54-15-E.*

Febex bentonite is composed of illite/smectite (I/S) mixed layers, and stratifications are common, either formed due to the experimental exposure conditions or simply because they are one of the most frequent clay components. Therefore, the identification of smectites and mixed-layers containing a smectitic component by XRD is based on the expansion of these clays by ethylene glycol [244].

The use of ethylene glycol complexes intensifies second order reflections and develops stable two-layer complexes by all varieties of dioctahedral smectites [244]. Mixed-layers clay mineral identification was performed following the recommendations of Moore and Reynolds [196], who provided the guidelines for I/S and chlorite/smectite (C/S) identification, which may also allow identification of possible mineral alterations. For this, the characteristic reflection at ~16Å (a.1) in the glycolated patterns was firstly examined (Figures 4.19 and 4.20, and Table 4.14). This particular reflection is presented, broadly-shaped, in each glycolated pattern, indicating that the observed interstratification is likely to be random and rich in smectite, as stated by Moore and Reynolds [196]. The subsequent observed peak at ~8.50Å (a.2) is also characteristic of interstratified illite (001)/glycolated smectite (002) reflections. The observed peak at ~5.55Å (a.3) bolsters the evidence of I/S presence, along with the presence of the sharp peak at ~3.30Å (a.5) due to the (003) illite and (005) smectite reflections. From the described observations in the glycolated patterns, it is logical to conclude that there are small amounts of illite, which were subsequently semi-quantified considering the d-spacings of a.2 and a.3 peaks and following the instructions provided by Moore and Reynolds [196].

Table 4.15: *Positions of reflections for percentage illite/glycolated smectite estimations. Adapted from* [196].

%Illite	001/002(Å)	002/003(Å)
10	8.58	5.61
20	8.67	5.58
30	8.77	5.53
40	8.89	5.50
50	9.05	5.44
60	9.22	5.34
70	9.40	5.28
80	9.64	5.20
0	9.52	5.10

Thus, using Table 4.15 it can be stated that the presence of I/S is about 10-15%. The final sample treatment consisted of heating at 550°C. Samples heated at this temperature showed a collapse between layers due to dewatering, resulting in new basal spacings. These new basal spacings, together with the basal spacings obtained through the air-dried and glycolation treatments, allowed the establishment of a conclusive determination of the clay minerals present in the samples. As observed in Figures 4.19 and 4.20, and Table 4.16, the decay of 001 reflection to values around 9Å is attributed to moisture loss or 0 hydration state, as shown in Table 4.12, and is characteristic of smectite being present [196].

Table 4.16: *d-spacing values of heating patterns.*

Position in Figures 4.19 and 4.20	Febex untreated	BM-B-41-1, section A	M-S-48-1	S-S-54-15-A	S-S-54-15-B	S-S-54-15-C	S-S-54-15-D	S-S-54-15-E
	d-spacing (Å)							
c.1 d(001)	9.81	9.86	9.77	9.94	9.99	9.99	9.71	9.84
c.2 d(002)	4.87	4.90	4.81	4.89	4.84	4.84	4.82	4.86
c.3 d(003)	3.22	3.22	3.21	3.22	3.22	3.22	3.22	3.22

Overall, from XRD of the Febex samples, we can conclude that, from a clay mineralogy perspective, no observable dissimilarities between the untreated material and the samples were found. Based on XRD and the positions of the 001/002 and 002/003 reflections [196], the smectitic phases of the Febex reference and in-situ test samples were shown to be made up of I/S mixed layers with 10-15% of illite layers [150]. Additionally, random powders from the reference and experimental samples revealed the presence of variable quantities of quartz, plagioclases, cristobalite, calcite and tridymite, common mineral structural components of Febex bentonite.

4.2.7 High resolution diffraction on Febex bentonite altered samples using synchrotron x-rays

Although XRD is one of the most commonly used techniques for routine characterisation of clays, their structural complexity, due to the presence of impurities, and the time required to collect an XRD pattern in a conventional diffractometer, make it difficult to obtain a diffractogram which enables an adequate semi-quantification of the constituent phases.

Moore and Reynolds [196] pointed out several disadvantages of laboratory-based XRD instruments to determine the bulk mineralogy of clay materials. The presence of non-clay minerals, such as quartz, K-feldspars, plagioclase, pyrite, gypsum and iron oxides, in large amounts within the clayey matrix can mask the clay peaks, jeopardising a suitable identification of the phases present. Besides, the use of a CuKα source in a conventional instrument could produce a high signal-to-noise ratio due to the fluorescence of the iron phases, significantly masking smaller peaks. To overcome these disadvantages, the use of synchrotron x-rays is proven to reduce the time required for collection of a diffraction pattern. In addition, the extremely high brilliance of the x-rays produced in a synchrotron allows the acquisition of highly-resolved diffraction patterns due to the notably improved signal-to-noise ratio compared to that the obtained by laboratory-based instruments. Therefore, to implement a better investigation of any possible alteration and/or transformation induced in the clayey matrix of the Febex bentonite, as well as the identification of iron phases, synchrotron analysis was selected as a supplemental technique to the laboratory diffraction previously performed.

High-resolution synchrotron diffraction data were collected using beamline I11 at the Diamond Light Source (UK). Each diffraction pattern was measured using Si-calibrated x-rays with a wavelength of 0.8245230Å and with the samples sealed in 0.5mm inner diameter borosilicate glass capillaries. Sample holder rotation was used together with a 1x1mm beam.

Samples were prepared as described in section 3.2.3.3.2.4 (Chapter 3). To assess the evidence of iron phases and identify any alteration and/or transformation in the Febex bentonite, preliminary high-resolution random powder diffraction was carried out on the reference sample. This initial analysis provided baseline data which was later utilised for comparative analysis of the bulk mineralogy of the reference sample with regard to the bulk mineralogy determined for each Febex experimental sample.

High-resolution synchrotron diffraction results are shown in Figures 4.21 to 4.23 and tabulated in Table 4.17. Estimates of mineral percentages (based on 100%) were determined using the MATCH! phase identification programme for powder diffraction, which utilises ICDD tabulated reference intensity ratios for each peak position (2θ) and relative intensity (I/I_0). MATCH! reports that the results have a standard deviation of ±10% of the calculated value [245].

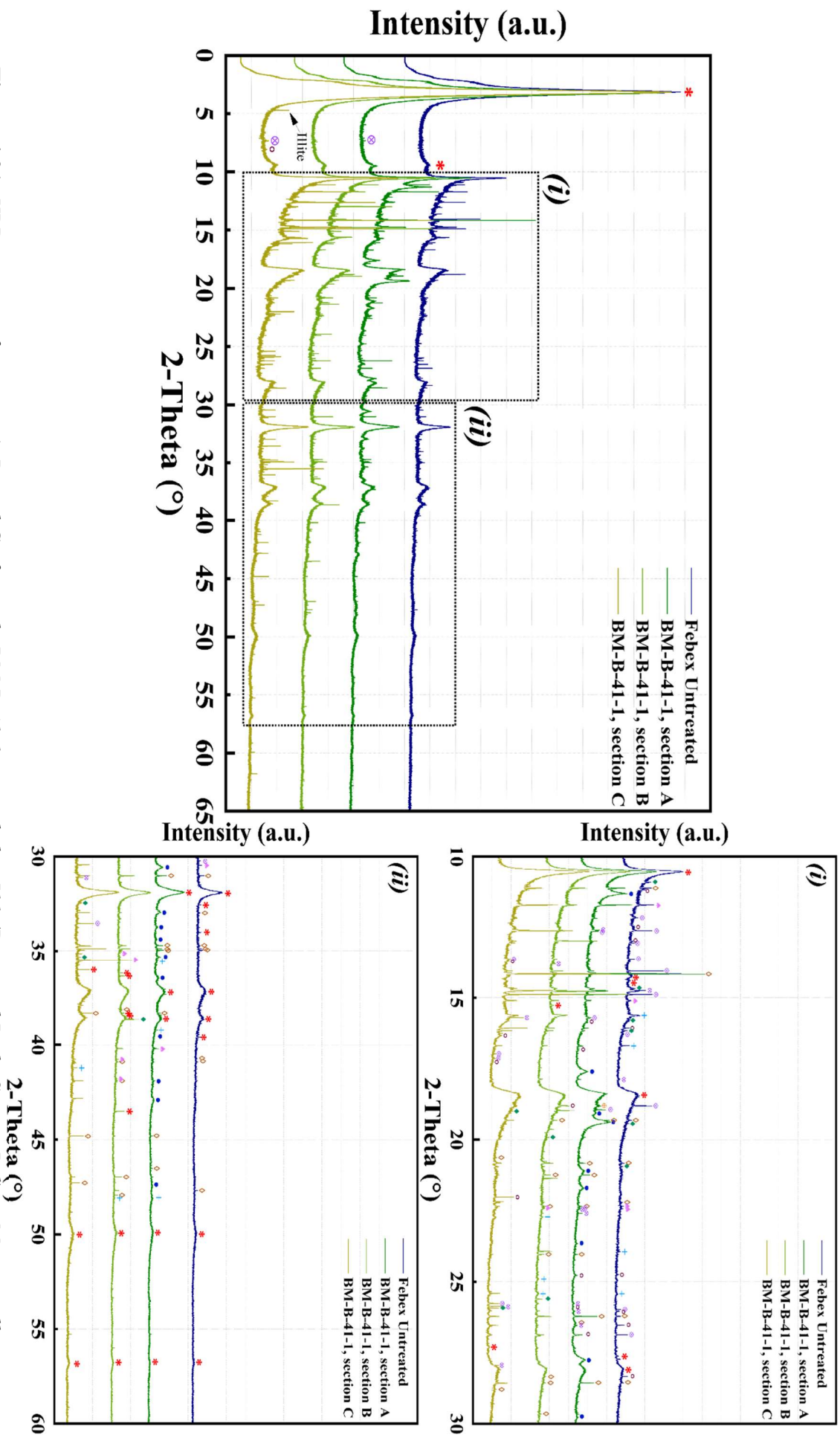

Figure 4.21: *XRD pattern of sections A, B, and C of sample BM-B-41-1, recorded at I11 (Diamond Light Source Ltd).* ✱*: Montmorillonite;* ⊗*: Plagioclase;* o*: K-Feldspar;* ●*: Goethite;* ⊕*: Magnetite;* ◆*: Tridymite;* +*: Carbonate;* ♣*: Cristobalite;* ◊*: Quartz. (i) Region between 10° and 30° in 2θ. (ii) Region between 30° and 55° in 2θ.*

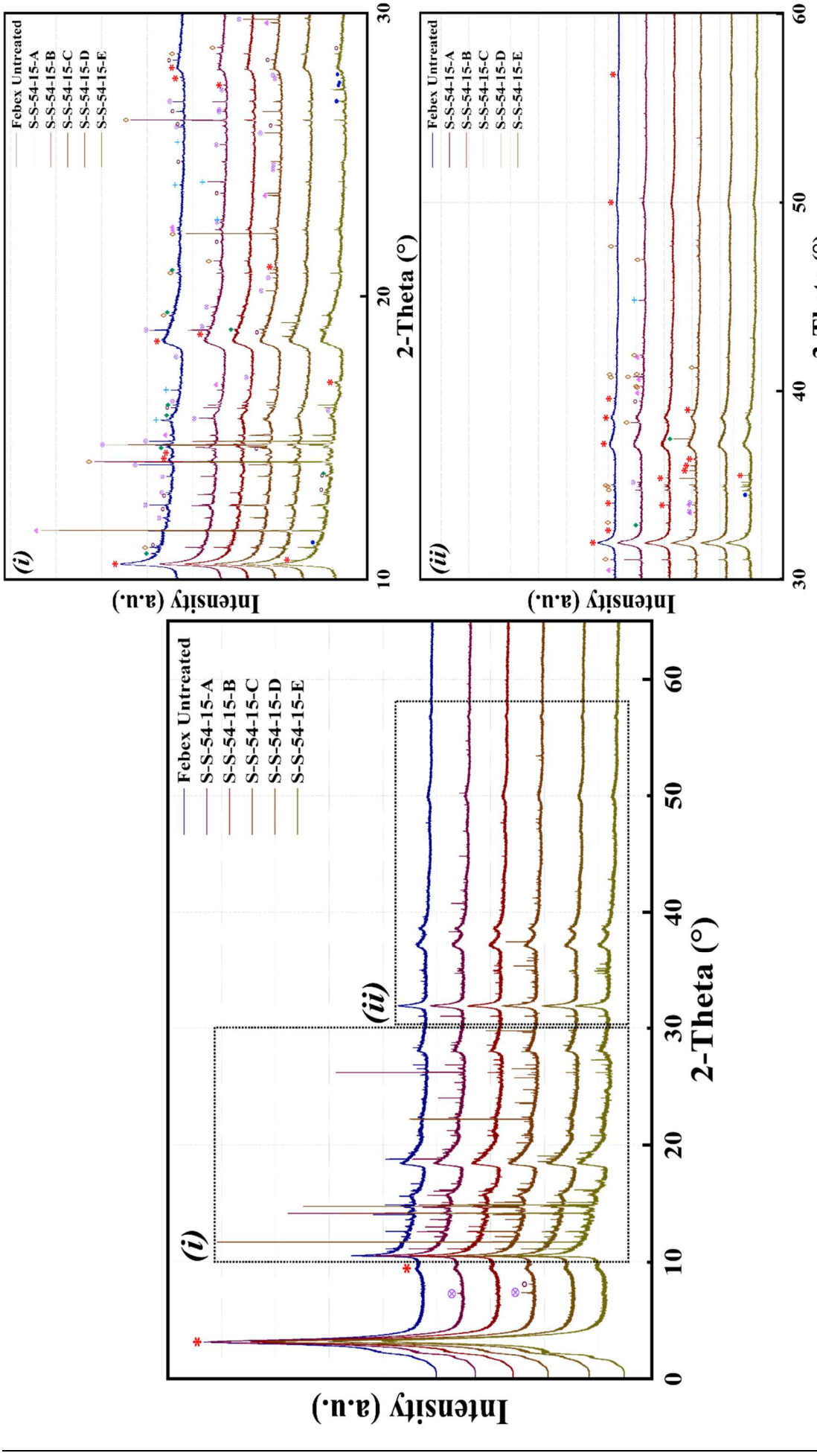

Figure 4.22: *XRD pattern of S-S-54-15-A/B/C/D and E, recorded at I11 (Diamond Light Source Ltd).* ✱*: Montmorillonite;* ⊗*: Plagioclase;* ○*: K-Feldspar;* ●*: Goethite;* ⊕*: Magnetite;* ◆*: Tridymite;* +*: Carbonate;* ◆*: Cristobalite;* ◇*: Quartz. (i) Region between 10° and 30° in 2θ. (ii) Region between 30° and 55° in 2θ.*

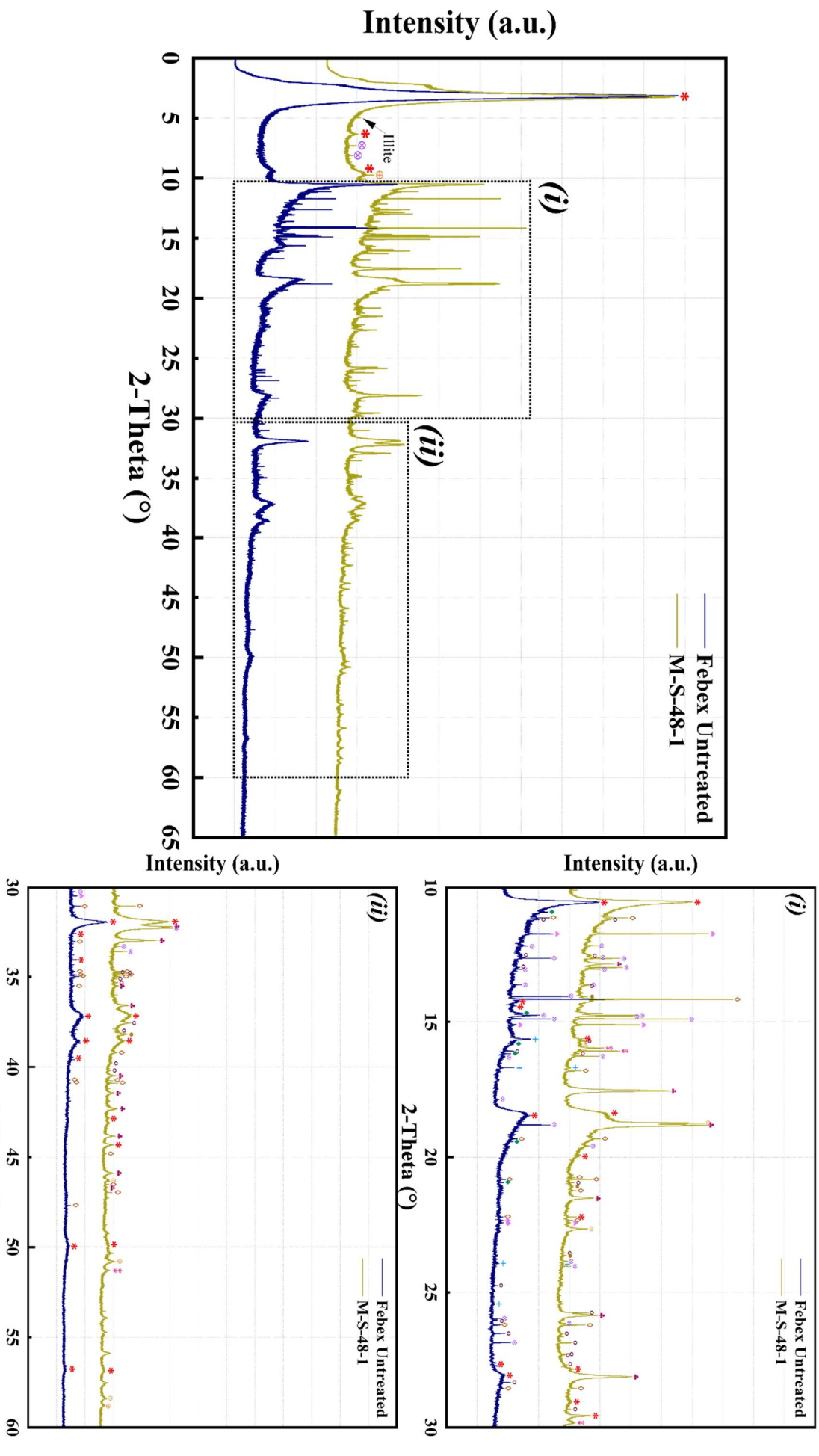

Figure 4.23: *XRD pattern of sample M-S-48-1, recorded at I11 (Diamond Light Source Ltd).* ✱*: Montmorillonite;* ⊗*: Plagioclase;* ○*: K-Feldspar;* ●*: Goethite;* ⊕*: Magnetite;* ◆*: Tridymite;* +*: Carbonate;* ♠*: Cristobalite;* ◇*: Quartz;* ●*: Siderite;* ♣*: Hematite;* ≠*: Maghemite. (i) Region between 10° and 30° in 2θ. (ii) Region between 30° and 55° in 2θ.*

Table 4.17: *Mineralogical composition of Febex bentonite samples compared with the Febex reference sample.*

Sample ID	Montmorillonite	Quartz	Tridymite	Plagioclase (albite/anorthite)	Carbonate (calcite/dolomite)	Cristobalite	K-Feldspar	Goethite	Hematite	Magnetite	Maghemite	Siderite
	(%)											
Febex Untreated	90.6	2.4	0.8	2.5	1.2	1.0	1.5	-	-	-	-	-
BM-B-41-1, section A	84.0	2.4	1.1	1.3	1.0	0.6	1.1	7.3	-	1.2	-	-
BM-B-41-1, section B	90.2	2.8	1.2	1.4	1.4	1.6	1.4	-	-	-	-	-
BM-B-41-1, section C	90.4	2.5	0.9	1.8	1.3	2.2	1.0	-	-	-	-	-
S-S-54-15-A	86.7	5.4	0.9	1.4	2.1	2.4	1.0	-	-	-	-	-
S-S-54-15-B	85.9	6.2	0.8	1.6	1.7	1.9	1.9	-	-	-	-	-
S-S-54-15-C	87.8	4.4	1.0	1.9	2.3	1.5	1.1	-	-	-	-	-
S-S-54-15-D	86.4	5.2	2.2	1.9	2.2	0.9	1.3	-	-	-	-	-
S-S-54-15-E	85.2	4.1	1.2	2.3	0.4	0.5	2.8	3.4	-	-	-	-
M-S-48-1	80.1	2.1	1.0	1.2	1.1	1.9	1.4	-	4.3	1.6	3.3	1.9

Figure 4.21 and Table 4.17 show the results obtained in the different sections of sample BM-B-41-1. The mineral phases observed in sections C and B were similar to those observed in the pristine sample. However, section A shows the presence of goethite and magnetite, coexisting in the bulk mineralogy together with variable quantities of the characteristic accessory minerals of Febex bentonite, that present values close to those observed in the bulk mineralogy of the untreated sample. The presence of goethite and magnetite could be explained due to their diffusion through the bentonite matrix and as a consequence of the liner corrosion. Although, iron phases are apparent, no evidence of neoformed minerals were detected, therefore, it can be stated that the main constituent clay mineral is montmorillonite, with no major indication of alteration.

Figure 4.22 and Table 4.17 display the results of high-resolution diffraction carried out on the extensometer samples. Overall, the phases observed in the bulk mineralogy of the samples are characteristic of the unaltered material. However, samples S-S-54-15-A, C and D showed a moderate growth of calcite, a primary mineral of Febex bentonite. Savage et al. [246], [247] modelled the mineralogical evolution of bentonite minerals in cement-bentonite systems, and concluded that the mineralogical composition of bentonite does not seem to be stable under hyperalkaline pore fluid conditions, leading to some of the bentonite's key accessory minerals, such as calcite, to dissolve and, later, re-precipitate. Savage et al. [246], [247] affirmed that most alteration was associated with the high pH of the fluid and the low temperature of the system, which determined the dissolution and precipitation kinetics. Although the extensometer samples were not retrieved from a cement-bentonite environment, their relative increase in calcite content might be explained due to the alkaline character of the GTS groundwaters and the low temperatures at which the samples were exposed (Table 3.5), which, in turn, might increase the alkalinity of the fluid occupying the pores and inter-aggregate spaces, favouring the dissolution and re-precipitation of calcite. In addition, sample S-S-54-15-E showed the presence of goethite that might be explained due to the corrosion experienced on the surface of the extensometer. Furthermore, sample S-S-54-15-E displayed a lower calcite concentration in comparison with the reference sample. The lesser calcite concentration might be attributed to its expected dissolution and subsequent precipitation in inter-aggregates [27], [89].

High-resolution diffraction was also conducted on the collected loose pieces from corrosion coupons. Results are presented in Figure 4.23 and Table 4.17. From Figure 4.23 and Table 4.17,

the presence of a variety of iron phases cohabiting in the clayey matrix was observed. The presence of iron phases confirms predictions reported in the literature, regarding container corrosion (section 2.3). As a result of the direct contact between the bentonite and the corrosion coupons, the local environment formed at the interface has led to the formation of iron oxides, such as hematite, magnetite and maghemite, and carbonates such as siderite, inhibiting the formation of a stable corrosion layer. However, the presence of Fe-rich clay mineral phases was not detectable and, therefore, it is logical to conclude that montmorillonite remained the predominant clay phase in sample M-S-48-1.

Overall, from high-resolution random powder diffraction analyses, we can conclude that no alteration and/or transformations were observed in the bulk mineralogy of each sample. Dissolution and re-precipitation of some of the primary minerals can be predicted due to changes in calcite content. In addition, the presence of iron oxides, oxyhydroxides and carbonates indicates the formation of a heterogenous corrosion layer on the surface of steel components which has released corrosion by-products, such as hematite, magnetite, maghemite, goethite and siderite, which, in turn, have diffused through the bentonite compacted body. However, the formation of Fe-rich clay minerals could not be detected. Therefore, to determine any subtle alteration and/or transformation, other analytical techniques were considered.

4.2.8 Fourier transform infrared spectroscopy analysis in the interface zone between the Febex in-situ test samples and metallic components

The chemical composition, isomorphic substitutions, layer stacking order and structural modifications of clay minerals are perceptible in an IR spectrum [248]. Therefore, IR constitutes a supplementary technique to XRD for evaluation of the physicochemical properties of the Febex in-situ test samples, since it allows us to examine not only their mineral composition and crystal chemistry but also possible interactions with organic and inorganic molecules. The IR technique is based on the vibrations of atoms in the mineral structure. Thus, the vibrations of silicate layers in phyllosilicates minerals can be ‘somewhat’ separated into their constituent units, i.e. the OH groups, silicate anion, octahedral vibration and interlayer cations [248]. The vibrations of the OH groups are the most frequently studied, since these are an indicator of their environment [248].

The OH stretching (υOH) and bending (δOH) vibrations occur in the 3700-3500 cm^{-1} and 950-650cm^{-1} regions of the MIR spectra, respectively [248]. These vibrations are, in practice, independent of the vibrations of the rest of the structure. However, they are strongly influenced by the nature of the ions coordinated with the OH group [248]. Therefore, OH vibrations are strongly affected by the octahedral cations to which the OH group is coordinated and, to a lesser state, by the tetrahedral and interlayer environments. Regarding the Si-O stretching modes, Farmer & Russell [249] reported that the Si-O stretching modes show at 1050-980cm^{-1} in the MIR spectra. Nonetheless, the most intense bands occur in the 550-400cm^{-1} region.

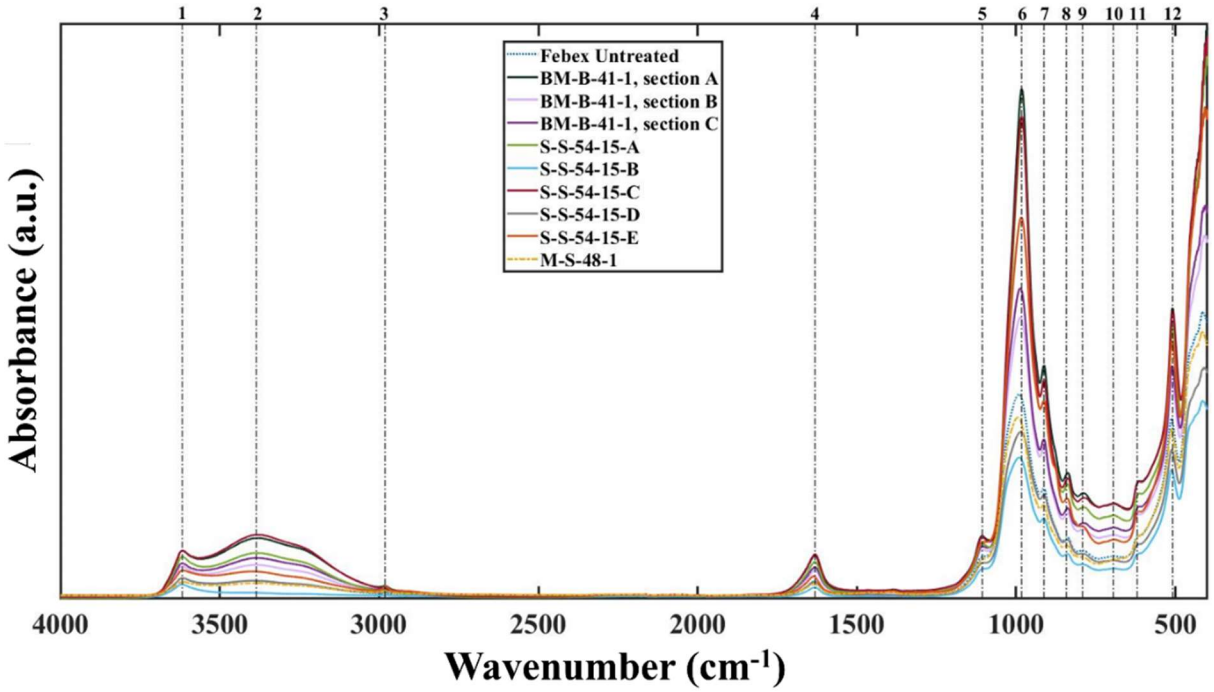

Figure 4.24: *ATR-FTIR spectra (4000-400cm^{-1}) of Febex samples and untreated sample. Peaks are indicated by dotted lines.*

As a first approximation, ATR spectroscopy was carried out on the Febex in-situ test samples to provide an initial absorption spectrum of a reference sample, as well as of the experimental samples (Figure 4.24 and Table 4.18). ATR spectroscopy is based on the phenomenon of total internal reflection (in this case) by a diamond prism [250]. When the IR radiation enters the diamond, the crystal undergoes a total internal reflection at the crystal-sample interface [250]. The fraction of light reaching the sample is known as the evanescent wave and is attenuated in the regions of the IR spectrum where the sample, in contact with the surface of the ATR crystal, absorbs energy [250]. ATR-FTIR spectra were recorded in the MIR region, and well-resolved and sharp bands were obtained for the ATR spectrum of each sample.

Table 4.18: *ATR-FTIR positions (cm^{-1}) and assignments of reference and assessed Febex samples in MID region of the IR spectra.*

Band positions in Figure 4.24	Febex Untreated	BM-B-41-1, section A	BM-B-41-1, section B	BM-B-41-1, section C	S-S-54-15-A	S-S-54-15-B	S-S-54-15-C	S-S-54-15-D	S-S-54-15-E	M-S-48-1	Assignments
	ATR-FTIR positions (cm^{-1})										
1	3617	3617	3617	3617	3617	3618	3616	3616	3616	3616	**OH stretching of structural hydroxyls groups**
2	3391	3389	3390	3391	3391	-	3370	3390	3399	3391	**OH stretching of water**
3	2979	2981	2981	2981	2981	2979	2979	2979	2978	2979	**C-H stretching**
4	1634	1632	1633	1633	1633	1632	1632	1633	1635	1634	**OH deformation of water**
5	1104	1107	1106	1106	1106	1107	1107	1102	1103	1110	**Si-O stretching (longitudinal mode)**
6	991	983	987	987	982	991	983	985	984	995	**Si-O stretching**
7	913	912	913	913	913	913	913	913	913	913	**δAlAlOH deformation**
8	839	838	838	838	838	839	838	839	840	840	**δAlMgOH deformation**
9	791	788	788	787	787	792	784	794	790	788	**Si-O stretching of quartz and silica**
10	694	694	694	693	694	694	694	693	693	690	**Si-O deformation and bending mode**
11	618	612	612	612	612	618	613	611	618	615	**Coupled Al-OH and Si-O, out of plane**
12	512	509	511	511	509	512	509	512	511	512	**Si-O-Al deformation**

Figure 4.24 presents the ATR recorded results of the reference and experimental samples, and their respective assignments are listed in Table 4.18. Overall, the IR spectra recorded for the reference sample and experimental samples indicate that montmorillonite is the dominant phase in accordance with the results obtained in XRD. The intense bands observed at ~3617cm^{-1} correspond to the OH stretching vibration of structural hydroxyl groups commonly observed in dioctahedral smectites [208], [251].

The broad bands observed at ~3390cm^{-1} are assigned to H_2O-stretching, with an overtone of the bending vibration of water observed around 1634cm^{-1} [208], [251]. The sharp peaks at ~990cm^{-1} correlate with the Si-O stretching vibrations typical of dioctahedral smectites, while the bands observed at ~512cm^{-1} are due to the Al-O-Si [208], [251]. In the ATR spectra, the occupancy of the octahedral layers strongly influences the position of the OH bending bands [208], [251].

The bands at ~913cm^{-1} and 838cm^{-1} correspond to δAlAlOH and δAlMgOH, i.e. the octahedral cation deformation bands, and they may suggest a partial substitution of Al by Mg [208], [251]. The subsequent bands around ~790cm^{-1} appertain to Si-O stretching of quartz and silica, and confirm the presence of quartz in the Febex samples [208], [251]. The noted bands at ~693cm^{-1} correlate with the deformation and bending modes of the Si-O bond [208], [251]. Finally, the observed peaks at ~618cm^{-1} correspond with the out of plane vibration of the coupled Al-O and Si-O [208], [251].

The absorption bands due to the structural OH and Si-O groups play an important role in clay mineral differentiation and, therefore, can provide some insights into any potential alteration and/or transformation of the experimental samples. Thus, a second FTIR analysis was conducted, but this time following the KBr technique to provide a routine characterisation of the experimental and reference samples in the MIR region of the IR spectra (Table 4.19 and Figure 4.25). On the whole, the bands observed in the KBr spectra correlate very well with those observed in the ATR spectrum.

The ATR technique depends on the angle at which the IR reaches the boundary between the sample and the crystal, therefore being a suitable technique for surface analysis. The KBr technique is frequently used for transmission analysis of powders, since the KBr is inert and transparent above 400cm^{-1}, and acts as an infrared transparent diluent [252].

Table 4.19: *KBr-FTIR positions (cm^{-1}) and assignments of reference and assessed Febex samples in MID.*

Band positions in Figure 4.25	Febex Untreated	BM-B-41-1, section A	BM-B-41-1, section B	BM-B-41-1, section C	S-S-54-15-A	S-S-54-15-B	S-S-54-15-C	S-S-54-15-D	S-S-54-15-E	M-S-48-1	Assignments
	KBr-FTIR positions (cm^{-1})										
1	3624	3625	3625	3625	3625	3624	3625	3265	3265	3620	**OH stretching of structural hydroxyl groups**
2	3421	3425	3415	3418	3418	3429	3418	3412	3430	3415	**OH stretching of water**
3	2982	2982	-	-	-	-	-	-	2981	2981	**C-H stretching**
4	1826	-	1831	1830	1828	1831	1827	1832	-	1827	**Quartz overtone**
5	1638	1639	1634	1640	1639	1635	1638	1634	1639	1636	**OH deformation of water**
6	1384	1384	1386	1383	1384	1384	1384	1385	1384	1384	**C-H bending vibrations**
7	1110	1108	1107	1110	1108	1103	1110	1109	1113	1110	**Si-O stretching (longitudinal mode)**
8	1036	1032	1047	1032	1035	1031	1036	1034	1032	1031	**Si-O stretching**
9	915	914	915	915	914	914	915	914	915	915	**δAlAlOH deformation**
10	842	842	843	842	841	842	842	844	842	847	**δAlMgOH deformation**
11	796	796	796	795	796	795	796	793	794	791	**Si-O stretching of quartz and silica**
12	697	696	696	695	696	695	697	693	697	694	**Si-O-Al bending**
13	627	625	624	624	626	623	628	627	624	625	**Coupled Al-OH and Si-O, out of plane**
14	520	520	523	522	521	520	520	521	520	520	**Al-O-Si deformation**
15	467	466	471	467	466	466	467	466	467	466	**Si-O-Si deformation**

Although, the KBr technique is used in transmission analysis, its results are presented as a function of the absorbance in Figure 4.25 and Table 4.19, to facilitate peak identification and correlate the results with the ATR measurements. Overall, the Febex samples in their KBr spectra displayed the characteristic bands related with the absorbed water at ~3400cm^{-1} and ~1630cm^{-1} (OH stretching) and vibration of the silicate group (Si-stretching and O-Si-O bending around 1110cm^{-1} and 466cm^{-1} respectively) [253], [254], [255], [256].

In addition, the KBr-FTIR spectra show characteristic bands around ~3620cm^{-1} which correspond with the OH stretching of structural hydroxyl groups of dioctahedral smectite with Al-rich octahedral sheets [253], [254], [255], [256]. The complex and sharp bands observed around 1030cm^{-1} are due to the Si-O typical of dioctahedral montmorillonites and are an indicator of the absence of tetrahedral Fe^{3+} substitutions [253], [254], [255], [256].

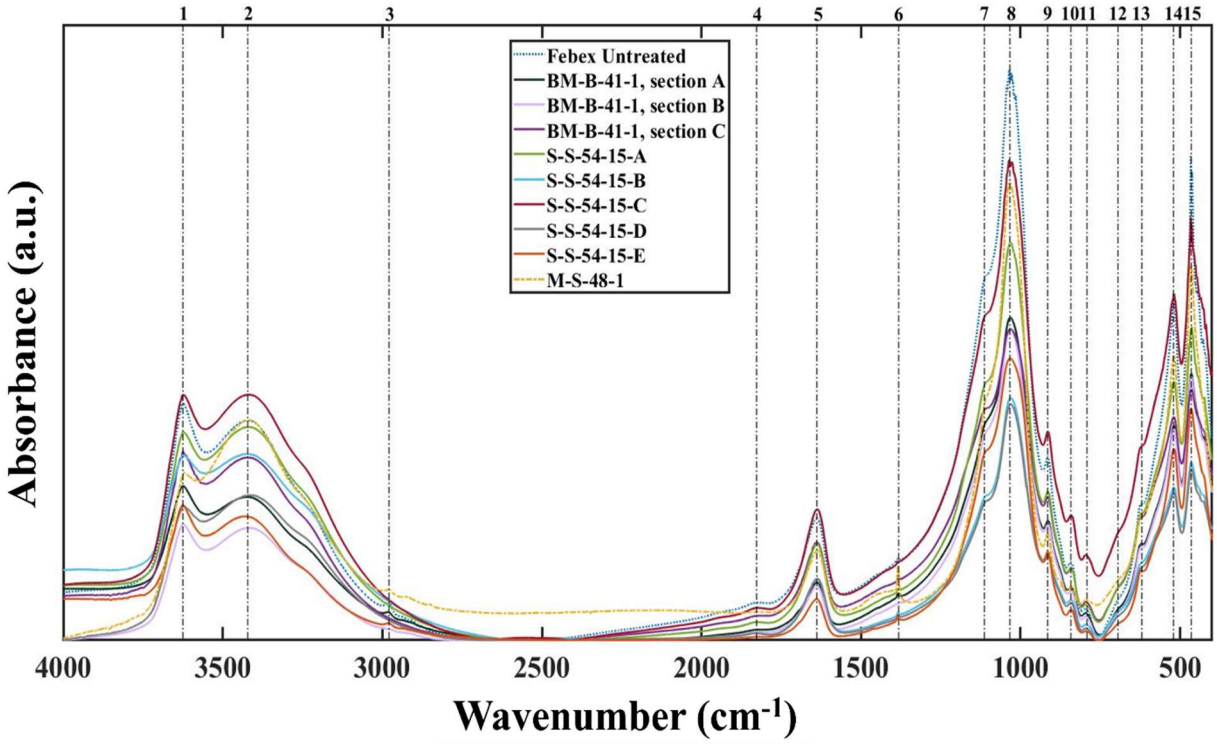

Figure 4.25: *KBr-FTIR spectra (4000-400cm^{-1}) of Febex samples and untreated sample. Peaks are indicated by dotted lines.*

The occupancy of the octahedral environment in smectites will determine the positions of the OH bending bands. The positioned bands around ~915cm^{-1} (δAlAlOH) and ~840cm^{-1} (δAlMgOH) could be indicators of partial substitution of Al by Mg, frequently observed in dioctahedral smectites [253], [254], [255], [256]. The bands at ~520cm^{-1} and ~466cm^{-1} correspond to Si-O-Al (octahedral Al) and Si-O-Si bending vibrations, respectively [253],

[254], [255], [256]. The bands around 796cm^{-1} are caused by the Si-O stretching of quartz. Additionally, the bands observed at ~2980cm^{-1} and ~1384cm^{-1}, in both ATR and KBr spectra, could be explained due to the stretching and bending vibrations of CH groups [257]. These bands are usually present in soils rich in organic substances as reported by Janik et al. [258]. Finally, the bands observed in the KBr spectra around ~1830cm^{-1} could be correlated with quartz [257]. Once the MIR region of the Febex and reference samples were evaluated to examine the octahedral cation distribution in the Febex experimental samples.

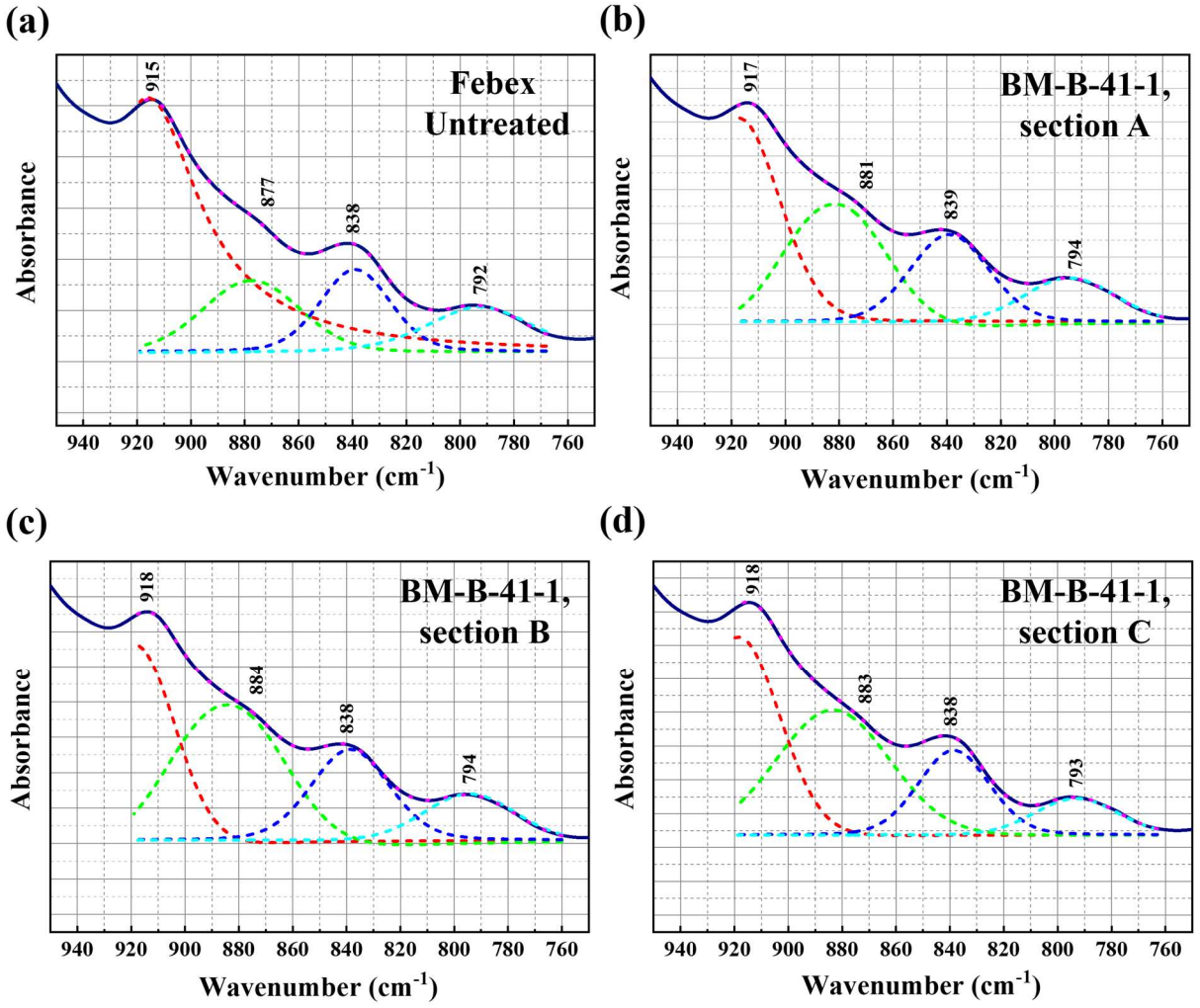

Figure 4.26: *(a), (b), (c) and (d) fitted band positions corresponding with the octahedral cation-OH deformation bands of Febex untreated and sections A, B and C of BM-B-41-1 sample in the KBr-FTIR spectra.*

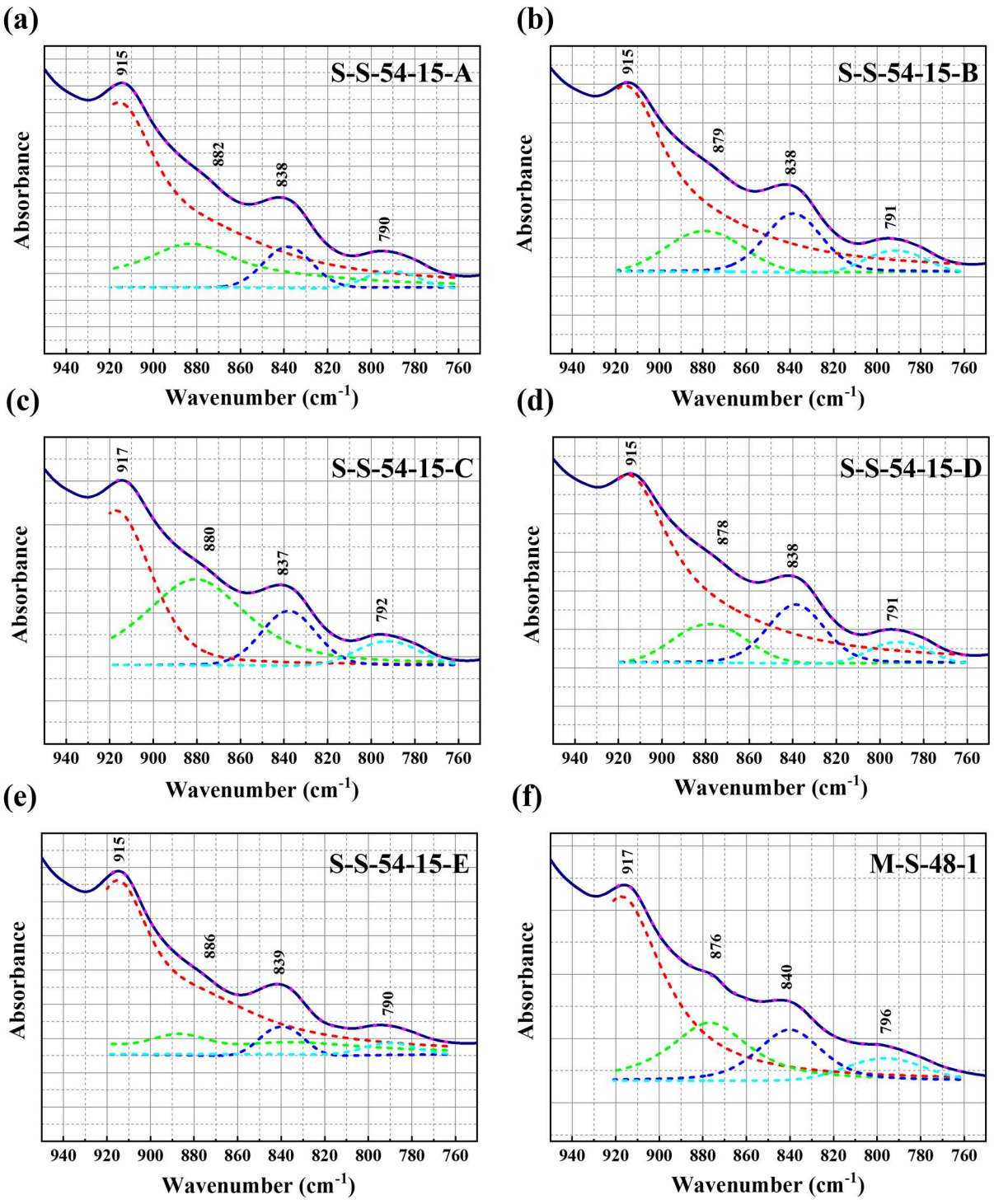

Figure 4.27: *(a), (b), (c), (d) and (e) fitted band positions corresponding with the octahedral cation-OH deformation bands of S-S-54-15-A/B/C/D/E samples. (f) Fitted band positions corresponding with the octahedral cation-OH deformation bands of M-S-48-1 sample.*

Figures 4.26 and 4.27, and Table 4.20 and 4.21, display the fitted results obtained from study of the octahedral cation distribution, particularly in the range of 950-750cm^{-1}, corresponding with the octahedral cation-OH lattice deformation bands. The fitted positions for each spectra do not deviate from those reported in the literature [138], [253], [254], [255], [256].

Table 4.20: *KBr-FTIR positions (cm^{-1}) corresponding to the graphs (a), (b), (c), and (d) in Figure 4.26, and assignments at 950-750cm^{-1} region corresponding to the δAl-Me^{2+}-OH bands.*

Febex Untreated	BM-B-41-1, section A	BM-B-41-1, section B	BM-B-41-1, section C	Assignments
ATR positions (cm^{-1})				
915.95±0.62	917.25±1.13	918.98±2.93	918.53±1.56	**δAlAlOH deformation**
877.50±0.90	881.70±2.67	884.29±6.51	883.44±4.23	**δAlFeOH deformation**
838.97±0.36	839.07±0.27	838.63±0.31	838.59±0.23	**δAlMgOH deformation**
792.69±0.58	794.37±0.27	794.32±0.48	793.07±0.37	**Si-O stretching of quartz and silica**

Table 4.21: *KBr-FTIR positions (cm^{-1}) corresponding to the graphs (a), (b), (c), (d), (e) and (f) in Figure 4.27, and assignments at 950-750cm^{-1} region corresponding to the δAl-Me^{2+}-OH bands.*

S-S-54-15-A	S-S-54-15-B	S-S-54-15-C	S-S-54-15-D	S-S-54-15-E	M-S-48-1	Assignments
ATR positions (cm^{-1})						
915.77 ±0.11	915.81 ±0.44	917.13 ±1.65	915.74 ±0.31	915.12 ±0.12	917.43 ±1.11	***δ*AlAlOH deformation**
882.82 ±1.38	879.16 ±3.91	880.59 ±2.97	878.22 ±2.82	886.95 ±0.83	876.81 ±1.17	***δ*AlFeOH deformation**
383.33 ±0.13	838.48 ±0.26	837.91 ±0.12	838.63 ±0.26	839.73 ±0.12	840.10 ±1.45	***δ*AlMgOH deformation**
790.50 ±0.72	791.49 ±0.44	792.48 ±1.13	791.46 ±0.43	790.04 ±0.21	796.31 ±3.07	**Si-O stretching of quartz and silica**

However, the fitted values are slightly higher than those reported in the literature, and in comparison, with the reference sample. This can be explained due to the selected fitting method for this region of the spectra. Thus, to achieve a much better screen of the octahedral cation distribution (Figure 4.28), the OH-bending region of the IR bentonite spectra was corrected. No appreciable differences between the reference sample and the experimental samples were found, except for sample M-S-48-1 1 (loose pieces of bentonite collected between the coupons

composing the Rack 1A) where the δAlFeOH band seems to be an accentuating feature in this region of the spectra.

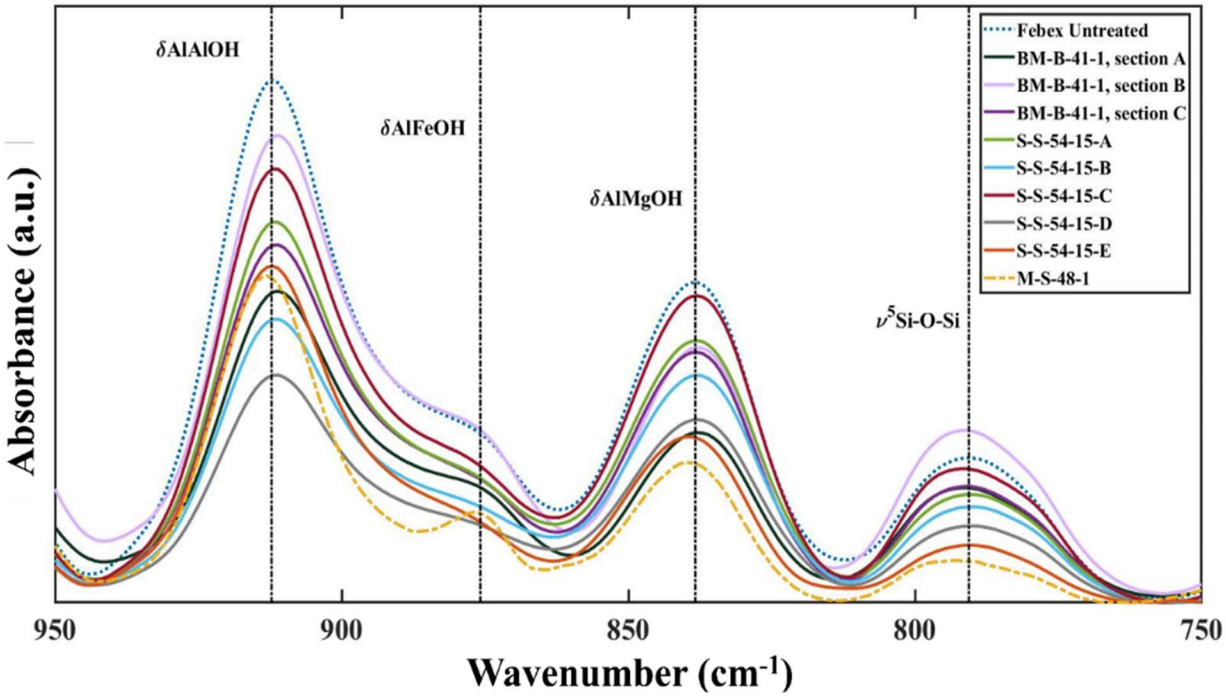

Figure 4.28: *Shows the octahedral cation-OH deformation bands of Febex bentonite samples and untreated sample once data was baselined. Peaks are indicated by dotted lines.*

One of the most important properties of smectites is their swelling ability. The swelling of these minerals occurs in a stepwise manner as the water enters the interlayer space and forms one-, two- and three-layer hydrates [251]. This process is controlled by the relative humidity, nature of the interlayer cation and the charge density of the clay mineral.

The interaction of water with smectites has been widely investigated [259], [260], [261], distinguishing two different water environments within their structure: (*i*) the water molecules coordinated with the exchangeable cations present in the interlayer; and (*ii*) the water molecules filling up the pores. The vibrational mode of strongly hydrogen-bonded water molecules differs to those water molecules weakly bound to the oxygen of the silicate anions and these specific features allow IR analysis. Therefore, when water in montmorillonite is low the water molecules in the interlayer space are strongly coordinated with the exchangeable cations and form an inner hydration sphere in the interlayer space. On the other hand, those structural water molecules not directly associated with interlayer cations tend to create an outer hydration sphere of interlayer cations. The latter water molecules are very similar to the water molecules occupying the pore, which are also hydrogen bonded.

As a consequence of the stretching and bending vibrations of water molecules, the MIR spectra of the water absorbed by the inner and outer surfaces of smectites frequently show strong absorption peaks in the 3600-3200cm^{-1} and 1630cm^{-1} regions [251]. The frequencies of these absorptions are strongly affected by the interlayer cations and the charge density of the oxygen surfaces, thus reflecting the strength of the hydrogen bonding between H_2O molecules [249]. The formation of strong and weak bonds between water molecules is reflected in the positioning of the water bands in the H_2O stretching and bending regions of the MIR region of the IR spectra. Consequently, an increase in the strength of hydrogen bonding is captured in a shift towards lower wavenumbers in the stretching region and higher wavenumbers in the bending region. This effect is also influenced by the increasing ionic potential of the exchangeable cations, reflected in a strengthening of water hydrogen bonds [262].

One emphasis in the study of water bands in the 3800-3100cm^{-1} region was to evaluate and relate the band position with the influence of the exchangeable cations present. On this basis, the specific water bands of the Febex in-situ test samples were individually fitted and analysed, along with an untreated sample to provide reference data. The results derived from the different sections of sample BM-B-41-1 (liner bentonite sample) are displayed in Table 4.22 and Figure 4.29, along with the results obtained from the reference sample.

Table 4.22: *KBr-FTIR positions (cm^{-1}) corresponding to the graphs (a), (b), (c), and (d) in Figure 4.29, and assignments at 3800-3100cm^{-1} region corresponding to the stretching water region.*

Febex Untreated	**BM-B-41-1, section A**	**BM-B-41-1, section B**	**BM-B-41-1, section C**	**Assignments**
ATR positions (cm^{-1})				
3623.99±0.16	3624.47±0.37	3624.95±0.13	3623.12±0.20	**OH stretching of structural hydroxyl groups**
3422.40±0.15	3424.05±0.18	3418.35±0.41	3423.47±0.16	**OH stretching of water**
3235.08±1.05	3235.46±0.62	3236.32±1.40	3236.47±1.51	

The spectra of the untreated sample, Figure 4.29 (a), shows a sharp strong peak at 3624cm^{-1} which corresponds with the OH stretching vibrations of the structural OH groups, this is accompanied by a broad band of water located at 3422 cm^{-1} originated by overlapping of the

asymmetric stretching vibrations of H-bonded water [251]. The small shoulder observed at 3235cm^{-1} is due to the overtone of the bending vibration mode of cation hydration water [251].

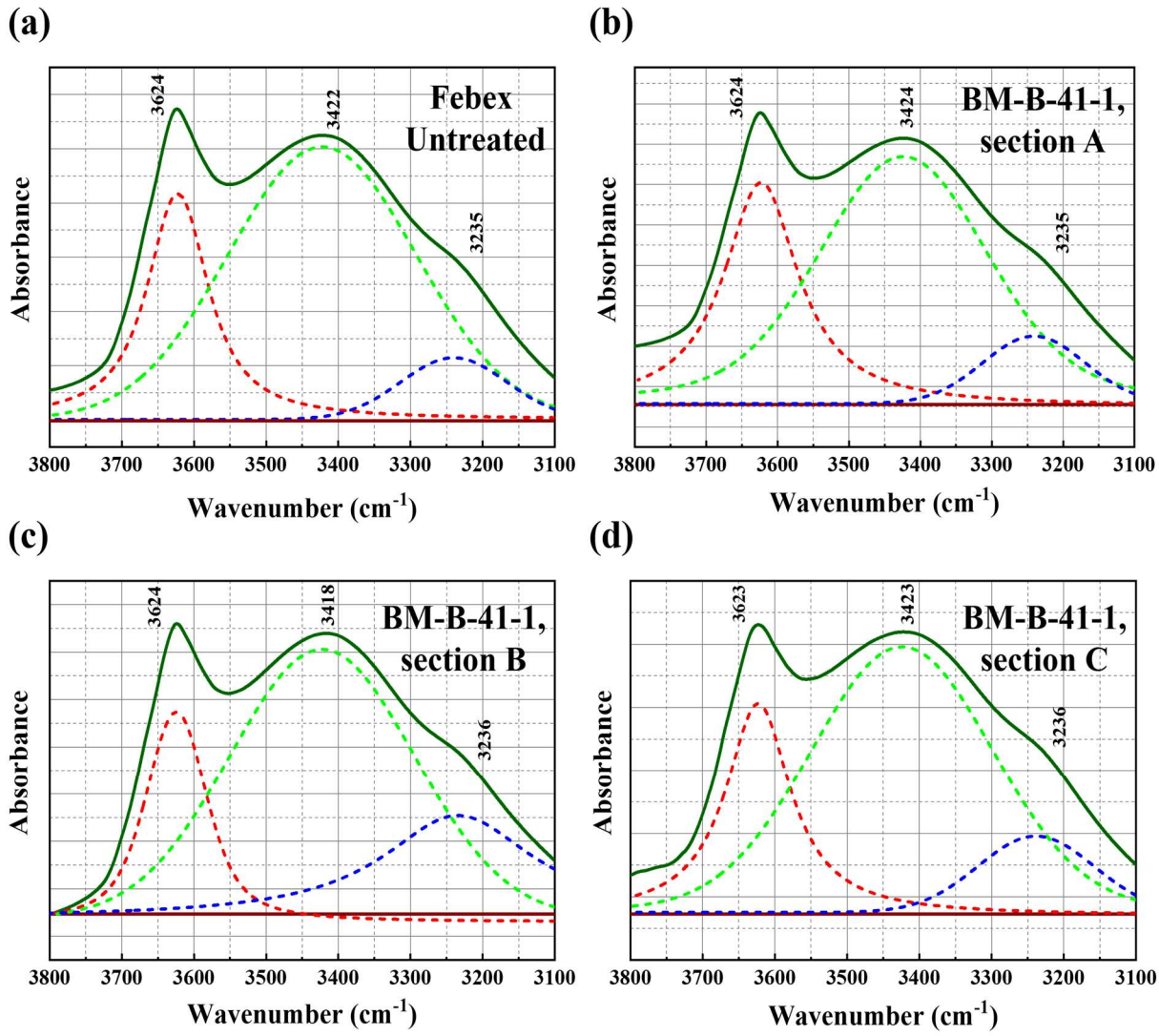

Figure 4.29: *Shows the fitted band positions corresponding with the water stretching bands of Febex Untreated (a), and BM-B-41-1 sample section A (b), B (c), and C (d) respectively.*

As stated by Madejová [251], the interlayer cations modify the intensity and position of the broad band located around 3400cm^{-1}. Madejová [251] also reported that the substitutions observed in MX-80 bentonite decrease in position in the following order K^+, Na^+, Ca^{2+} and Mg^{2+} (Figure 4.30). From Figures 4.29 (b), (c) and (d), no appreciable differences were detected with regard to the reference sample.

Analysis of the water bands of the extensometer samples and sample M-S-48-1 (loose pieces of bentonite collected between the coupons composing the Rack 1A) was also performed, and the results are presented in Table 4.23 and Figure 4.31.

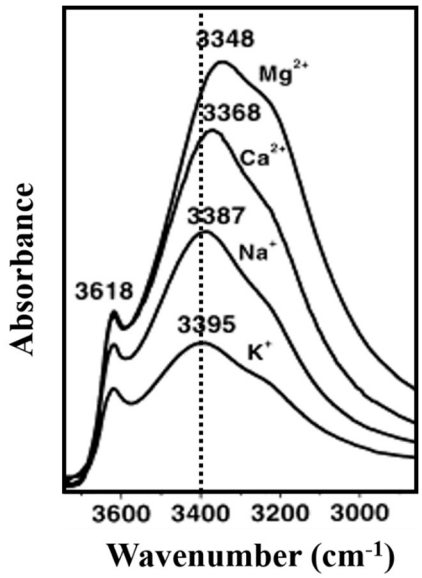

Figure 4.30*: ATR spectra of the OH stretching region of MX-80 montmorillonite saturated with different cations. Adapted from* [251].

From Figures 4.31 (a), (b), and (e), which correspond with samples S-S-54-15-A/B/E (extensometer samples), no observable differences with respect to the reference sample were detected. However, in Figures 4.31 (c), (d) and (f) show a small shift in position towards lower values for the bands corresponding to the vibrations of H-bonded water. Band shifting in sample M-S-48-1 is observable at a lower wavenumber, which could mean that the cations present in this specific sample is of different nature to those observed in part A of sample BM-B-41-1 (liner bentonite sample).

Table 4.23: *KBr-FTIR positions (cm^{-1}) corresponding to the graphs (a), (b), (c), (d), (e) and (f) in Figure 4.31 and assignments at 3800-3100cm^{-1} region corresponding to the water stretching bands.*

S-S-54-15-A	S-S-54-15-B	S-S-54-15-C	S-S-54-15-D	S-S-54-15-E	M-S-48-1	Assignments
ATR positions (cm^{-1})						
3622.45± 0.19	3622.836 ±0.37	3622.31± 0.16	3623.19± 0.17	3626.42± 1.49	3618.19± 1.25	**OH stretching of structural hydroxyl groups**
3422.85± 0.84	3425.25± 0.34	3419.74± 0.71	3418.11± 0.78	3424.39± 0.99	3414.21± 0.88	**OH stretching of water**
3237.57± 1.73	3235.11± 1.09	3238.62± 2.45	3233.24± 1.28	3233.48± 1.53	3239.61± 1.30	

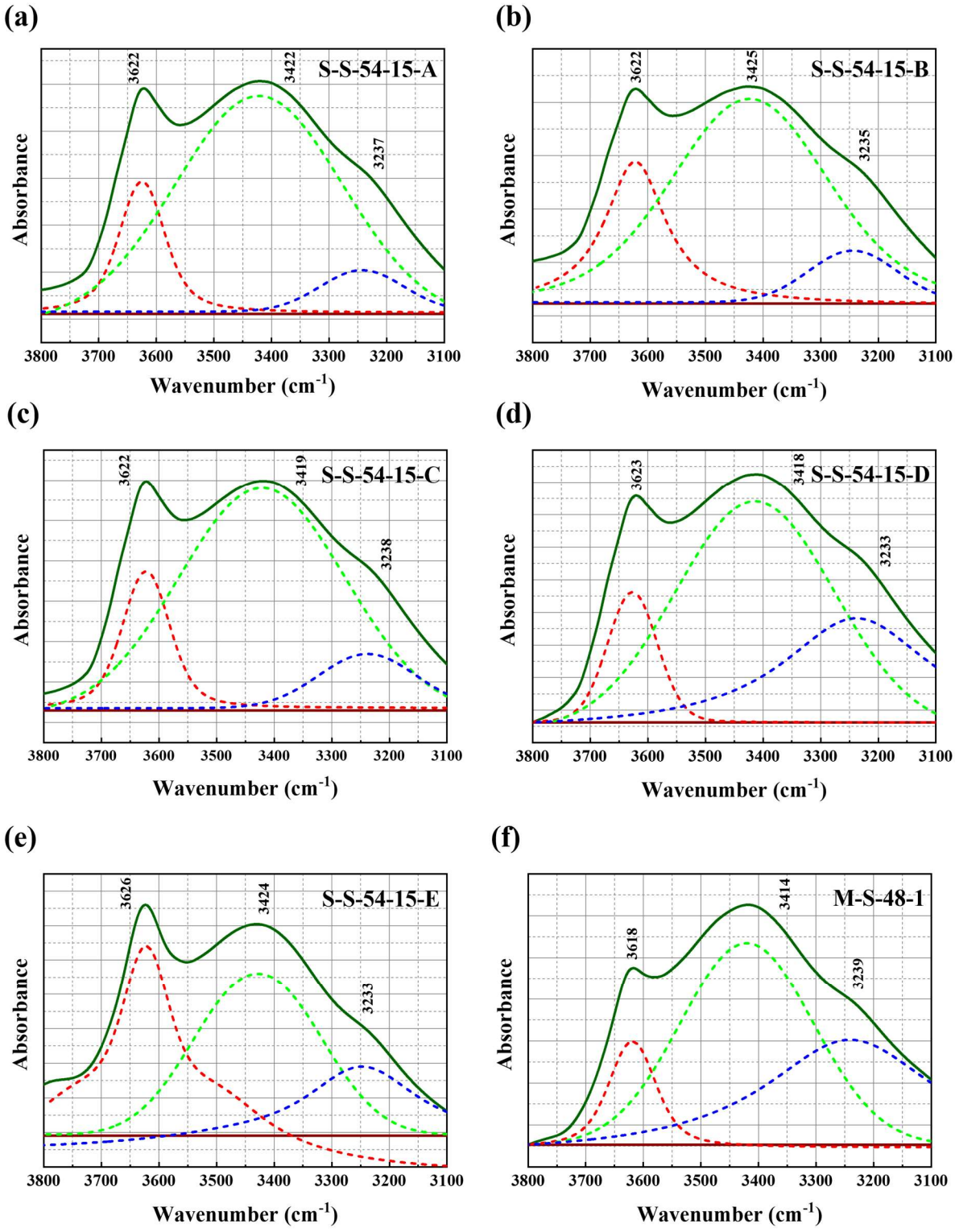

Figure 4.31: *Shows the fitted band positions corresponding with the water stretching bands of S-S-54-15-A (a), B (b), C (c), D (d), E (e) and M-S-48-1 (f).*

To better identify if any deviation has occurred in the water bands of the Febex samples, this region of the spectra was plotted against the results obtained from the untreated material and results are presented in Figure 4.32.

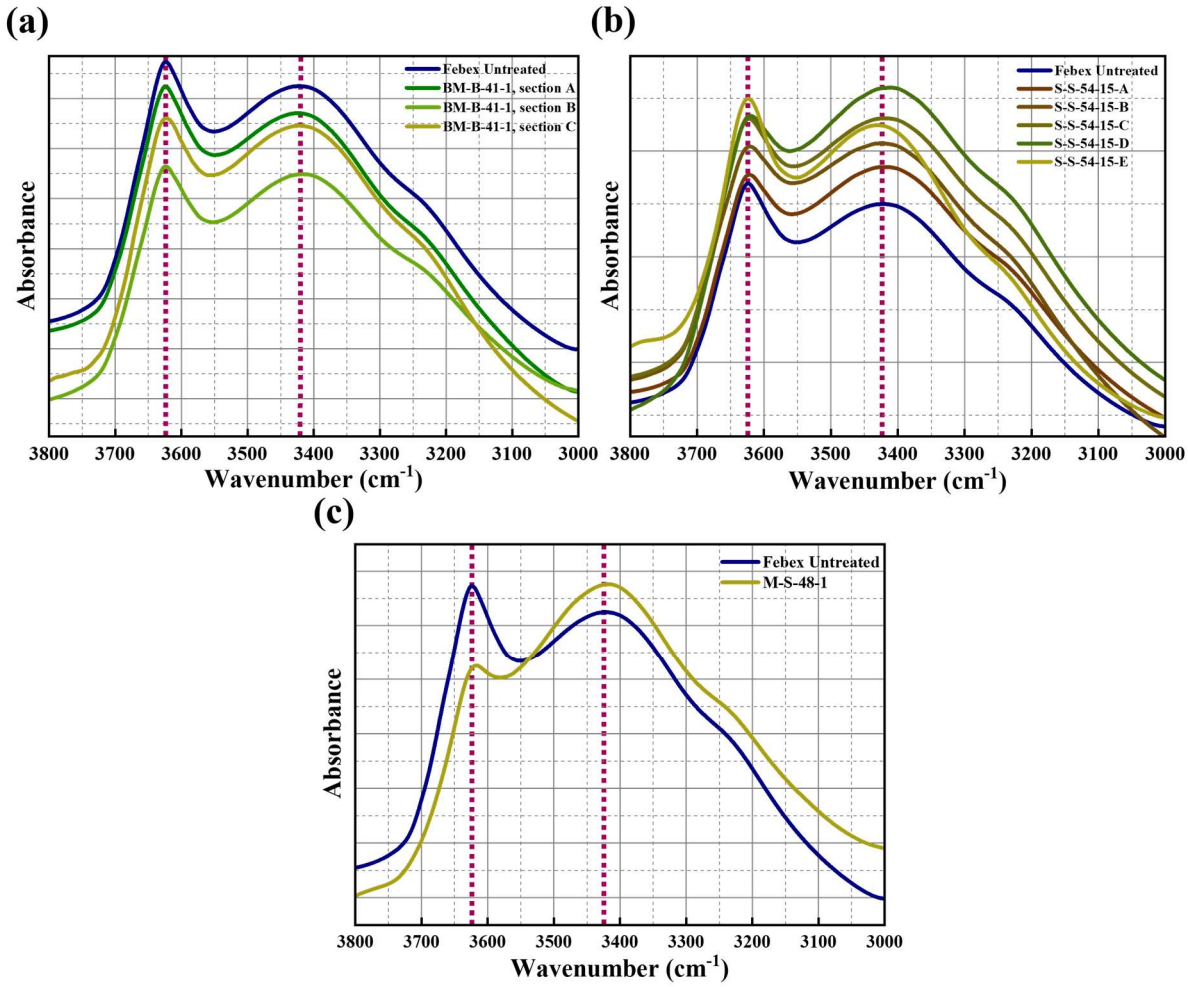

Figure 4.32: *(a)-(c) Water stretching bands.*

No appreciable differences between the reference sample and the different sections of BM-B-41-1 were found. However, sample S-S-54-15-D (Figure 4.32 (b)) shows a small deviation on OH stretching vibrations of the structural OH groups that might be caused by cation exchange in the interlayer space. The same observation can be made for sample M-S-48-1 (Figure 4.32 (c)).

From ATR-FITR and KBr-FTIR analysis, it was observed the characteristic bands corresponded to dioctahedral smectites. No observable alteration and/or transformation was recorded. However, the bentonite fragments collected from sample M-S-48-1 presented a moderate increase in absorbance that might suggest an iron enrichment of the δAlFeOH deformation at octahedral cation-OH lattice deformation region. In addition, from the stretching water region analysis, a shift in position of the band corresponding to OH stretching of S-S-54-15-D and M-S-48-1 samples was observed, which may be explained by replaceability of the interlayer cations.

4.2.9 Thermal analysis on Febex bentonite samples

Heat affects clays in varied ways and produces changes in their many properties. Consequently, thermogravimetric analysis is a technique frequently used for clay characterisation. This technique is based on mass changes as a result of exposure to a controlled variation of temperature and, in combination with the analyses carried out so far, this technique can provide valuable information, not only about the thermal behaviour of bentonite but also aspects derived from its chemical behaviour, since it is possible to determine the conditions under which the clays decompose, inferring on the products of such a decomposition.

Bentonite contains mineral components in varying amounts. In general, these minerals are intimately mixed within the clay matrix. The behaviour of bentonite under the influence of temperature may be governed by several factors, including chemical composition, predominant interlayer cation, hydration state and the presence of other interstratified clay minerals. The processes occurring in bentonite can be as follows [263]: (*i*) dehydration; (*ii*) dehydroxylation; (*iii*) decomposition or transformation into an amorphous form and; (*iv*) recrystallisation or formation of new crystal structures.

Dehydration, dehydroxylation and decomposition are of endothermic character, but the first two differ from the third in that the associated mass loss that occur during the dehydration and dehydroxylation does not happen during the decomposition. Conversely, recrystallisation is of an exothermic process [263]. Therefore, by evaluating the thermal effect over bentonite, some predictions may be made concerning the behaviour of bentonite against iron diffusion and identify its effect in the clayey matrix. Thermal decomposition of the bentonite experimental samples was investigated using TGA. The results obtained are visualised and presented as derivative weight loss or derivative thermogravimetric data (DTG) in Figures 4.33 and 4.34 and summarised in Table 4.24 and 4.25.

The temperature range covered was from ambient to 1000°C. Prior to experimental sample examination, an untreated sample was subjected to a controlled variation of temperature to identify the mass variation and decomposition processes for comparison, as shown in Figure 4.33 (a) and Table 4.24. Figures 4.33 (b), (c) and (d) and Table 4.24 also show the results obtained from TGA analysis performed on each section of sample BM-B-41-1. The first temperature interval, from ambient to 150-200°C, shows two initial endothermic peaks, (a) and (b), which are ascribed to the dehydration of the samples. Dehydration implies the desorption

of physiosorbed water, including water present in the interlayer spaces. This endothermic process also exposes the heterovalent character of the cations occupying the interlayer space [264], [265], [266], [267].

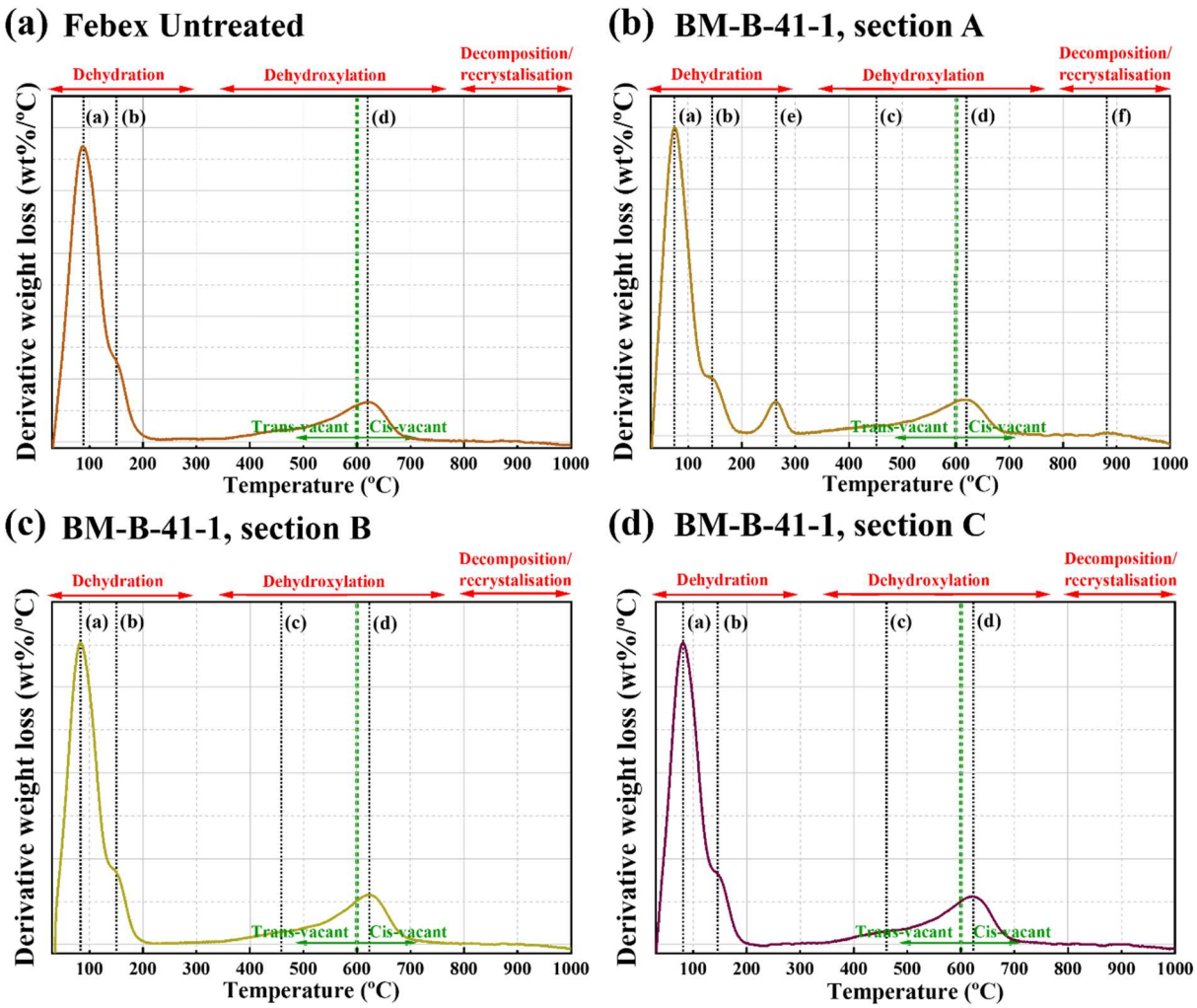

Figure 4.33: *(a) DTG results of reference sample. (b) DTG results of BM-B-41-1, section A. (c) DTG results of BM-B-41-1, section B. (d) DTG results of BM-B-41-1, section C. Peaks are indicated by dotted lines.*

The second next endothermic event is observed at 350°C-750°C, and it can be assigned to the dehydroxylation of the montmorillonite component [264]. This temperature region is characterised by the presence of a prominent peak around 620°C (c), which is attributable to the loss of lattice water [264] or, as stated by Wolters and Emmerich [268], the occurrence of montmorillonite dehydroxylation due to the migration of structural water from two hydroxyl groups per formula unit (half unit cell) out of the clay mineral structure. This process is led by the following reaction: $2(OH) \rightarrow H_2O + O_r$ (r, residual), and influenced by: (*i*) the nature of the interlayer cation; (*ii*) the nature of the octahedral cations which increase the dehydroxylation

temperature with the following sequence: Fe-OH<Al-OH<Mg-OH; and (*iii*) the percentage of cis- and trans-vacant positions leading to different dehydroxylation temperatures.

Table 4.24: *Temperature values of peaks observed in TGA. Temperature accuracy = ±0.25°C* [269].

Positions in Figure 4.33	Febex Untreated	BM-B-41-1, section A	BM-B-41-1, section B	BM-B-41-1, section C
	Temperature (°C)			
(a)	88.41	74.72	83.56	80.61
(b)	149.60	142.67	150.64	144.75
(c)	456.59	451.56	458.49	461.44
(d)	620.21	619.35	623.34	623.34
(e)	-	264.18	-	-
(f)	-	880.74	-	-

Mackenzie & Bishui [270] affirmed that the boundary between cis- (cv) and trans-vacant (tv) montmorillonites is at 600°C. Thus, above 600°C, cv montmorillonite predominates, while dehydroxylation values below 600°C indicate a tv character of the montmorillonite component. In addition, montmorillonites are classified as 'ideal' or 'normal' when dehydroxylation undergoes at temperatures around 700°C, and/or 'abnormal' when dehydroxylation undergoes at temperatures around 500°C, exhibiting in some of the abnormal montmorillonites a double peak, the first at ~550°C and the second located around 700°C [271], [272]. This two-stage dehydroxylation was explained by Heller and Kalman [273], who asserted that this effect was due to the iron isomorphic substitutions in octahedral allocations, while other authors assign this double peak occurrence to possible defects in the montmorillonite structure [274] or due to differences in mineral particle sizes [275].

From Figures 4.33 (a), (b), (c) and (d) it can be affirmed that both the untreated sample and the different sections of sample BM-B-41-1 are mostly composed of cv dioctahedral smectite clay particles which are characteristic of Febex bentonite. As part of the main dehydroxylation peak at around 620°C, a new peak between 450-500°C (c) (Table 4.24), appeared in the total fraction. The presence of this peak, together with the abnormal dehydroxylation peak, might be an indicator of the presence of another type of clay mineral in addition to the cv dioctahedral smectite clay particles. As postulated by Fernández et al. [256], this peak could be explained due to the presence of smectite particles with high-iron content, since the presence of iron in

octahedral sites will decrease the dehydroxylation peak towards temperatures ranging between 450-520°C, as observed in dioctahedral Fe-smectites such as nontronite.

Decomposition and recrystallisation occur around 850°C and 1000°C [268], respectively. The endothermic decomposition leads to the breakdown of the montmorillonite crystalline structure and formation of amorphous products, whose visibility is not always apparent in DTG diffractograms [276]. The exothermic reactions occur when the amorphous phases recrystalise at high temperatures (probably spinel), and this process is strongly dependant on the chemical composition of the sample [277].

The peak associated with decomposition (f) was only observed in section A of sample BM-B-41-1. This peak is not apparent in the reference material. Fernández et al. [256], who analysed several Febex bentonite samples from heater no.2 along with the unaltered material, located the endothermic peak associated with the decomposition of the unaltered sample at around 867°C. The peak observed in section A occurred around 880°C, indicating a modification of the high temperature endothermic peak. Finally, it is noteworthy that sample A exhibited a remarkable endothermic peak at around 250°C (e) in the DTG diffractogram of sample BM-B-41-1 (section A). The occurrence temperature of such peak might be associated with goethite dehydroxylation, which is reported at temperatures around 250-300°C [256], [278], [279].

Table 4.25: *Temperature values of peaks observed in TGA. Temperature accuracy =±0.25°C* [269].

Positions in Figure 4.34	**S-S-54-15-A**	**S-S-54-15-B**	**S-S-54-15-C**	**S-S-54-15-D**	**S-S-54-15-E**	**M-S-48-1**
	Temperature (°C)					
(a)	84.56	80.61	81.38	83.56	84.60	88.20
(b)	150.64	147.69	148.43	146.66	146.66	146.82
(c)	455.55	451.56	452.22	455.55	458.49	504.04
(d)	623.34	620.22	619.48	619.35	614.32	628.33
(e)	-	-	-	-	257.25	-
(f)	-	-	-	-	-	800.59
(g)	-	-	-	-	353.97	-

TGA analysis was also conducted in the extensometer samples (S-S-54-15-A/B/C/D/E) and the bentonite sample belonging to the surface of the corrosion coupons. Results are presented in Table 4.25 and Figure 4.34.

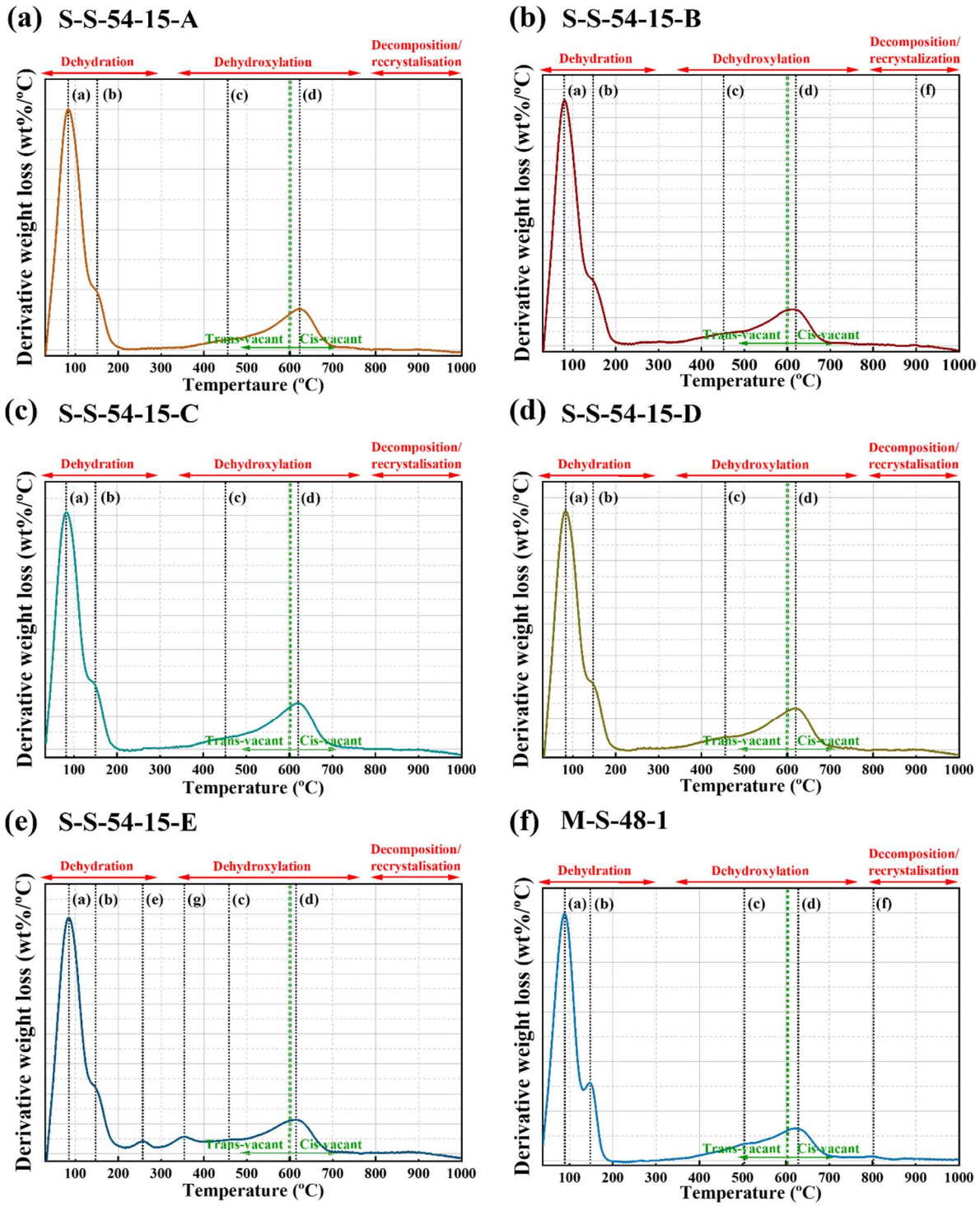

Figure 4.34: *(a) DTG results of S-S-52-15-A sample. (b) DTG results of S-S-52-15-B sample. (c) DTG results of S-S-52-15-C sample. (d) DTG results of S-S-52-15-D sample. (e) DTG results of S-S-52-15-E sample. (f) DTG results of M-S-41-1 sample. Peaks are indicated by dotted lines.*

The peaks observed at (a), (b), (c) and (d) correspond to the dehydration and dehydroxylation reactions mentioned for sample BM-B-41-1. Therefore, it can be established, as previously observed in sample BM-B-41-1, that both extensometer and corrosion coupon bentonite are characterised by the presence of cv dioctahedral smectite clay particles.

Nonetheless, sample S-S-54-15-E showed the presence of two endothermic peaks: (*i*) the first one (e) might again be explained by the dehydroxylation of goethite (e) [256], [278], [279], [280]; and (*ii*) the second endothermic peak at 353.97°C (g) might correlate with the gradual conversion of goethite to hematite which seems to occur at temperatures between 300-400°C [271], [281].

4.3 Concluding statement

This chapter has presented results obtained from the physicochemical evaluation of the samples from the Febex in-situ test. The aim was to provide consistent data on the residual state of the samples versus analyses performed on unaltered bentonite supplied by CIEMAT. This study has allowed an exhaustive examination of possible chemical and structural differences between the samples from the in-situ test and the pristine material.

Overall, there is little information regarding the expected processes during the first operational stages of a GDF. Thus, the Febex in-situ test was devised with numerous steel components due to its proven corrosion instability under geological disposal conditions, to investigate the degree of degradation between bentonite and the released corrosion by-products. The chemically reducing local environment at the contact interface between the steel components and the bentonite buffer could lead to bentonite alteration and/or transformation, which would result in the formation of new minerals with reduced swelling capabilities, that would undermine the plasticity and shear strength of bentonite.

After the immediate placement of the HAW containers, the evaporation of water absorbed/present in the bentonite structure is expected, giving rise to a momentary increase of relative humidity in the vicinity of the containers [27], [89]. The generated vapour would also migrate towards peripheral zones. This-coupled with the presence of residual oxygen trapped in the geotechnical barrier could favour the initial formation of hydroxides and oxyhydroxides

[27], [89]. It has been deemed that the corrosion processes during these initial stages will therefore be similar to those expected under atmospheric corrosion [282], [283]. To date, the most reliable data obtained was derived from the partial dismantling carried out in 2005 [242]. The major corrosion products identified at structural metallic component surfaces were goethite (α-FeOOH) and iron(III) hydroxide ($Fe(OH)_3$). These results coincided with a mechanism of electrochemical corrosion in aqueous medium under aerobic conditions [27], [89] and can be summarised in the following equations:

$$Fe(s) \rightarrow Fe^{2+} + 2e^{-}$$ Equation 4.1 [284]

$$Fe^{2+} + 2OH^{-} \rightarrow 2Fe(OH)_2$$ Equation 4.2 [284]

$$4Fe(OH)_2 + 2H_2O + O_2 \rightarrow 4Fe(OH)_3$$ Equation 4.3 [284]

Giving the global reaction:

$$4Fe + 6H_2O + 3O_2 \rightarrow 4Fe(OH)_3$$ Equation 4.4 [284]

However, the heat emitted by the nuclear waste will produce an increase of temperature at container surfaces and, in general, in the barrier system due to thermal gradients [27], [89]. Most of the international programmes that contemplate geological disposition of HAW have delimited the temperature at container surfaces to a maximum of 100°C. Therefore, the temperature at container surfaces will be close to the boiling point of water, giving rise to an environment with low relative humidity (≤20%) during the first 10 years [27], [89]. During this stage, low relative humidity and oxygen availability is expected to slow down corrosion rates.

Once this period of time has elapsed, the temperature at container surfaces will begin to decay, favouring the progressive re-saturation of the clay barrier, thus increasing the relative humidity around the containers. The re-saturation of the clay barrier together with decreasing thermal gradients will lead to a highly dynamic environment characterised by a great variety of geochemical phenomena with direct effects on corrosion of structural metallic components such as: (*i*) dissolution of sulphates and carbonates; (*ii*) redistribution of salts; (*iii*) precipitation and deposition of salts over metal surfaces; and (*iv*) deliquescence phenomena. In addition, any remaining oxygen will be consumed early in this stage, leading to anaerobic conditions, prevailing during most of the operational period of the repository [27], [89]. Therefore, the

corrosion mechanism will essentially be a function of the relative humidity and oxygen present. Once complete saturation of the barrier has occurred, and electrochemical corrosion is established under anoxic conditions, the steel will continue to corrode according to the following equation:

$$Fe + 2H_2O \rightarrow Fe(OH)_2 + H \uparrow$$ Equation 4.5 [284]

$Fe(OH)_2$ is thermodynamically unstable and will rapidly evolve to precipitate magnetite. Although magnetite is the most favoured end product, aqua-$Fe(OH)_2$ can predominate at temperatures below 60°C, inhibiting the formation of magnetite.

As it has been stated, magnetite is the more likely corrosion by-product and it tends to form a stable corrosion layer over the steel components. The development of such a layer inhibits the ongoing diffusion rate since it acts as a passivator in non-dynamic environments [285]. However, in highly dynamic environments, it has been speculated that due to the direct contact of bentonite with steel components, in conjunction with the heat released by the HAW and the hydrodynamics of the bentonite-bedrock system, the formation of a stable magnetite layer will be inhibited, giving rise to the formation of a double corrosion layer that will be a function of the relative humidity and remaining oxygen. The double corrosion layer will be formed by an outer layer of oxyhydroxide compounds, such as maghemite, lepidocrocite, goethite and akaganeite and iron oxides such as magnetite and hematite, and an inner ferrous corrosion layer just behind the outer layer. Wilson et al. [90] predicted that the formation of a dual corrosion layer will facilitate the free diffusion of ions into the bounding bentonite until the corrosion of the canister is complete.

Our metallographic analyses over the surface of the carbon steel corrosion coupons confirmed the speculations of Wilson et al. [90]. The environment at the interface between the bentonite and corrosion coupons did indeed indicate the formation of a double corrosion layer on the carbon steel coupons. XRD and Raman analysis allowed the identification of iron oxides (magnetite and hematite) and oxyhydroxides (lepidocrocite, maghemite, goethite and akaganeite) together with traces of calcite.

Reviewed studies (section 2.3) suggest that due to the formation of a double corrosion layer, iron diffusion into the bentonite will be less impeded than if a competent layer existed. Hence a greater degree of alteration in the bentonite buffer is expected through its complexation at the

edges or occupying exchanges sites and, therefore, this electron transfer will lead to a dynamic redox environment. As a result, the formation of iron-rich smectites such as saponite, nontronite and ferrosaponite are likely to occur. However the amount of structural Fe will determine the formation of trioctahedral smectites or 1:1 phyllosilicates such as berthierine-type [70], [129], [130], [132], [286].

Initially, to evaluate the degree of degradation, if any, bentonite samples were visually inspected. Section A of BM-B-41-1 showed a clear change of colouration was observed in the region of immediate contact of the sample with the liner, which might suggest the concurrence of certain chemical changes in the bentonite structure. Tomographic analysis of the sample revealed the presence of microparticles of a denser material and higher attenuation coefficient, which were attributed to the presence of iron oxides, later confirmed by synchrotron XRD analysis.

The results obtained from CEC showed values close to those displayed by the reference sample. The dissimilarities encountered between the reference sample, M-S-48-1 sample and the different sections of BM-B-41-1 might be attributable to isomorphic substitutions that are characteristic of clay minerals or due to the migration of Fe^{2+} through the clay matrix.

The exchangeable cations analysis indicated that in the area of direct contact with the liner (BM-B-41-1, section A) there are higher concentrations of Mg^{2+}. Moving towards the interior of the clay matrix, the exchangeable cations are those observed in the reference material. The increase of Mg^{2+} can be explained due to the predicted dissolution of carbonates, mostly calcite, at very early stages after repository closure and its later precipitation in areas close to the heater as a result of the re-saturation of the barrier aided by the thermal gradients, favouring the increase of exchangeable Mg^{2+} at expenses of Na^{+}.

However, sample S-S-54-15-E showed a general decrease in exchangeable cation population. Although, the individual value deviations are close to the values obtained in the untreated sample, these deviations might be explained due to the occupation of migrated Fe^{2+} in the interlayer space. This specific sample was collected in the immediate contact with the extensometer component. Furthermore, the saline content of the Grimsel groundwater (Table 3.20) might have facilitated the sorption of the Fe^{2+} liberated due to extensometer corrosion, since at basic pH, Fe^{2+} sorption shows a selectivity coefficient very similar to that of Ca^{2+}.

The results obtained through XRD do not show significant crystallographic changes between the experimental samples and the reference sample. Nevertheless, these results differ from those obtained through high-resolution diffraction and thermal analysis. Despite the fact that no newly-formed minerals were observed, the presence of iron phases was strongly apparent in particular in section A of BM-B-41-1 and M-S-48-1 sample, which is not characteristic of the mineralogical composition of Febex material. Mössbauer analyses confirmed the existence of goethite and hematite in the section A (BM-B-41-1) and M-S-48-1 samples, in addition to Fe^{2+} and Fe^{3+} coexisting in octahedral positions, suggesting a small degree of structural reduction or electron transfer in the montmorillonite. In addition, thermal analysis of sample S-S-54-15-E and section A of BM-B-41-1 displayed the presence of goethite and hematite. The presence of iron oxides blended in the bentonite body is explained due to the corrosion of the metallic components and its dissolution and diffusion through the compacted barrier, before precipitating at grain boundaries or dilation spaces in the bentonite matrix as iron oxide.

Overall, the obtained results indicate the formation of a double corrosion layer on C-steel surfaces, characterised by the presence of iron oxides and oxyhydroxides. From evaluation of the bentonite samples, it can be affirmed that some crystallographic changes might have occurred. It can be clearly stated that due to the advective effect caused by the re-saturation of the barrier and the thermal gradients, there were clear changes to the cation population in the areas close to the liner, manifested in dissolution of carbonates such as calcite, in contrast to areas further away from the heater/liner. However, the overall CEC remained in the range of values expected for Febex bentonite.

Accordingly, the most significant alteration of the bentonite in contact with the heated liner (simulated HAW surface) is caused by precipitation of iron oxide minerals which contribute to volumetric dilution of the properties of the bentonite. Presumably over longer periods, this alteration front would propagate further into the bentonite, with the zone closest to the liner becoming further enriched in iron oxides precipitates and, therefore, further compromising the bentonite properties. Although we tentatively suggest small changes in the montmorillonite structure, in material immediately surrounding the liner these alterations are relatively indistinct. This does not rule out more significant alteration over longer periods but certainly indicates that such alterations would likely not occur to any substantial degree within the first 20-50 years of GDF operation, which coincides with the period when HAW heat output is greatest.

Chapter 5 Effect of metallic corrosion on the properties of Alternative Buffer Material bentonite samples

5.1 Chapter overview

In the field of bentonite research applied to geological disposal, the Alternative Buffer Material (ABM) experiment was conceived to examine different bentonite types. This in-situ test aimed to evaluate the following properties of each bentonite involved in the experiment [47]: (*i*) amount of smectite; (*ii*) mineralogy of the bentonites investigated, (*iii*) organic carbon and sulphur content; (*iv*) effects of microorganism; (*v*) CEC; (*vi*) cations and anions present in the clays; (*vii*) iron redox chemistry; and (*viii*) hydromechanical properties of the buffer.

The most important feature of any bentonite buffer is to ensure its long-term mineralogical stability. The mineralogical stability of bentonite can be compromised by the occurrence of the following processes [47]: (*i*) conversion to illite; (*iii*) dissolution of certain structural components and the formation of new minerals; (*iii*) changes in its CEC; and (*iv*) influence of salt transport through the clayey matrix. In addition, it has been pointed out regularly in the literature (Chapter 2) that the bentonite interaction with released iron corrosion by-products seems to lead to its alteration and/or transformation and, so, the formation of new non-swelling minerals. Bearing in mind this assumption, the ABM project was designed with an steel heater due to its known corrosion susceptibility in a repository environment [47]. The ensuing container corrosion yielded the opportunity to investigate the scenarios under which different bentonite-types may interact with the corroded species released from the container, such as [47]: (*i*) iron incorporation by cation exchange into the interlayer or by complexation at the edges; (*ii*) reduction of iron in octahedral sites; (*iii*) bentonite transformation by dissolution processes; and (*iv*) cementation of corrosion products in the buffer body.

This present chapter focusses on bentonite-iron interactions in different sourced clay materials. The ABM in-situ test targeted a maximum temperature of 130°C, and the buffer materials were

naturally wetted by the surrounding water from the host rock, with a calculated water inflow of 0.06l/min [47]. Figure 5.1 shows the temperature distribution of parcel 1 from the surface of the container-heater to 60mm depth into the bentonite body. From Figure 5.1 we can assume that the Kunigel V1 bentonite sample (ABM 1) was subjected to a temperature range of 120-130°C. Due to the absence of data relating to the temperature distribution in parcel 2, the distribution of temperatures in parcel 1 was taken as an approximation of that in parcel 2, assuming, therefore, that the bentonite samples from this parcel were also exposed to the same temperature range. We believe that the error introduced by this assumption does not invalidate the conclusions presented in this chapter.

In addition, both parcels were equipped with an artificial water system to guarantee complete saturation of the bentonite blocks; the water composition is given in Table 5.1.

Table 5.1: *Main elements in the water supply. Adapted from* [47]*.*Sulphate-sulphur.*

Element	Amount (mg/l)
Na^+	2470
K^+	12.40
Ca^{2+}	2560
Mg^{2+}	64.80
HCO_3^-	51.70
Cl^-	8580
SO_4^{2-}	483
$SO_4\_S^*$	171
Br^-	59
F^-	1.50
Si	6.30
pH	7.33

The bentonite samples further evaluated in the present chapter were retrieved from the contact interface with the container-heater system. Since parcels 1 and 2 were both naturally and artificially wetted over the experiment, and as a result of the experimental temperature selected (130°C), it is logical to assume that the degree of saturation and, therefore, the water content of the samples was lower than that expected in those samples retrieved in areas further away from the immediate contact with the canister-heater. Svensson et al. [47] evaluated the water content in a large number of positions of each bentonite block from parcel 1. They

concluded that the material properties and bulk densities achieved after strong compaction reached influenced water distribution along the different bentonite blocks, therefore; the water content increased as the distance from the container surface increased.

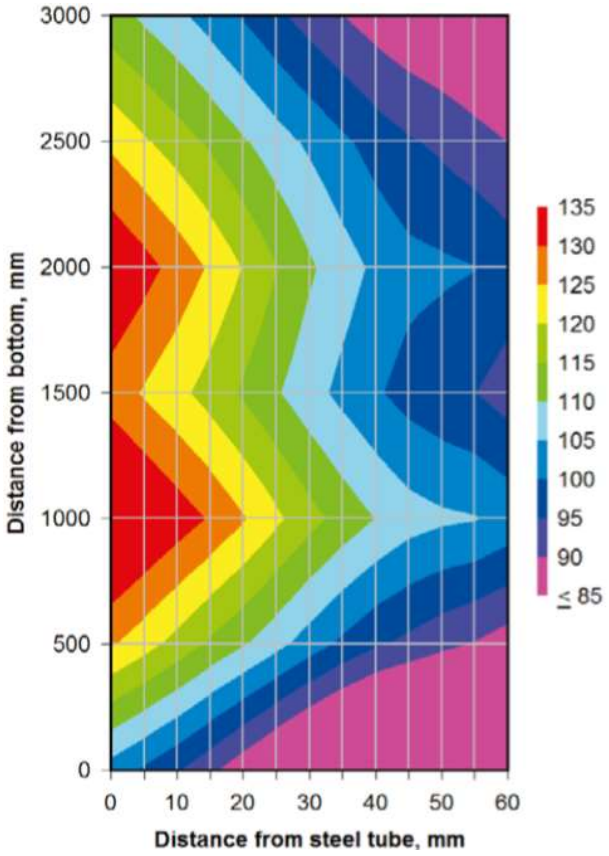

Figure 5.1: *Temperature distribution in parcel 1 from the surface of the heater up to 60mm in the bentonite body. Adapted from* [47].

The experimental work presented in this chapter aimed to provide a parallel and complementary vision to the results obtained in Chapter 4, since the main focus of the present chapter is also to evaluate any possible physicochemical alteration that bentonite may have experienced during the ABM in-situ test. The ABM experiment design and, therefore, the boundary conditions differed from those imposed in the Febex in-situ test. Most notable was the higher peak temperature (130°C).

The samples examined in this chapter pertain to different bentonite source deposits, located in different worldwide regions. Although all the evaluated samples are bentonites, the mineralogical composition and smectite content vary from one source to another. This fact, together with the experimental conditions to which the bentonite samples were subjected, may provide different insights into the parameters that govern the bentonite alteration and/or transformation, e.g. if they were in geological disposal conditions.

5.2 Characterisation of the effect of metallic container corrosion of different types of bentonite

5.2.1 Visual examination of physical condition of bentonite samples

Samples were received at the University of Bristol as described in Chapter 3 and were sequentially opened in a nitrogen-purged glovebox (Saffron Scientific Equipment Ltd).

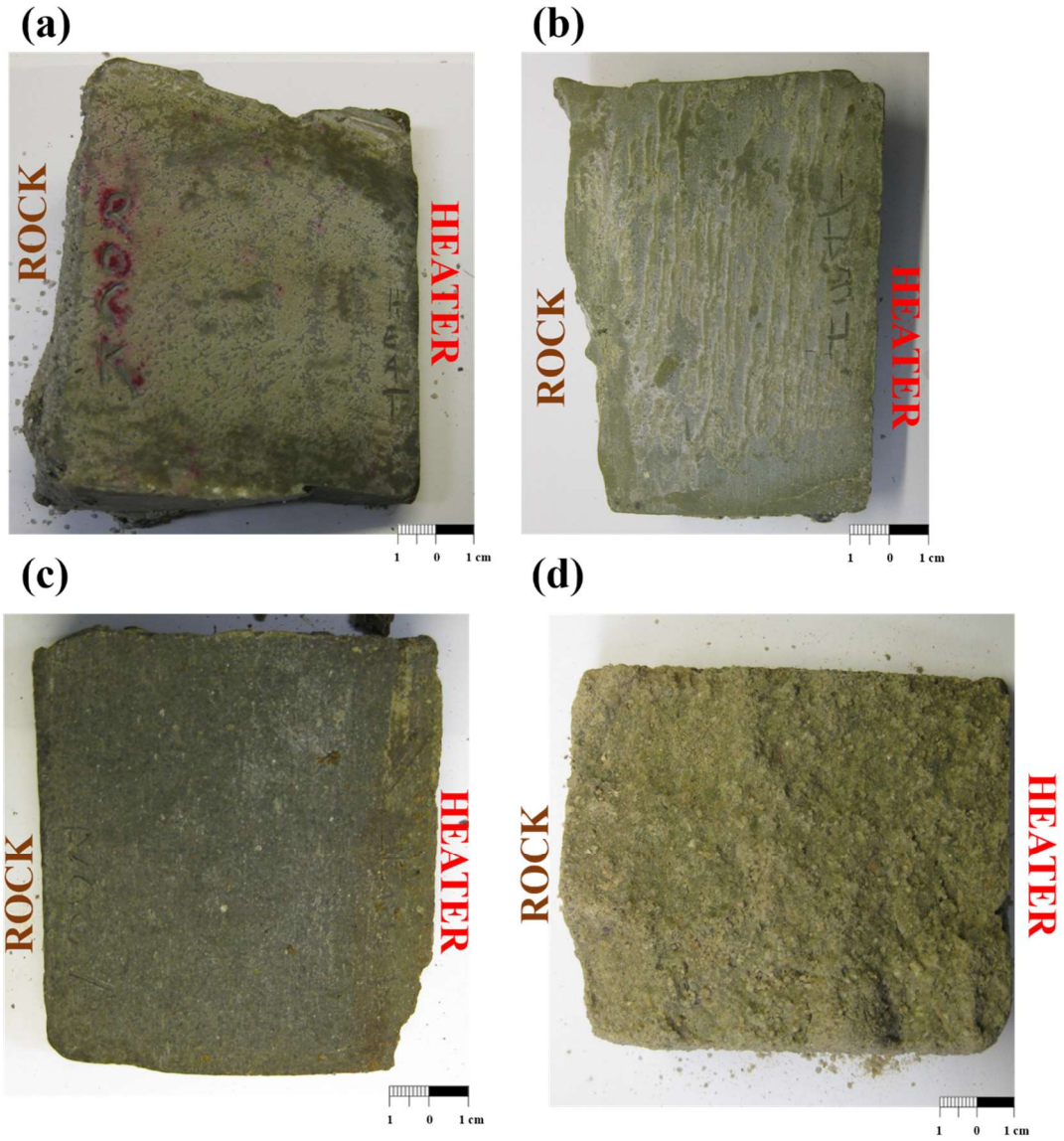

Figure 5.2: *(a) Physical appearance of Kunigel V1(ABM 2) sample. (b) Physical appearance of Deponit C-AN (ABM 2) sample. (c) Physical appearance of MX-80 (ABM 2) sample. (d) Physical appearance of Febex (ABM 2) sample.*

As a first pass analysis method, samples were visually inspected and photographed to identify any possible discolouration along the samples, as observed in sample BM-B-41-1 (liner bentonite sample) from the Febex in-situ test (Figure 4.8).

Figure 5.2 shows the physical state of the samples upon their reception at the University of Bristol. Overall, samples presented a homogeneous colouration, in contrast to BM-B-41-1 (Figure 4.8). No colour change was seen on the sample surfaces or areas of the samples that had been in immediate contact with the heater-container. The absence of colouration in the areas of the bentonite samples proximal to the heater was initially attributed to the high degree of saturation presented in each sample that could have concealed the colour degradation due to bentonite when saturated acquires a darker colouration. Although no physical discolouration was observed, further analyses were needed to evaluate the physicochemical conditions of samples after several years of heating exposure.

5.2.2 Cation exchange capacity determination in the contact area between the bentonite and the metallic canister

CEC determines the ability of the geotechnical barrier to absorb or retain certain radionuclides, thus defining the importance of CEC analyses since any fluctuation from normal CEC values may be indicative of mineralogical alterations, as has been explained in section 4.2.3. CEC was initially determined following the guidelines described in Chapter 3. The values are presented in mmol(+)/100g in Figure 5.3 and Table 5.2. Determinations were performed twice for each sample, following the Cu-trien method, to ensure consistency. Unaltered samples provided by SKB were also analysed to generate baseline data.

Smectites are ion exchangers. This exchange capability is defined by their high specific surface areas, which are determined by their structural characteristics (section 4.2.3). It can be said that smectites are composed of a ‘stationary phase’ or, silicate structure, and a ‘mobile phase’, or interlayered cations. The most common cations in the interlayer space of smectites are Na^{+} and Ca^{2+} (section 2.1.1), and their abundance determines the smectite’s sodium or calcic nature. As the charge of the stationary phase increases, there are a greater number of cations occupying the interlaminar space, so that CEC will be larger. Consequently, the greater the smectite component in bentonite, the higher the CEC. Hence, CEC of bentonite is a combined function of the amount of montmorillonite and the montmorillonite surface charge. Table 5.3 collects data relative to the montmorillonite content of each of the ABM bentonite samples examined.

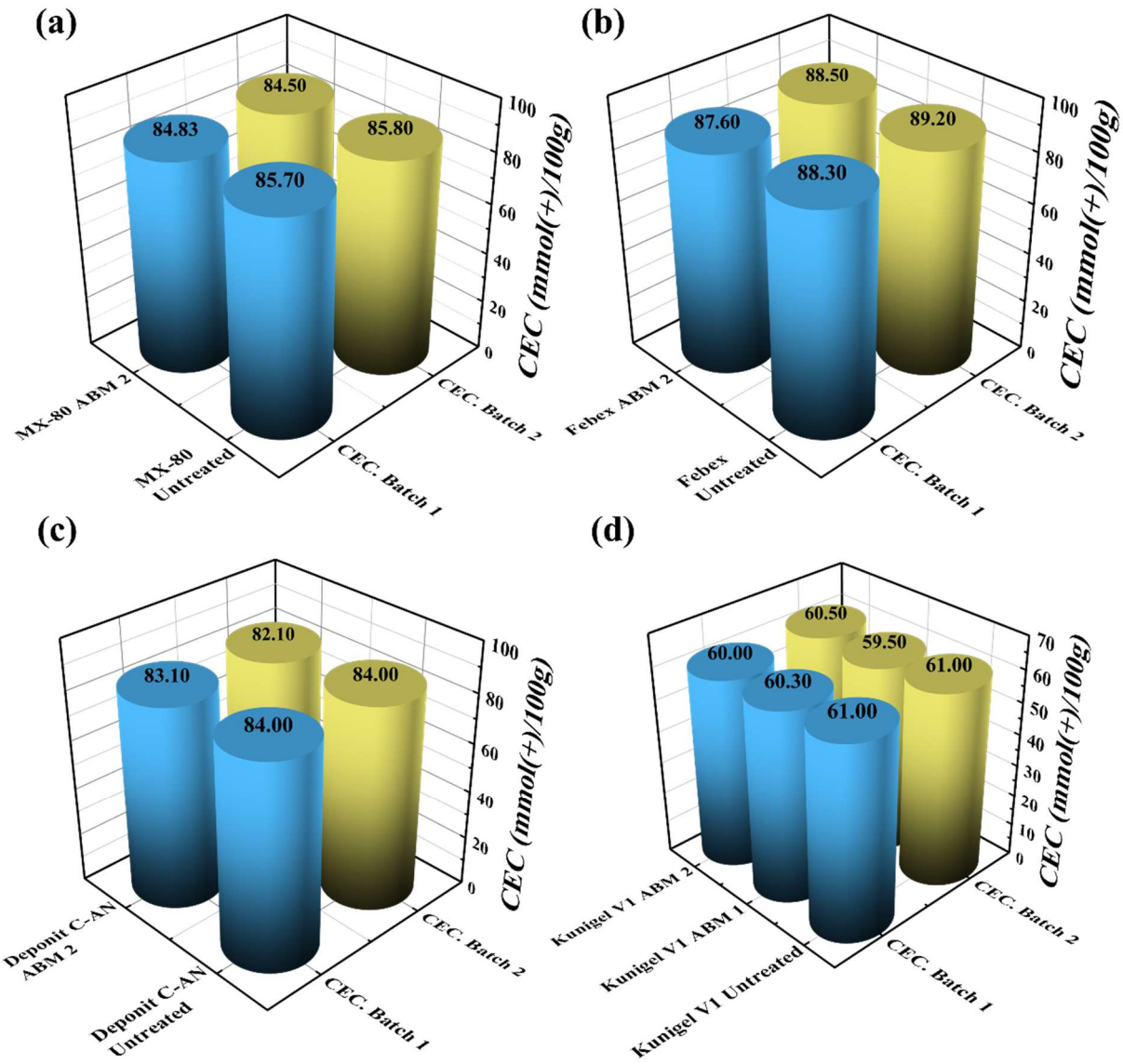

Figure 5.3: *(a)-(d) Cation exchange capacity (CEC, mmol(+)/100g) measured in all ABM bentonite samples vs reference material.*

Table 5.2: *Literature data of montmorillonite content of each sample measured by XRD.*

Sample	Montmorillonite content (wt%)	Literature source
MX-80	62-82	Villar & Gómez-Espina [175]
Febex	92	LLoret & Villar [81]
Deponit C-AN	79.5-82.50	Laine & Karttunen [178]
Kunigel V1	46-49	Tachi, Ochs & Suyama [169]

From data presented in Table 5.2 and Table 5.3, it is natural to conclude that the lower CEC values obtained from the pristine Kunigel V1 bentonite are due to its lower montmorillonite content in comparison with the other unaltered materials analysed.

Table 5.3: *CEC measured on ABM bentonite samples and CEC reported in the literature.* [1]*Standard error* ($SE_{MX\text{-}80\ first\ batch}$) = *1.44mmol(+)/100g,* [2]*Standard error* ($SE_{Febex\ first\ batch}$) = *1.35mmol(+)/100g,* [3]*Standard error* ($SE_{Kunigel\ V1\ first\ batch}$) = *1.30mmol(+)/100g,* [4]*Standard error* ($SE_{Deponit\ C\text{-}AN\ first\ batch}$) = *1.45mmol(+)/100g,* [5] *Standard error* ($SE_{MX\text{-}80\ second\ batch}$) = *1.65mmol(+)/100g,* [6]*Standard error* ($SE_{Febex\ second\ batch}$) = *1.35mmol(+)/100g,* [7]*Standard error* ($SE_{Kunigel\ V1\ second\ batch}$) = *1.32mmol(+)/100g,* [8]*Standard error* ($SE_{Deponit\ C\text{-}AN\ second\ batch}$) = *1.27 mmol(+)/100g.*

ID sample	CEC (mmol(+)/100g) First batch	CEC (mmol(+)/100g) Second batch	CEC (mmol(+)/100g) reported in the literature
MX-80 Untreated[1, 5]	85.70	85.80	74 [175]
MX-80 ABM 2[1, 5]	84.83	84.50	-
Febex Untreated[2, 6]	88.30	89.20	111 [81]
Febex ABM 2[2, 6]	87.60	88.50	-
Kunigel V1 Untreated[3, 7]	61.00	61.00	60.1 [169]
Kunigel V1 ABM 1[3, 7]	60.30	59.50	-
Kunigel V1 ABM 2[3, 7]	60.00	60.50	-
Deponit CA-N Untreated[4, 8]	84.00	84.00	81 [178]
Deponit CA-N ABM 2[4, 8]	83.10	82.10	-

Table 5.3 shows results obtained from CEC analysis carried out on the ABM bentonite samples after underground retrieval. Overall, the results obtained correlate very well with determinations performed on the untreated materials. Discrete fluctuations between values were also observed, but can be considered negligible. CEC values of MX-80, Febex and Deponit differ from those presented in the literature (Table 5.3). This variation can be explained due to the sensitivity of the equipment utilised, since the values obtained from the experimental samples were a close match to those obtained in the unaltered samples. Hence, it is logical to assume that no major alterations have occurred. However, the extent of any possible alteration and/or transformation must be evaluated by complementary analysis, not CEC alone.

5.2.3 Study of the evolution of exchangeable cations in the ABM bentonite samples

Once CEC is established, the occupancy and nature of the cations filling up the interlayer space can provide information about the underlying processes affecting the contact interface between the bentonite and embedded metallic components. The precipitation, and later dissolution, of

certain bentonite structural components, together with progressive concentration of sulphates and carbonates at the bentonite-container interface and the expected re-saturation processes, will favour re-dissolution of the precipitated salts [27], [89], which may then facilitate cation migration through the clayey matrix, affecting the occupancy of the interlayer space, which in some cases may alter the bentonite's swelling capability. Determinations of soluble ions were performed on the reference and experimental ABM samples. Exchangeable cations were determined in the immediate contact regions of the bentonite samples with the steel heater. The analysis was duplicated to ensure repeatability and a $CsNO_3$ solution was used to displace the cations in the interlayer. The examinations of soluble ion evolution are presented in Figures 5.4 to 5.7 and Tables 5.4 to 5.7; determinations were performed for Na^+, K^+, Mg^{2+} and Ca^{2+}.

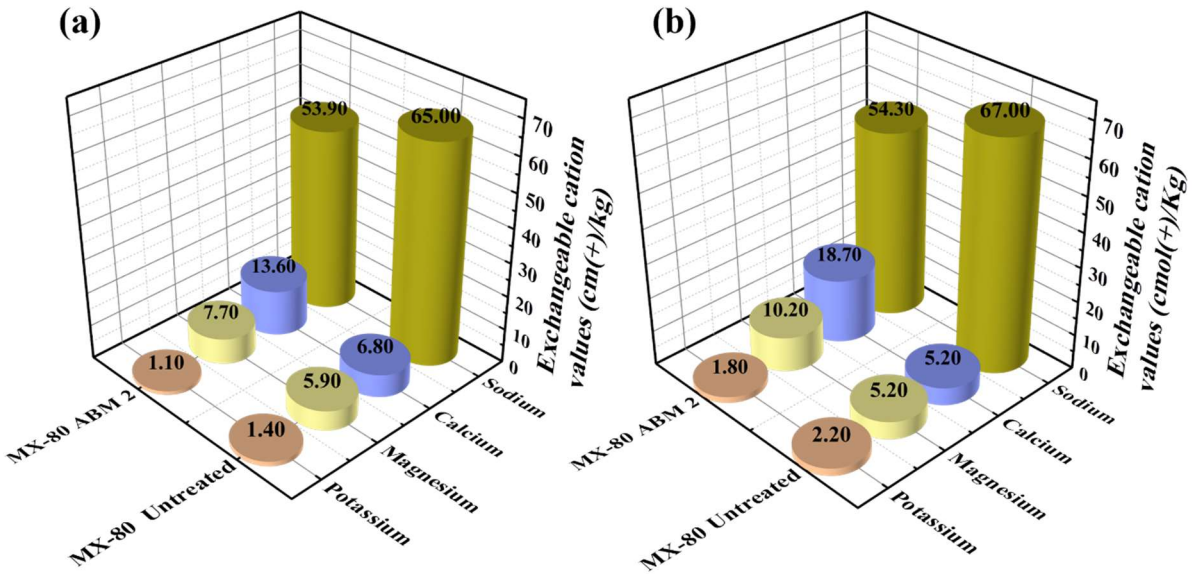

Figure 5.4: *(a)-(b) Results of exchangeable cation analysis (cmol(+)/kg) in two determinations conducted in the areas of immediate contact with the heater of MX-80 ABM 2 sample, and results obtained from the untreated MX-80 sample.*

As explained in Chapter 4 (section 4.2.4), the replacement of cations in the exchange complex is dominated by: (*i*) the cationic valence, the greater the valence of the cation the higher is the replacement potential; and (*ii*) the ionic diameter or the size of the cation, the potential replacement increases with the size of the cation. However, it is ultimately the size of the hydrated cation that controls the replacement ability. Therefore, those cations less hydrated will be more difficult to replace and vice versa.

CEC data of the MX-80 sample (ABM 2) and the reference material are presented in Table 5.4 and Figure 5.4. From Figure 5.4 and Table 5.4, subtle differences can be observed between the experimental sample and the reference material. Variations in Na^+, Ca^{2+} and Mg^{2+}

concentrations in the experimental sample are significant in comparison with the reference material. These variations could be explained due to replacement of Na^+ by Ca^{2+} and Ca^{2+} by Mg^{2+} as a result of the higher ionic diameter of Na^+ regarding Ca^{2+} and the higher ionic diameter of Ca^{2+} regarding Mg^{2+}. Besides, the total CEC values between duplicates are slightly different. This could be explained by the possible replacement of Ca^{2+} by Fe^{2+}, in the exchange complex, whose selectivity coefficient is very similar to that of Ca^{2+} at basic pH (Chapter 2, section 2.3.1).

Table 5.4: *Results of exchangeable cation values variation (measured in cmol(+)/kg) estimated in MX-80 ABM 2 and reference samples. [1]SE(Na^+) = 5.55cmol(+)/kg, [2]SE(K^+) = 0.15cmol(+)/kg, [3]SE(Mg^{2+}) = 0.90cmol(+)/kg, [4]SE(Ca^{2+}) = 3.4cmol(+)/kg, [5]SE(Na^+) = 6.35cmol(+)/kg, [6]SE(K^+) = 0.20cmol(+)/kg, [7]SE(Mg^{2+}) = 2.50cmol(+)/kg, [8]SE(Ca^{2+}) = 1.75cmol(+)/kg.*

Determination 1					
Total CEC	**Na^+ [1]**	**K^+ [2]**	**Mg^{2+} [3]**	**Ca^{2+} [4]**	**Sample**
76.30	53.90	1.10	7.70	13.60	**MX-80 ABM 2**
79.10	*65.00*	*1.40*	*5.90*	*6.80*	***MX-80 Untreated***
Determination 2					
Total CEC	**Na^+ [5]**	**K^+ [6]**	**Mg^{2+} [7]**	**Ca^{2+} [8]**	**Sample**
75.00	54.30	1.80	10.20	8.70	**MX-80 ABM 2**
79.60	*67.00*	*2.20*	*5.20*	*5.20*	***MX-80 Untreated***

Table 5.5 and Figure 5.5 display the results of CEC estimations in the Febex ABM 2 sample and the reference material.

Table 5.5: *Results of exchangeable cation values variation (measured in cmol(+)/kg) estimated in Febex ABM 2 sample and untreated samples. [1]SE(Na^+) = 3.20cmol(+)/kg, [2]SE(K^+) = 0.75cmol(+)/kg, [3]SE(Mg^{2+}) = 7.20cmol(+)/kg, [4]SE(Ca^{2+}) = 8.80cmol(+)/kg, [5]SE(Na^+) = 2.70cmol(+)/kg, [6]SE(K^+) = 0.20cmol(+)/kg, [7]SE(Mg^{2+}) = 4.90cmol(+)/kg, [8]SE(Ca^{2+}) = 6.25cmol(+)/kg.*

Determination 1					
Total CEC	**Na^+ [1]**	**K^+ [2]**	**Mg^{2+} [3]**	**Ca^{2+} [4]**	**Sample**
93.10	19.20	1.10	19.30	52.50	**Febex ABM 2**
96.80	*25.60*	*2.60*	*33.70*	*34.90*	***Febex Untreated***
Determination 2					
Total CEC	**Na^+ [5]**	**K^+ [6]**	**Mg^{2+} [7]**	**Ca^{2+} [8]**	**Sample**
93.60	20.50	1.90	23.90	47.30	**Febex ABM 2**
96.70	***25.90***	***2.30***	***33.70***	***34.80***	***Febex Untreated***

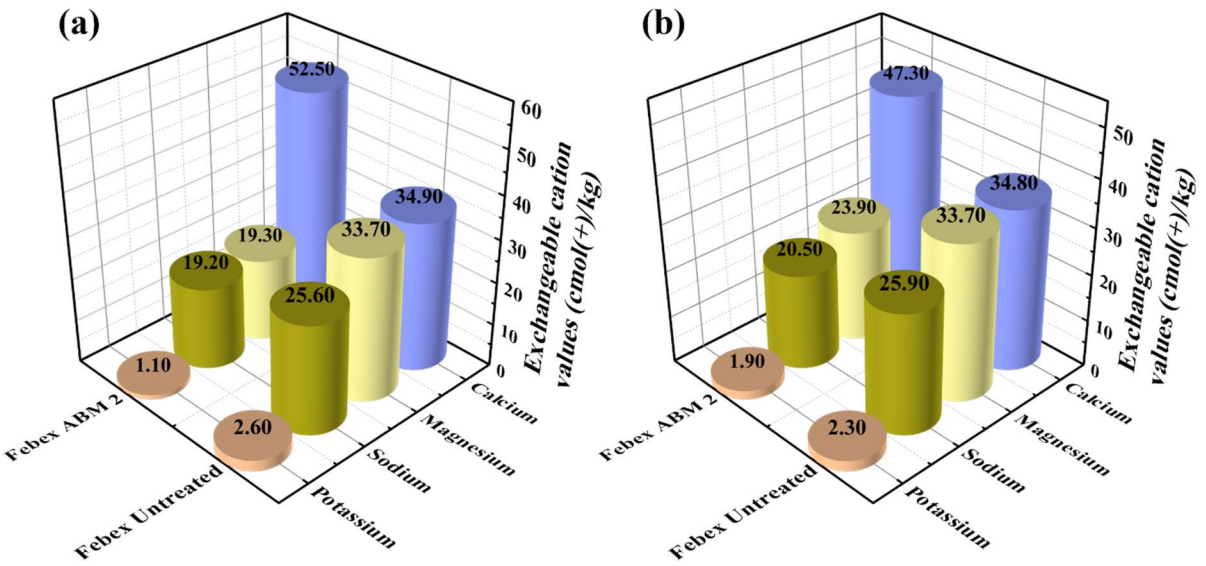

Figure 5.5*: (a)-(b) Results of exchangeable cation analysis (cmol(+)/kg) in two determinations conducted in the areas of immediate contact with the heater of Febex ABM 2 sample, and results obtained from the untreated Febex sample.*

As noted in the CEC values from the MX-80 ABM 2 sample, the Febex ABM 2 sample shows a replacement of Na^{+} by Ca^{2+} (Table 5.5 and Figure 5.5). However, the concentration of Mg^{2+} decreases with respect to the reference sample, entailing an overall decrease of the total CEC in determination 1 and 2 (Table 5.5). As already stated in the MX-80 ABM 2 sample conclusions, the decrease of the total CEC could have been caused by the incorporation of Fe^{2+} in the exchange complex.

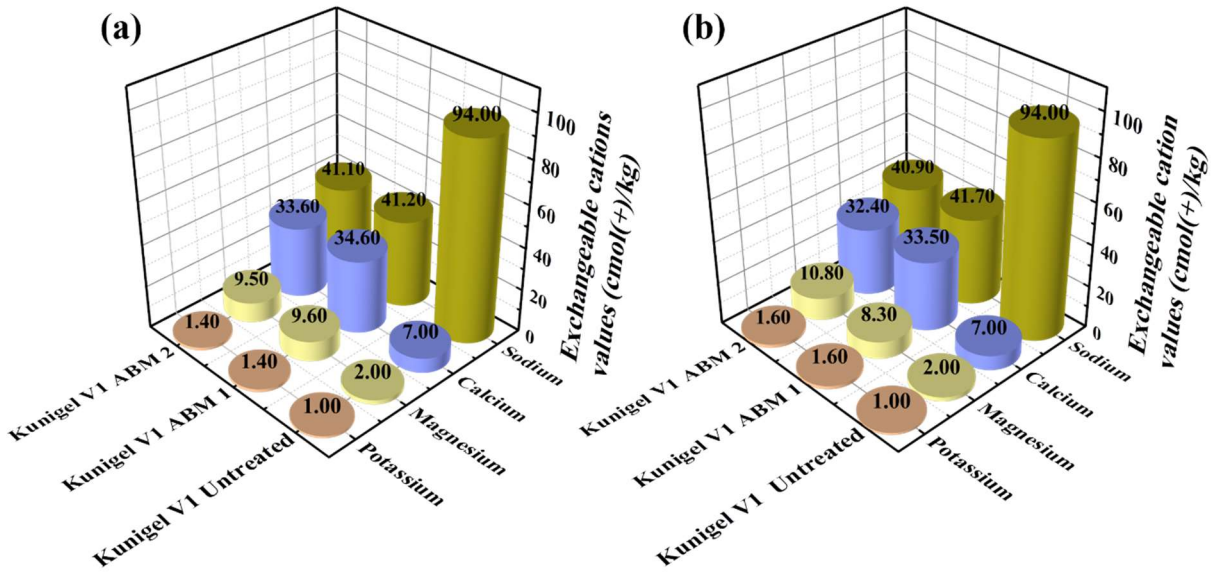

Figure 5.6: *(a)-(b) Results of exchangeable cation analysis (cmol(+)/kg) in two determinations conducted in the areas of immediate contact with the heater of Kunigel V1 samples from parcels 1 and 2, and results obtained from the untreated Kunigel V1 sample.*

Table 5.6: *Results of exchangeable cation values variation (measured in cmol(+)/kg) estimated in Kunigel V1 from parcels 1 and 2, and untreated samples.* $^{[1]}SE(Na^{+})$ *= 11.95cmol(+)/kg,* $^{[2]}SE(K^{+})$ *= 0.13cmol(+)/kg,* $^{[3]}SE(Mg^{2+})$ *= 2.52cmol(+)/kg,* $^{[4]}SE(Ca^{2+})$ *= 9.03cmol(+)/kg,* $^{[5]}SE(Na^{+})$ *= 11.90cmol(+)/kg,* $^{[6]}SE(K^{+})$ *= 0.20cmol(+)/kg,* $^{[7]}SE(Mg^{2+})$ *= 2.61cmol(+)/kg,* $^{[8]}SE(Ca^{2+})$ *= 8.65cmol(+)/kg.*

Determination 1					
Total CEC	**Na^{+} [1]**	**K^{+} [2]**	**Mg^{2+} [3]**	**Ca^{2+} [4]**	**Sample**
86.80	41.20	1.40	9.60	34.60	**Kunigel V1 ABM 1**
85.60	41.10	1.40	9.50	33.60	**Kunigel V1 ABM 2**
87.00	*77.00*	*1.00*	*2.00*	*7.00*	***Kunigel V1 Untreated***
Determination 2					
Total CEC	**Na^{+} [5]**	**K^{+} [6]**	**Mg^{2+} [7]**	**Ca^{2+} [8]**	**Sample**
85.10	41.70	1.60	8.30	33.50	**Kunigel V1 ABM 1**
85.70	40.90	1.60	10.80	32.40	**Kunigel V1 ABM 2**
87.00	*77.00*	*1.00*	*2.00*	*7.00*	***Kunigel V1 Untreated***

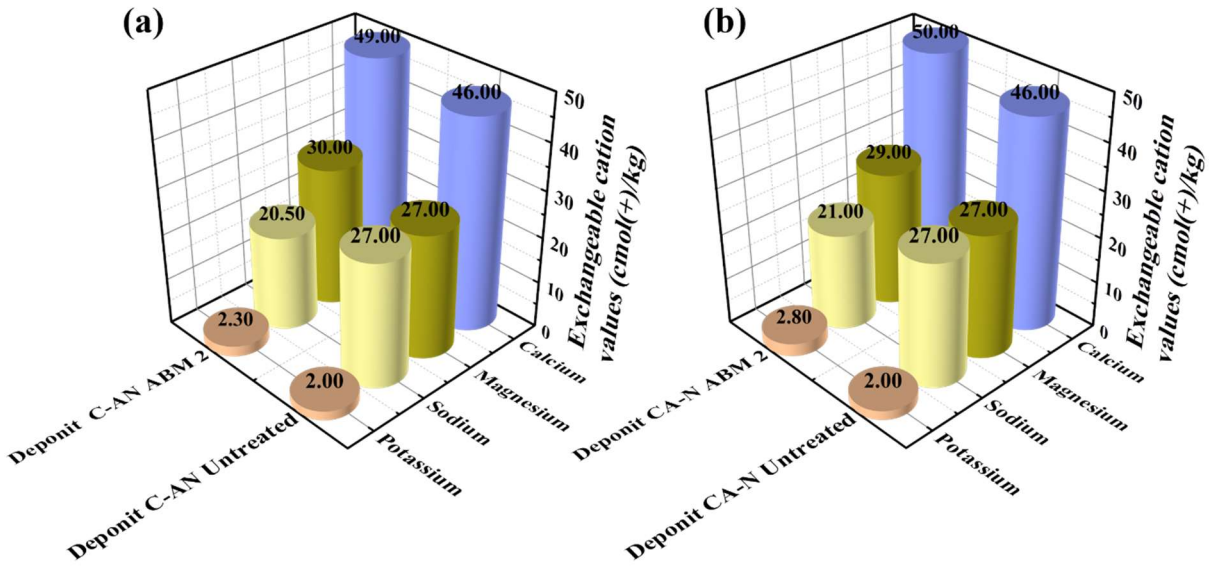

Figure 5.7: *(a)-(b) Results of exchangeable cation analysis (cmol(+)/kg) in two determinations conducted in the areas of immediate contact with the heater of Deponit C-AN ABM 2 sample, and results obtained from the untreated Deponit C-AN sample.*

Figure 5.6 and Table 5.6 present the CEC data obtained from Kunigel V1 ABM 1 and 2 samples in comparison with the reference sample. As observed in the MX-80 and Febex samples from the package 2, there is a clear replacement of Na^{+} by Ca^{2+}, as well as a replacement of Ca^{2+} possibly by Mg^{2+}. Besides, the concentration of K^{+} in the exchange complex in the Kunigel V1 samples is slightly higher than the recorded in the reference material. Nevertheless, the

variation in K^+ concentration corresponds well with other literature sources that analysed the same bentonite [85], [169].

Table 5.7: *Results of exchangeable cation values variation (measured in cmol(+)/kg) estimated in Deponit C-AN ABM 2 and untreated samples.* $^{[1]}SE(Na^+) = 3.25cmol(+)/kg$, $^{[2]}SE(K^+) = 0.15cmol(+)/kg$, $^{[3]}SE(Mg^{2+}) = 1.50cmol(+)/kg$, $^{[4]}SE(Ca^{2+}) = 1.50cmol(+)/kg$, $^{[5]}SE(Na^+) = 3.00cmol(+)/kg$, $^{[6]}SE(K^+) = 0.40cmol(+)/kg$, $^{[7]}SE(Mg^{2+}) = 1.00cmol(+)/kg$, $^{[8]}SE(Ca^{2+}) = 2.00cmol(+)/kg$.

Determination 1					
Total CEC	**Na^+ [1]**	**K^+ [2]**	**Mg^{2+} [3]**	**Ca^{2+} [4]**	**Sample**
101.80	20.50	2.30	30.00	49.00	**Deponit C-AN ABM 2**
102.00	*27.00*	*2.00*	*27.00*	*46.00*	***Deponit C-AN Untreated***
Determination 2					
Total CEC	**Na^+ [5]**	**K^+ [6]**	**Mg^{2+} [7]**	**Ca^{2+} [8]**	**Sample**
102.80	21.00	2.80	29.00	50.00	**Deponit C-AN ABM 2**
102.00	*27.00*	*2.00*	*27.00*	*46.00*	***Deponit C-AN Untreated***

Figure 5.7 and Table 5.7 show the CEC determinations of Deponit C-AN both in the experimental sample (package 2) and the reference material. From CEC determinations, in the experimental and reference sample and in accordance with the observations from the previous samples, a replacement of Na^+ by Ca^{2+} and, in lesser degree, of Ca^{2+} by Mg^{2+} has occurred.

Overall, exchangeable cation analyses performed in each bentonite sample showed a clear exchange of Na^+ possibly by Ca^{2+} and Ca^{2+} by Mg^{2+} in areas close to the heater. These results are in accordance with that observed in the BM-B-41-1 sample (Febex bentonite in contact with the liner) form the Febex experiment. Therefore, it is logical to conclude that cation migration and redistribution of cations has occurred in those areas of the clayey matrix that have been in direct contact with the heater liner, as observed by Wilson et al. [136] on samples examined from parcel 1, and by Torres et al. [138] on several samples examined from the Febex in-situ test. However, the major cation exchanged in the Febex, Kunigel V1 and Deponit C-AN samples was Ca^{2+}, compared to Mg^{2+} in sample MX-80. The partial replacement observed of Na^+ observed in MX-80 and Kunigel V1 samples, bentonites of sodium nature, might have induced a reduction in their swelling capability. Since the expandable capability of sodium bentonites due to the presence of monovalent cations in the interlayer is approximately six times greater than calcium bentonites, whose plasticity and swelling properties are expected to be lower [173]. The partial replacement of Na^+ by Ca^{2+} in the interlayer space might have impaired their desired swelling properties.

5.2.4 X-ray diffraction studies performed on bentonite samples in contact with the experimental iron canister

XRD analysis was conducted to identify any mineral alteration and/or formation of new mineral phases during progression of the ABM in-situ test. As a prior analysis, the (001) reflection was studied, aiming to examine the nature of the smectite component, and identify any possible alteration and/or transformation experienced by the samples over the experiment duration. The typical spacing of the 001 reflection of smectites ranges from 12Å to 15Å, and initially depends on the ambient relative humidity and the nature of the cations occupying the interlayer space [241]. Table 5.8 and Figure 5.8 display values of the 001 spacing of each bentonite sample from the ABM in-situ test.

Table 5.8: *001 spacings values of ABM samples and reference materials. [1]Standard error (SE_{MX-80}) = 1.43%, [2]Standard error (SE_{Febex}) = 0.19%, [3]Standard error ($SE_{Kunigel\ V1}$) = 0.84%, [4]Standard error ($SE_{Deponit\ C-AN}$) = 0.40%.*

Sample	d-spacing (Å)
MX-80 Untreated[1]	12.03
MX-80 ABM 2[1]	14.89
Febex Untreated[2]	14.62
Febex ABM 2[2]	14.99
Kunigel V1 Untreated[3]	12.45
Kunigel V1 ABM 1[3]	14.98
Kunigel V1 ABM 2[3]	14.98
Deponit C-AN Untreated[4]	14.17
Deponit C-AN ABM 2[4]	14.96

Table 5.8 and Figures 5.8 (a) and (c) present results derived from the 001 spacing analysis of MX-80 and Kunigel V1. The basal spacing results show a shift in position for both sodium bentonites that could be explained due to the displacement of the interlayer Na^+ by Ca^{2+} and/or Mg^{2+} and the hydration state of the samples. Table 5.8 and Figures 5.8 (b) and (d) show results of the 001 reflection analyses of Febex and Deponit C-AN samples. In contrast to the shifts observed in the sodium bentonites, the calcium bentonites show values close to those observed in the untreated materials, i.e. little or no change had occurred.

XRD was also utilised to determine the presence of iron phases and derived possible alteration and/or transformation that samples could have undergone after several years of being heating

in the experiment. Preliminary random powder diffraction of unaltered samples was carried out and, subsequently, comparative analysis was made with the experimental samples to provide semi-quantitative data pf their bulk mineralogy. Results of random powder diffraction are presented in Figure 5.9 and Table 5.9.

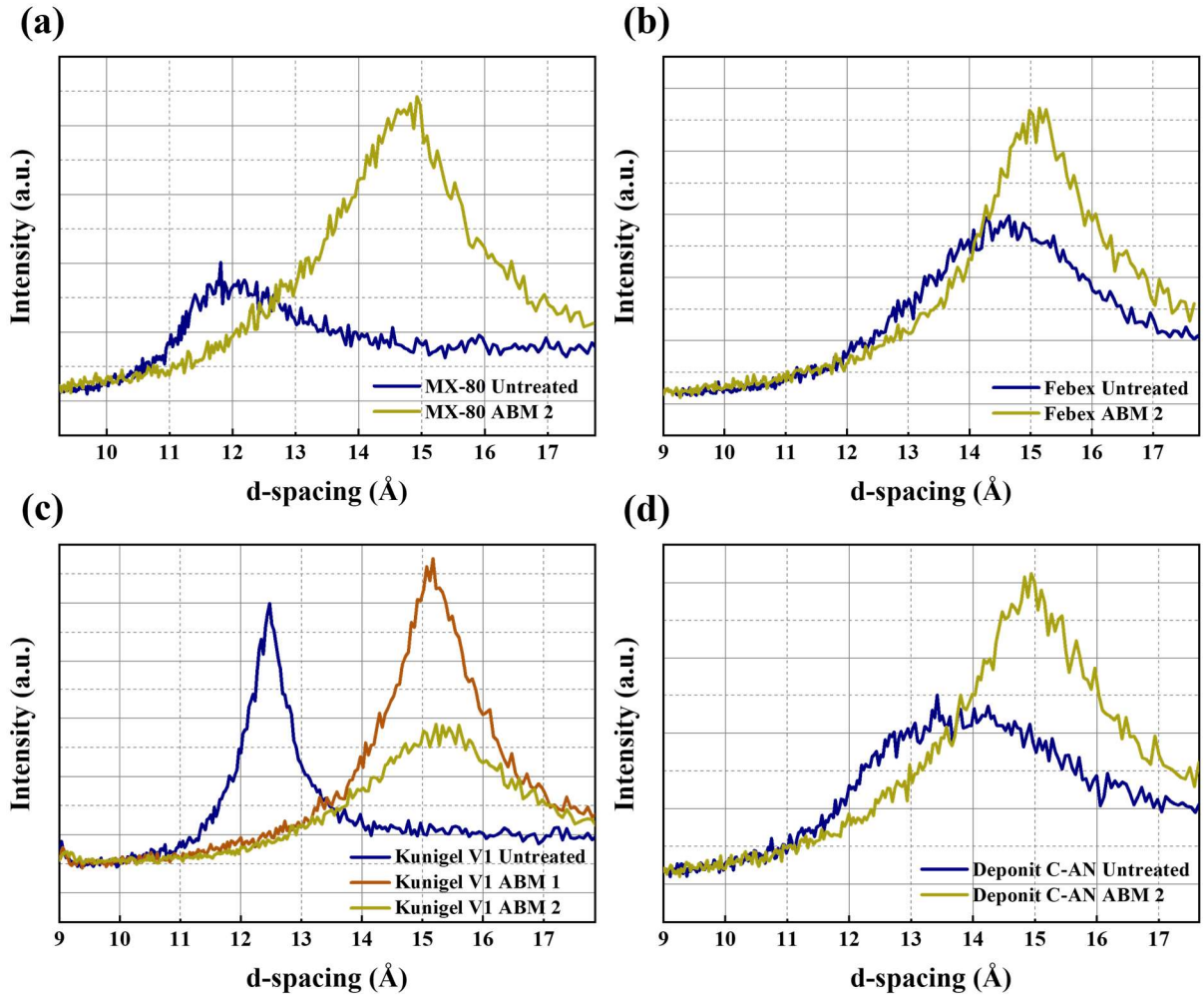

Figure 5.8: *(a) 001 spacing of MX-80 ABM 2 sample and untreated material. (b) 001 spacing of Febex ABM 2 sample and untreated material. (c) 001 spacing of Kunigel V1 ABM 1 and ABM 2 samples and untreated material. (d) 001 spacing of Deponit C-AN ABM 2 and untreated sample.*

Overall, from XRD analysis (Table 5.9 and Figure 5.9), no appreciable differences in mineralogy between the pristine materials and the experimental samples were detected. Therefore, based on mineralogical compositional, it can be affirmed that the ABM and reference samples were similar. The presence of iron (Table 5.9) was detected in samples MX-80 and Deponit C-AN but, it can be stated that this iron was present as a natural component of the bentonite since it was also present in the virgin materials. Additionally, no evidence of alteration or presence of new minerals was detected.

Table 5.9: *Mineralogy of ABM and untreated samples. [1]Standard error ($SE_{MX\text{-}80\ Quartz}$) = 0.28%, [2]Standard error ($SE_{Febex\ Quartz}$) = 2.50%, [3]Standard error ($SE_{Kunigel\ V1\ Quartz}$) = 1.86%, [4]Standard error ($SE_{Deponit\ C\text{-}AN\ Quartz}$) = 0.50%, [5]Standard error ($SE_{MX\text{-}80\ Tridymite}$) = 0.50%, [6]Standard error ($SE_{Febex\ Tridymite}$) = 0.50%, [7]Standard error ($SE_{Deponit\ C\text{-}AN\ Tridymite}$) = 0.50%, [8]Standard error ($SE_{MX\text{-}80\ Phyll}$) = 1.50%, [9]Standard error ($SE_{Febex\ Phyll}$) = 2.00%, [10]Standard error ($SE_{Kunigel\ V1\ Phyll}$) = 0.88%, [11]Standard error ($SE_{Deponit\ C\text{-}AN\ V1\ Phyll}$) = 0.50%, [12]Standard error ($SE_{MX\text{-}80\ Calcite}$) = 0.50%, [13]Standard error ($SE_{Kunigel\ V1\ Calcite}$) = 1.67%, [14]Standard error ($SE_{Deponit\ C\text{-}AN\ Calcite}$) = 0.50%, [15]Standard error ($SE_{Deponit\ C\text{-}AN\ Dolomite}$) = 0.50%, [16]Standard error ($SE_{Deponit\ C\text{-}AN\ Gypsum}$) = 0.50%, [17]Standard error ($SE_{MX\text{-}80\ Goethite}$) = 0.50%, [18]Standard error ($SE_{Kunigel\ V1\ Clinop}$) = 0.58%, [19]Standard error ($SE_{Kunigel\ V1\ Analcime}$) = 0.41%, [20]Standard error ($SE_{MX\text{-}80\ Plagio}$) = 0.50%, [21]Standard error ($SE_{Febex\ Plagio}$) = 0.50%, [22]Standard error ($SE_{Kunigel\ V1\ Plagio}$) = 0.58%, [23]Standard error ($SE_{Kunigel\ V1\ Cristob}$) = 0.33%.*

Mineral (%)	MX-80 Untreated	MX-80 ABM 2	Febex Untreated	Febex ABM 2	Kunigel V1 Untreated	Kunigel V1 ABM 1	Kunigel V1 ABM 2	Deponit C-AN Untreated	Deponit C-AN ABM 2
Quartz[1, 2, 3, 4]	4	8	2	7	31	37	32	1	2
Tridymite[5, 6, 7]	4	5	4	3	-	-	-	5	6
Phyllosilicates[8, 9, 10, 11]	79	76	88	84	55	53	52	77	76
K-feldspars	-	-	-	-	-	-	-	4	4
Calcite[12, 13, 14]	1	1	1	2	1	1	6	6	5
Dolomite[15]	-	-	-	-	1	1	1	2	1
Gypsum[16]	1	1	-	-	-	-	-	1	2
Goethite[17]	2	1	-	-	-	-	-	2	2
Magnetite	1	1	-	-	-	-	-	1	1
Pyrite	-	-	-	-	1	1	1	1	1
Clinoptilolite (zeolite)[18]	-	-	-	-	4	2	3	-	-
Analcime[19]	-	-	-	-	1	-	1	-	-
Plagioclase[20, 21, 22]	7	8	4	3	6	5	4	-	-
Cristobalite[23]	1	1	1	1	1	-	-	-	-

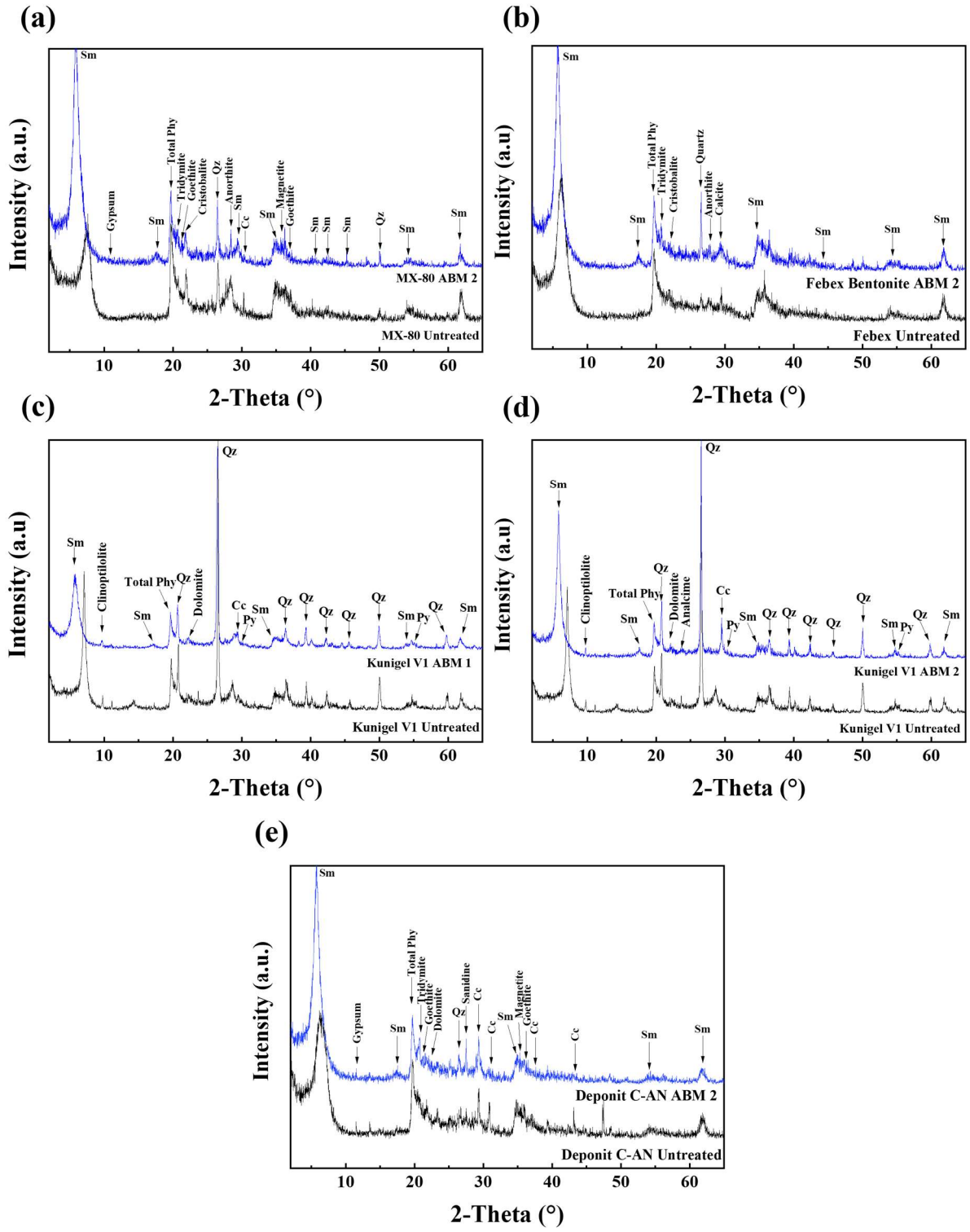

Figure 5.9: *(a) XRD pattern of MX-80 (ABM 2) and reference sample. (b) XRD pattern of Febex (ABM 2) and reference sample. (c) XRD pattern of Kunigel V1 (ABM 1) and reference sample. (d) XRD pattern of Kunigel V1 (ABM 2) and reference sample. (e) XRD pattern of Deponit C-AN (ABM 1) and reference sample. Sm: Smectite, Total Phy: Total phyllosilicates, Qz: Quartz, Cc: Calcite.*

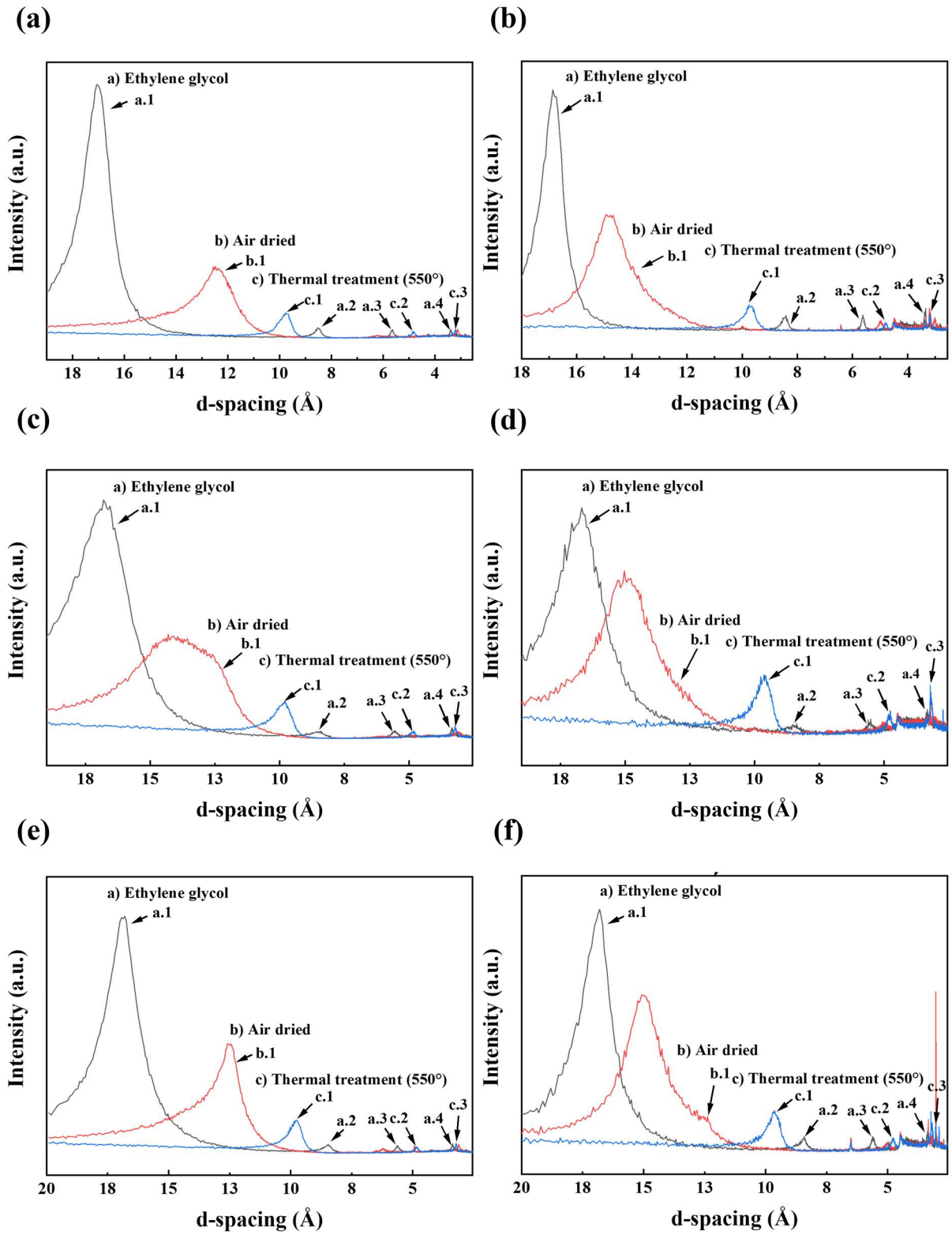

Figure 5.10: *(a) OM patterns of MX-80 Untreated. (b) OM patterns of MX-80 ABM 2. (c) OM patterns of Febex Untreated. (d) OM patterns of Febex ABM 2. (e) OM patterns of Deponit C-AN Untreated. (f) OM patterns of Deponit C-AN ABM 2.*

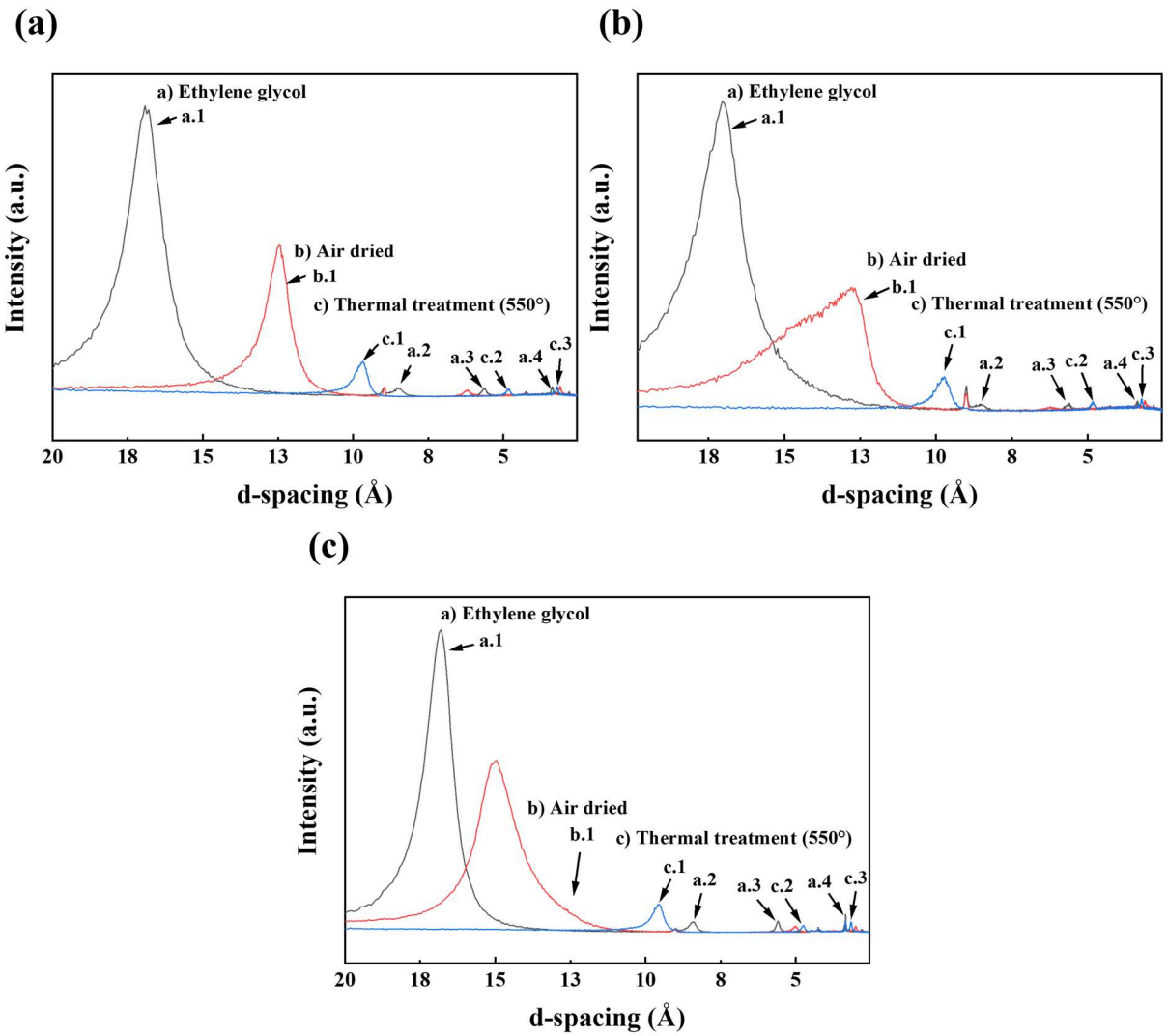

Figure 5.11: *(a) OM patterns of Kunigel V1 Untreated. (b) OM patterns of Kunigel V1 ABM 1. (c) OM patterns of Kunigel V1 ABM 2.*

Table 5.10: *d-spacing values of air-dried patterns.*

Position in Figures 5.10 and 5.11	MX-80 Untreated	MX-80 ABM 2	Febex Untreated	Febex ABM 2	Kunigel V1 Untreated	Kunigel V1 ABM 1	Kunigel V1 ABM 2	Dep. C-AN Untreated	Dep. C-AN ABM 2
	d-spacing (Å)								
b.1 d(001)	12.47	12.71	12.63	12.83	12.45	12.84	12.68	12.51	12.91

The study of clay mineralogy, and, thus, the identification of any alteration and/or transformation of the smectite component of each ABM samples, was carried out by oriented mounts (OM) preparation, as described in section 4.2.4. Figures 5.10 and 5.11, and Tables 5.10

and 5.12, show the results obtained from OM. As a prior identification of the smectitic nature of the samples, the values of the 001 reflection of air-dried patterns were analysed, using Table 4.10. Figures 5.10 and 5.11, and Table 5.10, collect the air-dried sample treatment data. From the recorded patterns (Figure 5.10 and 5.11 and Table 5.10), it can be observed that the samples were in a 1-2 hydration state, confirming, therefore, the presence of smectite minerals.

Table 5.11: *d-spacing values of ethylene glycol patterns.*

Position in Figures 5.10 and 5.11	MX-80 Untreated	MX-80 ABM 2	Febex Untreated	Febex ABM 2	Kunigel V1 Untreated	Kunigel V1 ABM 1	Kunigel V1 ABM 2	Dep. C-AN Untreated	Dep. C-AN ABM 2
	d-spacing (Å)								
a.1 d(001)	16.79	16.82	16.99	16.69	16.89	16.82	16.96	16.87	16.81
a.2 d(002)	8.55	8.46	8.50	8.49	8.47	8.42	8.49	8.47	8.43
a.3 d(003)	5.69	5.62	5.55	5.53	5.62	5.62	5.56	5.53	5.57
a.4 d(005)	3.40	3.34	3.34	3.34	3.36	3.34	3.34	3.37	3.34

Table 5.12: *d-spacing values of thermal treatment patterns.*

Position in Figures 5.10 and 5.11	MX-80 Untreated	MX-80 ABM 2	Febex Untreated	Febex ABM 2	Kunigel V1 Untreated	Kunigel V1 ABM 1	Kunigel V1 ABM 2	Dep. C-AN Untreated	Dep. C-AN ABM 2
	d-spacing (Å)								
c.1 d(001)	9.80	9.78	9.82	9.76	9.70	9.71	9.74	9.70	9.70
c.2 d(002)	4.85	4.81	4.87	4.86	4.83	4.78	4.84	4.85	4.80
c.3 d(003)	3.21	3.20	3.22	3.22	3.22	3.22	3.22	3.22	3.22

The identification of the smectite component was also performed for glycolated samples, since the use of ethylene glycol allows the development of stable two-layer complexes. To do this, the reflection observed around ~16Å (a.1) was examined (Figures 5.10 and 5.11 and Table 5.11). Upon glycolation, this characteristic reflection shifts position towards higher

values ranging between 16-17Å. In addition, the reflections observed around ~8Å (a.2), ~5Å (a.3) and ~3Å (a.4) confirmed the smectitic nature of MX-80, Kunigel V1 and Deponit C-AN samples. This result matches those already reported in the literature [169], [175], [178]. In the case of Febex samples, the confirmation of mixed-layers was carried out following the guidelines provided by Moore & Reynolds [196], as described in section 4.2.4, and the presence of small amounts of the illite were semi-quantified using Table 4.15, concluding that the I/S rating is about 10-15%. Finally, heated samples at 550°C were analysed to confirm their smectitic nature (Figures 5.10 and 5.11 and Table 5.12). When samples are subjected to high temperatures their layers tend to collapse as water is expelled and a new basal spacing ~9Å (c.1) typically confirms the presence of smectite.

From XRD analysis of ABM in-situ specimens, it was concluded that the bulk mineralogy point was the same as the starting materials. Once analysed, the following clay mineralogy observations were made: (*i*) MX-80: 100% of the phyllosilicates present are dioctahedral-type smectite; (*ii*) Febex: Based on XRD, the presence of illite-smectitic mixed layers with around 10-15% of illite layers was confirmed; (*iii*) Kunigel V1: 100% of the phyllosilicates present are dioctahedral-type smectite; and (*iv*) Deponit C-AN: 100% of the phyllosilicates present in the untreated and ABM samples are dioctahedral-type smectite.

The observations described above correspond well with other literature sources that analysed the same bentonites through XRD [81], [169], [175], [178].

5.2.5 High resolution diffraction on ABM bentonite samples using synchrotron x-rays

As previously described in section 4.2.6, the use of synchrotron x-rays to reduce the collection time of a diffraction pattern and achieve better signal-to-noise ratio allows the acquisition of highly-resolved diffraction patterns with a reduced background noise in comparison with the diffraction patterns obtained by laboratory-based instruments, enabling the visualisation of small peaks that could have been masked by the fluorescence of the iron phases present in the clayey matrix.

Data collected on beamline I11 (Diamond Light Source, UK) is presented in Figures 5.12 to 5.15 and Table 5.13. Data were recorded using a 1x1mm beam with a wavelength of 0.8245230Å over powdered samples embedded in microcapillaries of 0.5mm inner diameter

and between 40-50mm length. The estimation of mineral percentages (section 4.2.6) was carried our using the MATCH! phase identification programme for powder diffraction. MATCH! reports that the results have a standard deviation of ±10% of the calculated value [245].

Figure 5.15 and Table 5.13 display the results obtained from high-resolution diffraction of the reference MX-80 material and the MX-80 bentonite sample from parcel 2 of the ABM project. Firstly, the basic identification of the clay component in the bulk mineralogy was made according to the position of basal reflection 001. The 001 spacing of the reference sample showed a value of 12.46Å, indicating the sodium character of MX-80 bentonite, while the ABM sample displayed a value of 14.72Å, which is more similar to calcium bentonites. This observed increase of the basal spacing, suggests a possible a possible exchange of Na^{+} for Ca^{2+} or Mg^{2+}, as observed in the determinations of the exchangeable cations and conventional XRD. In addition, a broad peak at 3.02Å was observed. However, the nature of this broad peak could not be identified by the processing program. We concluded that this peak might be attributed to the presence of saponite, a trioctahedral smectite; more specifically to ferrosaponite, an Fe-dominant end-member of the beidellite-saponite series. This are a phases reported in other literature sources [287], [288]. The presence of goethite and magnetite was detected in both the experimental and reference samples. However, it can be said that the percentages of goethite and magnetite found in the experimental sample are the naturally occurring levels in the MX-80 bentonite.

Results of the Febex ABM sample are presented in Figure 5.16 and Table 5.13. The basal 001 reflections of the experimental and reference samples showed values of 14.29Å and 14.87Å respectively, indicating the calcic nature of the Febex bentonite. Additionally, the broad peak observed at 3.02Å was also present in the Febex bentonite, and it was also assigned to ferrosaponite [287], [288]. Iron phases, such as goethite and magnetite, were also present in the Febex ABM sample which are not mineralogical phases of the Febex bentonite. The results obtained from high resolution diffraction of Deponit C-AN and Kunigel V1 samples are presented in Figures 5.14 and 5.15 and Table 5.13. Due to the absence of a specific reference material, the data presented in Figures 5.14 and 5.15 are those of the ABM sample. The bulk mineralogy of the samples correlates well with the values reported from other literature sources on the same bentonites [169], [178]. The presence of goethite and magnetite was identified in each sample, and these results correlate with those obtained from laboratory diffraction.

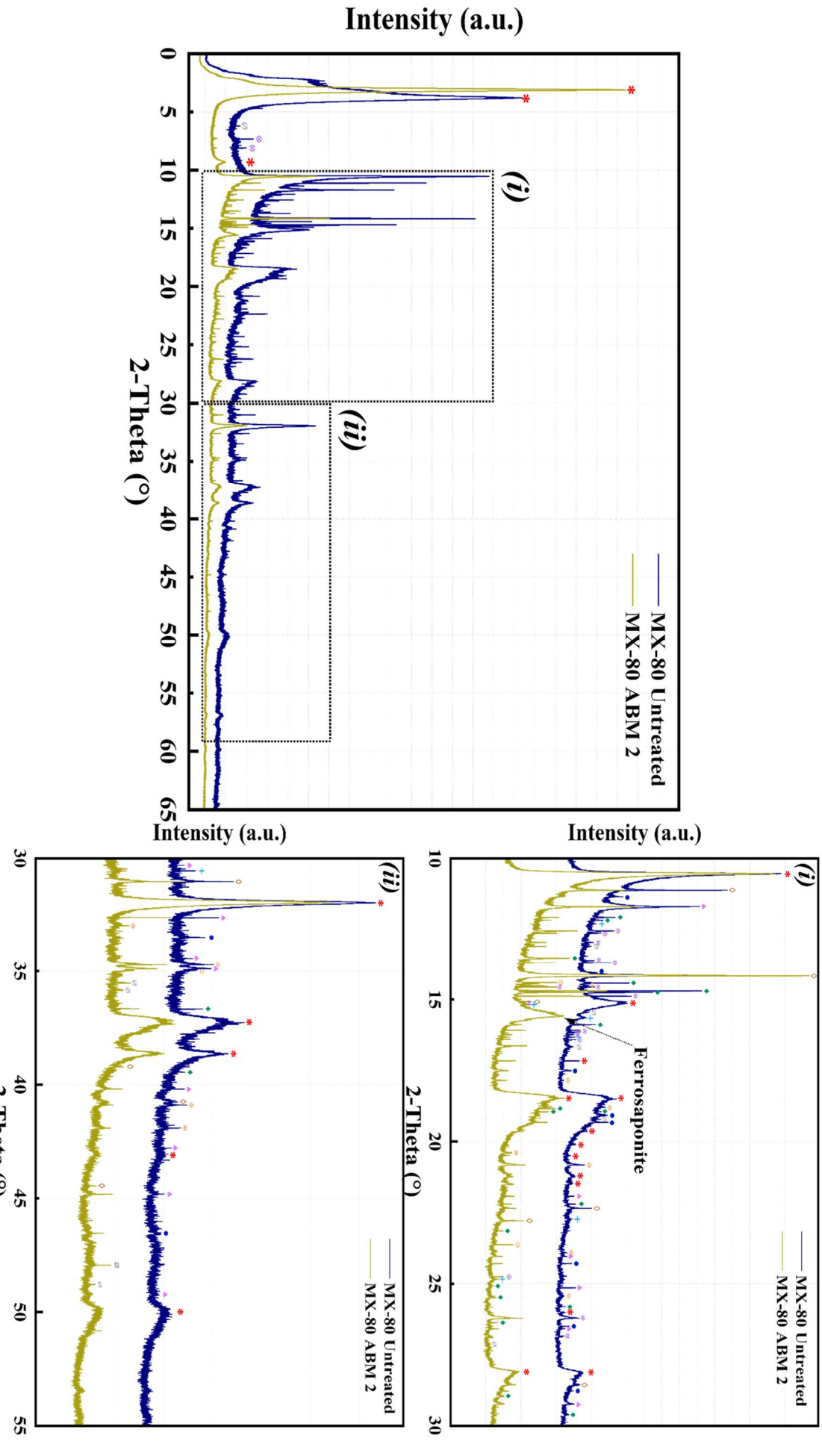

Figure 5.12: *XRD pattern of MX-80 ABM 2 sample, recorded on beamline I11 (Diamond Light Source).* ✱*: Montmorillonite;* ⊗*: Plagioclase;* o*: K-Feldspar;* ●*: Goethite;* ⊕*: Magnetite;* ◆*: Tridymite;* +*: Carbonate;* ♣*: Cristobalite;* ◇*: Quartz,* ∅*: Gypsum. (i) Region between 10° and 30° in 2θ. (ii) Region between 30° and 55° in 2θ.*

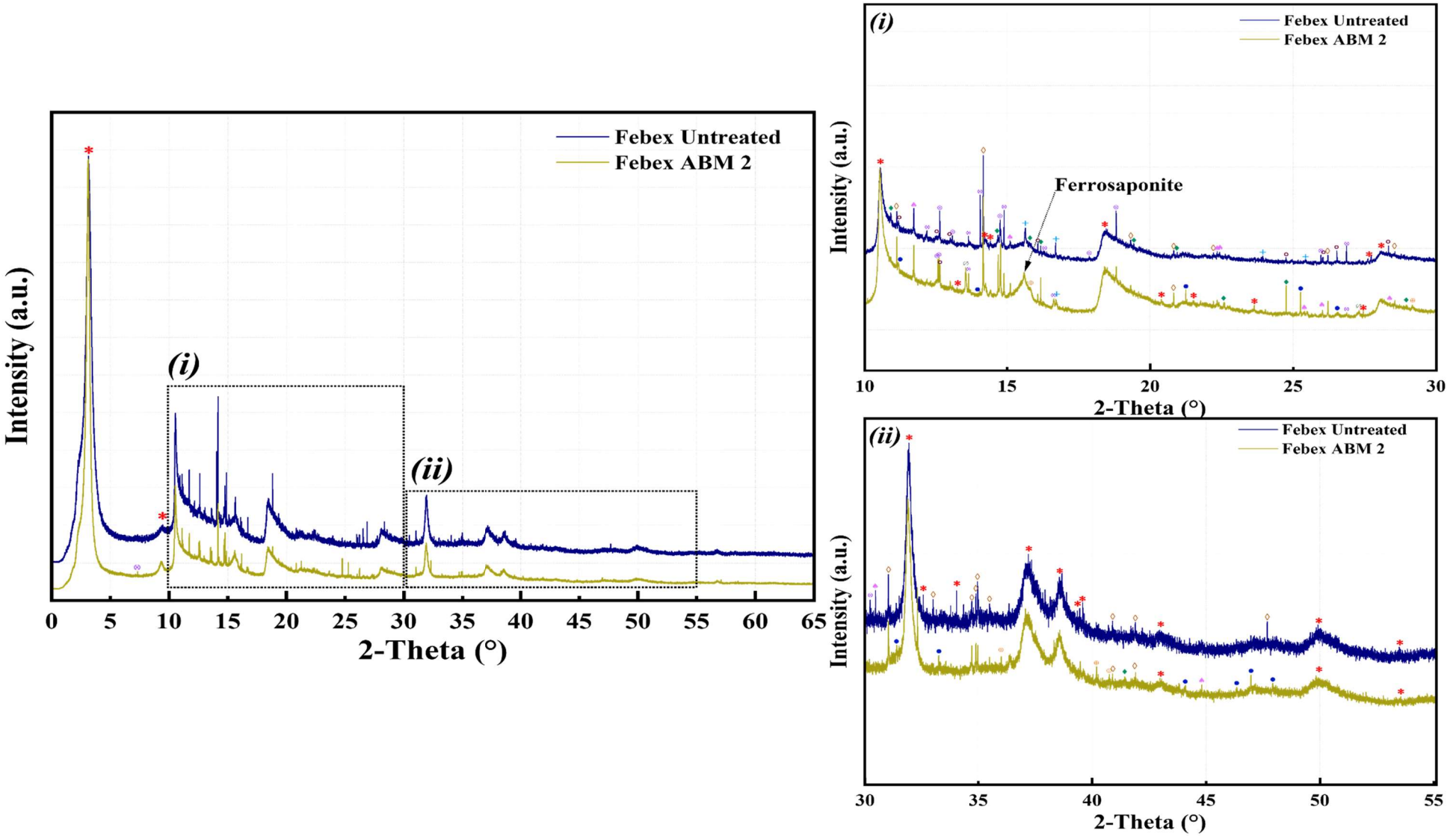

Figure 5.13: *XRD pattern of Febex ABM 2 sample, recorded on beamline I11 (Diamond Light Source).* ✱*: Montmorillonite;* ⊗*: Plagioclase;* o*: K-Feldspar;* ●*: Goethite;* ⊕*: Magnetite;* ♦*: Tridymite;* +*: Carbonate;* ♠*: Cristobalite;* ◊*: Quartz,* ∅*: Gypsum. (i) Region between 10° and 30° in 2θ. (ii) Region between 30° and 55° in 2θ.*

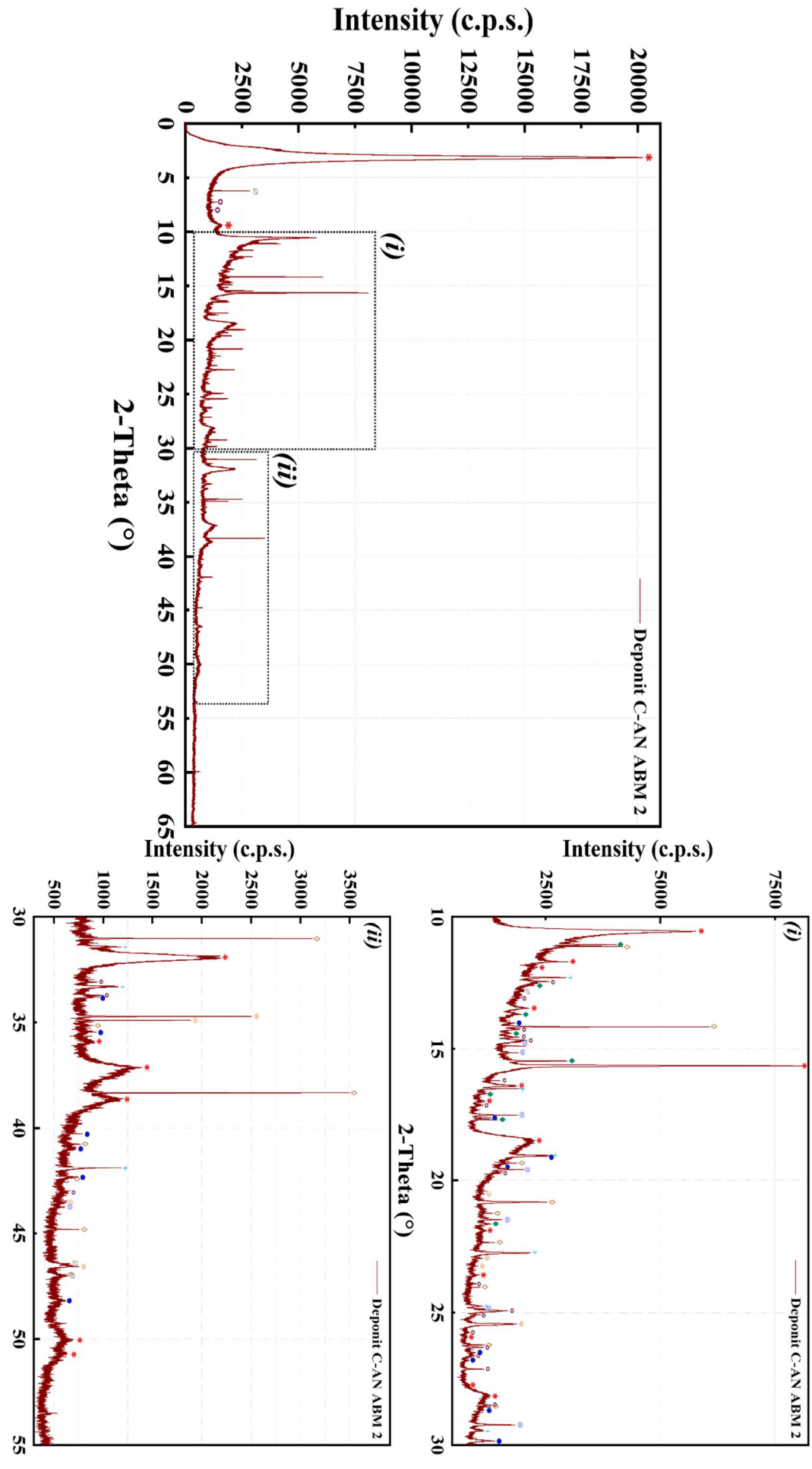

Figure 5.14: *XRD pattern of Deponit C-AN ABM 2 sample, recorded on beamline I11 (Diamond Light Source).* ✱*: Montmorillonite;* ⊗*: Plagioclase;* o*: K-Feldspar;* ●*: Goethite;* ⊕*: Magnetite;* ◆*: Tridymite;* +*: Carbonate;* ♣*: Cristobalite;* ◇*: Quartz,* ∅*: Gypsum;* ⊗*: Plagioclase. (i) Region between 10° and 30° in 2θ. (ii) Region between 30° and 55° in 2θ.*

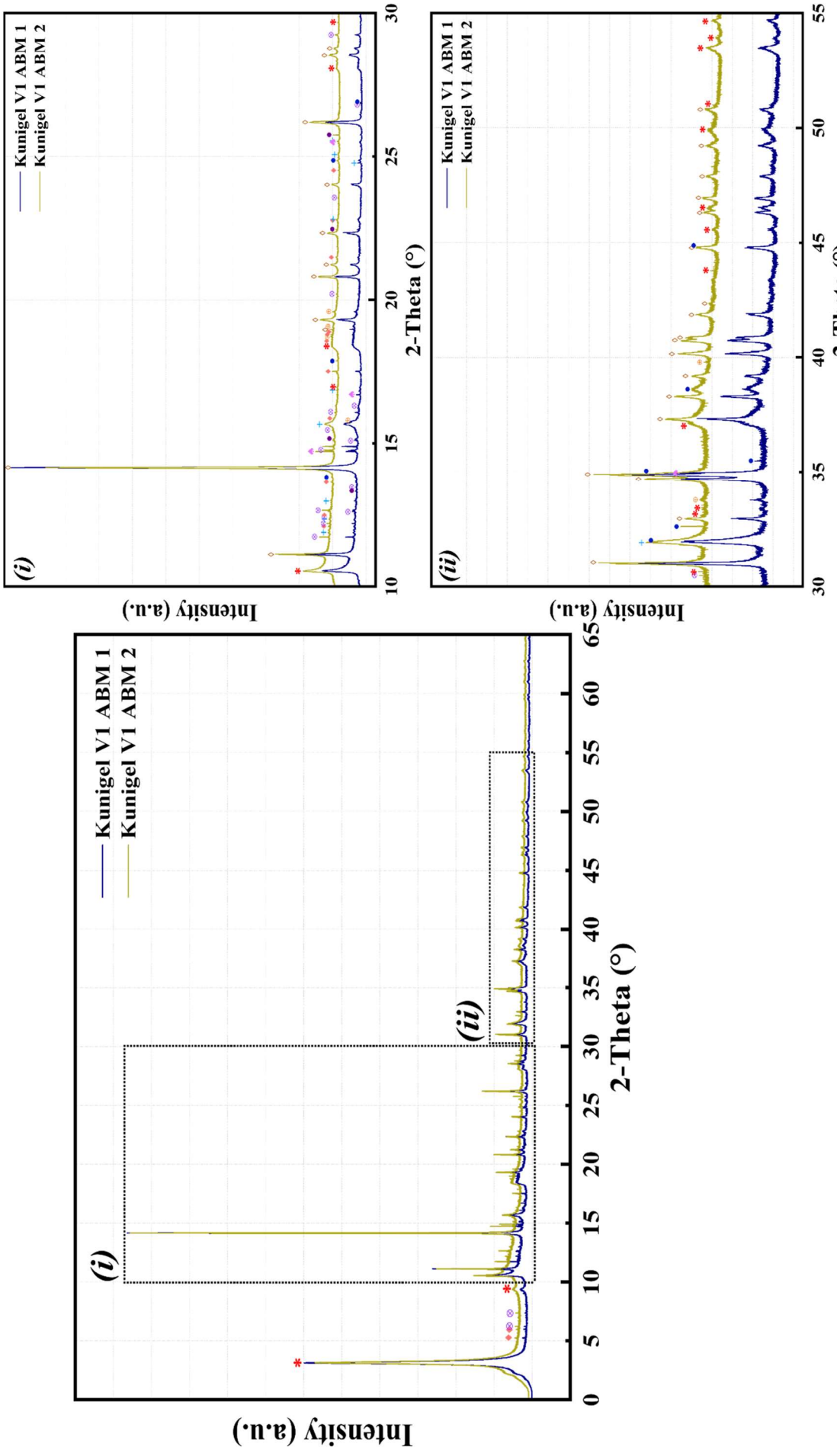

Figure 5.15: *XRD patterns of Kunigel V1 ABM 1 and 2 samples, recorded at 111 (Diamond Light Source). ✱: Montmorillonite; ⊗: Plagioclase; o: K-Feldspar; ●: Goethite; ⊕: Magnetite; ◆: Clinoptilolite; +: Carbonate; ✦: Cristobalite; ◇: Quartz, ●: Analcime. (i) Region between 10° and 30° in 2θ. (ii) Region between 30° and 55° in 2θ.*

Table 5.13: *Mineralogy of the ABM samples.*

Sample ID	Montmorillonite	Ferrosaponite	Trydimite	Cristobalite	Quartz	Plagioclase (albite/anorthite)	K-feldspar	Carbonate (calcite/dolomite)	Gypsum	Pyrite	Analcime	Clinoptilolite	Magnetite	Goethite
	%													
MX-80 Untreated	81.5	-	8.9	3.9	1.9	0.6	-	0.4	0.2	-	-	-	1.5	1.1
MX-80 ABM 2	82.6	3.0	9.9	0.2	1.5	0.8	-	0.7	0.3	-	-	-	0.7	0.3
Febex Untreated	87.7	-	3.6	2.6	2.8	2.1	1.4	1.8	-	-	-	-	-	-
Febex ABM 2	82.9	2.8	3.7	1.4	1.0	0.3	0.4	0.5	0.4	-	-	-	3.0	3.7
Deponit C-AN ABM 1	78.5	-	8.2	-	2.6	-	3.5	0.3	0.1	1.3	-	-	2.1	3.5
Kunigel V1 ABM 1	51.8	-	-	0.6	32.2	1.0	-	1.4	-	0.1	0.2	1.4	7.0	4.3
Kunigel V1 ABM 2	52.6	-	-	0.4	32.5	0.6	-	2.0	-	-	0.1	0.9	6.9	4.2

5.2.6 Fourier transform infrared spectroscopy analysis in the interface zones

As a part of the physicochemical evaluation of the ABM experimental samples, FTIR was utilised as a complementary technique to XRD and high resolution diffraction to evaluate the mineral composition, as well as the crystal chemistry. Therefore, the following subsections present comprehensive FTIR results of each bentonite sample from the ABM project.

5.2.6.1 MX-80 bentonite ABM parcel 2

Data presented in Table 5.14 and Figures 5.16 and 5.17 correspond with the ATR and KBr spectra recorded from MX-80 bentonite sample and untreated material.

Table 5.14: *ATR-FTIR and KBr-FTIR positions (cm^{-1}) and assignments of reference and MX-80 samples in mid-region of the spectra. Numbers in parentheses indicate band numbers in Figures 5.16 and 5.17.*

MX-80 Untreated		**Assignment**	**MX-80 AMB 2**	
ATR	**KBr**		**ATR**	**KBr**
Position (cm^{-1})			Position (cm^{-1})	
$3625^{(1)}$	$3632^{(1)}$	OH stretching of structural hydroxyl groups	$3625^{(1)}$	$3628^{(1)}$
-	$3433^{(2)}$	OH stretching of water	$3392^{(2)}$	$3436^{(2)}$
-	$2980^{(3)}$	C-H stretching vibration	$2978^{(3)}$	$2979^{(3)}$
$1634^{(4)}$	$1639^{(4)}$	OH deformation of water	$1633^{(4)}$	$1638^{(4)}$
-	-	Fe asymmetric vibration	-	$1428^{(5)}$
-	$1384^{(6)}$	C-H bending vibrations	-	$1384^{(6)}$
$1117^{(7)}$	$1117^{(7)}$	Si-O stretching (longitudinal mode)	$1117^{(7)}$	$1120^{(7)}$
$995^{(8)}$	$1047^{(8)}$	Si-O stretching	$997^{(8)}$	$1043^{(8)}$
$916^{(9)}$	$917^{(9)}$	δAlAlOH deformation	$916^{(9)}$	$919^{(9)}$
-	$880^{(10)}$	δAlFeOH deformation	-	$881^{(10)}$
$847^{(11)}$	$844^{(11)}$	δAlMgOH deformation	$844^{(11)}$	$843^{(11)}$
$795^{(12)}$	$797^{(12)}$	Si-O stretching of quartz and silica	$793^{(12)}$	$796^{(12)}$
$694^{(13)}$	$695^{(13)}$	Si-O-Al bending	$693^{(13)}$	$695^{(13)}$
$620^{(14)}$	$624^{(14)}$	Coupled Al-OH and Si-O, out of plane	$618^{(14)}$	$627^{(14)}$
$512^{(15)}$	$523^{(15)}$	Al-O-Si deformation	$512^{(15)}$	$523^{(15)}$
-	$467^{(16)}$	Si-O-Si deformation	-	$465^{(16)}$

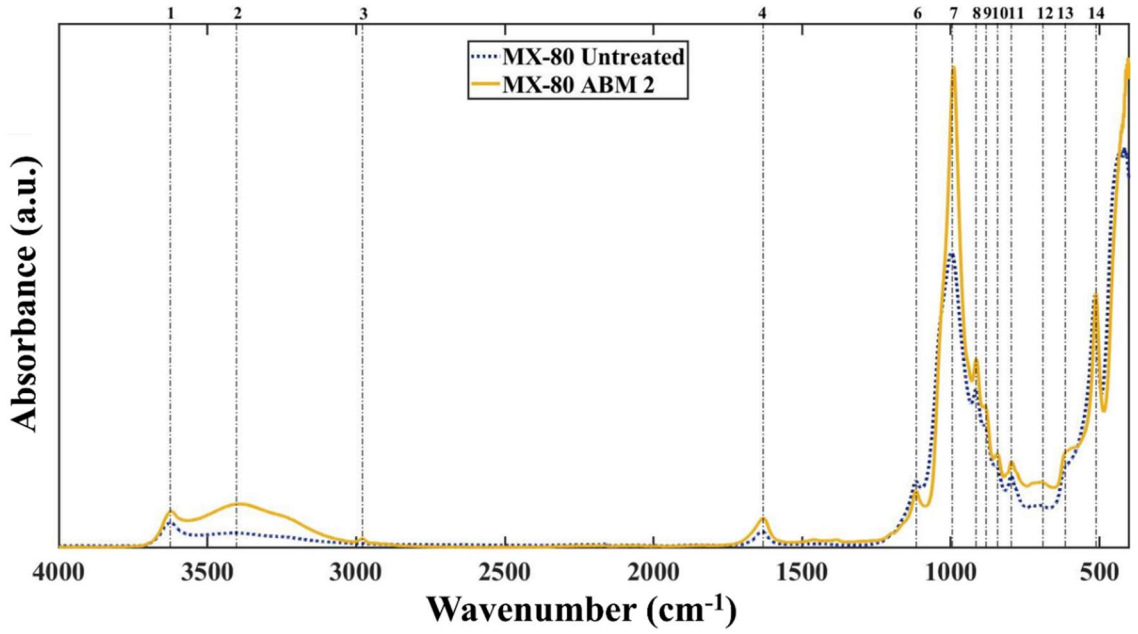

Figure 5.16: *ATR-FTIR spectra (4000-400cm^{-1}) of MX-80 ABM 2 and untreated samples. Peaks are indicated by dotted lines.*

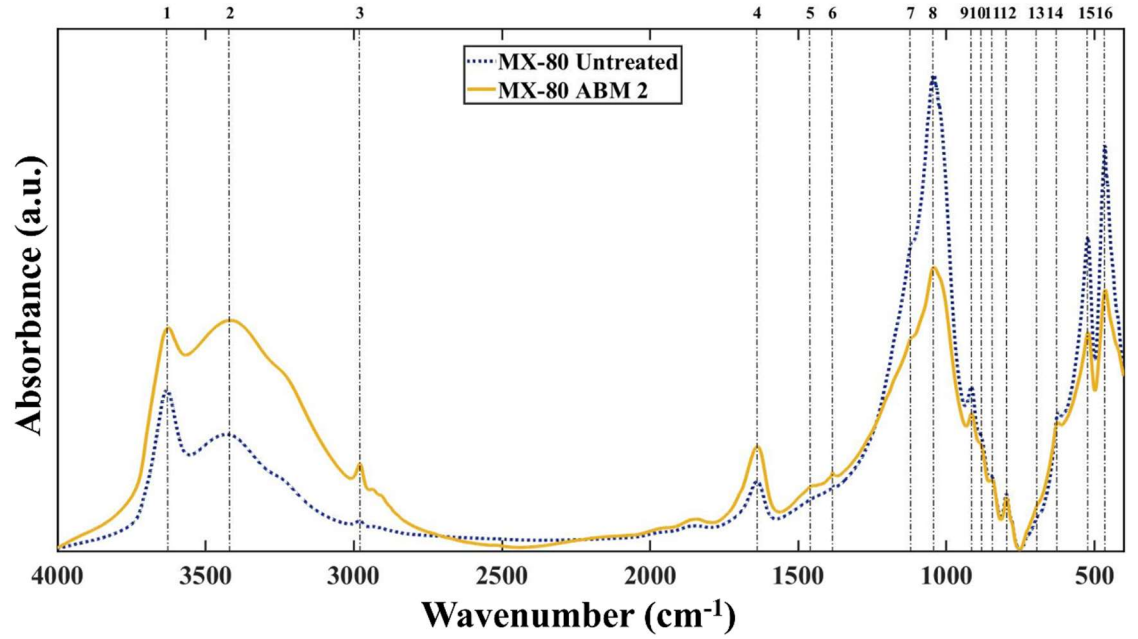

Figure 5.17: *KBr-FTIR spectra (4000-400cm^{-1}) of MX-80 ABM 2 and untreated samples. Peaks are indicated by dotted lines.*

Table 5.14 presents the corresponding bands of the mid-region of the spectra (4000-400cm^{-1}) of the MX-80 sample and unaltered bentonite recorded in ATR and KBr. Overall, the bands recorded by both FTIR preparation methods of the reference and experimental samples correlate very well, and it can be affirmed that montmorillonite is the dominant phase in both the pristine material and the in-situ test sample. A general description of the bands observed in both spectra is as follows. The well-resolved band observed at (1), in both ATR and KBr

spectra, is assigned to the OH-stretching vibration of structural hydroxyl groups. The broad band observed at (2) corresponds with the H_2O-stretching vibration with an overtone of the water bending vibration observed at (4). The bands observed at (3) and (6) could be explained due to the stretching and bending vibrations of CH groups owing to the presence of organic matter, although (6) was only observed in the KBR spectra. The broad band observed at (5) can be explained due to significant accumulation of inorganic carbon at the contact between the bentonite and simulated canister, and it might be associated with the Fe corrosion due to siderite formation, as already stated by Kaufhold et al. [289]. The intense bands observed at (7) and (16), the latter only apparent in the KBr spectrum, correspond with the stretching (longitudinal mode) and bending of the Si respectively. The sharp band at (8) correlates with the characteristic Si-O stretching vibration of octahedral smectites.

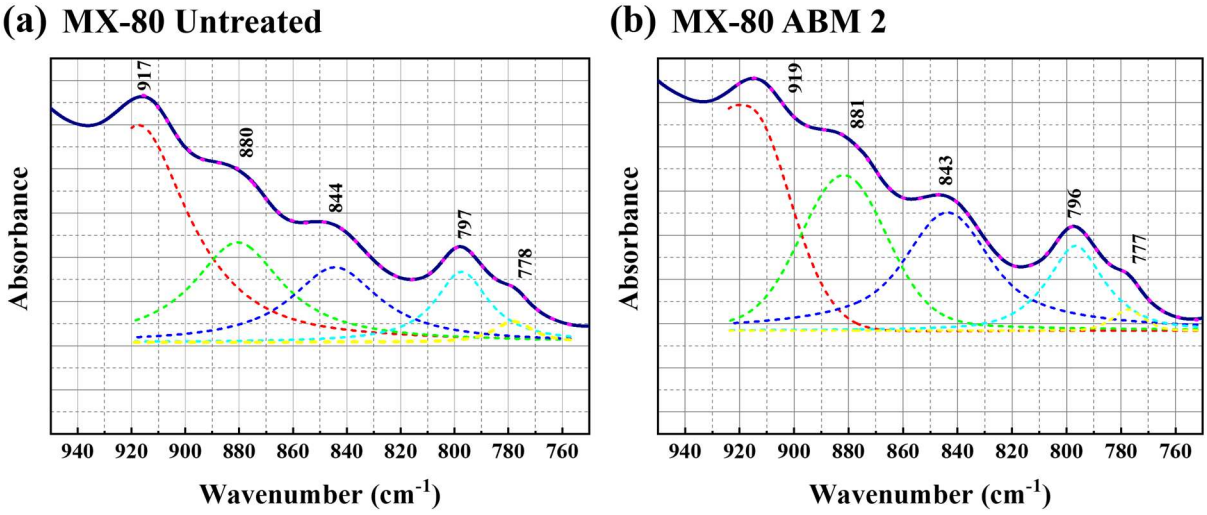

Figure 5.18: *(a)-(b) Fitted band positions corresponding with the octahedral cation-OH deformation bands of MX-80 untreated and ABM 2 samples in the KBr-FTIR spectra.*

Table 5.15: *KBr-FTIR positions (cm^{-1}) corresponding to graphs (a) and (d) in Figure 5.18, and assignments in the 950-750cm^{-1} region corresponding to the δAl-Me^{2+}-OH bands.*

MX-80 Untreated	MX-80 ABM 2	Assignments
ATR positions (cm^{-1})		
917.42±1.08	919.57±1.37	δAlAlOH deformation
880.52±0.88	881.78±1.11	δAlFeOH deformation
844.38±0.19	843.73±1.08	δAlMgOH deformation
797.27±0.13	796.65±0.30	Si-O stretching of quartz and silica
778.11±0.21	777.34±0.30	

In smectites, the occupancy of the octahedral layers strongly determines the position of the OH bending bands. The bands observed at (9), (10) and (11) correspond to δAlAlOH, δAlFeOH and δAlMgOH respectively, or with the octahedral cation deformation bands. Therefore, to evaluate any possible iron enrichment within octahedral allocations, the region of the spectra between 950-750cm^{-1} was further examined. Figures 5.18 (a) and (b) and Table 5.15 present the fitted data of the octahedral cation distribution of the reference sample (Figure 5.18 (a)) and in-situ test sample (Figure 5.18 (b)). From the results obtained, it can be inferred that there are no differences between the untreated bentonite and the experimental sample, and the band positions do not deviate from those reported in the literature [290], [286]. Nevertheless, to accomplish a more precise determination of the octahedral cation distribution within the 950-750cm^{-1} range, this region was baselined following the description provided in section 4.2.8, and the resulting spectra is presented in Figure 5.19. By comparing the reference and experimental samples, it can be stated that no appreciable differences regarding the wavenumber position of the iron octahedral band were detected, whereas certain displacement of the octahedral aluminium and magnesium was detected, which might be explained due to isomorphic substitutions within octahedral sites.

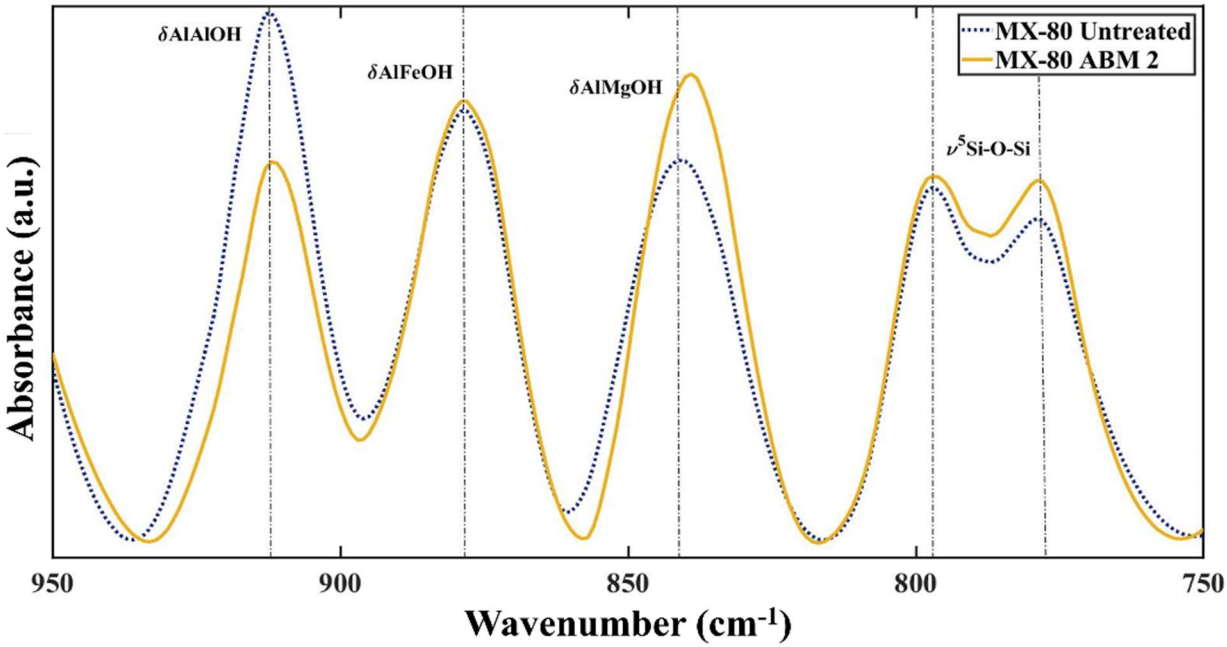

Figure 5.19: *Octahedral cation-OH deformation bands of MX-80 ABM 2 (KBr-FTIR) and untreated samples once data were baselined. Peaks are indicated by dotted lines.*

Figures 5.16 and 5.17 also show the characteristic Si-O stretching of quartz and silica, and Si-O-Al bending bands, at (12) and (13) respectively. Finally, the bands observed at (14) and (15) are caused by the coupled Al-OH and Si-O out-of-plane and Al-O-Si deformation.

Additionally, to complete a full evaluation of the mid-region of the spectra, the influence of the exchangeable cations was examined over the region between 3800-3100cm^{-1}, and results are presented in Figure 5.20 and Table 5.16. The spectra of the untreated and MX-80 samples showed a sharp peak at 3632cm^{-1} and 3628cm^{-1}, respectively. This band corresponds with OH stretching vibrations of the structural OH groups. The mentioned bands, in both cases, are accompanied by a broad band of water located at 3433cm^{-1} and 3436cm^{-1} caused by overlapping of the asymmetric stretching vibrations of H-bonded water.

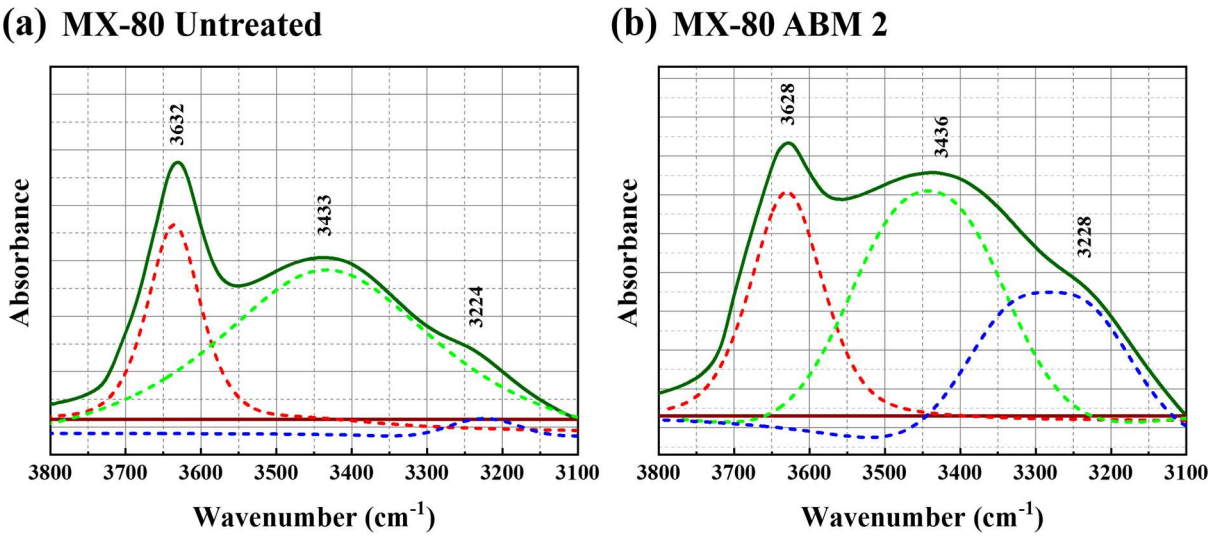

Figure 5.20: *(a) and (b) Fitted band positions corresponding with the water stretching bands of MX-80 untreated and ABM 2 samples.*

Table 5.16: *KBr-FTIR positions (cm^{-1}) corresponding to the graphs (a) and (b) in Figure 5.20, and assignments at 3800-3100cm^{-1} region corresponding to the stretching water region.*

MX-80 Untreated	MX-80 ABM 2	Assignments
ATR positions (cm^{-1})		
3632.75±0.14	3628.01±0.34	OH stretching of structural hydroxyl groups
3433.70±0.98	3436.45±1.43	OH stretching of water
3224.23±1.46	3228.28±1.41	

The small shoulders observed at 3224cm^{-1} and 3228cm^{-1} are due to the overtone of the bending vibration mode of cation hydration water. Although there is a small shift regarding to the wavenumber, the values observed are a close match to those already reported in the literature [290], [286].

5.2.6.2 Febex bentonite ABM parcel 2

The Febex bentonite was also examined by ATR and KBr and results are presented in Figures 5.21 and 5.22 and Table 5.17.

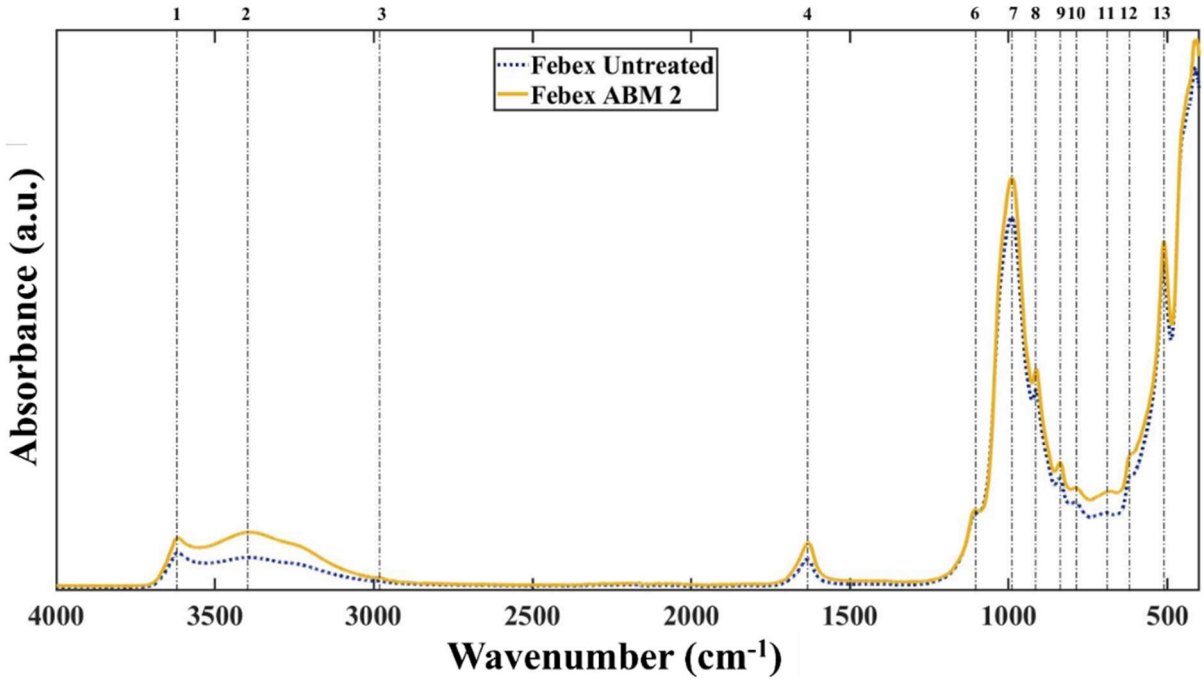

Figure 5.21: *ATR-FTIR spectra (4000-400cm^{-1}) of Febex ABM 2 and untreated samples. Peaks are indicated by dotted lines.*

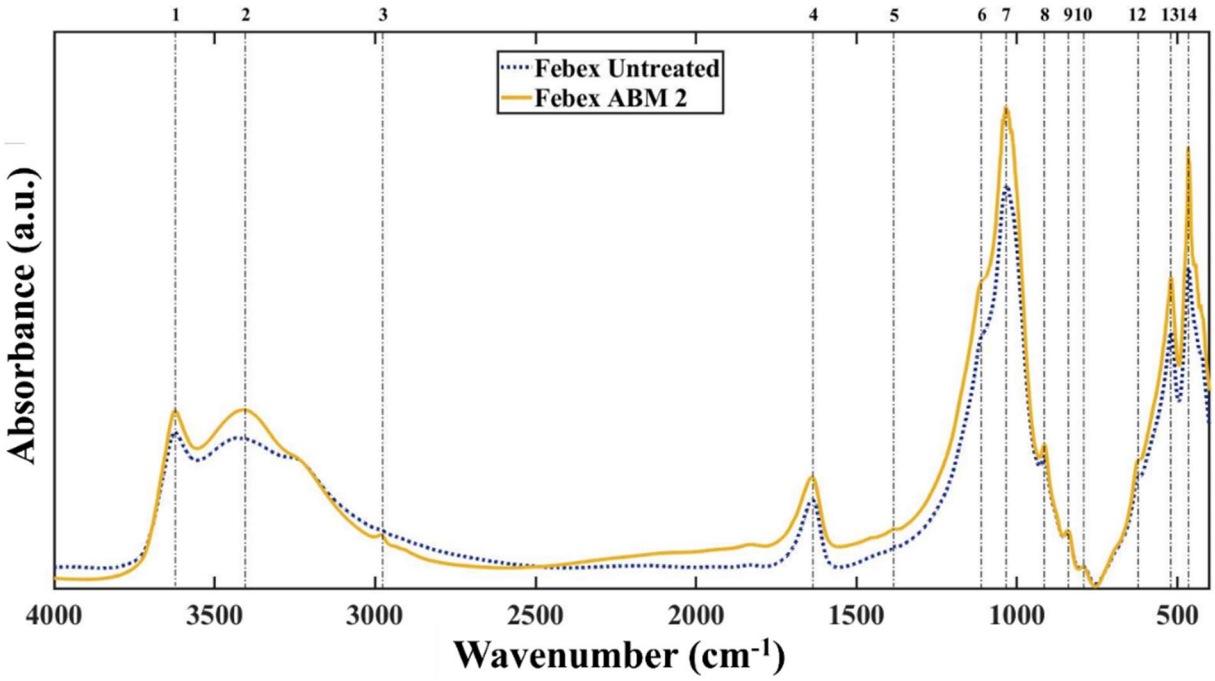

Figure 5.22: *KBr-FTIR spectra (4000-400 cm^{-1}) of Febex ABM 2 and untreated samples. Peaks are indicated by dotted lines.*

Table 5.17 shows the assignments corresponding with the bands obtained by ATR and KBr-FTIR. Overall, the dominant phase present in the untreated and Febex ABM samples is montmorillonite, and the bands observed are a close match to those previously described in section 4.2.8 for FTIR analysis of Febex in-situ test samples.

Table 5.17: *ATR-FTIR and KBr-FTIR positions (cm^{-1}) and assignments of reference and Febex sample in mid-region of the spectra. Numbers in parentheses indicate band numbers in Figures 5.21 and 5.22.*

Febex Untreated		**Assignment**	**Febex AMB 2**	
ATR	**KBr**		**ATR**	**KBr**
Position (cm^{-1})			Position (cm^{-1})	
3617(1)	3627(1)	OH stretching of structural hydroxyl groups	3616(1)	3629(1)
3391(2)	3422(2)	OH stretching of water	3391(2)	3426(2)
-	2982(3)	C-H stretching vibration	2982(3)	2983(3)
1634(4)	1638(4)	OH deformation of water	1633(4)	1638(4)
-	-	C-H bending vibrations	-	1384(5)
1104(6)	1110(6)	Si-O stretching (longitudinal mode)	1106(6)	1113(6)
991(7)	1036(7)	Si-O stretching	990(7)	1031(7)
913(8)	915(8)	δAlAlOH deformation	913(8)	915(8)
839(9)	838(9)	δAlMgOH deformation	838(9)	838(9)
791(10)	792(10)	Si-O stretching of quartz and silica	790(10)	790(10)
694(11)	-	Si-O-Al bending	693(11)	--
618(12)	627(12)	Coupled Al-OH and Si-O, out of plane	615(12)	625(12)
512(13)	520(13)	Al-O-Si deformation	511(13)	520(13)
-	467(14)	Si-O-Si deformation	-	467(14)

From Figures 5.21 and 5.22, the following assignments can be drawn. The band observed at (1) corresponds with the OH-stretching vibration of the structural montmorillonite hydroxyls groups, which is closely accompanied by a shoulder (2) that corresponds with the H_2O-stretching vibration with an overtone of the water bending vibration observed at (4). The bands at (3) and (5) are due to the stretching and bending vibration of CH groups present in the montmorillonite structure. The bands at (6) and (14) are assigned to the stretching (longitudinal mode) and bending of the Si respectively, while the sharp band at (7) is attributed to the Si-O stretching vibration of octahedral smectites. The bands at (10), (12) and (13) are ascribed to

the Si-O stretching of quartz and silica, coupled Al-OH and Si-O out-of-plane and Al-O-Si deformation.

The bands observed at (8) and (9) are attributed to δAlAlOH and δAlMgOH, respectively. The δAlFeOH octahedral band is not discernible in the spectra and, thus, to assess any iron enrichment between octahedral allocation, this specific region of the spectrum was examined in detail, and the results are presented in Figures 5.23 (a) and (b) and Table 5.18.

Results obtained from octahedral cation distribution analysis show a slight shift of the δAlFeOH band position, which might be an indicator of iron enrichment within octahedral allocations in the montmorillonite structure. On viewing the fitting results obtained, the region between 950-750cm^{-1} was baselined to better identify any possible displacement of the octahedral cations towards lower or higher wavenumbers, and results are presented in Figure 5.24. Contrary to observations from Figure 5.23, the iron band position in the ABM sample does not show any displacement towards higher values. Therefore, the observed effect on the prior fitting analysis can be explained due to the sensitivity of the utilised program while fitting this region of the spectra.

To complete the evaluation of the mid-region of the spectra, the influence of the cations present in the interlayer space corresponding to the region of the spectra between with 3800-3100cm^{-1} was also studied, and results are presented in Figure 5.25 and Table 5.19.

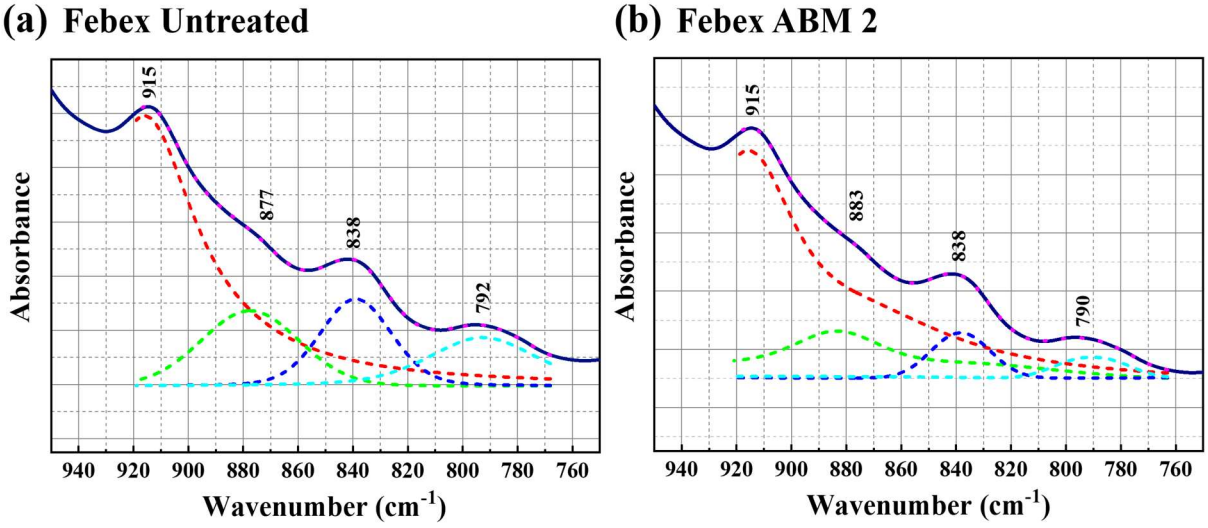

Figure 5.23: *(a)-(b) Fitted band positions corresponding with the octahedral cation-OH deformation bands of Febex untreated and ABM 2 samples in the KBr-FTIR spectra.*

Table 5.18: *KBr-FTIR positions (cm^{-1}) corresponding to graphs (a) and (d) in Figure 5.23, and assignments in the 950-750cm^{-1} region corresponding to the δAl-Me^{2+}-OH bands.*

Febex Untreated	Febex ABM 2	Assignments
ATR positions (cm^{-1})		
915.95±0.62	915.79±0.15	δAlAlOH deformation
877.50±0.90	883.49±0.97	δAlFeOH deformation
838.97±0.36	838.36±0.16	δAlMgOH deformation
792.69±0.58	790.45±0.31	Si-O stretching of quartz and silica

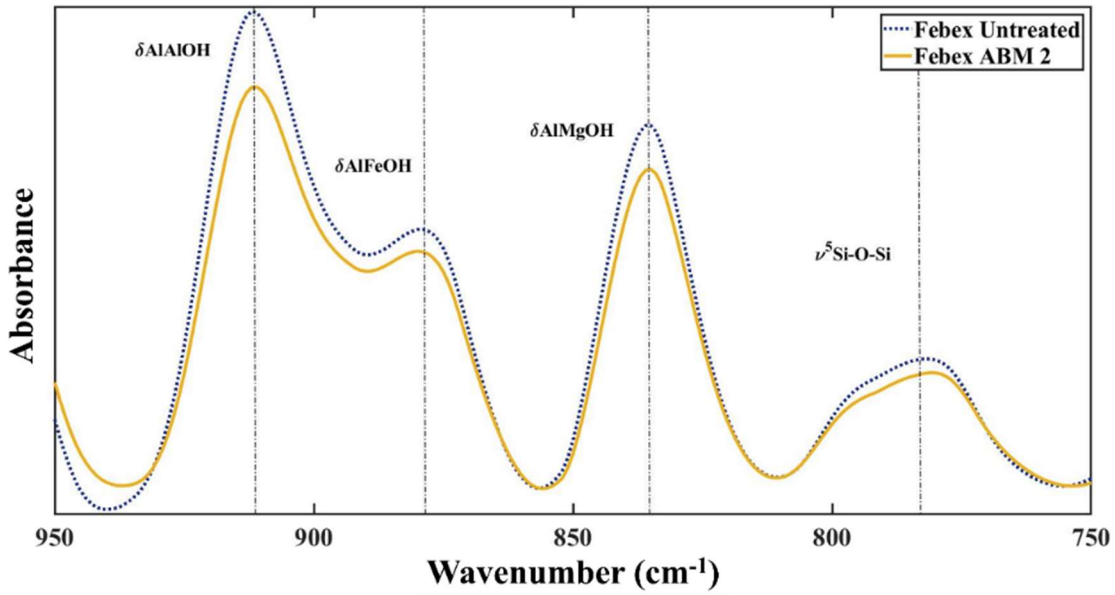

Figure 5.24: *Octahedral cation-OH deformation bands of Febex ABM 2 (KBr-FTIR) and untreated samples once data was baselined. Peaks are indicated by dotted lines.*

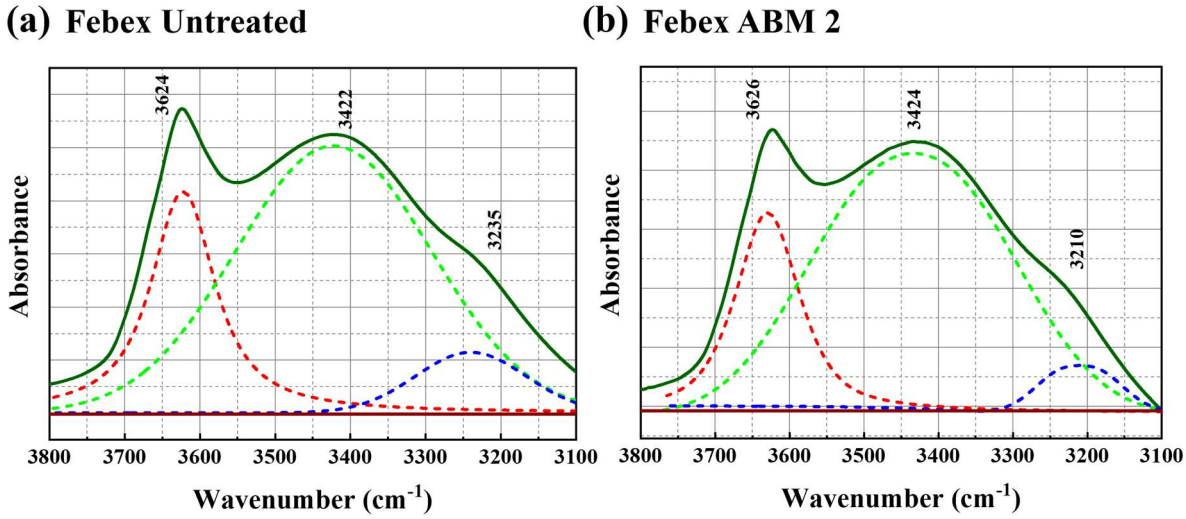

Figure 5.25: *(a) and (b) Fitted band positions corresponding with the water stretching bands of Febex untreated and ABM 2 samples.*

The shape of the peaks observed in this region of the spectra are very similar between the reference and the ABM 2 sample. There was no obvious/discernible difference.

Table 5.19: *KBr-FTIR positions (cm^{-1}) corresponding to graphs (a) and (b) in Figure 5.25, and assignments in the 3800-3100cm^{-1} region corresponding to the stretching water region.*

Febex Untreated	Febex ABM 2	Assignments
ATR positions (cm^{-1})		
3623.99±0.16	3626.59±0.13	OH stretching of structural hydroxyl groups
3422.40±0.15	3424.02±0.52	OH stretching of water
3235.08±1.05	3210.44±1.76	

The bands observed can clearly be assigned to the OH stretching of structural hydroxyl groups (3624cm^{-1} and 3626cm^{-1}) and OH stretching of water (3422cm^{-1}, 3424cm^{-1}, 3235cm^{-1} and 3210cm^{-1}). As previously observed in the MX-80 sample, there is a small shift in wavenumber, but it can be explained due to the sensitivity of Origin while performing the spectral fitting, since the values reported correlate with those reported in the literature [254], [256].

ATR and KBr-FTIR analyses in the Febex ABM sample did not show differences compared to similar measurements carried out on the Febex samples from the Febex in-situ test. No appreciable variations between wavenumber position of the stretching and bending bands were identified in the Febex bentonite samples from the Febex in-situ test and the Febex bentonite sample from the ABM project. Therefore, it can be affirmed that no differences between the Febex bentonite samples from both experiments were detected, despite the different experimental set-up.

5.2.6.3 Deponit C-AN bentonite ABM parcel 2

Results obtained from the FTIR Deponit C-AN bentonite are presented in Figures 5.26 and 5.27 and Table 5.20. The bands observed in the mid-region of the spectra (4000-400cm^{-1}) correlate with the characteristic bands of dioctahedral smectites. Therefore, it can be inferred that the main dominant phase in Deponit C-AN bentonite is montmorillonite. The description of the bands provided for the MX-80 sample and Febex samples are the same as those observed in the ATR and KBr-FTIR analysis, and their assignments are compiled in Table 5.20. As also observed in the MX-80 sample, the presence of a broad band (5) might be explained due to Fe asymmetric vibration, although in the MX-80 bentonite the presence of this band was only

apparent in the experimental sample. In the case of Deponit C-AN, this band was observed in both the experimental and reference material. Overall, the bands evidenced in the mid-region of the spectra are a close match to those observed in the literature [291].

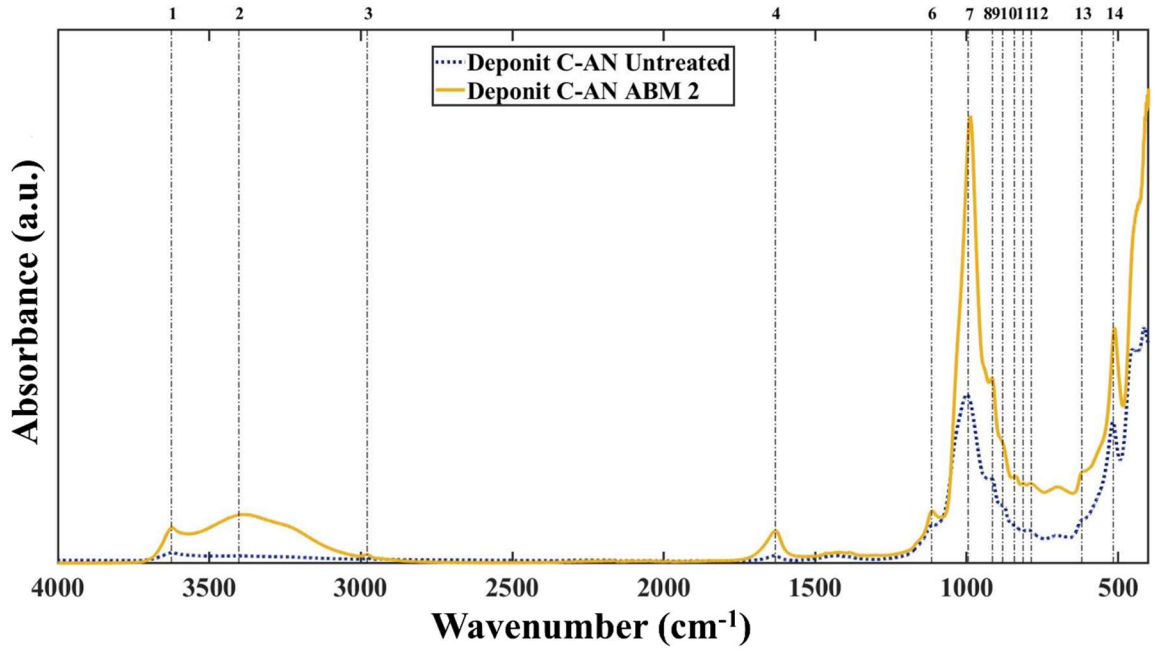

Figure 5.26: *ATR-FTIR spectra (4000-400 cm^{-1}) of Deponit C-AN ABM 2 and untreated samples. Peaks are indicated by dotted lines.*

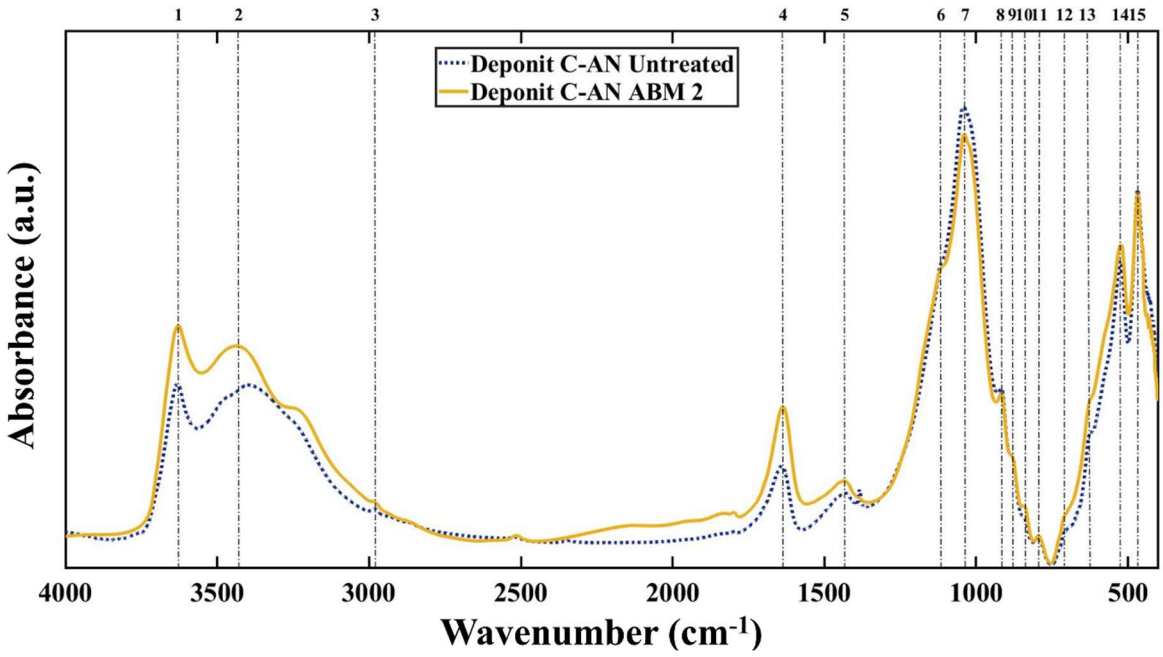

Figure 5.27: *KBr-FTIR spectra (4000-400 cm^{-1}) of Deponit C-AN ABM 2 and untreated samples. Peaks are indicated by dotted lines.*

However, as was determined previously in MX-80 and Febex samples, evaluation of the octahedral cation distribution over the range of 950-750cm^{-1} was also carried out and results

obtained from the analysis of the octahedral cation-OH lattice deformation bands are presented in Figure 5.28 and Table 5.21.

Table 5.20: *ATR-FTIR and KBr-FTIR positions (cm^{-1}) and assignments of reference and Deponit C-AN sample in mid-region of the spectra. Number in parentheses indicates band numbers in Figures 5.26 and 5.27.*

Deponit C-AN Untreated		**Assignment**	**Deponit C-AN AMB 2**	
ATR	**KBr**		**ATR**	**KBr**
Position (cm^{-1})			Position (cm^{-1})	
$3625^{(1)}$	$3638^{(1)}$	OH stretching of structural hydroxyl groups	$3625^{(1)}$	$3636^{(1)}$
-	$3435^{(2)}$	OH stretching of water	$3393^{(2)}$	$3442^{(2)}$
-	$2980^{(3)}$	C-H stretching	$2980^{(3)}$	-
$1632^{(4)}$	$1639^{(4)}$	OH deformation of water	$1632^{(4)}$	$1639^{(4)}$
-	$1428^{(5)}$	Fe asymmetric vibration	-	$1428^{(5)}$
$1114^{(6)}$	$1118^{(6)}$	Si-O stretching (longitudinal mode)	$1114^{(6)}$	$1114^{(6)}$
$1000^{(7)}$	$1043^{(7)}$	Si-O stretching	$1001^{(7)}$	$1043^{(7)}$
$918^{(8)}$	$919^{(8)}$	δAlAlOH deformation	$918^{(8)}$	$919^{(8)}$
$882^{(9)}$	$877^{(9)}$	δAlFeOH deformation	$883^{(9)}$	$881^{(9)}$
$843^{(10)}$	$839^{(10)}$	δAlMgOH deformation	$844^{(10)}$	$839^{(10)}$
$795^{(11)}$	$792^{(11)}$	Si-O stretching of quartz and silica	$794^{(11)}$	$792^{(11)}$
$693^{(12)}$	$712^{(12)}$	Si-O-Al bending	$692^{(12)}$	$712^{(12)}$
$620^{(13)}$	$626^{(13)}$	Coupled Al-OH and Si-O, out of plane	$618^{(13)}$	$626^{(13)}$
$516^{(14)}$	$526^{(14)}$	Al-O-Si deformation	$515^{(14)}$	$526^{(14)}$
-	$468^{(15)}$	Si-O-Si deformation	-	$468^{(15)}$

The reported values of the ABM sample, particularly the values corresponding with the octahedral iron band are slightly shifted towards higher wavenumber values, suggesting that some iron enrichment may have occurred. Thus, to evaluate any possible shifting of the octahedral cation-OH deformation bands, this specific region of the spectra was baselined, and results are presented in Figure 5.29.

From Figure 5.29, it can be concluded that there was no displacement concerning the Fe octahedral band, despite prior observations. However, the baselined spectra showed a small variation relative to wavenumber in the octahedral Al^{3+} and Mg^{2+} bands. This variation might (again) be explained due to possible isomorphic substitutions within the octahedral sites.

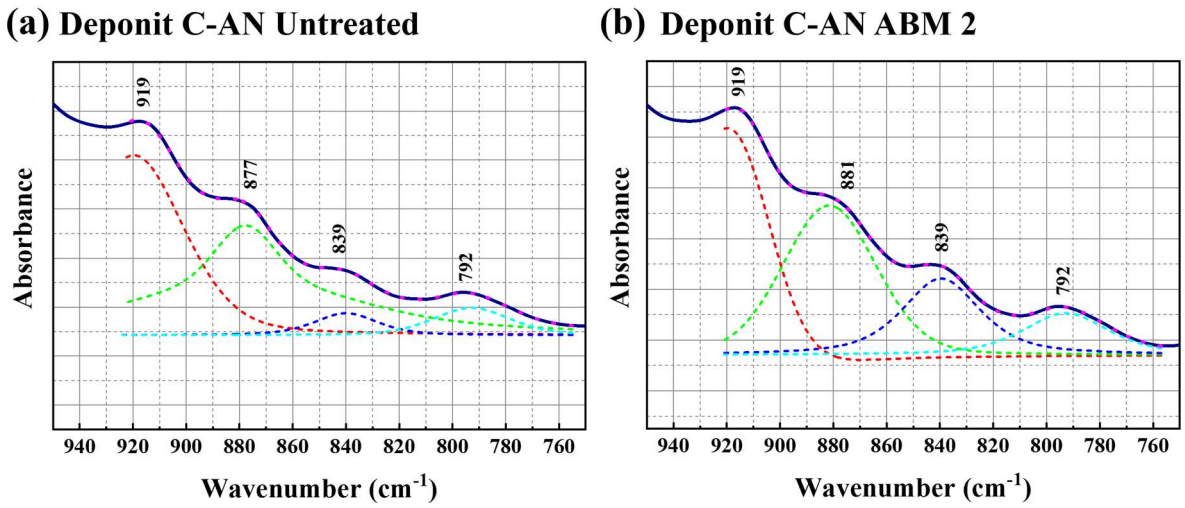

Figure 5.28: *(a)-(b) Fitted band positions corresponding with the octahedral cation-OH deformation bands of Deponit C-AN untreated and Deponit C-AN ABM 2 samples in the KBr-FTIR spectra.*

Table 5.21: *KBr-FTIR positions (cm^{-1}) corresponding to graphs (a) and (d) in Figure 5.28, and assignments in the 950-750cm^{-1} region corresponding to the δAl-Me^{2+}-OH bands.*

Deponit C-AN Untreated	Deponit C-AN ABM 2	Assignments
ATR positions (cm^{-1})		
919.68±0.21	919.76±0.27	δAlAlOH deformation
877.75±0.32	881.52±0.97	δAlFeOH deformation
839.99±0.61	839.58±0.18	δAlMgOH deformation
792.83±0.35	792.79±0.21	Si-O stretching of quartz and silica

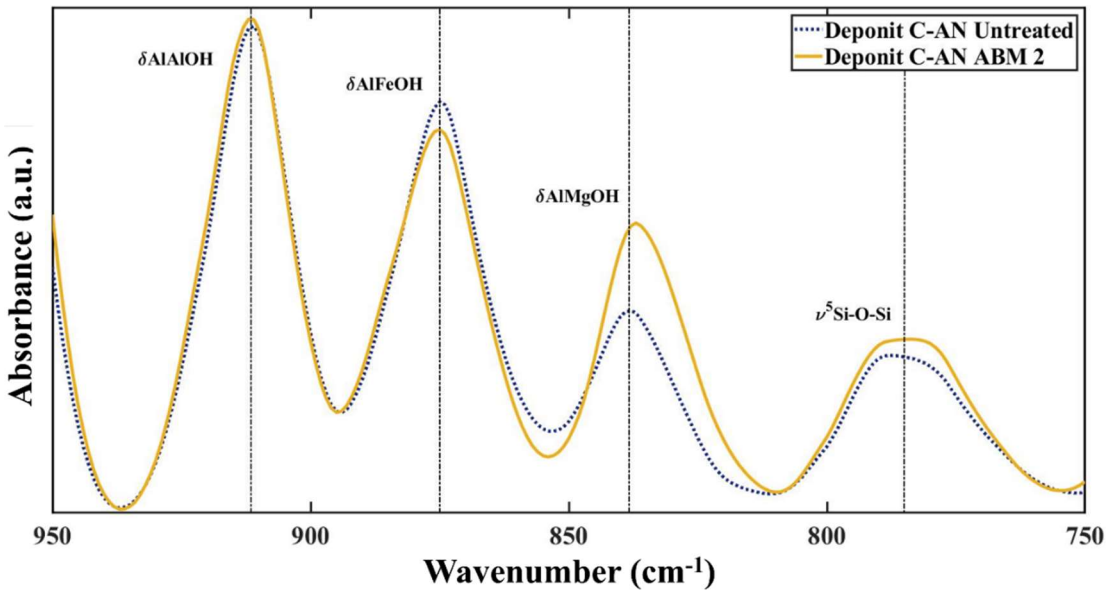

Figure 5.29: *Octahedral cation-OH deformation bands of Deponit C-AN (KBr-FTIR) and untreated samples once data were baselined. Peaks are indicated by dotted lines.*

Finally, the influence of the exchangeable cations was evaluated through study of the water bands in the range 3800-3100cm^{-1} of the IR spectra, and results are presented in Figure 5.30 and Table 5.22.

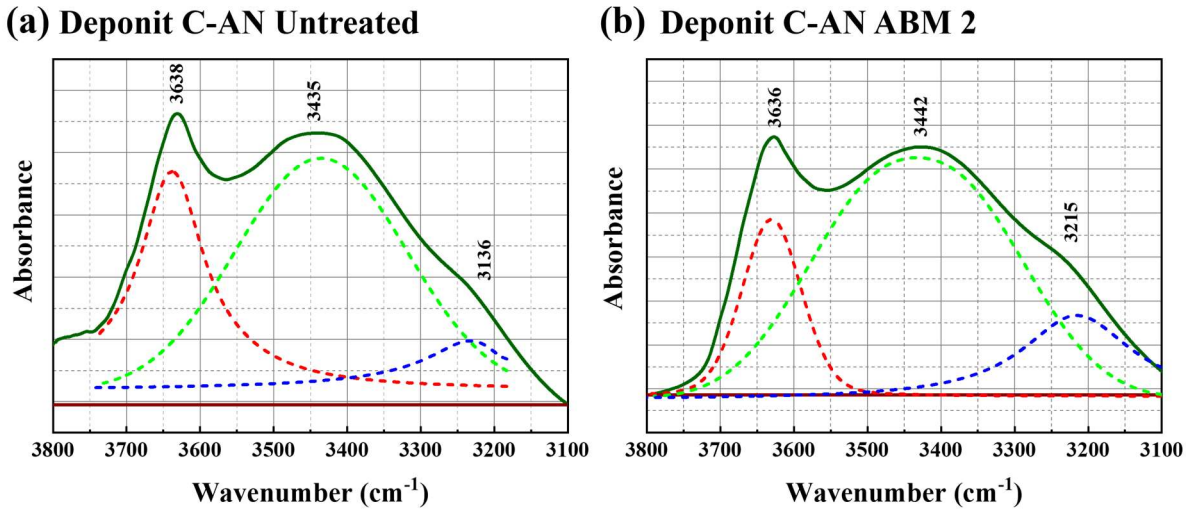

Figure 5.30: *(a) and (b) Fitted band positions corresponding with the water stretching bands of Deponit C-AN untreated and ABM 2 samples.*

Table 5.22: *KBr-FTIR positions (cm^{-1}) corresponding to the graphs (a) and (b) in Figure 5.30, and assignments at 3800-3100cm^{-1} region corresponding to the stretching water region.*

Febex Untreated	**Febex ABM 2**	**Assignments**
ATR positions (cm^{-1})		
3638.11±0.14	3636.27±0.14	OH stretching of structural hydroxyl groups
3435.43±1.25	3442.58±0.81	OH stretching of water
3136.08±6.68	3215.37±1.09	

The spectra collected from the pristine material (Figure 5.30 (a)) and the experimental sample (Figure 5.30 (b)) showed strong peaks at 3638cm^{-1} and 3636cm^{-1}, which correspond with the OH stretching of structural hydroxyl groups. The peaks at 3638cm^{-1} and 3636cm^{-1} are accompanied by a broad band (3435cm^{-1} and 3442cm^{-1}) of water which is created by overlapping of the asymmetric stretching vibrations of H-bonded water. The small shoulders observed at 3136cm^{-1} and 3215cm^{-1} correspond to the overtone of the bending vibration mode of the cation hydration water. From analysis of the water bands, it can be affirmed that there were no observable differences with the reference sample.

5.2.6.4 Kunigel V1 bentonite ABM parcel 1 and 2

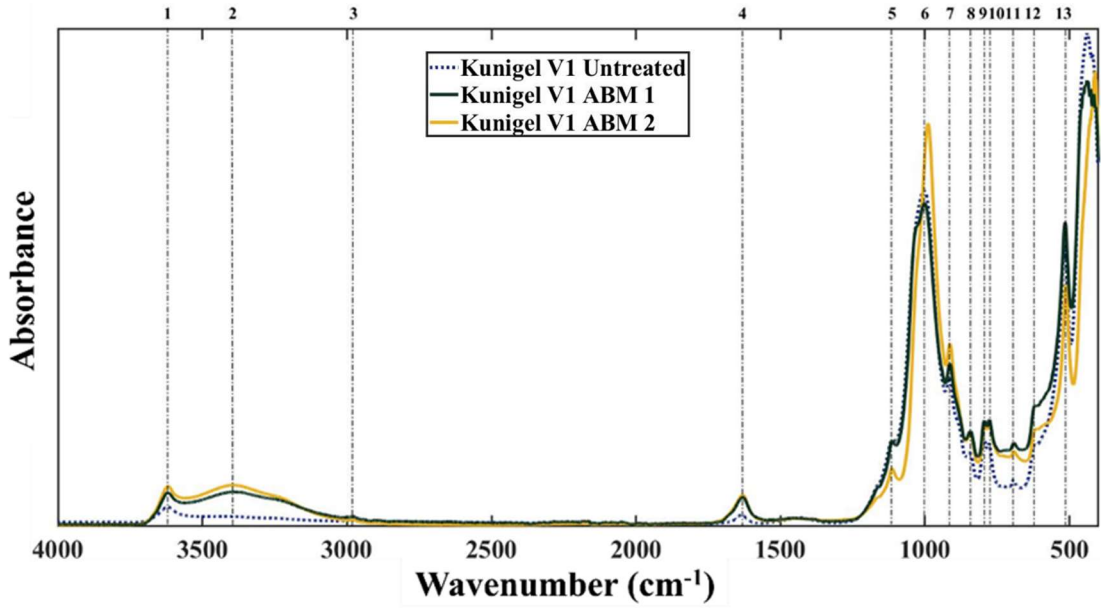

Figure 5.31: *ATR-FTIR spectra (4000-400cm^{-1}) of Kunigel V1 (ABM 1 and ABM 2) and untreated samples. Peaks are indicated by dotted lines.*

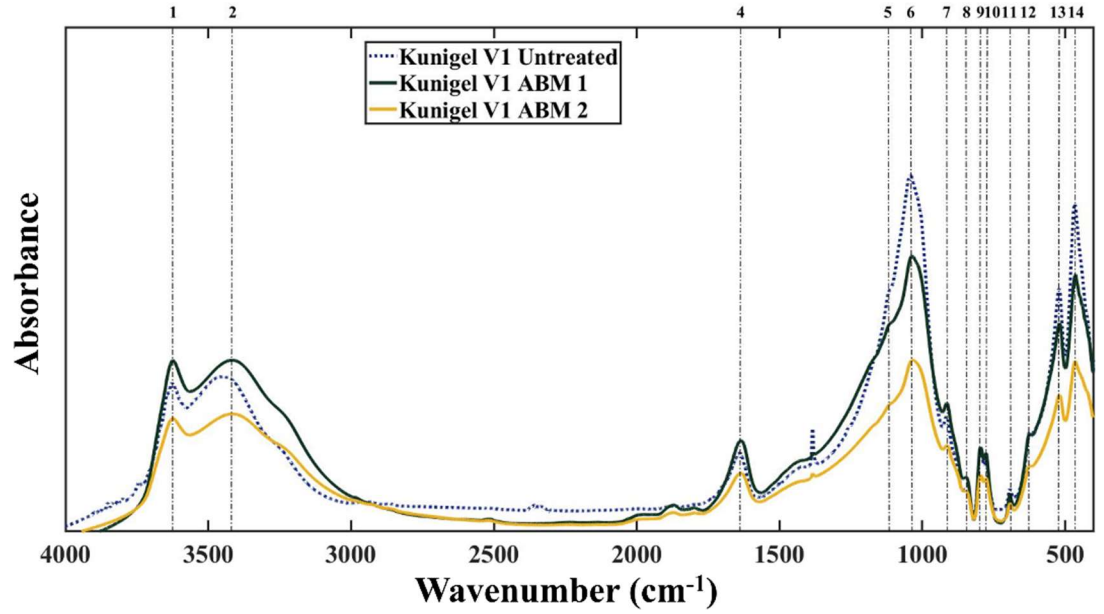

Figure 5.32: *KBr-FTIR spectra (4000-400cm^{-1}) of Kunigel V1 (ABM 1 and ABM 2) and untreated sample. Peaks are indicated by dotted lines.*

The results obtained from FTIR analysis of the Kunigel V1 bentonite are presented in Figures 5.31 and 5.32 and Table 5.23. The observed bands in the mid-region of the spectra (4000-400cm^{-1}) are close matches to those observed in the MX-80, Febex and Deponit C-AN samples. Therefore, it can be inferred that montmorillonite is the dominant phase. The assignments of the bands are provided in Table 5.23, and the band allocations correspond to

those observed in the previously described ABM samples. As for MX-80, Febex and Deponit C-AN samples, analysis of the octahedral cation-OH deformation bands was carried out. Overall, the observed bands (Figure 5.33 and Table 5.24) in the experimental samples corresponded to those observed in the reference Kunigel V1 samples and do not deviate from those reported in the literature [292].

Table 5.23: *ATR-FTIR and KBr-FTIR positions (cm^{-1}) and assignments of reference and Kunigel V1 ABM 1 and ABM 2 samples in mid-region of the spectra. Numbers in parentheses indicate band numbers in Figures 5.31 and 5.32.*

Kunigel V1 Untreated		**Assignment**	**Kunigel V1 ABM 1**		**Kunigel V1 ABM 2**	
ATR	**KBr**		**ATR**	**KBr**	**ATR**	**KBr**
Position (cm^{-1})			Position (cm^{-1})		Position (cm^{-1})	
$3618^{(1)}$	$3634^{(1)}$	OH stretching of structural hydroxyl groups	$3618^{(1)}$	$3633^{(1)}$	$3618^{(1)}$	$3625^{(1)}$
-	$3424^{(2)}$	OH stretching of water	$3393^{(2)}$	$3428^{(2)}$	$3392^{(2)}$	$3426^{(2)}$
-	-	C-H stretching vibration	$2981^{(3)}$	-	$2980^{(3)}$	-
$1634^{(4)}$	$1639^{(4)}$	OH deformation of water	$1633^{(4)}$	$1634^{(4)}$	$1633^{(4)}$	$1636^{(4)}$
-	$1428^{(5)}$	Fe asymmetric vibration	-	$1427^{(5)}$	-	$1428^{(5)}$
$1114^{(5)}$	$1121^{(5)}$	Si-O stretching (longitudinal mode)	$1114^{(5)}$	$1118^{(5)}$	$1114^{(5)}$	$1113^{(5)}$
$1001^{(6)}$	$1041^{(6)}$	Si-O stretching	$1000^{(6)}$	$1036^{(6)}$	$988^{(6)}$	$1034^{(6)}$
$914^{(7)}$	$918^{(7)}$	δAlAlOH deformation	$914^{(7)}$	$917^{(7)}$	$914^{(7)}$	$917^{(7)}$
$845^{(8)}$	$843^{(8)}$	δAlMgOH deformation	$843^{(8)}$	$842^{(8)}$	$842^{(8)}$	$841^{(8)}$
$795^{(9)}$	$798^{(9)}$	Si-O stretching of quartz and silica	$795^{(9)}$	$798^{(9)}$	$795^{(9)}$	$799^{(9)}$
$777^{(10)}$	$776^{(10)}$	Si-O stretching of quartz and silica	$776^{(10)}$	$776^{(10)}$	$777^{(10)}$	$774^{(10)}$
$694^{(11)}$	$694^{(11)}$	Si-O-Al bending	$694^{(11)}$	$694^{(11)}$	$694^{(11)}$	$694^{(11)}$
$620^{(12)}$	$625^{(12)}$	Coupled Al-OH and Si-O, out of plane	$618^{(12)}$	$627^{(12)}$	$618^{(12)}$	$627^{(12)}$
$512^{(13)}$	$522^{(13)}$	Al-O-Si deformation	$512^{(13)}$	$520^{(13)}$	$512^{(13)}$	$521^{(13)}$
-	$467^{(14)}$	Si-O-Si deformation	-	$467^{(14)}$	-	$467^{(14)}$

Despite this, the reported values of the iron band (δAlFeOH) of the sample belonging to the second parcel show a displacement towards lower values, suggesting a lesser degree of iron within the octahedral allocations.

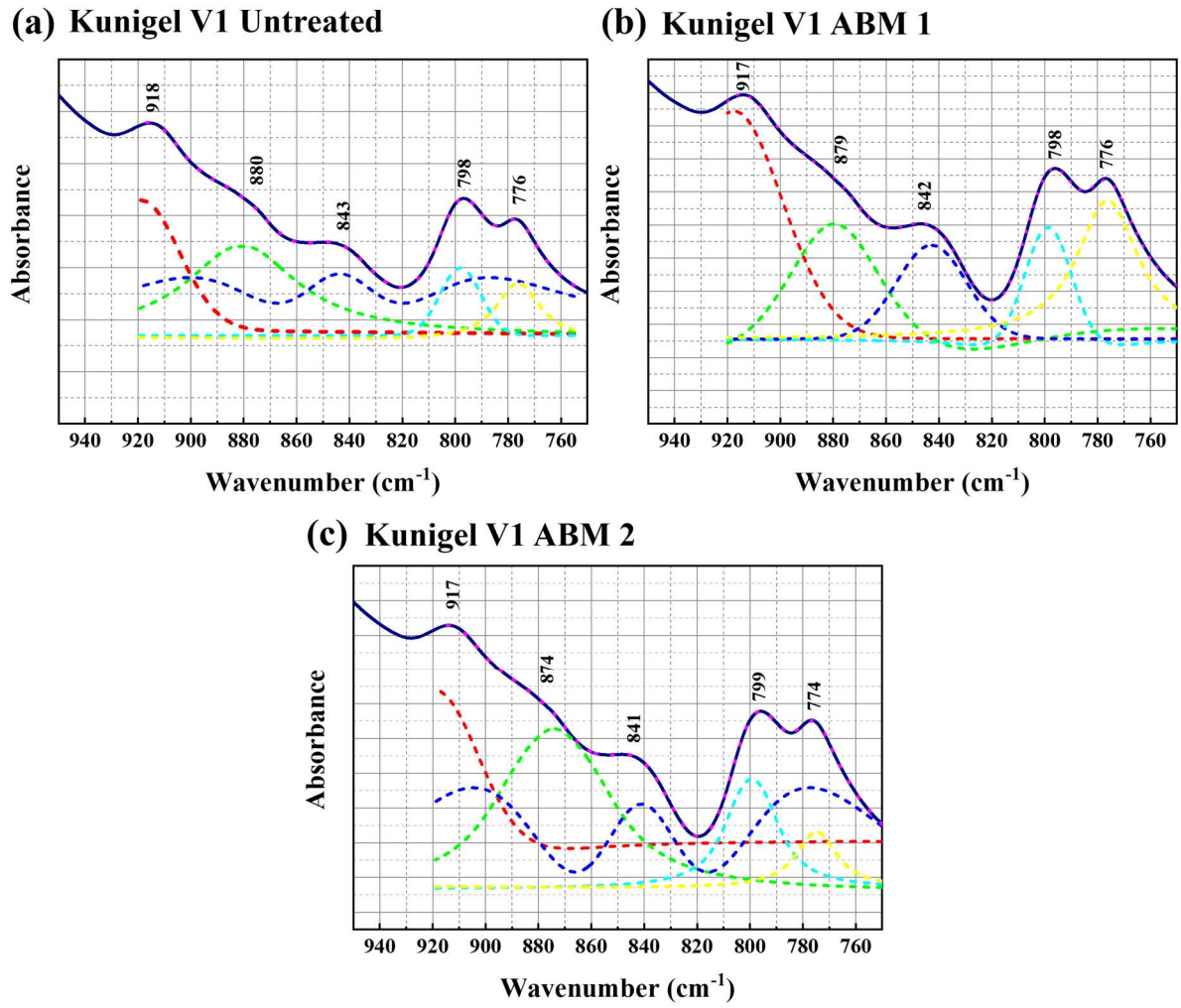

Figure 5.33: *(a)-(c) Fitted band positions corresponding with the octahedral cation-OH deformation bands of Kunigel V1 untreated and ABM 1 and 2 samples in the KBr-FTIR spectra.*

Table 5.24: *KBr-FTIR positions (cm^{-1}) corresponding to graphs (a) and (d) in Figure 5.33, and assignments in the 950-750cm^{-1} region corresponding to the δAl-Me^{2+}-OH bands.*

Kunigel V1 Untreated	Kunigel V1 ABM 1	Kunigel V1 ABM 2	Assignments
ATR positions (cm^{-1})			
918.82±2.47	917.48±1.29	920.08±1.95	δAlAlOH deformation
880.74±1.56	879.53±3.66	874.11±0.66	δAlFeOH deformation
843.66±0.79	842.79±0.06	841.01±0.39	δAlMgOH deformation
798.02±0.24	798.70±0.32	799.32±0.12	Si-O stretching of quartz and silica
776.18±0.23	776.24±0.50	774.85±0.14	Si-O stretching of quartz and silica

To confirm this spectral shift, this specific region of the spectra (950-750cm^{-1}) was baselined. Figure 5.34 shows that there is a clear shift in the Fe octahedral band on both bentonite samples retrieved from parcel 1 and 2, as well as a shift in the Mg^{2+} and Al^{3+} bands, which might be explained due to isomorphic substitutions, occurring in octahedral positions and correlating with observed changes in CEC.

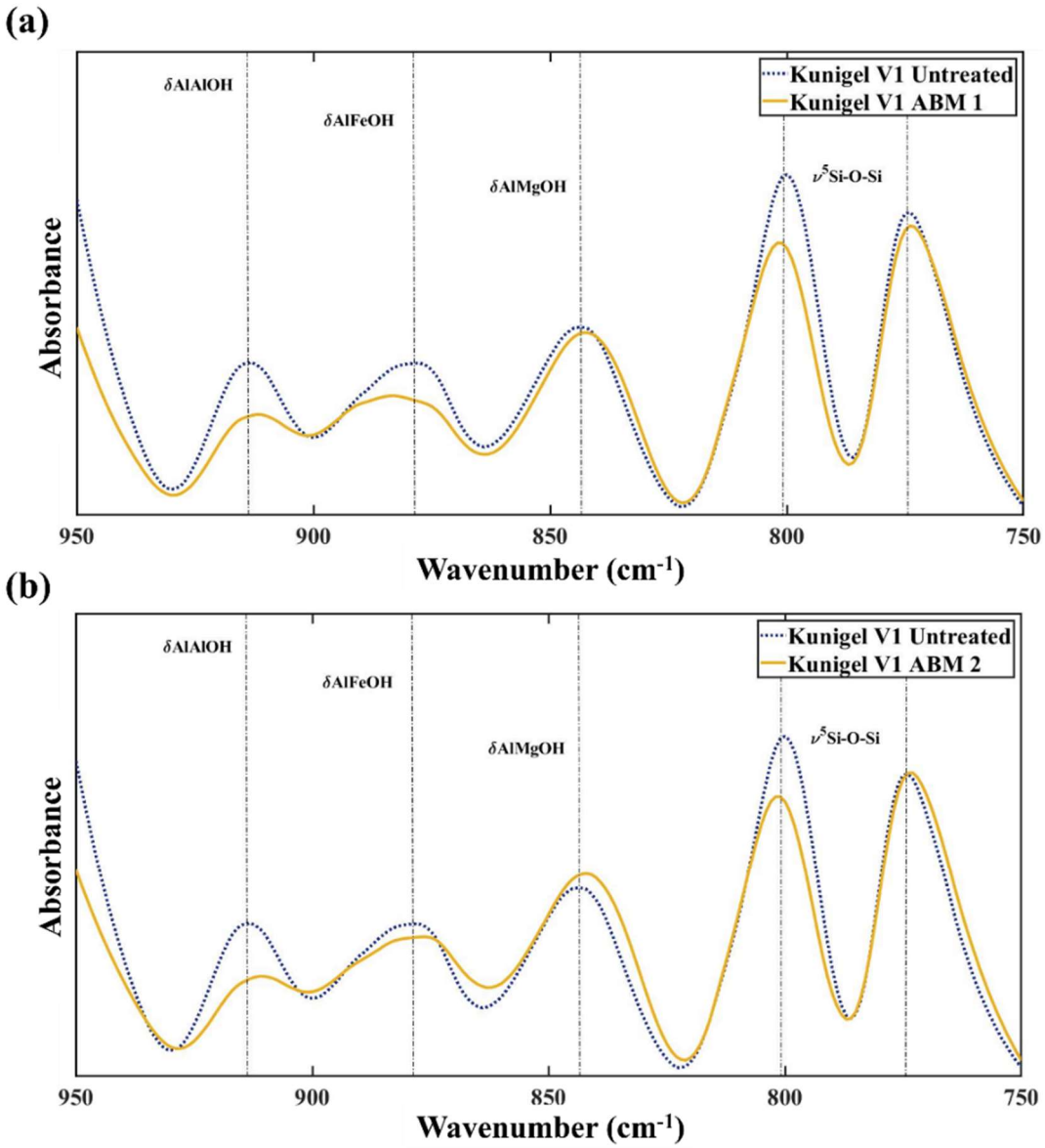

Figure 5.34: *(a) Octahedral cation-OH deformation bands of Kunigel V1 ABM 1 vs. reference sample. (b) Octahedral cation-OH deformation bands of Kunigel V1 ABM 2 vs. reference sample. Peaks are indicated by dotted lines.*

The influence of the cations present within the interlayer space in the montmorillonite component of the Kunigel V1 samples were evaluated. Results are presented in Figure 5.35 and Table 5.25.

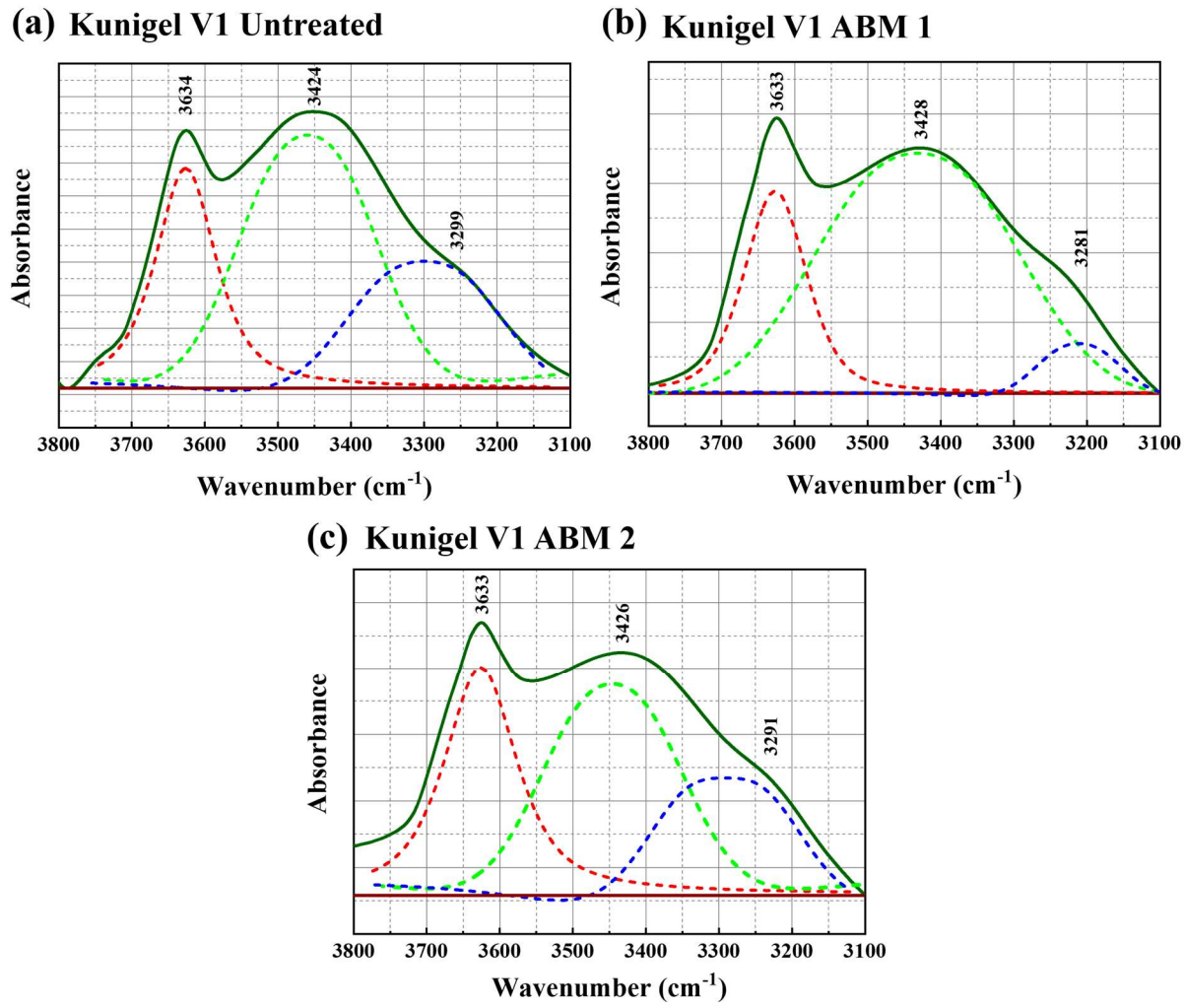

Figure 5.35: *(a)-(c) Fitted band positions corresponding with the water stretching bands of Kunigel V1 untreated and ABM 1 and ABM 2 sample.*

Table 5.25: *KBr-FTIR positions (cm^{-1}) corresponding to graphs (a) and (d) in Figure 5.35, and assignments in the 950-750cm^{-1} region corresponding to the δAl-Me^{2+}-OH bands.*

Kunigel V1 Untreated	Kunigel V1 ABM 1	Kunigel V1 ABM 2	Assignments
ATR positions (cm^{-1})			
3634.21±0.16	3633.65±0.18	3633.15±0.33	OH stretching of structural hydroxyl groups
3424.21±0.74	3428.85±0.63	3426.04±1.26	OH stretching of water
3299.41±1.11	3281.27±0.89	3291.31±1.13	

Overall, the results obtained show the characteristics bands of the OH structural hydroxyl groups, accompanied by the broad band due to the overlapping of the asymmetric stretching vibration of the H-bonded water. Finally, a small shoulder is observed which is assigned to an overtone of the bending vibration mode of the cation hydration water. From evaluation of the

water bands, it can be affirmed that no observable differences regarding compared to the reference sample were detected.

5.2.7 Thermal analysis on ABM bentonite samples

TGA was utilised to provide sensitive information about the thermal and chemical behaviour of the ABM bentonite samples.

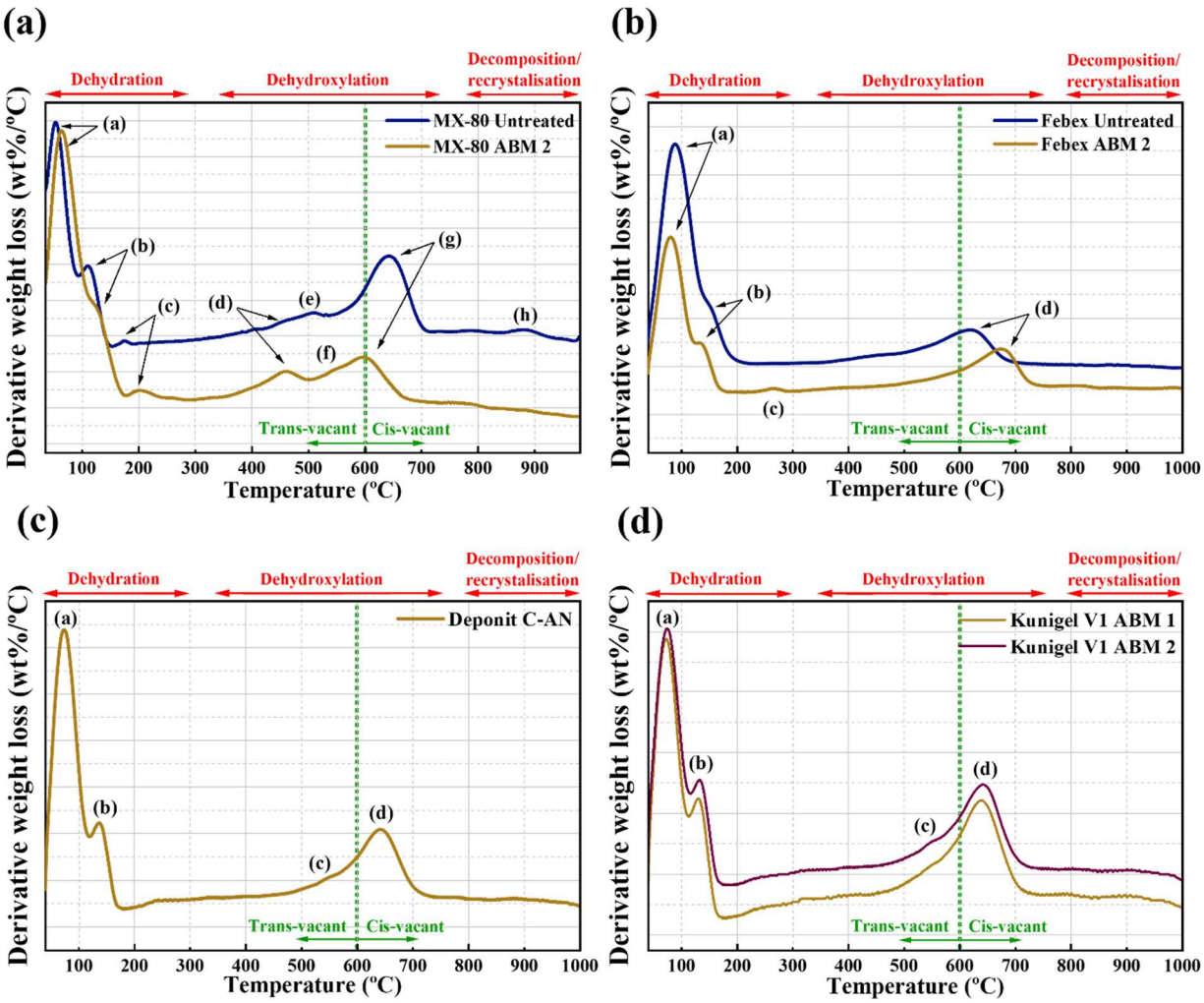

Figure 5.36: *(a) DTG results on MX-80 ABM 2 vs. untreated samples. (b) DTG results Febex ABM 2 vs. untreated samples. (c) DTG results on Deponit C-AN ABM 2 (d) DTG on Kunigel V1 ABM 1 and ABM 2.*

Since, TGA allows determination of the conditions under which the clays decompose and, therefore, identify the products of such decomposition, it constitutes a complementary technique for physicochemical analysis of ABM samples. Results obtained from TGA analysis are presented in Figure 5.36 and Table 5.26. The temperature test range ran from ambient to

1000°C. Due to the unavailability of pristine/reference Kunigel V1 and Deponit C-AN samples, only the experimental samples and MX-80 and Febex reference samples were examined.

Table 5.26: *Temperature values of peaks observed in TGA. Temperature accuracy = ±0.25°C* [269].

Sample	Peak position Figure 5.36							
	Temperature (°C)							
	(a)	(b)	(c)	(d)	(e)	(f)	(g)	(h)
MX-80 Untreated	53.54	109.97	173.84	461.16	509.28	-	642.12	881.42
MX-80 ABM 2	64.41	122.60	199.76	460.21	-	553.08	598.14	-
Febex Untreated	88.41	149.60	-	433.62	620.21	-	-	-
Febex ABM 2	81.43	109.97	267.59	-	677.99	-	-	-
Deponit C-AN ABM 2	73.71	137.61	554.88	643.61	-	-	-	-
Kunigel V1 ABM 172.70	72.70	130.06	551.03	638.91	-	-	-	-
Kunigel V1 ABM 2	73.71	131.91	551.03	641.76	-	-	-	-

The bulk matrix of bentonite is characterised by the constituent-assembly of minerals, as reflected in XRD. Consequently, progressively heating this material results in characteristic decomposition of these different products at different temperatures. Thus, TGA can be used to confirm mineral composition but also the presence of new minerals which began to form during the course of the in-situ AM test. The expected alteration and/or transformation processes in bentonite are those described in section 4.2.9. Figure 5.36 shows the results obtained from TGA analysis, which are presented as derivative weight loss or derivative thermogravimetric data (DTG). Table 5.26 presents the peaks identified in each sample. Significant differences between the ABM retrieved and the untreated samples were found in the DTG curves, which indicate the presence of corrosion by-products and possible structural modifications of the montmorillonite component of the experimental samples. Figure 5.36 (a) and Table 5.26 show the corresponding DTG curves of the MX-80 bentonite sample compared with the reference material. When comparing the respective curves, the differences discussed below were observed. In both DTG curves, the peaks related to the water loss occurring on the external surfaces and interlayer space due to sample dehydration were observed at (a), (b) and (c) respectively. The different thermal peak positions might be explained due to the heterovalent

character of the cations inhabiting the interlayer space, and it might also suggest certain migration and cation exchange in the areas in contact with the canister, as indicated in section 5.2.2. Continuing with the reference sample, the main dehydroxylation peak (g) is observed at 642.12°C, indicating the presence of cv dioctahedral smectite particles. When analysing this same peak (g) in the sample from the ABM in-situ test, a shift towards lower temperatures (598.14°C) was seen. This displacement is ascribed as an indicator of a structural modification within the montmorillonite component, since an increase in tv positions is observed. Structural transformations towards tv 2:1 layers caused by the heating or reduction of the octahedral Fe^{3+} could lead to the transformation of a cv montmorillonite into a mixed structure, with cohabiting tv and cv 2:1 layers, as suggested by Drits et al. [293] and Emmerich et al. [294]. The peaks observed at (e) and (f) could be ascribed to the two-stage dehydroxylation observed in 'abnormal' montmorillonites [271], [272] or, as stated by Heller and Kalman [273] caused by iron isomorphic substitutions within octahedral allocations. In addition, the peaks at (d) in both curves might indicate the presence of smectite particles with high iron content, since dehydroxylation of Fe-smectites (tv) occurs around 450-520°C [256]. Finally, one further peak (h) appeared in the decomposition zone that was not seen in the untreated material. The presence of this peak is associated with the displacement of the dehydroxylation peak that occurred in the experimental sample at 553.08°C (f) related to the endothermic-exothermic decomposition of the clayey matrix between 850 and 1000°C.

Figure 5.36 (b) and Table 5.26 displays the results obtained from TGA analysis carried out on the Febex and untreated bentonite samples. From comparing the DTG curves, several conclusions can be drawn. The observed peaks at (a) and (b), in both DTG curves, are due to dehydration of the samples and, therefore, there is a loss of water present on the external surfaces and in the interlayer space of the smectite component. This is also indicative of the heterovalent composition of the cations occupying the interlayer space [264], [265], [266], [267]. The peak observed at (c), only present in the ABM sample, might be explained because of the presence of goethite, since its dehydroxylation occurs at temperatures ranging from 250°C and 300°C [256], [278], [279], [280]. The peaks observed at (d) were assigned to the main dehydroxylation peak characteristic of montmorillonite, which indicates the presence of cis-vacant dioctahedral smectite clay particles. However, while this main peak in the reference sample is present at temperatures of about 620.21°C, in the ABM sample it shifts to a higher temperature value (677.99°C). Since the octahedral cations determine the dehydroxylation

temperature, this shift might be explained by the greater presence of dioctahedral Al-smectites (cis-vacant) whose dehydroxylation occurs at temperatures ranging between 670-730°C [256].

Figures 5.36 (c) and (d) display the DTG curves of Deponit and Kunigel V1 samples. Despite the differences observed in the previous samples, the DTG curves of Deponit and Kunigel V1 show the characteristic thermal peaks of bentonites and the values correlate well with those already reported in the literature [295]. There appears to be no significant differences.

5.2.8 Mössbauer spectroscopy analysis of iron valence state in ABM bentonite samples

As explained in section 4.2.6 and 5.2.4, Fe^{3+} oxides are common constituents of the bentonite matrix, but also, as predicted by the literature, the corrosion of the container and the local environment created in the interface between bentonite and the HAW container might have liberated iron by-products that could have diffused and interacted with the montmorillonite component. From XRT data of the Febex in-situ test sample (BM-B-41-1), the presence of small iron oxide particles, characterised by higher density and greater attenuation coefficient than the surrounding were visualised.

Since the ABM bentonite samples were in direct contact with the simulated steel container, it was expected that any container corrosion could contribute similar iron by-products into the bentonite that could be identified by Mössbauer. Mössbauer spectra of phyllosilicates usually consist of two doublets resulting from the presence of Fe^{3+} and Fe^{2+} in octahedral positions, influenced to a lesser degree by the presence of Fe^{3+} in tetrahedral positions [296]. Nonetheless, the complex structure of clays owing to the association of a variety of minerals, and the frequent isomorphic substitutions within their structure, may alter the Mössbauer effect, due to: (*i*) the substitution of iron by aluminium, leading to a decrease of the magnetic order of some iron oxyhydroxides, such as goethite and lepidocrocite [237], [238]; and (*ii*) the influence exerted by the presence of oxyhydroxides in the clayey matrix, which may change the magnetisation direction [237], [238]. Consequently, Mössbauer spectroscopy of clays is a reliable technique for the determination of Fe^{2+}:Fe^{3+} ratios and, therefore, indicates the ambient environmental redox conditions at the canister interface zone [296].

Table 5.27: *Mössbauer data of reference and ABM samples. Measurements performed at room temperature. B_{hf}: hyperfine magnetic field, δ: Isomer shift relative to ^{57}Fe, Δ: Quadrupole splitting, and RA: Relative spectral area (data acquired by Dr. María Sánchez Arenillas and Dr. Juan de la Figuera Bayón from Consejo Superior de Investigaciones Científicas (CSIC, Spanish National Research Council)). $^{1}SE_{(standard\ error\ RA\ MX\text{-}80)}$ =8%. $^{2}SE_{(standard\ error\ RA\ Febex)}$ =15%. $^{3}SE_{(standard\ error\ RA\ Kunigel\ V1)}$ =7%. $^{4}SE_{(standard\ error\ RA\ Deponit\ C\text{-}AN)}$ =16%.*

Sample	Assignment	B_{hf} (T)	δ (mmS^{-1})	Δ (mmS^{-1})	RA (%)[1, 2, 3, 4]
MX-80 Untreated	Fe^{3+} OH	-	0.48	1.11	10
	Fe^{3+} OH	-	0.34	0.54	53
	Fe^{2+} OH	-	1.15	2.83	23
	Fe^{2+} Td	-	0.94	2.50	14
MX-80 ABM 2	Fe^{2+} OH	-	1.15	2.81	42
	Fe^{3+} OH	-	0.32	0.57	58
Febex Untreated	Fe^{3+} OH	-	0.36	0.59	92
	Fe^{2+} Td	-	0.85	2.50	2
	Fe^{2+} OH	-	1.22	2.70	6
Febex ABM 2	Fe^{2+} OH	-	0.38	1.10	22
	Fe^{3+} OH	-	0.35	0.47	71
	Fe^{2+} Td	-	0.95	2.70	7
Kunigel V1 Untreated	Fe^{3+} (ultra-distorted)	-	0.31	1.46	14
	Fe^{2+} OH	-	1.20	1.80	15
	Fe^{2+} OH	-	1.18	2.86	17
	Fe^{3+} OH	-	0.32	0.61	54
Kunigel V1 ABM 1	Fe^{3+} OH	-	0.33	0.57	63
	Fe^{3+} OH	-	1.16	2.78	24
	Fe^{2+} OH	-	0.78	2.50	13
Kunigel V1 ABM 2	Fe^{2+} OH	-	1.10	2.83	27
	Fe^{3+} Td/OH	-	0.29	0.59	73
Deponit C-AN Untreated	Fe^{3+} OH	-	0.42	1.18	16
	Fe^{3+} OH	-	0.34	0.51	76
	Fe^{2+} Td	-	0.80	2.50	5
	Fe^{2+} OH	-	1.14	2.87	3
Deponit C-AN ABM 2	Fe^{2+} OH	-	1.12	2.78	9
	Fe^{3+} Td/OH	-	0.35	0.53	91

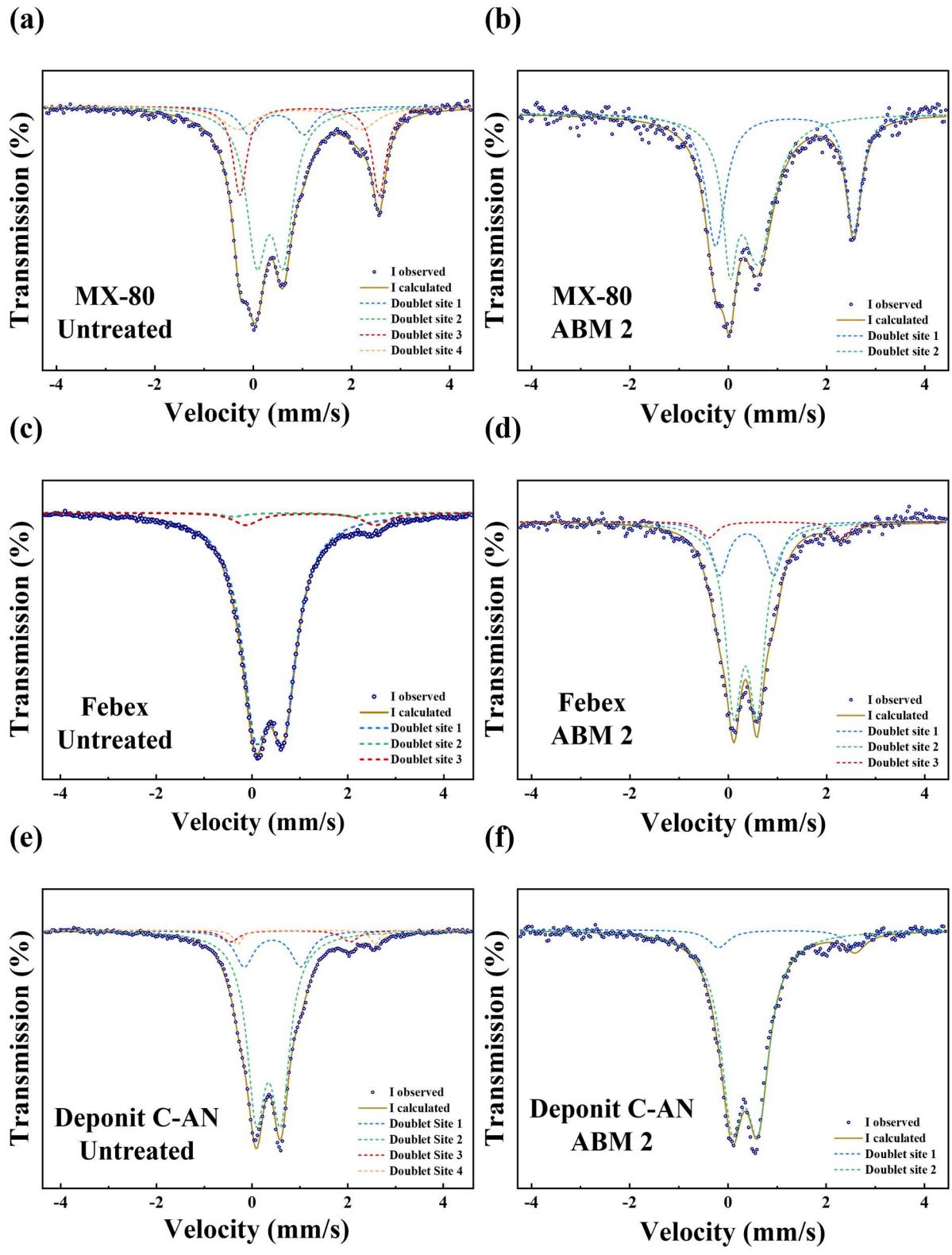

Figure 5.37: *(a) Mössbauer spectra of MX-80 reference sample. (b) Mössbauer spectra of MX-80 ABM 2. (c) Mössbauer spectra of Febex reference sample. (d) Mössbauer spectra of Febex ABM 2. (e) Mössbauer spectra of Deponit C-AN reference sample. (f) Mössbauer spectra of Deponit C-AN ABM 2 (data acquired by Dr. María Sánchez Arenillas and Dr. Juan de la Figuera Bayón from Consejo Superior de Investigaciones Científicas (CSIC, Spanish National Research Council)).*

Mössbauer analyses were initially carried out on pristine samples of each sample to provide reference data. The Mössbauer analyses were performed at CSIC. Comparison of the hyperfine parameters between the ABM samples and the untreated materials aimed to quantify the presence of Fe^{2+} and Fe^{3+} within the structure of the experimental samples. Figures 5.37 and 5.38 and Table 5.27 display the results obtained through Mössbauer analysis.

Figure 5.37 (a) and Table 5.27 show the data collected from the unaltered MX-80 bentonite sample. From Figure 5.37 (a), it can be stated that the spectrum is asymmetric and can be fitted by four doublets. The spectrum is best defined with two Fe^{3+} and two Fe^{2+} sites. The first Fe^{3+} site (double site 1), with an isomeric or centre shift (δ) at 0.48mmS^{-1} and a quadrupole splitting (Δ) of 1.11mmS^{-1}, was assigned to trans-octahedral Fe^{3+}. The second Fe^{3+} site (double site 2, δ=0.34mmS^{-1}, Δ=0.54mmS^{-1} and RA=53%) was characterised as cis-octahedral Fe^{3+}. The third Fe^{2+} site (doublet site 3, δ=1.15mmS^{-1}, Δ=2.83mmS^{-1} and RA=23%) was fitted as Fe^{2+} occupying octahedral positions. The fourth Fe^{2+} site (doublet site 4, δ=0.94mmS^{-1}, Δ=2.50mmS^{-1} and RA=14%) was assigned to Fe^{2+} occupying tetrahedral sites.

Figure 5.37 (b) and Table 5.27 display results from the MX-80 ABM 2 bentonite sample. The spectrum is asymmetric and can be fitted by two doublets; one Fe^{2+} site and one Fe^{3+}. The first Fe^{2+} site (doublet site 1, δ=1.15mmS^{-1}, Δ=2.81mmS^{-1} and RA=42%) was assigned as Fe^{2+} occupying octahedral locations. The second Fe^{3+} site (doublet site 2, δ=0.32mmS^{-1}, Δ=0.57mmS^{-1} and RA=58%) was characterised to cis-octahedral Fe^{3+}. Therefore, from the MX-80 Mössbauer results it can be stated that in the experimental sample Fe^{2+} and Fe^{3+} coexists in octahedral locations. Although, the coexistence of iron in both oxidation states was also observed in the untreated sample, the relative spectral area (RA) of the Fe^{2+} in octahedral sites of the ABM sample is higher than in the untreated sample.

Figures 5.37 (c) and (d), and Table 5.27 display results from the Mössbauer analysis performed in the Febex untreated and ABM samples. It can be said that both spectra are asymmetric and can be fitted in three doublets. Overall, the experimental and untreated samples present Fe^{3+} and Fe^{2+} coexisting in octahedral locations, as well as Fe^{2+} occupying tetrahedral sites. However, as previously observed in the MX-80 bentonite sample, the RA of the Fe^{2+} in octahedral locations is again higher in the experimental sample than in the untreated sample.

Figures 5.37 (d) and (e), and Table 5.27, present data relating to the Deponit C-AN bentonite sample. The observed asymmetry in the previous samples is also seen in the Deponit C-AN

spectra. The spectrum of the untreated Deponit C-AN bentonite (Figure 5.33 (d)) can be fitted by four doublets with two Fe^{3+} and Fe^{2+} sites. The first Fe^{3+} site (doublet site 1, δ=0.42mmS^{-1}, Δ=1.18mmS^{-1} an RA=16%) was characterised as trans-octahedral Fe^{3+}.

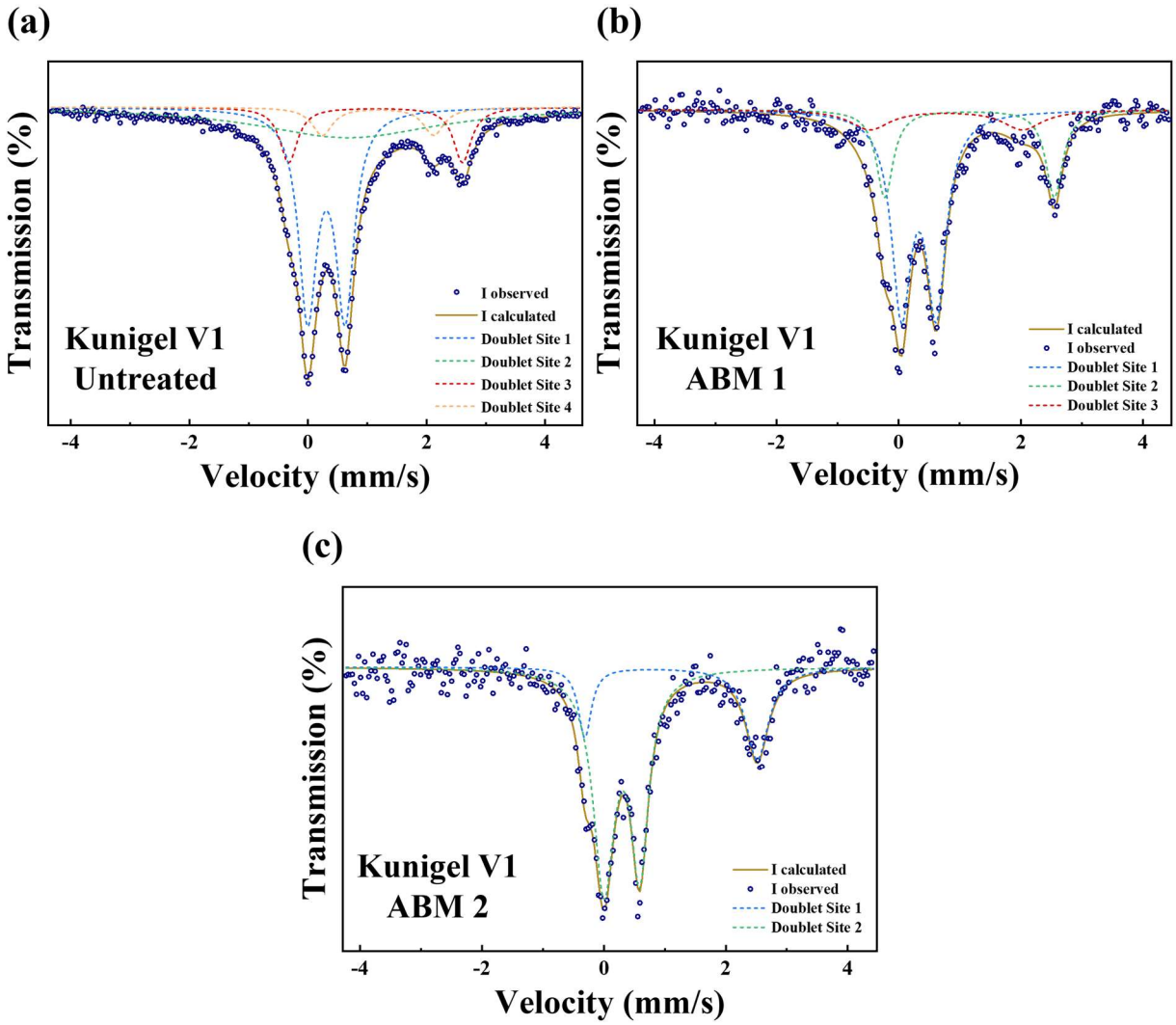

Figure 5.38: *(a) Mössbauer spectra of Kunigel V1 reference sample. (b) Mössbauer spectra of Kunigel V1 ABM 1. (c) Mössbauer spectra of Kunigel V1 ABM 2 (data acquired by Dr. María Sánchez Arenillas and Dr. Juan de la Figuera Bayón from Consejo Superior de Investigaciones Científicas (CSIC, Spanish National Research Council)).*

The second Fe^{3+} site (doublet site 2, δ=0.34mmS^{-1}, Δ=0.51mmS^{-1} and RA=76%) was characterised as cis-octahedral Fe^{3+}. The third Fe^{2+} site (doublet site 3, δ=0.80mmS^{-1}, Δ=2.50mmS^{-1} and RA=3) was assigned to Fe^{2+} in octahedral positions. The fourth Fe^{2+} site (doublet site 4, δ=1.14mmS^{-1}, Δ=2.87mmS^{-1} and RA=5%) is assigned to Fe^{2+} occupying octahedral positions. The spectrum of the Deponit C-AN sample (Figure 5.37 (e)) can be fitted by two doublets corresponding with one Fe^{2+} site and one Fe^{3+} sites. The first Fe^{2+} site (double site 1, δ=1.20mmS^{-1} and Δ=2.78mmS^{-1} and RA=9%) was characterised as Fe^{2+} occupying

octahedral positions. The second Fe^{3+} site (doublet site 2, δ=0.35mmS^{-1}, Δ=0.53mmS^{-1} and RA=91%) was characterised as cis-tetrahedral Fe^{3+}. From these results, it can be concluded that the iron present in the experimental sample is mostly trivalent, i.e. the iron is fully oxidised.

Figure 5.38 and Table 5.27 show results obtained from the pristine Kunigel V1 and the samples extracted from the parcel 1 and 2. Overall, all the spectra are asymmetric and the proportion of Fe^{2+} coexisting with Fe^{3+} is similar between samples.

In summary, from Mössbauer analysis it can be stated that in all the samples we see the coexistence of Fe^{3+} and Fe^{2+} in octahedral locations. The proportion of Fe^{3+} and Fe^{2+} with respect to RA is variable between samples. Of possible significance is the notable increase in Fe^{2+}:Fe^{3+} ratio for iron in octahedral coordination that appears in MX-80 and Febex samples versus their reference counterparts. This indicates that chemical reduction of heater-proximal bentonite has occurred.

5.3 Concluding statement

This chapter has presented results obtained from physicochemical evaluation of samples from the ABM project. Analyses were carried out on untreated samples to provide baseline data, allowing an exhaustive examination of any chemical or structural degradation within the samples. Initially, the ABM project was conceived to evaluate the performance of bentonite from different worldwide deposits under simulated geological disposal conditions. However, since the in-situ test was designed with an iron heater this also provided an opportunity to investigate the effect of iron corrosion on different bentonite types.

As discussed in Chapter 2 (section 2.3), after canister emplacement in a GDF the environment at the interface between bentonite and the canister is expected to be initially highly-dynamic, driven by the high starting surface temperatures of the canister surfaces, and the interface may partially dry out as a result of this. The oxygen trapped in the clayey matrix, after facility closure, will result in oxidation of the metal container. The rate of corrosion is based on the metal or alloy selected for the container. As temperature decreases and the barrier slowly re-saturates, the formation of oxyhydroxides is likely to occur. During this stage, the developed pH is expected to be extremely basic and, consequently, dissolution of the smectite component,

together with the corrosion by-products, will occur. The dissolved silica will migrate from the hotter areas (close to the canister) and re-precipitate in cooler zones further away from the container surfaces. Once free oxygen has been consumed, chemically-reducing conditions will become established and give rise to the formation of magnetite and carbonates, such as siderite. Under these conditions, the resulting environment will be highly complex and the expected, but very slow, alteration and/or transformation of the smectite component will cause incremental degradation of the clay barrier, detrimentally affecting some of its mechanical and chemical properties, such as its swelling capability, hydraulic conductivity and CEC.

CEC evaluation of the different bentonite materials did not show any deviation from the values obtained from the untreated materials. However, exchangeable cation analyses displayed a clear migration of Ca^{2+} and Mg^{2+} towards the canister, as observed in the BM-B-41-1 sample. In addition, the sodium bentonites (MX-80 and Kunigel V1) showed a partial replacement of the interlayered Na^{+} with Ca^{2+} and Mg^{2+}. This finding was confirmed through examination of the 001 reflection, both in XRD and synchrotron data. Such an alteration would cause a reduction in the swelling capacity.

From the bulk and clay mineralogy point of view, there was no evidence of alteration and/or transformation of the montmorillonite in any of the evaluated samples. However, synchrotron analysis, which is arguably more sensitive, showed the presence of ferrosaponite, in the Febex and MX-80 bentonite samples also indicated by TGA. The presence of ferrosaponite suggests that, due to canister corrosion, the liberated ions had subsequently undergone sufficient electron transfer with cations in the montmorillonite structure to form to a very limited extent of new minerals. In addition, synchrotron examination confirmed the presence of iron phases blended in the clayey matrix. These results were in accordance with those obtained through FTIR. TGA analysis confirmed a structural modification within the montmorillonite component, particularly noticeable in the MX-80 sample where the presence of a tv layer could have been caused by transformation of a cv montmorillonite into a mixed structure. Mössbauer analysis showed Fe^{3+} and Fe^{2+} cohabiting in octahedral allocations, and with ratios varying between samples. The high proportion of Fe^{2+} in MX-80 and Febex samples within their structures suggests partial chemical reduction of structural Fe^{3+}.

Results indicate that, due to the presence of ferrosaponite, very limited alteration of the montmorillonite has occurred. Nonetheless, this alteration was not observable in all different bentonite samples analysed. The highly-dynamic environment developed at the interface might

have defined the local degree of alteration. Therefore, to further evaluate the degree of alteration, a batch test was conducted to examine the kinetics of the physicochemical processes expected at the bentonite-container interface. Potential alteration will be 'measured' by comparing the physicochemical state of the samples and the results obtained in Chapter 4 and the present chapter.

Pragmatically, it would seem that the alterations indicated in the current chapter cannot be associated with a significant progressive diffusion of iron into the bentonite matrix. This is not evidenced to have occurred. Accordingly, the alterations observed must be driven partially by the higher heat flux being supplied to the system, which could have induced more rapid kinetic reactions. Consequently, the ABM experiment could have exhibited greater alteration kinetics than the Febex experiment due to the higher heater temperature. This may highlight how important it will be for any GDF facility to ensure the lowest possible canister temperatures for waste or SNF emplacement. If canister temperatures are well above 100°C, then deleterious alterations could have progressed rapidly, with alterations being, perhaps, very significant over many decades. Therefore, alteration kinetics warrant further research.

Alterations seem to be driven by a combination of chemical reduction of octahedral iron in the montmorillonite structure, concurrent with a substantial local shift in exchangeable cations, with expulsion of Na^{+} in exchange for Ca^{2+} and Mg^{2+} driven by hydrothermal effects, also seen in the Febex experiment.

Indeed, for both the Febex and ABM experiments, the analysis indicates that chemically-reducing conditions had established themselves in the bentonites at the container interfaces. The strongest evidence for this is within the Mössbauer data. Establishment of reducing conditions is, again, logical and somewhat inevitable, because the heated canister surfaces will consume free oxygen very rapidly (on geological timescales) through corrosion reactions. Once this free (presumably water-dissolved) oxygen is consumed then progressive corrosion will consume water, stripping the molecular oxygen to form oxides and releasing hydrogen as a by-product. Hence, redox conditions will get progressively more negative (reducing) as corrosion progresses.

The observed alteration of the ABM bentonites, some of which naturally have measurable iron content, is most notable and potentially of significance if the rates of alteration can, in the future, be defined experimentally (or through modelling). The results also show that this

alteration is likely to occur for waste canisters made from other materials, such as copper or titanium, which are regarded as more corrosion-resistant but also more expensive.

Further research will need to better define the rates for bentonite alteration and/or transformation, and determine whether they change substantially during the transition from oxic to anoxic conditions and how the gradual cooling of the containers may curtail the alteration rates. .

Chapter 6 Experimental time-resolved x-ray analysis study on the anaerobic interactions between carbon steel and bentonite under simulated geological disposal conditions

6.1 Chapter overview

The current chapter provides a time-resolved investigation of the corrosion of carbon steel in bentonite under simulated GDF conditions at a range of temperatures in comparison to copper and titanium metal. In-situ batch tests without braking experimental containment were conducted under at temperatures, ranging between 55°C and 100°C. These temperatures were selected as representative of the temperatures expected in the interface environment between the compacted bentonite body and the waste canister. Landolt et al. [27] and Leupin et al. [89] set an initial surface-canister temperature between 100-150°C several years after the emplacement of the containers in their respective boreholes (section 2.3). Despite this, the upper thermal limit for the work presented in this chapter was set at 100°C, in accordance with the thermal limit of the UK disposal concept [297], and also being representative of the selected thermal limits of many countries (Table 6.1).

The temperatures were selected to investigate the thermal impact exerted by the heat released from the containers and were representative of those expected under real geological disposal conditions. The different considered scenarios regarding temperature, time and saturation were intended to provide complementary insight to the Febex and ABM bentonite sample characterisation and, therefore, provide additional information on the kinetics of the mineralogical transformation and/or alteration that bentonite might experience over the timescales considered. The intention of the experiment was to simulate the expected anaerobic conditions. Therefore, special attention was given to the experimental design and set up of the

experimental cells and conservation of the metal samples after their preparatory chemical pickling, as well as the compaction process. However, it could not be guaranteed that aerobic conditions were not initially present, since the compaction bentonite process implied exposure of the samples, as well as the wires, to air. To gain comprehensive knowledge of possible bentonite alteration and/or transformation, the exposure time and temperature were sequentially varied. This sequential variation was intended to evaluate the extent of alteration and/or transformation (outlined in Chapter 2), if any, and results were compared to unaltered Febex bentonite.

Table 6.1: *Thermal limits imposed by some countries.*

Country	Host rock	Thermal limit	Reference
United States	Yucca Mountain	300°C first 500 years, and 200°C the following 9,500 years	Sandia National Laboratories (2007) [298]
Switzerland	Opalinus clay formation	125°C	Nagra (2002) [26]
Sweden	Crystalline rock	100°C	Hökmark and Fälth [299]
Spain	Crystalline rock	100°C	ENRESA (2000) [43]
Japan	Crystalline rock	100°C	JNC (2000) [300]
South Korea	Crystalline rock	100°C	Choi and Choi (2008) [301]
Germany	Salt host rock	200°C	Rothfuchs [302]
France	Callovo-Oxfordian formation	100°C	Andra (2005) [34]
Finland	Crystalline rock	100°C	Smith et al. [303]
Canada	Granitic host rock	100°C	Johnson et al. [304]
Belgium	Boom clay formation	100°C	Wickham [305]

The experimental methodology for this work was described in section 3.2.3. Saturation of the samples was performed using granitic water, characterised by a high salinity (Table 3.23) as representative of groundwaters expected at great depths in a crystalline basement bedrock. Additionally, two cells conforming the batch test were saturated with Grimsel Test Site water (Table 3.24) to provide consistent and complementary information to the experimental work carried out in Chapter 4.

The Febex bentonite, a bentonite of Ca-Mg type, was selected for the present experimental procedure due to its elevated montmorillonite content [43]. The bentonite was received in

granular form provided courtesy of CIEMAT. Once the experiment was completed, sub-samples were from the alteration zones at the interface contact between the bentonite and the metallic wires. The degree of alteration of bentonite in contact with C-steel bodies varied from one sample to another (Figure 6.1). Initially, this observation was attributed to the degrees of compaction, saturation and porosity in the vicinity of the metallic wires. Furthermore, in the contact interface of bentonite with titanium and copper metal bodies no discolouration was observed. Therefore, only the samples arose from the contact between bentonite and C-steel bodies will be discussed in this chapter.

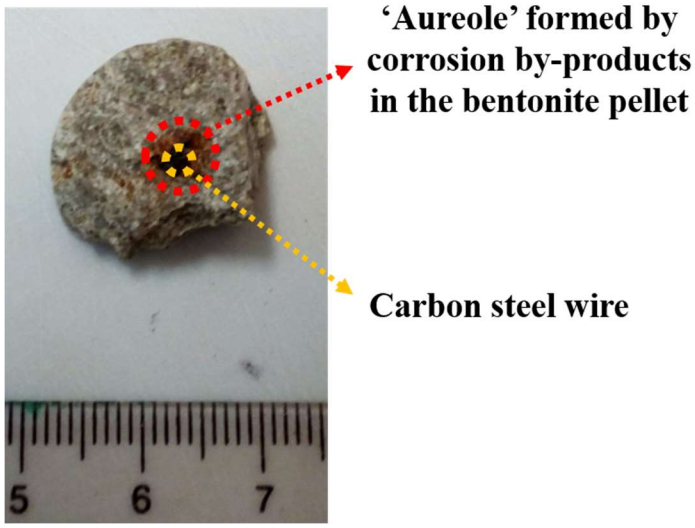

Figure 6.1: *Carbon steel wire in contact with compacted Febex bentonite.*

The main experimental aims for the work presented in this chapter were to determine the effects of temperature, corrosion and water salinity on the functionality of the clay barrier. The different thermal loadings and the duration of the test were chosen to isolate the combined effects of temperature and salinity on the physicochemical properties of the bentonite. The following describes the applied methodology to evaluate the durability of the cells employed during the batch test, followed by comprehensive results of μCT and high-resolution diffraction conducted on the bentonite samples to evaluate the physicochemical state after the experiment.

6.2 Experimental set-up

The present section depicts the results of a short test performed to evaluate the pressure evolution within the cells during heating and to ensure stability of the experiment in the

long-term. For this purpose, a cell was equipped with an analogue pressure gauge screwed onto a hollow tube (whose dimensions are presented in Table 6.2) welded to an upper stainless steel 316L lid replacing the original upper closing due to the 'poor' welding properties of the original aluminium lid. Since the main purpose of this preliminary test was to evaluate the performance of the cells in the long-term, as well as the swelling pressure exerted by the bentonite over the course of an experiment, a sample was prepared following the protocol described in Chapter 3.

Table 6.2: *Tube dimensions.*

Dimensions	
Length	400mm
Inner diameter	4.75mm
Outer diameter	6.35mm
Inner volume hollow tube	12,667.69mm^3

To record the temperature profile during cell heating, a thermocouple was secured onto the external body of the cell. Sequential heating on sealed cells was performed inside an oven and, therefore, under isothermal conditions. The test was initiated at 50°C, and the temperature was increased in 25°C steps at 24 hour intervals, until >150°C was reached. The temperatures selected for this preliminary test were not those considered for the final test, but more to test a wider envelope of temperature conditions with regards to cell durability and the pressure exerted by bentonite swelling.

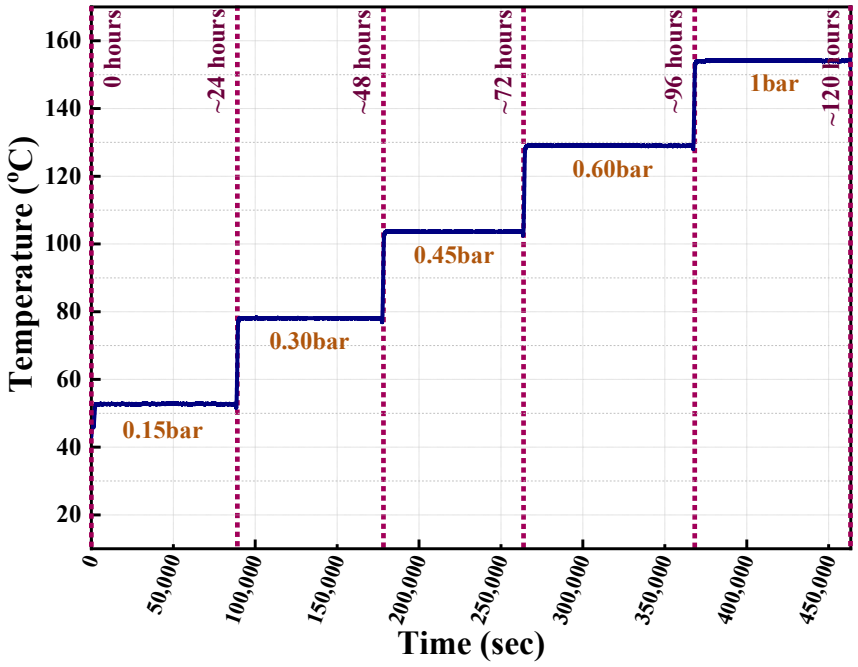

Figure 6.2: *Pressure evolution within the cell with increasing time and temperature.*

Figure 6.2 and Table 6.3 show the pressure changes registered with increasing temperature. From Table 6.3, a linear pressure increase can be observed as the temperature increases. Nonetheless, in the range of 125°C to 150°C, the pressure inside the cell abruptly increased by 0.40bar. Despite the change observed in pressure and, after experiment completion, once the cell was dismantled, no visual changes were observed in the compacted body cell. However, given the consensus regarding the upper thermal limit selected by many countries (Table 6.1), temperature ranges between 100°C and 150°C were ruled out since they would not be representative of temperatures under geological disposal conditions.

Table 6.3: *Pressure evolution with increasing time and temperature.*

Time (hours)	Temperature	Pressure increasing (bar)
0-24	0°C to >50°C	0.15
24-48	>50°C to >75°C	0.3
48-72	>75°C to >100°C	0.45
72-96	>100°C to >125°C	0.6
96-120	>125°C to >150°C	1

It should be noted that since a hollow tube of 400mm length was welded onto the cell lid with an attached pressure gauge, the water-vapour developing inside the cell headspace had a greater expansion volume, so that the measured pressures were not entirely representative of the pressures likely to develop inside the actual experimental cells. Thus, the dimensions of the device (cell and tube) were considered (Table 6.4) to calculate the expected internal pressures for the real experimental cells.

Table 6.4: *Device dimensions. Volume of each piece of the device was calculated by means of Autodesk Fusion 360.*

Cell + tube volume	$2.98 \cdot 10^4 mm^3$
Body cell volume	$8{,}906.947 mm^3$
Liner volume	$5{,}376.086 mm^3$
Bentonite pellet volume	$15{,}942.086 mm^3$

Since Febex bentonite itself contains water in its structure (13.70%) and considering that the sample was fully-saturated during preparation (section 3.2.3), the theoretical amount of water within its structure was considered to be 7.60ml. In addition, the granular bentonite was compacted considering the inner volume of the compaction tool (section 3.2.3.3.2.3).

Therefore, the 'free space' for water to move was the inter-aggregate space within the bentonite pellet. To calculate the porosity of the pellet Table 6.5 and Equation 6.1 were utilised.

Table 6.5: *Febex bentonite total porosity at a dry density of 1.65 (g/cm^3)* [306].

Φ (%)	38.90

$$Total\ porosity\ (\Phi) = \frac{Pore\ volume}{Bulk\ volume} \qquad \text{Equation 6.1}$$

The final estimation space for water-vapour phase to move is tabulated in Table 6.6.

Table 6.6: *Space for water-vapour phase to move in the interior space of the device.*

Free space inside experimental cells	6,328.2mm^3
Free space inside test cell	18,995.9mm^3

The estimated pressure inside the experimental cells are displayed in Table 6.7. The calculations were conducted by considering Boyle's law.

Table 6.7: *Pressure changes registered with increasing temperature.*

Time (hours)	**Temperature**	**Pressure increasing (bar)**
0-24	0°C to >50°C	0.45
24-48	>50°C to >75°C	0.90
48-72	>75°C to >100°C	1.35
72-96	>100°C to >125°C	1.80
96-120	>125°C to >150°C	3.00

Although the integrity of the cells was physically demonstrated by means of this short-term experiment, a thermal stress simulation was also carried out, using Autodesk Fusion 360, to assure the viability and structural integrity of the call and the experiment in the long-term.

The boundary conditions were defined considering an inner pressure of 4 bars (0.40 MPa), the selected experimental temperatures (50°C; 70°C; 90°C; and 100°C) and the physical properties of the aluminium 6082 T6 utilised for the manufacture of the cells (Table 6.8). To perform the simulation, the cell body was modelled in Autodesk Fusion 360, including the Teflon liner and the upper lid with sealing O-ring. The Von Mises values derived from the simulation are presented in Table 6.9 and Figure 6.3. The Von Mises stress is mostly used for ductile materials, such as metals, to determine if a given material will yield or fracture. The Von Mises yield

criterion establishes that if the Von Mises stress of a ductile material, under load, is equal or greater than the yield strength of that given material under a simple tension, the material will yield.

Table 6.8: *Physical properties of the aluminium 6082 T6, data provided by Goodfellow.*

Density	$2.7 \cdot 10^{-6} kg/mm^3$
Young's Modulus	70,000MPa
Poisson's Ratio	0.33
Yield Strength	250MPa
Ultimate Tensile Strength	260MPa
Thermal Conductivity	0.17W/(mm°C)
Thermal Expansion Coefficient	$2.31 \cdot 10^{-5}$/°C
Specific Heat	900J/Kg°C

Table 6.9: *Results simulation body cell.*

Boundary conditions simulation	**Von Mises**	
	Minimum	**Maximum**
50°C (0.40MPa)	$7.848 \cdot 10^{-4}$MPa	92.18MPa
70°C (0.40MPa)	0.001346MPa	153.7MPa
90°C (0.40MPa)	0.001908MPa	215.1MPa
100°C (0.40MPa)	0.002189MPa	245.9MPa

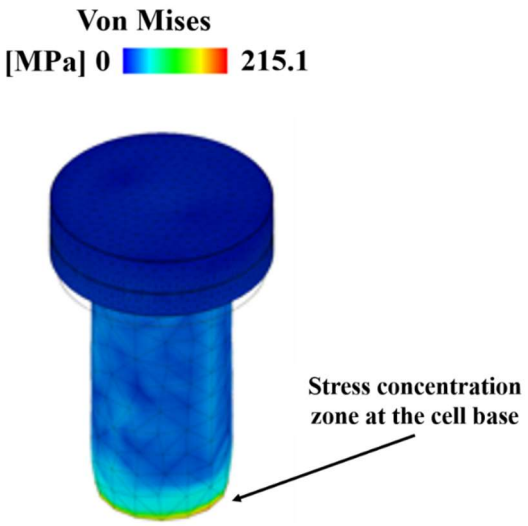

Figure 6.3: *Simulation result at 0.40MPa and 90°C, including mesh.*

Therefore, by comparing the aluminium 6082 T6 yield strength value (Table 6.8) and results obtained from the simulation, that is to say, with the Von Mises yield criterion obtained, it can

be affirmed that even under the most severe experimental pressurisation scenario the cells will preserve their physical integrity, since the calculated Von Mises values at a given scenario remain below the yield strength. With this now understood, the experiment was set and run for seven months.

6.3 Laboratory x-ray tomography studies to chart the in-situ evolution of wire corrosion

As indicated in section 1.4, bentonite has been selected as vital component in most international programmes for the safe disposition of HAW. The primary application of bentonite is its use as a buffer material in an EBS, confining the radioactive waste inside metallic containers. Containers would be deposited into drilled boreholes at great depths, and the pre-compacted bentonite would be placed around the containers, initiating the post-closure phase of the waste facility and saturation of the clay barrier. The saturation of the geotechnical barrier would provide an environment of low oxygen availability and low permeability at the contact interface between the bentonite and the containers [89], [90], [307]. This is the generally accepted expectation.

The design basis of an EBS is centred on the principle of preventing accelerated corrosion, decreasing the release rate of actinides, inhibiting microbial growth and providing a plastic deformation zone to mitigate against displacements of the host rock. However, it has been predicted in the literature (Chapter 2) that due to anoxic local conditions developed at the contact interface, the ineluctable container degradation will give rise to corrosion by-products that might interact with the buffer material, inducing its alteration and/or transformation towards mineral phases that will degrade its ability to swell and, therefore, its self-healing capability. The container impairment will occur over time scales in the order of 10^5 years [89], [119]. Therefore, corrosion of steel base metallic components, and later interactions of the corrosion products with the buffer, is arguably the one most significant problem in an EBS. Thus, to visualise the development of expected corrosion inside a simulated system, we have used x-ray tomography to study the corrosion of small steel wires embedded in bentonite.

The x-ray tomography technique is based on the fact that a material can potentially attenuate an x-ray flux passing through it (section 3.3.4.3). The degree of attenuation experienced depends on the energy of the x-rays and the elemental composition of the object. In general, the x-rays generated have a wide energy range and, therefore, do not attenuate equally when passing through an object. For example, when passing though the central areas of the metal wires, the x-rays would be more attenuated compared with those passing through the edges. Thus, the reconstructed images of the wires have brighter voxels at the edges. This effect is known as 'beam-hardening' and is caused by the technique itself and not by the density of the material. However, the use of filters reduces this effect, as well as the scattering effect. A Zeiss HE1 filter was used for this study (composition undisclosed) to reduce the effect of beam hardening. Scan parameters were 2001 projections, 140kV and 71µA. Analysis was performed over the 24 C-steel wires. However, the representative data presented below belong to sample 18 and 24, exposed to 100°C for 183 and 211 days, respectively.

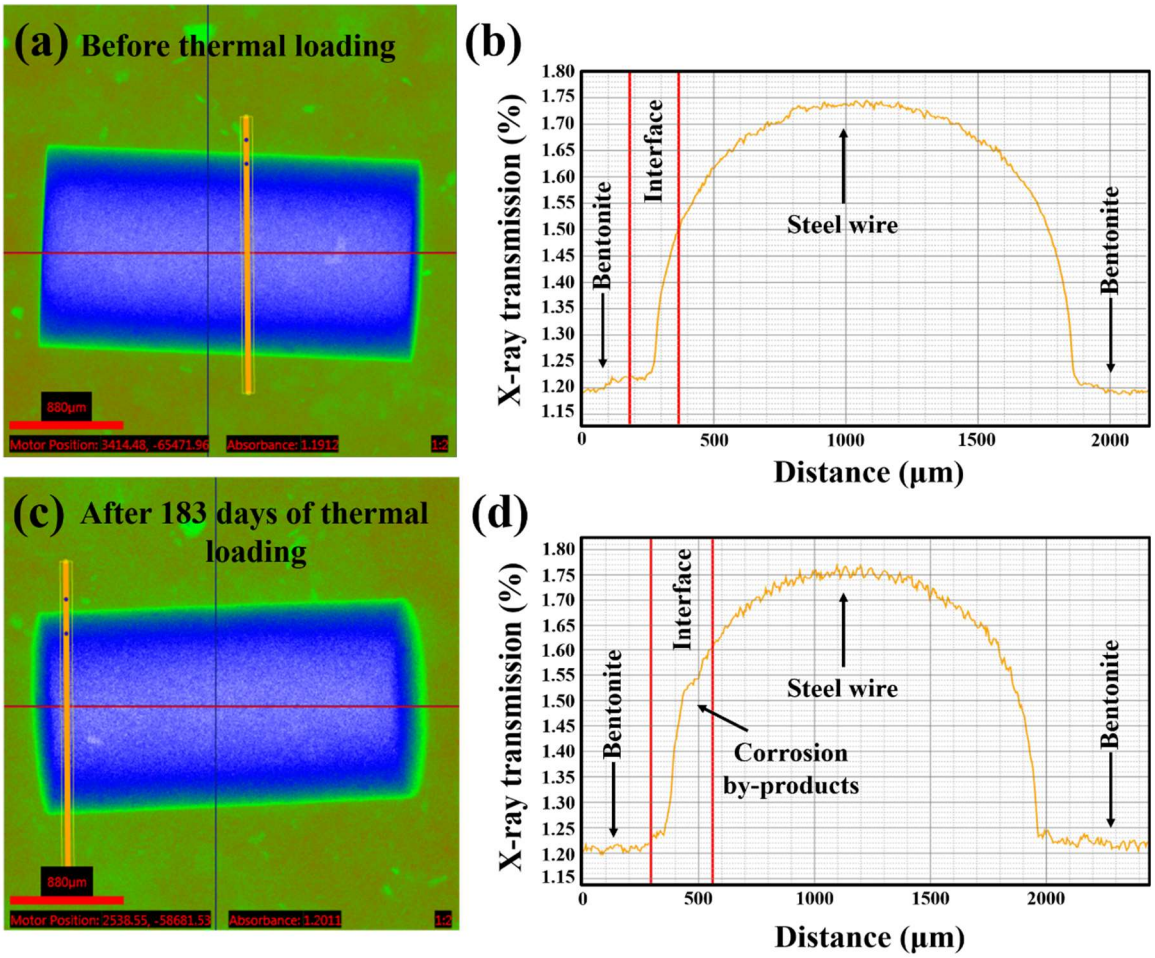

Figure 6.4: *(a) C-steel wire of sample 18 before heating. (b) Variation in transmission on sample 18 before heating. (c) C-steel wire of sample 18 after heating at 100ºC for 183 days. (d) Variation in transmission on sample 18 after heating at 100ºC for 183 days .*

In CT, x-ray attenuation varies depending on the material scanned. Steel materials, corrosion products and bentonite have all different densities. Therefore, the x-ray attenuation will be different. Figures 6.4 and 6.5 show the variation in x-ray transmission along a probing line which passes through the bentonite, corrosion products and steel wire.

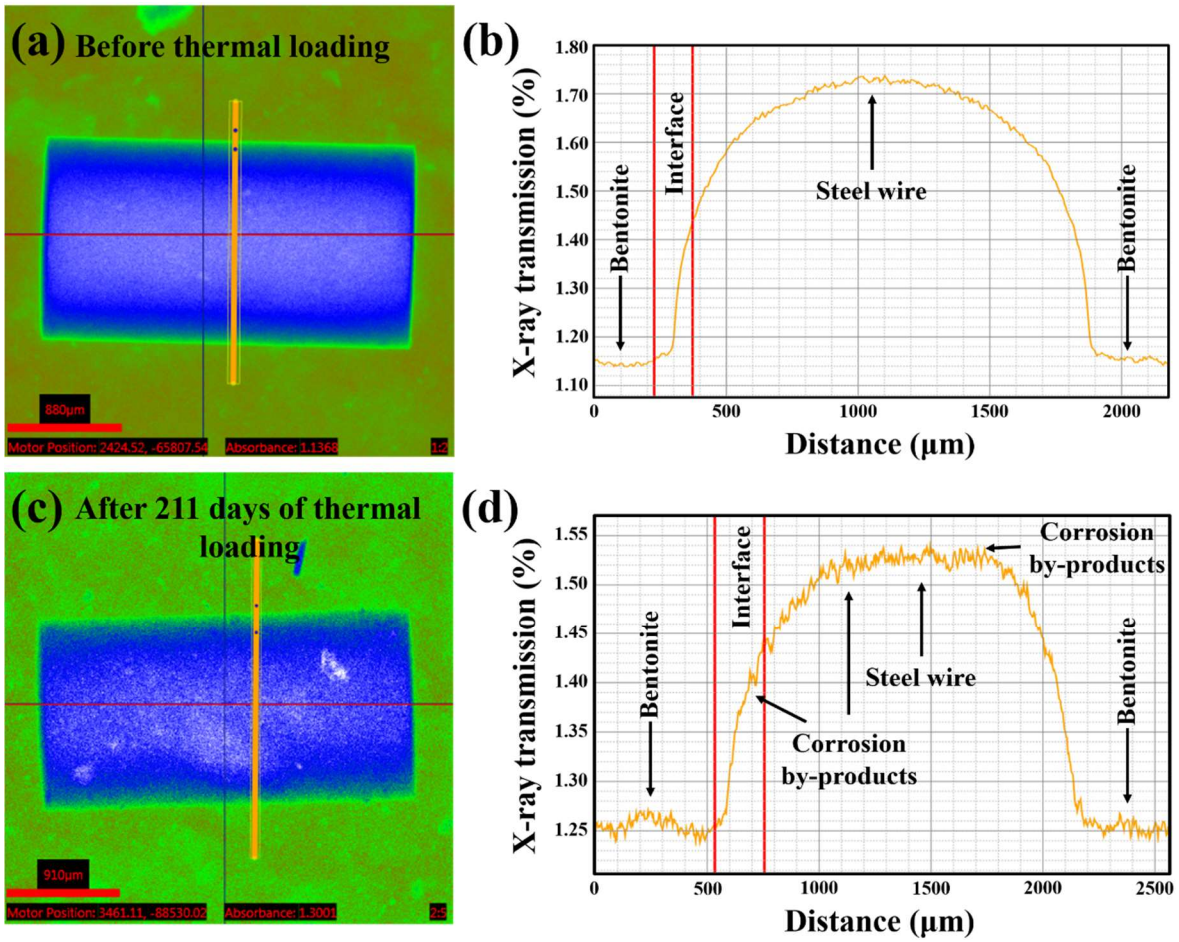

Figure 6.5: *(a) C-steel wire of sample 24 before heating. (b) Variation in transmission on sample 24 before heating. (c) C-steel wire of sample 24 after heating at 100ºC for 211 days. (d) Variation in transmission on sample 24 after heating at 100ºC for 211 days .*

Figure 6.4 visualises the C-steel wires before and after heating and the probing line of the sample exposed to 100°C for 183 days. Figures 6.4 (b) and (d) show the variation in transmission as a function of distance. In Figure 6.4 (d) we can observe a variation in transmission in the interface zone that might be an indicator of the formation of corrosion by-products.

Figure 6.5 shows the C-steel wires before and after heating and the probing line of the sample exposed to 100°C for 211 days. Figure 6.6 (b) and (d) show the variation on transmission as a function of the distance. Figure 6.6 (d) depicts a variation in transmission at the interface and

over the surface of the C-steel wire, as observed in Figure 6.5 (d), indicating the possible formation of corrosion by-products due to the experimental conditions. Since there was a variation in transmission in the examined metal bodies at high temperatures, their reconstruction was carried out using Avizo Lite to better visualise the degree of their degradation (Figure 6.7). The previous figures (Figure 6.4 and 6.5) aimed to show a variation in transmission due to the formation of corrosion by products, to visualise how the corrosion has been evolving over C-steel wire surfaces considering time, thermal loading and different water composition. Reconstructed 3D volumes were also obtained from samples exposed to less experimental time (Figure 6.6).

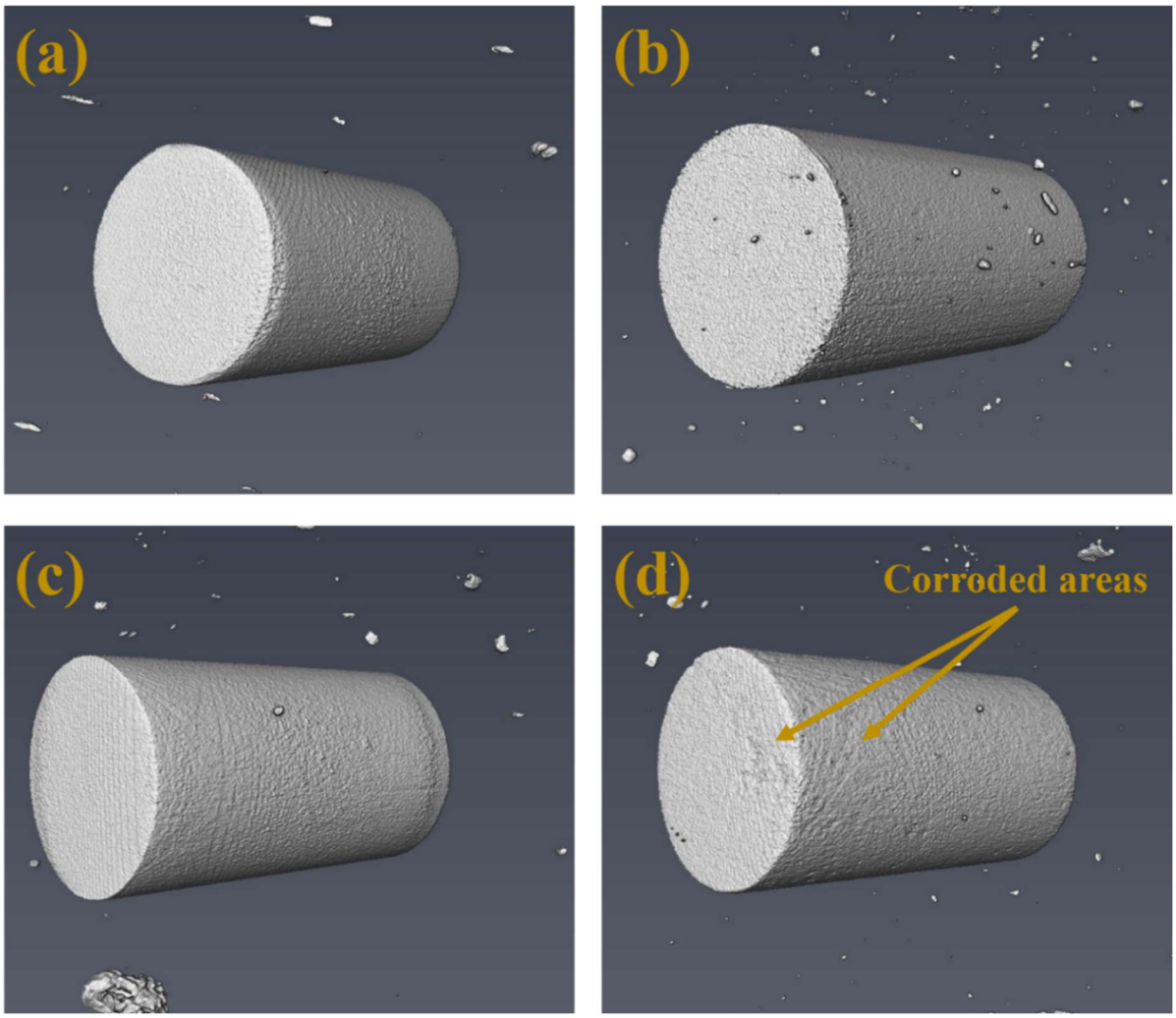

Figure 6.6: *(a) Micro-tomographical surface of C-steel wire before heating (sample 6). (b) Micro-tomographical surface of C-steel wire after 61 days of heating at 100°C (sample 6). (c) Micro-tomographical surface of C-steel wire before heating (sample 12). (d) Micro-tomographical surface of C-steel wire after 122 days of heating at 100°C (sample 12).*

The tomographic stack recorded form the C-steel bodies were processed to provide visualisation of their initial state (Figures 6.6 and 6.7). Figures 6.6 (a) and (c) and Figures 6.7

(a) and (c) show the reconstructed images of the specimens not yet exposed to 100°C thermal loading. To better analyse the spatial distribution of wire corrosion, the 3D structure of the C-steel wires exposed to a thermal loading of 100°C for 61, 112, 183 and 211 days are presented in Figures 6.6 (b) and (d) and Figures 6.7 (b) and (d).

From reconstructed images, it can be affirmed that corrosion on the wire surfaces seems to have progressed in the form of pitting. However, contrary to the corrosion observed over the surface of the corrosion coupons, the formation of a 'double layer' could not be observed (section 4.2.1). This may be explained due to the oxygen trapped in the bentonite bodies during the compaction process i.e. anoxic conditions may not have been established.

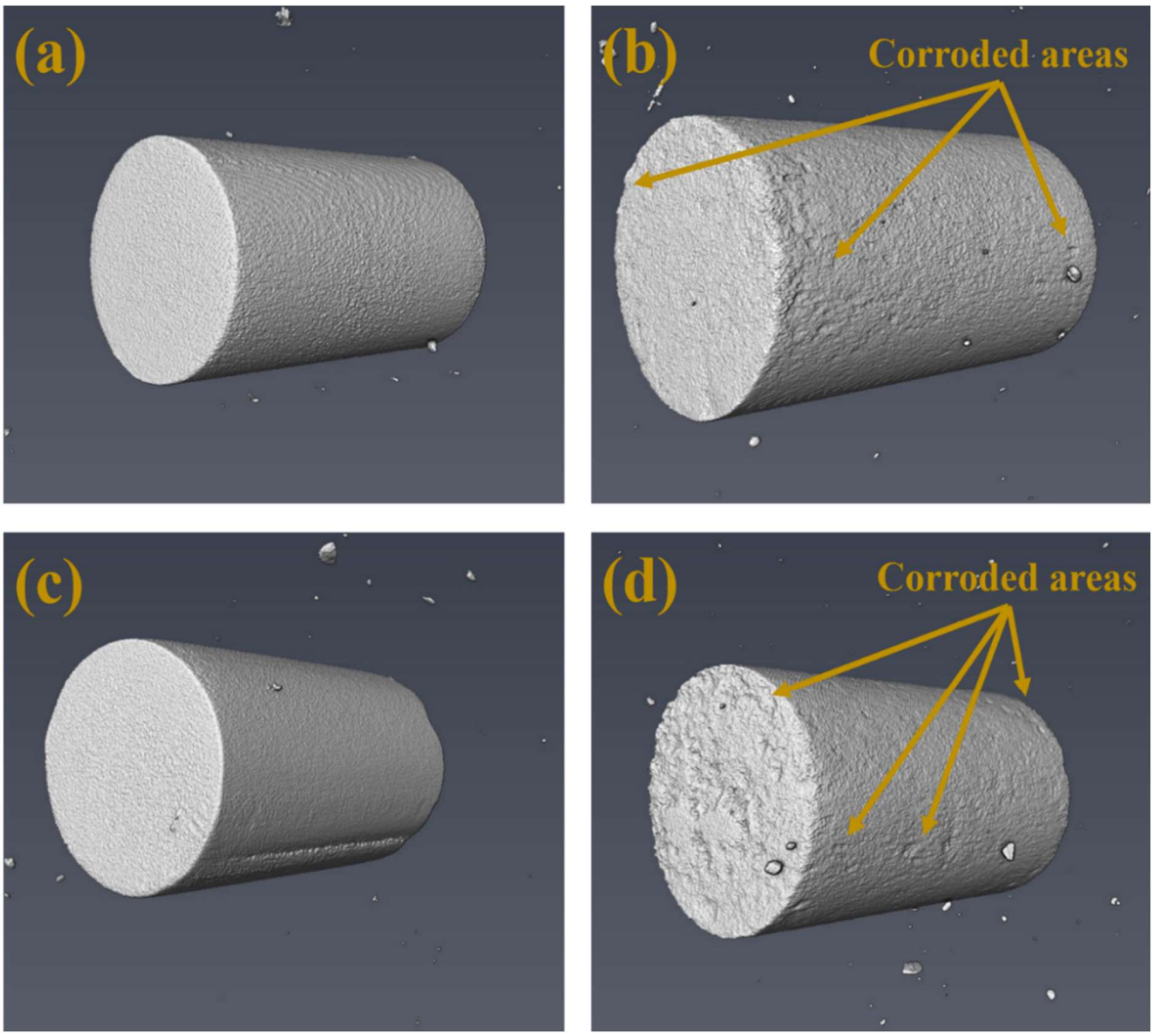

Figure 6.7: *(a) Micro-tomographical surface of C-steel wire before heating (sample 18). (b) Micro-tomographical surface of C-steel wire after 183 day of heating at 100°C (sample 18). (c) Micro-tomographical surface of C-steel wire before heating (sample 24). (d) Micro-tomographical surface of C-steel wire after 211 day of heating at 100°C (sample 24).*

Finally, Table 6.10 shows the measured volumes of the corroded layer of the samples exposed at 100°C, since alteration was noticeable in the surface of these samples, while it could not be observed in the samples exposed to lower temperatures. Estimations were achieved due to the variation of the thickness of the reconstructed wires before and after the thermal loading.

Table 6.10: *Thickness of corrosion layer on experimental samples.*

Sample ID	Total volume before heating (μm^3)	Total volume after heating (μm^3)	Volume of corrosion layer (μm^3)	Volume of the corrosion layer (mm^3)	Volume of the corrosion layer per experimental time (mm^3/day)
6	5916554296	5916553586	710	$7.10 \cdot 10^{-7}$	$1.16 \cdot 10^{-8}$
12	5592939881	5591996406	943475	$9.43 \cdot 10^{-4}$	$7.73 \cdot 10^{-6}$
18	5844325394	5779414177	64911217	$6.49 \cdot 10^{-2}$	$3.55 \cdot 10^{-4}$
24. Grimsel	5577393492	5419335175	158058317	$1.58 \cdot 10^{-1}$	$7.49 \cdot 10^{-4}$
Standard error (SE)	-	-	-	$3.73 \cdot 10^{-2}$	$1.78 \cdot 10^{-4}$

From Table 6.10 and Figures 6.6 and 6.7, it can be concluded that corrosion on C-steel wires seems to be progressive with time exposition. The estimates shown in Table 6.10 are intended to show the relative volume of the corrosion layer formed on the surfaces of C-steel wires. However, these should not be taken as absolute values due to the uncertainty associated with the volumetric reconstructed values carried out with Avizo Lite.

6.4 High-resolution selected volume diffraction with synchrotron x-rays

HAW containers will provide confinement and mechanical resilience over the geological time-scales envisaged for a GDF. During 'mid-life' for a repository, the transient saturation of the geotechnical barrier and the thermal gradients in the vicinity of the bentonite-container system are relevant to understanding the dynamics of the processes involved. The slow saturation of the clay barrier and dissolution of certain structural minerals in the bentonite will result in by-products from these secondary minerals. The transport of these by-products

towards the contact interface between the bentonite barrier and the container will contribute to acceleration of the corrosion thereof, and the resulting corrosion by-products will migrate through the compacted bentonite by diffusive transport.

Throughout the literature, evidence has been presented of the formation of Fe-rich minerals, as a result of diffusional transport of corrosion by-products [103], [129], [130], [131], [132], [133], [134]. This evidence may have been confirmed in bentonite samples of the ABM project that were measured using synchrotron (section 5.2.5). As a result of the alteration of bentonite the partial or total loss of its swelling and self-healing capability is expected. It is believed that such alteration/degradation is caused by loss of the layer charge due to isomorphic substitutions and the occupation of vacant tetrahedral and octahedral sites.

In GDF concepts based in crystalline host rock, the dissolution of secondary minerals will contribute to an increase in the alkalinity of the migrating water towards the interface regions, reducing corrosion rates at the interface itself. Once deposition tunnels are closed, the oxygen trapped in the compacted body of bentonite will eventually be consumed through container corrosion. The total consumption of free oxygen in the system will lead to anaerobic/reducing conditions that will now dominate the corrosion processes. The increased pH, along with the anaerobic environment, makes the chemistry developed in the near-field dominated by the presence of OH^- ions which favour the formation of oxyhydroxides [308]. The complete saturation of the geotechnical barrier will give rise to a wet corrosion process, resulting in the formation of magnetite. This process will be reinforced by the total consumption of free oxygen. However, the alkaline and anaerobic environment during the last stages of evolution of a crystalline rock repository will favour the formation of ferrous hydroxide (Equation 4.5), which will rapidly evolve to magnetite releasing additional hydrogen. Furthermore, the formation of green oxide compounds and iron carbonates, such as siderite, together with magnetite, hematite and goethite on C-steel surfaces has been also observed [126], [309], [310].

Against this backdrop, the experiment discussed in this chapter was performed to evaluate the kinetics governing the alteration and/or transformation of bentonite under repository-scale simulated conditions. XRT analysis of the embedded C-steel bodies evidenced that active corrosion was occurring. Thus, a basis for montmorillonite alteration and/or transformation may be invoked for investigation. To evaluate the degree of alteration and/or transformation, samples from the cell experiments were examined by synchrotron x-rays. High-resolution x-ray diffraction was performed on the I11 beamline at Diamond Light Source (UK). Each diffraction

pattern was collected using Si-calibrated x-rays with a wavelength of 0.8245230Å. Samples were prepared as described in section 3.2.3.3.2.4 (Chapter 3). Sample holder rotation was used together with a 1x1mm beam. Preliminary high-resolution random powder diffraction was carried out on a reference sample to provide accurate baseline data.

Table 6.11: *001 spacing values of Febex experimental and reference materials.*

Sample	d-spacing (Å)			
	61 days	**122 days**	**183 days**	**211 days**
Febex reference	14.6546	14.6546	14.6546	14.6546
55°C	14.5917	14.8455	14.6837	14.8580
65°C	14.7760	14.9023	14.5996	14.8174
75°C	14.7133	14.8751	14.5528	14.8094
85°C	14.5515	14.8484	14.5601	14.8421
95°C	14.7942	14.9326	14.9105	14.7893
100°C	14.8536	14.9390	14.8132	14.9230

Owing to the widening of basal spacing observed by XRT in section A of BM-B-41-1, MX-80 and Febex samples from the Febex in-situ test and ABM project, respectively, we first assessed the characteristic (001) reflection of each sample.

The (001) reflection of smectites varies from 12Å in Na-montmorillonites to 15Å in Ca-montmorillonites. This variation is conditioned by the ambient relative humidity and the nature of the cations occupying the interlayer space [241]. Results of the 001 spacing of the experimental samples are listed in Table 6.11 and presented in Figure 6.8. From Table 6.11 and Figure 6.8, we concluded that the experimental samples exhibit a basal spacing similar to that measured in the reference material and close to 15Å which confirmed the expected Ca-Mg character of the Febex bentonite. Overall, there are no clear differences in basal spacings between samples, and the deviations observed with respect to the reference sample could be explained due to the hydration state of each sample.

High-resolution diffraction was utilised to determine the bulk mineralogy of each experimental sample and, thus, identify the presence of iron phases and possible alterations and/or transformations that samples might have experienced due to the combination of thermal loading, saturation and time. Results of high-resolution random powder diffraction are presented in Figures 6.9 to 6.12 and tabulated in Table 6.12. The determination of the percentage (based on 100%) of each mineral present was carried out using the MATCH! Phase

identification programme for powder diffraction. MATCH! reports that the results have a standard deviation of ±10% of the calculated value [245].

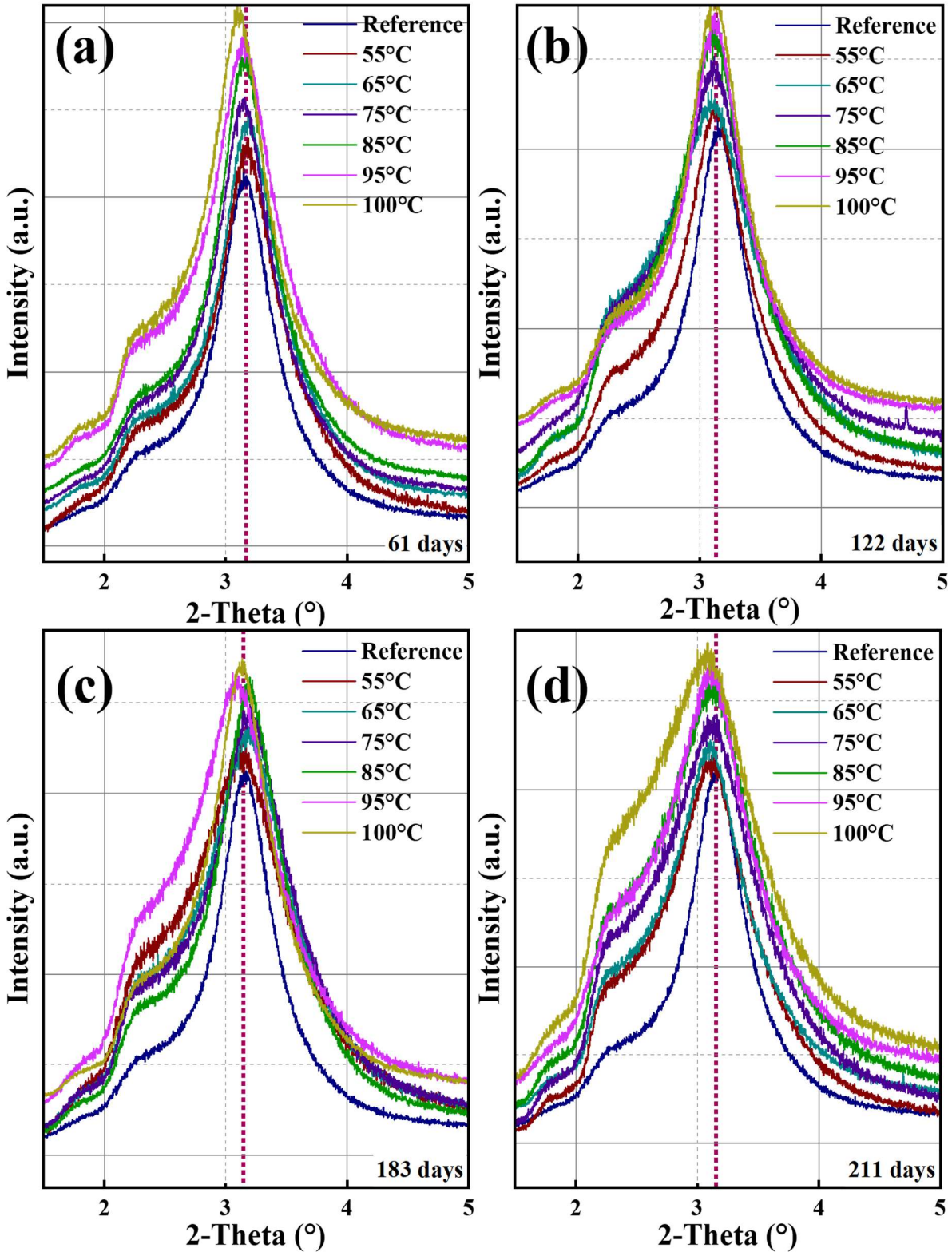

Figure 6.8: *(a)-(d) XRD peak positions of 001 spacings of Febex experimental vs reference samples at different temperatures for 61, 122, 183 and 211 days, respectively.*

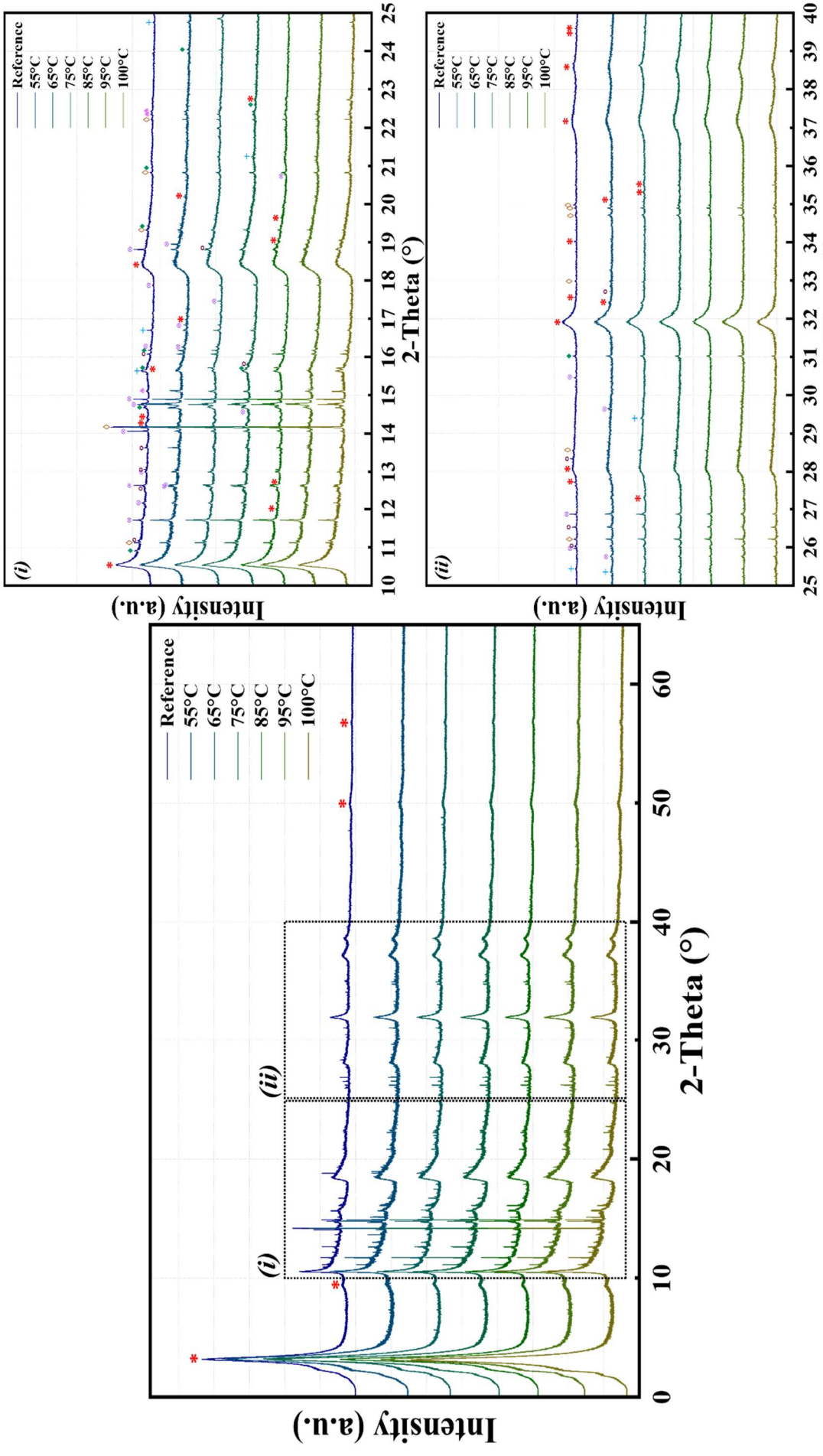

Figure 6.9: *XRD patterns of Febex experimental samples after 61 days of heating, recorded on beamline I11 (Diamond Light Source).* ✱*: Montmorillonite;* ⊗*: Plagioclase;* o*: K-Feldspar;* ◆*: Tridymite;* +*: Carbonate;* ◆*: Cristobalite;* ◇*: Quartz. (i) Region between 10° and 25° in 2θ. (ii) Region between 25° and 40° in 2θ.*

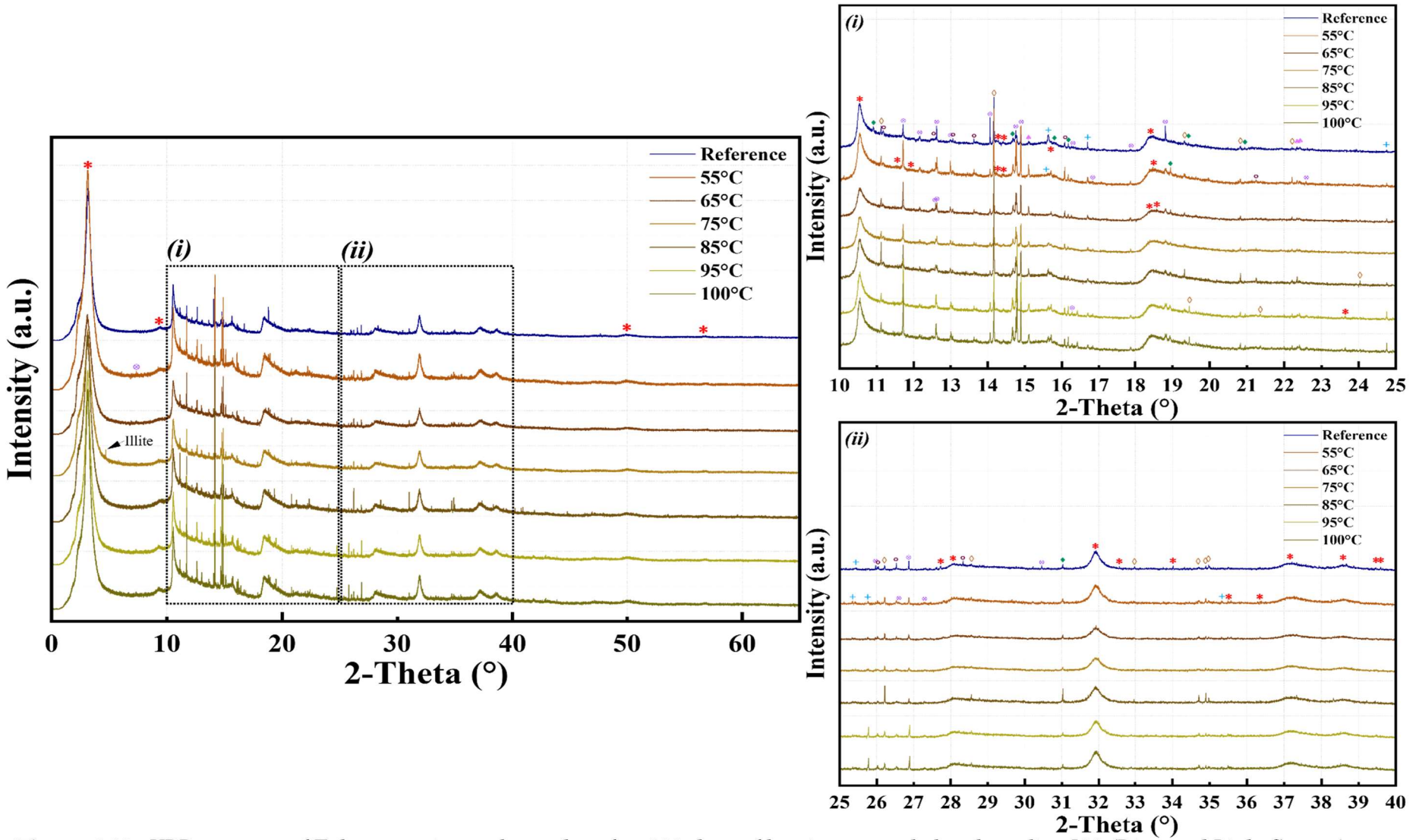

Figure 6.10: *XRD patterns of Febex experimental samples after 122 days of heating, recorded on beamline I11 (Diamond Light Source).* ✱*: Montmorillonite;* ⊗*: Plagioclase;* o*: K-Feldspar;* ♦*: Tridymite;* +*: Carbonate;* ♠*: Cristobalite;* ◊*: Quartz. (i) Region between 10° and 25° in 2θ. (ii) Region between 25° and 40° in 2θ.*

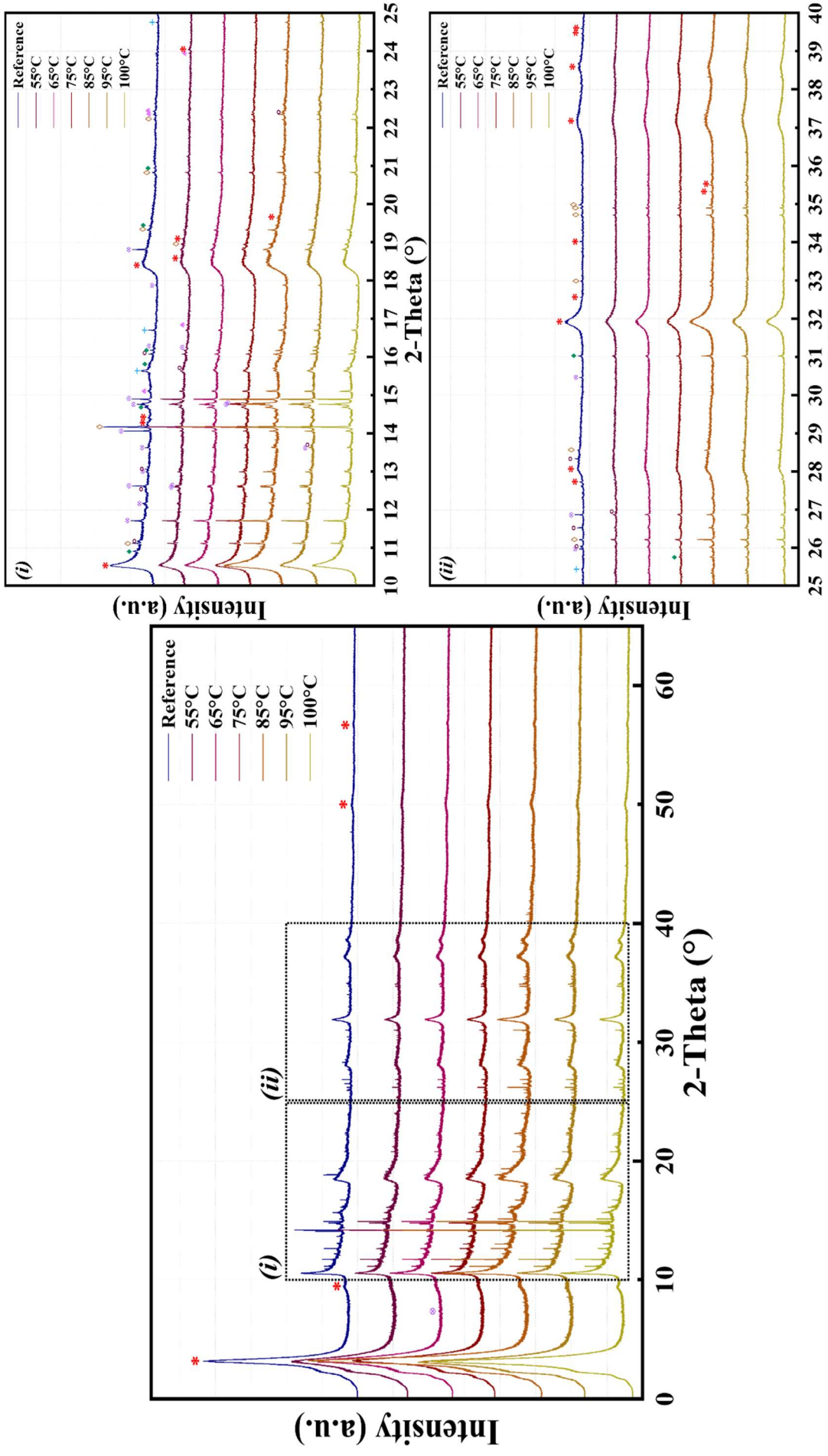

Figure 6.11: *XRD patterns of Febex experimental samples after 183 days of heating, recorded on beamline I11 (Diamond Light Source).* ✱*: Montmorillonite;* ⊗*: Plagioclase;* ○*: K-Feldspar;* ◆*: Tridymite;* +*: Carbonate;* ♣*: Cristobalite;* ◇*: Quartz. (i) Region between 10° and 25° in 2θ. (ii) Region between 25° and 40° in 2θ.*

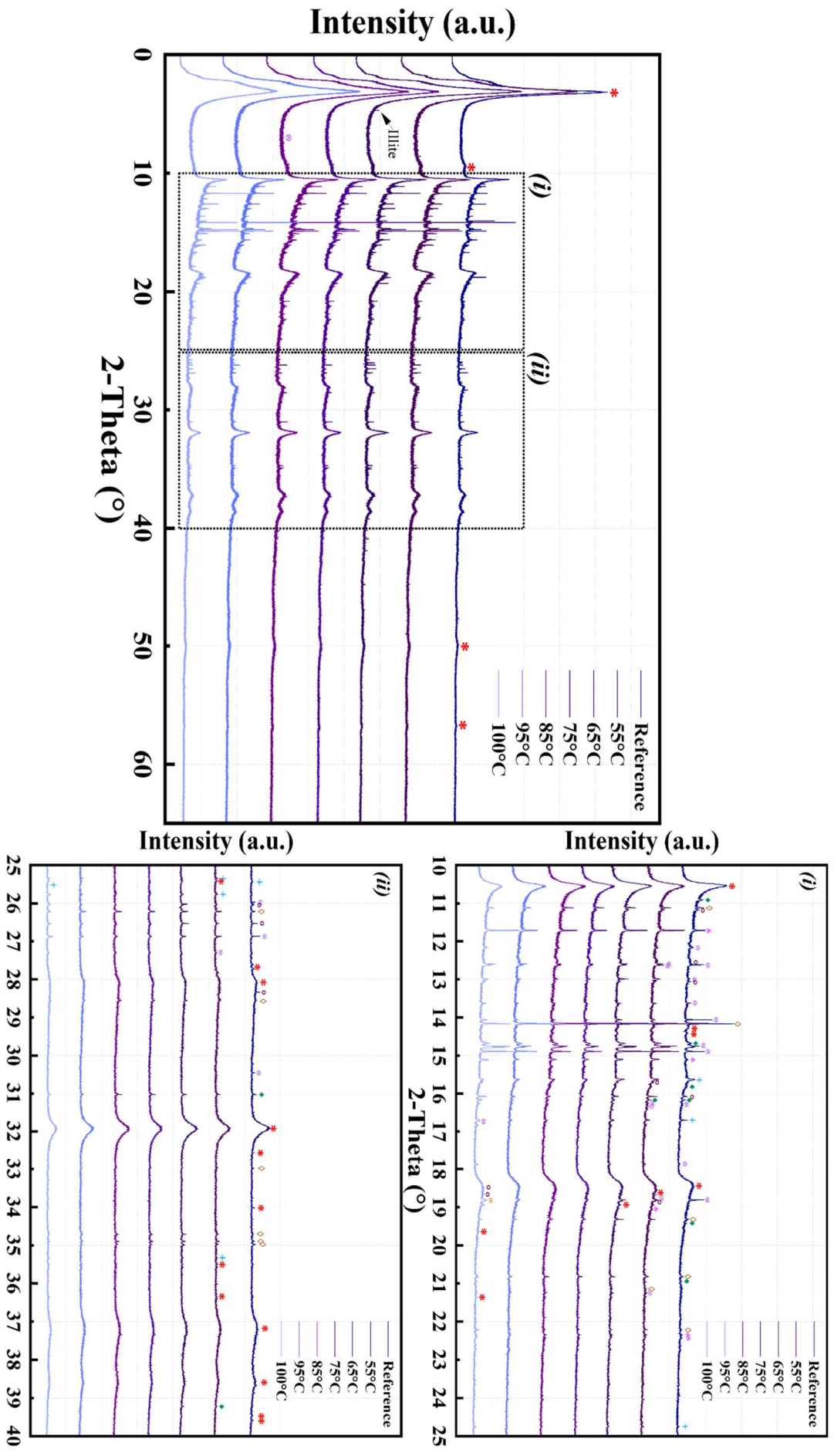

Figure 6.12: *XRD patterns of Febex experimental samples after 211 days of heating, recorded on beamline I11 (Diamond Light Source). *: Montmorillonite; ⊗: Plagioclase; o: K-Feldspar; ◆: Tridymite; +: Carbonate; ♣: Cristobalite; ◊: Quartz. (i) Region between 10°and 25° in 2θ. (ii) Region between 25° and 40°in 2θ.*

Table 6.12: *Bulk mineralogy of Febex experimental samples.*

Mineral (%)	Reference	55ºC	65ºC	75ºC	85ºC	95ºC	100ºC
61 days of thermal loading							
Montmorillonite	90.6	90.0	89.0	89.0	90.2	89.0	89.2
Quartz	2.4	2.7	2.5	2.4	2.1	2.2	2.7
Tridymite	0.8	1.0	1.2	1.7	1.7	2.0	1.6
Plagioclase	2.5	1.8	1.7	2.2	2.1	1.1	1.7
Calcite	1.2	0.9	1.5	1.4	0.4	1.6	1.2
Cristobalite	1.0	1.6	1.9	1.5	1.3	1.9	1.4
K-Feldspar	1.5	2.0	2.2	1.8	2.1	2.2	2.2
Total	*100*	*100*	*100*	*100*	*100*	*100*	*100*
122 days of thermal loading							
Montmorillonite	90.6	90.3	89.0	89.1	90.3	89.1	89.2
Quartz	2.4	2.9	3.2	2.7	2.1	2.2	2.2
Tridymite	0.8	1.4	1.6	1.3	1.3	2.5	1.8
Plagioclase	2.5	2.2	2.2	2.5	2.5	1.8	1.4
Calcite	1.2	0.4	0.4	2.1	1.4	1.3	1.9
Cristobalite	1.0	1.2	1.4	1.0	1.0	1.4	1.5
K-Feldspar	1.5	1.6	2.2	1.3	1.4	1.7	2.0
Total	*100*	*100*	*100*	*100*	*100*	*100*	*100*
183 days of thermal loading							
Montmorillonite	90.6	89.1	90.0	89.7	89.1	90.5	90.6
Quartz	2.4	2.8	1.8	2.1	2.8	2.1	2.6
Tridymite	0.8	1.4	1.0	0.8	1.1	1.2	1.0
Plagioclase	2.5	2.5	2.9	2.8	2.8	2.3	1.5
Calcite	1.2	0.7	0.5	1.0	0.8	1.4	0.5
Cristobalite	1.0	2.5	2.4	1.6	2.3	1.2	1.9
K-Feldspar	1.5	1.0	1.4	2.0	1.1	1.3	1.9
Total	*100*	*100*	*100*	*100*	*100*	*100*	*100*
211 days of thermal loading							
Montmorillonite	90.6	90.1	90.0	89.3	89.0	89.0	90.2
Quartz	2.4	2.2	2.4	3.1	3.4	3.0	3.0
Tridymite	0.8	1.6	1.1	1.7	1.7	1.9	1.2
Plagioclase	2.5	1.1	1.0	1.5	1.4	1.2	1.8
Calcite	1.2	1.3	1.9	1.8	0.8	1.2	0.5
Cristobalite	1.0	2.5	1.6	1.4	2.0	1.8	1.8
K-Feldspar	1.5	1.2	2.0	1.2	1.6	1.9	1.1
Magnetite	**-**	**-**	**-**	**-**	**-**	**-**	**0.4**
Total	*100*	*100*	*100*	*100*	*100*	*100*	*100*

Figures 6.9 to 6.12 and Table 6.12 gather the data concerning the samples heated for 61, 122 and 183 days. From data presented in Figures 6.9 to 6.11 and Table 6.12 it can be seen that the mineralogical phases are those observed in the reference samples. It is noteworthy, however, that during sample disassembly a corrosion aureole with variable diameter was observed in the perimeter of the metallic bodies, suggesting an interaction had occurred. Therefore, we can conclude that no alteration and/or transformation of the montmorillonite component had occurred during the experimental time selected.

Figure 6.12 and Table 6.12 show the data corresponding with different thermal loadings after 211 days. The mineral phases observed at 55ºC, 65ºC, 75ºC, 85ºC and 95ºC are those observed in the reference material. However, data corresponding to a thermal loading of 100ºC and 211 days of exposure showed the presence of magnetite traces. The presence of magnetite traces has led us to speculate that a stable corrosion layer has been formed on the metallic body surfaces due to consumption of oxygen trapped in the compacted bentonite bodies and, after a reasonable experimental time (211 days), the corrosion by-products have begun to diffuse through the clayey matrix (Figure 6.1). Despite this observation, the presence of neoformed minerals could not be detected.

6.5 Concluding statement

The present chapter has presented results derived from physicochemical evaluation of compacted Febex bentonite which had undergone different exposure regarding thermal loading, duration and different saturation water compositions. The performed testing intended to evaluate the processes governing the alteration and/or transformation of bentonite. It is clear that the testing conditions were very limited in duration compared with the in-situ conditions of the Febex and ABM near-field experiments; furthermore the time-scales expected in a GDF are considerably longer than those large internationally in-situ tests. However, the experimental work could assist in improving the understanding achieved to date regarding interactions involved over the lifespan of an underground repository. This, combined with computational work, could provide different insights into the processes developed in highly-dynamic environments, as expected in an underground repository.

It is evident from results presented that thermal load, exposure time and water composition are key factors in the corrosion processes of containers, as well as the diffusion of corrosion by-products through the clayey matrix and, therefore, in its alteration and/or transformation.

Upon comparing the results obtained for shorter exposure times (61, 122 and 183 days), no significant mineralogical changes were observed and iron phases, that could indicate a diffusive process of corrosion by-products through the compacted clay matrix were not detected. The mineralogical phases observed in 23 of 24 samples analysed in the synchrotron do not indicate any mineralogical change or presence of new phases, either by the diffusion of iron or by the presence of new minerals that may have been formed due to experimental conditions. The sample subjected to a thermal load of 100ºC for 211 days showed the presence of magnetite traces, which are not characteristic of the Febex bentonite. With the support of previously conducted studies [70], [106-111], [129], [130], [132], [286], it can be concluded that the formation of magnetite as the main corrosion product resulted in a corrosion layer that could have acted as a passivator of the corrosion rate.

Despite the presence of iron phases, the analysed samples did not show any evidence of bentonite alteration and/or transformation. The observed basal spacings in the experimental samples are characteristic of the reference material. Therefore, it can be stated that there was no cation exchange due to dissolution of certain structural bentonite components, as observed in the Febex and ABM samples (Chapter 4 and 5). The basal spacing deviations with respect to the reference material could be explained due to the hydration state of the samples, which would indicate that the cells were completely sealed.

With regard to the bulk mineralogy, no changes were observed in any of the samples analysed. This could be explained owing to: (*i*) the experimental methodology selected, since the compaction process was performed under atmospheric conditions and, therefore, oxygen could have been trapped in the compacted bentonite pellets, initiating a corrosion process similar to that expected in atmospheric corrosion and, thus, the oxygen availability could have slowed down the corrosion rates; or (*ii*) the experimental times considered were not adequate for the observation/examination of alteration and/or transformation of the smectite component. It is considered that a combination of both factors is more likely.

Chapter 7 Conclusions and suggestions for further work

Most international concepts for a GDF involve a 'multibarrier' approach for confinement of the waste, utilising natural and engineering materials. Due to the different physical and chemical characteristics of the materials composing each barrier, it is not only crucial to study the long-term chemical and physical behaviour and transformation of these materials, but also to study the interfacial interactions between them. This thesis has specifically examined the interactions between the metallic container surfaces of HAW and bentonite. The work developed throughout this thesis has aimed to address the scientific issues arising from uncertainties related to the interactions occurring at contact interface, and has been benefited from several samples recovered from the Febex and long-term field experiments. Such samples combined with novel short duration experiments using analysis have improved understanding of interface evolution with time and under different experimental conditions.

Firstly, a detailed characterisation of several samples from the Febex in-situ test was carried out. All samples discussed in Chapter 4 were in contact with metallic components or were retrieved from the vicinity of metal components integrated into the compacted body of bentonite, providing the opportunity to evaluate the degree of interaction of bentonite with released corrosion by-products in a confined anoxic and chemically reducing environment, as expected after 20 years of repository closure. The experimental investigation evaluated the state of each sample to understand the underlying processes at the bentonite-container interface during the mid-life of an underground repository. As a part of this, the correct preservation of the samples was also crucial. Physicochemical examination of these samples has allowed us to draw several conclusions about the state of the geotechnical barrier after nearly two decades of exposure.

The second experimental study involved the evaluation of various bentonite types sourced from different worldwide regions, utilised in the ABM experiment for intercomparing, to extend knowledge of how different bentonite types would behave under repository-like conditions. The samples evaluated in Chapter 5 were also retrieved from being in contact with a simulated heater-container. The preliminary aim of this study was to assess the extent to which the

corrosion by-products had integrated into the bentonite barrier, as well as possible bentonite alteration and/or transformation due to interaction of such by-products. This involved a detailed analysis of the mineralogical composition of the bentonite and specifically the smectite content of each sample. The methodological guidelines used for this study are well founded in literature by prior works [57], [188], [196], [208], that have deeply investigated clays for a large variety of industrial applications.

Finally, the last experimental chapter in this thesis developed and implemented a novel laboratory-scale experiment. The main focus was to investigate the possible physical and chemical alterations of bentonite owing to interaction and iron incorporation arising from corrosion by-products in the bentonite structure. The experimental design incorporated carbon steel, titanium and copper metallic bodies integrated in the compacted bentonite, all contained within aluminium cells lined with Teflon to guarantee seclusion from atmosphere conditions. The experiment aimed to establish the pressure, temperature and redox conditions expected in an early to mid-life repository, with the premise that the most significant alterations would occur over this period of time, as a combined result of temperature, progressive barrier saturation and saline content of groundwaters.

The key research questions stipulated in section 2.5 allowed us to follow a research methodology to provide scientifically rigorous answers. The following sections summarise the main findings from experimental investigations carried out throughout this thesis.

7.1 Febex in-situ test sample findings summary

Upon post-mortem sampling of Febex samples, the extent to which the corrosion by-products had diffused and precipitated into the compacted body was only significantly apparent within sample BM-B-41-1. This specific sample showed a clear change of colouration in the region of immediate contact with the liner. Therefore, it was clear that there was a gradational concentration of corrosion by-products away from the liner surface. This finding was supported by a tomographic study carried out on this section (section A) of the sample that unequivocally showed the presence of microparticles of much denser material than bentonite. These denser

particles, with higher attenuation coefficient, were attributed to the presence of iron compounds intercalated within the clayey matrix.

Metallographic studies on metallic coupons showed the presence of a double corrosion layer whose composition was determined by XRD and Raman spectroscopy. It is considered that the magnetite layer on the surface of the C-steel coupons probably acted as a passivator of corrosion processes, and therefore slowed down the corrosion rates once it had established. However, due to the direct contact of the corrosion film with the Febex bentonite, the passivating effect of the magnetite layer was inhibited, and thus Fe was slowly released, giving rise to oxyhydroxide formation. For example, the orange-reddish colouration in section A of BM-B-41-1 indicated that bentonite was acting as a graded precipitation zone for corrosion by-products.

A combination of laboratory analytical techniques unequivocally revealed the presence of corrosion by-products within the Febex bentonite matrix. This observation was supported by results from high-resolution diffraction, XRT and TGA analysis that showed the presence of goethite and magnetite in the bentonite matrix with a gradational concentration away from the heated metal surface.

Exchangeable cation analysis indicated an increase in Mg^{2+} in areas close to the liner, where the temperatures were higher and saturation degree of the clay barrier were probably less than that observed in peripheral areas of the in-situ test. The presence of Mg^{2+} could be an indicator of the dissolution of secondary minerals, mostly calcite and dolomite, in areas further away from the liner. As re-saturation of the barrier occurred, these dissolved minerals were transported towards the liner interface zone and re-precipitated aided by the thermal gradients and favouring the increase of exchangeable Mg^{2+} and Ca^{2+} at the expense of Na^{+}. Similar observations were apparent in FTIR from analysis of the water stretching band. However, the sum of total exchangeable cations remained close to that observed in the reference material, indicating that the exchange capacity was not greatly altered. The slight alteration in the CEC observed for liner-proximal samples is attributed to a dilution of the bentonite with iron-oxide and hydroxides precipitates. Hence per cubic millimetre of material there was slightly less bentonite (by 2-4%) relative to reference material. It is interesting to note a graded distribution of iron oxides/hydroxides precipitating away from the immediate liner surface. This observation implies that the corrosion layer is unstable (as already indicated) and iron is

dissolving into contacting pore water at the interface and then precipitating further into the bentonite.

Crystallographic observations of the montmorillonite component after long-term exposure (18 years) of simulated geological conditions indicated that no alteration and/or transformation had occurred. This conclusion was achieved through the examination of the characteristic d-spacing upon glycolation (17Å). The lack of smectite alteration allows us to conclude that the swelling or self-healing capability of Febex bentonite remained unimpaired over the in-situ test duration. Furthermore, oriented mounts highlighted an interstratified structure with 10-15% of illite present, similar to the observed in the control material.

Analysis of the bulk mineralogy by XRD and high-resolution diffraction showed clear dissolution of cristobalite in the sample material in contact with the liner and, therefore, exposed to higher temperature. Nonetheless, the majority of the secondary minerals remained in concentrations similar to those observed in the pristine material.

More work is necessary to further investigate the impact of the evolving redox front on the overall performance of the barriers. For example, it is not clear how much precipitate the bentonite at the interface will accumulate to reach saturation and what this will do to the thermo-hydro-chemical-mechanical properties. When considering that Fe is more soluble in a reduced (Fe^{2+}) state, it may indicate that anoxic conditions have quickly established at the bentonite-metal interface, with oxygen consumed by corrosion, and allowing some Fe^{2+} dissolution. Diffusional transport of the iron-bearing solution into the bentonite, which still held pore oxygen, would the result in iron oxidation (Fe^{2+} to Fe^{3+}) with an associated precipitation of ‘rust’ phases. Hence, we ascribe the graded iron zone as representing the location of the redox front in the bentonite (Figure 7.1).

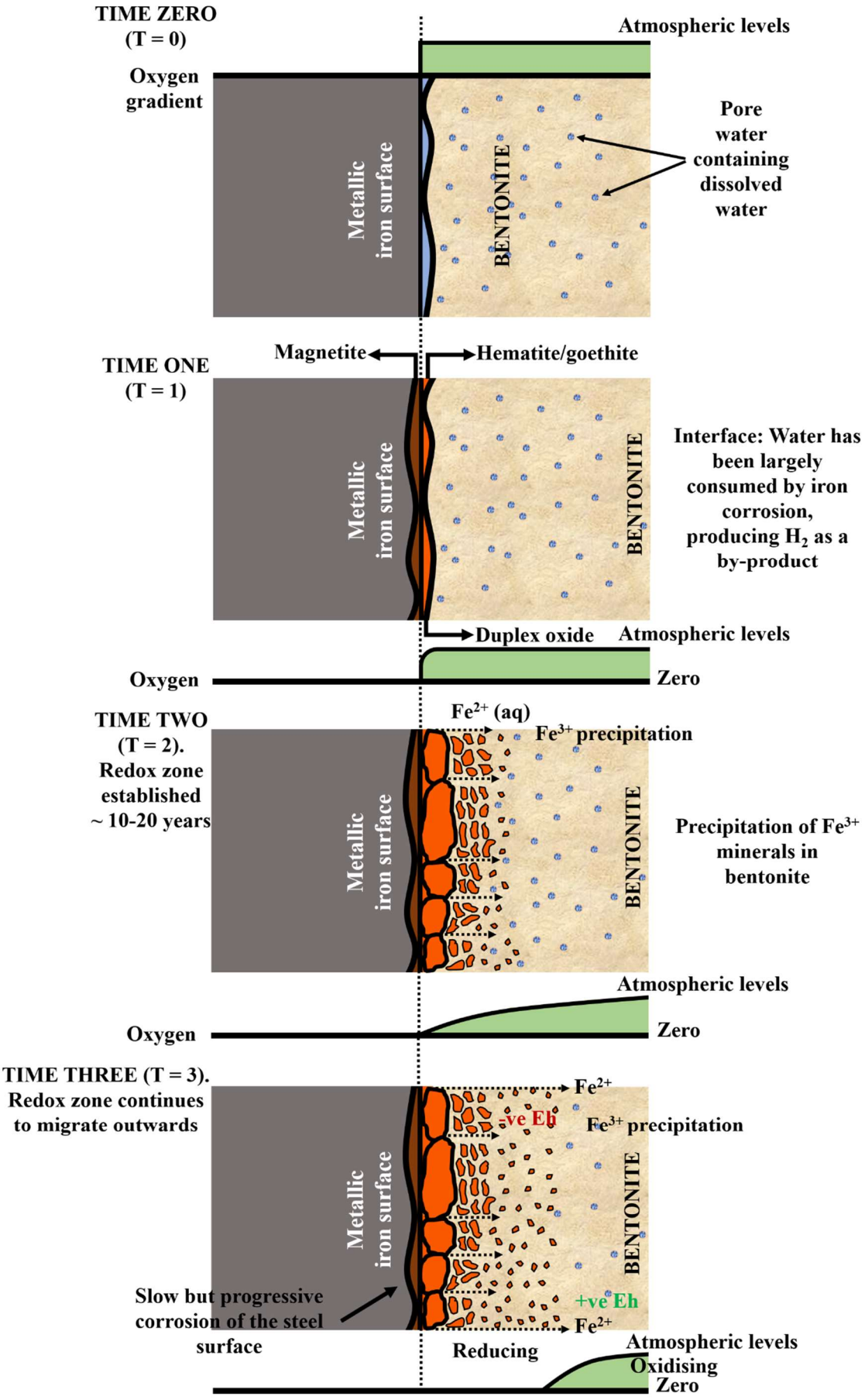

Figure 7.1: *Schematic of the evolution of the contact interface between bentonite and metallic container.*

7.2 ABM project sample findings summary

This section of the experimental work aimed to provide a complementary vision of the alteration and/or transformations possibly experienced by bentonite samples from the ABM in-situ test. Upon visual examination of the samples, no colour changes were observed on surfaces in direct contact with the metal liner of the container-heater system. CEC analysis showed values close to those observed in the control materials. However, exchangeable cation examinations displayed a greater concentration of Ca^{2+} and Mg^{2+} in bentonite samples taken from immediate contact with the heater-container. This finding correlates with exchangeable cation examinations carried out on bentonite surfaces of Febex samples in contact with metallic components and confirms a consistent exchange of Mg^{2+} and Ca^{2+} at the expense of Na^{+} in the vicinity of the container-heater. This result was especially noticeable within sodium bentonites and, was also confirmed by XRD 001 reflection examination.

XRD analysis of the bulk mineralogy of the samples did not identify the presence of any iron phases which correlates with visual observations. Crystallographic observations of the smectite component of each sample indicated that no alteration and/or transformation took place. This observation was accomplished through the XRD examination of glycolated patterns of each sample, allowing us to conclude that bentonite samples did not undergo changes on its self-healing capacity. In addition, oriented mount of Febex sample remained interstratified with 10-15% of illite present.

Analysis of the bulk mineralogy of ABM-derived Febex and MX-80 samples by high-resolution diffraction showed the presence of a broad peak attributed to ferrosaponite. The presence of saponite is an indicator that the smectite component of bentonite had slightly altered, becoming ferro-saponitic in those areas where the effect of thermal gradients were strong, and samples were in direct contact with the container-heater. This finding was later confirmed by TGA analysis. Both Febex and MX-80 bentonites samples showed shifts of the main dehydroxylation peak towards lower temperature values. This displacement regarding position indicated an increase on trans-vacant positions that could have been caused by the chemical reduction of structural Fe^{3+} giving rise to a mixed structure of tv and cv 2:1 layers. Furthermore, the MX-80 sample showed an additional dehydroxylation peak at temperatures between 400 and 500°C which indicated the presence of smectite particles with high iron content, since dehydroxylation of Fe-smectite as ferrosaponite occurs at said temperatures. In

addition TGA examination showed the presence of iron particles in both Febex and MX-80 samples.

Overall, it can be concluded that Fe hydroxides were formed at the contact interface between bentonite and the heater-container. The presence of ferrosaponite indicates a certain degree of alteration of the clay minerals at the immediate heater interface. However, the degree of alteration considering the time-scale of the experiment does not seem to be significant, since the bentonite maintained a good swelling capacity as observed in glycolated patterns.

From this study, it has been shown that the most relevant processes affecting the stability of bentonite under early post-closure periods of a GDF are likely to be container corrosion and smectite alteration. With regards to the implications for the engineered barrier system the degradation mechanism of steel surfaces is important because it has knock-on influence for smectite transformation into an iron-rich from, probably aided by the high thermal gradients experienced by the barrier and the saline composition of groundwaters. However, as with the Febex experiment, more work is needed to understand the combined effects of temperature, salinity and the evolving steel corrosion mechanism on the rate of smectite alteration to determine the likely timescales for significantly deleterious alteration to be reached, if at all.

7.3 Batch test findings summary

From the batch test experiment, the relatively short experimental durations compared to the Febex and ABM experiments did not allow us to draw decisive conclusions for post-closure evolution of a GDF.

The immediate effects on the barrier are related to high thermal load, salinity of groundwaters and rapid development of a chemically reducing environment at the contact interface between the bentonite and the container. However, the experimental methodology developed for this experiment, and to evaluate the combined effect of these three factors on bentonite, was not entirely adequate.

From tomographic studies performed in-situ, the development and growth of a corrosion layer on the embedded steel wires could clearly be charted with good success. The presence of

magnetite traces in the bentonite samples analysed in synchrotron indicated the formation of a stable corrosion layer on the wire surfaces.

Similar to the Febex samples (Chapter 4), a diffusion process was evidenced by the presence of reddish coloured aureoles in the immediate vicinity of the metal bodies. Bentonite samples from these aureoles were analysed at the national synchrotron facility at Diamond Light Source. The bentonite samples analysed at synchrotron did not show any significant evidence for iron phases or alteration products within the bulk mineralogy of the samples, except for the samples exposed to the highest thermal loading for a period of 211 days and, therefore, experienced the most rapid corrosion kinetics.

The experimental configuration was intended to replicate the expected pressure-temperature conditions for a deep underground repository. However, it is not clear how well the negative redox conditions became established throughout the cells. The preparatory bentonite compaction process was carried out under atmospheric conditions and, therefore, there was clearly oxygen trapped in the clayey matrix from the outset. Whilst this was experimentally undesirable it was arguably close to what will/would happen in a GDF, where compacted bentonite blocks likely be prepared ex-situ and transported to GDF site for emplacement.

From results of high-resolution diffraction and micro-CT, it can be speculated that initial corrosion was oxic but transitioned to anoxic during the selected experimental period as evidenced by the presence of magnetite. Nevertheless, to reach an observation close to that expected in an underground repository the experimental time need to be far longer, on the order of years, to achieve more robust results.

Overall, from this study it is logical to conclude that time plays an important role for alteration and/or transformation observation of the smectite component. This observation is supported by results derived from Febex and ABM sample characterisation, where it is also clear that the magnitude of thermal gradients and the salinity of the enveloping medium are other strong factors that condition the degree and progression of alteration.

7.4 Suggestions for further work

From the scientific work described in this thesis, several areas of further research can be highlighted. Most generally, additional scientific exploration is needed to better define the rates and timescales for alteration of the clay barrier in underground repositories.

During the batch test, it became clear that achieving chemically reducing conditions from the outset is difficult. Therefore, it is evident that additional experimental work is needed to define the time required to achieve reducing conditions once corrosion by-products have diffused through the bentonite, to replicate the medium- and long- term conditions. Equally, the selected time-scales for the batch test reported here have not been sufficient to develop a well-established corrosion front. The rapid chemical reduction of iron within the bentonite matrix could be accomplished by using sodium dithionite or by the hydroxylamine method, since both methodologies have been proven efficient for bentonite Fe structural reduction. Subsequently, the compaction process should be carried out in an inert atmosphere, as provided by a glovebox, to ensure the preservation of a reduced state, which would require the development of a device to achieve compaction in an inert atmosphere. In addition, it would also be desirable to combine longer time-scales and greater variations of the pore water salinity, since salinity certainly has an important impact/influence on the degradation of the barrier.

Additional characterisation/examination of the swelling capability of Febex and ABM samples could have provided additional information on the state of the barrier with regards to its self-healing capacity. This could be easily achieved by oedometer testing. Despite exchangeable cations being determined for each sample, the presence of sorbed iron in the interlayer space was not determined; this could be achieved by use of inductively coupled plasma mass spectrometry. The presence of a superparamagnetic component in Mössbauer spectroscopy results indicated the need for further analysis at lower temperatures. Although, Mössbauer results allowed us to draw some conclusions, these were not entirely conclusive regarding the structural oxidation state of the samples.

Finally, during this study, microbial effects that could have accelerated the corrosion and, therefore, caused a physical and chemical alterations in the barrier has not been studied or taken into account. The presence of sulphate reducing bacteria, once anoxic conditions are established, could have had and interesting impact on the iron phases precipitating, e.g. FeS_2, assuming they could access the container surfaces. These alterations, together with the

processes described, could adversely affect the barrier properties and its performance in the long-term.

Reference list

[1] Department for Business Energy and Industrial Strategy (2017). The clean growth strategy. Leading the way to a low carbon future.

[2] R. Cowan (1990). Nuclear power reactors: A study in technological lock. *J. Econ. Hist.*, vol. 50, no. 3, pp. 541-567.

[3] Foreign and commonwealth office (2017). Paris agreement. Treaty series no.4 web version.

[4] Department of Energy & Climate Change (2008). Climate change Act: Chapter 27.

[5] W. Space (2006). Nuclear power and climate change: Aspects of the current debate. *Electr. J.*, vol. 19, no. 6, pp. 73-82.

[6] W.M. Stacey (2004). Chapter 2. Neutron nuclear reactions, in *Nuclear reactor physics*, pp. 1-32.

[7] W.R. Harper (1961). Basic principles of fission reactors.

[8] Westinghouse technology system manual (2011). Section 1.2. Introduction to pressurized water reactor generating systems. USNRC HRTD 0519-R304.

[9] OECD (2006). Physics and safety of transmutation systems. Technical Report NEA No. 6090.

[10] IAEA (1963). A basic toxicity clasifficiation of radionuclides. Technical Report no. 15.

[11] I. Hore-Lacy (2012). The world nuclear university primer. Nuclear energy in the 21st Century. 3rd Edition.

[12] IAEA Safety Glossary (2006). Terminology used in nuclear, radiation, radioactive waste and transport safety. International Atomic Energy Agency, Version 2.0.

[13] G. Choppin, J.O. Liljenzin, J. Rydberg, and C. Ekberg (2013). Chapter 21. The nuclear fuel cycle, in *Radiochemistry and Nuclear Chemistry (Fourth Edition)*.

[14] J. Prawitz and J. Rydberg (1958). Composition of products formed by thermal neutro fission of ^{235}U. *Acta Chem. Scand.*, vol. 12, pp. 377-398.

[15] B. Flowers (1976). Royal commission on environmental pollution: Sixth report-nuclear power and the environment.

[16] NDA (2010). Geological disposal: An overview of the generic disposal system safety case. NDA/RWM/010.

[17] CoRWM (2006). Managing our radioactive waste safely, CoRWM's recommendations to Goverment.

[18] NDA (2017) Radioactive waste in UK. Context and Methodology. Report. ISBN: 978-1-905985-32-6.

[19] NDA (2017). Radioactive waste in the UK. UK radioactive waste. Inventory Report. ISBN: 978-1-905985-33-3.

[20] NDA (2016). Higher activity waste strategy.

[21] LLW Repository Ltd, "Guidance for the management of Lower Active Waste," 2016.

[22] Department of Energy & Climate Change (2014). Implementing geological disposal: A framework for the long-term management of higher activity radioactive waste. DECC Report URN 14D/235.

[23] SKB (2011). Environmental impact statement. Interim storage, encapsulation and final disposal of spent nuclear fuel. Svensk Kärnbränslehantering AB. Doc no. 1208391.

[24] S. Berglund, U. Kautsky, T. Lindborg, and J.O. Selroos (2009). Integration of hydrological and ecological modelling for the assessment of a nuclear waste repository. *Hydrogeol. J.*, vol. 17, no. 1, pp. 95-113.

[25] SKB (2006). Long-term safety for KBS-3 repositories at Forsmark and Laxemar-a first evaluation: Main Report of the SR-Can project. Svensk Kärnbränslehantering AB Technical Report TR-06-09.

[26] NAGRA (2002). Opalinus Clay Project. Demonstration of disposal feasibility for spent fuel, vitrified high-level waste and long-lived intermediate-level waste. Svensk Kärnbränslehantering AB. Technical Report 02-05.

[27] NAGRA (2009). A review of materials and corrosion issues regrading canisters for disposal of spent fuel and high-level waste in opalinus clay. Technical Report 09-02.

[28] NAGRA (2016). Waste management programme of the waste producers. (Entsorgungsnachweis). Technical Report 16-01E.

[29] DETEC (2008). Department of the environment, transport and communications. Sectoral plan for deep geological repositories. Conceptual part.

[30] Posiva (2014). Safety case for the disposal of spent fuel at Olkiluoto-Definition of reference and bounding groundwaters, buffer and backfill porewaters. Technical Report 2014-04.

[31] C. Cosma, N. Enescu, K. Kemppainen, and T. Ahokas (2007). Seismic prediction of hard rock fault zones and confirmation by tunnel observations. Conference: ISRM. The 7th International workshop on the application of geophysics to rock engineering.

[32] Andra (2005). Dossier 2005 Argile-architecture and management of a geological repository.

[33] Andra (2005). Dossier 2005 Granite-assets of granite formations for deep geological disposal.

[34] Andra (2005). Dossier 2005. Andra research on the geological disposal of high-level long-lived radiactive waste. Results and perspectives.

[35] R. Dohrmann, S. Kaufhold, and B. Lundqvist (2013). The role of clays for safe storage of nuclear waste, in *Developments in Clay Science*, vol. 5, pp. 667-710.

[36] K. Thatcher, R. Newson, S. Watson, and S. Norris (2018). Review of data and models on the mechanical properties of bentonite available at the start of BEACON.

[37] Posiva (2015). Designing, commssioning and monitoring of 40% scale bentonite buffer test. Workreport 2015-8.

[38] Herwig R. Müller et al. (2017). Implementation of the full-scale emplacement (FE) experiment at the Mont Terri rock laboratory. *Swiss J. Geosci.*, vol. 110, pp. 287-306.

[39] N. Giroud et al. (2018). On the fate of oxygen in a spent fuel emplacement drift in Opalinus Clay. *Appl. Geochemistry*, vol. 97, pp. 270-278.

[40] SKB (2000). Long term test of buffer material: Final report on the pilot parcels. Svensk Kärnbränslehantering AB. Technical Report TR-00-22.

[41] Posiva (2006). Chemical conditions in the A2 parcel of the long-term test of buffer material in Äspö. Workreport 2006-83.

[42] SKB (2012). Temperature buffer material. Final report. Svensk Kärnbränslehantering AB. Technical report TR-12-04.

[43] ENRESA (2000). FEBEX Project: Full-scale engineered barriers experiment for a deep geological repository for high level radioactive waste in crystalline host rock. Technical

Report 1/2000.

[44] NAGRA (1989). Grimsel test site. Geology. Technical Report 87-14E.

[45] NAGRA (2008). Impact of corrosion-derived iron on the bentonite buffer within the KBS-3H disposal concept. Technical Report R-08-34.

[46] M.V. Villar and A. Lloret (2007). Dismantling of the first section of the FEBEX in situ test: THM laboratory tests on the bentonite blocks retrieved. *Phys. Chem. Earth*, vol. 32, no. 8-14, pp. 716-729.

[47] SKB (2011). Alternative buffer material: Status of the ongoing laboratory investigation of reference materials and test package 1. Svensk Kärnbränslehantering AB. Technical Report TR-11-06.

[48] J.R. Lovering, A. Yip, and T. Nordhaus (2016). Historical construction costs of global nuclear power reactors. *Energy Policy*, vol. 91, pp. 371-382.

[49] R. Pusch (1992). Use of bentonite for isolation of radioactive waste products. *Clay Miner.*, vol. 27, no. 3, pp. 353-361, 1992.

[50] SKB (2010). Design, production and initial state of the buffer. Svensk Kärnbränslehantering AB. Technical Report TR-10-15.

[51] R.E. Grim and N. Güven (1978). Geology, mineralogy, properties and uses.

[52] P.C. Wright (1968). The meandu creek bentonite-A reply. *J. Geol. Soc. Aust.*, vol. 15, no. 2, pp. 347-350.

[53] F. Bergaya and G. Lagaly (2013). Chapter 1. General introduction: Clays, clay minerals, and clay science, in *Handbook of clay sciences. Part A: Fundamentals*, vol. 5, pp. 1-19.

[54] M.F. Brigatti, E. Galan, and B.K. Theng (2013). Chapter 2. Structures and mineralogy of clay minerals, in *Handbook of clay sciences. Part A: Fundamentals*, vol. 5, pp. 21-81.

[55] C. Ma and R.A. Eggleton (1999). Cation exchange capacity of kaolinite. *Clays Clay Miner.*, vol. 47, no. 2, pp. 174-180.

[56] S.J. Anderson and G. Sposito (1991). Caesium-adsorption method for measuring accessible structural surface charge. *Soil Sci. Soc. Am. J.*, vol. 55, no. 6, pp. 1569-1576.

[57] L.P. Meier and G. Kahr (1999). Determination of the cation exchange capacity (CEC) of clay minerals using the complexes of copper(II) ion with triethylenetetramine and

tetraethylenepentamine. *Clays Clay Miner.*, vol. 47, no. 3, pp. 386-388.

[58] A.F. Gualtieri et al. (2008). Structural characterization of the clay mineral illite-1M. *J. Appl. Crystallogr.*, vol. 41, no. 2, pp. 402-415.

[59] D.M.C. MacEwan (1958). Fourier transform methods for studying x-ray scattering from lamellar systems-II. The calculation of x-ray diffraction effects for various types of interstratification. *Kolloid-Zeitschrift*, vol. 156, no. 1, pp. 61-67.

[60] P.H. Nadeau, M.J. Wilson, W.J. McHardy, and J.M. Tait (1985). The conversion of smectite to illite during diagenesis: Evidence from some illitic clays from bentonites and sandstones. *Mineral. Mag.*, vol. 49, pp. 393-400.

[61] S.P. Altaner and R.F. Ylagan (1997). Comparison of structural models of mixed-layer illite-smectite and reaction mechanisms of smectite illitization. *Clays Clay Miner.*, vol. 45, no. 4, pp. 517-533.

[62] H. Komine and N. Ogata (1996). Prediction for swelling characteristics of compacted bentonite. *Can. Geotech. J.*, vol. 33, no. 1, pp. 11-22.

[63] M.V. Villar and A. Lloret (2008). Influence of dry density and water content on the swelling of a compacted bentonite. *Appl. Clay Sci.*, vol. 39, no. 1-2, pp. 38-49.

[64] W.M. Ye, Y.G. Chen, B. Chen, Q. Wang, and J. Wang (2010). Advances on the knowledge of the buffer/backfill properties of heavily-compacted GMZ bentonite. *Eng. Geol.*, vol. 116, no. 1-2, pp. 12-20.

[65] P. Delage, M.D. Howat, and Y.J. Cui (1998). The relationship between suction and swelling properties in a heavily compacted unsaturated clay. *Eng. Geol.*, vol. 50, no. 1-2, pp. 31-48.

[66] E. Romero, A. Gens, and A. Lloret (1999). Water permeability, water retention and microstructure of unsaturated compacted Boom clay. *Eng. Geol.*, vol. 54, pp. 117-127.

[67] A. Tarantino and E. De Col (2008). Compaction behaviour of clay. *Géotechnique*, vol. 58, no. 3, pp. 199-213.

[68] S.M. Rao and K. Ravi (2015). Influence of initial degree of saturation on swell pressures of compacted Barmer bentonite specimens. *Ann. Nucl. Energy*, vol. 80, pp. 303-311.

[69] M.V. Villar and A. Lloret (2004). Influence of temperature on the hydro-mechanical behaviour of a compacted bentonite. *Appl. Clay Sci.*, vol. 26, pp. 337-350.

[70] M.V. Villar, R. Gómez-Espina, and A. Lloret (2010). Experimental investigation into temperature effect on hydro-mechanical behaviours of bentonite. *J. Rock Mech. Geotech. Eng.*, vol. 2, no. 1, pp. 71-78.

[71] R.A. Couture (1985). Steam rapidly reduces the swelling capacity of bentonite. *Nature*, vol. 318, pp. 50-52.

[72] R. Pusch, P. Bluemling, and L. Johnson (2003). Performance of strongly compressed MX-80 pellets under repository-like conditions. *Appl. Clay Sci.*, vol. 23, pp. 239-244.

[73] W.M. Ye, Z.J. Zheng, B. Chen, Y.G. Chen, Y.J. Cui, and J. Wang (2014). Effects of pH and temperature on the swelling pressure and hydraulic conductivity of compacted GMZ01 bentonite. *Appl. Clay Sci.*, vol. 101, pp. 192-198.

[74] W.J. Cho, J.O. Lee, and C.H. Kang (2000). Influence of temperature elevation on the sealing performance of a potential buffer material for a high-level radioactive waste repository. *Ann. Nucl. Energy*, vol. 27, pp. 1271-1284.

[75] R. Bag and A. Rabbani (2017). Effect of temperature on swelling pressure and compressibility characteristics of soil. *Appl. Clay Sci.*, vol. 136, pp. 1-7.

[76] R. Yong, L.O. Taylor, and B.P. Warkentin (1962). Swelling pressure of sodium montmorillonite at depressed temperature. *Clays Clay Miner.*, vol. 11, pp. 268-281.

[77] SKB (2006). Mineralogy and Sealing Properties of Various Bentonites and Smectite-Rich Clay Materials. Svensk Kärnbränslehantering AB. Technical Report TR-06-30.

[78] E. Castellanos, M.V. Villar, E. Romero, A. Lloret, and A. Gens (2008). Chemical impact on the hydro-mechanical behaviour of high-density FEBEX bentonite. *Phys. Chem. Earth*, vol. 33, no. Supplement 1, pp. S516-S526.

[79] SKB (1997). Bentonite swelling pressure in strong NaCl solutions: Correlation between model calculations and experimentally determined data. Svensk Kärnbränslehantering AB. Technical Report TR-97-31.

[80] H.J. Herbert, J. Kasbohm, H. Sprenger, A.M. Fernández, and C. Reichelt (2008). Swelling pressures of MX-80 bentonite in solutions of different ionic strength. *Phys. Chem. Earth*, vol. 33, pp. S327-S342.

[81] A. Lloret and M.V. Villar (2007). Advances on the knowledge of the thermo-hydro-mechanical behaviour of heavily compacted 'FEBEX' bentonite. *Phys.*

Chem. Earth, vol. 32, no. 8-14, pp. 701-715.

[82] M.K. Gueddouda, I. Goual, B. Benabed, S. Taibi, and N. Aboubekr (2016). Hydraulic properties of dune sand-bentonite mixtures of insulation barriers for hazardous waste facilities. *J. Rock Mech. Geotech. Eng.*, vol. 8, no. 4, pp. 541-550.

[83] W.J. Cho, J.O. Lee, and K.S. Chun (1999). The temperature effects on hydraulic conductivity of compacted bentonite. *Appl. Clay Sci.*, vol. 14, no. 1-3, pp. 47-58.

[84] IAEA (2001). Swelling and hydraulic properties of Ca-bentonite for the buffer of a waste repository. Technical Report IAEA-CSP--6/C.

[85] H. Komine (2004). Simplified evaluation on hydraulic conductivities of sand-bentonite mixture backfill. *Appl. Clay Sci.*, vol. 26, no. 1-4, pp. 13-19.

[86] Y. He, W.M. Ye, Y.G. Chen, B. Chen, B. Ye, and Y.J. Cui (2016). Influence of pore fluid concentration on water retention properties of compacted GMZ01 bentonite. *Appl. Clay Sci.*, vol. 129, pp. 131-141.

[87] A.-M. Tang and Y.-J. Cui (2005). Controlling suction by the vapour equilibrium technique at different temperatures and its application in determining the water retention properties of MX80 clay. *Can. Geotech. J.*, vol. 42, no. 1, pp. 287-296.

[88] J.A. Blatz, J. Graham, and N.A. Chandler (2002). Influence of suction on the strength and stiffness of compacted sand-bentonite. *Can. Geotech. J.*, vol. 39, no. 5, pp. 1005-1015.

[89] NAGRA (2014). Montmorillonite stability under near-field conditions. Technical Report 14-12.

[90] NDA (2011). Bentonite: A review of key properties, processes and issues for consideration in the UK context. Technical Report QRS-13788ZG-1.

[91] Sven Knutsson (1983). On the thermal conductivity and thermal diffusivity of highly compacted bentonite. University of Luleå. Technical Report 83-72.

[92] A.M. Tang, Y.J. Cui, and T.T. Le (2008). A study on the thermal conductivity of compacted bentonites. *Appl. Clay Sci.*, vol. 41, no. 3-4, pp. 181-189.

[93] NDA/RWN (2016). Geological Disposal High Heat Generating Wastes Project: Final Report. Technical Report NDA/RWM/136.

[94] A. Beziat, M. Dardaine, and E. Mouche (1992). Measurements of the thermal

conductivity of clay-sand and clay-graphite mixtures used as engineered barriers for high-level radioactive waste disposal. *Appl. Clay Sci.*, vol. 6, no. 4, pp. 245-263.

[95] M. Jobmann and G. Buntebarth (2009). Influence of graphite and quartz addition on the thermo-physical properties of bentonite for sealing heat-generating radioactive waste. *Appl. Clay Sci.*, vol. 44, no. 3-4, pp. 206-210.

[96] L. Xu, W.M. Ye, B. Chen, Y.G. Chen, and Y.J. Cui (2016). Experimental investigations on thermo-hydro-mechanical properties of compacted GMZ01 bentonite-sand mixture using as buffer materials. *Eng. Geol.*, vol. 213, pp. 46-54.

[97] F.T. Madsen (1998). Clay Mineralogical Investigations Related to Nuclear Waste Disposal. *Clay Miner.*, vol. 33, no. 1, pp. 102-109.

[98] NAGRA (2008). Impact of corrosion-derived iron on the bentonite buffer within the KBS-3H disposal concept. Technical Report R-08-34.

[99] L. Charlet and C. Tournassat (2005). Fe(II)–Na(I)–Ca(II) Cation exchange on montmorillonite in chloride medium: Evidence for preferential clay adsorption of chloride-metal ion pairs in seawater. *Aquat. Geochemistry*, vol. 11, no. 2, pp. 115-137.

[100] P. Wersin, L. Johnson, and M. Snellman (2006). Impact of iron released from steel components on the performance of the bentonite buffer: A preliminary assessment within the framework of the KBS-3H disposal concept. MRS Proceedings, 932, 117.1.

[101] S. Lantenois, B. Lanson, F. Muller, A. Bauer, M. Jullien, and A. Plançon (2005). Experimental study of smectite interaction with metal Fe at low temperature: 1. Smectite destabilization. *Clays Clay Miner.*, vol. 53, no. 6, pp. 597-612.

[102] J. Wilson, D. Savage, J. Cuadros, M. Shibata, and K.V. Ragnarsdottir (2006). The effect of iron on montmorillonite stability. (I) Background and thermodynamic considerations. *Geochim. Cosmochim. Acta*, vol. 70, no.2, pp 306-322.

[103] J. Wilson *et al.* (2006). The effect of iron on montmorillonite stability. (II) Experimental investigation. *Geochim. Cosmochim. Acta*, vol. 70, no. 2, pp. 323-336.

[104] N. Kohyama, S. Shimoda, and T. Sudo (1973). Iron-rich saponite (ferrous and ferric forms). *Clays Clay Miner.*, vol. 21, pp. 229-237.

[105] D. Badaut, G. Besson, A. Decarreau, and R. Rautureau (1985). Occurrence of a ferrous, trioctahedral smectite in recent sediments of Atlantis II Deep, Red Sea. *Clay Miner.*, vol.

20, no. 3, pp. 389-404.

[106] J.W. Stucki and C.B. Roth (1977). Oxidation-reduction mechanism for structural iron in nontronite. *Soil Sci. Soc. Am.*, vol. 41, no. 4, pp. 808-814.

[107] J.W. Stucki, D.C. Golden, and C.B. Roth (1984). Effects of reduction and reoxidation of structural iron on the surface charge and dissolution of dioctahedral smectites. *Clays Clay Miner.*, vol. 32, no. 5, pp. 350-356.

[108] J.W. Stucki and D. Tessier (1991). Effects of iron oxidation state on the texture and structural order of Na-nontronite gels. *Clays Clay Miner.*, vol. 39, no. 2, pp. 137-143.

[109] J.W. Stucki, G.W. Bailey, and H. Gan (1996). Oxidation-reduction mechanisms in iron-bearing phyllosilicates. *Appl. Clay Sci.*, vol. 10, no. 6, pp. 417-430.

[110] A. Manceau et al. (2000). Oxidation-reduction mechanism of iron in dioctahedral smectites: II. Crystal chemistry of reduced Garfield nontronite. *Am. Mineral.*, vol. 85, no. 1, pp. 153-172.

[111] V.A. Drits and A. Manceau (2000). A model for the mechanism of Fe^{3+} to Fe^{2+} reduction in dioctahedral smectites. *Clays Clay Miner.*, vol. 48, no. 2, pp. 185-195.

[112] J.E. Kostka, J. Wu, K.H. Nealson, and J.W. Stucki (1999). The impact of structural Fe(III) reduction by bacteria on the surface chemistry of smectite clay minerals. *Geochim. Cosmochim. Acta*, vol. 63, no. 22, pp. 3705–3713.

[113] J. Cervini-Silva, R.A. Larson, J. Wu, and J.W. Stucki (2001). Transformation of chlorinated aliphatic compounds by ferruginous smectite. *Environ. Sci. Technol.*, vol. 35, no. 4, pp. 805-809.

[114] J. Cervini-Silva, J.E. Kostka, R.A. Larson, J.W. Stucki, and J. Wu (2003). Dehydrochlorination of 1,1,1-trichloroethane and pentachloroethane by microbially reduced ferruginous smectite. *Environ. Toxicol. Chem.*, vol. 22, no. 5, pp. 1046-1050.

[115] K. Ikonen, J. Kuutti, and H. Raiko (2018). Thermal Dimensioning fot the Olkiluoto Repository-2018 Update. WR 2018-26.

[116] M. Juvankoski (2018). Bentoniittipuskurit, jarjestermakuvaus. Internal Posiva Memorandum. POS-01445.

[117] L.L. Hench, D.E. Clark, and J. Campbell (1984). High level waste immobilization forms. *Nucl. Chem. Waste Manag.*, vol. 5, no. 2, pp. 149-173.

[118] P. Wersin, L. H. Johnson, and I. G. McKinley (2007). Performance of the bentonite barrier at temperatures beyond 100 °C: A critical review. *Phys. Chem. Earth*, vol. 32, no. 8-14, pp. 780-788.

[119] NDA/Amec (2012). Project Ankhiale: Disposability and full life cycle implications of high-heat generating UK wastes. Technical Report no. RP51.

[120] NAGRA (1991). Investigation into the behaviour of bentonite in contact with magnetite and iron under the conditions of a final repository. Technical Report NTB--91-14.

[121] M. Perronnet, M. Jullien, F. Villiéras, J. Raynal, D. Bonnin, and G. Bruno (2008). Evidence of a critical content in Fe(0) on FoCa7 bentonite reactivity at 80°C. *Appl. Clay Sci.*, vol. 38, no. 3-4, pp. 187-202.

[122] M. Osackỳ, V. Šucha, A. Czímerová, and J. Madejová (2010). Reaction of smectites with iron in a nitrogen atmosphere at 75°C. *Appl. Clay Sci.*, vol. 50, no. 2, pp. 237-244.

[123] G. de Combarieu et al. (2011). Glass-iron-clay interactions in a radioactive waste geological disposal: An integrated laboratory-scale experiment. *Appl. Geochemistry*, vol. 26, no. 1, pp. 65-79.

[124] B. Lanson, A. Plançon, S. Lantenois, P.A. van Aken, and A. Bauer (2012). Experimental investigation of smectite interaction with metal iron at 80°C: Structural characterization of newly formed Fe-rich phyllosilicates. *Am. Mineral.*, vol. 97, no. 5-6, pp. 864-871.

[125] C. Rivard et al. (2015). Reactivity of callovo-oxfordian claystone and its clay fraction with metallic Iron: Role of non-clay minerals in the interaction mechanism. *Clays Clay Miner.*, vol. 63, no. 4, pp. 290-310.

[126] L. Carlson *et al.* (2007). Experimental studies of the interactions between anaerobically corroding iron and bentonite. *Phys. Chem. Earth*, vol. 32, no. 1-7, pp. 334-345.

[127] O. Bildstein, L. Trotignon, M. Perronnet, and M. Jullien (2006). Modelling iron-clay interactions in deep geological disposal conditions. *Phys. Chem. Earth*, vol. 31, no. 10-14, pp. 617-625.

[128] D. Savage, C. Watson, S. Benbow, and J. Wilson (2001). Modelling iron-bentonite interactions. *Appl. Clay Sci.*, vol. 47, no. 1-2, pp. 91-98.

[129] D. Guillaume et al. (2003). Experimental synthesis of chlorite from smectite at 300ºC in the presence of metallic Fe. *Clay Miner.*, vol. 38, no. 1, pp. 281-302.

[130] D. Guillaume et al. (2004). Experimental study of the transformation of smectite at 80 and 300°C in the presence of Fe oxides. *Clay Miner.*, vol. 39, no. 1, pp. 17-34.

[131] Andra (2005). Dissolution-crystallization processes affecting di-octahedral smectite in presence of iron metal: implication on mineral distribution in clay barriers. Clays in Natural and Engineered Barriers for Radioactive Waste Confinement.

[132] D. Charpentiera, K. Devineau, R. Mosser-Ruck, M. Cathelineau, and F. Villiéras (2006). Bentonite-iron interactions under alkaline condition: An experimental approach. *Appl. Clay Sci.*, vol. 32, no. 1-2, pp. 1-13.

[133] M.C. Jodin-Caumon, R. Mosser-Ruck, D. Rousset, A. Randi, M. Cathelineau, and N. Michau (2010). Effect of a thermal gradient on iron-clay interactions. *Clays Clay Miner.*, vol. 58, no. 5, pp. 667-681.

[134] M. C. Jodin-Caumon, R. Mosser-Ruck, A. Randi, O. Pierron, M. Cathelineau, and N. Michau, "Mineralogical evolution of a claystone after reaction with iron under thermal gradient," *Clays Clay Miner.*, vol. 60, no. 5, pp. 443–455, 2012.

[135] SKB (2008). Impact of corrosion-derived iron on the bentonite buffer KBS-3H disposal concept. Svensk Kärnbränslehantering AB. Technical Report R-08-34.

[136] P. Wersin, A. Jenni, and U.K. Mäder (2015). Interaction of corroding iron with bentonite in the ABM1 experiment at ÄSPÖ, Sweden: A microscopic approach. *Clays Clay Miner.*, vol. 63, no. 1, pp. 51-68.

[137] D. Svensson and S. Hansen (2013). Redox chemistry in two iron-bentonite field experiments at Äspö Hard Rock Laboratory, Sweden: An XRD and Fe K-Edge XANES study. *Clays Clay Miner.*, vol. 61, no. 6, pp. 566–579.

[138] E. Torres, M.J. Turrero, D. Moreno, L. Sánchez, and A. Garralón (2017). FEBEX in-situ test: Preliminary results of the geochemical characterization of the metal/bentonite interface. *Procedia Earth Planet. Sci.*, vol. 17, pp. 802-805.

[139] M.J. Apted (1992). Natural analogues for predicting the reliability of the engineered barrier system for high-level waste. *J. Geochemical Explor.*, vol. 46, pp. 35-62.

[140] J.H. Ahn and D.R. Peacor (1986). Transmission and analytical electron microscopy of the smectite-to-illite transition. *Clays Clay Miner.*, vol. 34, no. 2, pp. 165-179.

[141] A. Inoue and M. Utada (1991). Smectite-to-chlorite transformation in thermally

metamorphosed volcanoclastic rocks in the Kamikita area, northern Honshu, Japan. *Am. Mineral.*, vol. 76, pp. 628-640.

[142] W.T. Jiang and D.R. Peacor (1994). Prograde transitions of corrensite and chlorite in low-grade pelitic rocks from the Gaspé Peninsula, Quebec. *Clays Clay Miner.*, vol. 42, no. 5, pp. 497-517.

[143] K.V. Ragnarsdóttir, J.V. Walther, and S. Arnórsson (1984). Description and interpretation of the composition of fluid and alteration mineralogy in the geothermal system, at Svartsengi, Iceland. *Geochim. Cosmochim. Acta*, vol. 48, no. 7, pp. 1535-1553.

[144] S.T. Schmidt and D. Robinson (1997). Metamorphic grade and porosity and permeability controls on mafic phyllosilicate distributions in a regional zeolite to greenschist facies transition of the North Shore Volcanic Group, Minnesota. *Bull. Geol. Soc. Am.*, vol. 109, no. 6, pp. 683-697.

[145] D. Beaufort and A. Meunier (1994). Saponite, corrensite and chlorite-saponite mixed-layers in the Sancerre-Couy deep drill-hole (France). *Clay Miner.*, vol. 29, no. 1, pp. 47-61.

[146] R.J. Merriman and D.R. Peacor (2009). Chapter 2. Very low-grade metapelites: Mineralogy, microfabrics and measuring reaction progress. in *Low-Grade Metamorphism*.

[147] ENRESA (1994). Almacenamiento geologico profundo de residuos radiactivos de alta actividad (AGP). Conceptos preliminares. Technical Publication 07/94.

[148] E. Caballero (1985). Quimismo del proceso de bentonitización en la región volcánica de cabo de gatA. Ph.D thesis (in Spanish). University of Granada, Madrid (Spain).

[149] ENRESA (1998). Full-scale engineered barrier experiment in crystalline host rock. Final design and installation of the in-situ test at Grimsel. Technical Publication 12/98.

[150] ENRESA (1998). FEBEX bentonite. Origin, properties and fabrication of blocks. Technical Publication 05/98.

[151] M.V. Villar (2000). Caracterización termo-hidro-mecánica de una bentonita de Cabo de Gata. Ph.D Thesis (in Spanish). Universidad Complutense de Madrid, Madrid (Spain).

[152] M.V. Villar and A. Lloret (2001). Variation of the intrinsic permeability of expansive

clay upon saturation. *Proceedings of the International Symposium on Suction, Swelling, Permeability and Structure of Clays*, Shizouka, pp. 259-266.

[153] E. Romero, M.V. Villar, and A. Lloret (2005). Thermo-hydro-mechanical behaviour of two heavily overconsolidated clays. *Eng. Geol.*, vol. 81, no. 3, pp. 255-268.

[154] CIEMAT (2002). Second report on thermo-hydro-mechanical laboratory test. Technical Report CIEMAT/DIAE--54520/6/02.

[155] X. Pintado, A. Ledesma, and A. Lloret (2002). Backanalysis of thermohydraulic bentonite properties from laboratory tests. *Eng. Geol.*, vol. 64, no. 2-3, pp. 91-115.

[156] M.V. Villar and A. Lloret (2004). Temperature influence on the mechanical behaviour of a compacted bentonite. *Elsevier Geo-Engineering B. Ser.*, vol. 2, pp. 305-310.

[157] A.M. Fernández (2003). Caracterización y modelización del agua intersticial en materiales arcillosos. Estudio de la bentonita de Cortijo de Archidona. Ph.D. Thesis (in Spanish). Universidad Autónoma de Madrid, Madrid (Spain).

[158] ENRESA (2004). FEBEX II Project final report on thermo-hydro-mechanical laboratory tests. Technical Publication 10/04.

[159] E.E. Alonso et al. (2005). The FEBEX benchmark test: Case definition and comparison of modelling approaches. *Int. J. Rock Mech. Min. Sci.*, no. 5-6, pp. 611-638.

[160] NAGRA (2016). FEBEX-DP on-site analyses report. Nagra. Arbeitsbericht NAB 16-12.

[161] ENRESA (2006). FEBEX Project Final Report. Addendum sensors data report. In situ experiment. Publicación Técnica Enresa 05-5/2006.

[162] NAGRA (2016). FEBEX-e: Final Sensor Data Report (FEBEX In Situ Experiment). Arbeitsbericht NAB 16-19.

[163] J. Hadi. Sampling section 54. University of Bern. p. 10, 2016.

[164] NAGRA (2017). FEBEX-DP. Metal Corrosion and Iron-Bentonite: Interaction Studies. Technical Report NAB 16-16.

[165] Kober, F. (2015). FEBEX-DP sample log book. Switzerland: Nagra Aktennotiz.

[166] S. Kumpulainen, L. Kiviranta, and P. Korkeakoski (2016). Long-term effects of an iron heater and Äspö groundwater on smectite clays: Chemical and hydromechanical results

from the in situ alternative buffer material (ABM) test package 2. *Clay Miner.*, vol. 51, no. 2, pp. 129-144.

[167] T. Takagi (2005). Bentonite in Japan-Geology and Industries. Open file report of geological survey of Japan, no. 425. *Research Center for Deep Geological Environments, Geological Survey of Japan National Institute of Advanced Industrial Science and Technology* (AIST). p. 13.

[168] S. Tripathy, A. Sridharan, and T. Schanz (2004). Swelling pressures of compacted bentonites from diffuse double layer theory. *Can. Geotech. J.*, vol. 41, no. 3, pp. 437-450.

[169] Y. Tachi, M. Ochs, and T. Suyama (2014). Integrated sorption and diffusion model for bentonite. Part 1: Clay-water interaction and sorption modeling in dispersed systems. *J. Nucl. Sci. Technol.*, vol. 51, no. 10, pp. 1191-1204.

[170] H. Komine and N. Ogata (2011). Experimental study on swelling characteristics of sand-bentonite mixture for nuclear waste disposal. *Soils Found.*, vol. 39, no. 2, pp. 83-97.

[171] H. Komine (2004). Simplified evaluation for swelling characteristics of bentonites. *Eng. Geol.*, vol. 71, no. 3-4, pp. 265-279.

[172] H. Komine and N. Ogata (2003). New equations for swelling characteristics of bentonite-based buffer materials. *Can. Geotech. J.*, vol. 40, no. 2, pp. 460-475.

[173] H. Komine and N. Ogata (2004). Predicting Swelling Characteristics of Bentonites. *J. Geotech. Geoenvironmental Eng.*, vol. 130, no. 8, pp. 818–829.

[174] M.M. Knechtel and S.H. Patterson (1962). Bentonite Deposits of the Northern Black Hills District Wyoming, Montana, and South Dakota. *Geological survey bulletin 1082-M*. p. 148.

[175] M.V. Villar and R. Gómez-Espina (2008). Effect of temperature on the water retention capacity of FEBEX and MX-80 bentonites, in *Unsaturated soils: Advances in Geo-engineering*, pp. 257–262.

[176] CIEMAT (2005). MX-80 Bentonite. Thermo-hydro-Mechanical characterisation performed at CIEMAT in the context of prototype project. Technical Report 1053.

[177] I.S. Parcharidis, E. Gartzos, and E.M. Psomiadis (2001). Evaluation of remote sensing

methods for the detection of hydrothermal alteration zones in Milos Island (Greece). *Conference paper-January* 2001, p. 8

[178] Posiva (2010). Long-term stability of bentonite: A literature review. Technical Report Posiva-WR--10-53.

[179] SKB (2008). Backfilling and closure of the deep repository. Phase 3- Pilot test to verify engineering feasibility. Geotechnical investigations made on unsaturated backfill materials. Svensk Kärnbränslehantering. Technical Report R-08-131.

[180] K. Ren, W. Dai, J. Zhou, J. Su, and H. Wu (2011). Whole-teflon microfluidic chips. *Proc. Natl. Acad. Sci.*, vol. 108, no. 20, pp. 8162-8166.

[181] Atomic energy of Canada Limited (1984). The Canadian nuclear fuel waste management program. Technical Report AECL-7787.

[182] F. King (2013). Container materials for the storage and disposal of nuclear waste. *Corrosion*, vol. 69, no. 10, pp. 986-1011.

[183] J.R. Davis (2001). ASM specialty hanbook: Copper and copper Alloys.

[184] M.J. Donachie (2000). Titanium: A technical guide, 2nd Edition, in *ASM International*.

[185] NAGRA (2008). Grimsel test site investigation phase IV. Borehole sealing. Technical Report 07-01.

[186] M.N. Wuddivira et al. (2012). Estimation of soil clay content from hygroscopic water content measurements. *Soil Sci. Soc. Am. J.*, vol. 76, no. 5, pp. 1529-1535.

[187] J. Fritz, D.T. Gjerde, and C. Pohlandt (1982). Ion chromatography (chromatographic methods). Heidelberg.

[188] Thermo Scientific (2006). ICS-90 Ion chromatography system operator's manual.

[189] B.L. Sawhney (1970). Potassium and caesium ion selectivity in relation to clay mineral structure. *Clays Clay Miner.*, vol. 18, no. 1, pp. 47-52.

[190] P.K. Gallagher, M.E. Brown and S.Z.D. Cheng and R.B. Kemp (1998). Handbook of thermal analysis and calorimetry, in *Elsevier*.

[191] J.C. Vickerman and I.S. Gilmore (2009). Surface analysis-the principal techniques: 2nd Edition.

[192] G. Brunker (2011). Introduction to XAFS: A Practical guide to x-ray absorption fine

structure spectroscopy, in *Cambridge University Press*.

[193] http://readingrat.net/block-diagram-of-x-ray-machine/

[194] M. Sowinska et al. (2014). In-operando hard x-ray photoelectron spectroscopy study on the impact of current compliance and switching cycles on oxygen and carbon defects in resistive switching Ti/HfO_2 /TiN cells. *J. Appl. Phys.*, vol. 115, no. 20, 204509.

[195] H. Pullin (2016). The fate and reactivity of zero-valent iron nanoparticles in the environment. Ph.D. dissertation, University of Bristol.

[196] D.M. Moore and R.C. Reynolds (1989). X-ray diffraction and the identification and analysis of clay minerals, in *Oxford University Press*.

[197] J.C.R. Giraldo, C.A. Clavijo, and C.H. McCollough (2008). Tomografía computarizada por rayos x: Fundamentos y actualidad. *Rev. Ing. Biomédica*, vol. 2, no. 4, pp. 54-66.

[198] S.K. Ali, U. Das, Y. Lu, V. Kundapur, and T. May (2011). Chapter 18. Synchrotron radiation: Applications in diagnosis and treatment of malignant brain tumors. *Synchrotron Radiation: Applications in Diagnosis and Treatment of Malignant Brain Tumors, InTech*.

[199] Diamod Light Source Ltd (2017). How diamond works-diamond light source.

[200] C. Murray, J. Parker, J. Potter, C. Tang, S. Thompson, and F. Yuan (2017). Beamline I11 user manual. BLS-I1-MAN-001. p. 58

[201] C.C. Tang, S.P. Thompson, T.P. Hill, G.R. Wilkin, and U.H. Wagner (2007). Design of powder diffraction beamline (BL-I11) at Diamond, in *Zeitschrift fur Kristallographie, Supplement*.

[202] S.P. Thompson et al. (2009). Beamline I11 at Diamond: A new instrument for high resolution powder diffraction. *Rev. Sci. Instrum.*, vol. 80, no. 075107.

[203] H. Günzler and A. Williams (2008). Handbook of analytical techniques.

[204] N.B. Colthup, L.H. Daly, and S.E. Wiberly (1975). Introduction to infrared and raman spectroscopy. 2nd edition.

[205] T. Olawumi 92015). Ultra-low k dielectrics and plasma damage control for advanced technology nodes (10nm and below). *AVS 60th International Symposium and Exhibition*.

[206] F. Rull-Perez (1993). Espectroscopia IR y raman de cristales y minerales. *Secretariado de publicaciones de la Universidad de Valladolid*.

[207] Metrohm (2013). NIR Spectroscopy. A guide to near-infrared spectroscopy analysis of industrial manufacturing process.

[208] J. Madejová and P. Komadel (2001). Baseline studies of the clay minerals society source clays: Infrared methods. *Clays Clay Miner.*, vol. 49, no. 5, pp. 410-432.

[209] I.R. Lewis and H. Edwards (2001). Handbook of Raman spectroscopy. *From the Research Laboratory to the Process Line*.

[210] C.C. Moura, R.S. Tare, R.O.C. Oreffo, and S. Mahajan (2016). Raman spectroscopy and coherent anti-Stokes Raman scattering imaging: Prospective tools for monitoring skeletal cells and skeletal regeneration. *J. R. Soc. Interface*, vol. 13, no. 118.

[211] L. Nasdala, D.C. Smith, R. Kaindl, and M.A. Ziemann (2004). Raman spectroscopy: Analytical perspectives in mineralogical research. *EMU Notes in Mineralogy 6-Spectroscopic methods in mineralogy*, vol. 6. p. 63.

[212] M. Kalvius and P. Kienle (2012). The Rudolf Mössbauer story. His scientific work and its impact on science and history, in *Springer*.

[213] L. May (1971). An introduction to Mössbauer spectroscopy, in *Springer*.

[214] H. Frauenfelder (1962). The Mössbauer effect.

[215] G. Vandegrift and B. Fultz (1998). The Mössbauer effect explained. *Am. J. Phys.*, vol. 66, pp. 593-596.

[216] A.J. Bearden, P.L. Mattern, and P.S. Nobel (1964). Mössbauer-Effect apparatus for an advanced undergraduate teaching laboratory. *Am. J. Phys.*, vol. 32, pp. 109-119.

[217] N.N. Greenwood and T.C. Gibb (1971). Mössbauer spectroscopy.

[218] Consejo Superior de Investigaciones Científicas (CSIC). 'Mössbauer spectrometers'. https://surfmoss.iqfr.csic.es/en/instruments/moessbauer-spectrometers.

[219] N. Buzgar and a I. Apopei (2009). The Raman study of certain carbonates. *Geol. Tomul LV*, vol. 2, pp. 97-112.

[220] S. Das and M.J. Hendry (2011). Application of Raman spectroscopy to identify iron minerals commonly found in mine wastes. *Chem. Geol.*, vol. 209, no. 3-4, pp. 101-108.

[221] T. Ohtsuka, K. Kubo, and N. Sato (1986). Raman spectroscopy of thin corrosion films on iron at 100 to 150ºC in air. *Corrosion*, vol. 42, no. 8, pp. 476-481.

[222] S. Oh, D.C. Cook, and H.E. Townsend (1998). Characterization of iron oxides commonly formed as corrosion products on steel. *Hyperfine Interact.*, vol. 112, no. 1-4, pp. 59-66.

[223] S. Yean et al. (2005). Effect of magnetite particle size on adsorption and desorption of arsenite and arsenate. *J. Mater. Res.*, vol. 20, no. 12, pp. 3255-3264.

[224] D.M. Cwiertny, R.M. Handler, M.V. Schaefer, V.H. Grassian, and M.M. Scherer (2008). Interpreting nanoscale size-effects in aggregated Fe-oxide suspensions: Reaction of Fe(II) with goethite. *Geochim. Cosmochim. Acta*, vol. 72, no. 5, pp. 1365-1380.

[225] R.J. Murphy, J.J. Lenhart, and B.D. Honeyman (1999). The sorption of thorium (IV) and uranium (VI) to hematite in the presence of natural organic matter. *Colloids Surfaces A Physicochem. Eng. Asp.*, vol. 157, no. 1-3, pp. 47-62.

[226] C. E. Harland (2007). Ion exchange: Theory and practice. 2nd Edition.

[227] O. Karnland, "Chemical and mineralogical characterization of the bentonite procedure in a KBS-3 repository.," *SKB Report. SKB-TR--10-60. Sweden*, vol. 43, no. 3, p. 25, 2010.

[228] D.J. Mulla, P.F. Low, and C.B. Roth (1985). Measurement of the specific surface area of clays by internal reflectance spectroscopy. *Clays Clay Miner.*, vol. 33, no. 5, pp. 391-396.

[229] D. Carroll and H.C. Starkey (1971). Reactivity of clay minerals with acids and alkalies. *Clays Clay Miner.*, vol. 19, pp. 321-333.

[230] A. Neumann, T.L. Olson, and M.M. Scherer (2013). Spectroscopic evidence for Fe(II)-Fe(III) electron transfer at clay mineral edge and basal sites. *Environ. Sci. Technol.*, vol. 47, pp. 6969–6977.

[231] A. Escribano, M.J. Turrero, E. Torres, and P.L. Martin (2008). Concrete/Febex bentonite interaction: Results on short-term column experiments. *Conference: IYNC 2008: International Youth Nuclear Congress 2008*, Interlaken (Switzerland). pp. 21-26.

[232] CIEMAT (2009). Report on thermo-hydro-mechanical laboratory tests performed by CIEMAT on Febex bentonite 2004-2008. Technical report CIEMAT--1178.

[233] S. Kaufhold, R. Dohrmann, and M. Klinkenberg (2010). Water-uptake capacity of bentonites. *Clays Clay Miner.*, vol. 57, no. 1, pp. 37-43.

[234] SKB (2001). The buffer and backfill handbook. Part 2: Materials and techniques. Svensk Kärnbränslehantering AB. Technical Report TR-02-12.

[235] E. Murad (2013). Chapter 2.1 Mössbauer spectroscopy of clays and clay minerals, in *Handbook of clay sciences. Part B: Techniques and Applications*, pp. 11-24.

[236] Y.V. Kolenko et al. (2014). High-temperature magnetism as a probe for structural and compositional uniformity in ligand-capped magnetite nanoparticles. J. Phys. Chem. C, vol. 118, no. 48, pp. 28322–28329.

[237] J.B. Forsyth, I.G. Hedley, and C.E. Johnson (1968). The magnetic structure and hyperfine field of goethite (α-FeOOH). *J. Phys. C Solid State Phys.*, vol. 1, no. 1, pp. 179-188.

[238] E. Murad and U. Schwertmann (1984). The influence of crystallinity on the Mössbauer spectrum of lepidocrocite. *Mineral. Mag.*, vol. 48, no. 349, pp. 507-511.

[239] E. Murad and J.H. Johnston (1987). Iron oxides and oxyhydroxides, in *Mössbauer spectroscopy applied to inorganic chemistry, vol. 2.*, pp. 507-582.

[240] Posiva (2004). Bentonite mineralogy. Part 1: Methods of investigation: A literature review. Part 2: Mineralogical research of selected bentonites.Technical Report 2004-02.

[241] D.M. Moore and J. Hower (1986). Ordered interstratification of dehydrated and dehydrated Na-smectite. *Clays Clay Miner.*, vol. 34, no. 4, pp. 379-384.

[242] ENRESA (2006). FEBEX Project final report. Post-mortem bentonite analysis. Technical Report ENRESA 05-1/2006.

[243] B.A. Sakharov and B. Lanson (2013). Chapter 2.3. X-ray identification of mixed-layer structures. Modelling of diffractions effects, in *Handbook of clay sciences. Part B: Techniques and Applications*, pp. 51–129.

[244] J. Srodon (1980). Precise identification of illite/smectite interstratifications by x-ray powder diffraction. *Clays Clay Miner.*, vol. 28, no. 6, pp. 401-411.

[245] https://www.crystalimpact.com/match/

[246] D. Savage, D. Noy, and M. Mihara (2002). Modelling the interaction of bentonite with hyperalkaline fluids. *Appl. Geochemistry*, vol. 17, no. 3, pp. 207-223.

[247] D. Savage, C. Walker, R. Arthur, C. Rochelle, C. Oda, and H. Takase (2007). Alteration of bentonite by hyperalkaline fluids: A review of the role of secondary minerals. *Phys. Chem. Earth*, vol. 32, no. 1-7, pp. 287-297.

[248] S. Petit and J. Madejová (2013). Chapter 2.7. Fourier transform infrared spectroscopy, in *Handbook of clay sciences. Part B: Techniques and Applications*, pp. 213-225.

[249] V.C. Farmer and J. D. Russell (1964). The infra-red spectra of layer silicates. *Spectrochim. Acta*, vol. 20, no. 7, pp. 1149-1173.

[250] M. Milosevic (2004). Internal reflection and ATR spectroscopy.

[251] J. Madejová (2003). FTIR techniques in clay mineral studies. *Vib. Spectrosc.*, vol. 31, no. 1, pp. 1-10.

[252] B.H. Stuart (2005). Infrared spectroscopy: Fundamentals and applications.

[253] I. Stríček, V. Šucha, P. Uhlík, J. Madejová, and I. Galko (2009). Mineral stability of Fe-rich bentonite in the Mock-Up-CZ experiment. *Geol. Carphatica*, vol. 60, no. 5, pp. 431-436.

[254] A. Fernández and M. V. Villar (2010). Geochemical behaviour of a bentonite barrier in the laboratory after up to 8 years of heating and hydration. *Appl. Geochemistry*, vol. 25, no. 6, pp. 809-824.

[255] R. Fernández et al. (2017). Interaction processes at the concrete-bentonite interface after 13 years of FEBEX-Plug operation. Part II: Bentonite contact. *Phys. Chem. Earth*, vol. 99, pp. 49-63.

[256] A.M. Fernández et al. (2018). Evolution of the THC conditions in the FEBEX in-situ test after 18 years of experiment: Smectite crystallochemical modifications after interactions of the bentonite with a C-steel heater at 100 °C. *Appl. Geochemistry*, vol. 98, pp. 152-171.

[257] F.J. Calderón, M.M. Mikha, M.F. Vigil, D.C. Nielsen, J.G. Benjamin, and J.B. Reeves (2011). Diffuse-reflectance mid-infrared spectral properties of soils under alternative crop rotations in a semi-arid climate. *Commun. Soil Sci. Plant Anal.*, vol. 42, pp. 2143-2159.

[258] L.J. Janik, J.O. Skjemstad, K.D. Shepherd, and L.R. Spouncer (2007). The prediction of soil carbon fractions using mid-infrared-partial least square analysis. *Aust. J. Soil Res.*,

vol. 45, no. 2, pp. 73-81.

[259] G. Sposito and R. Prost (1982). Structure of water absorbed on smectites. *Chem. Rev.*, vol. 82, no. 6, pp. 553-573.

[260] J. Madejová, J. Kečkéš, H. Pálková, and P. Komadel (2016). Identification of components in smectite/kaolinite mixtures. *Clay Miner.*, vol. 37, no. 2, pp. 377-388.

[261] C.E. Clarke, J. Aguilar-Carrillo, and A.N. Roychoudhury (2011). Quantification of drying induced acidity at the mineral-water interface using ATR-FTIR spectroscopy. *Geochim. Cosmochim. Acta*, vol. 75, no. 17, pp. 4846-48-56.

[262] K.M. Dontsova, L.D. Norton, C.T. Johnston, and J.M. Bigham (2010). Influence of exchangeable cations on water adsorption by soil clays. *Soil Sci. Soc. Am. J.*, vol. 68, no. 4, pp. 1218-1227.

[263] S. Żymankowska-Kumon, M. Holtzer, and G. Grabowski (2011). Thermal analysis of foundry bentonites. *Arch. Foundry.*, vol. 11, no. 4, pp. 209-213.

[264] J.V. O'Gorman and P.L. Walker (1973). Thermal behaviour of mineral fractions separated from selected American coals. *Fuel*, vol. 52, no. 1, pp. 71-79.

[265] S.V. Vassilev, C. Braekman-Danheux, and P. Laurent (1999). Characterization of refuse-derived char from municipal solid waste: 1. Phase-mineral and chemical composition. *Fuel Process. Technol.*, vol. 59, no. 2-3, pp. 95-134.

[266] C.B. Hedley, G. Yuan, and B.K.G. Theng (2007).Thermal analysis of montmorillonites modified with quaternary phosphonium and ammonium surfactants. *Appl. Clay Sci.*, vol. 35, no. 3-4, pp. 180-188.

[267] B. Makhoukhi, D. Villemin, and M.A. Didi (2013). Preparation, characterization and thermal stability of bentonite modified with bis-imidazolium salts. *Mater. Chem. Phys.*, vol. 138, no. 1, pp. 199-203.

[268] F. Wolters and K. Emmerich (2007). Thermal reactions of smectites-relation of dehydroxylation temperature to octahedral structure. *Thermochim. Acta*, vol. 462, no. 1-2, pp. 808-888.

[269] https://fdocuments.us/document/mettler-toledo-tgadsc-1-star-e-system.html.

[270] R.C. Mackenzie and B.M. Bishui (1958). The montmorillonite differential thermal curve. II. Effect of exchangeable cations on the dehydroxylation of normal

montmorillonite. *Clay Miner.*, vol. 3, no. 20, pp. 276-286.

[271] R.C. Mackenzie (1957). The differential thermal investigation of clays. *Mineralogical society (clay minerals group), London.*

[272] L. Heller, V. Farmer, R.C. Mackenzie, and B.D. Mitchell (1962). The dehydroxylation and rehydroxylation of triphormic dioctahedral clay minerals. *Clay Miner.*, vol. 5, no. 28, pp. 56-72.

[273] L. Heller and Z.H. Kalman (1961). An approximate determination of the position of some cations in dehydroxylated montmorillonite. Clay Miner., vol. 4, no. 25, pp. 213 220.

[274] R. Greene-Kelly (1957). The montmorillonite minerals, in *The Differential Thermal Investigation of Clays, Mineralogical Society, London*.

[275] R. Gauglitz and H.E. Schwiete (1961). Thermochemical investigations on montmorillonite with regards to type, grain size, and cation loading. *Berichte Dtsch. Keramik Ges*, vol. 38, p. 43.

[276] R.E. Grim and W.F. Bardley (1940). Investigation of the effect of heat on the clay minerals illite and montmorillonite. *Am. Ceram. Soc.*, vol. 23, no. 8, pp. 242-248.

[277] W.F. Cole (1955). Interpretation of differential curves of mixed-layer minerals of illite and montmorillonite. *Nature*, vol. 175, pp. 384-385.

[278] M.V. Fey and J.B. Dixon (1981). Synthesis and properties of poorly crystalline hydrated aluminous goethites. *Clays Clay Miner.*, vol. 29, no. 2, pp. 91-100.

[279] D.G. Schulze and U. Schwertmann (1984). The influence of aluminum on iron oxides: X. Properties of aluminum-substituted goethites. *Clay Miner.*, vol. 19, no. 4, pp. 521-539.

[280] Y.H. Chen (2013). Thermal properties of nanocrystalline goethite, magnetite, and maghemite. *J. Alloys Compd.*, vol. 553, pp. 194-198.

[281] R.J. Tullock and C.B. Roth (1975). Stability of mixed iron and aluminum hydrous oxides on montmorillonite. *Clays Clay Miner.*, vol. 22, pp. 27-32.

[282] C. Padovani (2014). Overview of UK research on the durability of container materials for radioactive wastes. *Corros. Eng. Sci. Technol.*, vol. 49, no. 6, pp. 402-409.

[283] A.J. Davenport et al. (2014). Mechanistic studies of atmospheric pitting corrosion of

stainless steel for ILW containers. Corros. Eng. Sci. Technol., vol. 49, no. 6, pp. 514-520.

[284] M. Marty et al. (2010). Dual alteration of bentonite by iron corrosion and concrete interaction under high temperature conditions, in *Clays in natural & engineered barriers for radiactive waste confinement*, vol. 46, no. 50, pp. 473-474.

[285] F.A. Martin, C. Bataillon, and M.L. Schlegel (2008). Corrosion of iron and low alloyed steel within a water saturated brick of clay under anaerobic deep geological disposal conditions: An integrated experiment. *J. Nucl. Mater.*, vol. 379, no. 1-3, pp 80-90.

[286] L. Xiaodong, R. Prikryl, and R. Pusch (2011). THMC-testing of three expandable clays of potential use in HLW repositories. *Appl. Clay Sci.*, vol. 52, no. 4, pp. 419-427.

[287] N.N. Zinchuk, D.D. Gorshkov, and A.I. Kotelnikov (2003). Identification and genesis of the mixed-layer lizardite-saponite phase in a Kimberlite Pipe, South Africa. *Lithol. Miner. Resour.*, vol. 38, no. 1, pp. 74-81.

[288] Z. Dali-Youcef and M. Queneudec (2011). Removal of phenol from aqueous solution by activated mud. *J. Encapsulation Adsorpt. Sci.*, vol. 1, pp. 35-42.

[289] S. Kaufhold, R. Dohrmann, T. Sandén, P. Sellin, and D. Svensson (2013). Mineralogical investigations of the first package of the alternative buffer material test – I. Alteration of bentonites. *Clay Miner.*, vol. 48, pp. 199-213..

[290] J. Madejová, M. Janek, P. Komadel, H.J. Herbert, and H. C. Moog (2002). FTIR analyses of water in MX-80 bentonite compacted from high salinary salt solution systems. *Appl. Clay Sci.*, vol. 20, no. 6, pp. 255-271.

[291] Posiva (2010). Mineralogical and chemical characterization of various bentonite and smectite-rich clay materials. Part B: Mineralogical and chemical characterization of clay materials. Working Report 2010-52.

[292] S. Kaufhold, R. Dohrmann, N. Götze, and D. Svensson (2017). Characterization of the second parcel of the alternative buffer material (ABM) experiment – I. Mineralogical reactions. *Clays Clay Miner.*, vol. 65, no. 1, pp. 27-41.

[293] V.A. Drits, G. Besson, and F. Muller (1995). An improved model for structural transformations of heat-treated aluminous dioctahedral 2:1 layer silicates. *Clays Clay Miner.*, vol. 43, pp. 718-731.

[294] K. Emmerich, F.T. Madsen, and G. Kahr (1999). Dehydroxylation behavior of heat-treated and steam-treated homoionic cis-vacant montmorillonites. *Clays Clay Miner.*, vol. 47, no. 5, pp. 591-604.

[295] IAEA (2013). Characterization of swelling clays as components of the engineered barrier system for geological repositories. Results of an IAEA Coordinated Research 2002–2007. IAEA-TECDOC-1718 Project.

[296] E. Murad (2004). Magnetic properties of microcrystalline iron (III) oxides and related materials as reflected in their Mössbauer spectra. *Phys. Chem. Miner.*, vol. 23, pp. 248-262.

[297] RWM (2009). Role of bentonite in determination of thermal limits of geological disposal facility design. Technical Report 0883-1 Version 2.

[298] SNL (2007). Total system performance assessment data input package for requirements analysis for DOE SNF/HLW and naval SNF waste package physical attributes basis for performance assessment. Technical Reprot TDR-TDIP-ES-000009 REV 00.

[299] SKB (2011). Thermal dimensioning of the deep repository. Influence of canister spacing, canister power, rock thermal properties and nearfield design on the maximum canister surface temperature. Svensk Kärnbränslehantering AB. Technical report TR-03-09.

[300] JNC (2000). H12: Project to Establish the Scientific and Technical Basis for HLW Disposal in Japan. Second Progress Report on Research and Development for the Geological Disposal of HLW in Japan. Supporting Report 2: Repository Design and JNC TN1410 2000-003.

[301] H.J. Choi and J. Choi (2008). Double-layered buffer to enhance the thermal performance in a high-level radioactive waste disposal system. Nucl. Eng. Des., vol. 238, no. 10, pp. 2815 2820.

[302] T. Rothfuchs (1986). Untersuchung der Thermisch Induzierten Wasserfreisetzung aus Polyhalitischem Steinsalz unter in situ Bedingungen. Temperaturversuch 5 im Salzbertgwerk Asse. European Commission Report EUR10392 DE. In German with English Abstract.

[303] SKB (2008). Safety assessment for a KBS-3H spent nuclear fuel repository at Olkiluoto. Evolution report. Svensk Kärnbränslehantering AB. Technical Report R-08-37.

[304] AECL (1994). Disposal of Canada's nuclear fuel waste: The vault model for postclosure assessment. Technical Report AECL-10714.

[305] ONDRAF/NIRAS (2008). Evolution of the Near-Field of the ONDRAF/NIRAS Repository Concept for Category C Wastes. Technical Report NIROND-TR 2007-07E.

[306] M. García-Gutiérrez, J.L. Cormenzana, T. Missana, M. Mingarro, and J. Molinero (2005). Overview of laboratory methods employed for obtaining diffusion coefficients in FEBEX compacted bentonite. *J. Iber. Geol.*, vol. 32, no. 1, pp. 37-53.

[307] P. Delage, Y.J. Cui, and A.M. Tang (2010). Clays in radioactive waste disposal. *J. Rock Mech. Geotech. Eng.*, vol. 2, no. 2, pp. 111-123.

[308] SKB (2014). KBS-3H reactive transport modelling of iron-bentonite interactions, an update for the Olkiuoto case. Svensk Kärnbränslehantering AB. Technical Report 2013-02.

[309] Y. Tamaura, T. Yoshida, and T. Katsura (1984). The synthesis of green rust II(FeIII1–FeII2) and its spontaneous transformation into Fe_3O_4. *Chem. Soc. Japan*, vol. 57, pp. 2411-2416.

[310] NAGRA (2003). Redox Conditions in the Near Field of a Repository for SF/HLW and ILW in Opalinus Clay. Technical Report 02-13.

Appendix A

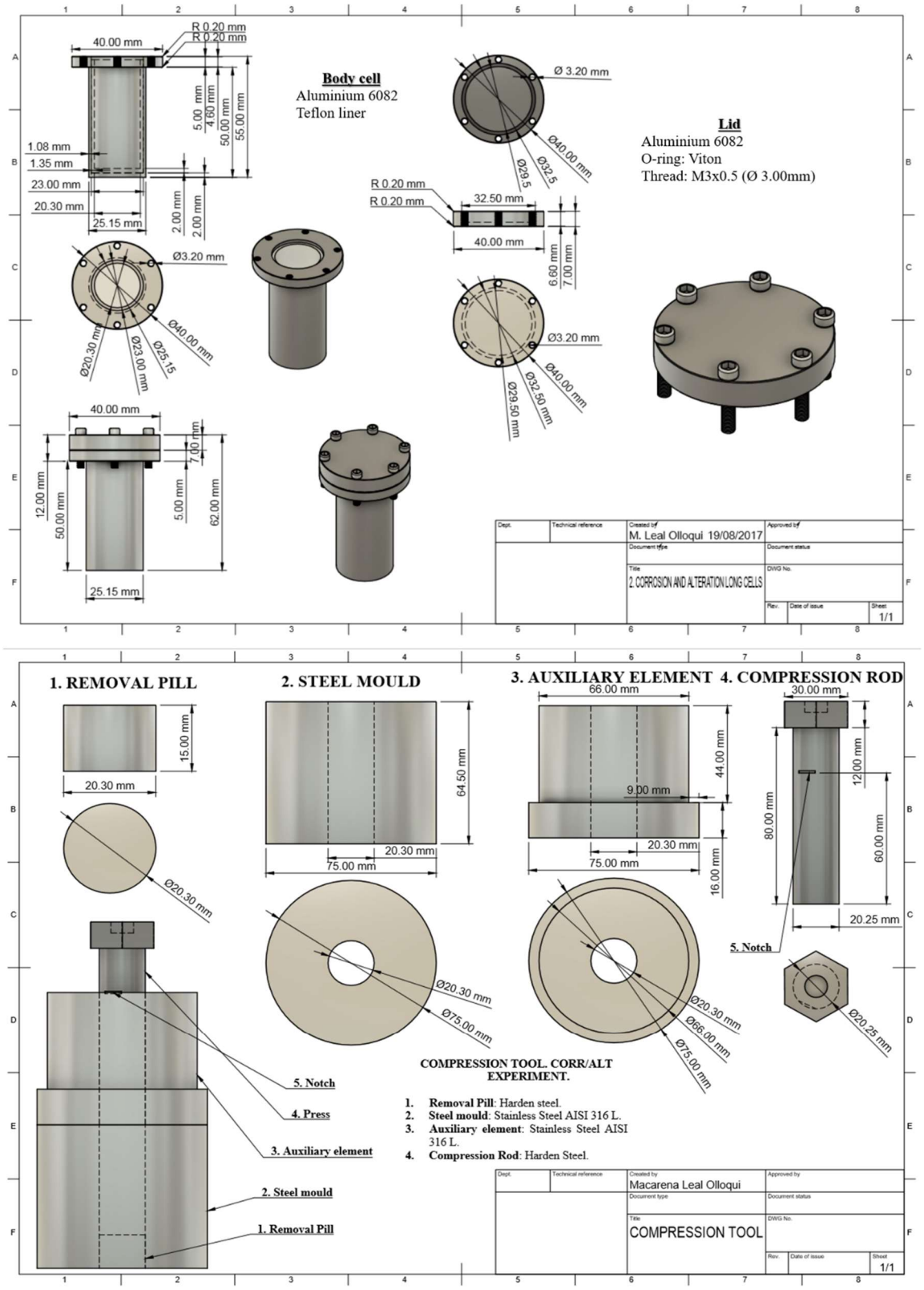

Plane A.1: *Corrosion-alteration cells design (upper plane). Compression tool design (lower plane).*